ESTEC contract 21022/07/NL/HE

Air density models derived from multi-satellite drag observations

Final report

Eelco Doornbos[1], Matthias Förster[2], Bent Fritsche[3],
Tom van Helleputte[1], Jose van den IJssel[1],
Georg Koppenwallner[3], Hermann Lühr[2,]
David Rees[4], Pieter Visser[1]

[1]DEOS / TU Delft	Delft Institute of Earth Observation and Space Systems Delft University of Technology Kluyverweg 1 2629 HS Delft, The Netherlands
[2]GFZ-Potsdam	Helmholtz Centre Potsdam GeoForschungsZentrum - German Centre for Geosciences Potsdam, Germany
[3]HTG	Hypersonic Technology Göttingen Katlenburg-Lindau, Germany
[4]Hovemere	Hovemere Ltd. Sevenoaks, United Kingdom

ESA study manager: Michael Kern

May 2009

European Space Agency
Contract Report

The work described in this report was done under ESA contract. Responsibility for the contents resides in the authors or organisation that prepared it.

TU Delft Delft University of Technology

Air density models derived from multi-satellite drag observations

Eelco Doornbos, Matthias Förster, Bent Fritsche, Tom van Helleputte, Jose van den IJssel, Georg Koppenwallner, Hermann Lühr, David Rees and Pieter Visser

DEOS/TU Delft scientific report 01/2009

ESA Study Contract Report

ESA Contract	Title	Contractor
21022/07/NL/HE	Air density models derived from multi-satellite drag observations	Delft Institute of Earth Observation and Space Systems (DEOS/TU Delft)

Abstract

Satellite accelerometers, such as those carried on the CHAMP and GRACE satellites, can provide valuable data for improving our knowledge of thermosphere density and winds. These data are now available over a wide range of the defining conditions, including more than half a solar cycle. Continuity and enhancement of this multi-satellite accelerometer data set will be provided by ESA's Swarm mission. This investigation covers the processing steps required for accurately converting accelerometer data into density and wind data, and the subsequent use of this data for improving the understanding of the thermosphere.

The investigation of the data processing is based on data from the CHAMP and GRACE accelerometers, star cameras and GPS receivers and equivalent simulated data that has been created for Swarm. The investigation encompasses the calibration of the accelerometer instrument, accurate aerodynamic and radiation pressure force modelling and the enhancement of processing algorithms. This has resulted in improved accuracy of the data and increased insight in the possible sources of error.

The largest remaining error sources in the density derivation are the gas-surface interaction modelling, modelling of the satellite geometry, the calibration scale factor for the in-track accelerometer component, and the knowledge of the atmospheric in-track wind speed, composition and temperature. These sources lead to density errors which are largely systematic in nature and are estimated at about 15% of the density signal for CHAMP, GRACE and Swarm.

The crosswind determination accuracy is very much dependent on the strength of the aerodynamic drag signal, compared to solar radiation pressure modelling errors and accelerometer cross-track calibration errors. Therefore, reliable results can only be obtained for a combination of a sufficiently low altitude, high enough solar activity and a favourable orbit geometry in terms of radiation pressure accelerations. For CHAMP, a multi-year time series of crosswind speeds has been obtained that is within the statistical uncertainty of current empirical thermosphere wind models. However, for the higher altitude GRACE satellites, radiation pressure modelling errors dominate.

The CHAMP- and GRACE-derived density and wind data has subsequently been used in extensive evaluations using empirical and physical models of the thermosphere, and geophysical studies of large scale structures and patterns in the data. Experiments with an accelerometer-calibrated empirical density model indicate that improvements in the standard deviation of data/model ratios of at least 30% are possible. The work concludes with recommendations for Swarm and other possible future thermosphere missions.

The work described in this report was done under ESA contract.
Responsibility for the contents resides in the author or organisation that prepared it.

Names of authors
Eelco Doornbos (DEOS/TU Delft), Matthias Förster (GFZ-Potsdam), Bent Fritsche (HTG), Tom van Helleputte (DEOS/TU Delft), Jose van den IJssel (DEOS/TU Delft), Georg Koppenwallner (HTG), Hermann Lühr (GFZ-Potsdam), David Rees (Hovemere), Pieter Visser (DEOS/TU Delft)

ESA study manager	ESA budget heading
Michael Kern **Division** Mission Science Division **Directorate** Directorate of Earth Observation Programmes	

Contents

Chapter 1
Introduction

Neutral density in the thermosphere is one of the most important variables to model for applications in satellite orbit determination and solar-terrestrial physics. The state of the neutral thermosphere can be expressed in terms of the densities of its constituents, its temperature and wind speeds. These parameters vary over a wide range of spatial and temporal scales. This complexity, combined with an undersupply of available observation data, has made the improvement of models quite a challenge.

Accelerometers carried by satellites provide valuable data for improving our understanding of the thermosphere density and winds, especially when these data are available over a wide range of the most important influencing parameters: Altitude, latitude, local solar time and solar and geomagnetic activity. The CHAMP and GRACE missions provide such data. These missions carry accelerometers in order to allow the removal of non-gravitational signals from ac-

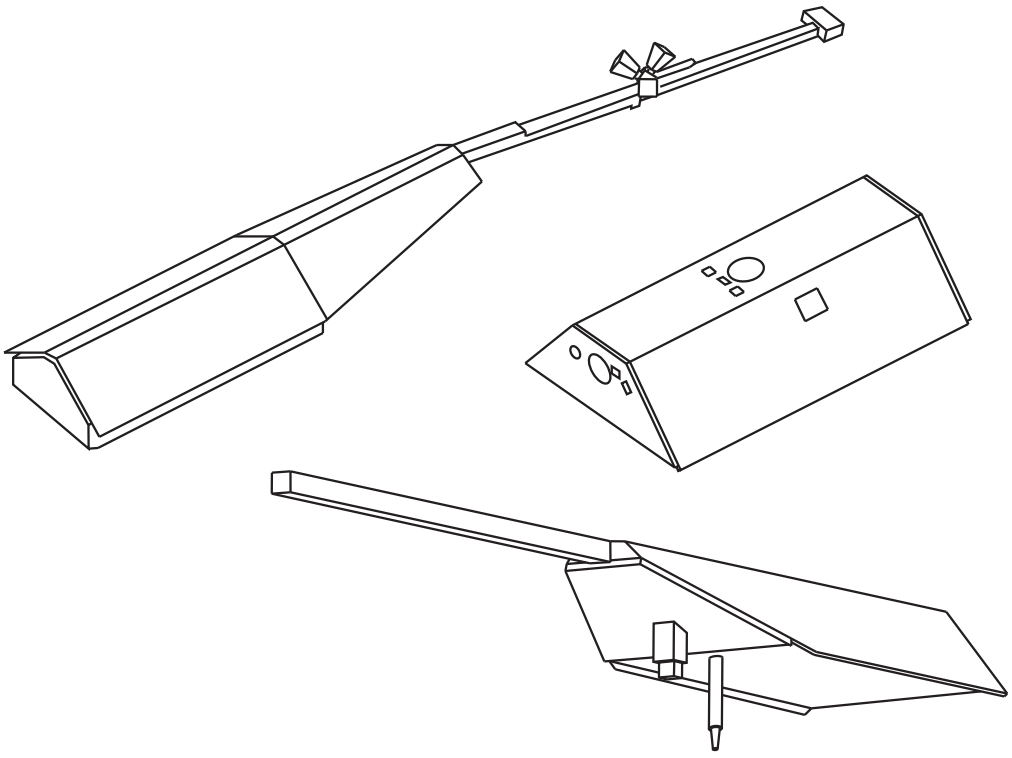

Figure 1.1 From top to bottom: The Swarm, GRACE and CHAMP satellites (not at the same scale).

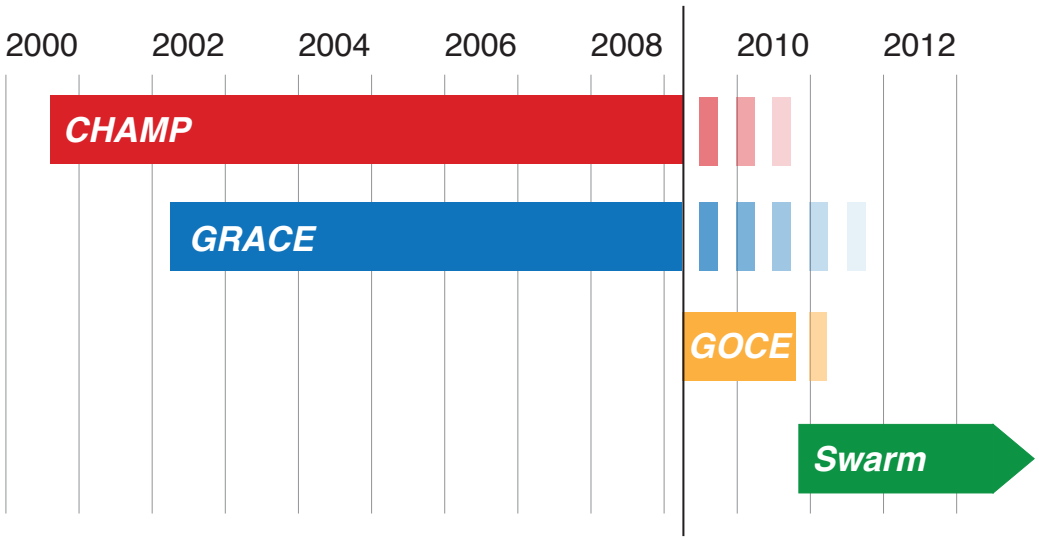

Figure 1.2 Timeline for current and future low Earth orbiting satellite missions carrying precision accelerometers.

celerations due to the Earth's gravity field. Even though studying thermospheric density is not part of their primary mission objectives, it is a very important spin-off application, which is generating important science. Since the satellites also carry accurate GPS receivers and star cameras, accelerometer calibration errors and attitude errors in the satellite aerodynamic model can be largely reduced.

The fact that the CHAMP and GRACE missions are largely overlapping in time (see Figure 1.2) offers the opportunity to study the synergy of their data. The twin GRACE satellites and the single CHAMP satellite form a constellation of which the geometrical configuration constantly changes over time. When the orbital planes are perpendicular, the instantaneous local solar time coverage will be doubled compared to having just one mission. At times when the orbits are coplanar it will be most interesting to study relatively short spatial scale features. Since both missions are in polar orbits, they offer unprecedented opportunities to study the complex dynamics of the thermosphere at high latitudes.

The trajectories of both missions are spiralling downwards due to the effect of drag, so they will sample density and wind speeds at a wide range of altitudes. This also implies that the satellites will likely perish in re-entry during the next solar cycle peak, CHAMP somewhat earlier than GRACE. That raises the question of continuity of their valuable data. This continuity could be provided by ESA's Swarm mission, a constellation of three satellites for studying the Earth's magnetic field. The Swarm constellation offers unique possibilities, not only for observing and separating different sources that contribute to the Earth's magnetic field, but also for improving the observation of atmospheric density and wind variations and their relation with geomagnetic activity. Also shown in Figure 1.2 is the very recently launched GOCE mission, which will fly under drag-free control [*Canuto et al.*, 2002] at a very low altitude. This drag-free control mode, required for its primary mission in gravity recovery, is a complicating factor for density determination, which leaves this mission outside the scope of this study. Nevertheless GOCE's data could be very valuable as well for thermospheric studies, and this certainly deserves further investigation.

The beneficial features of these combined accelerometer datasets have not yet

been fully exploited in the study of thermospheric density and air dynamics and in density modelling at satellite altitudes.

1.1 Study goals

The purpose of this study is to investigate the optimal derivation, calibration and use of density and wind data derived from the combination of instruments on CHAMP, GRACE, Swarm and other (future) accelerometer missions.

During the study, the CHAMP and GRACE accelerometer datasets have been processed using state-of-the-art models and techniques. Special attention has been given to aerodynamic modelling of the satellites, accelerometer calibration, the combination of data from both missions and the separation of density and winds from the accelerations.

The resulting densities and wind fields have been visualized and analyzed in several ways, including the use of the density observations as input in density model calibration software.

Using the knowledge gained during this work on CHAMP and GRACE, simulations have been performed on the capabilities for thermosphere studies of the future Swarm constellation of three satellites, in order to provide further insight on how Swarm and possible other future missions can contribute to this field of research.

1.2 Study approach and overview

A number of distinct steps can be identified in the processing of accelerometer data for the retrieval of thermospheric densities and wind speeds. These are listed below:

1. Retrieval of input data (accelerometer data, attitude quaternions from star trackers, GPS tracking data, orbits, housekeeping data, such as a list of thruster events, mass changes, etc.);
2. Conversion of input data to formats suitable for further processing;
3. Calibration of the accelerometer data using GPS tracking data;
4. Removal of accelerations affected by thrusters;
5. Computation of radiation pressure forces;
6. Removal of radiation pressure forces from the accelerometer data, leaving the aerodynamic accelerations;
7. Retrieving density and wind speeds from the accelerations, making use of an aerodynamic model;
8. Data validation, for instance by comparisons with models
9. Geophysical interpretation of the results.

The work for this study was broken down into 5 tasks and 23 work packages, as listed in Table 1.1. These work packages cover all of the above mentioned steps. For this final report, the results of several of the work packages have been combined into single chapters, which more closely match these processing steps.

Chapter 2 will start with an overview of thermospheric modelling, and implementation details on the density and wind models used for this study. Chapter 3

WP	Title	Partner
WP1000	**Project management**	
WP1100	Study organization	DEOS
WP1200	Project control	DEOS
WP2000	**Data and modelling state of the art (Task 1)**	
WP2100	Description and selection of present thermospheric models	Hovemere
WP2200	Description and selection of CHAMP/GRACE instruments and...	GFZ
WP2300	State of the art aerodynamic and radiation pressure modelling...	HTG
WP2400	Algorithms for accelerometer calibration	DEOS
WP2500	Algorithms for density and wind retrieval from accelerometer data	GFZ+Hovemere
WP3000	**CHAMP/GRACE single satellite processing and analysis (Task 2)**	
WP3100	Accelerometer and quaternion data preprocessing	DEOS
WP3200	Accelerometer calibration - single satellite approach	DEOS
WP3300	Satellite aerodynamic and radiation pressure calculations	HTG
WP3400	Density and wind determination - single satellite approach	DEOS
WP3500	Density and wind model comparison - single satellite approach	Hovemere
WP3600	Density and wind geophysical interpretation - single satellite...	GFZ
WP4000	**CHAMP/GRACE combined processing and analysis (Task 3)**	
WP4100	Accelerometer calibration - constellation approach	DEOS
WP4200	Density and wind determination - constellation approach	DEOS
WP4300	Density and wind model comparison - constellation approach	Hovemere
WP4400	Density and wind geophysical interpretation - constellation approach	GFZ
WP4500	Density model calibration using multi-satellite accelerometer...	DEOS
WP5000	**Simulations for Swarm and other future constellations (Task 4)**	
WP5100	Specification of simulated reference atmosphere	Hovemere
WP5200	Producing simulated accelerometer and tracking measurements	DEOS
WP5300	Accelerometer calibration - simulated constellations	DEOS
WP5400	Density and wind determination - simulated constellations	DEOS
WP6000	**Conclusions and recommendations (Task 5)**	
WP6100	Synthesis of results and recommendations for future work	All

Table 1.1 List of work packages

will give a description of the CHAMP and GRACE missions and the data sets that were used for this study. Chapter 4 describes the way the infrastructure for the data processing is set up, and discusses the preprocessing steps and their resulting data products.

The next section of the report focuses on the non-gravitational force modelling: Chapter 5 describes how the radiation pressure model calculations were made. The closely related, but more complicated topic of aerodynamic modelling of satellites is described in Chapter 6.

In the following section, the focus is returned to the data processing. Chapter 7 presents the approach for the calibration of the accelerometer measurements. The core of this report is Chapter 8, in which the processing of all the input data sets into density and crosswind information is described in detail.

The second half of the report is concerned with the use of this data, and the lessons that can be learned from the data itself, and the processing steps that were required to create it.

In Chapter 9, the density and wind data sets from CHAMP and GRACE are compared with various thermosphere models. Chapter 10 goes one step further, in an attempt to calibrate empirical density models using the accelerometer-derived data. The results are evaluated by examining residuals and using independent data. Several methods to investigate the geophysical content of the data are presented in Chapter 11, including a study of the variations with latitude, local solar time, level of solar activity, etc.

In the final chapters of this report, the focus is turned towards the future. Chapter 12 presents a study using simulated data for the 3-satellite Swarm mission. Chapter 13 gives an overview of other current and planned missions used for studying the thermosphere, and looks even further ahead, in order to give recommendations for missions after those that are currently already planned or under construction.

Finally, the conclusions and recommendations from the study are brought together in the final Chapter 14

Chapter 2
Modelling the thermosphere

This Chapter will describe the history, use and limitations of empirical thermosphere models.

2.1 Atmospheric structure and variability

The Earth's atmosphere is often portrayed as a fragile, finite and thin layer of gases surrounding our planet. However, since the number of atmospheric particles decreases exponentially with altitude, there is no definite boundary between the atmosphere and outer space. Even though the density at satellite altitudes is at least a billion times lower than at sea level, the velocities of orbiting objects are so high that there is still a drag force that can be measured. This force can currently be derived from operational space surveillance satellite tracking orbit data for altitudes up to around 500 km and by using more specialized methods or equipment up to about 1500 km. Tracking measurements on the very first artificial satellites [*Jacchia*, 1959; *King-Hele*, 1992] resulted in the identification of several important variations in density, which will be briefly introduced here. Figure 2.1 illustrates the magnitude of density variations at a single geographical

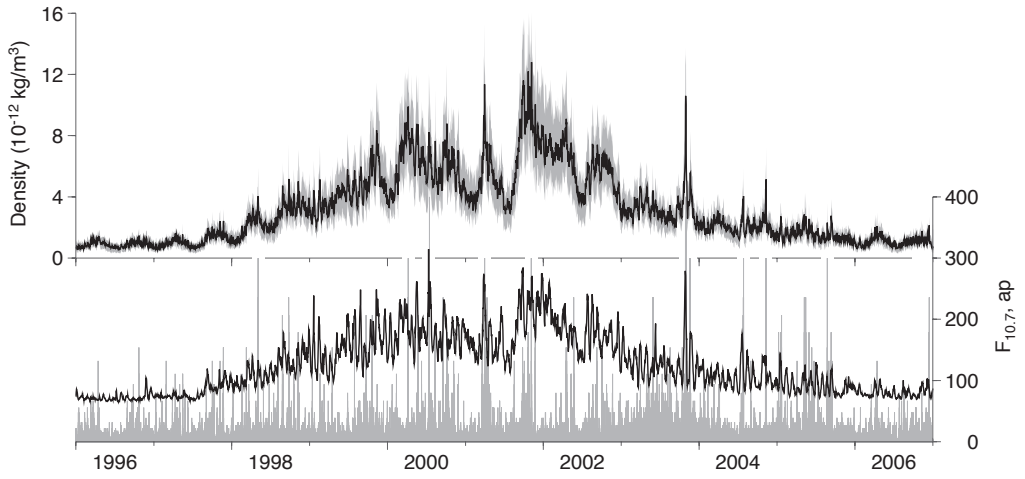

Figure 2.1 *Top*: Time series over the last solar cycle of daily averaged densities (black line), and daily minimum and maximum values (grey area), at 400 km altitude over a mid-latitude location, from the NRLMSISE-00 model [*Picone et al.*, 2002]. *Bottom*: The $F_{10.7}$ solar activity proxy (black line) and ap geomagnetic activity index (grey spikes) drive the irregular density variations in empirical models such as NRLMSISE-00.

location (400 km above Delft, the Netherlands) over the course of an 11-year solar cycle. The various processes affecting density will be introduced in more detail below.

2.1.1 Vertical structure of the atmosphere

On approximation, the pressure p, density ρ and temperature T of the Earth's atmosphere obey the ideal gas law,

$$\frac{p}{\rho} = \frac{RT}{M}, \tag{2.1}$$

where R is the gas constant (8.31 J K^{-1} mol^{-1}) and M is the molecular weight of the gas. The vertical structure of the Earth's atmosphere is largely governed by hydrostatic equilibrium, a balance between gravity and pressure. The hydrostatic equation relates the decrease of pressure p with height y to the density ρ and gravitational acceleration g:

$$\frac{dp}{dy} = -\rho(y)g(y) \tag{2.2}$$

Combining these two equations, atmospheric pressure can be expressed as a function of altitude:

$$p(z) = p(0)e^{-\int_0^z \frac{1}{H(r)}dr} \tag{2.3}$$

where H is the pressure scale height:

$$H(z) = \frac{RT(z)}{g(z)M(z)} \tag{2.4}$$

The variation of density with height can be derived similarly, resulting in:

$$\rho(z) = \rho(0)e^{-\int_0^z \frac{1}{H^*(r)}dr}, \tag{2.5}$$

with the density scale height H^* defined as

$$\frac{1}{H^*(z)} = \frac{1}{T(z)}\frac{dT(z)}{dz} + \frac{g(z)M(z)}{RT(z)} \tag{2.6}$$

For regions where temperature is constant, such as the upper thermosphere, the density scale height is equal to the pressure scale height. These scale heights, which depend on the temperature, represent the vertical distances over which the pressure or density decreases by a factor e. At sea level, the scale height is about 8.5 km, while in the thermosphere it is of the order of 50 kilometers.

Figure 2.2 shows the temperature and density profiles, according to the NRLMSISE-00 model, for day and night conditions at very low and very high solar activity conditions. Below 100 km, a variety of heat sources and energy transport processes result in distinct temperature minima and maxima, which delineate the named layers of the atmosphere. With ascending altitude these are the *troposphere*, the *stratosphere* and the *mesosphere*. Our interest is in the top layer, the *thermosphere*, which is governed by the absorption of solar extreme-ultraviolet radiation, causing an asymptotically increasing temperature with altitude.

The Sun's radiation causes part of the gas particles in the thermosphere to become ionized, creating the Earth's *ionosphere*. Ionized particles and electrons

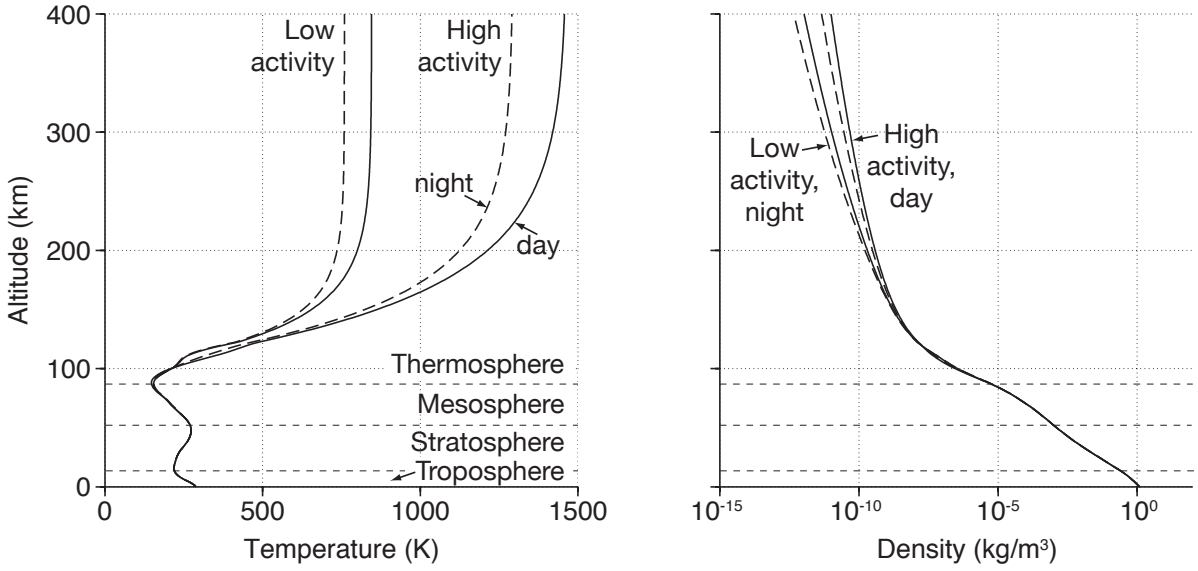

Figure 2.2 Altitude profiles of atmospheric temperature (*left*) and density (*right*), according to the NRLMSISE-00 model.

tend to be greatly outnumbered by neutral particles, at least at altitudes below 800 km. Above that altitude, data on the composition of the thermosphere is very scarce. The presence of oxygen ions as a significant contributor to satellite drag is taken into account in the NRLMSISE-00 model [*Picone et al.*, 2002], but not in other models. In any case, the fact that charged particles are present in the upper atmosphere has a profound effect on the medium's electrical properties, which affect its heating and dynamics.

The *mean free path length* of the atmospheric gas is another important parameter. Below the thermosphere, the mean free path length is short, and there are many collisions between the gas molecules. This causes the constituents of the gas to remain well-mixed. This region is called the *turbosphere* or *homosphere*. In the *heterosphere*, collisions are much less frequent. The gases can separate through gaseous diffusion more rapidly than they are mixed by turbulence. According to equation (2.6), the density scale height of light-weight constituents is larger than for heavier constituents. Therefore, with increasing altitude, the major thermospheric species are molecular nitrogen (N_2), atomic oxygen (O), helium (He) and hydrogen (H), as can be seen in Figure 2.3.

The *exosphere* is the region, above approximately 400–600 km (depending on the level of solar activity), from which particles may escape from the atmosphere. This occurs when the kinetic energy of the particle exceeds the gravitational binding energy, and if the mean free path length is long enough to prevent collisions with other particles.

2.1.2 Energy sources

The temperature profile of the atmosphere, discussed in the previous section, results from the balance between heat sources, loss processes and transport mechanisms. In the thermosphere, the most important sources of heat are solar EUV radiation, related to solar activity, and energetic charged particles, related to geomagnetic activity. Dissipation of tidal motions and gravity waves are minor heat sources, which are neglected in current empirical models. Heat is transported

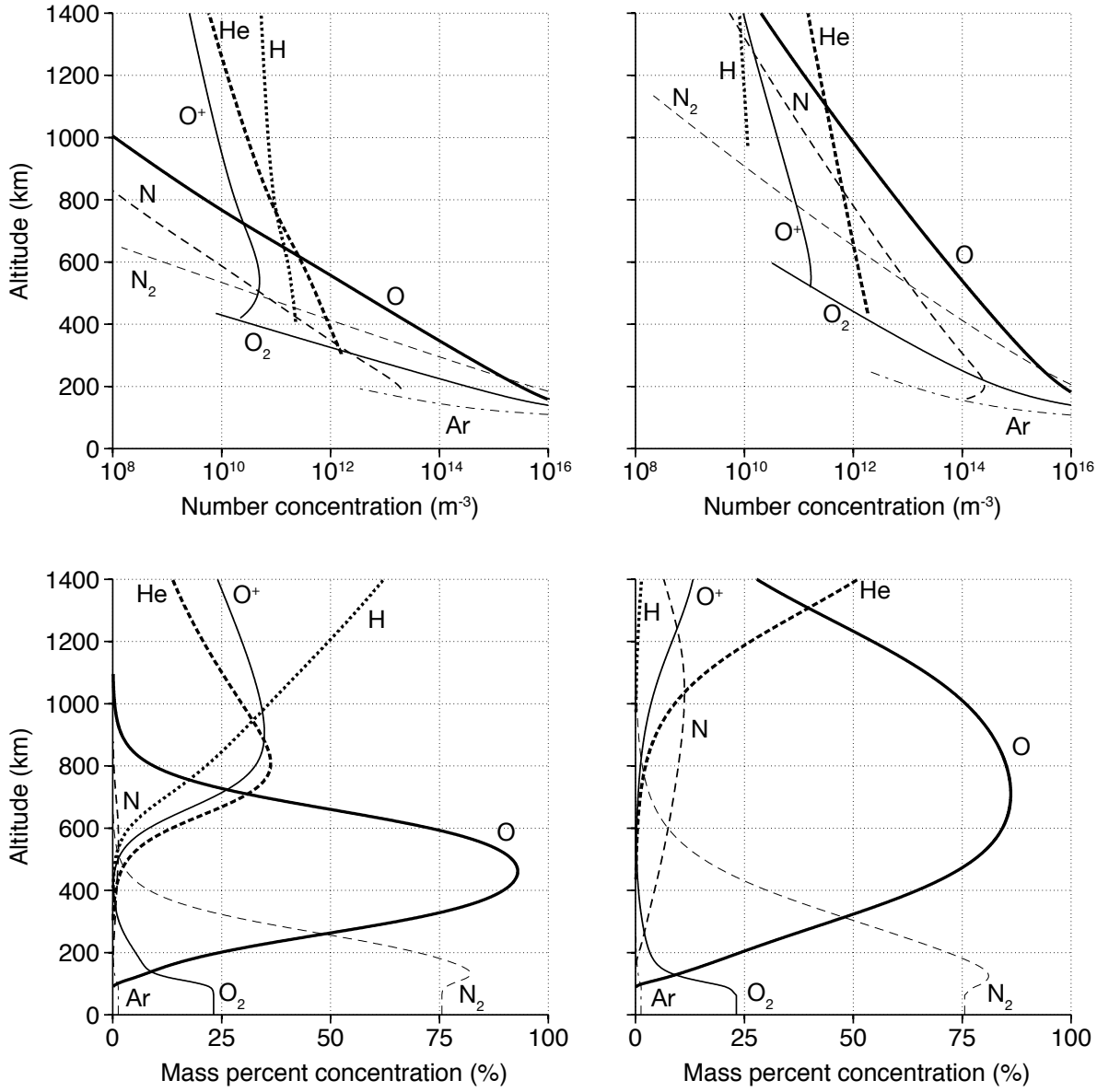

Figure 2.3 Altitude profiles of atmospheric number concentrations (*top*) and mass percent concentrations (*bottom*), for low (*left*) and high (*right*) solar activity levels, according to the NRLMSISE-00 model.

around and out of the thermosphere by conduction, radiation and convection [*Hargreaves*, 1992].

For empirical modelling, the representation of density variations with solar and geomagnetic activity are of prime importance. They will be discussed in the next sections.

Solar EUV radiation

The Sun emits electromagnetic radiation across a wide spectrum. At the wavelengths of visible light, where the solar irradiance is at its maximum, the emission is quite constant, but both at shorter wavelengths (ultraviolet) and longer wavelengths (radio), the level of emission is related to the level of activity of the Sun's magnetic field, and the interaction of this magnetic field with gases on the solar surface, the *photosphere*, and in its atmosphere, the *chromosphere* and *corona*. The emissions at the shortest wavelengths, of 170 nm and less, are responsible for heating the Earth's thermosphere. Radiation in this wavelength range is often designated Extreme Ultraviolet, or EUV radiation. Note that different publications might use slightly different definitions for the wavelength ranges in this part of the spectrum. The designations XUV (soft X-rays), EUV and FUV (Far Ultraviolet) may be encountered. In the following, we will simply use the term EUV for all solar radiation that affects the thermosphere, unless otherwise noted.

The heating of the thermosphere by EUV radiation occurs through excitation, dissociation or ionization of the atoms or molecules (primarily O, O_2 and N_2). The excess energy of each photon is converted into kinetic energy of the reaction products [*Rees*, 1989; *Hargreaves*, 1992].

Variations in EUV radiation are wavelength-dependent, as the shortest wavelengths are generally formed higher in the Sun's atmosphere and are more variable than shorter wavelengths [*Lean*, 1991]. They are also generally absorbed at higher altitudes in the Earth's atmosphere [*Tobiska et al.*, 2006]. Ideally, knowledge of the variability in irradiance over the entire UV and EUV spectrum is required in order to model the heating input in the atmosphere correctly.

The absorption of EUV radiation in the thermosphere results in a so-called diurnal bulge in temperature and density, on the daylight side of the Earth. For this reason, density variations in a horizontal plane are usually mapped in a coordinate system of local solar time versus latitude (see Section 2.1.3). Local solar time (LST) is equivalent to the longitude coordinate on normal maps, but usually expressed in hours instead of degrees, and with the defining meridian, at 12h (noon) LST, passing through the sub-solar point instead of through Greenwich. Due to thermal inertia, the diurnal bulge has its peak at around 14h–15h local solar time.

Solar wind and magnetospheric and ionospheric interactions

The Sun constantly emits a stream of particles out into space, called the *solar wind*. The solar wind consists mostly of electrons and protons, with a minor fraction of heavier ions [*Hargreaves*, 1992]. The motion of these solar wind particles forms the *interplanetary magnetic field*, which interacts with the terrestrial magnetic field, forming the Earth's *magnetosphere* (see Figure 2.4). In effect, the terrestrial magnetic field shields the Earth from the solar wind. Solar wind particles can only enter the magnetosphere and upper atmosphere through the *polar cusps*.

During quiet times at the Sun, the solar wind originates mainly through *coronal holes*. These occur where magnetic field lines open up into interplanetary

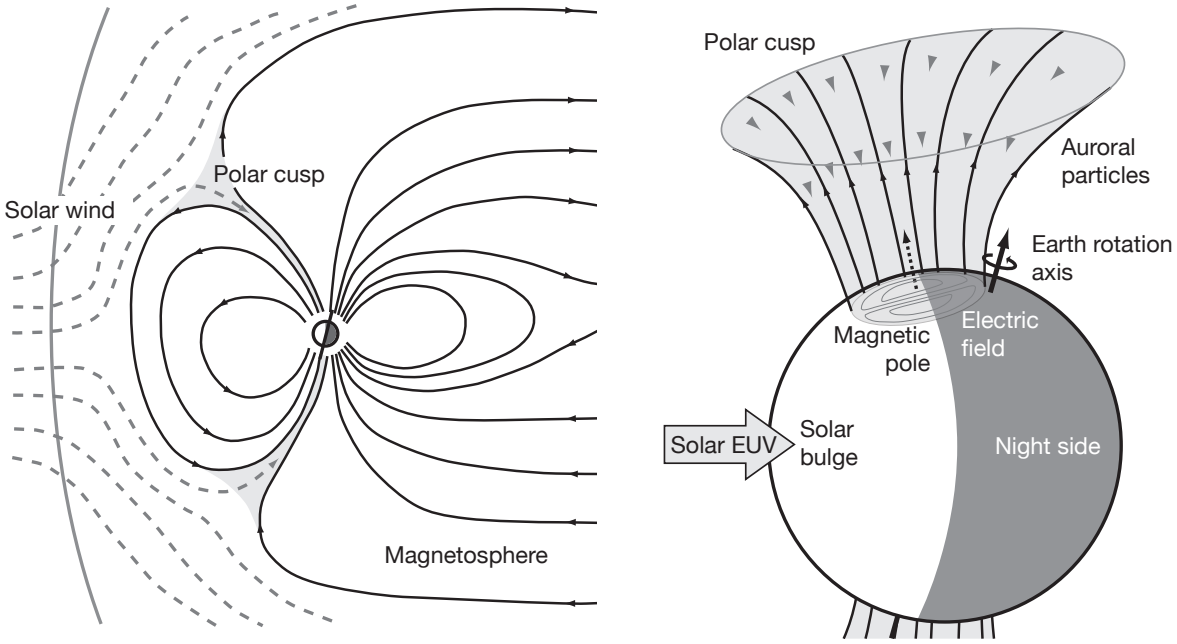

Figure 2.4 Schematic views of the Earth's magnetosphere, the polar cusps and their relation with processes affecting thermosphere density variations.

space. Sudden increases in the number of solar wind particles, and their speed, are related to *coronal mass ejections*, during which huge amounts of material are injected with high speed into the solar wind, and with *solar flares*, which are sudden short outbursts of electromagnetic energy and particles over a small area on the Sun. These phenomena are all closely related to the complexities of the Sun's magnetic field and occur more often during peak years of the 11-year solar activity cycle. The differences in speed between solar wind particles from various solar sources can cause interplanetary shocks and compressions [*De Pater and Lissauer*, 2001; *Hargreaves*, 1992]. The relationship between the Sun's magnetic field and these processes is the subject of ongoing investigations, with the aid of observatories both on the ground and in space, such as the SOHO [*Domingo et al.*, 1995] and STEREO [*Kaiser*, 2005] missions.

Near the Earth, the interactions between the solar wind, the magnetosphere and the ionosphere are very complex. The solar wind particles are slowed down at the bow shock and are largely deflected around the magnetopause. They can only enter at the geomagnetic poles, where the Earth's magnetic field lines are open. Inside the magnetosphere, an extensive system of currents is present, as well as regions where charged particles are trapped. The system is complex, because the motion of the charged particles induces the currents and electric fields, which in turn influences the magnetic field, which alter the motion of the charged particles. The end result is that the processes on the Sun which are briefly described above can result in large disturbances, called *geomagnetic storms*, at the Earth [*e.g.*, *McPherron and Baker*, 1993; *Fuller-Rowell et al.*, 1994; *Forbes et al.*, 1996; *Zhang et al.*, 2007]. The physics of magnetospheric processes is a subject of intensive ongoing study. Several space missions, including ESA's Cluster constellation [*Escoubet et al.*, 1997], are helping to unravel the intricacies. These physical processes are extensively studied making use of extensive coupled thermosphere, ionosphere and magnetosphere models (see the references in Section 2.8.3 for more details).

For the thermosphere, the most important aspect of this complex system is the mechanism in which energy is deposited. A relatively small part of this is due to particle precipitation. A larger contribution is due to Joule heating by ionospheric electric currents. The amount of energy deposited in the thermosphere through these two processes combined normally amounts to about one fourth of the energy deposited by EUV radiation. After extraordinary large solar flares and coronal mass ejections however, the energy deposited in the auroral zone can be up to twice that of the EUV energy [*Knipp et al.*, 2004].

Because there is an offset between the Earth's magnetic pole and its rotation axis (see Figure 2.4), the location of maximum energy absorption in the auroral zone shows a diurnal shift when viewed in the local solar time versus geographic latitude reference frame. Variations in the thermosphere that are affected by geomagnetic activity are therefore often calculated and viewed in a system of geomagnetic coordinates.

2.1.3 Horizontal structure

Now that the different energy inputs have been introduced, it is possible to have a look at how they affect variations in the thermosphere in a horizontal plane. Figures 2.5 and 2.6 show temperatures, densities and wind speeds from the NRLMSISE-00 [*Picone et al.*, 2002] and HWM-93 [*Hedin et al.*, 1996] models, at 400 km altitude above the Earth's surface. Figure 2.5 shows the situation at low solar activity, when solar EUV radiation is the dominant energy source. Figure 2.6 shows the situation for the exact same time of day and day of year, only six years earlier. The factors influencing the diurnal and seasonal variation are exactly the same, however the energy input is completely different. The $F_{10.7}$ proxy has a three times higher value in 2000, compared with 2006. Even more importantly, the snapshot of model values in Figure 2.6 is taken at the peak of a major geomagnetic storm. How these circumstances affect the temperature, density and wind speeds will be explained in the following paragraphs.

Temperature and density variations at 400 km altitude

The diurnal bulge, caused by EUV heating, is the dominant feature in the horizontal plane for temperature and density at low solar activity as seen in the top two frames of Figure 2.5. The maximum density, at around 1.2 10^{-12} kg/m^3, is located several hours East of the sub-solar point. It is summer in the Northern hemisphere, and the maximum temperature there is around 900 K. The temperature minimum, of around 600 K is close to the South Pole.

At high solar and geomagnetic activity, Joule heating and particle precipitation in the auroral zones have become the dominant energy sources, so that the diurnal variation is hardly visible anymore. Temperatures have become twice as large as at solar minimum, and now there are maxima around both the Poles. The temperature minimum is located near the night-side equator.

The density at high solar activity is more than a factor 10 larger than at low activity. The density maximum has shifted towards the auroral zone, while there are now minima at mid-latitudes on the night-side.

This Figure is just a snapshot image of the model at one specific moment in time. Although the NRLMSISE-00 model shows increased variability during this geomagnetic storm, compared to low activity conditions, its spatial resolution is actually quite coarse when compared with density observations derived from

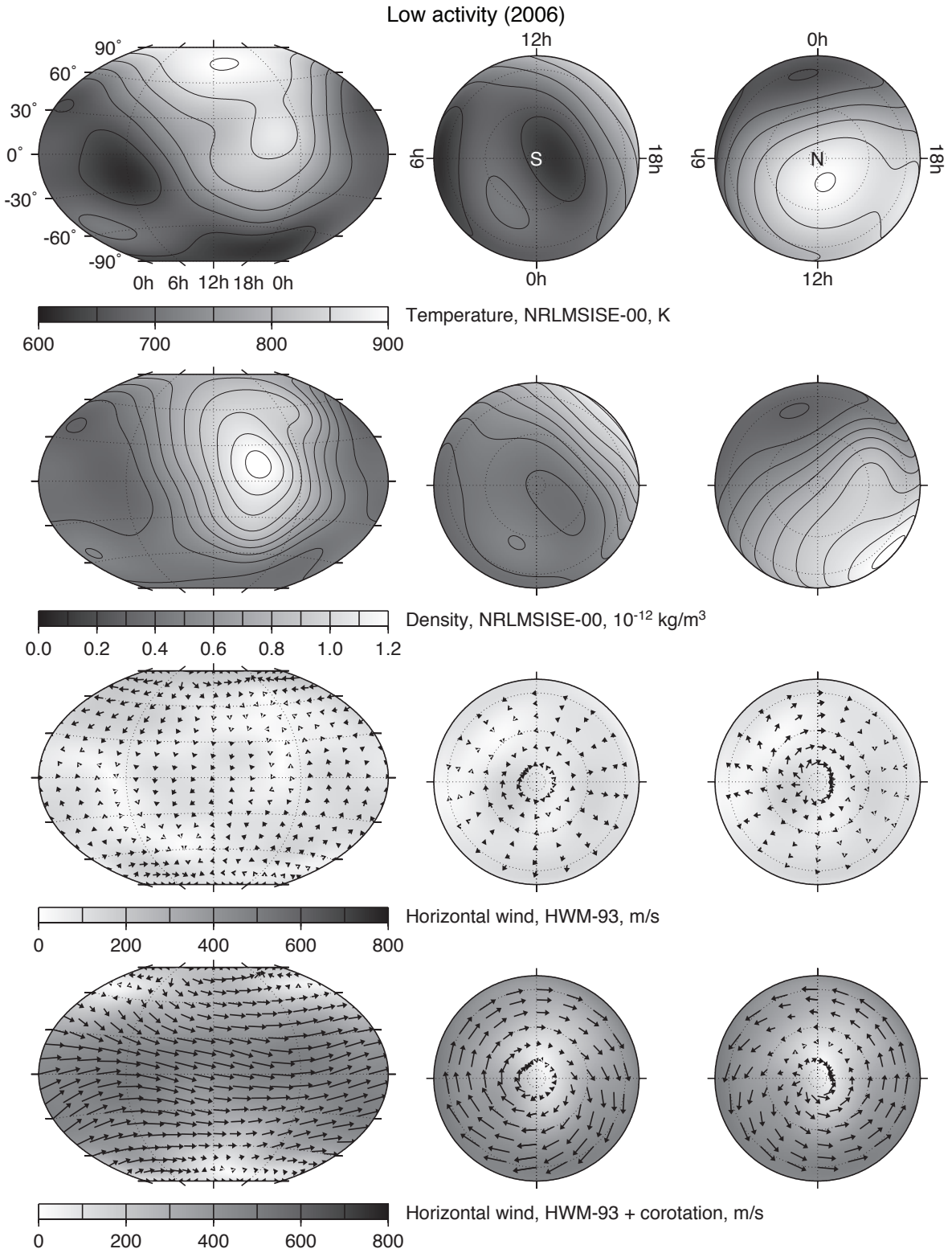

Figure 2.5 Maps of modelled temperature, density and wind speeds at 400 km altitude, on July 15, 2006 at 18:00:00 UTC ($F_{10.7}$=70.2, ap=3). The map projections are, from left to right, a Winkel Tripel projection, and two orthographic hemispherical projections centered on the geographic South Pole and North Pole.

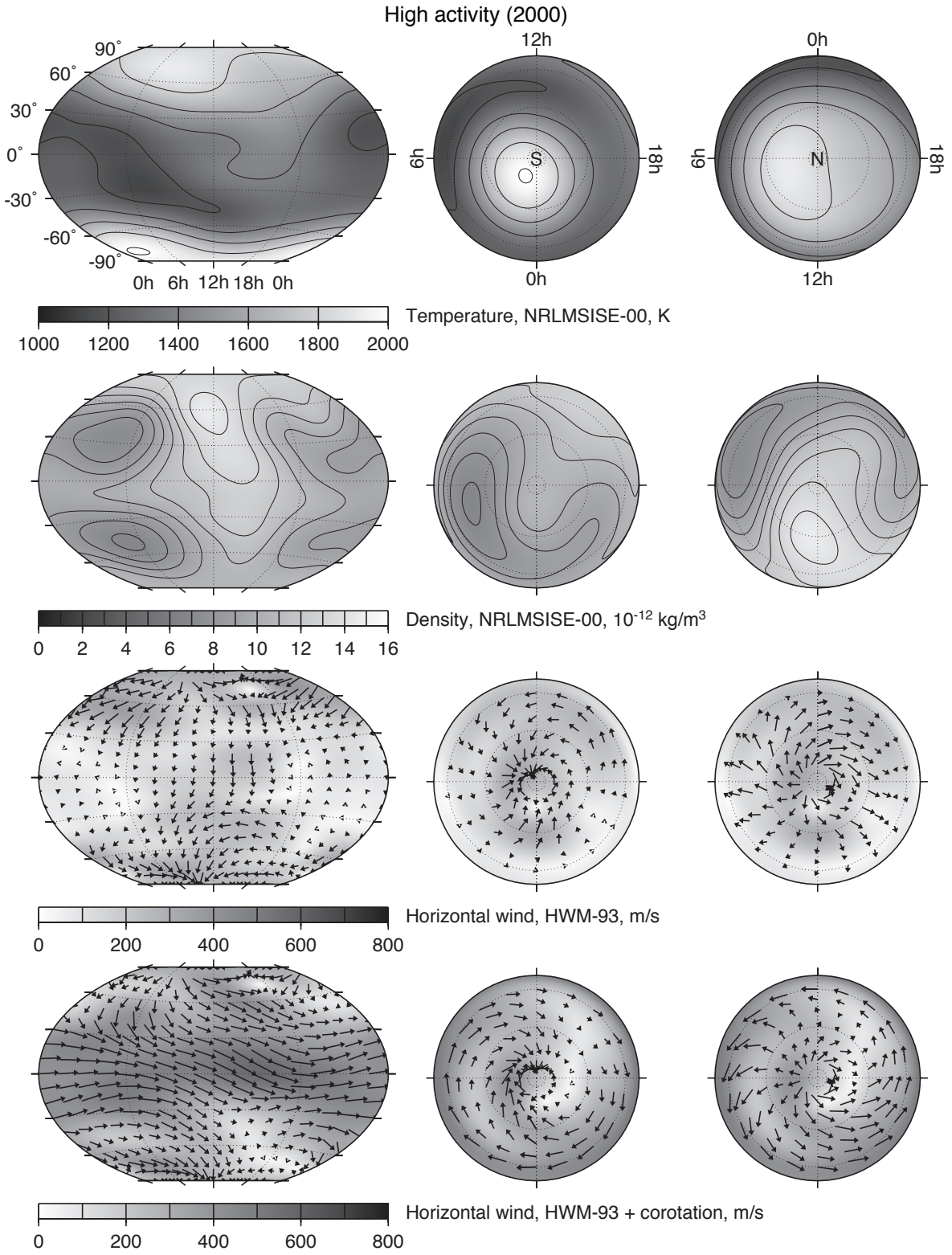

Figure 2.6 Same as Figure 2.5, but for July 15, 2000 at 18:00:00 UTC ($F_{10.7}$=213.1, ap=400).

accelerometer measurements. Such observations will be shown in later chapters, and they will be compared with model values in Chapter 9.

Horizontal winds in the thermosphere

The bottom two rows in Figures 2.5 and 2.6 show horizontal wind speeds and directions at 400 km altitude, obtained from the HWM-93 model. This model outputs zonal and meridional wind speeds, with respect to a corotating atmosphere. The wind direction at the Poles is therefore undefined.

The third row in the Figures shows just the output of the model, which is a representation of the wind that could be measured by an observer on the ground. The bottom row adds the speed of the Earth's rotation to the output of the model. This is a representation of the wind that influences the motion of satellites. The corotation velocity is proportional to the cosine of the latitude, which goes from a maximum at the equator to zero at the poles. Figure 2.5 shows that the HWM-93 output is below 200 m/s and is therefore nearly negligable compared to the corotation velocity at low latitudes. The deviation from corotation becomes more important in the polar areas, and at high activity, as can be seen in Figure 2.6. Unfortunately, the observation data at high latitudes on which models such as HWM-93 are based, is very sparse. Accelerometer-derived wind data, if properly calibrated, could be very helpful in that respect.

Altitude dependence of the horizontal density structure

Figures 2.2 and 2.3 have provided a representation of the variation of density with height at a single location, while Figures 2.5 and 2.6 have shown the variations in the horizontal plane at a single altitude level of 400 km. Now, in Figure 2.7, both views are combined, to get a more coherent picture of density variations in the thermosphere.

It is clear from the Figure that the situation at 400 km is quite representative for a large range in altitude. This is especially true at low solar activity, when the diurnal bulge is the dominant feature. However, at 100 km, *semi-diurnal tides* dominate. In this region, the behaviour of the thermosphere is tightly linked to that of the mesosphere, and density levels are actually lower during solar maximum than at solar minimum, according to the model.

The behaviour of total density above approximately 600–800 km is also quite different. There is a distinct density peak over the winter hemisphere. This *winter helium bulge* is caused by the atmospheric dynamics of lower altitudes [*Mayr et al.*, 1978], where helium is a minor constituent. The minor light-weight gas is dragged along with the circulation of the major gas flow at lower altitudes, but because of its large scale height, more helium is transported to the winter pole than is returned to the summer pole [*Cageao and Kerr*, 1984].

2.1.4 Temporal variability

Up to this point, the figures in this chapter have focussed on two distinct times with extreme low and high solar and geomagnetic activity conditions. To complete our overview of the major variations in the thermosphere, Figure 2.8 shows two zoomed in views of Figure 2.1, showing the magnitude of the day-to-day variability of density over the course of the years 2000 and 2006, as modelled by

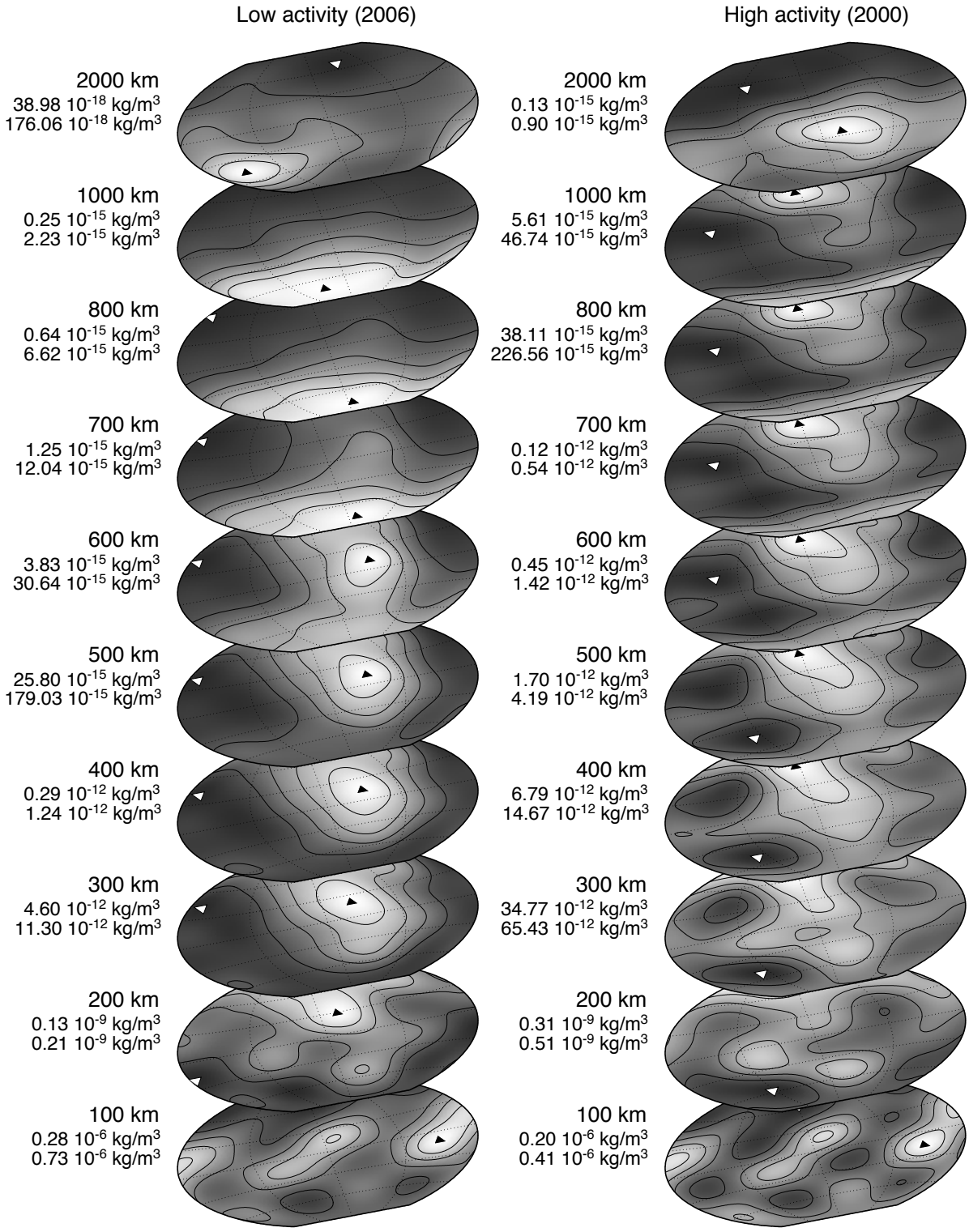

Figure 2.7 Maps of modelled density on July 15, 2006 at 18:00:00 UTC (*left*) and at the same date and time in 2000 (*right*). The locations of the absolute minimum and maximum values at each altitude are indicated by the white and black triangles. The corresponding values are provided alongside the map. Contour lines are drawn at 20% intervals between the minimum and maximum.

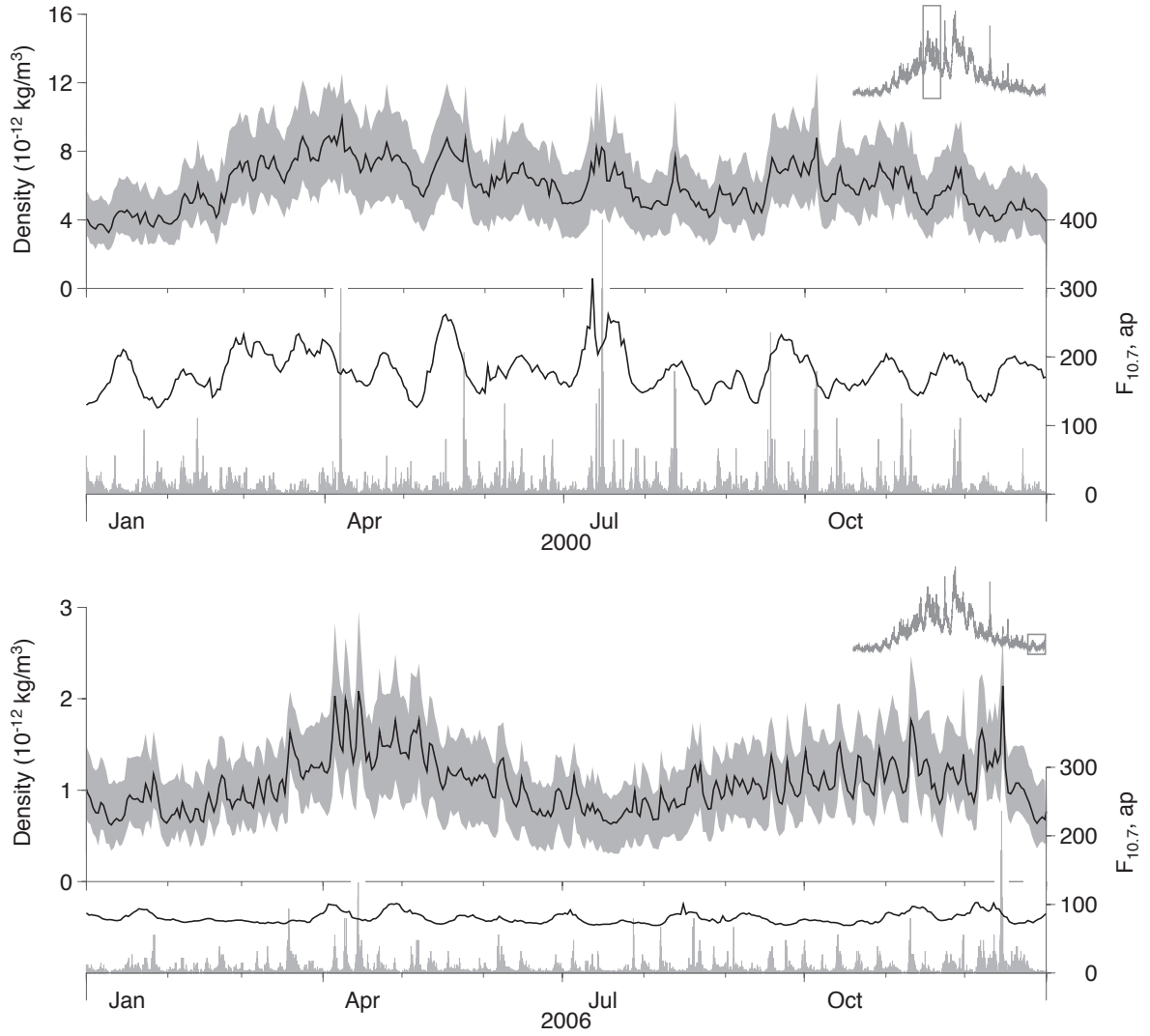

Figure 2.8 Yearly time series of daily minimum and maximum (grey area) and average values (black line), as well as $F_{10.7}$ (black line) and ap (grey spikes). Densities are evaluated from the NRLMSISE-00 model at 400 km altitude over a mid-latitude location (Delft, The Netherlands). The insets show the years in context of the 11-year solar cycle.

NRLMSISE-00. During the year 2000, the approximately 27-day solar rotation period is a dominant feature in both $F_{10.7}$ and density. During the more quiet year of 2006, the semi-annual variation with maxima in April and October is more clearly visible, and the relative effect of occasional peaks in geomagnetic activity are larger. Note for example the three peaks in April 2006.

2.2 Observations, proxies and indices of thermospheric energy inputs

In the previous Sections, the large influence of processes on the Sun, in the magnetosphere and in the ionosphere on the thermosphere has been explained. In order to study and model the thermosphere, observations of these processes are therefore very useful.

These observations are often available in the form of *proxies* and *indices*. A

proxy is an observation that is related to, and shows similar behaviour as the phenomena of interest, but that is easier to obtain, or for which the historical record is more complete, than a direct observation. An index is a quantity that is derived from observations according to a pre-designed standard. Indices are often designed to summarize complex phenomena from multiple observations, facilitating the representation in models and the quick identification of disruptive events.

2.2.1 Solar EUV observations and proxies

Measurements of the Sun's radiative output at EUV wavelengths are difficult, as they need to be made by satellites above the absorbing atmosphere. To make matters worse, instrumentation sensitive to this radiation also degrades significantly under its influence [*Lean*, 1991; *Floyd et al.*, 2005]. Measurements from satellites started in the 1960's, but they have only been available on a regular basis since the 1990's. These recent missions have also introduced calibration techniques to account for the effects of instrument degradation. Such missions include UARS [*Reber et al.*, 1993], launched in 1991, SOHO [*Domingo et al.*, 1995], launched in 1995, TIMED [*Paxton et al.*, 1999], launched in 2001 and SORCE [*Rottman*, 2005], launched in 2003.

It is important to note that investigations on the thermosphere before the 1990's had to be made without reliable direct and continuous observations of variations in EUV radiation, contemporaneous with the available data on density. Instead, investigators had to rely on observations of solar activity in parts of the spectrum that are available on the ground, such as the number of sunspots visible on the solar disc, or the level of radiation at radio-wavelengths, which can be used as proxies for the EUV radiation.

10.7-cm radio flux

Sunspot numbers have been recorded since Galileo first observed them in 1610, but a better correlation with thermospheric density was found with $F_{10.7}$ [*Jacchia*, 1959], which is the amount of energy received from the Sun at 10.7 cm wavelength. $F_{10.7}$ measurements have been made daily by radio telescope, operated by the National Research Council at Ottawa from 1947 to 1991 and at Penticton, British Columbia from 1991 onwards. $F_{10.7}$ is always supplied in units of 10^4 Jansky (Jy) = 10^{-22} W/m^2/s. In plots and publications, the units are usually omitted, or designated simply as solar flux units (s.f.u.). The proxy ranges from below 70 during solar minimum, to around 370 during extremely active days.

Early researchers such as *Jacchia* [1959] first recognized the solar radiation influence on the thermosphere from the 27-day variations which was found in orbital drag time series. It was later found that a more slowly varying component of solar radiation was also present. The moving average of $F_{10.7}$ over three or four solar rotations (81 or 108 days), denoted $\bar{F}_{10.7}$ was used to represent this component.

The $F_{10.7}$ data are published in two forms: the *observed* fluxes are the actual measured values, while the *adjusted* fluxes are scaled to a standard distance of 1 AU, to compensate for the varying distance between the Earth and Sun through the year. While the adjusted values give a better representation of the processes taking place on the Sun, the observed values better represent the EUV heating

input in the upper atmosphere. Therefore, the latter should be used as input to the density models.

Mg II core-to-wing ratio

It is now widely recognized that the use of $F_{10.7}$ and $\bar{F}_{10.7}$ as proxies in empirical density models has become a limiting factor in further improving their accuracy. With the availability of better satellite observations and empirical models of solar irradiances, researchers have started looking for alternative, more representative proxies, of which the most widely studied example is Mg II.

The use of the Mg II core-to-wing ratio (or just Mg II for short), was first proposed by *Heath and Schlesinger* [1986], and is computed by taking the ratio of the intensity of the Mg II emission at 280 nm over that of the nearby line wings. The use of this ratio makes the index much less sensitive to instrument trends, since the wavelength dependence of degradation is limited. Mg II observations have been made from various satellites with different instrument characteristics. From these different datasets, composite time series have been constructed that often do not go further back than the 1990's. These time series correlate well with $F_{10.7}$. For density studies, the Mg II time series are often scaled using linear regression with $F_{10.7}$ so that they can be expressed in the same units.

Combinations of EUV proxies

Of specific interest with regard to the use of EUV measurements for thermosphere modelling is the work by *Dudok de Wit et al.* [2005], who performed a principal component analysis on EUV spectra recorded by the TIMED satellite. An important result of this analysis is that the full EUV spectrum can be reconstructed with high accuracy from just a small number of spectral lines. The work confirms that a single spectral line or proxy is clearly not sufficient to represent variability at the different wavelengths within the EUV spectrum that affect the thermosphere. This technique provides graphical representations of the similarity and dissimilarity of the behaviour of the various spectral lines and EUV proxies.

The use of a combination of proxies for representing EUV input in the thermosphere has been the strategy of *Tobiska et al.* [2006] and *Bowman and Tobiska* [2006] in preparation for the JB2006 density model. After testing several combinations, they arrived at the use of $F_{10.7}$, Mg II and S_{EUV}, and their 81-day averages. The S_{EUV} index is a measure of the integrated 26–34 nm emission, observed by SOHO. The Mg II and S_{EUV} measurements have been averaged to daily values and converted by linear regression to the same value range as $F_{10.7}$, resulting in the new indices M_{10} and S_{10}. For the update of the Jacchia-Bowman model to its 2008 version, JB-2008 [*Bowman et al.*, 2008*a*], an additional solar activity index was added, designated Y_{10}. It is a composite index, designed to represent 0.1–0.8 nm X-ray emissions during solar maximum and Lyman-α emissions during moderate and low solar activity. Separately from these modelling efforts, solar indices have recently been analyzed, making use of CHAMP accelerometer data, in the work of *Guo et al.* [2007].

2.2.2 Geomagnetic activity observations and indices

Satellite observations of charged particles from the solar wind and their interaction with the magnetosphere and ionosphere have been available since the late

Kp	00	0+	1-	10	1+	2-	20	2+	3-	30	3+	4-	40	4+
ap (nT)	0	2	3	4	5	6	7	9	12	15	18	22	27	32
Kp	5-	50	5+	6-	60	6+	7-	70	7+	8-	80	8+	9-	90
ap (nT)	39	48	56	67	80	94	111	132	154	179	207	236	300	400

Table 2.1 Relation of geomagnetic Kp to ap values.

1970's and early 1980's. These observations were made from NOAA's TIROS and POES satellites, as well as by the DMSP program [*Knipp et al.*, 2004]. More recently, observatories of the Sun, the magnetosphere and the interplanetary environment such as SOHO, ACE, Cluster and STEREO, have greatly increased our knowledge of these complex environments and their interactions.

These measurements have never been used in empirical thermosphere models however. Thermosphere models have traditionally made use of the Kp and ap geomagnetic indices, which are extensively described in the monograph by *Mayaud* [1980], and the more accesible review article by *Menvielle and Berthelier* [1991]. The information in this section draws heavily from these sources.

The Kp and ap geomagnetic indices

The Kp index is derived from measurements made at 11 geomagnetic observatories at mid-latitudes, through a rather intricate procedure, described in [*Menvielle and Berthelier*, 1991]. At these stations, the horizontal magnetic components are separated in regular and irregular variations. The intensity of the irregular variations is expressed in a K index at each station, over each three-hour period.

This K index, as defined by *Bartels et al.* [1939], ranges from 0 to 9, in discrete steps of one thirds, specified by plus and minus signs, as follows: 0$_0$, 0$_+$, 1$_-$, 1$_0$, 1$_+$, ..., to 9$_0$. The K indices from the 11 stations are standardized to avoid local time influences and averaged to form the planetary index Kp. Since Kp is a true index, it carries no physical units. It can be converted to the approximate amplitude of geomagnetic perturbation by the use of a conversion table (see Table 2.1), resulting in ap (planetary equivalent amplitude) values, expressed in units of nanoTesla (nT). These ap values should be multiplied by two to represent the magnitude of the observed variation in the magnetic field. Since the ap index is related directly to Kp, it also has a 3-hourly cadence, and can take no other values than those listed in the conversion table. The average of all eight ap values in a UTC day is denoted as the Ap index. Time series of Ap can be useful for creating plots and quickly identifying active days, but the loss of temporal resolution with respect to ap makes the daily index less suitable for use in density models.

Alternative geomagnetic indices

Kp and related indices are widely used in many applications, including thermosphere models. However, by today's standards, they show some obvious shortcomings [*Menvielle and Berthelier*, 1991; *Menvielle and Marchaudon*, 2007]. Since the Kp network was set up at the start of the cold war period, most stations are located in Western Europe and North America. Relatively minor magnetic disturbances over one of these areas will therefore result in high values of the index, while disturbances of similar magnitude in uncovered areas might go largely unnoticed.

$F_{10.7}$	f	ftp://ftp.ngdc.noaa.gov/STP/SOLAR_DATA/SOLAR_RADIO/FLUX
	c	ftp://sec.noaa.gov/pub/indices/quar_DSD.txt
	p	ftp://sec.noaa.gov/pub/latest/45DF.txt
S_{10}	f	http://sol.spacenvironment.net/~JB2006/SD_delivery_folder/JB06_delivery0_v4_0h.txt
M_{10}	f	http://sol.spacenvironment.net/~JB2006/SD_delivery_folder/JB06_delivery0_v4_0h.txt
Y_{10}	f	http://sol.spacenvironment.net/~JB2008/indices/SOLFSMY.TXT.zip
Kp	f	ftp://ftp.ngdc.noaa.gov/STP/GEOMAGNETIC_DATA/INDICES/KP_AP
	c	ftp://sec.noaa.gov/pub/indices/quar_DGD.txt
	p	ftp://sec.noaa.gov/pub/latest/45DF.txt
ap	a	Converted from K_p
am	f	http://isgi.cetp.ipsl.fr/source/indices/am/
Dst	f	ftp://ftp.ngdc.noaa.gov/STP/GEOMAGNETIC_DATA/INDICES/DST
ΔT_C^{Dst}	f	http://sol.spacenvironment.net/~JB2008/indices/DTCFILE.TXT.zip

Table 2.2 Sources of the solar and geomagnetic activity proxies used in this study. The letters in the second column stand for f=final, c=current, p=predicted or a=all values.

A new global network, with a much better geographical distribution, was set up after the International Geophysical Year (1957/1958), coinciding with the beginning of the space age. The *an*, *as* and *am* indices, all expressed in nT are derived from the *K* indices measured at these stations. The *an* index represents the northern hemisphere, *as* the southern, and *am* (where *m* stands for 'mondial') is the average of both hemispherical indices. The *am* index can therefore be considered an improved version of ap.

The *longitude sector geomagnetic indices*, or aλ indices, are *K*-derived indices which are provided for various pre-defined longitude sectors [*Menvielle and Paris*, 2001]. Five of these sectors, each of which contains two or more observing stations, are in the Northern hemisphere, and four are in the Southern. These indices are thus able to represent variations with longitude.

Other parameters, such as the *Dst* (*disturbance storm time*) and *PC* (*polar cap*) indices represent only certain parts of the geomagnetic activity, at low and high latitudes respectively, which are mainly driven by distinct current systems. See for example, *Campbell* [1996], *Troshichev et al.* [2006] and references therein. These two indices are available at an hourly or higher rate and therefore offer improved temporal resolution compared to the 3-hourly *K*-derived indices. The work of *Knipp et al.* [2004] provides an empirical model for the power input by Joule heating in the thermosphere, based on quadratic equations using these two indices.

2.2.3 Comparison of proxies and indices

Table 2.2 lists the sources of the geomagnetic and solar activity values which have been obtained and used in this study. A distinction is made between *predicted*, *current* and *final* values, which are available in order of increasing accuracy and latency. The availability of current and predicted values is especially important for near real-time applications. This thesis will be mostly concerned with performance of models under historical circumstances however, so unless otherwise noted, the final values are used.

Figure 2.9 shows a comparison of time series of several of the proxies and indices described in the previous Sections. During the period of late October to the end of November 2003, the variations in solar activity were especially large, due to the presence of large active regions on the Sun (see Figure 2.1 for context).

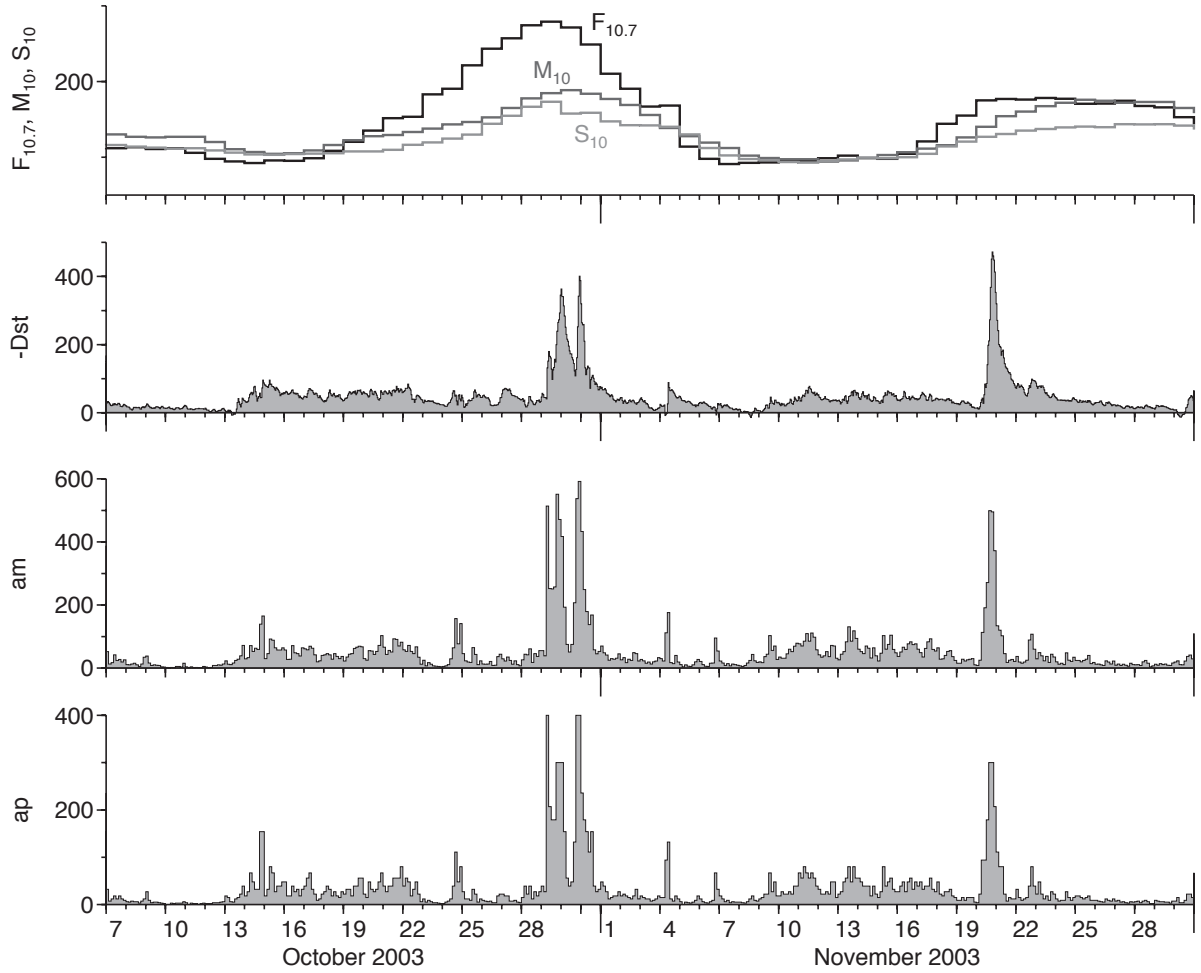

Figure 2.9 Comparison of solar activity proxies and geomagnetic indices.

Two of the largest geomagnetic storms of the last solar cycle occurred during the last days of October and on 20 and 21 November. Note that the behaviour of these indices during this time period is not necessarily indicative for other time periods.

The top panel in the plot shows the variation of the three daily solar radiation proxies that are provided for the JB2006 model. During this period, $F_{10.7}$, which is used by older models as well, shows the largest amplitude. The new M_{10} and S_{10} proxies show similar values during low activity, but differences are considerable around the time of the storms.

The bottom three panels show the hourly *Dst* and the three-hourly *am* and *ap* indices. The *am* and *ap* plots look quite similar. The main difference between these indices is in the improved global distribution of the observation network for the *am* index. The result of this is especially apparent in the relative magnitudes of the three peaks of the October storm. The *Dst* index, which returns predominantly negative values, has been multiplied by -1 here for easier comparison with the other indices. *Dst* provides more detail, because of its hourly rate, but it only represents the geomagnetic disturbances in the equatorial region. After major disturbances, *Dst* takes longer to recover than the *am* and *ap* values. Notice also how the disturbance on October 24 is not clearly present in the *Dst* plot, and how the maximum amplitude of the November storm exceeds that of the October storm in *Dst*, but not in *am* or *ap*.

From this example and the discussion in the previous Sections, it is clear that there is a wide variety of observations, proxies and indices available for research in thermospheric density and its connection to processes on the Sun. In the early 1960's, the combination of $F_{10.7}$ and ap was chosen to represent all non-periodic variations in density. This was a convenient choice, because long time series for these values were already easily available at the time. Empirical modellers have stuck to this choice until only very recently.

2.3 Empirical density models

The development of new density models has been largely driven by the availability of new sources of observation data. With the availability of more data, the models have become able to represent more subtle variations in density. Table 2.3 lists the most widely known models and their references. Jacchia, MSIS and DTM are the three major families of models, which have been under development since the 1960's and 1970's. Several models of these families will be evaluated and used in this research, and they are therefore introduced in the remainder of this Chapter.

2.3.1 Early models and Jacchia's models

The first observations of orbital motions of satellites under the influence of drag in the late 1950's paved the way for the first generation of general empirical density models in the 1960s and early 1970s. Examples of these models include those by Harris and Priester [*Harris and Priester*, 1962] and L.G. Jacchia [*Jacchia*, 1964, 1971*a*, 1971*b*, 1977]. The Jacchia-71 model was adopted as the COSPAR International Reference Atmosphere in 1972, and is therefore also known as CIRA-72 [*Jacchia*, 1972]. Later models by Jacchia, such as the those published in *Jacchia* [1977], have not led to accuracy improvements with respect to this model [*Marcos*, 1990]. The Jacchia-70 and -71 models have been used at the basis of the NASA Marshall Engineering Thermosphere (MET) models [*Hickey*, 1988; *Owens*, 2002], which have been applied in satellite lifetime predictions. More recently, Jacchia's models have been further improved under an initiative of the US Air Force Space Command, with new algorithms for computing the semi-annual density variation and the use of additional solar and geomagnetic activity proxies. This effort has resulted in the Jacchia-Bowman 2006 (JB2006) and 2008 (JB2008) models [*Bowman et al.*, 2008*b*, 2008*a*].

2.3.2 DTM models

The first of the DTM models was published in 1978 [*Barlier et al.*, 1978]. Like the Jacchia models, DTM was based solely on observations of satellite drag, however it used a more sophisticated and generalised model formulation. A major update, named DTM-94, was published by *Berger et al.* [1998]. DTM-94 is based on an extended satellite drag dataset for improved accuracy at solar minimum and solar maximum conditions. DTM model improvement is ongoing. Recent developments include the introduction of the Mg II solar EUV proxy [*Thuillier and Bruinsma*, 2001] in DTM-2000 [*Bruinsma et al.*, 2003] and incorporation of new data such as that from the CHAMP accelerometer [*Bruinsma and Biancale*, 2003].

Model family	*Model name*	*Reference*	*Source code*
Jacchia	Jacchia '64	*Jacchia* [1964]	
	Jacchia '70	*Jacchia* [1971*a*]	
	Jacchia '71	*Jacchia* [1971*b*]	
	Jacchia-Roberts '71	*Roberts* [1971]	
	CIRA-72	*Jacchia* [1972]	In reference
	Jacchia '77	*Jacchia* [1977]	
	MET	*Hickey* [1988]	
	MET 2.0	*Owens* [2002]	
	JB2006	*Bowman et al.* [2008*b*]	Internet[1]
	JB2008	*Bowman et al.* [2008*a*]	Internet[2]
DTM	DTM	*Barlier et al.* [1978]	In reference
	DTM-94	*Berger et al.* [1998]	From author
	DTM-2000	*Bruinsma et al.* [2003]	
MSIS	MSIS	*Hedin et al.* [1977*a*, 1977*b*]	
	MSIS-83	*Hedin* [1983]	
	MSIS-86	*Hedin* [1987]	Internet[3]
	CIRA-86	*Hedin* [1988]	
	MSISE-90	*Hedin* [1991]	
	NRLMSISE-00	*Picone et al.* [2002]	Internet[3]
HWM	HWM-87	*Hedin et al.* [1988]	
	HWM-90	*Hedin et al.* [1991]	
	HWM-93	*Hedin et al.* [1996]	Internet[4]
	HWM07	*Drob et al.* [2008]	Internet[4]
	DWM07	*Emmert et al.* [2008*b*]	Internet[4]
Others	Harris-Priester	*Harris and Priester* [1962]	
	TD 88	*Sehnal* [1988]	
	GOST	see *Vallado* [2001, App. B]	

[1] http://sol.spacenvironment.net/~jb2006/
[2] http://sol.spacenvironment.net/~jb2008/
[3] http://uap-www.nrl.navy.mil/models_web/msis/msis_home.htm
[4] http://uap-www.nrl.navy.mil/models_web/hwm/hwm_home.htm

Table 2.3 List of empirical thermosphere models, their literature references, and the source of the FORTRAN code for the models that have been obtained and implemented for use and evaluation in this study.

2.3.3 MSIS and HWM models

Starting in the late 1970's Alan Hedin created a new class of density models, named MSIS. His models [*Hedin et al.*, 1977*a*, 1977*b*] were based solely on mass spectrometer and incoherent scatter radar observations. The main advantage of the use of these datasets over the drag-derived datasets is that they consist of independent observations of both temperature and number densities for the atmospheric constituents. The MSIS-86 model replaced Jacchia-71 as the COSPAR International Reference Atmosphere thermosphere model, and is therefore also known as CIRA-86 [*Hedin*, 1987, 1988]. An extension to the model was published as MSISE-90 [*Hedin*, 1991]. This model is identical to MSIS-86 for the thermosphere region, but extends down to zero altitude.

At the end of the 1990's, development of the MSIS-class models was continued at the US Naval Research Laboratory (NRL). The resulting NRLMSISE-00 model [*Picone et al.*, 2002] includes additional mass spectrometer and incoherent scatter radar data, as well as accelerometer data and the DTM and Jacchia satellite orbit decay databases. An additional constituent, anomalous oxygen, was introduced in the model to investigate apparent discrepancies between the datasets at higher altitudes.

The HWM series of thermospheric horizontal wind models was created alongside the MSIS model series. The model subroutine accepts the same inputs as the MSIS series of density models and returns zonal and meridional wind speeds. The models are based on gradient winds from CIRA-86 plus rocket soundings, incoherent scatter radar, MF radar and meteor radar data. Further development of the HWM model series is now continued at the Naval Research Lab. The latest edition is HWM07 [*Drob et al.*, 2008], which has a companion model for high geomagnetic activity, the Disturbance Wind Model DWM07 [*Emmert et al.*, 2008*b*].

2.4 Empirical model input and output

In its most simple form, a density model returns an estimate of density based on time and location, where the location is usually expressed in terms of the geodetic height h, latitude ϕ and longitude λ:

$$\rho \approx \rho_{\text{model}}(t, \phi, \lambda, h) \tag{2.7}$$

In reality, there are many differences between the way the input parameters of the various models are defined. An exact specification of the input parameters is not always even clearly identified in the model source code comments or documentation. The MSIS models allow the user program to make settings before calling the model subroutine, which affect their output. Part of the temporal variation of the model output is driven by solar and geomagnetic activity indices and proxies, which can sometimes be obtained from multiple sources or in various formats. These issues can easily cause inconsistent results and errors. Such practical challenges in implementing thermosphere density models for the purpose of the exact reproduction of results have been identified and summarized for the NRLMSISE-00 model by *Wilkins et al.* [2006]. In order to obtain reproducible results from the density models, including the calibrated models which will be described in later Chapters, it is therefore necessary to give a strict definition of the input parameters and settings with which the models are called. These will be provided in the following Section.

Function	Description
	Time/date conversion functions
$sec(t)$	Number of seconds since the start of the UTC day, in the range 0–86400.
$yy(t)$	Last two digits of the year.
$doy(t)$	Day of the year, in the range 0-366.
$mjd(t)$	Modified Julian Date and fraction of the day.
$lst(t,\lambda)$	Local solar time in hours: $lst(t,\lambda) = sec(t)/3600 + \lambda/(2\pi/24)$.
	Solar and geomagnetic proxy and index functions
$Kp(t)$	Planetary geomagnetic activity index Kp for the time t, piecewise constant over the 3-hour time interval.
$Kp^i(t)$	Planetary geomagnetic activity index Kp, linearly interpolated between the mid-points of the two three-hour time intervals that are closest to t.
$ap(t)$	Planetary geomagnetic activity index ap for the time t, piecewise constant over the 3-hour time interval.
$F_{10.7}(t)$	Observed 10.7 cm solar flux for the UTC day of t.
$\bar{F}_{10.7}(t,m)$	Moving average of $F_{10.7}(t)$ over a time span with length m, centered on the UTC day of t. $\bar{F}_{10.7}(t,m) = \frac{1}{2m+1}\sum_{j=-m}^{m} F_{10.7}(t+j)$
$S_{10}(t)$	EUV index for JB2006, scaled to $F_{10.7}$.
$\bar{S}_{10}(t,m)$	Moving average of $S_{10}(t)$ over a time span with length m, centered on the UTC day of t.
$M_{10}(t)$	Mg II index for JB2006, scaled to $F_{10.7}$.
$\bar{M}_{10}(t)$	Moving average of $M_{10}(t)$ over a time span with length m, centered on the UTC day of t.
$Y_{10}(t)$	X-Ray index for JB2008, scaled to $F_{10.7}$.
$\bar{Y}_{10}(t)$	Moving average of $Y_{10}(t)$ over a time span with length m, centered on the UTC day of t.
$\Delta T_C^{Dst}(t)$	Change in culmination point temperature during high geomagnetic activity, for the JB2008 model, computed offline from the Dst index.

Table 2.4 Auxiliary functions for the computation of density model subroutine input variables.

2.4.1 Definition of model inputs

Unless otherwise noted, all times are in the UTC time system, and all coordinates will be with respect to the International Terrestrial Reference Frame ITRF-2000. The geodetic coordinates ϕ, λ and h are with respect to the GRS80 reference ellipsoid.

All of the density model subroutines are called using wrapping subroutines, which translate the four arguments of (2.7) to the actual model subroutine arguments as defined by their respective authors. Several auxiliary functions for time conversions and the retrieval of solar and geomagnetic activity proxies and indices, listed in Table 2.4, are called by the wrapping subroutines. These proxies and indices were retrieved from the Internet locations listed in Table 2.2. The conversions themselves are provided in Tables 2.5, 2.6 and 2.7. As can be seen in these Tables, these conversions are not trivial. All models require the user to apply a latency and smoothing to the solar activity inputs, and often to the geomagnetic activity input as well. The DTM-94 model even incorporates a latitude dependent latency on Kp, from 3 hours at the poles to 6 hours at the equator. The local solar time is an important parameter in all models. It is directly related to the time of day and longitude, according to the equation in Table 2.4. This equation is used in order to provide consistent time, longitude and local solar time to the MSIS models.

The MSIS and HWM models contain switches with which various features of the model can be turned on or off. For this research, the switch to use the 3-hourly

Variable	*Units*	CIRA-72	JB2006	JB2008
AMJD	days	$mjd(t)$	$mjd(t)$	$mjd(t)$
SUN(1)	rad	$\lambda_\odot$	$\lambda_\odot$	$\lambda_\odot$
SUN(2)	rad	$\phi_\odot$	$\phi_\odot$	$\phi_\odot$
SAT(1)	rad	λ	λ	λ
SAT(2)	rad	ϕ	ϕ	ϕ
SAT(3)	km	h	h	h
GEO(1)	10^4 Jy	$F_{10.7}(t - 1.71\text{d})$	$F_{10.7}(t - 1\text{d})$	$F_{10.7}(t - 1\text{d})$
GEO(2)	10^4 Jy	$\bar{F}_{10.7}(t, 108\text{d})$	$\bar{F}_{10.7}(t - 1\text{d}, 81\text{d})$	$\bar{F}_{10.7}(t - 1\text{d}, 81\text{d})$
GEO(3)	–	$Kp(t - 0.279\text{d})$	$ap(t - 0.279\text{d})$	$ap(t - 0.279\text{d})$
S10	–	–	$S_{10}(t - 1\text{d})$	$S_{10}(t - 1\text{d})$
S10B	–	–	$\bar{S}_{10}(t - 1\text{d}, 81\text{d})$	$\bar{S}_{10}(t - 1\text{d}, 81\text{d})$
XM10	–	–	$M_{10}(t - 5\text{d})$	$M_{10}(t - 5\text{d})$
XM10B	–	–	$\bar{M}_{10}(t - 5\text{d}, 81\text{d})$	$\bar{M}_{10}(t - 5\text{d}, 81\text{d})$
Y10	–	–	–	$Y_{10}(t - 5\text{d})$
Y10B	–	–	–	$\bar{Y}_{10}(t - 5\text{d}, 81\text{d})$
DSTDTC	K	–	–	$\Delta T_C^{Dst}(t)$

Table 2.5 Conversion formulas for the input variables of the CIRA-72, JB-2006 and JB-2008 subroutines.

Variable	*Units*	DTM	DTM-94
DAY	days	$doy(t)$	$doy(t)$
ALTI	km	h	h
HL	h	$lst(t, \phi)$	$lst(t, \phi)$
ALAT	deg	ϕ	–
APHI	deg	–	ϕ
XLON	deg	–	λ
F	10^4 Jy	$F_{10.7}(t - 1\text{d})$	$F_{10.7}(t - 1\text{d})$
FBAR	10^4 Jy	$\bar{F}_{10.7}(t, 81\text{d})$	$\bar{F}_{10.7}(t, 81\text{d})$
AKP	–	$Kp(t - 3\text{h})$	$Kp^i(t - 6\text{h} + \lvert\phi\rvert \cdot 0.033\text{h})$

Table 2.6 Conversion formulas for the input variables of the DTM subroutines.

ap values for the geomagnetic indices instead of the daily Ap values is set, and all model features are switched on.

2.4.2 Model output

All density models return the total density and atmospheric temperature as outputs. In addition, the partial densities or concentrations for each of the atmospheric constituents considered by the models can be retrieved as well, either directly or with only slight modifications to the model source code. Table 2.8 lists which constituents are considered by which models, and gives an approximate validity range for the altitude. The HWM models return zonal (eastward) and meridional (northward) wind speed components relative to a co-rotating atmosphere. The wrapping subroutines convert the model outputs of the various models to the same units.

Variable	*Units*	MSIS and HWM
IYD	days	$1000 \cdot yy(t) + doy(t)$. Note that the value of $yy(t)$ is ignored by the models.
SEC	s	$sec(t)$
ALT	km	h
GLAT	deg	ϕ
GLONG	deg	λ
STL	hours	$lst(t, \lambda)$
F107A	10^4 Jy	$\bar{F}_{10.7}(t, 81\text{d})$
F107	10^4 Jy	$F_{10.7}(t - 1\text{d})$
AP(1)	nT	$Ap(t)$. Note that either the daily Ap in AP(1) or the array of six values in AP(2:7), based on the history of 3-hourly ap indices, is used by the models, depending on a switch setting.
AP(2)	nT	$ap(t)$
AP(3)	nT	$ap(t - 3\text{h})$
AP(4)	nT	$ap(t - 6\text{h})$
AP(5)	nT	$ap(t - 9\text{h})$
AP(6)	nT	$\frac{1}{8}(ap(t - 12\text{h}) + ap(t - 15\text{h}) + \cdots + ap(t - 30\text{h}) + ap(t - 33\text{h}))$
AP(7)	nT	$\frac{1}{8}(ap(t - 36\text{h}) + ap(t - 39\text{h}) + \cdots + ap(t - 54\text{h}) + ap(t - 57\text{h}))$
MASS	–	Mass number for the gas of which the density is to be calculated. Set to 48 for all. Not applicale for HWM models.

Table 2.7 Conversion formulas for the input variables of the MSIS-86, NRLMSISE-00 and HWM subroutines.

Model	*Altitude range*	H	He	O	O^+	N	O_2	N_2	Ar
CIRA-72	110–2000 km	•	•	•			•	•	•
DTM-78	200–1200 km		•	•			•	•	
MSIS-86	90–2000 km	•	•	•		•	•	•	•
DTM-94	200–1400 km	•	•	•		•	•	•	
NRLMSISE-00	0–2000 km	•	•	•	•	•	•	•	•
JB2006	110–2000 km	•	•	•			•	•	•
JB2008	110–2000 km	•	•	•			•	•	•

Table 2.8 Valid altitude range and output of the thermospheric density models.

2.5 Empirical model algorithms

The empirical models considered in this Chapter were all created by fitting a set of parametric equations to an underlying database of observations. The accuracy of the models is therefore dependant on both the strength of the database as well as the ability of the parametric equations to reproduce this data for interpolation and extrapolation. There are considerable differences between the number and complexity of the parametric equations used in the various models. Full details on the model formulations and generation can be found in the references provided in Table 2.3. A few details which are of importance for this study will be provided here however.

2.5.1 Jacchia's CIRA-72 algorithm

In short, the Jacchia models use the exospheric temperature T_∞ as a defining parameter. This temperature is calculated for each location from the solar activity

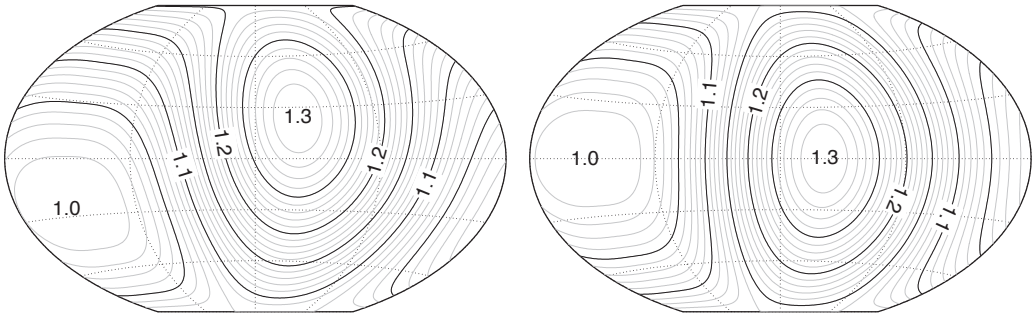

Figure 2.10 The CIRA–72 diurnal function at solstice (*left*) and equinox (*right*). The map is a Winkel-Tripel projection in local solar time versus latitude.

data, in combination with a model of the diurnal variation. Additional corrections are applied, depending on time and altitude. These include the semi-annual variation, a seasonal-latitudinal variation and an additional geomagnetic activity term. The exospheric temperature is then used as input for a temperature profile, which forms the basis for the integration of the diffusion equation.

The first step in the CIRA-72 density computation is the calculation of the culmination point temperature. This temperature, denoted by T_c, is the nighttime minimum of the global exospheric temperature field, when the geomagnetic index K_p is zero. It is a function of the solar activity proxy and its 81-day average, and three empirical constants (α, β and γ):

$$T_c = \alpha + \beta \bar{F}_{10.7} + \gamma(F_{10.7} - \bar{F}_{10.7}) \tag{2.8}$$

T_c is then multiplied with the diurnal variation function $D(t, \phi, lst)$. This function, which does not depend on the solar or geomagnetic activity, defines the shape of the diurnal bulge for the model, as shown in Figure 2.10. It provides a smooth variation between the minimum temperature T_c and a maximum temperature of 1.3 times T_c to the East of the sub-solar point.

The calculation of the local exospheric temperature T_∞ is completed by adding a temperature correction for geomagnetic activity ΔT_G:

$$T_\infty(t, \phi, \lambda) = T_c(t)\ D(t, \phi, \lambda) + \Delta T_G(a_p) \tag{2.9}$$

Jacchia's temperature profile is further defined by a boundary condition of $T = 183$ K and $dT/dh = 0$ at the minimum altitude of 90 km and an inflection point at an altitude of 125 km. The inflection point temperature T_x is a function of T_∞ and four empirical constants (a, b, c and k):

$$T_x(T_\infty, \Delta T_x) = a + bT_\infty + c\ \exp(kT_\infty) \tag{2.10}$$

With the complete temperature profile now in place, the model computes the number density of each individual species by integrating the diffusion equation. Empirical corrections are added for geomagnetic activity variations, the semi-annual variation and seasonal-latitudinal variations.

2.5.2 The DTM and MSIS algorithms

In the DTM and MSIS models, the temperature profile with height is a function of the exospheric temperature. Just as in Jacchia's model, the exospheric temperature is determined from solar and geomagnetic activity proxies and indices. Un-

like Jacchia's models however, the density in the DTM and MSIS models is not derived from a direct integration with altitude over the temperature profile. Instead these models basically contain independent sub-models for the thermospheric temperature T_∞ and number densities n_i of each of the constituents. The index i is used to iterate over each of the atmospheric constituents (H, He, O, etc.), and a set of model coefficients a_j (with $j = 0 \ldots N$) is defined for the temperature and densities of each of the constiuents. We will use the notation and equations from the DTM-94 model [*Berger et al.*, 1998] in this Section. The formulation for the thermospheric part of the MSIS models is largely similar. The modelled thermospheric temperature and concentrations are expressed using a function $G(L)$ of the input parameter vector L as follows:

$$T_\infty = a^0_{T_\infty}(1 + G_{T_\infty}(L)) \tag{2.11}$$

$$n_i(z) = a^0_i \exp(G_i(L)) f_i(z) \tag{2.12}$$

The total density can then be computed from the concentrations by multiplying with the molecular mass m_i of the constituents and summing all constituents.

$$\rho_i = m_i n_i \tag{2.13}$$

$$\rho = \sum_i \rho_i \tag{2.14}$$

The functions $G(L)$ can contain a large number of terms, for instance:

- Polynomial terms with the solar and geomagnetic activity proxies and indices.
- Spherical harmonic terms in geodetic latitude and local solar time.
- Spherical harmonic terms in geomagnetic latitude and geomagnetic local time.
- Periodic terms in day of year and time of day.
- Cross terms of solar and geomagnetic activity with the periodic variations.

The coefficients for these terms have been determined in a least squares adjustment using a large database of density and temperature measurements. There is a large difference between the complexity of the DTM models and that of the MSIS-86 models. This is mainly due to the fact that the MSIS models incorporate much more variations of density and temperature in the lower atmosphere. As an example, the DTM-94 model is defined by 172 non-zero coefficients, while the NRLMSISE-00 model requires approximately 2200.

2.6 Emprical model accuracy

Nearly half a century of thermosphere studies has led to many advances in the understanding of the processes which govern the upper atmosphere (see for example *Kockarts* [2002] and *Marcos et al.* [1997] for an overview). Unfortunately, recent density models, such as NRLMSISE-00, hardly perform better than their predecessors. The upper atmosphere has proven to be extremely dynamic in nature, and models are only able to capture part of the variations.

2.6.1 General limitations

Several reasons for the apparent barrier in accuracy can be identified:

- The $F_{10.7}$ proxy and its mean over several solar rotations are inadequate to represent the complex interactions between the solar EUV and the upper atmosphere. Similarly, the K_p and a_p proxies are planetary indices, based on measurements by a network of mid-latitude observatories. In reality, the spatial and temporal evolution of geomagnetic disturbances on the thermospheric density is very complex. Significant progress has been made on these problems in recent years, with the development of the Jacchia-Bowman models, which introduced the use of multiple improved proxies and indices.
- The data underlying the models does not comprehensively cover the full range of the input variables. The models must therefore extrapolate under some conditions, especially at low and high altitudes and extreme solar and geomagnetic activity. In addition, during the generation of the model, it is not possible to resolve variations which have temporal and spatial characteristics that are beyond the resolution of the data. The current availability of data from CHAMP and GRACE, and in the future of Swarm, are important improvements in this respect.
- The parameterized equations in the models are unable to represent many of the observed variations in the atmosphere. For example, the well-observed year-to-year differences in amplitude and phase of the semi-annual variation are often not taken into account. There are also strong indications of a slow but steady decrease in thermospheric density [*Roble and Dickinson*, 1989; *Emmert et al.*, 2004], possibly caused by increased concentrations of greenhouse gases in the lower atmosphere, which none of the models is currently taking into account. This will likely be improved in future models, as these variations are more easily resolved from the expanding dataset.
- Features such as planetary and gravity waves are unpredictable and short-lived events, that are currently impossible to capture in an empirical model.

2.6.2 Historical and forecast modelling

In the current thermospheric density models, there is no distinction between the use in terms of historical representation of the atmosphere and forecast capabilities. For most of the operational applications of the models, the forecast capabilities are most important. These forecast capabilities are currently completely dependent on the forecasts of the geophysical proxies (such as $F_{10.7}$ and K_p), which will of course be much less accurate than the measured values. In other words, For many purposes, the accuracy of the density models suffers from the fact that the already inadequate proxies are themselves inaccurate predictions.

One of the required proxies in the current models is the 81-day averaged $F_{10.7}$ centred on the epoch in question. Therefore, the extra disadvantage of density predictions does not only come into play when the density at a future epoch is required, but also for one in the past 40 days. In this case, the user of the model can only choose between averaging over partly measured, and partly predicted values, or taking the average over the measured values of the past 81 days. In both cases, the density output from the model will be most likely less accurate than the output when final values are used according to their proper definition.

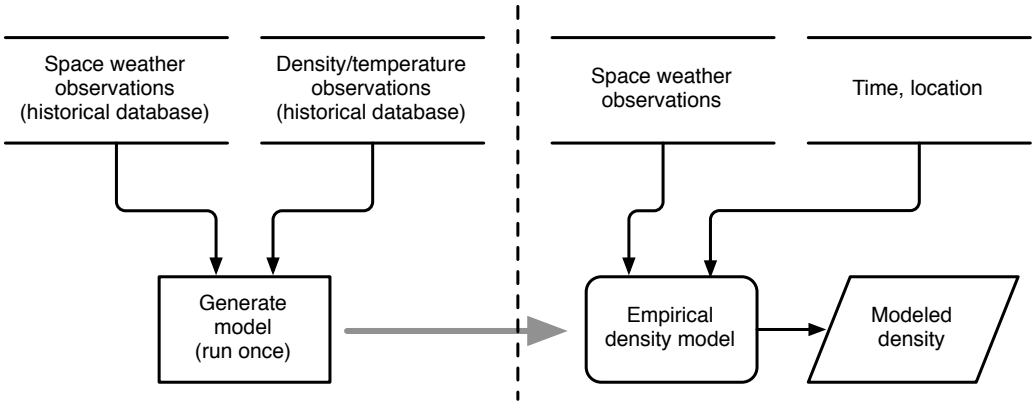

Figure 2.11 Flow chart of traditional empirical density models. The one-time model generation is depicted on the left, the use of the model in applications on the right.

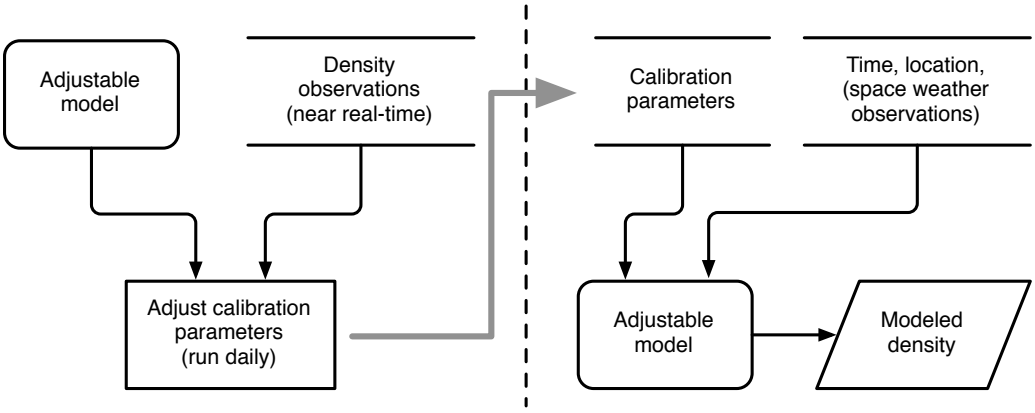

Figure 2.12 Flow chart of a near real-time calibrated density model. The daily model calibration procedure is displayed on the left, the use of the model in applications on the right.

2.7 Calibration of empirical density models

Density calibration involves the calculation of corrections to existing density models using an ongoing analysis of drag accelerations on a number of low perigee satellites and debris objects. The correction parameters, determined from assimilated satellite drag data, can then contribute to, or even replace the role of solar and geomagnetic activity indices, in driving the irregular variations in the density model [*Marcos et al.*, 1998]. For use in operational applications, the estimation of calibration parameters must be done in near real-time, preferably at regular intervals, such as daily or 3-hourly. Figure 2.12 shows the flow chart of this process, to be compared with Figure 2.11. Even though the empirical model that is being adjusted still requires space weather observations as inputs, the calibration process should be able to absorb any errors. The calibration parameters, estimated from satellite drag data, therefore largely replace the role of the space weather observations for the historical representation of the atmospheric state.

Using this method, a significantly better level of accuracy than that of the uncalibrated empirical models can be reached. Two distinct density calibration initiatives were started by scientists in the space tracking community several years ago.

A United States-Russian collaborative density calibration project involved the

estimation of daily scale factors, varying linearly with altitude, which multiply the original model density to better represent orbit data. The analysis was performed for both the Russian GOST model [*Cefola et al.*, 2003] and the US NRLMSISE-00 model [*Yurasov et al.*, 2005*b*]. Trajectory information for the calibration objects was taken from publicly available TLE data. A statistical analysis, investigating the possibility to predict correction parameters into the future has also been performed by this group [*Yurasov et al.*, 2005*a*]. As expected, the accuracy behaviour of predictions depends on the forecasting interval. While near-term results are significantly improved, forecasts over more than a few days can apparently no longer provide additional density accuracy over uncalibrated models.

Another density model calibration project, the United States Air Force Space Command's Dynamic Calibration Atmosphere (DCA) for the High-Accuracy Satellite Drag Model (HASDM) [*Storz et al.*, 2005], uses the more accurate tracking data from the Space Surveillance Network (SSN), to adjust simultaneously the trajectories of around 75-80 calibration objects with spherical harmonic expansions of two temperature parameters from the Jacchia-70 thermosphere model [*Casali and Barker*, 2002]. Within Jacchia's models, these two temperatures define the vertical density profile completely. The spherical harmonic expansion allows corrections to the modelling of the diurnal variation. HASDM also includes a method for predicting the corrections three days into the future as a function of solar and geomagnetic indices. A follow-on project, named Sapphire Dragon, is aimed at improving the prediction capabilities of HASDM through a series of enhancements, including an increase in the number of calibration objects and a more sophisticated use of various space weather proxies [*Bowman*, personal communication, 2006]. Unfortunately, the resulting calibrated model and the underlying precise SSN tracking data are not made publicly available. However, the HASDM model densities, computed along the CHAMP and GRACE tracks by Bruce Bowman, were kindly made available for evaluation (see Section 4.8.5).

Part of the work done for the current project involves density model calibration using satellite drag data. The NRTDM software [*Doornbos*, 2006], which was initially developed for ESA/ESOC, for use with TLE-derived density data, has been modified to incorporate accelerometer-derived densities. This will be described in detail in Chapter 10.

2.8 Physical models

Physical models (also called theoretical models or numerical models) are based on the fundamental physical equations that govern the atmosphere ionosphere system. Compared to empirical models, physical models are very computationally intensive, and require more expert knowledge to run. In addition, the finest spatial and time-dependent features of the energetic and momentum inputs are still difficult to describe on a global scale. These energy and momentum inputs are largest and most prevalent at high latitudes during periods of high geomagnetic activity, and are due to energetic particle precipitation, Joule heating from ionospheric currents and Lorentz forcing. The spatial resolution of the fully global theoretical models is also still challenged by computational limitations. As a result, there are still limitations regarding the accuracy of the physical models, which need to be understood when interpreting their output. One means of getting around the limitation of resolution is to use a "Nested Grid" approach. Under some conditions, it is possible to describe the magnetospheric inputs in

high resolution for example using specific satellite overpasses of a ground-based network of suitable optical and radar instrumentation. The global physical model keeps the boundary conditions "honest", while the Nested Grid Model handles the high resolution computations within a limited and well-described region, perhaps several hundred km in 2-D extent.

This tends to make the physical models less suitable for routine applications in orbit determination, and more suitable for detailed scientific investigations of the thermosphere-ionosphere system. However, physical models can describe the detailed spatial and temporal changes of thermospheric density, temperature, composition and winds during periods of elevated geomagnetic activity in a way that cannot as yet be derived from empirical models.

Physical models may be particularly valuable in terms of providing a first-order estimate of thermospheric winds, particularly at high geomagnetic latitudes, and during periods of elevated geomagnetic activity.

2.8.1 Development of physical models

In the early 1980s it was realized that to obtain a self-consistent description of solar-related processes that heated the global thermosphere and created most of the global ionosphere, it would be essential to develop fully-coupled physical/theoretical models of the thermosphere-ionosphere system. Early tests with these models confirmed the strong interactions between the ionosphere and thermosphere. Of additional importance was their success in evaluation of the then newly-available global data sets from Projects such as the NASA Dynamics Explorer and UARS Missions. Many of the critical features of the thermospheric response to the highly dynamic processes occurring during periods of high geomagnetic activity can only be simulated by means of the fully-coupled thermosphere – ionosphere physical/theoretical models.

Its not only ionosphere-thermosphere (I-T) models which are of interest here. They marked the beginning of this kind of studies in the early 1980s with the development of thermospheric general circulation models (TGCMs) such as those by the UCL [*Fuller-Rowell and Rees*, 1980, 1983] and NCAR [*Dickinson et al.*, 1981, 1984]. These early models are, however, rather simple, considering the state-of-art of global modelling which developed during the last two decades.

The first step toward more complex models was to include the energetic, chemical and dynamical interactions between the ionosphere and thermosphere, within the TIGCMs (thermosphere ionosphere general circulation models), e.g., *Fuller-Rowell et al.* [1987, 1988], *Roble et al.* [1988]. This was followed by the inclusion of the plasmasphere (e.g. *Namgaladze et al.* [1988, 1991]).

Because large-scale electrodynamics play an important role in the neutral and plasma dynamics of the upper atmosphere (not only at high latitudes), further developments of these global models resulted in TIEGCMs, i.e. they include the interplay with the plasmasphere, magnetosphere and the electrodynamics of the whole system [*Richmond et al.*, 1992; *Namgaladze et al.*, 1994; *Peymirat et al.*, 1998].

2.8.2 WACCM

One of the current theoretical models that is widely used within the scientific community is the Whole Atmosphere Community Climate Model (WACCM). It has been developed as an interdisciplinary project, bringing together physical components or models from three ESSL divisions of NCAR. These include:

- The physics and dynamics of the lower atmosphere;
- The chemistry of the middle and upper atmosphere;
- The physical processes of the upper atmosphere.

As far as the thermosphere and exospheric regions are concerned, WACCM can be considered to be the direct descendent of the TIEGCM's developed by R.G. Roble and colleagues, hosted at NCAR, Boulder. The main issues in terms of the changes incorporated are the ways in which the interactions with the behaviour of the lower and middle regions of the atmosphere are taken into account. In particular, tidal variations caused by solar heating of water vapour and ozone within the troposphere and stratosphere are better accounted for, as are chemical, thermal and dynamical changes within the mesosphere.

The scientific goal of WACCM is to study the couplings (chemical, dynamical and radiative) among atmospheric layers, from the near surface to the the exosphere [*Roble*, 2000]. From the first version of WACCM, which did not include interactive chemistry [*Sassi et al.*, 2002], through an intermediate version with limited interactive chemistry [*Sassi et al.*, 2005], to the current, fully interactive model [*Garcia et al.*, 2007], the project has grown from an in-house effort to a small community of users and developers, both inside NCAR and from universities, government laboratories and non-profit research groups.

2.8.3 CTIPe

The Coupled Thermosphere Ionosphere Plasmasphere Electrodynamics (CTIPe) model is a global, three-dimensional, time-dependent, non-linear code that is a union of three physical components. The first is a global, non-linear, time-dependent neutral thermosphere code developed by *Fuller-Rowell and Rees* [1980, 1983]. The second is a mid- and high-latitude ionosphere convection model developed by *Quegan et al.* [1982]. These first two components were initially coupled self-consistently and are known as the Coupled Thermosphere-Ionosphere Model (CTIM) [*Fuller-Rowell et al.*, 1996]. CTIM was further extended by including a third component, a plasmasphere and low latitude ionosphere [*Millward et al.*, 1996], to produce CTIP. Later the electrodynamics was solved self-consistently with the neutral dynamics and plasma components.

The thermospheric code simulates the time-dependent structure of the wind vector, temperature and density of the neutral thermosphere by numerically solving the non-linear, first-principles, equations of momentum, energy and continuity. The global atmosphere is divided into a series of elements in geographic latitude, longitude and pressure. Each grid point rotates with the Earth to define a non-inertial frame of reference in a spherical polar coordinate system. The latitude resolution is 2°, longitude resolution 18°, and each longitude slice sweeps through local time with a one-minute time step. In the vertical direction the atmosphere is divided into 15 levels in logarithm of pressure from a lower boundary of 1 Pa at 80 km altitude.

A time-dependent mean mass equation was incorporated into the model by *Fuller-Rowell and Rees* [1983]. This formalism assumed the upper atmosphere could be approximated by two species, atomic oxygen and the sum of molecular nitrogen and oxygen. Later the major species composition was improved to include solution of the three major species, O, O_2 and N_2, including chemistry, transport and the mutual diffusion between the species. Using a combination of

the generalized diffusion equation [*Chapman and Cowling*, 1970] and the continuity equations, the change in mass mixing ratio of the three species is evaluated self-consistently with the wind and temperature fields. Allowance is made for mutual molecular diffusion, horizontal and vertical advection, turbulent mixing vertically and horizontally, and production and loss mechanisms. The time dependent variables of southward and eastward wind, total energy density, and concentrations of O, O_2 and N_2 are evaluated at each grid point by an explicit time-stepping numerical technique. After each iteration, the vertical wind is derived, together with temperature, density, and heights of pressure surfaces. The parameters can be interpolated to fixed heights for comparison with experimental data.

The equations for the neutral thermosphere are solved self-consistently with a high latitude ionosphere convection model [*Quegan et al.*, 1982]. Traditionally, ionosphere models are evaluated in a Lagrangian system, where the evolution of ion density and temperature of parcels of plasma are computed as they are traced along their convection paths. In the high latitude ionosphere model the Lagrangian frame has been modified to be more compatible with the Eulerian frame by implementing a semi-Lagrangian technique [*Fuller-Rowell et al.*, 1987, 1988]. Adoption of a rotating frame of reference for the ionosphere implicitly includes the "co-rotation potential". Transport under the influence of the magnetospheric electric field is explicitly treated, assuming $E \times B$ drifts and collisions with the neutral particles. The atomic ions H^+ and O^+, and ion temperature are evaluated over the height range from 100 to 10,000 km, including horizontal transport, vertical diffusion and the ion-ion and ion-neutral chemical processes. Below 400 km the additional contribution from the molecular ion species N_2^+, O_2^+ and NO^+, and the atomic ion N^+ are included.

The model of the Earth's mid- and low-latitude plasmasphere and ionosphere is based on the code of *Bailey et al.* [1997]. The densities, temperatures, and velocities are calculated for H^+ and O^+ along closed flux-tubes with geometry defined by the tilted dipole approximation to the Earth's magnetic field. The model solves the coupled equations of continuity, momentum, and energy balance along the flux-tubes to yield ion density, field-aligned velocity, and temperature, including the effects of inter-hemispheric coupling. The plasmasphere component of the CTIPe model also adopts an Eulerian framework in which individual flux-tubes are fixed in space. This represents a modification to the original *Bailey et al.* [1997] code that used the more conventional Lagrangian scheme, where individual flux-tubes are followed as they drift under the influence of the electric field. The Eulerian fixed frame, where cross flux tube plasma transport is accommodated by advection, has been adopted to enable storm-time low latitude electric fields to be used without incurring the problem of flux tubes not returning to their initial position after a full diurnal cycle. To produce a global model of the ionosphere, 1400 individual flux-tubes are computed concurrently and defined by magnetic longitude, i.e., constant along a tube. The L value determines the equatorial crossing height relative to the centre of the dipole in units of the Earth's radius. The plasma moves across flux-tubes under the effect of electric fields where the velocity is assumed to be completely decoupled from the field aligned velocities of the ions, which are the result of winds, diffusion, and space-charge electric fields. The mid and low latitude electric fields are computed self-consistently within the model using the code of *Richmond and Roble* [1987]. The temperatures of the two ion species are also solved by the coupled energy balance equations. A reliable and

reasonably realistic ionosphere is important for the calculation of neutral winds because of the ion drag process. At high latitudes ion drag acts more as a driver, elsewhere more as a drag on the neutral winds.

The magnetosphere input is based on the statistical models of auroral precipitation and electric fields described by *Fuller-Rowell and Evans* [1987] and *Weimer* [2005], respectively. The auroral precipitation is keyed to the hemispheric power index (PI), based on the TIROS/NOAA auroral particle measurements, and has been available since the mid 1970s. The PI index runs from 1 to 10 to cover very quiet to storm levels of geomagnetic activity; the relationship between PI and Kp can be found in *Foster et al.* [1986]. The Weimer electric field model is keyed to the solar wind parameters impinging the Earths magnetosphere. The input drivers include the magnitude of the interplanetary magnetic field (IMF) in the Y-Z plane, together with the velocity of the solar wind.

The (2,2), (2,3), (2,4), (2,5), and (1,1) propagating tidal modes are imposed at 80 km altitude [*Fuller-Rowell et al.*, 1991] with a prescribed amplitude and phase. Ionization rates from the EUV flux are evaluated from the *Hinteregger et al.* [1981] reference spectra for high and low solar activity based on the Atmospheric Explorer (AE) measurements.

The latest version of the CTIPE model has very recently been adapted, to better follow significant atmospheric changes during geomagnetic storms such as the creation, transport and dissipation of Nitric Oxide. NO plays a critical role in the ionosphere, and it also has a very important role in the cooling of the thermosphere following major geomagnetic disturbances. CTIPe additionally includes atomic Hydrogen as an additional species. This may be significant during periods of low solar and geomagnetic activity, as have occurred since 2004 / 2005. Results from this very latest version have only been available since January 20th 2009.

Description of the CTIPe data format

It was possible to obtain simulations using CTIPe that related directly to periods of high interest for this study. The CTIPe Model Output Data format provides information on a large number of atmospheric and ionospheric parameter at a function of 15 pressure levels, pressure level 1 being close to 80 km altitude, while pressure level 15 is at or about the exobase (400 800 km depending on solar and geomagnetic activity. The computational time resolution within the model is 60 seconds (for most simulations). The output is normally provided at steps of 1.2 hours, or 20 steps per 24 hours of UT. The model has a resolution of 18 degrees in longitude and 2 degrees in latitude.

Interpolation/extrapolation to the CHAMP and GRACE trajectories

Information on the satellite location versus time is provided as an input file. A programme is then used to interpolate in the horizontal plane between the model grid points in spatial coordinates, and between the time-steps of the model output to trace the horizontal and temporal locations of the satellite.

Since the data are sensitive functions of pressure level or altitude, a further interpolation / extrapolation routine is applied to compute the information, such as wind velocity, density or temperature etc. at the actual altitude of the satellite (again as a function of space and time). Interpolation is used when the satellite is below pressure level 15, while a simple exponential extrapolation is use when the

satellite is above pressure level 15. This is based (when appropriate) on knowing that of all the important atmospheric parameters, only density varies with the altitude, following an exponential variation in terms of the density scale height (which can itself be computed from atmospheric parameters computed by the model itself. Wind and temperature have only a small variation with altitude above 300 km, due to the high dynamic viscosity of the upper thermosphere and the fact that the mean free path is approaching the scale height near the exobase altitude (near pressure level 15).

The Primary CTIPe output variables are:

- meridional neutral wind
- zonal neutral wind
- vertical neutral wind
- neutral temperature
- neutral density

These are provided as a function of the satellite:

- date/time
- altitude
- latitude
- longitude

These four parameters are being taken from the satellite trajectory input file and are linearly interpolated in height from the data grids.

2.9 Selection of models for use in the study

The NRLMSISE-00 model has been selected for providing the temperature and composition inputs that are required for aerodynamic model calculations. The HWM-93 model was initially selected for providing a priori information on the horizontal winds, and it is used in all of the GRACE-derived results presented in this report. During the course of the project, the HWM07 model became available, and this model has replaced HWM-93 in the latest reprocessing of the CHAMP accelerometer data. Wherever results are presented for which the use of these models is relevant, such as in Chapter 9, it will be specifically stated which model was used.

Other models, such as the Jacchia-Bowman and CTIPe models, were extensively used during the course of this study for comparison and evaluation purposes.

Chapter 3

CHAMP and GRACE missions, instruments and data products

3.1 Satellites and instruments

CHAMP (CHAllenging Minisatellite Payload) is a German small satellite mission for geoscientific and atmospheric research and applications, managed by GFZ. It was launched on July 15, 2000, into a near-circular orbit with 87.3° inclination at an altitude of ∼460 km [*Reigber et al.*, 2002]. Its orbital altitude gradually decayed to ∼400 km in 2003 and ∼350 km in 2008. It is expected that CHAMP will provide highly valuable data for another 2 years from low altitude. CHAMP performs simultaneously highly precise gravity and magnetic field measurements together with plasma density and GPS tracking methods like atmospheric limb sounding and is therefore equipped with magnetometers, an accelerometer, star sensors, GPS receivers, a laser retro reflector, a planar Langmuir probe (PLP), and DIDM, the digital ion drift meter (see Figure 3.1).

GRACE (Gravity Recovery and Climate Experiment) is a joint project between the National Aeronautics and Space Administration (NASA) and the Deutsches Zentrum für Luft- und Raumfahrt (DLR) [*Tapley et al.*, 2004]. This pair of identical spacecraft were launched on March 17, 2002, into very close near-circular polar orbits at initial altitudes of ∼500 km and an inclination of ≈89°. The GRACE spacecrafts are similarly equipped and are of similar design with respect to the main S/C body like CHAMP, but without DIDM/PLP for plasma measurements and without the large frontal boom because magnetic measurements are not part of the GRACE mission (see Figure 3.2). GRACE has succeeded the CHAMP mission in the area of Earth gravity field measurements; like CHAMP they perform highly precise measurements of attitude and non-gravitational forces with star cameras and accelerometers. The increase in accuracy of gravity field measurements has been achieved by utilizing two satellites following each other on the same orbital track. These satellites are interconnected by a K-band microwave link to measure the exact separation distance and its rate of change to an accuracy of better than 1 μm/s.

The position and velocity of both CHAMP and GRACE satellites are measured with high precision using onboard GPS antennae. The precise attitude is measured with several Advanced Stellar Compasses (ASCs) onboard the S/C. As for the CHAMP satellite, they are installed both at the boom near the mag-

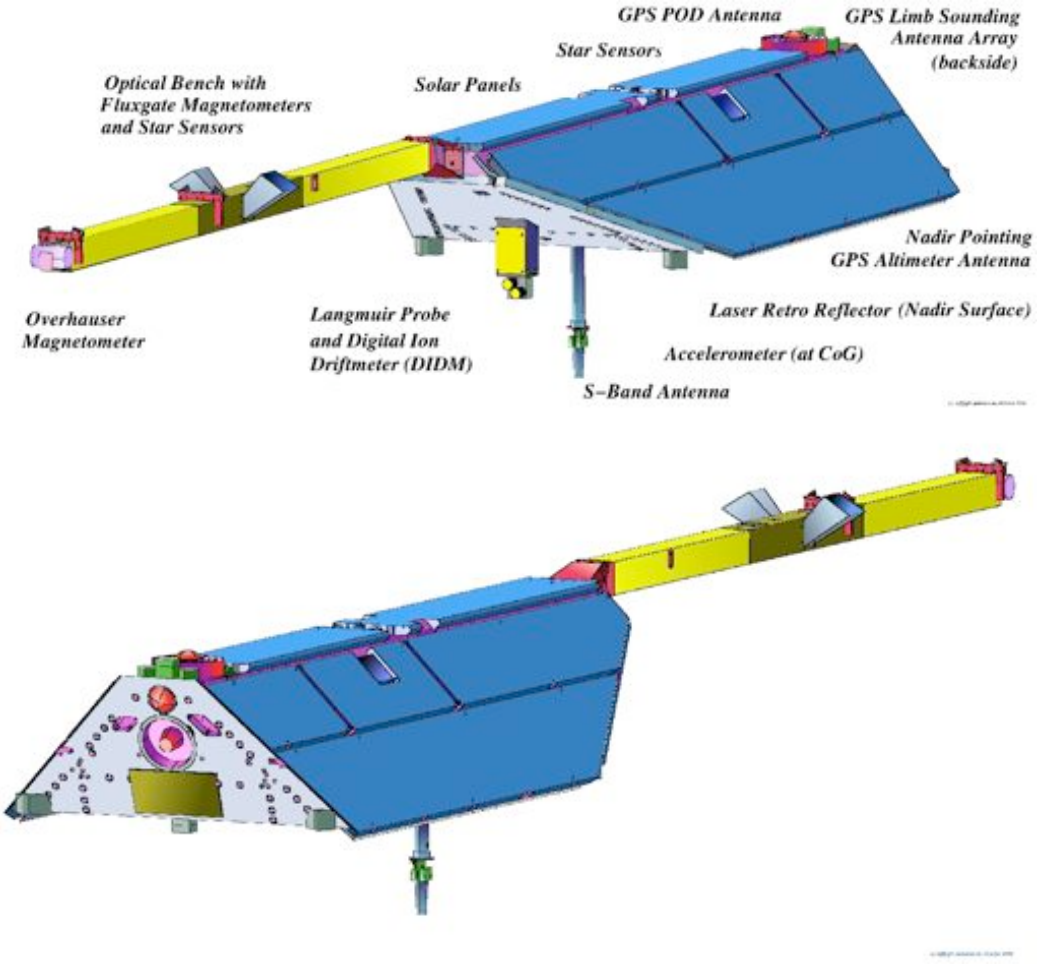

Figure 3.1 Schematic view of the CHAMP satellite from two perspectives. In the upper panel the scientific instruments onboard CHAMP are listed with their approximate positioning. The accelerometer (indicated at bottom) is located at the Center of Gravity (CoG) in the main body's interior.

netometer and at the S/C main body, rigidly connected to the three component STAR accelerometer.

The Reference Systems, Transformations and Standards used for the CHAMP mission are documented in the official GFZ documentation **CH-GFZ-RS-002**, which can be found under the web-address:

$\Longrightarrow$ http://www.gfz-potsdam.de/pb1/op/champ/more/index_MORE.html

with direct access to the pdf-file mentioned via the link:

$\Longrightarrow$ http://www.gfz-potsdam.de/pb1/op/champ/docs_CHAMP/...

CH-GFZ-RS-002.PDF.

3.1.1 STAR accelerometer (ACC)

The STAR (Spatial Triaxial Accelerometer for Research) sensor is provided by the Centre National d'Etudes Spatiales (CNES) and was manufactured by the Office National d'Etudes et de Recherches Aerospatials (ONERA). It serves for measuring the non-gravitational accelerations such as air drag, Earth albedo and solar radiation acting on the CHAMP satellite. The STAR accelerometer uses the

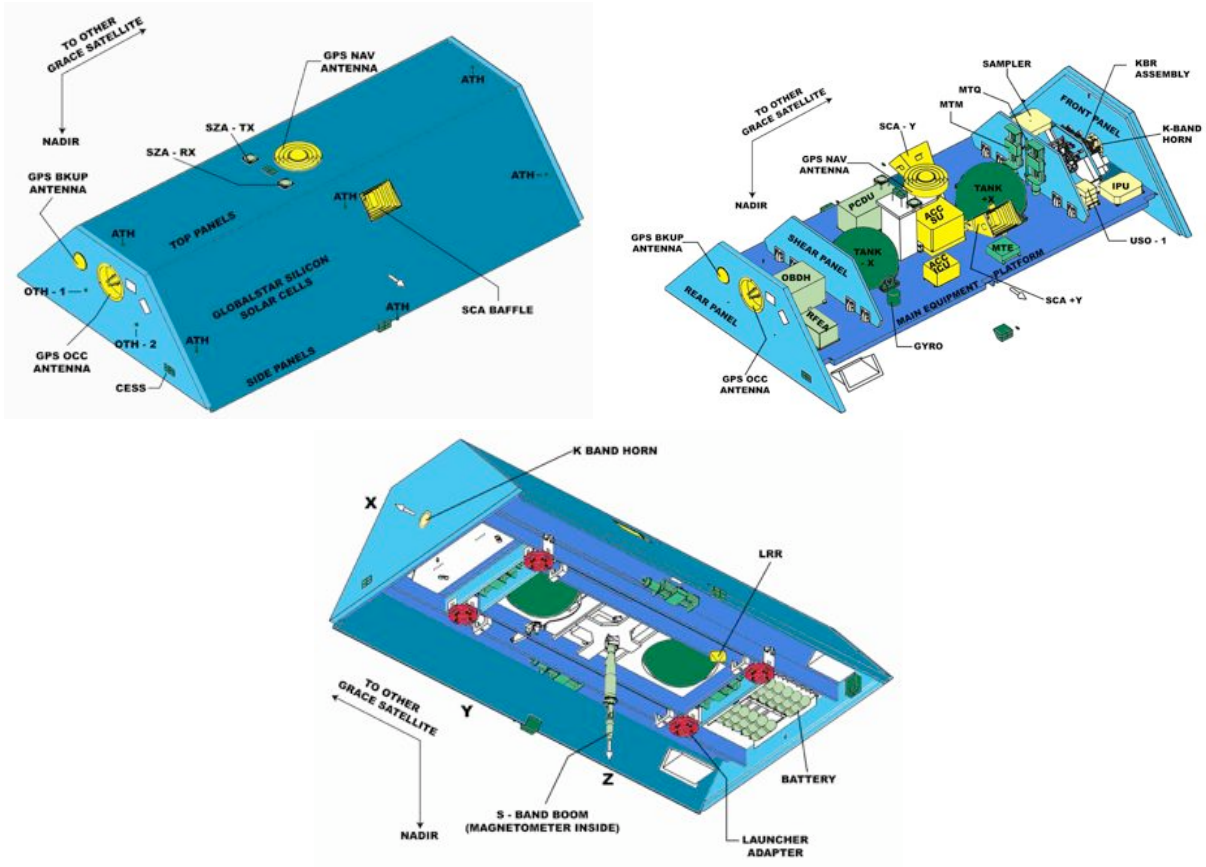

Figure 3.2 Schematic views of a GRACE satellite. The top-right and bottom views show the satellite with some of the exterior panels removed, to show the internal configuration.

basic principle of an electrostatic micro-accelerometer: a proof-mass is floating freely inside a cage supported by an electrostatic suspension. The cavity walls are equipped with electrodes thus controlling the motion (both translation and rotation) of the test body by electrostatic forces.

The STAR accelerometer sensor axes are defined via the surface normals of the parallelepipedic proof-mass as shown in Table 3.1. The origin of the measurement frame is the centre of the proof-mass. The orthogonality of the axes of this frame is better than $2.5\,10^{-5}$ rad. Due to some failure within the accelerometer onboard CHAMP, the X-axis sensor (parallel to the Z-axis of the S/C body system) which is less sensitive than the sensors in the two other spatial direction, cannot sensibly be used for the data interpretation. Consequently, two of the three angular acceleration measurements are of no use as well.

The SuperSTAR accelerometer onboard the GRACE satellites is also manufactured by ONERA/CNES (France) and represents a modified version of the STAR accelerometer that operates onboard the CHAMP satellite. As for the GRACE accelerometer instruments, malfunctions of that kind are not known. Their measurements are supposed to be reliable and their sensitivities are listed in Table 3.2 according to *Frommknecht et al.* [2003]. They are high-sensitive (better than CHAMP) for the along-track and radial axes, but less sensitive in the cross-track direction.

Component	Coordinate system reference	Sensitivity	Comments
X (STAR)	parallel to S/C Z-axis	$< 3 \cdot 10^{-8} m\,s^{-2}$	affected axis, NOT recommended
Y (STAR)	parallel to S/C X-axis	$< 3 \cdot 10^{-9} m\,s^{-2}$	high sensitive axis
Z (STAR)	parallel to S/C Y-axis	$< 3 \cdot 10^{-9} m\,s^{-2}$	high sensitive axis
ϕ (phi)	rotation about X-axis of acc.	$< 1 \cdot 10^{-7} rad\,s^{-2}$	highly sensitive
θ (theta)	rotation about Y-axis of acc.	$< 5 \cdot 10^{-7} rad\,s^{-2}$	NOT useable
ψ (psi)	rotation about Z-axis of acc.	$< 5 \cdot 10^{-7} rad\,s^{-2}$	NOT useable

Table 3.1 Characteristics of the STAR accelerometer sensor onboard CHAMP for both the linear (upper three lines) and angular (lower three lines) accelerations.

Component	Coordinate system reference	Sensitivity	Comments
X (STAR)	parallel to S/C Z-axis	$< 1 \cdot 10^{-10} m\,s^{-2}$	high sensitive axis
Y (STAR)	parallel to S/C X-axis	$< 1 \cdot 10^{-10} m\,s^{-2}$	high sensitive axis
Z (STAR)	parallel to S/C Y-axis	$< 1 \cdot 10^{-9} m\,s^{-2}$	less sensitive axis

Table 3.2 Characteristics of the SuperSTAR accelerometer sensors onboard the GRACE satellites for the linear accelerations along the three S/C axes.

3.1.2 Advanced Stellar Compasses (ASCs)

The Advanced Stellar Compass (ASC) has been developed and fabricated under contract by the DTU (Technical University of Denmark, Lyngby). The design of this star imager is based on a new development that was flown on the Ørsted satellite. On CHAMP, there are two ASC systems each consisting of two Camera Head Units (CHU) and a common Data Processing Unit (DPU). One ASC is part of the magnetometry optical bench unit on the boom and the other provides high precision attitude information for the instruments fixed to the spacecraft body. Additionally the ASCs serve as sensors for the satellite attitude control system which consists of three magneto-torquers and of a set of 12 cold gas thrusters, pointing pairwise in the six principle directions. The S/C attitude is kept within a tolerance range of $\pm 2^\circ$ for all three axes.

3.1.3 GPS receiver

The GPS Receiver TRSR-2 onboard CHAMP is provided by NASA and manufactured at NASA's Jet Propulsion Laboratories (JPL). A zenith mounted antenna on a choke ring on the top rear side of CHAMP is mainly used for the Precise Orbit Determination (POD). This is the so-called tracking mode, which is the default mode of this zenith mounted GPS receiver.

The low orbiting CHAMP satellite and each spacecraft of the high orbiting GPS satellite configuration establish a so-called high-low satellite-to-satellite (SST) link. Each of the GPS S/C is transmitting modulated L1 and L2 signals which the TSRS-2 receiver onboard of CHAMP acquires for a maximum of 12 satellites at the same time. From these signals the orbiting receiver generates at a frequency of 0.1 Hz pseudo-ranges and carrier phases for all satellites which were in lock at this time instant. By using pseudo-ranges from at least 4 different GPS S/C with known ephemeris at the same time, both the three-dimensional coordinates of the CHAMP receiver and their respective change with time can be

solved for, thus a navigation solution is obtained. The accuracy of this solution depends on the availability of the classified P-code inside the receiver and the satellite constellation used for coordinate determination and can range down to a few meters after post-processing. With the less precise but unclassified C/A-code an accuracy of several tens of meters is still obtainable after post-processing.

There are two other GPS receivers for different tasks onboard CHAMP. One on the rear side is used for the observation of radio occultation of GPS S/C by approaching the Earth's limb. For this purpose the GPS signal of the satellite to be occulted is sampled with considerably higher frequency than usual (50 Hz instead of 0.1 Hz) during crossing the lower layers of the Earth atmosphere in comparison to a non-occulted GPS S/C. A downward positioned GPS antenna on the bottom side of CHAMP is used to collect specular reflections of GPS signals from the ocean's surface. Knowing the precise position of the transmitting GPS S/C and of the CHAMP satellite as well, quasi-altimetry measurements are carried out.

On the GRACE satellites, GPS "TurboRogue Space Receiver" assemblies provided by JPL are used which perform the POD with cm-accuracy. The GPS receiver assembly is fully autonomous: initialisation, GPS satellite acquisition and signal processing are performed automatically once the instrument is switched on.

3.2 Data sets

Generally, data of both (CHAMP and GRACE) missions are accessible and available via the **Information System and Data Center (ISDC)**, hosted by the Helmholtz Centre Potsdam, Deutsches GeoForschungsZentrum (GFZ), Germany:

$\Longrightarrow$ http://isdc.gfz-potsdam.de/.

3.2.1 CHAMP input data products

Accelerometer and attitude data

The preprocessing of the accelerometer and attitude data of CHAMP is described in the publication of *Förste and Choi* [2005]. The preprocessing comprises several correction steps, filterings, smoothing of data and outlier/spike identification and elimination. The intervals of thruster pulses are cut out, including the three subsequent seconds of data [*Förste and Choi*, 2005].

The original CHAMP accelerometer sampling rate of 1 Hz is then transformed by smoothing and averaging of the cleaned data to a data set with 0.1 Hz sampling rate (10 sec resolution). These time series of CHAMP accelerometer and attitude data are stored as 1-day packages (dat-files as ASCII) in the level-2 data product **"CH-OG-2-ACC"** that is described in the following documentation:
$\Longrightarrow$ http://www.gfz-potsdam.de/pb1/op/champ/docs_CHAMP/CH-GFZ-RS-001.PDF.

The naming convention of this level-2 product is **"CH-OG-2-ACC+yyyy_ddd_hh.vv.dat"** with:

yyyy	as the 4-digit year
ddd	as the 3-digit day of year count (DOY)
hh	as the 2-digit hour of the day for data start, and

vv as the 2-digit version number of the data set

Version numbers 09, 10, 11, and 12 are the most recent, actually valid updates with the highest number as the best choice. The data files contain the following parameters:

- STAR Accelerometer Data for both linear and angular accelerations; the linear acceleration components are give in the Spacecraft Body Fixed System (S/C), i.e. with X aligned with the long side main axis parallel to the boom with the nominal attitude in flight direction, Z points toward the S/C bottom side or nominally toward Nadir, and Y completes the right-hand system
- attitude data of the Body Advanced Stellar Compass (ASC) are given as quaternions with respect to the Conventional Inertial System (cis) according to the format description; this inertial system is probably better known as the International Celestial Reference System (ICRS) or International Celestial Reference Frame (ICRF)
- thruster firing events with time, duration and thruster number
- S/C total mass and cold gas mass in $\sim$ 4 hr intervals, given in the header of each file
- acceleration calibration parameters (bias and scale factor for each component) with the following definition: Corrected_measurement = (Uncorrected_measurement - Bias) $\times$ Scale-factor

Satellite mass

As for CHAMP, the information about the S/C mass and the cold gass mass used for the thrusters are given within the header lines of the data product which was described in the previous Section 3.2.1. The difference between both masses is constant within computer precision; therefore one can deduce the "empty S/C" mass of CHAMP to 488.893 kg.

Orbit data

A documentation about the CHAMP orbital data formats is given in:
CH-GFZ-FD-002.pdf, issue date 2002-06-28, which is entitled:
"Format Description, The CHAMP orbit format" by R. König.
Download from:
http://www.gfz-potsdam.de/pb1/op/champ/docs_CHAMP/

There are three different orbit data products:

- Level-4 data product: CH-OG-4-PSO post-processed science orbits
- Level-3 data product: CH-OG-3-PDO predicted science orbits or
- Level-3 data product: CH-OG-3-RSO rapid science orbits.

They have the usual naming convention as, e.g.,
CH-OG-3-RSO+yyyy_ddd_hh.vv.dat.

The RSOs are most recommended; they are produced in packages of two per day, comprising each 14 hrs from 10 pm/am to 12 am/pm.

GPS data

GPS Ground tracking data are given in the files named as, e.g., **CH-OG-1-GPS-10S** for 10 sec sampling rates (alternatively for 30 sec samples "...-30S"). The data files comprise 1 hour per station; the data are given in the so-called "Receiver Independent Exchange Format" (Rinex), Version 2.20, which is an exchange format developed by the international geodetic user community.

3.2.2 GRACE input data products

Accelerometer and attitude data

As for the GRACE satellites (A & B), the information about data products are given in the "GRACE Level 1B Data Product User Handbook". The corresponding accelerometer are "level-1B" products which are stored in data files like **"GA-OG-1B-ACCDAT+JPL-ACC1B_yyyy-mm-dd_S_vv.ext"** with the following naming conventions:

GA...	product identification label, where "ACC1B" stands for accelerometer data of level 1B
yyyy	as the 4-digit year
mm	as the 2-digit month of the year
dd	as the 2-digit day of the month
S	as GRACE satellite identifier, i.e. A, B, or X = combined product of GRACE A and B
vv	as the 2-digit version number of the data set
ext	file extension indicating binary (dat) or ASCII (asc) files

The GRACE-A/B Level-1B star camera data are stored in the files named **"GA-OG-1B-SCAATT-..."** and **"GB-OG-1B-SCAATT-..."** for GRACE-A and GRACE-B, respectively. These are preprocessed and calibrated star camera quaternion data edited and decimated from instrument high-rate (1 sec) to low-rate (5 sec) sampling rates for science use. There are one file per day, given in the level-1 data format.

Satellite mass

As for the GRACE satellites, there are independent data products of level 1B which describe the mass evolution of the S/C with an resolution of 60 sec in data files which comprise one day each:
"GA-OG-1B-MASDAT+FFF-MAS1B_yyyy-mm-dd_S_vv.ext" or **"GB-..."**
The naming convention of these files is as follows:

GA... or GB...	product identification label, where "MAS1B" stands for S/C total mass data of level 1B
GA/GB	product derived from GRACE-A or GRACE-B data
FFF	processing facility ('JPL' or 'GFZ')
yyyy	as the 4-digit year
mm	as the 2-digit month of the year
dd	as the 2-digit day of the month
S	as GRACE satellite identifier, i.e. A, B, or X = combined product of GRACE A and B

vv	as the 2-digit version number of the data set (product release)
ext	file extension indicating binary (dat) or ASCII (asc) files

Orbit data

The orbital data of both GRACE satellites can be retrieved from ISDC level-1 files named **"GA-OG-1B-NAVSOL-..."** and **"GB-OG-1B-NAVSOL-..'** for GRACE-A and GRACE-B, respectively. These GPS navigation data are edited and decimated from instrument high-rate to low-rate (30 sec) samples for science use (1 file per day, level-1 format).

GPS data

As for CHAMP orbit tracking (cf. section 3.2.1), there are also GPS ground tracking data for both GRACE satellites in files named as, e.g., **GA-OG-1B-GPSDAT** for GRACE-A ("GB-..." accordingly for GRACE-B).

These are preprocessed and calibrated GPS code and phase tracking data edited and decimated from the instrument's high-rate to low-rate (10 sec) samples for science use. The files comprise one file per day and per station.

Chapter 4
Data preprocessing

The data preprocessing is required to prepare the satellite data products for the density and wind processing. The distinction between preprocessing and processing in this case is rather arbitrary. Preprocessing is defined here as all the actions performed with the data that are not dependent on the inputs from the calibration work. These include:

- Retrieval from the ISDC (GFZ Information Systems and Data Centre) of CHAMP level 1/2/3 and GRACE level 1B input data.
- Conversion of the ISDC data files to the project's data storage system.
- Conversion to different reference frames and coordinate systems.
- Data-screening, editing and interpolation of data gaps.
- Computation of density and wind model outputs at the satellite orbit locations.

In addition, the following tasks which were done to support both the preprocessing and processing will be discussed in this chapter as well:

- Development of software for data storage and retrieval
- Development of a web interface for distribution of data and metadata to users.

4.1 Data product storage and metadata

The data storage and retrieval system, and many of the processing subroutines, are based on the software library developed for the ESA/ESOC Near Real Time Density Model (NRTDM) project [*Doornbos*, 2006].

The data storage part of the NRTDM software has been expanded in order to be able to store metadata, which is available for display on the project website and which helps automate data conversions. The following sections will describe the storage system and data retrieval in more detail. A preprocessing flowchart is provided in Figure 4.1 for reference.

4.1.1 Product naming convention

Each of the data fields in the storage system has a unique identifier, consisting of a category, a product name, and a field number.

The category generally refers to the satellite, which is abbreviated (CH for CHAMP, GA and GB for GRACE-A and -B), and might also include information

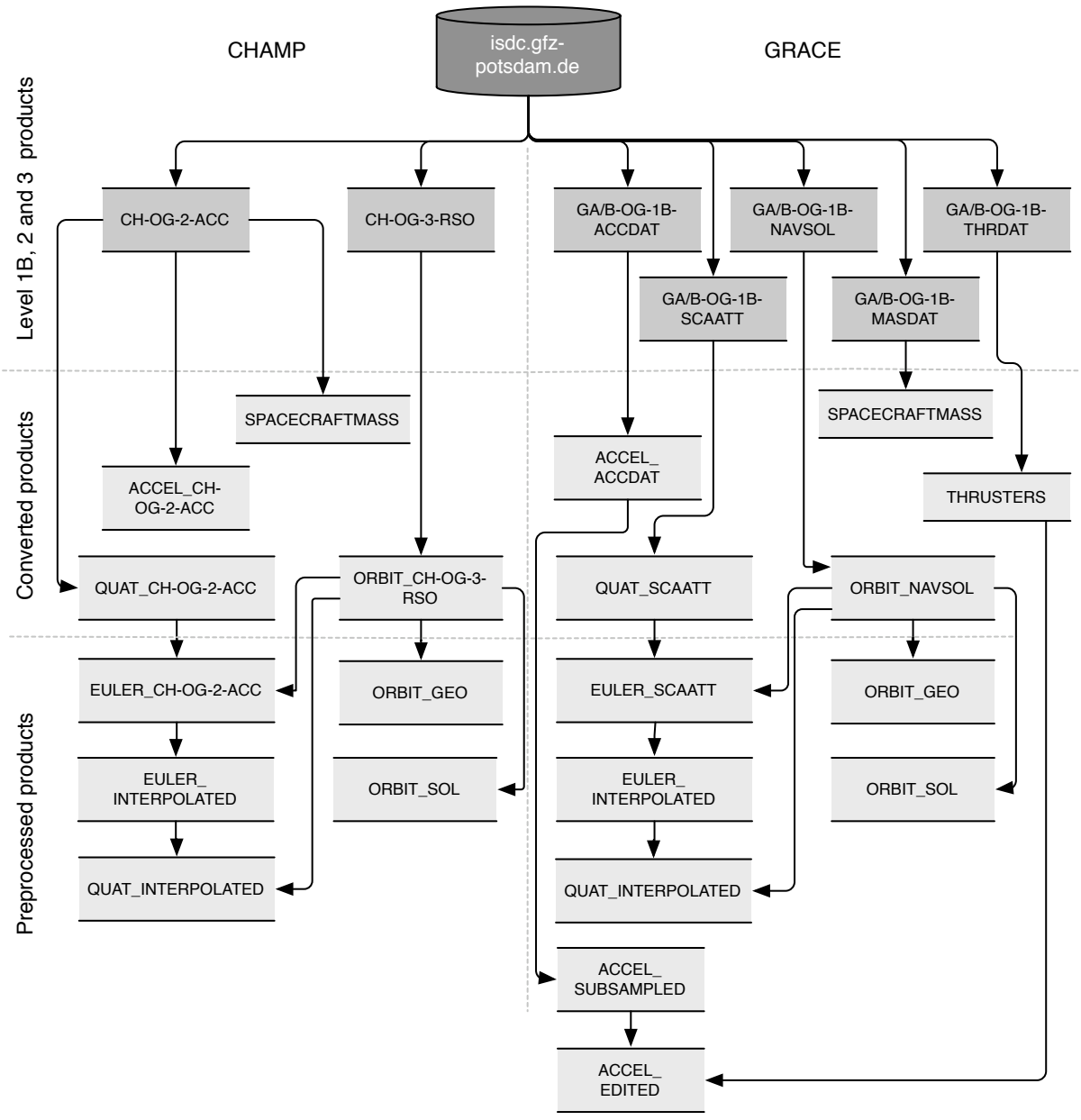

Figure 4.1 Flowchart of the preprocessing products.

on the force modelling (PN for panels and AN for ANGARA models) and calibration (R02, R03, ...) that have been applied (see also Section 7.4). These segments are separated by underscore characters. So the CH category contains general, mostly low-level CHAMP data, the CH_PN category contains CHAMP data with panel model calculations applied, and the CH_PN_R03 category contains further processed data for which the R03 calibration parameters have been used as well. The categories have been implemented as an easy way to browse through the different products. The categories are directories in the file system of the project data server.

Product names describe the data which they contain. These descriptive elements in the name are also separated by underscores. Examples include DENSMODEL_NRLMSISE-00, ACCEL_CALIBRATED, etc. Each of the products will be described in detail later in this Chapter and in Chapter 8 on the density and wind processing.

Each product can contain a number of related data fields. For example the DENSMODEL_NRLMSISE-00 products contain fields containing the density, temperature and composition. These fields are indicated with numbers.

4.1.2 Metadata properties

Each of the data products contains a set of metadata. The following metadata elements are possible:

Satellite Name of the satellite, current options are CHAMP, GRACE-1 and GRACE-2.

Public Sets the visibility of the product on the project web site, options are Yes or No.

ShortDescription A short description of the data product, for display in an overview table on the website.

LongDescription A longer description of the data product, for display on the product page on the website. If this metadata item is not available, the ShortDescription is used instead.

Orbital-in List of the names of high-rate data products on which this product depends.

epoch Date and time string, which serves as a reference date for the data.

timestep The timestep in seconds at which data records are spaced. Most high-rate products are produced at a 10-second time step. Exceptions are some products that are direct derivatives of the original CHAMP and GRACE Level 1B/2/3 products, which are converted to the 10 second time step by interpolation, averaging or subsampling during the preprocessing. These include the orbits, which are provided every 30 seconds for CHAMP and 60 seconds for GRACE, the GRACE quaternions, which are provided every 5 seconds, and the GRACE accelerometer data, which are provided at 1 second intervals.

InterpolationType Handles whether, and how, data are interpolated when values are requested at epochs which are not in step with the timestep. Possible values are *None*, *Linear*, *Lagrange* (9-point Lagrange interpolation) and *FStep* (step-function, the value for the last time step is used).

timesystem Timesystem in which the data are stored. Common options are UTC, TAI, GPS.

offset Number of seconds since the start of the day in the current time system for the first data record.

dimension Number of data fields per record in the data product.

field List of descriptions for each of the data fields, for display on the website, in data product headers and in plots. The descriptions also contain the units, if applicable to the data.

4.2 Retrieval of input data

The latest CHAMP and GRACE data are automatically retrieved each night from the GFZ ISDC system at http://isdc.gfz-potsdam.de/, using a Perl script that interacts with the ISDC server. The following data products are downloaded:

CH-OG-3-RSO CHAMP rapid science orbits.

CH-OG-2-ACC CHAMP accelerometer data - includes attitude quaternions, thruster events and satellite mass changes.

CH-OG-1-SST CHAMP GPS data (satellite-to-satellite tracking data).

GA/GB-OG-1B-ACCDAT GRACE accelerometer data.

GA/GB-OG-1B-NAVSOL GRACE navigation solution orbits.

GA/GB-OG-1B-SCAATT GRACE quaternions from star camera data.

GA/GB-OG-1B-MASDAT GRACE spacecraft mass history.

GA/GB-OG-1B-THRDAT GRACE thruster events.

GA/GB-OG-1B-GPSDAT GRACE GPS data.

This automatic synchronization script makes a copy of the data files on ISDC to the local server, by using the following procedure:

1. Submit a request for the list of available data files for the time period and products of interest to ISDC.
2. After one hour, retrieve the requested list of available data files from the ISDC ftp-server.
3. Check for new data files by comparing the list of files available on ISDC with the list of locally available files.
4. Create a request file for the new data files, making sure that the ISDC bandwidth limits of 1 GB and 1000 files per day are not exceeded.
5. Send the request for the new data files to the ISDC server.
6. After three hours, retrieve the requested data files from the ISDC FTP-server.

As a result of this procedure, local copies of the product files on the ISDC are available for preprocessing. The conversion of these files to the internal project formats is described in Sections 4.4, 4.5, 4.6.

In addition, the software uses the scripts from the NRTDM software for the automatic retrieval of solar and geomagnetic activity proxies and indices from the National Geophysical Data Center (NOAA/NGDC, at www.ngdc.noaa.gov) and Space Weather Prediction Centre (NOAA/SWPC at www.swpc.noaa.gov) and of Earth-orientation parameters from the International Earth Orientation and Reference Systems Service (IERS, at www.iers.org). For the Jacchia-Bowman 2006 and 2008 models, indices are downloaded from

Figure 4.2 Screenshot of the data section of the project website, including a downloaded data file and plot.

their respective websites as well (http://sol.spacenvironment.net/~JB-2006 and http://sol.spacenvironment.net/~JB-2008).

4.3 Web interface

In order to be able to distribute the data and provide quick overviews of availability, data ranges and data behaviour, a web interface was built. The web interface is run from the project server, at http://thermosphere.deos.tudelft.nl/. Features of this web interface include:

- Display of a data product overview.
- Display of data product metadata.
- Display of data product availability.
- Quick download of text files and time series plots with all fields from a single data product.
- Download of text files and time series plots with a combination of fields from several data products.

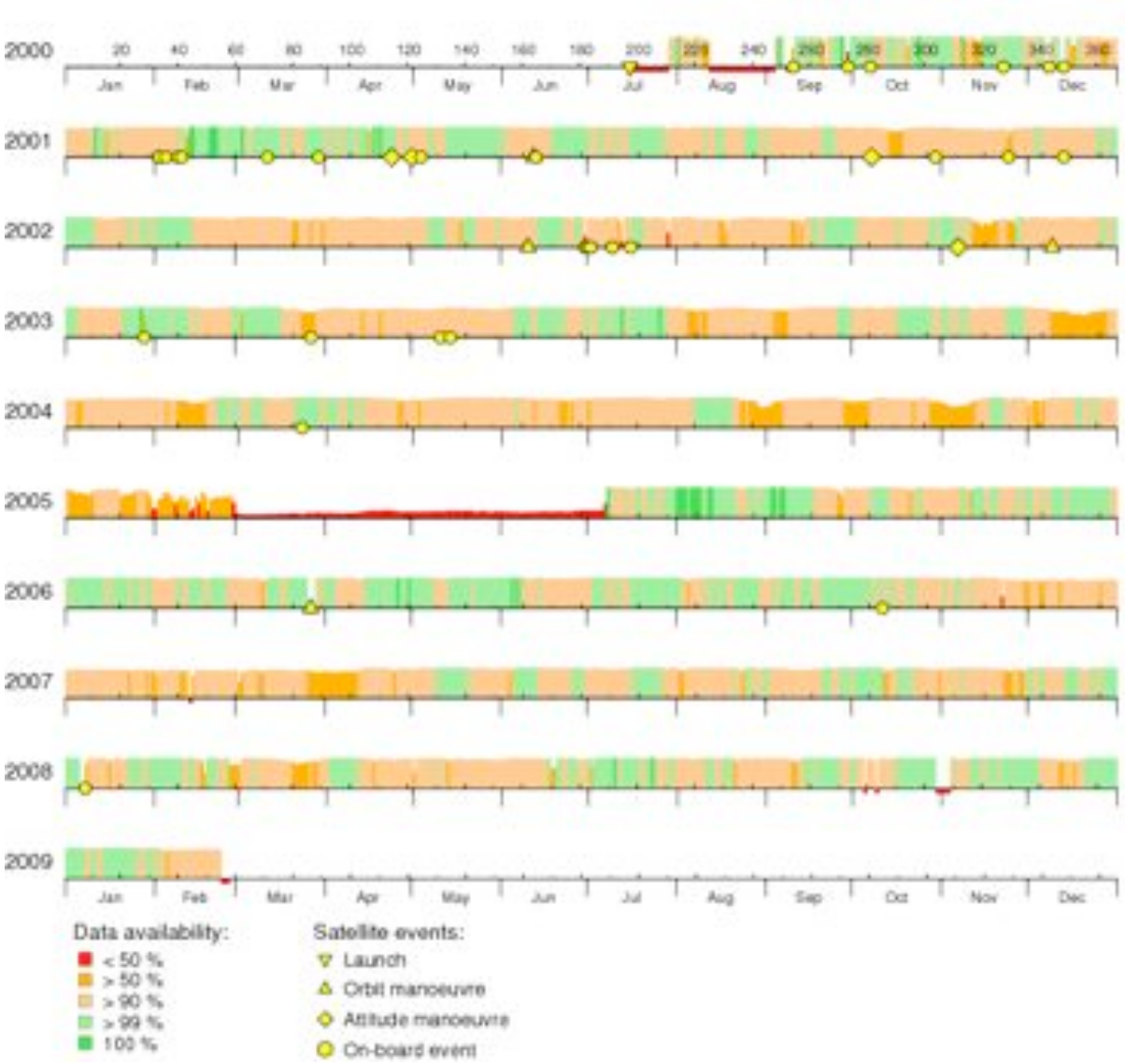

Figure 4.3 Data availability chart for unprocessed CHAMP attitude quaternion data (CH:QUAT_CH-OG-2-ACC).

Figure 4.2 shows a view of the website, a downloaded data file and a downloaded data plot.

The website is often updated, and will always contain the latest data products, metadata and availability information, which may have superseded the information in this report. The availability charts on the website also contain indicators of important satellite orbit and attitude manoeuvres, which may affect the data. Such a chart for CHAMP attitude data is shown in Figure 4.3.

4.4 Low data rate products

This section will give a description of the low-rate auxiliary data products, resulting from the data preprocessing.

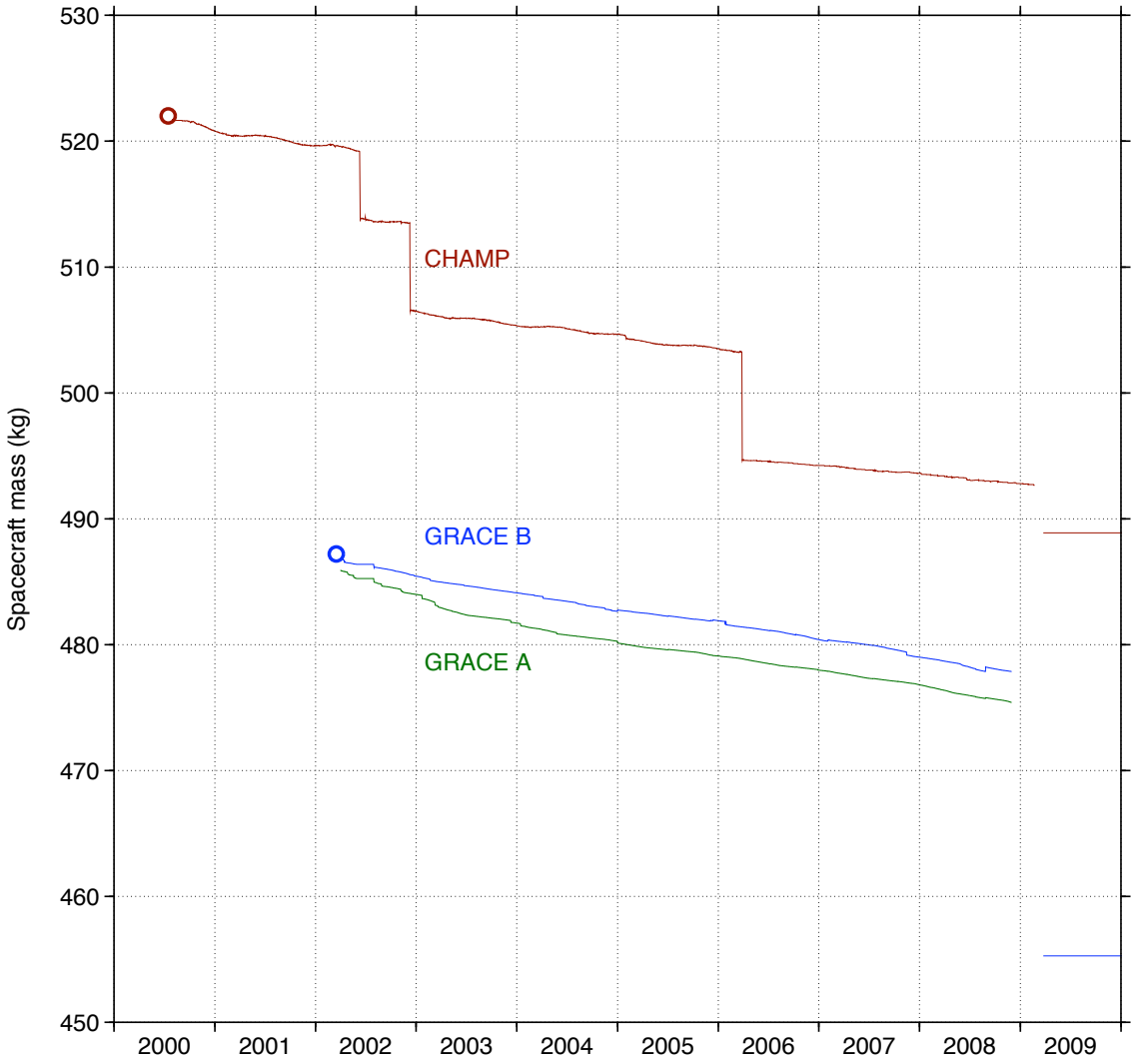

Figure 4.4 Time series of spacecraft mass from the CH-OG-2-ACC product for CHAMP and GA/B-OG-1B-MASDAT for GRACE. The open circles indicate the values of the published spacecraft mass at launch. The horizontal lines extending from the right edge represent the values of the dry spacecraft mass, without propellant.

4.4.1 Spacecraft mass variations: SPACECRAFTMASS

The SPACECRAFTMASS products contain just one field:

1. Estimated spacecraft mass (kg)

The data are copied and resampled from the CH-OG-2-ACC data for CHAMP and from the GA/GB-OG-1B-MASDAT data for GRACE. A plot of this data can be seen in Figure 4.4. The mass values are based on precise measurements of the pre-launch satellite masses and either computations of the propellant mass used in manoeuvres or computations based on tank pressure observations. The mass data in the CH-OG-2-ACC product seems to have a time step of four hours, although variations are apparent. For GRACE, the records in the original product appear at irregular intervals as well. In these preprocessed products, the data rate is set to one record per hour.

4.4.2 Thruster activity: THRUSTERS

The THRUSTERS product is only generated for the GRACE satellites. It contains one data field, which is derived from the GA/B-OG-1B-THRDAT product:

1. Time to closest thruster activation time (s)

The time to the closest thruster activation time can be used to edit data that might be affected by thruster activity. Although the attitude thruster activation duration is generally measured in milliseconds, the GRACE Level 1B processing applies a filter which spreads out the acceleration over tens of seconds. Unfortunately, this makes it necessary to remove a substantial number of data points.

4.5 Orbit products

4.5.1 Imported orbits: ORBIT_CH-OG-3-RSO and ORBIT_NAVSOL

The ORBIT products contain the Cartesian position and velocity in the international terrestrial reference frame (ITRF). These data are copied from the CH-OG-3-RSO (Rapid Science Orbits) for CHAMP and from GA/GB-OG-1B-NAVSOL (Navigation Solution) for GRACE. The 3D-position accuracy of these orbits is believed to be well below the 5 cm level [*König et al.*, 2005; *Kang et al.*, 2006] for recent data. The CHAMP orbits had a lower accuracy, of around 20 cm, during the first period of the mission, when satellite parameters still had to be tuned and the gravity field models were not yet as accurate as they are today [*König et al.*, 2005]. This lower accuracy is still sufficiently accurate for the purposes of this project. The following data fields are available in the ORBIT products:

1. X-component of position in ITRF (m)
2. Y-component of position in ITRF (m)
3. Z-component of position in ITRF (m)
4. X-component of velocity in ITRF (m/s)
5. Y-component of velocity in ITRF (m/s)
6. Z-component of velocity in ITRF (m/s)

4.5.2 Orbit in geodetic and geomagnetic coordinates: ORBIT_GEO

The ORBIT_GEO product contains orbit information in geodetic and geomagnetic coordinates. The list of data fields is as follows:

1. Altitude (m)
2. Geodetic longitude (deg)
3. Geodetic latitude (deg)
4. Local solar time (hours)
5. Argument of latitude (deg)
6. Geomagnetic longitude (deg)
7. Geomagnetic latitude (deg)
8. Geomagnetic local solar time (hours)

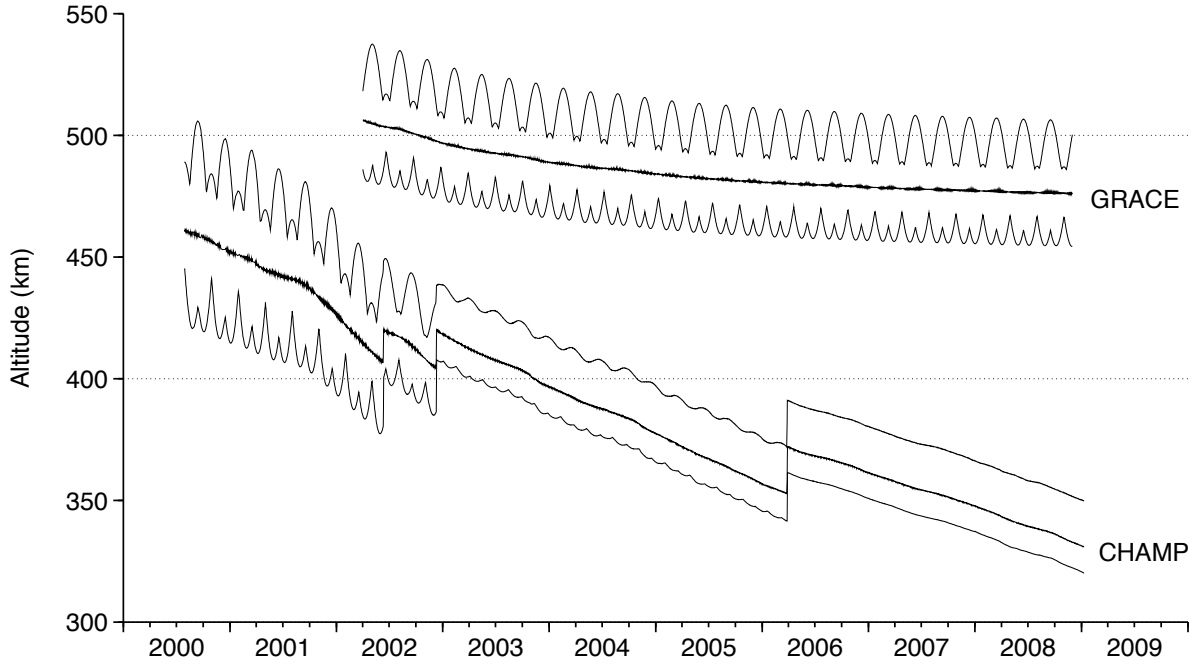

Figure 4.5 Time series of daily mean, minimum and maximum orbital altitudes for CHAMP and GRACE.

The geodetic coordinates (height, latitude and longitude) are with respect to the ITRF reference ellipsoid. Figure 4.5 shows the height variations of CHAMP and GRACE over the course of the years.

Local solar time is computed using the longitude and the number of UTC seconds in the day. The geomagnetic coordinates are with respect to the IGRF dipole, based on the GEOPACK subroutine library by Dr. N. A. Tsyganenko, obtained from http://geo.phys.spbu.ru/∼tsyganenko/. The argument of latitude is the position angle along the orbit, measured from the ascending node, computed by summing two Keplerian elements: the argument of perigee and the true anomaly. Figure 4.6 shows the position of the CHAMP satellite in geodetic and geomagnetic coordinates for one day (January 1, 2003). The figures give a good idea of the coverage with respect to these coordinate frames during the course of a single day.

4.5.3 Orbit geometry with respect to the Moon and Sun: ORBIT_SOL

The ORBIT_SOL product contains information on the geometry of the satellite with respect to the Sun and Moon. The data fields are as follows:

1. Beta prime (deg)
2. Shadow function for solar eclipse by the Earth
3. Shadow function for solar eclipse by the Moon
4. Time with respect to closest Earth shadow transition (seconds)
5. Solar zenith angle (deg)
6. Lunar zenith angle (deg)

Beta prime is the angle between the orbital plane and the Sun-Earth vector. The shadow functions provide information on when the satellite is in the Earth's or

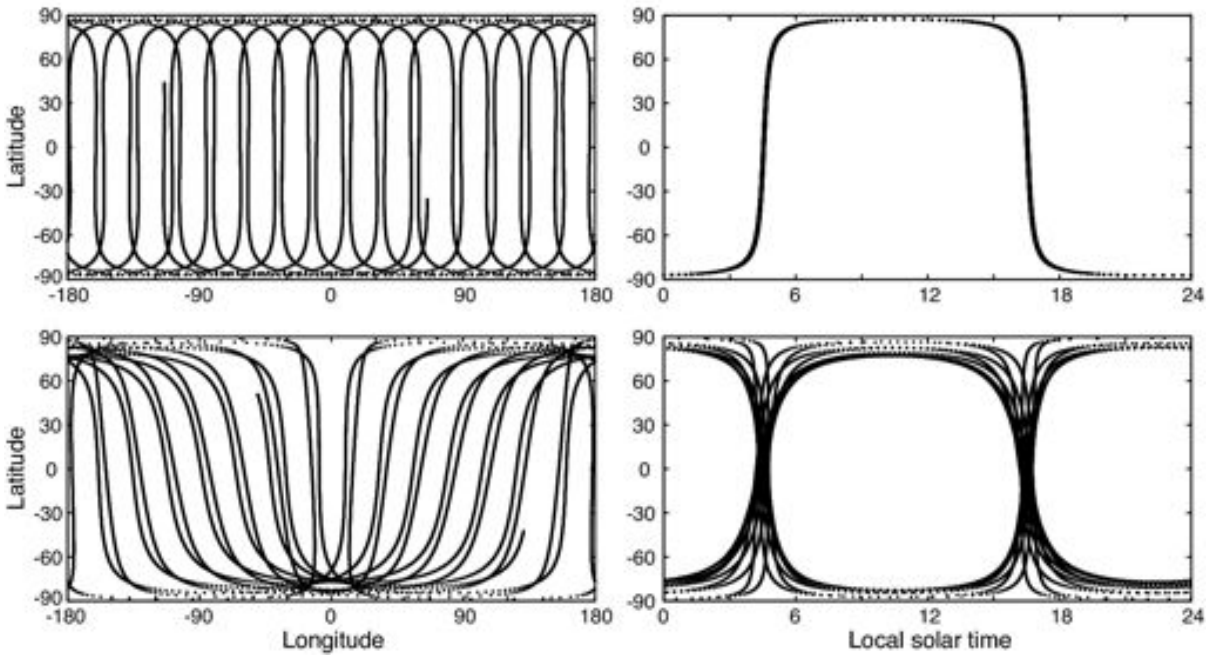

Figure 4.6 Positions of CHAMP during January 1, 2003, using longitude (left) and local solar time (right), in geodetic coordinates (top) and geomagnetic coordinates (bottom).

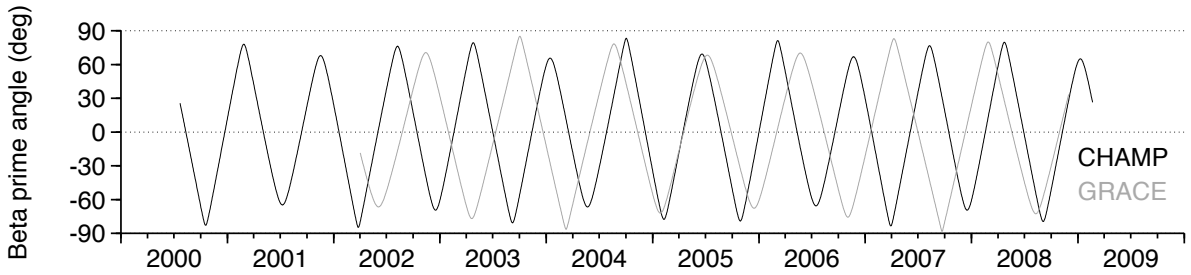

Figure 4.7 Time series of beta prime, which is the angle between the orbital plane and the Sun-Earth vector.

Moon's eclipse. It has a value of 0 when in full sunlight, of 1 when eclipsed, and a value in between when it is in the semi-shadow region. The time with respect to the closest shadow transition can be used for data editing and error analysis, since the modelled radiation pressure will likely be less accurate, close to shadow transitions. The solar and lunar zenith angles are the angles between the satellite position vector and solar and lunar position vectors, respectively.

Figure 4.7 shows the variation of beta prime for the CHAMP and GRACE orbits over the course of the years. This variation is mainly driven by the orbit perturbation due to the Earth's flattening. The plot shows when the orbits of both missions were nearly coplanar, which is an important characteristic for the sampling of density and winds in a multi-satellite approach.

Figure 4.8 shows how eclipses occur over the CHAMP orbit during the year 2002. This pattern is mainly driven by the precession of the orbital plane with respect to the Sun. There were two periods during this year (in March/April and July/August) without eclipses, where CHAMP was in a dawn-dusk orbit. In December, the satellite was in a dawn-dusk orbit again, but encountered only very short eclipses over the North Pole, with prolonged semi-shadow periods,

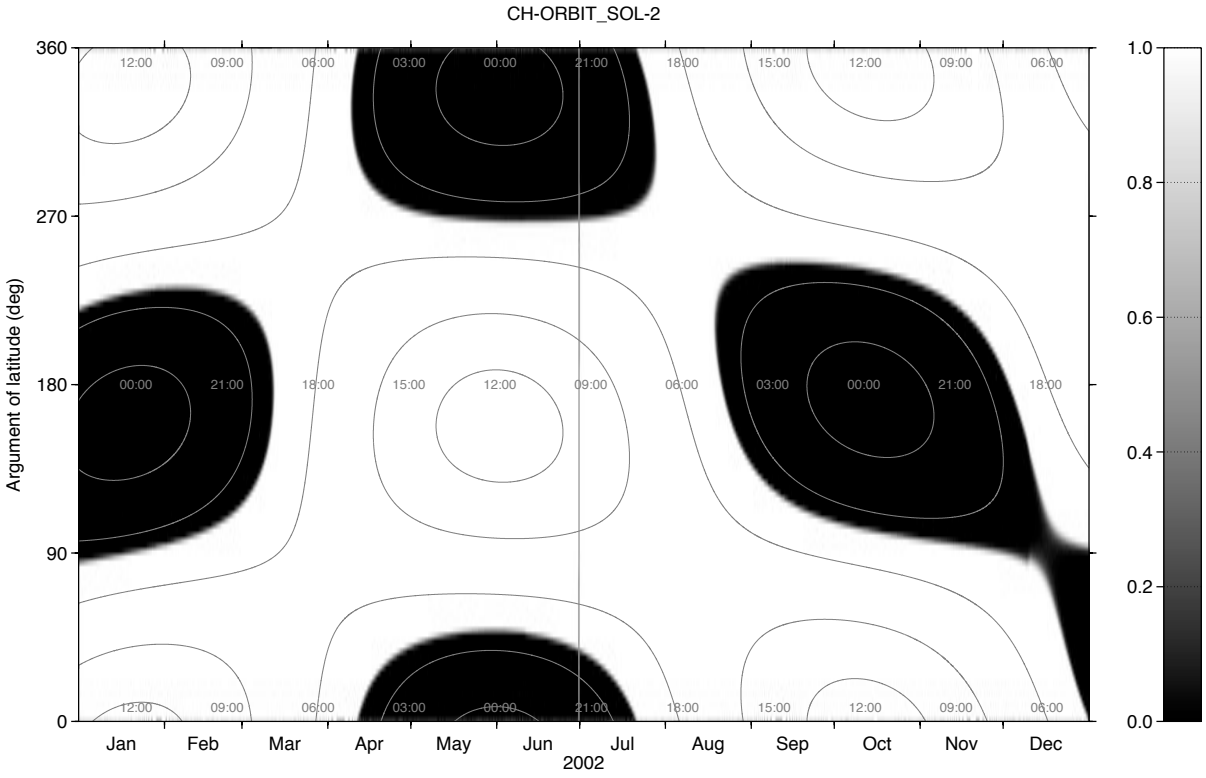

Figure 4.8 Shadow function and solar zenith angle for CHAMP during the year 2002, as a function of time (X-axis) and argument of latitude (Y-axis). The white-grey-black scale represents the amount of sunlight that is blocked by the Earth (white is full sunlight, black is eclipse). The contour lines represent the solar zenith angle at intervals of 30 degrees. The single vertical line at the end of June appears because CH-OG-3-RSO orbit information was missing for a single day.

which show up as the fuzzy grey boundaries in this plot. There is a discontinuity at the start of this period, which is due to the orbit raising manoeuvre, which occurred on December 9 and 10, 2002.

4.6 Attitude products

The attitude data from the spacecraft star cameras has required most of the pre-processing effort. An approach as described in *Neumayer et al.* [2005] has been adopted, which will be described below. For both CHAMP and GRACE, the attitude quaternion data contains many data gaps. These data gaps can often be filled by linear interpolation. The quaternions, which describe the rotation between the inertial frame and the spacecraft body-fixed frame, are macroscopic quantities however, which vary over their complete range in the course of each orbit. In addition, there is an ambiguity because a quaternion of which all four components have been multiplied by minus one, represents the same rotation as the original quaternion. For this project, the scalar component of processed quaternions are therefore always set to positive values, but as a side effect, sharp edges in the time series occur each orbit, when the scalar component is close to zero, so that interpolation leads to inaccurate results.

For this reason, the quaternions are first converted to Euler angles between the spacecraft body fixed frame and an orbit-fixed frame, of which the axes point

in the along-track, cross-track and near-radial directions. Due to the controlled attitude of the satellites, these Euler angles generally have values between -3 and +3 degrees for CHAMP and -1 and +1 degrees for GRACE. These small values of the Euler angles can be interpolated much more accurately than the quaternions. An additional benefit of the conversion to Euler angles is that it is much easier to create a mental picture of the satellite attitude behaviour. With the quaternions this is virtually impossible.

The conversion between quaternions, rotation matrices and Euler angles is based on the description in the "Matrix and quaternions FAQ", available at http://www.j3d.org/matrix_faq/matrfaq_latest.html, accessed in December 2007.

The complete attitude preprocessing chain is visualized in the flow chart of Figure 4.1. Each of the products and the way they are derived will be described in the following sections.

4.6.1 Imported quaternions: QUAT_CH-OG-2-ACC and QUAT_SCAATT

These products contain direct copies of the quaternion data from the CHAMP level 2 and GRACE level 1B data files. These quaternions describe the rotation between the ICRS inertial reference frame and the spacecraft body-fixed (S/C or SRF) frame.

The data rate is one record every 10 seconds for CHAMP and one record every 5 seconds for GRACE. The products contain the following data fields:

1. First vector component of quaternion
2. Second vector component of quaternion
3. Third vector component of quaternion
4. Scalar component of quaternion

Note that the ordering of vector and scalar components has been modified with respect to the original GRACE Level 1B SCAATT product, in order to achieve consistency among the satellite products.

4.6.2 Converted Euler angles: EULER_CH-OG-2-ACC and EULER_SCAATT

These products contain the Euler angles (roll, pitch and yaw) between the orbit-fixed frame (along-track, cross-track and nearly-radial) and a pseudo-orbit-fixed frame, defined below. The three data fields per record are defined as follows:

1. Euler angle rotation around the S/C X-axis (roll) (radians)
2. Euler angle rotation around the S/C Y-axis (pitch) (radians)
3. Euler angle rotation around the S/C Z-axis (yaw) (radians)

The products are available at a 10 second time step. This means that half of the quaternions from the GRACE product, which contains data at a 5 second time step, are simply discarded.

The orientation of the spacecraft body-fixed axes and of the traditional orbit-fixed axes is illustrated in Figure 4.9 [*Lühr et al.*, 2002; *Case et al.*, 2004]. The pseudo-orbit-fixed frame to which the Euler angles refer is defined to be closely aligned with the spacecraft body-fixed frame during nominal attitude control. This means that during normal spacecraft operations, the values of these angles

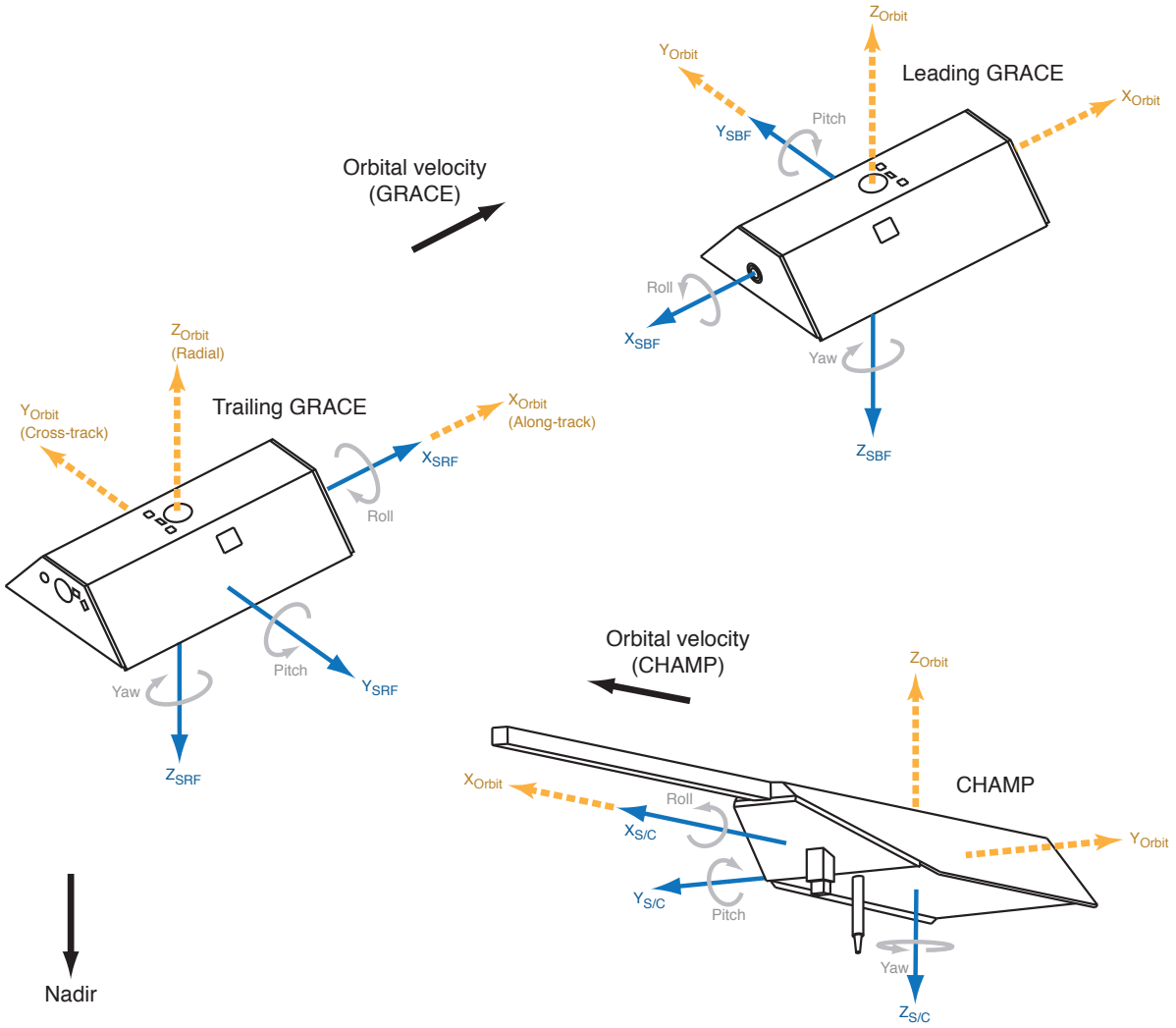

Figure 4.9 Orientation of the spacecraft body-fixed frames (S/C for CHAMP, SRF for GRACE), and of the orbit-fixed frame (along-track, cross-track and radial). The orientation of the orbit-fixed axes is shown for the nominal attitude of both missions, with all Euler angles at zero.

remain within plus or minus 2–3 degrees for CHAMP and within plus or minus one degree for the GRACE satellites.

Formally, the conversion between frames can be described using a set of rotation matrices R_{12} from frame 1 to frame 2, where the subscripts i, o, p and b are used for the inertial, orbit-fixed, pseudo-orbit-fixed and spacecraft body-fixed reference frames, respectively. The Euler angles can then be obtained from the rotation matrix R_{op}, which is computed as follows:

$$R_{op} = R_{bp} R_{ib} R_{oi} \tag{4.1}$$

The matrix R_{oi} is defined by the satellite's orbital position and velocity in inertial space. The Earth-fixed orbit is first converted to the inertial frame by applying the standard Earth orientation transformations (see, e.g. *Montenbruck and Gill* [2000]). The Earth orientation implementation of the NRTDM software is used for this purpose. If $\vec{r}$ is the inertial position vector and $\vec{v}$ the inertial velocity vector, then the three rows of R_{oi} are constructed from the three transposed unit vectors

that point in the along-track, cross-track and pseudo-radial directions: $\vec{v}$, $\vec{r} \times \vec{v}$ and $\vec{v} \times (\vec{r} \times \vec{v})$. The matrix R_{ib} is the rotation matrix that is constructed from the quaternion in the QUAT product. Finally, the matrix R_{bp} is defined by the definition of the nominal attitude control and the spacecraft body-fixed reference frame.

For CHAMP and the trailing GRACE satellite, this matrix is:

$$R_{bp} = \begin{bmatrix} 1 & 0 & 0 \\ 0 & -1 & 0 \\ 0 & 0 & -1 \end{bmatrix} \tag{4.2}$$

For the leading GRACE satellite, which is flying backwards with respect to the trailing satellite, the matrix is:

$$R_{bp} = \begin{bmatrix} -1 & 0 & 0 \\ 0 & 1 & 0 \\ 0 & 0 & -1 \end{bmatrix} \tag{4.3}$$

The two GRACE satellites have switched positions in December 2005. In the current version of the software, GRACE-A is considered to be leading until December 11, 2005, and trailing afterwards. The switch manoeuvre started earlier for GRACE-B. It is considered trailing until December 9, 2005, and leading afterwards. Note that there are also some shorter periods at which the orientation of the CHAMP and GRACE satellites has been changed from their nominal attitude. These periods are currently not taken into consideration in the definition and selection of the R_{bp} matrices. These periods can be identified by the fact that the Euler angles on the data products are not within a few degrees of zero, and by the markers on the data availability charts on the project website (such as the example in Figure 4.3).

Figure 4.10 shows the variation of the yaw angle for CHAMP during the year 2002, from the raw data. The data gaps, which form a geometric pattern, related to the solar zenith angle (compare with Figure 4.8), are clearly visible. Note also the correlation of yaw angle values with argument of latitude.

4.6.3 Interpolated Euler angles: EULER_INTERPOLATED

The EULER_INTERPOLATED products are derived from the EULER_CH-OG-2-ACC and EULER_SCAATT products by filling data gaps using linear interpolation of the two points adjacent to the gap. If there are data gaps that are longer than ten days, or for which the end points are more than 6 degrees apart, around any of the three axes, then the gap is not interpolated. Since there are many short data gaps, and only a few periods where the attitude is not nominal, the EULER_INTERPOLATED product contains many more records than the original Euler angle data.

The data fields in this product are similar to those of the original EULER products, but with one additional field:

1. Euler angle rotation around the S/C X-axis (roll) (radians)
2. Euler angle rotation around the S/C Y-axis (pitch) (radians)
3. Euler angle rotation around the S/C Z-axis (yaw) (radians)
4. Length of data gap, if interpolation is applied (s)

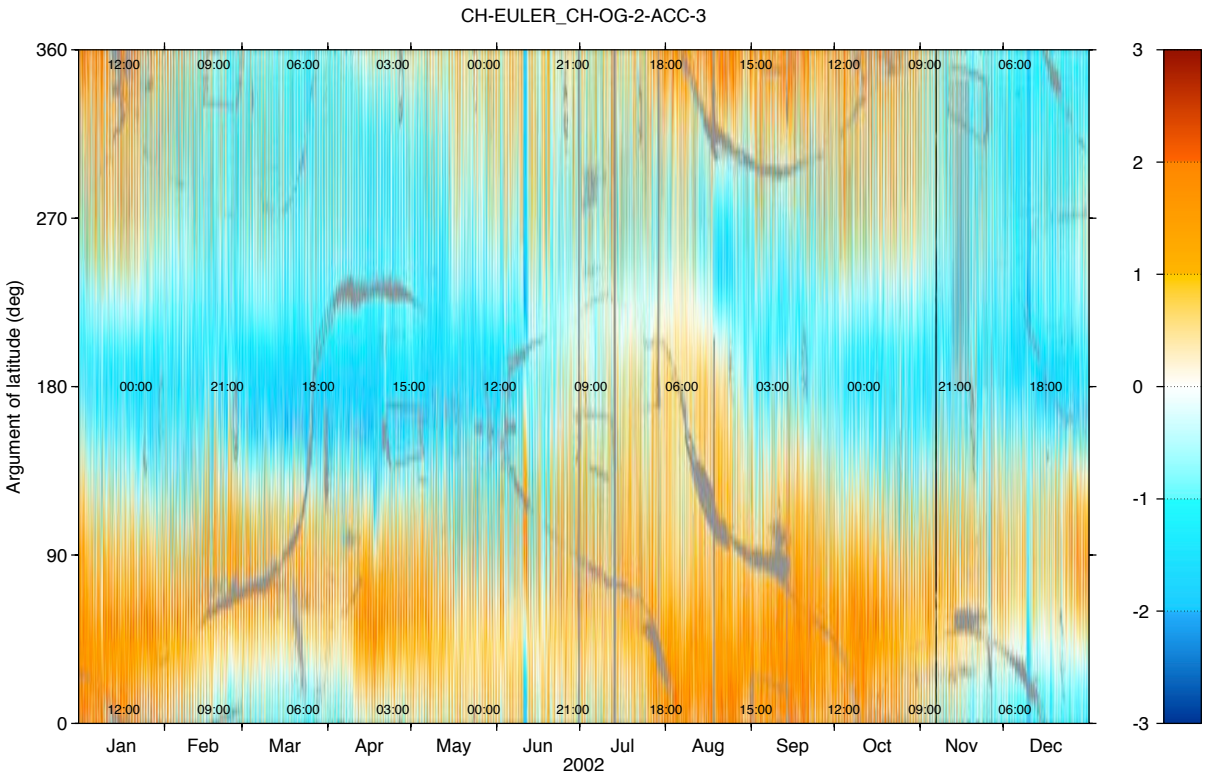

Figure 4.10 Variations of the CHAMP yaw angle (in degrees) over 2002, derived from the quaternion data in the CH-OG-2-ACC product. Grey areas represent data gaps.

The fourth field, which contains the length of the data gap in seconds, or zero if there was no gap, can be used for data editing. In general however, the error due to interpolation of the attitude data is much smaller than other error sources in the density and wind determination or orbit determination using this data, and the presence of the attitude data gaps only obstructs the further analysis of the accelerometer data. For the most precise applications however, data for which interpolation has taken place can be removed by checking this data field.

4.6.4 Interpolated quaternions: QUAT_INTERPOLATED

The QUAT_INTERPOLATED product is generated from the interpolated Euler angles and the satellite orbit data by applying the transformations of Section 4.6.2 in reverse. The product has the same data fields as the original quaternion data of Section 4.6.1

4.7 Accelerometer products

4.7.1 Imported accelerations: ACCEL_CH-OG-2-ACC and ACCEL_ACCDAT

The ACCEL_CH-OG-2-ACC and ACCEL_ACCDAT products contain copies of the linear acceleration data from the Level 2 CHAMP and Level 1B GRACE files, respectively. The data rate is one record for every 10 seconds for CHAMP, and one record per second for GRACE. For the CHAMP data, the Lorentz force correction and radial correction are applied. No calibration is applied to the data at this point. The CHAMP data are converted from the accelerometer reference

frame (ACC) to the spacecraft body-fixed (S/C) frame using the following rotation matrix:

$$\ddot{\vec{r}}_{S/C} = \begin{bmatrix} 0 & 1 & 0 \\ 0 & 0 & -1 \\ -1 & 0 & 0 \end{bmatrix} \ddot{\vec{r}}_{ACC} \tag{4.4}$$

The GRACE data are already provided in the spacecraft body-fixed frame (SRF). The data fields are defined as follows:

1. Linear acceleration in S/C X-direction (m/s^2)
2. Linear acceleration in S/C Y-direction (m/s^2)
3. Linear acceleration in S/C Z-direction (m/s^2)

4.7.2 Subsampled accelerations: ACCEL_SUBSAMPLED

The GRACE accelerometer data in the Level 1B product is provided at 1-second intervals, compared to 10 seconds for CHAMP. Upon first inspection, this higher temporal resolution does not provide a significant amount of additional information for atmospheric research. This is probably due to the fact that the data has been smoothed. The ACCEL_SUBSAMPLED product, which is only available for GRACE, provides the same accelerometer data, but subsampled at 10-second time steps. This reduces disk space usage and processing time for derived products. Each record in the ACCEL_SUBSAMPLED product is computed by taking the average value of the 1-second data records that are within five seconds before to five seconds after its time stamp. If invalid records are present, they are discarded. If less than eight valid records are present, the record is set to invalid. So in effect, each record represents the average of 8 to 11 records of the 1-second product. The definition of the data fields is the same as in the ACCEL_ACCDAT product (see Section 4.7).

1. Linear acceleration in S/C X-direction (m/s^2)
2. Linear acceleration in S/C Y-direction (m/s^2)
3. Linear acceleration in S/C Z-direction (m/s^2)

4.7.3 Edited accelerations: ACCEL_EDITED

The ACCEL_EDITED data product is a subset of the ACCEL_ACCDAT data. All accelerations in the spacecraft Y- and Z-directions which are closer than a certain threshold to a reported attitude thruster firing are removed. Although the thruster firings last only a fraction of a second each, the threshold is currently set at 25 seconds, in order to remove most of the visible acceleration spikes in the data. This longer time interval is necessary because the Level 1B ACCDAT data was smoothed, so that the influence of acceleration spikes is spread out over much longer time intervals. The data editing results in about 20% to 30% of the data to be removed.

4.8 Density and wind model products

The first products that will be described are the density and wind products based on empirical models. These models require the time, geodetic latitude, longitude and local solar time as inputs, which can all be retrieved from the GEO products.

They also require solar activity and geomagnetic indices, for which the processing uses the relevant NRTDM routines, behind the scenes.

4.8.1 Empirical density model output: DENSMODEL

The DENSMODEL products contain the density, temperature and composition from the empirical models that were selected for this study. The product depends only on the GEO product, so records are available wherever orbit information is available. The data fields per record are as follows:

1. Density at satellite altitude (kg/m^3)
2. Temperature (K)
3. Mass concentration of H
4. Mass concentration of He
5. Mass concentration of N
6. Mass concentration of O
7. Mass concentration of O+/anomalous Oxygen
8. Mass concentration of N2
9. Mass concentration of O2
10. Mass concentration of Ar
11. Density at 475 km (kg/m^3)
12. Density at 450 km (kg/m^3)
13. Density at 425 km (kg/m^3)
14. Density at 400 km (kg/m^3)
15. Density at 375 km (kg/m^3)
16. Density at 350 km (kg/m^3)
17. Density at 325 km (kg/m^3)
18. Density scale height at satellite altitude (m)

The model densities at fixed altitudes in records 11–17 can be used for normalization of the accelerometer-derived density to a fixed reference height. The density scale height H in record 18 is computed by calculating the model density ρ twice, for heights 1 km below and 1 km above the satellite altitude, denoted by h_1 and h_2 respectively, and subsequently applying the following equation:

$$H = \frac{h_2 - h_1}{\ln(\rho(h_1)/\rho(h_2))} \tag{4.5}$$

Note that not all atmospheric constituents are computed in several of the models. If that is the case, their concentration values are always set to zero. Figure 4.12 shows time series for 2007 of the mass concentrations as encountered by CHAMP and GRACE, according to the NRLMSISE-00 model. The figure shows that atomic oxygen is the dominant species for both satellites. At the lower altitude of CHAMP, molecular nitrogen has a large contribution as well, while at the higher altitude of GRACE, the lighter Helium atoms are abundant. There is a clear seasonal variation, and smaller variations dependent on the local solar time coverage and level solar EUV radiation and geomagnetic activity.

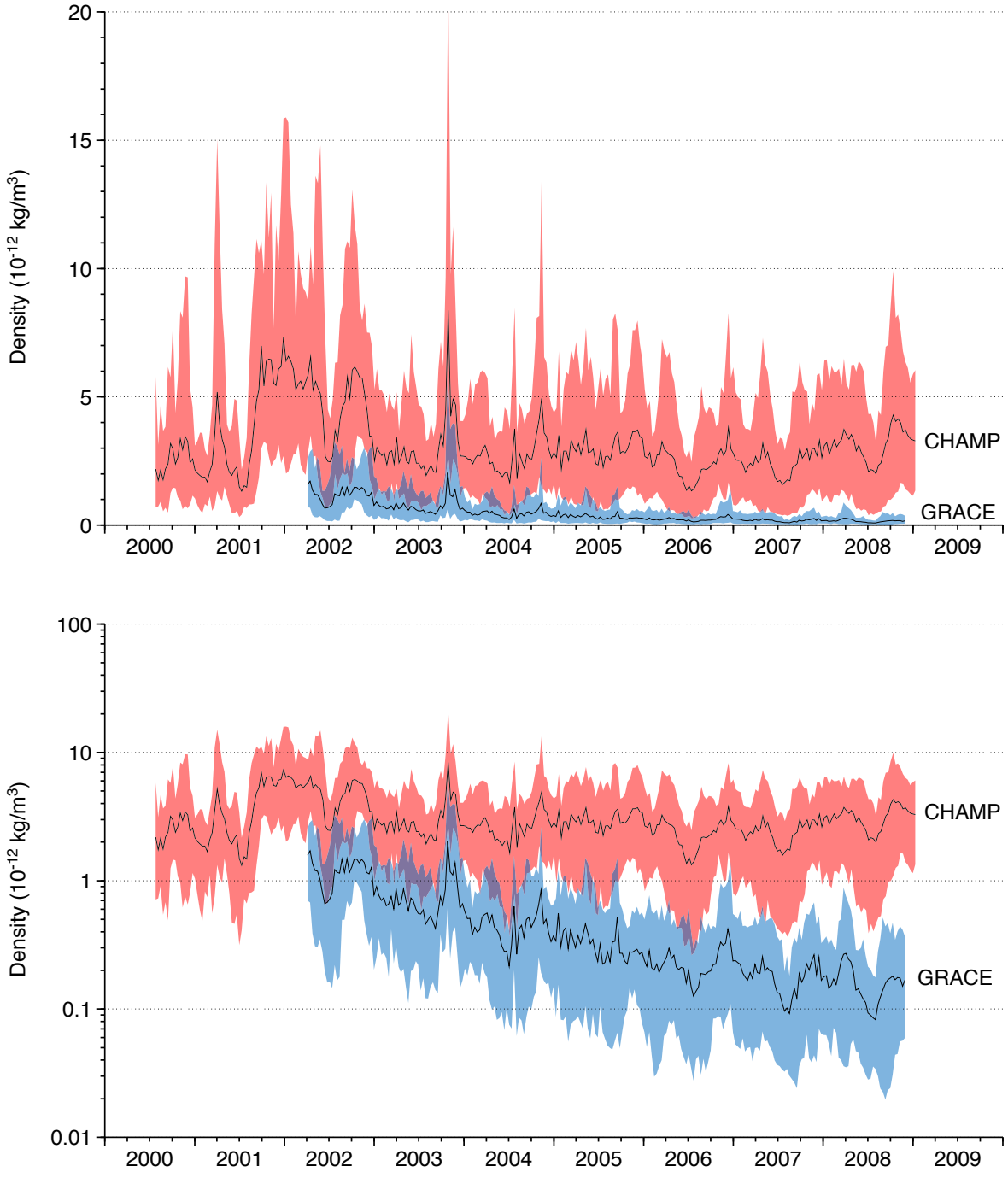

Figure 4.11 Time series of NRLMSISE-00 densities along the CHAMP and GRACE orbits, plotted against a linear (top) and logarithmic (bottom) Y-axis scale. The shaded areas show the minimum and maximum values, and the black lines the mean values, evaluated over 10-day intervals.

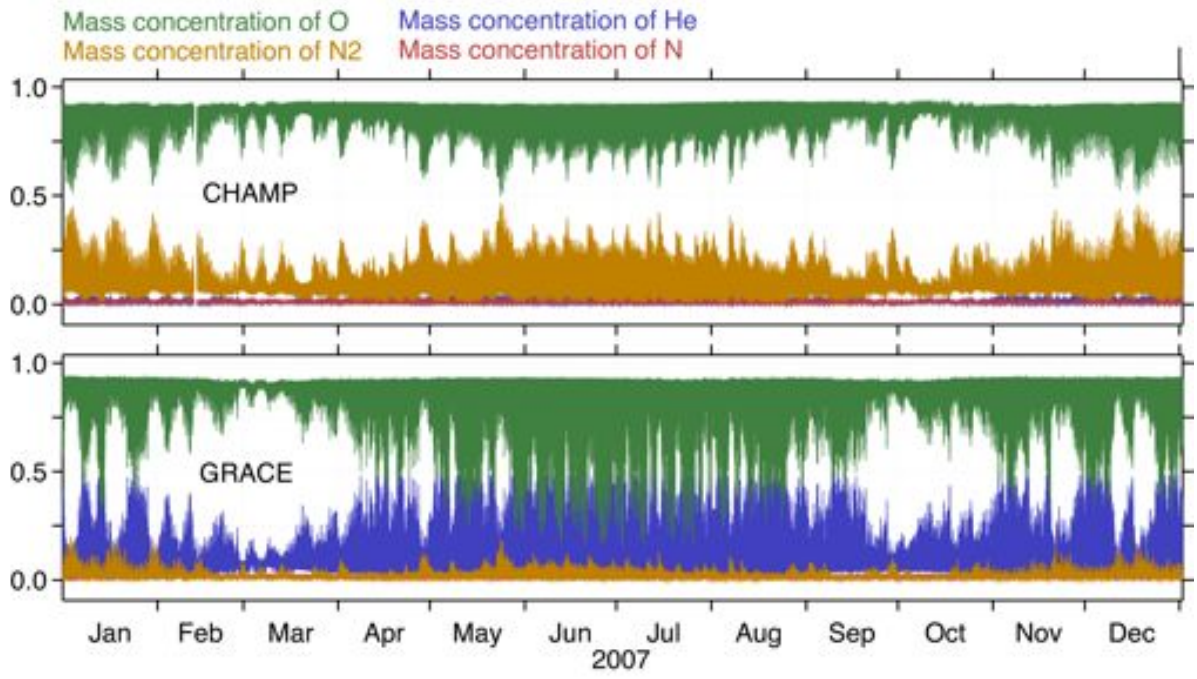

Figure 4.12 Time series for 2007 of the atmospheric composition at the position of CHAMP (top) and GRACE (bottom), according to the NRLMSISE-00 model.

4.8.2 Air flow velocity due to the orbit and atmosphere corotation: WINDMODEL_SC_ORBITCOROTATION

This product contains two vectors representing contributors to the velocity of the atmosphere relative to the satellite, expressed in the spacecraft body-fixed frame. The first component is the orbital velocity of the satellite, which is derived from the ORBIT product. This component is predominantly along the X-axis, but has small components in the other two directions due to deviations from the ideal attitude. The second component is due to the corotation of the atmosphere with respect to the Earth, and is predominantly in the Y-direction. The product fields are:

1. Wind speed due to orbital velocity along the S/C X-axis (m/s)
2. Wind speed due to orbital velocity along the S/C Y-axis (m/s)
3. Wind speed due to orbital velocity along the S/C Z-axis (m/s)
4. Wind speed due to atmosphere corotation along S/C X-axis (m/s)
5. Wind speed due to atmosphere corotation along S/C Y-axis (m/s)
6. Wind speed due to atmosphere corotation along S/C Z-axis (m/s)

If $\vec{r}_i$ and $\vec{v}_i$ are the inertial position and velocity vector from the ORBIT product, and R_{ib} is the rotation matrix derived from the quaternion data, then the wind speed due to the orbital velocity is simply

$$\vec{w}_b^o = -R_{ib}\vec{v}_i \tag{4.6}$$

The wind speed due to orbit corotation is

$$\vec{w}_b^c = R_{ib}(\vec{\omega}_\oplus \times \vec{r}_i) \tag{4.7}$$

where

$$\vec{\omega}_{\oplus} = (0, 0, 0.729210^{-4})^T \text{rad/s} \tag{4.8}$$

is the rotation rate vector for the Earth.

4.8.3 Empirical wind model output in the local frame: WINDMODEL_LOCAL

The HWM-93 and HWM07 models are companion models to the MSIS series of density models. The models return horizontal wind speeds in meters per second with respect to a co-rotating atmosphere, in a local North-East coordinate system. The following data fields are available:

- Zonal (Eastward) wind speed (m/s)
- Meridional (Northward) wind speed (m/s)

4.8.4 Empirical wind model output in the spacecraft frame: WINDMODEL_SC

This product contains the modelled wind speeds, taken from the WINDMODEL_LOCAL products, but converted to the spacecraft body-fixed coordinate system. The following fields are included:

1. HWM-93 local wind speed along the S/C X-axis (m/s)
2. HWM-93 local wind speed along the S/C Y-axis (m/s)
3. HWM-93 local wind speed along the S/C Z-axis (m/s)

The transformation of model wind speed $\vec{w}^m$ from local coordinates (index l) to the spacecraft body-fixed coordinates (index b) requires several rotation matrices:

$$\vec{w}_b^m = R_{ib} R_{ei} R_{le}\, \vec{w}_l^m \tag{4.9}$$

The rotation R_{ib} from inertial to body-fixed is derived from the quaternions of the QUAT_INTERPOLATED product. The Earth-fixed to inertial rotation matrix R_{ei} is computed using the standard transformations that were implemented for the NRTDM software. Finally, the rotation matrix from local to Earth-fixed coordinates R_{le} requires the longitude ϕ and latitude λ from the GEO_RSO or GEO_NAVSOL product:

$$R_{le} = \begin{bmatrix} -\sin\phi & -\sin\lambda\cos\phi & \cos\lambda\cos\phi \\ \cos\phi & -\sin\lambda\sin\phi & \cos\lambda\sin\phi \\ 0 & \cos\lambda & \sin\lambda \end{bmatrix} \tag{4.10}$$

Figure 4.13 illustrates that on ascending tracks and at mid-latitudes, the wind speed in the Y-direction coincides with Eastward wind and the X-direction with Northward winds. This is due to the very high inclination of the CHAMP orbit. At descending tracks, the spacecraft body-fixed X- and Y-axes are pointed in the opposite directions.

Figure 4.14 shows a comparison of the different contributions to the wind speed, or relative velocity $\vec{v}_r$. Clearly, the nearly constant orbital velocity is the dominant component in the X-direction of the S/C frame. In the Y-direction, the three contributions are of the same order of magnitude. The atmospheric corotation is slightly larger than the other two, showing a nice sinusoidal pattern.

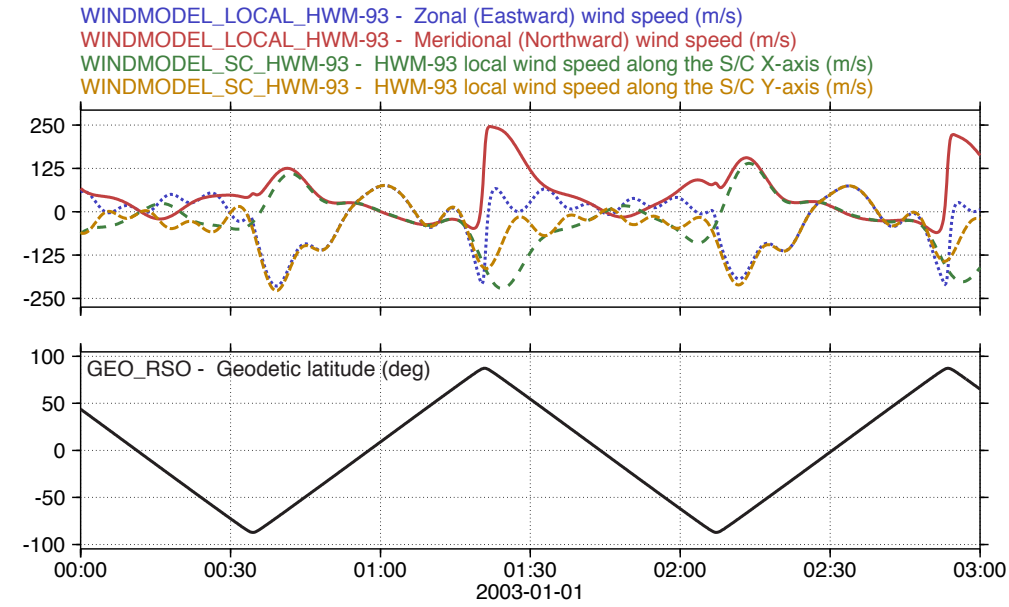

Figure 4.13 Comparison of HWM-93 model winds in local and spacecraft body-fixed coordinate system.

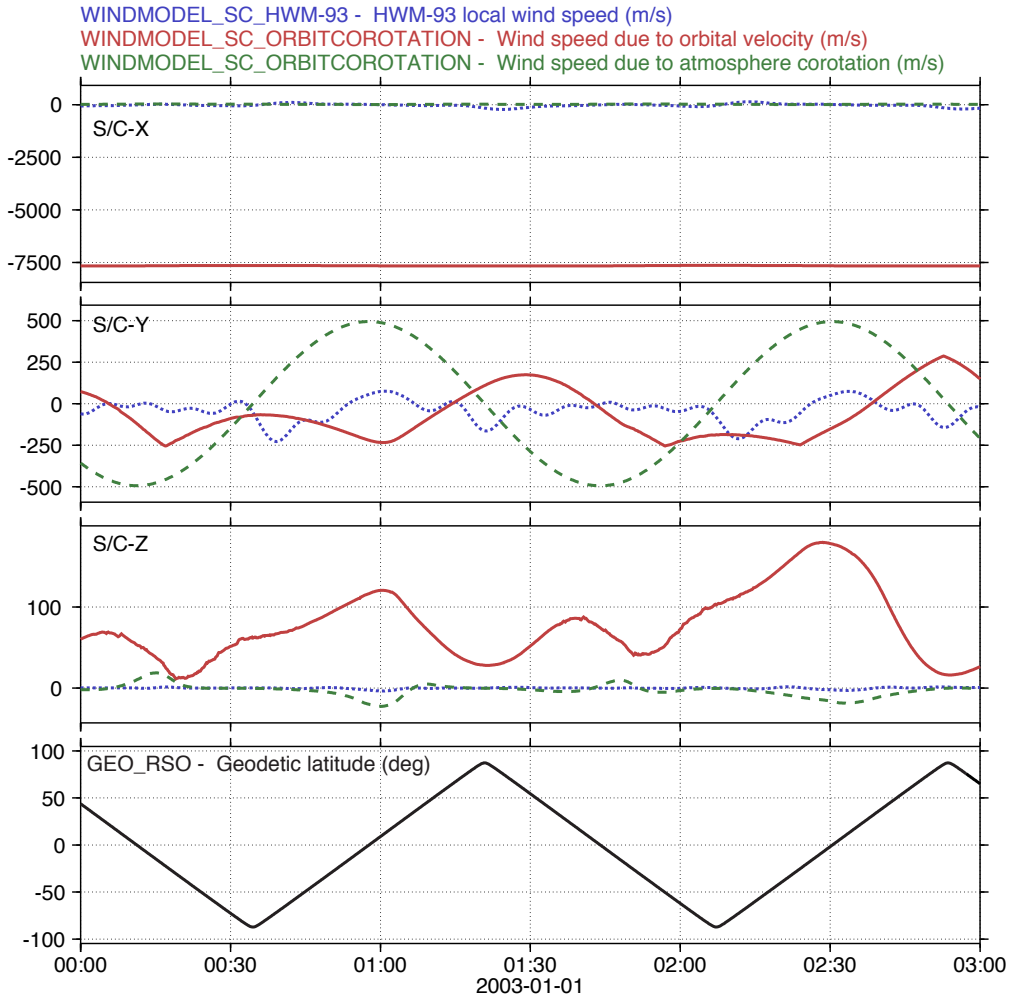

Figure 4.14 Comparison of HWM-93 model winds in local and spacecraft body-fixed coordinate system.

In the Z-direction, the horizontal wind speeds are necessarily very small, as they are proportional to the sine of the pitch angle, which is kept within plus and minus three degrees. The contribution due to the orbital velocity is by far the largest.

4.8.5 HASDM calibrated density model output: DENSDATA_HASDM

HASDM (High Accuracy Satellite Drag Model) data, evaluated along the tracks of CHAMP and GRACE, was kindly provided by Bruce Bowman. These datasets were imported into the database, providing the following fields:

1. HASDM density at satellite altitude (kg/m3)
2. HASDM time tag offset with CHAMP 10 sec GPS-time interval (sec)
3. HASDM data altitude (m)
4. HASDM data latitude (deg)
5. HASDM data longitude (deg)
6. HASDM data local solar time (hours)

The CHAMP and GRACE orbits, along which HASDM was evaluated were computed at Air Force Space Command, so the positions are not exactly the same as the CHAMP Rapid Science Orbits, or GRACE Navigation Solution orbits. The time tags of orbit and model evaluation were also not quite the same as that on the rest of the products in the database. These differences are generally small. They can be checked using fields 2–6 in this product, and comparing with the data in the ORBIT_GEO products.

4.8.6 CTIPe physical density and wind model output: DENSWINDDATA_CTIPE

The density and wind model data from the CTIPe physical model does not fit into the same data format as the empirical models. For that reason, a modified format is applied, containing the following records:

1. CTIPe density at satellite altitude (kg/m3)
2. CTIPe thermospheric temperature (K)
3. CTIPe zonal (Eastward) wind speed (m/s)
4. CTIPe meridional (Northward) wind speed (m/s)
5. CTIPe vertical (upward) wind speed (m/s)
6. CTIPe atomic oxygen density
7. CTIPe molecular oxygen density
8. CTIPe molecular nitrogen density

The original CTIPe data are delivered as NetCDF files, which contain grids at regular intervals of time, longitude, latitude and several pressure levels. The interpolation and extrapolation to the satellite position is performed in a separate piece of software, which reads in data from both the ORBIT_GEO product and the CTIPe NetCDF data, and outputs the time series which is then read into the database to form this product.

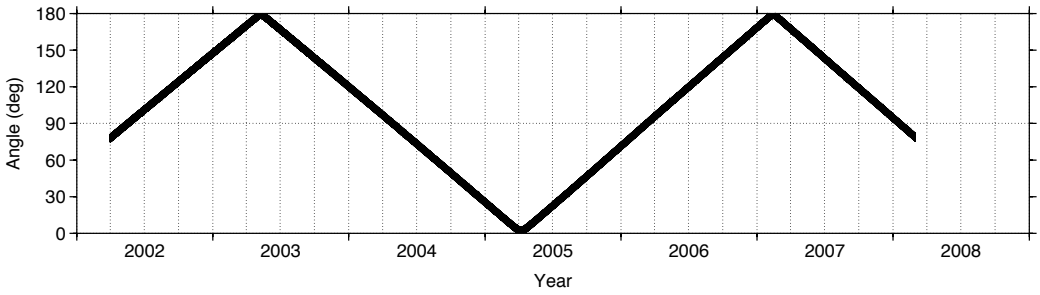

Figure 4.15 Time evolution of the angle between the orbital planes of CHAMP and GRACE.

MultiSat

The MultiSat category contains data products that aid in the processing of multi-satellite data. It currently contains the products ORBITDIFF_GRACE-1_CHAMP and ORBITDIFF_GRACE-1_GRACE-2. It contains the following data fields, which help in selecting periods with interesting observation geometry by the different satellites:

1. Distance (straight-line) between satellites (m)
2. Height difference (m)
3. Angle between the two position vectors (deg)
4. Angle between the two orbital planes (deg)

The angle between the orbital planes of both missions is plotted in Figure 4.15. Since the start of the mission, there have been only three occasions where the two satellites were in the same plane:

- Around May 10, 2003: The orbit planes are at 180 degrees, so the satellites are flying in opposite direction (retrograde). This was a period of elevated to high geomagnetic activity, throughout.
- Around April 4, 2005: This is the only occasion where the satellites were flying in the same direction in the same orbital plane. There was a clearly defined storm exactly on the day of closest approach, and a longer period of higher geomagnetic activity a few days later (Apr 12-16).
- Around February 12, 2007: The orbit planes are again at 180 degrees. There is again a peak in geomagnetic activity almost exactly at the same time as the conjunction of the orbit planes. A few days later there were some very quiet days as well. Unfortunately, CHAMP data are missing on the exact day of conjunction. A further investigation of this data gap has shown that both the orbit and accelerometer data products are not available on the ISDC/GFZ-Potsdam website. It is therefore likely due to an event on the satellite, or the ground segment, and not in the project's data processing. The CHAMP newsletters, which might contain more information on the missing data, were not available online at the time of writing.

SolGeoActivity

The SolGeoActivity category currently contains one data product, called SOLARGEO_PROXIES_INDICES, with the following fields:

1. F10.7 - Daily observed 10.7-cm flux (sfu)

2. F10.7_BAR - 81-day average of observed 10.7-cm flux (sfu)
3. kp - 3-hourly planetary geomagnetic index
4. ap - 3-hourly planetary equivalent geomagnetic amplitude (nT)

These fields are helpful in selecting and binning data according to the level of solar EUV or geomagnetic activity. Note that in empirical models, time delays are usually applied to these proxies and indices, which is not the case here.

Chapter 5
Radiation pressure modelling

5.1 Radiation force analysis methods

For satellites like CHAMP, with low Earth orbits, the radiation forces may be one order of magnitude smaller than the aerodynamic drag forces. Due to the small aerodynamic lift, solar radiation forces may however become comparable to the aerodynamic lift force.

Radiation pressure perturbation is one of the most important non-gravitational forces acting upon a spacecraft, especially at the altitudes where aerodynamic effects become small and/or for spacecraft of large dimensions and small specific mass. Radiant energy effects on the orbital motion of satellites became of interest to celestial mechanics during pioneering missions of the Van-

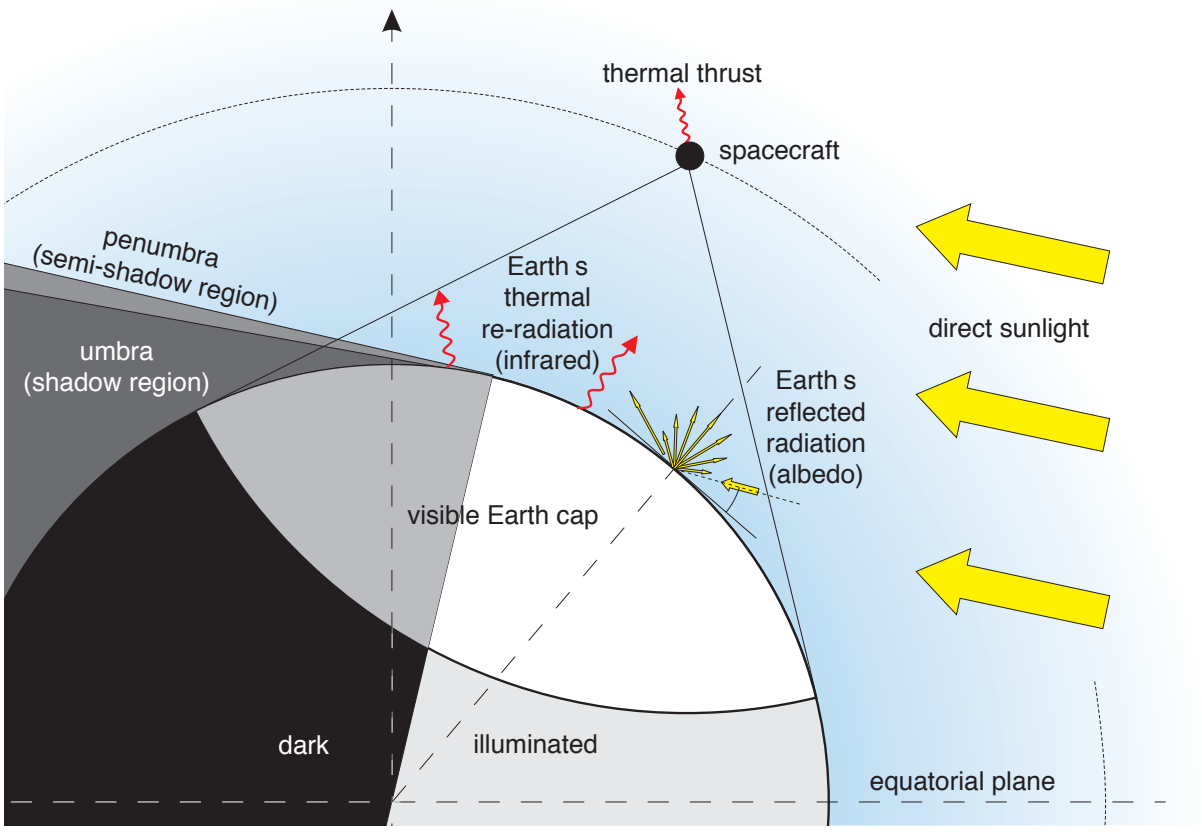

Figure 5.1 Radiative and aerodynamic environment of a satellite.

Radiation source	acceleration (nm/s^2)
Direct solar radiation	65–73
Earth Albedo	2–12
Earth IR	5–10
Spacecraft IR	5–6

Table 5.1 Accelerations on TOPEX/Poseidon due to various radiation sources

guard I and Echo I satellites. A summary of radiation forces and the corresponding radiation sources is shown in Figure 5.1.

To take account of these effects, simple solar radiation pressure models have been derived. The authors of [*Musen*, 1960; *Parkinson et al.*, 1960] determined the most important perturbations induced by radiation pressure for the Vanguard I satellite. The shadow effect was neglected, and the specular reflection of the sun rays on the satellite surface was assumed. Further investigations of the radiation pressure effects were stimulated by the launch of balloon satellites Echo 1, Echo 2, and Pageos. The perturbations in the motion of these satellites caused by solar radiation reach a considerable magnitude, they are fairly accurately determined from observations. Thus, more detailed studies of radiation pressure effects became necessary including firstly the Earth's shadowing effects, This was the subject of papers [*Ferraz-Mello*, 1964; *Lala and Sehnal*, 1969; *Lala*, 1971; *Ferraz-Mello*, 1972; *Vashkovyak*, 1973, 1976]. The disturbances related to reflection of sun rays on the Earth surface were also taken into account [*Sehnal*, 1966; *Baker*, 1966; *Wyatt*, 1963; *Sehnal*, 1970]. A brief review of papers published before mid-70s can be found in [*Aksenov*, 1977].

The development of space technology has required appreciably more accurate predictions of the satellite orbit perturbations. In particular, an extremely high accuracy is required for satellites included into Global Positioning System (GPS) [*Lichten and Border*, 1987; *Vigue et al.*, 1994], geophysical satellites such as LAGEOS [*Rubincam and Weiss*, 1986; *Rubincam*, 1987] and TOPEX/POSEIDON [*Marshall et al.*, 1992; *Antreasian and Rosborough*, 1992]. Thus, for instance, the orbit of the TOPEX/POSEIDON satellite designed for oceanographical research is to be calculated with an error not higher than 10 cm in the radial direction in ten days. This requires the effects which had been previously considered negligible, to be taken into account. In particular, the following sources of radiation , can be identified as contributors for radiation pressure forces [*Carrou*, 1995]:

- Direct solar radiation
- Solar radiation reflected on the Earth (Albedo)
- Infrared thermal radiation of the Earth
- Thermal radiation of the spacecraft

Radiation emitted by the instruments installed on a spacecraft (radar, altimeter, etc.) can be mentioned as an additional factor. According to [19], however, the recoil forces caused by it are negligibly small, namely by three orders of magnitude less than other radiation forces.

The relative contribution of the other sources can be estimated, for example, on the basis of data for the TOPEX/POSEIDON satellite [*Antreasian and Rosborough*, 1992]. This satellite moves along a circular orbit at the altitude of 1336 km. The maximum accelerations induced by various sources of radiation depend on

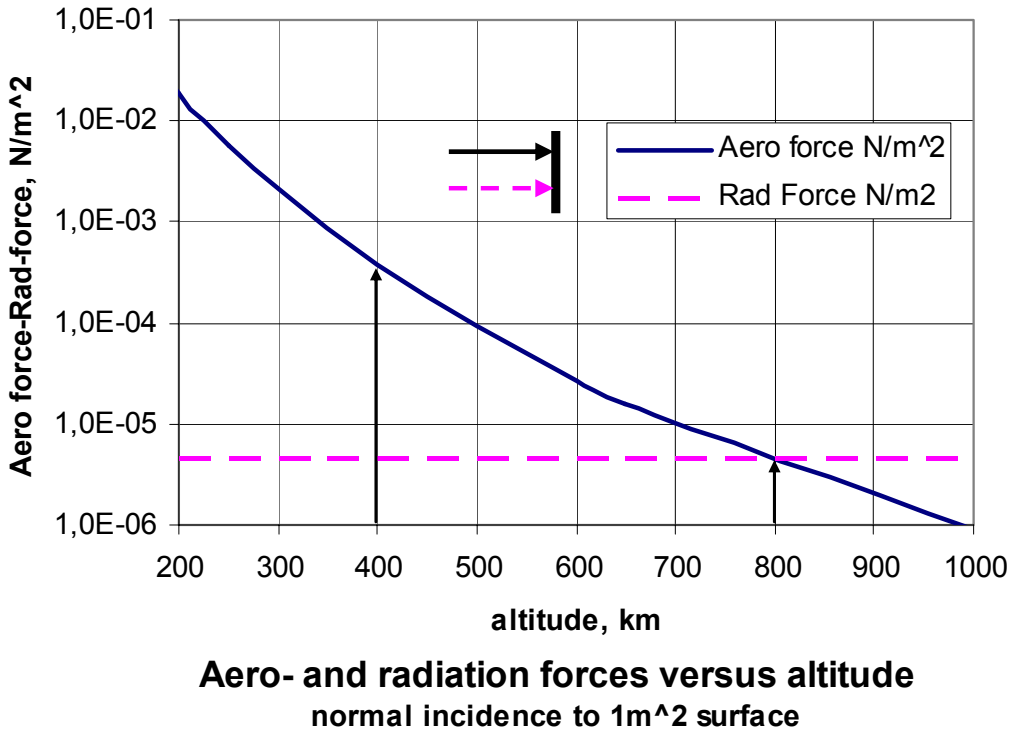

Figure 5.2 Aerodynamic and radiation forces versus altitude.

the orbit orientation and vary for TOPEX/Poseidon within the limits provided in Table 5.1.

Thus, it is obvious that though the direct solar radiation makes the major contribution, the effect of other factors cannot be neglected when the spacecraft orbit is to be determined with a high accuracy. Albedo and infrared radiation effects are approximately 10 percent of those of the direct solar radiation. The effect of thermal emission of spacecraft surfaces has been found to be of the same magnitude as the Earth infrared radiation effect. A complete radiation force analysis requires the consideration of each radiation source and is conducted in 2 steps:

1. Calculation of the flux incident onto the spacecraft from a given source.
2. Calculation of the force acting upon the spacecraft as a result of interaction of the spacecraft surface with this flux.

The second stage requires a certain model to describe the interaction of electromagnetic radiation with the spacecraft surface. This interaction is a very sophisticated physical process [*Born and Wolf*, 1999; *Landsberg*, 1976; *Kisel*, 1973; *Kittel*, 1971] whose particular features are determined by the surface material. For practical applications, however, it is sufficient to characterize the material by several coefficients:

- absorption factor α
- diffuse reflection factor ρ_d
- specular reflection factor $\rho_s = 1 - \rho_d$
- emissivity ϵ

If these quantities and the incident radiation fluxes are known, the resulting forces can be calculated with similar formulations as for satellite aerodynamics

with speed ratio $S = \infty$ (see Chapter 6). Due to the analogy between infinite speed ratio particle flow and the photon flow, the analysis tools for molecular particle flux can easily be extended to conduct radiation force analysis. This was a main reason for ESA and HTG to initiate the development of the ANGARA system, which incorporates the RAMSES aerodynamic analysis modules.

The radiative photon flux sources to a satellite are completely different to the atmospheric molecular particle source. It was therefore necessary to incorporate models in ANGARA, for all radiation sources to which an orbiting satellite is exposed. During ANGARA development, this required the main effort. As result of the very detailed photon source modelling, ANGARA now includes the following force contributions:

- Direct solar radiation including semi shadowing, and absorption and refraction by the Earth's atmosphere
- Indirect solar radiation considering the visible part of the Earth and its albedo
- Thermal radiation from the visible Earth
- Self radiation from hot satellite surfaces

Figure 5.2 compares aerodynamic and radiation forces for normal incidence to unit area. At 800km both forces are of equal magnitude.

At 400km altitude, which is of interest to the study, the aerodynamic force exceeds the radiation force by a factor of 100. In this case radiation, can only produce forces comparable to aerodynamic forces, if it is acting in directions, where aerodynamic forces are small. These are side force and lift directions.

5.2 Implementation of radiation pressure models in the data processing

Several satellite non-gravitational force models have been implemented in the project software. This includes the highly detailed ANGARA software package, as well as the often-used models based on a set of panels. The availability of multiple models allows for comparisons to be made, which gives some insight into the precision of the models.

5.2.1 Normalized force coefficients

The basis for the calculation of the non-gravitational forces is formed by the normalized force coefficient vectors which will be designated by the symbol $\vec{C}_F$. For this study, the vector components will be expressed in the spacecraft body-fixed reference frame.

The definition of the force coefficient vector for aerodynamics follows from the equation:

$$\ddot{\vec{r}}_a = \vec{C}_F \frac{A_{ref}}{m} \frac{1}{2} \rho v_r^2 \tag{5.1}$$

Here, $\ddot{\vec{r}}_a$ is the aerodynamic acceleration, A_{ref} is a reference area, ρ is the atmospheric density and v_r is the magnitude of the velocity of the atmosphere, relative to the spacecraft body. This equation is very similar to that used in low-speed

aerodynamic computations, where the product $\frac{1}{2}\rho v_r^2$ is called the dynamic pressure[1].

A similar equation defines $\vec{C}_F$ for radiation pressure calculations:

$$\ddot{\vec{r}}_r = \vec{C}_F \frac{A_{ref}}{m} P \tag{5.3}$$

where $\ddot{\vec{r}}_r$ is the radiation pressure acceleration and P is the radiation pressure, which is computed as follows:

$$P = \frac{\Phi}{c} = \frac{\Delta E}{A \Delta t c} \tag{5.4}$$

where Φ is the energy flux and c the speed of light. Φ is defined as the amount of energy ΔE of the photons that passes through an area A during a time interval of Δt. For a satellite in orbit around the Earth, the precise value of P should be computed by taking into account eclipses and the varying distance between the satellite and the Sun, as explained in 5.2.6. For Earth albedo and infrared radiation pressure, the matter becomes more complicated, as will be explained in Section 5.2.8.

Note that when values of $\vec{C}_F$ are presented, they should always be accompanied by the value of A_{ref} to which they apply. Confusion can arise when comparing values of $\vec{C}_F$ computed using different definitions for A_{ref}. It is a convention in aerodynamics to hold A_{ref} at a predefined constant value, regardless of the direction of flow. In surface force modelling for satellites however, the true frontal area with respect to the flow, or an approximation of it is often used.

In the processing software for this project, the latter approach is adopted, and the product $(\vec{C}_F A)$ is used as a single vector quantity in the data storage and computations. Instead of defining a new, single-letter symbol for this quantity, in this report it will be used as written above, between brackets, to keep the connection with the familiar equations used elsewhere in literature.

The equations (5.1) and (5.3) can then be put into a subtly different form:

$$\ddot{\vec{r}}_a = \frac{(\vec{C}_F A)}{m} \frac{1}{2} \rho v_r^2 \tag{5.5}$$

$$\ddot{\vec{r}}_r = \frac{(\vec{C}_F A)}{m} P \tag{5.6}$$

The values of $(\vec{C}_F A)$ represent the interaction between the incoming particles and the satellite. When the satellite shape and surface characteristics are defined, $(\vec{C}_F A)$ is a function of the direction of the incoming particles for both aerodynamics and radiation pressure calculations. For aerodynamics, the force coefficient vector is also a function of the composition and temperature of the atmosphere, and of the velocity of the incoming particles.

[1] In textbooks on satellite orbits, the aerodynamic lift force is usually neglected, and only the drag component is considered. Equation (5.1) then simplifies to the familiar equation

$$\ddot{r}_a = C_D \frac{A}{m} \frac{1}{2} \rho v_r^2 \tag{5.2}$$

where the direction of acceleration is in the opposite direction of the satellite velocity with respect to the atmosphere. The vector $\vec{C}_F$, in contrast, is not necessarily in this direction, since lift and sideways forces can be considered, in addition to drag.

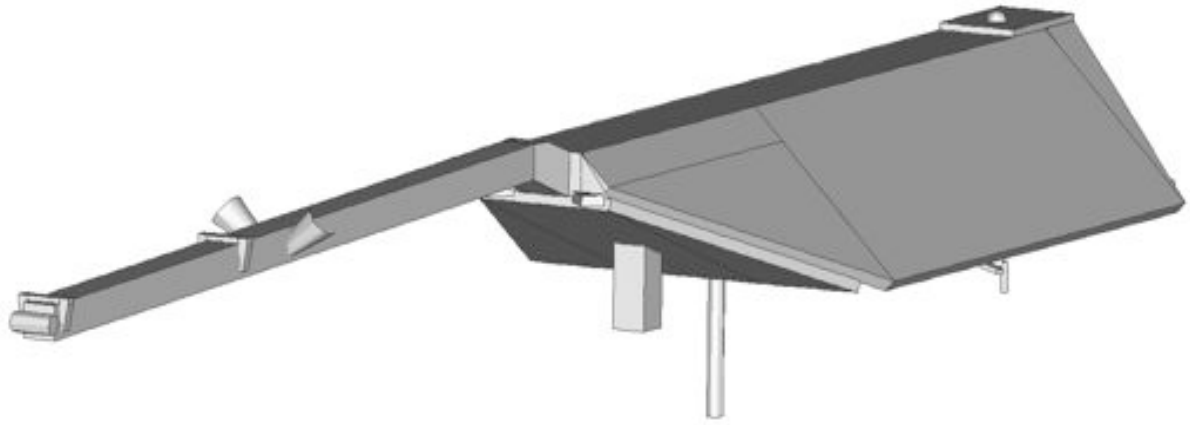

Figure 5.3 The CHAMP ANGARA model.

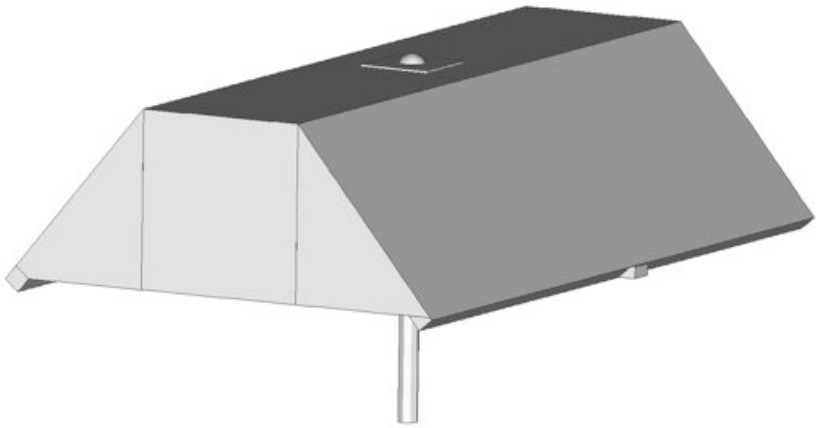

Figure 5.4 The GRACE ANGARA model.

The computation of $(\vec{C}_F A)$ as a function of its defining parameters is the main subject of this Chapter and the next.

In the next section, the representation of the satellite surface forces within the ANGARA and panel models will be discussed. The approaches of these two types of model for the implementation in the processing software are quite different, but in the end, they both provide values of $(\vec{C}_F A)_s$ as a function of the same input parameters.

5.2.2 ANGARA force models

The ANGARA software, developed by HTG under ESA/ESOC contract is extensively described in *Fritsche et al.* [1998]. Only a brief summary will be provided here. The software comprises of computational modules for aerodynamics and radiation pressure, both with options for Monte Carlo Test Particle methods and integral methods. Only the Monte Carlo Test Particle computation modules have been used for the data processing in this study. The aerodynamics module computations are described in more detail in Chapter 6. Both forces and moments can be calculated using the software. Only the force computations are used in this study.

Both the aerodynamics and radiation pressure computation modules make use of satellite geometry models that are built in a separate 3D modelling module. The geometry of the satellite outer surfaces can be constructed from primitive shapes such as boxes, panels, spheres, ellipsoids and cones. Each of the surfaces can be assigned surface properties, using yet another module.

The Monte Carlo Test Particle computations can be time-consuming, and therefore the computation of forces (and moments) or accelerations is split in two phases. In Phase 1, the time-consuming computations take place, and the results are output as normalized force and moment coefficients, tabulated according to the incidence direction of the particle stream and other parameters. In phase 2, which requires comparatively very little computation time, these coefficients are interpolated from the tabular data stored in computer memory, and de-normalized. The phase 2 software is completely integrated with the project's accelerometer processing software. Several models that were originally developed for ANGARA phase 2, such as the eclipse and Earth radiation pressure models, were adapted for use by both the ANGARA and panel model calculations. These phase 2 ANGARA models will be described in more detail in this Chapter and in Chapter 6

The CHAMP and GRACE models which were developed specifically for this project are visualized in Figures 5.3 and 5.4. A preliminary CHAMP model, with a much simplified geometry, developed as a M.Sc. thesis project using ANGARA at DEOS/TU Delft in 2005/2006 [*Caluwaerts*, 2006] was available as well and was used for comparisons.

5.2.3 ANGARA force model computations

In the processing software, the ANGARA force coefficient tables are read into memory at the start of each program execution. When a force model calculation is required, the relevant value of $(\vec{C}_F A)$ is determined by interpolation.

For radiation pressure calculations, two tables are available, one for visible wavelengths, and one for infrared wavelengths. Once the table for the proper wavelength is selected, only the direction of the incoming radiation is of importance, so the interpolation of the table takes place in two dimensions, representing the attack angle α and sideslip angle β in the spacecraft body-fixed frame, expressed in degrees. These angles are determined from the unit vector $\vec{u}$ with components u_x, u_y and u_z in the satellite body-fixed frame (see Figure 4.9), pointing from the source to the satellite. The angle of attack α, in the range $-180^\circ \leq \alpha \leq 180^\circ$, is computed by using the FORTRAN intrinsic atan2 function, as follows:

$$\alpha = \frac{180^\circ}{\pi} \operatorname{atan2}(u_z, u_x) \tag{5.7}$$

The sideslip angle β in the range $-90^\circ \leq \beta \leq 90^\circ$ is computed from the Y-component of $\vec{u}$:

$$\beta = \frac{180^\circ}{\pi} \arcsin(u_y) \tag{5.8}$$

For aerodynamic calculations, an additional parameter is required, which represents the speed ratio S, which is defined as the ratio between the relative velocity v_r of the particles with respect to the spacecraft, and the most probable thermal

speed of the molecules. The speed ratio can be expressed using

$$S = \frac{v_r}{\sqrt{\frac{2RT}{m}}} \tag{5.9}$$

where T is the temperature of the gas, taken from an empirical model, and $R = 8314$ J kmol^{-1}K^{-1} is the universal gas constant. The ANGARA phase 1 aerodynamic calculations result in two tables of vectors, one for the effect of the momentum exchange due to the incoming particles (subscript in), and one for the effect of the outgoing particles, including multiple reflections (subscript out + mr). The total effect for the complete satellite model (subscript s) is computed by applying the following equation:

$$(\vec{C}_F A)_{\mathrm{s}} = (\vec{C}_F A)_{\mathrm{in}} + \sqrt{\frac{T_w}{T}}(\vec{C}_F A)_{\mathrm{out+mr}} \tag{5.10}$$

where T_w is the spacecraft wall temperature ($T = 273$ K is assumed), and T is the temperature of the gas from the NRLMSISE-00 model.

ANGARA offers the possibility of modelling satellites with moving external parts, such as rotating solar arrays, by making use of a geometry parameter ϕ. The use of this parameter is not required for CHAMP and GRACE, so it is set to zero in the calls to the ANGARA phase 2 software.

5.2.4 Panel force model computations

For the panel models, the force coefficient vectors are computed by summing the contribution of each of the N panels with index i that make up the model. The value of $(\vec{C}_F A)_{\mathrm{s}}$ with subscript s for the whole satellite can be found using the summation:

$$(\vec{C}_F A)_{\mathrm{s}} = \sum_{i=1}^{N} (\vec{C}_F A)_i \tag{5.11}$$

A panel model consists of a set of panel areas A and outward normal unit vectors $\vec{u}_N$ that define their orientations in the body-fixed frame. As far as the force model computations are concerned, the panels are one-sided. In other words, the backside of each panel can be considered transparent for the atmospheric particles and photons that act upon the panel.

For each panel, reflectivity properties in the form of diffuse and specular reflectivities ρ_d and ρ_s, for both visible and infrared light, are available. The values for these properties were taken from technical reports [*Lühr et al.*, 2002; *Bettadpur*, 2007] and literature [*Bruinsma and Biancale*, 2003], and are summarized in Tables 5.2 and 5.3. Note that the GRACE table contains an entry for the nadir-pointing boom containing the S-band communications antenna. In the current processing software, the area of this part of the satellite can not be represented in the panel model.

5.2.5 Radiation pressure for a single panel

The derivation of an equation for the radiation pressure force coefficient for a single panel is much simpler than the aerodynamic equation. First, γ is the cosine of the angle between the panel normal and the direction vector.

$$\gamma = -\vec{u}_s \cdot \vec{u}_N \tag{5.12}$$

		Area (m^2)			Outward normal			Visible refl.		IR refl.	
i	Description	GFZ	Bruinsma	DEOS	$X_{S/C}$	$Y_{S/C}$	$Z_{S/C}$	spec.	diff.	spec.	diff.
1	Top	1.2920	1.2920	1.1500	0.0000	0.0000	-1.0000	0.05	0.30	0.03	0.16
2	Bottom	3.6239	3.6239	4.0000	0.0000	0.0000	1.0000	0.68	0.20	0.19	0.06
3	Left solar panel	3.1593	3.1593	3.1000	0.0000	-0.7071	-0.7071	0.05	0.30	0.03	0.16
4	Left panel rear	0.3020	0.3020	0.0000	0.0000	0.7071	0.7071	0.40	0.26	0.23	0.15
5	Right solar panel	3.1593	3.1593	3.1000	0.0000	0.7071	-0.7071	0.05	0.30	0.03	0.16
6	Right panel rear	0.3020	0.3020	0.0000	0.0000	-0.7071	0.7071	0.40	0.26	0.23	0.15
7	Aft	0.4902	0.4902	0.8000	-0.9397	0.0000	0.3420	0.40	0.26	0.23	0.15
8	Front	1.2199	1.2199	1.2199	0.3420	0.0000	0.9397	0.20	0.40	0.26	0.51
9	Boom top	0.5110	0.5110	0.5110	0.0000	0.0000	-1.0000	0.40	0.26	0.23	0.15
10	Boom top 2	0.4190	0.4190	0.4190	0.0000	0.0000	-1.0000	0.64	0.20	0.71	0.22
11	Boom bottom	0.9300	0.9300	0.9300	0.0000	0.0000	1.0000	0.40	0.26	0.23	0.15
12	Boom right	0.9300	0.9300	0.9300	0.0000	1.0000	0.0000	0.40	0.26	0.23	0.15
13	Boom left	0.9300	0.9300	0.9300	0.0000	-1.0000	0.0000	0.40	0.26	0.23	0.15
14	Boom front	0.0529	0.0880	0.0529	1.0000	0.0000	0.0000	0.20	0.40	0.26	0.51
15	Boom front 2	0.0000	0.1314	0.1314	1.0000	0.0000	0.0000	0.40	0.26	0.23	0.15
16	Front 2	0.0000	0.0000	0.1500	0.7170	0.0000	0.7170	0.40	0.26	0.23	0.15

Table 5.2 CHAMP panel model properties, based on *Bruinsma and Biancale* [2003] and *Lühr et al.* [2002]. The DEOS model was created by tweaking towards the values in the CH-IT-DID-0001 document.

			Outward normal			Visible refl.		IR refl.		
i	Description	Area (m^2)	X_{SRF}	Y_{SRF}	Z_{SRF}	spec.	diff.	spec.	diff.	Material
1	Front	0.9551567	1.0000	0.0000	0.0000	0.40	0.26	0.23	0.15	SiOx/Kapton
2	Rear	0.9551567	-1.0000	0.0000	0.0000	0.40	0.26	0.23	0.15	SiOx/Kapton
3	Starboard (outer)	3.1554792	0.0000	0.7660	-0.6428	0.05	0.30	0.03	0.16	Si glass
4	Starboard (inner)	0.2282913	0.0000	-0.7660	0.6428	0.40	0.26	0.23	0.15	SiOx/Kapton
5	Port (outer)	3.1554792	0.0000	-0.7660	-0.6428	0.05	0.30	0.03	0.16	Si glass
6	Port (inner)	0.2282913	0.0000	0.7660	0.6428	0.40	0.26	0.23	0.15	SiOx/Kapton
7	Nadir	6.0711120	0.0000	0.0000	1.0000	0.68	0.20	0.19	0.06	Teflon
8	Zenith	2.1673620	0.0000	0.0000	-1.0000	0.05	0.30	0.03	0.16	Si glass
–	Boom	0.0461901	–	–	–	0.40	0.26	0.23	0.15	SiOx/Kapton

Table 5.3 GRACE panel model properties, based on *Bettadpur* [2007]

For negative γ, the panel is in darkness, so that

$$(\vec{C}_F A) = \vec{0} \quad \text{for} \quad \gamma \leq 0 \tag{5.13}$$

For positive values of γ, a photon arriving at the panel is either absorbed, reflected diffusely or reflected specularly (see Figure 5.5). If ρ_d is the proportion of diffusely reflected photons and ρ_s the proportion of specularly reflected photons, then $(1 - \rho_s - \rho_d)$ is the proportion of absorbed photons. Let $\vec{u}_s$ represent the unit vector from the light source to the panel and $\vec{u}_N$ the outward panel normal, both in the spacecraft body-fixed frame, then the radiation pressure coefficient can be expressed in vector form as:

$$\vec{C}_R = (1 - \rho_s - \rho_d)\vec{u}_s - 2\rho_s(\vec{u}_s \cdot \vec{u}_N)\vec{u}_N + \rho_d(\vec{u}_s - \frac{2}{3}\vec{u}_N) \tag{5.14}$$

The calculation of $(\vec{C}_F A)$ is completed by multiplying $\vec{C}_R$ with the projected area $A\gamma$, where A is the full panel area as listed in Tables 5.2 and 5.3.

$$(\vec{C}_F A) = \vec{C}_R A\gamma \quad \text{for} \quad \gamma > 0 \tag{5.15}$$

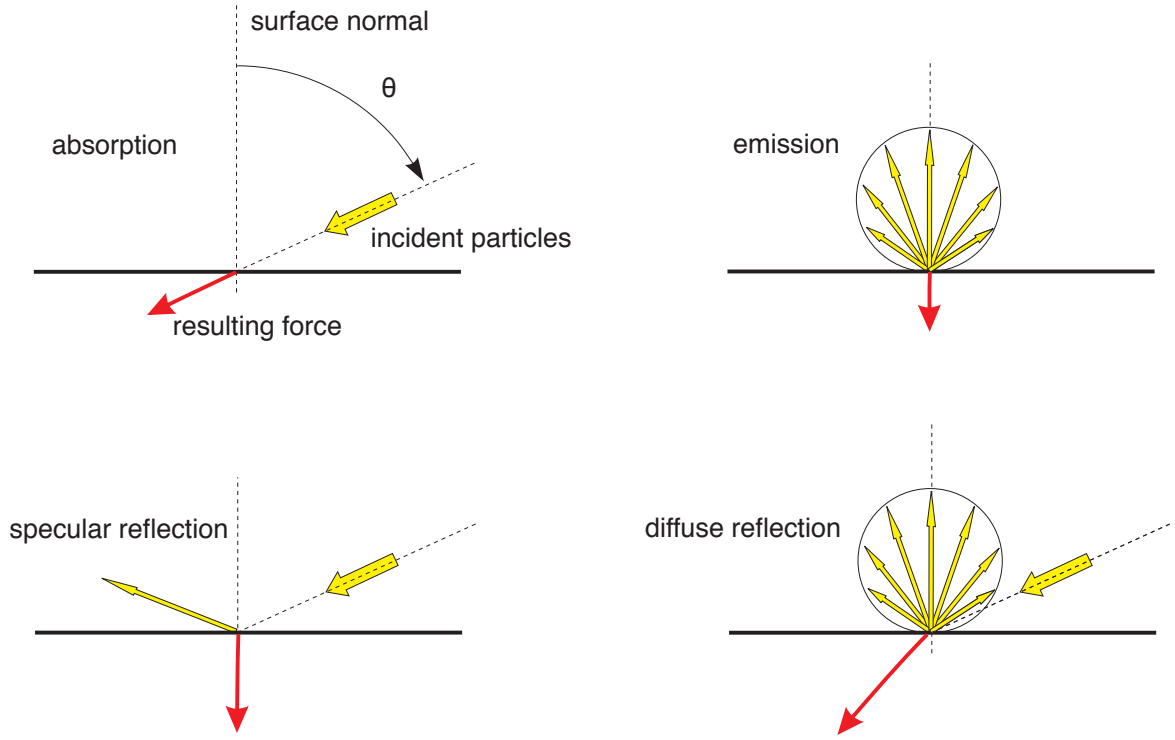

Figure 5.5 Absorption, reflection and emission of photons on a surface.

The next step in the force model calculations is to model the characteristics of the space environment in a way that is as realistic as possible. The next section will discuss how the various radiation sources are modelled.

5.2.6 Eclipses

The satellite shall often be eclipsed by the Earth. For this purpose a shadow function $f_s = f(\vec{r}, \vec{r}_\odot)$ is introduced, which is computed from the geocentric satellite position $\vec{r}$ and Sun position $\vec{r}_\odot$. The shadow function is defined to have a value of one when the satellite is in full sunlight, and zero when the satellite is fully eclipsed. Because the Sun forms a solid disc of about 0.5°, the Earth casts a semi shadow region, or pen-umbra around the core shadow, or umbra. In addition, sunlight which passes through the atmosphere is refracted, increasing the geometrically defined semi-shadow region. So in effect, the Earth's shadow works like an on/off switch on the direct solar radiation pressure, with the semi-shadow region smoothening this transition.

Different algorithms exist in order to determine whether a satellite is in eclipse [*Montenbruck and Gill*, 2000; *Vallado*, 2001; *Adhya et al.*, 2004]. An especially elaborate treatment of the problem can be found in the series of papers by *Vokrouhlický et al.* [1993, 1994, 1996]. The method outlined below is provided in the ANGARA level 2 software [*Fritsche et al.*, 1998]. It can be used to describe atmospheric effects on the semi-shadow boundaries. The basis of this method is a conical shadow model, where the Sun's disc is projected on an Earth radius vector which is perpendicular to the Sun-satellite line (see Figure 5.6).

The symbols $\oplus$ and $\odot$ are used for the positions of centres of the Earth and Sun, respectively, while s is used to denote the satellite position. Let $\vec{r}_{\oplus\to s}$ and

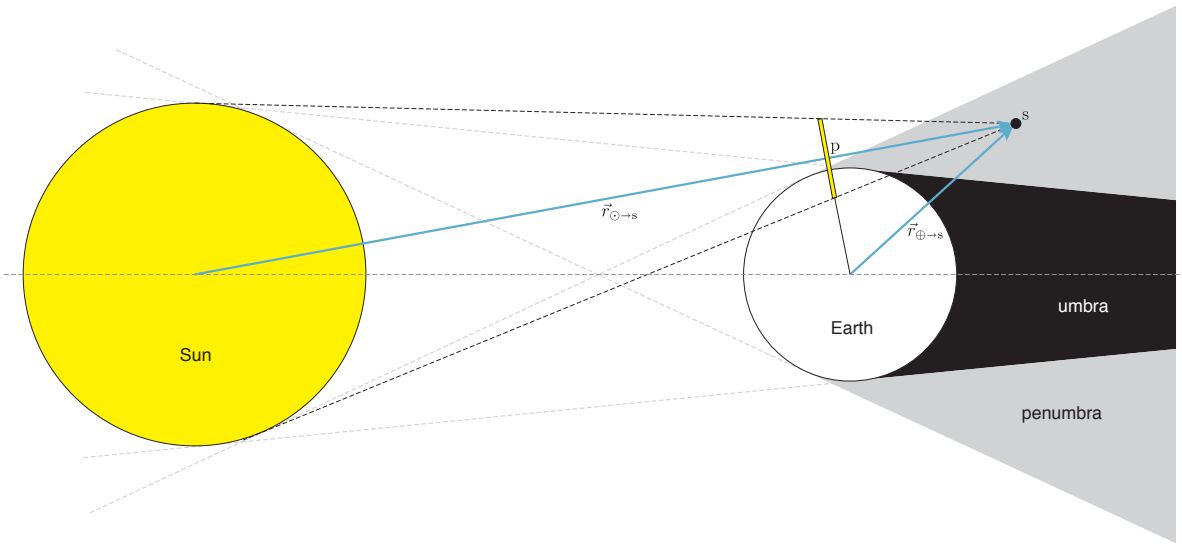

Figure 5.6 Eclipse geometry

$\vec{r}_{\odot\to s}$ then denote the position vectors of the satellite with respect to the centres of these two bodies. Their unit vectors are $\vec{u}_{\oplus\to s}$ and $\vec{u}_{\odot\to s}$.

The vector

$$\vec{r}_{p\to s} = (\vec{u}_{\odot\to s} \cdot \vec{r}_{\oplus\to s})\, \vec{u}_{\odot\to s} \tag{5.16}$$

then points along the Sun-satellite vector to the satellite center of mass from the point p, which is the closest point to the Earth's centre. The vector from the Earth's centre to this point p is then

$$\vec{r}_{\oplus\to p} = \vec{r}_{\oplus\to s} - \vec{r}_{p\to s} \tag{5.17}$$

The height above the Earth's surface of a line connecting the center of the Sun with the satellite is equal to

$$h_g = |\vec{r}_{\oplus\to p}| - R_\oplus \tag{5.18}$$

and the apparent radius of the solar disc projected on a plane through this point, perpendicular to the satellite-Sun vector is

$$R_p = \frac{|\vec{r}_{p\to s}|}{|\vec{r}_{\odot\to s}|} R_\odot \tag{5.19}$$

In these equations, $R_\oplus$ and $R_\odot$ are the radiuses of the Earth and Sun, respectively. A spherical Earth is assumed in the current version of the algorithm. A future implementation will include an oblate Earth, which is expected to improve the accuracy of the algorithm further.

Let $f_{ah}(h, d)$ be a function that returns the apparent height of a ray of light under the influence of refraction in the atmosphere, where h is the height without refraction and $d = |\vec{r}_{\oplus\to p}|$ the distance from the satellite to the point p. The derivation of the function f_{ah} is available in *Fritsche et al.* [1998]. Then

$$h_c = f_{ah}(h_g, d)$$

$$h_t = f_{ah}(h_g + R_p, d)$$

$$h_b = f_{ah}(h_g - R_p, d)$$

denote the apparent height above the Earth's surface of the beams from the center, top and bottom of the solar disc, respectively. A negative value indicates that the beam is blocked by the Earth (see Figure 5.6).

The effect of atmospheric refraction on the eclipse is that the semi-shadow region will be considerably expanded. This effect will be especially important for satellites in high orbits.

A geometric parameter η can now be introduced such that

$$\eta = \frac{h_c}{h_c - h_b} \quad , \tag{5.20}$$

where

$$\begin{aligned} \eta < -1 &\quad \text{if the satellite is in full eclipse} \\ -1 \leq \eta \leq 1 &\quad \text{if the satellite is in partial eclipse} \\ \eta > 1 &\quad \text{if the satellite is in full sunlight} \end{aligned}$$

Two effects can be recognized that determine the value of the shadow function f_s. The geometric shadowing factor f_g indicates the fractional area of the solar disc that is blocked by the Earth. It can be calculated using the method of *Carrou* [1995], resulting in the following formula:

$$f_g = \frac{A_{\odot,\text{eff}}}{A_\odot} = 1 - \frac{1}{\pi}\arccos(\eta) + \frac{\eta}{\pi}\sqrt{1-\eta^2} \tag{5.21}$$

The amount of sunlight that is not absorbed in the Earth's atmosphere is represented by the factor f_a. An algorithm to determine it is described by *Fritsche et al.* [1998]. The complete shadow function can then be computed by multiplying the geometric and absorption contributions.

$$f_s = f_g f_a \tag{5.22}$$

5.2.7 Varying Sun-Earth distance

For a realistic solar radiation pressure calculation, the varying distance of the spacecraft from the Sun has to be taken into account. For sunlight at a distance of 1 astronomical unit (1AU = 149,597,870,660 m) from the Sun, P has a value of $P_{1\text{AU}} = 4.56\ 10^{-6}$ N/m^2. Taking the varying Sun-satellite distance $r_{\odot\to\text{s}}$ into account and applying the inverse square law, equation (5.6) becomes

$$\ddot{\vec{r}}_{\text{srp}} = \frac{(\vec{C}_F A)_s}{m}\left(\frac{1\text{AU}}{r_{\odot\to\text{s}}}\right)^2 f_s P_{1\text{AU}} \tag{5.23}$$

For the panel model, once more equation (5.11) should be substituted, resulting in

$$\ddot{\vec{r}}_{\text{srp}} = \frac{1}{m}\left[\sum_{i=1}^{N}(\vec{C}_F A)_i\right]\left(\frac{1\text{AU}}{r_{\odot\to\text{s}}}\right)^2 f_s P_{1\text{AU}} \tag{5.24}$$

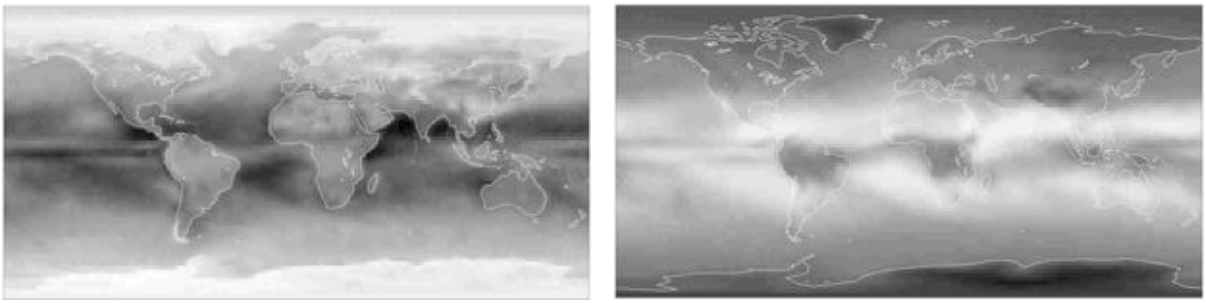

Figure 5.7 Example of a monthly ANGARA Earth albedo map (left) and an Earth infrared radiation map, based on ERBE data. The shade of grey is proportional to the percentage of sunlight that is reflected, or the infrared radiation that is emitted by the Earth surface elements, respectively.

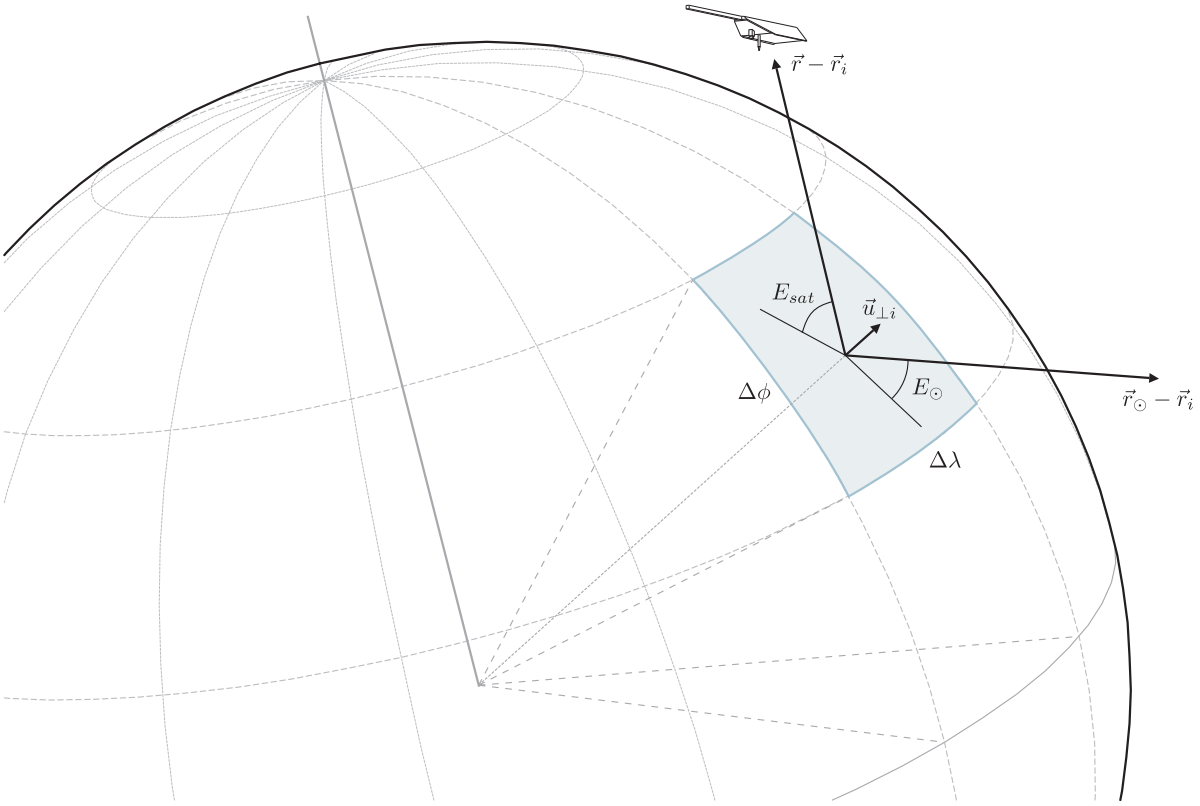

Figure 5.8 Definition of geometrical parameters in the computation of Earth radiation pressure.

5.2.8 Earth albedo and infrared radiation pressure

Because of the proximity of the satellite to the surface, we can not treat the Earth as a single light source. Therefore, the Earth radiation pressure accelerations are calculated by summation of the contributions of a number of Earth elements.

The ANGARA software provides detailed Earth maps of Earth Radiation Budget Experiment (ERBE) satellite data (see Figure 5.7). These bitmaps have a resolution of 144×72 pixels, corresponding to surface elements of $2.5^\circ \times 2.5^\circ$. The ERBE data, spanning several years in the late 1980's, are available in the form of monthly averaged maps containing albedo coefficients and infrared intensity data.

The Earth albedo and infrared radiation maps are stored in bitmap files in

equidistant cylindrical projection, with the top left corner of the map corresponding to +90° latitude and -180° longitude. Figure 5.8 shows various parameters involved in the following calculations.

If the map has a resolution of $L \times M$ pixels and

$$\Delta\lambda = \frac{360^\circ}{L} \tag{5.25}$$

$$\Delta\phi = \frac{180^\circ}{M} \tag{5.26}$$

then each pixel corresponds to an Earth surface element measuring $\Delta\lambda \times \Delta\phi$ degrees.

If a certain pixel is in column m and row l (with $1 \leq m \leq M$ and $1 \leq l \leq L$), the longitude ϕ_k and latitude λ_k of the center of the corresponding Earth surface element with index $k = m(l-1)/L$ can be found from

$$\phi_k = 180^\circ - (l - 0.5)\Delta\phi \tag{5.27}$$

$$\lambda_k = -90^\circ + (m - 0.5)\Delta\lambda \tag{5.28}$$

These coordinates can easily be transformed into Earth-fixed Cartesian coordinates, and subsequently to spacecraft body-fixed coordinates, which then form the vector $\vec{r}_k$.

The area of the Earth surface element is a function of the map resolution and the element's latitude.

$$A_k = \frac{4\pi R_E^2}{L} \sin\left(\frac{\pi/2}{M}\right) \sin\left(\frac{(m-0.5)\,\pi}{M}\right) \tag{5.29}$$

In order to find the albedo radiation pressure at the satellite position P_{alb_k} from a surface element k, we first need to find the incoming radiation pressure from the Sun on this element. This value can be found from the radiation pressure at a mean distance of 1 AU, corrected for the actual distance between the Sun and the surface element.

$$P_{\odot,k} = P_{1\mathrm{AU}} \left(\frac{1\mathrm{AU}}{|\vec{r}_\odot - \vec{r}_k|}\right)^2 \tag{5.30}$$

The percentage of this radiation that actually arrives at the satellite depends on the albedo coefficient C_{alb} and on the elevation angles of the Sun $E_\odot$ and the satellite E_{sat}. These two angles can be found from the following unit vectors, pointing from the surface element to the Sun, the satellite and the surface normal, respectively:

$$\vec{u}_{k\to\odot} = \frac{\vec{r}_\odot - \vec{r}_k}{|\vec{r}_\odot - \vec{r}_k|}, \quad \vec{u}_{k\to\mathrm{s}} = \frac{\vec{r} - \vec{r}_k}{|\vec{r} - \vec{r}_k|}, \quad \vec{u}_{\perp k} = \frac{\vec{r}_k}{|\vec{r}_k|} \tag{5.31}$$

The solar and satellite elevation angles for the surface element can then be found using

$$\sin E_{\odot,k} = \vec{u}_{k\to\odot} \cdot \vec{u}_{\perp k} \tag{5.32}$$

$$\sin E_{sat,k} = \vec{u}_{k\to\mathrm{s}} \cdot \vec{u}_{\perp k} \tag{5.33}$$

The albedo radiation pressure for the surface element is zero if either the satellite or the Sun have a negative elevation angle. Otherwise the sunlight will be reflected following the Lambert law for a diffuse body, and decrease with distance

according to the inverse square law, resulting in the following expression:

$$P_k^{alb} = \begin{cases} 0 & \text{if } \sin E_{sat,k} < 0 \text{ or } \sin E_{\odot,k} < 0 \\ C_k^{alb} A_k P_{\odot,k} \sin E_{\odot,k} \frac{\sin E_{sat,k}}{\pi} \frac{1}{|\vec{r}_k - \vec{r}|^2} & \text{if } \sin E_{sat,k} > 0 \text{ and } \sin E_{\odot,k} > 0 \end{cases} \tag{5.34}$$

The Earth infrared radiation pressure for each Earth element k, denoted by $P_{\oplus,k}^{IR}$ can be read directly from the map. The resulting radiation pressure at the satellite position then becomes

$$P_k^{IR} = \begin{cases} 0 & \text{if } \sin E_{sat,k} < 0 \\ A_k P_{\oplus,k}^{IR} \frac{\sin E_{sat,k}}{\pi} \frac{1}{|\vec{r}_k - \vec{r}|^2} & \text{if } \sin E_{sat,k} > 0 \end{cases} \tag{5.35}$$

Since for each of the Earth's surface elements, the vector to the satellite is different, a summation should take place to determine the accelerations. Note also that the optical properties of the satellite for visible light (albedo) and infrared light are different, requiring separate calculations of $(C_F A)$.

$$\ddot{\vec{r}}_{alb} = \frac{1}{m} \sum_{k=1}^{L \times M} (\vec{C}_F A)_k^{alb} P_k^{alb} \tag{5.36}$$

$$\ddot{\vec{r}}_{IR} = \frac{1}{m} \sum_{k=1}^{L \times M} (\vec{C}_F A)_k^{IR} P_k^{IR} \tag{5.37}$$

For the panel model, substitution in equation (5.11) results in a double summation, over the panels and over the Earth surface elements:

$$\ddot{\vec{r}}_{alb} = \frac{1}{m} \sum_{k=1}^{L \times M} \sum_{i=1}^{N} (\vec{C}_F A)_{k,i}^{alb} P_k^{alb} \tag{5.38}$$

$$\ddot{\vec{r}}_{IR} = \frac{1}{m} \sum_{k=1}^{L \times M} \sum_{i=1}^{N} (\vec{C}_F A)_{k,i}^{IR} P_k^{IR} \tag{5.39}$$

5.3 Geometric and radiation pressure modelling sensitivity analysis

In this section, the accuracy of satellite surface models is analyzed. Surface force models for CHAMP and GRACE are available both in the form of ANGARA force coefficient tables [*Fritsche et al.*, 1998] and of simplified sets of panels [*Bruinsma and Biancale*, 2003; *Bettadpur*, 2007].

5.3.1 Projected area

A good choice for a first test is to check whether these models return the appropriate projected area of the satellite. The projected area of a satellite is completely defined by its three-dimensional geometry and the angle under which this geometry is viewed. The results from the ANGARA and panel models may differ because they do not exactly represent the geometry of the true satellite. To what extent this is the case will be presented in this Section.

Available data and models

Reference values for the projected area along the axes of the spacecraft body-fixed reference frames are available for CHAMP and GRACE as part of the technical documentation. For CHAMP, this document has the code CH-IT-DID-001, and the relevant pages were obtained from Hermann Lühr in March 2008. For GRACE, similar information is available, for the X- and Y-axes only, in document CSR-GR-03-02 [*Bettadpur*, 2007]. The values in these documents are provided in Table 5.4, along with equivalent values computed from the ANGARA and panel models.

Three slightly different CHAMP panel models are now available. The panel areas for these three models are given in Table 5.2.

- The geometry (panel normals and areas) of CH-GFZ-RS-002 [*Lühr et al.*, 2002], combined with optical properties from *Bruinsma and Biancale* [2003], indicated in this document by the name GFZ panels.
- The slightly modified panel areas of *Bruinsma and Biancale* [2003], resulting in a larger frontal area.
- Another modification of the panel areas, known in this document as DEOS panels, was created by tweaking the areas and adding an extra panel, so that the frontal areas along the principal axes matches the values in the CH-IT-DID-0001 document closely.

The panel model information for GRACE is from *Bettadpur* [2007] (CSR-GR-03-02). The panel listing also contains an entry for the cylindrical nadir-pointing antenna-boom on GRACE, which is difficult to model in 3D with flat panels only, and has therefore been neglected in the Task 2 processing so far. Here, the panel model with and without this additional area are listed separately in Table 5.4.

The ANGARA software does not by default output information on the projected area. However, these values can be obtained by just performing a radiation pressure force coefficient calculation on a satellite model for which the material property has been set to zero reflection and full absorption of the photons. If the ANGARA internal reference area has been set to unity, the magnitude of the resulting force coefficient is then equal to the projected area of the 3D ANGARA spacecraft model.

For CHAMP, both the old ANGARA model created by Dries Caluwaerts [*Caluwaerts*, 2006], and the new, much more detailed model created by HTG for this project (see Figure 5.3) have been included. Note that the old DEOS ANGARA CHAMP model created by *Caluwaerts* [2006] was based on outdated satellite drawings, and did not contain all protruding spacecraft elements, such as the star camera baffles on the boom. This model is only used for comparisons in this and the subsequent chapter. For the accelerometer data processing, the detailed new HTG ANGARA CHAMP model is used.

For GRACE, there is a single ANGARA model available, created by HTG for this project, based on detailed satellite drawings.

Internal inconsistency in satellite surface geometry models

Table 5.4 provides projected area values for viewing angles along both the positive and negative axes. Although these values should be equal for any physical object, this is not the case with the models discussed here. The panels in the panel model do not form a completely closed shape. For computing the area as

Model / source	Front (+X)	Back (-X)	Left (+Y)	Right (-Y)	Bottom (+Z)	Top (-Z)
CHAMP						
CH-IT-DID-0001	0.7425	0.7425	3.1203	3.1203	6.4442	6.4442
ANGARA (DEOS, old)	0.5764	0.6419	2.9922	2.9944	6.5105	6.4380
ANGARA (HTG)	0.7944	0.7837	3.2446	3.2396	6.6210	6.5860
Panels (GFZ)	0.4701	0.4606	3.3775	3.3775	6.6899	6.2950
Panels (Bruinsma)	0.6366	0.4606	3.3775	3.3775	6.6899	6.2950
Panels (DEOS)	0.7427	0.7518	3.1220	3.1220	6.4560	6.4641
GRACE						
CSR-GR-03-02	1.0013	1.0013	2.4634	2.4634	–	–
ANGARA (HTG)	1.0433	1.0305	2.5496	2.5421	6.1530	6.1295
Panels (no boom)	0.9552	0.9552	2.5921	2.5921	6.2240	6.3646
Panels (boom)	1.0013	1.0013	2.6383	2.6383	6.2240	6.3646

Table 5.4 Projected areas of CHAMP and GRACE as viewed along the spacecraft body-fixed axes, as provided by the CH-IT-DID-0001 and CSR-GR-03-02 documents, and computed from the ANGARA and panel models.

viewed from the top, for example, the solar panels are used, when viewed from the bottom, the bottom panel is the most important contributor. The solar panels are then viewed from their backsides and are therefore considered 'transparent' in the area calculation. For the GFZ and Bruinsma panel models, this leads to a 6.3% lower area for CHAMP's view of the top, while for GRACE the top is 2.3% larger than the bottom.

For the more sophisticated ANGARA model, shadowing or blocking is accounted for in the projected area calculations with the Monte Carlo test particle method. The modeller using the ANGARA software has to personally make sure that the model is closed however. Nevertheless, even on a closed geometry, the values from opposite sides of the spacecraft model can still differ due to the statistical uncertainty, based on the limited number of test particles used. In Table 5.4, this difference is generally below 1.3% based on a rather coarse preliminary calculation. The exception is the X-direction in the ANGARA (DEOS) model, which shows a 10% difference. Fortunately, such a glitch is not present in the new ANGARA (HTG) model.

Comparison of model results

With a few exceptions, the calculated projected areas are within a few percent of the advertised values in the technical documentation. The ANGARA values are in general closer to these advertised values than the panel model values. The largest discrepancies occur for the CHAMP satellite, when viewed along the X-axis. The GFZ panels return a 37% lower area than stated in the CH-IT-DID-0001 document. The panel model in *Bruinsma and Biancale* [2003] has an increased front panel area, but is still 14% too low. The original DEOS ANGARA model did not yet include a geometric modelling of the boom star camera baffles, instruments and thrusters, and returns a 22% lower frontal area. The new HTG-developed ANGARA model comes closest, with a result that is 7% higher than the reference. Apparently the shape of CHAMP, with its slender body and large appendages, leads to a large uncertainty in the modelling of the frontal area in the flight (X) direction.

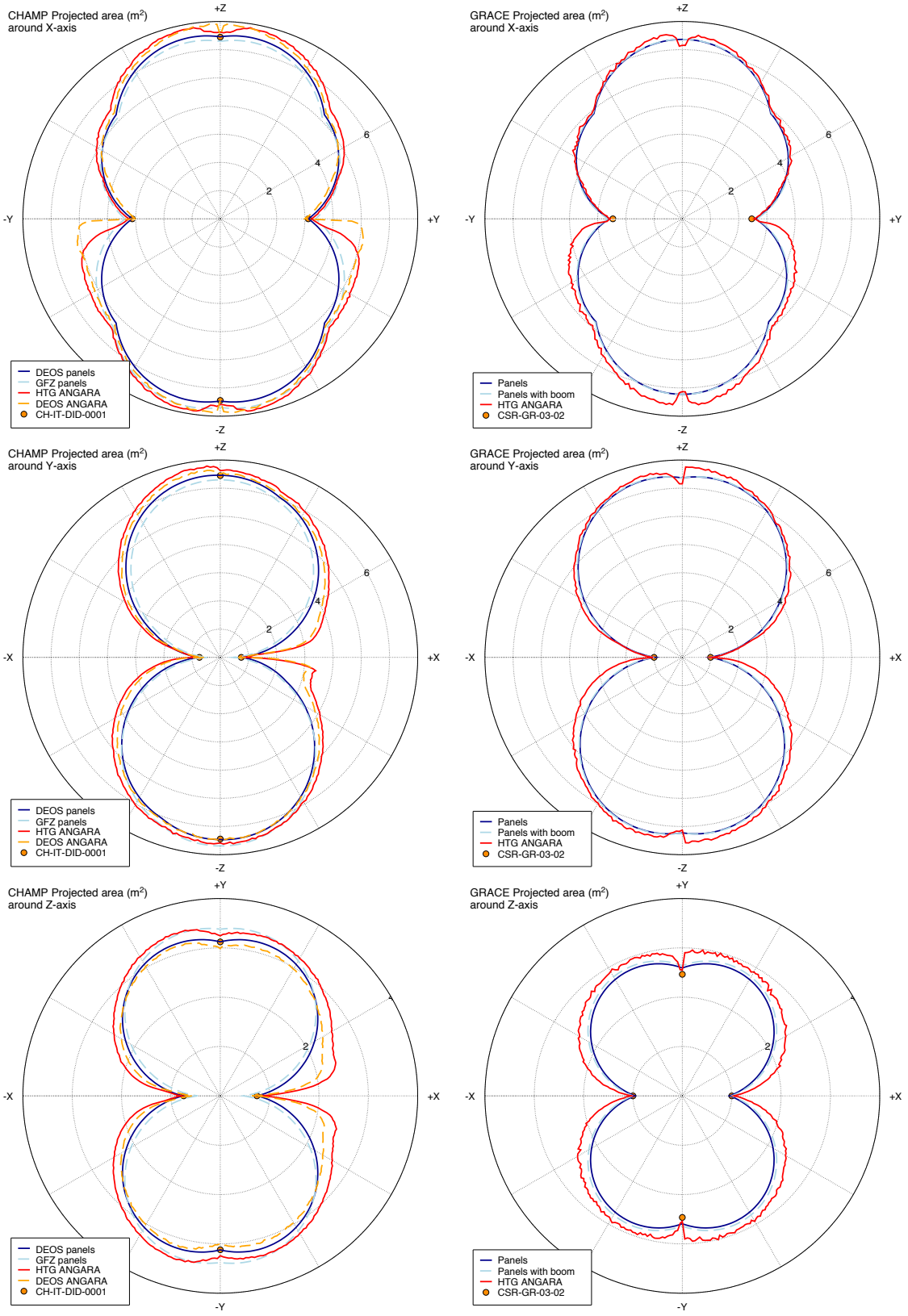

Figure 5.9 Comparison of projected areas for CHAMP (*left*) and GRACE (*right*) as a function of viewing angle in the planes defined by the axes of the satellite body-fixed frames (from *top* to *bottom*, the YZ-, XZ- and XY-planes).

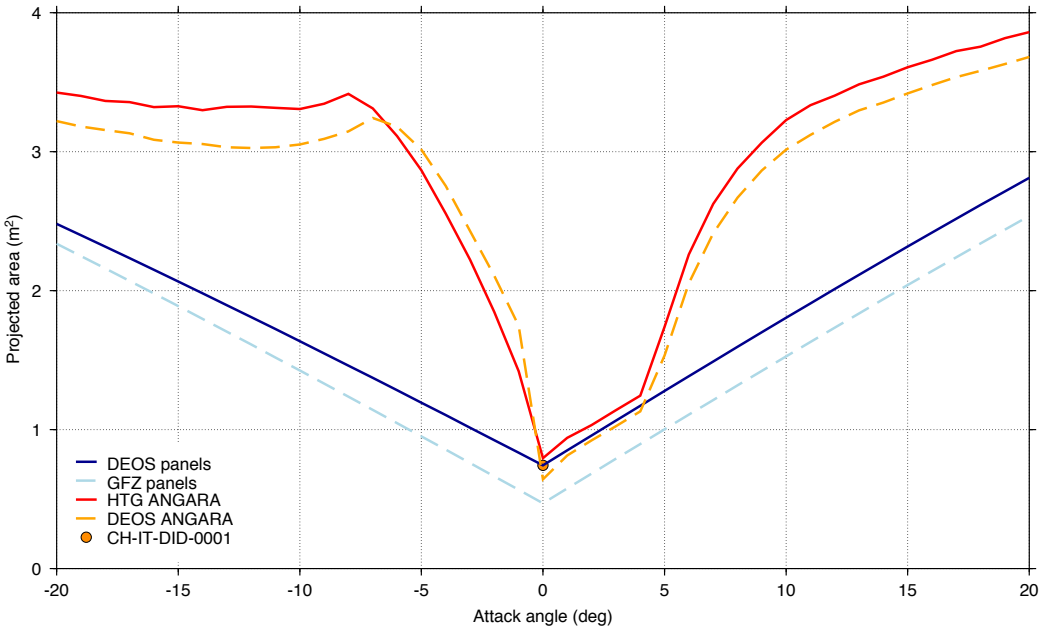

Figure 5.10 Comparison of projected areas for CHAMP as a function of viewing angle in the XZ-plane. This plot contains a more detailed view of part of the data in Figure 5.9.

The projected area results from Table 5.4 are also plotted in Figure 5.9, in which the results at oblique viewing angles in the YZ-, XZ- and XY-planes are made visible as well. The new HTG ANGARA model results, in red, seem to fit better than the GFZ panel model results, in light blue, with the values from the technical documentation, which are indicated by the orange dots on the principal axes. The results are certainly not perfect however. In general, ANGARA returns larger areas than the panels, which is to be expected, since the panel models do not include details on the contribution of small appendages, such as the star camera baffles and instruments on the CHAMP boom. The effect is more pronounced for CHAMP than for GRACE, and especially large for relatively small angular deviations from the X-axis. The new DEOS panel model was hand-tweaked to fit with the data points from the technical documentation. For several differences between the behaviour of the projected area models in these plots, no satisfactory explanations have been found so far. These include the following:

- Figure 5.10 gives a zoomed-in, more detailed view of the differences in the modelled projected area for CHAMP for small changes in the viewing angle in the XZ-plane. For an angle of -5°, the ANGARA results are approximately three times as large as the panel results. The ANGARA calculations also show a local minimum in projected area for a viewing angle of around -12°, which perhaps might be explained by shadowing of the S-band antenna and ion drift meter by the long boom. However, it is not likely that the presence of these appendages can completely explain the very large difference between ANGARA and panel areas for this viewing geometry.
- The curve for the ANGARA (DEOS) CHAMP model in the YZ-plane in Figure 5.9 shows a large jump, from around 3 m^2 to around 5 m^2, when the viewing angle moves below the Z-axis. For the panel model, this increase in area when transitioning from a side-view (Y) to a top-view (-Y) is more gradual. The curve for the new HTG ANGARA model lies somewhere in between.

- For both satellites, there are slight jumps and/or local minima when the Y- and Z-axes are crossed, for the ANGARA model, but not for the panel model. The jumps are more pronounced for the GRACE model than for the CHAMP model.

5.3.2 Radiation pressure model

Figure 5.11 shows the radiation pressure coefficients, in a similar manner to the projected areas in the previous Section. The radiation pressure coefficient values have been calculated by taking the magnitude of the total radiation pressure force coefficient vector $(\vec{C}_F A)$, as derived in Section 5.2.1, and dividing by the projected areas from Figure 5.9.

The figure shows good agreement between the various models. Notice the more complex variations of the reflectivity for viewing angles closely aligned with CHAMP's X-axis, which could be caused by the influence of shadowing by elements with different geometry and reflectivity, such as the satellite's boom, magnetometer instrument and communications antenna.

5.4 Analysis of force models using accelerometer data

In this section, the force models will be compared directly with the satellite accelerometer data, under conditions where one or more of the error sources either disappear, or where there is a variation in the sensitivity. This type of analysis will give more insight in the fidelity of the models and the data.

5.4.1 Solar radiation pressure accelerations during eclipse transitions

Figures 5.12 and 5.13 show plots of the acceleration changes around eclipse transitions. The uncalibrated accelerometer data are compared with the panel and ANGARA solar radiation pressure model, respectively. Figures 5.14 and 5.15 show the same type of analysis for CHAMP. Since the eclipse transitions contain a half-shadow phase, for which the timing is difficult to model exactly, the transition jumps were determined by averaging the 10-second accelerations found during a minute just before the modelled transition start time and subtracting the data found during one minute of 10-second data just after the modelled transition end time. Since a difference in acceleration is examined, only the accelerometer calibration scale factor can affect the result. A calibration bias will not have any influence.

The figures show distinct patterns caused by the repeating rotation of the orbital plane with respect to the Sun. The gaps in the pattern are the periods where eclipse transitions did not occur, when the satellite was in a dawn-dusk or dusk-dawn orbit.

The GRACE results show a good match between the data and the models, especially in the Y-direction. The X-direction shows much higher noise in the data, due to the difference in drag acceleration just before and after the transition. This noise was much larger during the high solar-actvity years 2002 and 2003, which are not shown here. The Z-direction shows less noise than the X-direction, but still more than the Y-direction. This is likely due to changes in the Earth radiation pressure during the minutes before and after the transition.

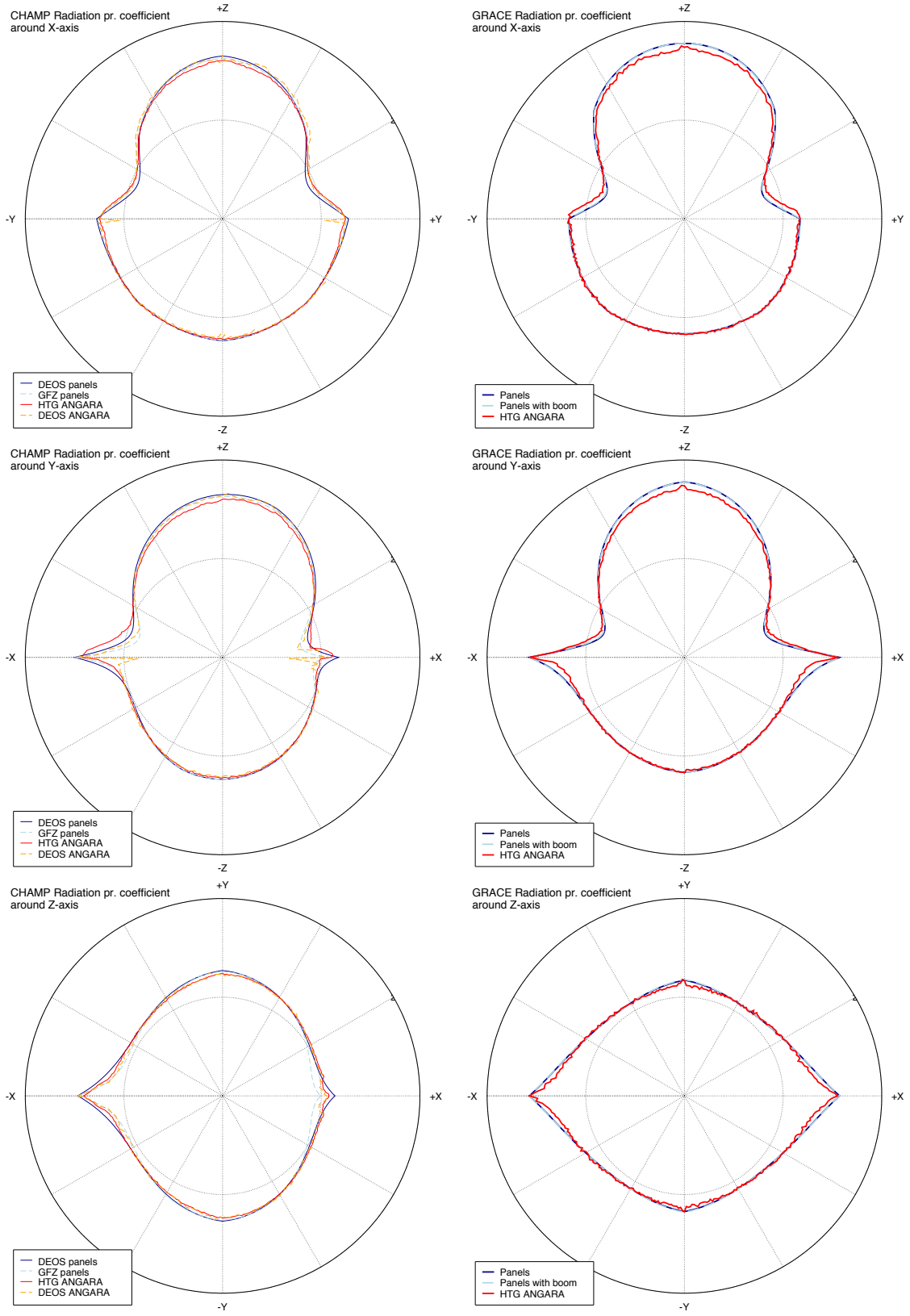

Figure 5.11 Comparison of radiation pressure coefficients for CHAMP (*left*) and GRACE (*right*) as a function of viewing angle in the planes defined by the axes of the satellite body-fixed frames (from *top* to *bottom*, the YZ-, XZ- and XY-planes).

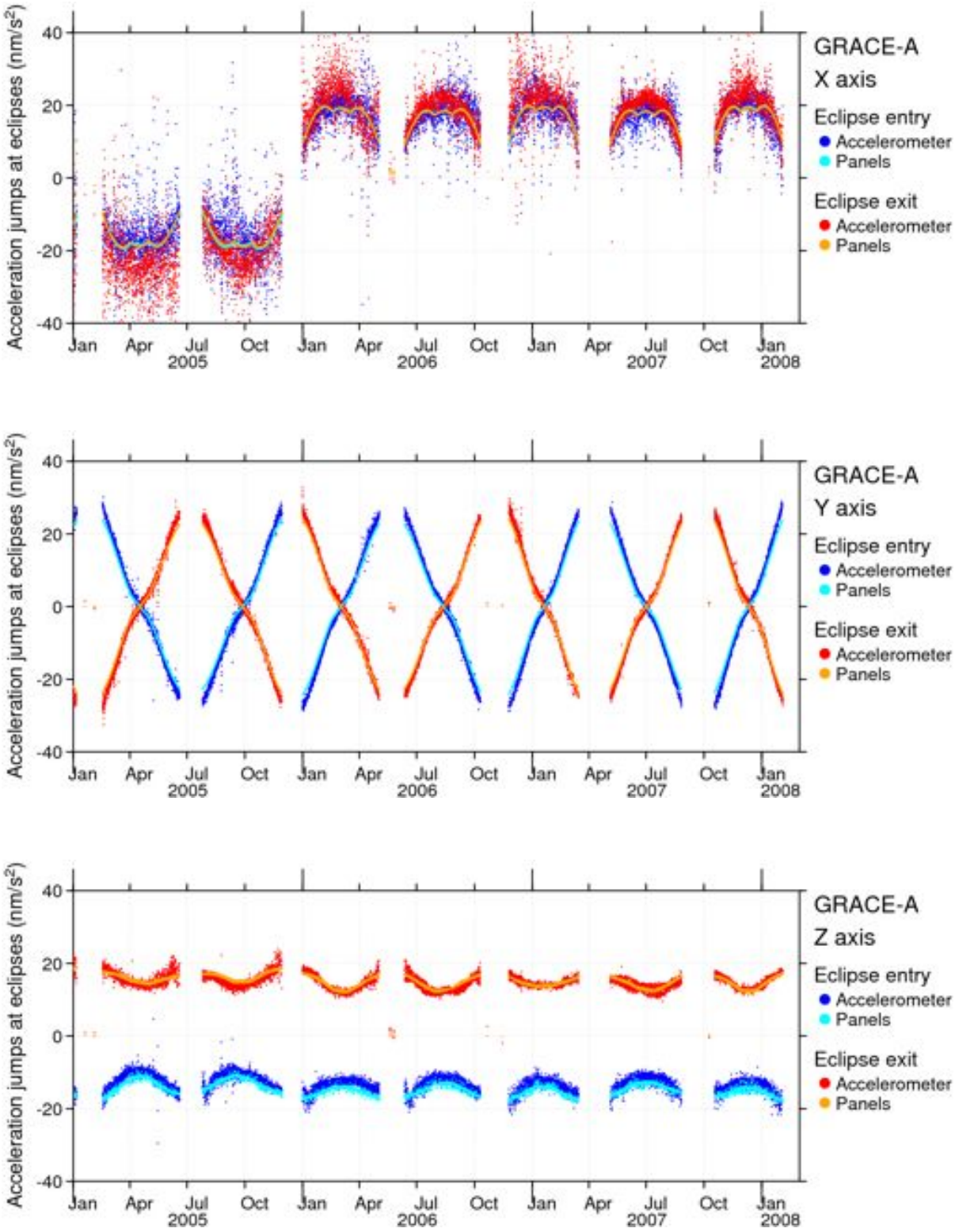

Figure 5.12 Comparison of acceleration jumps at eclipse transitions for GRACE-A. The uncalibrated accelerometer data are compared with the panels solar radiation pressure model.

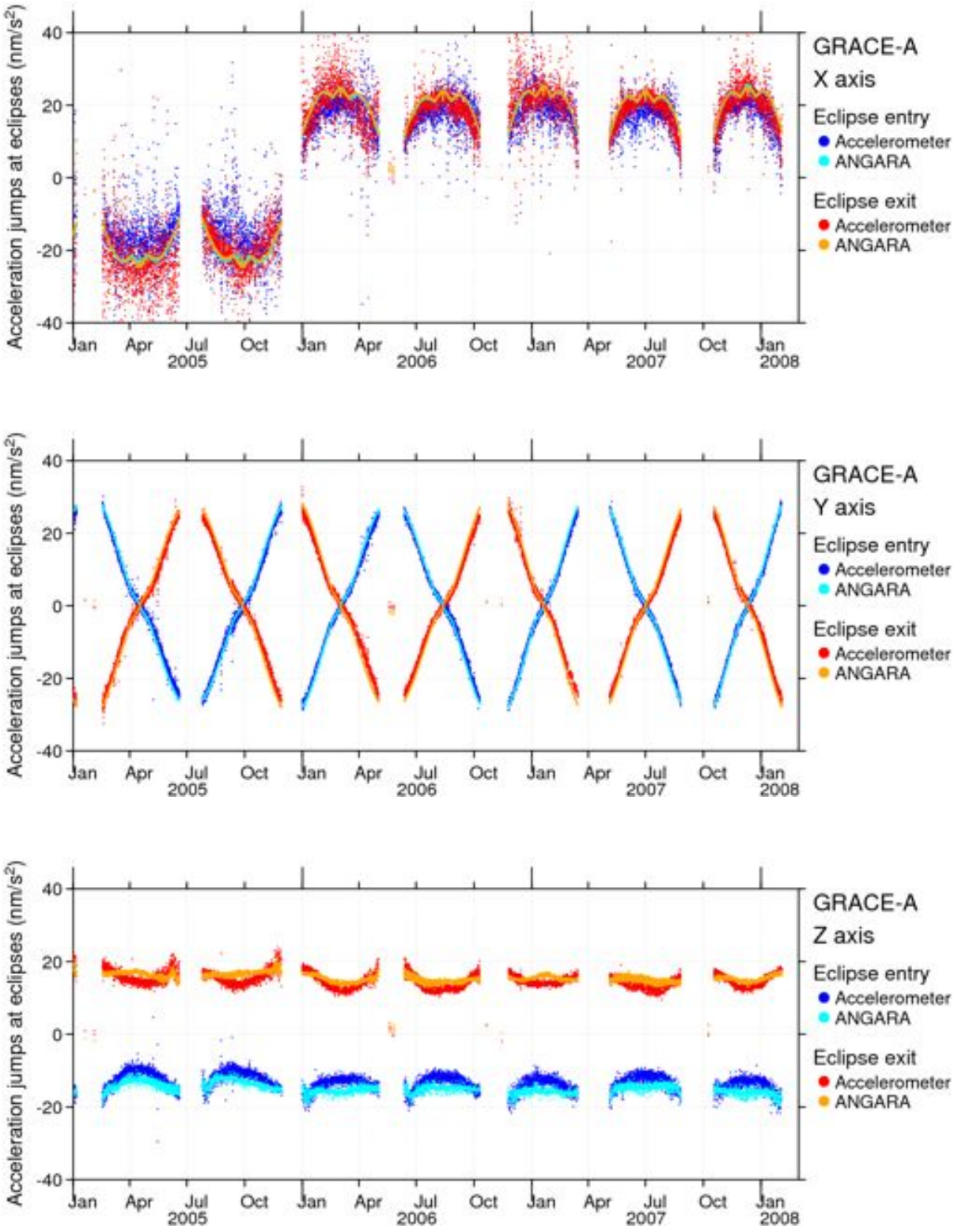

Figure 5.13 Same as the previous figure, but for the ANGARA solar radiation pressure model.

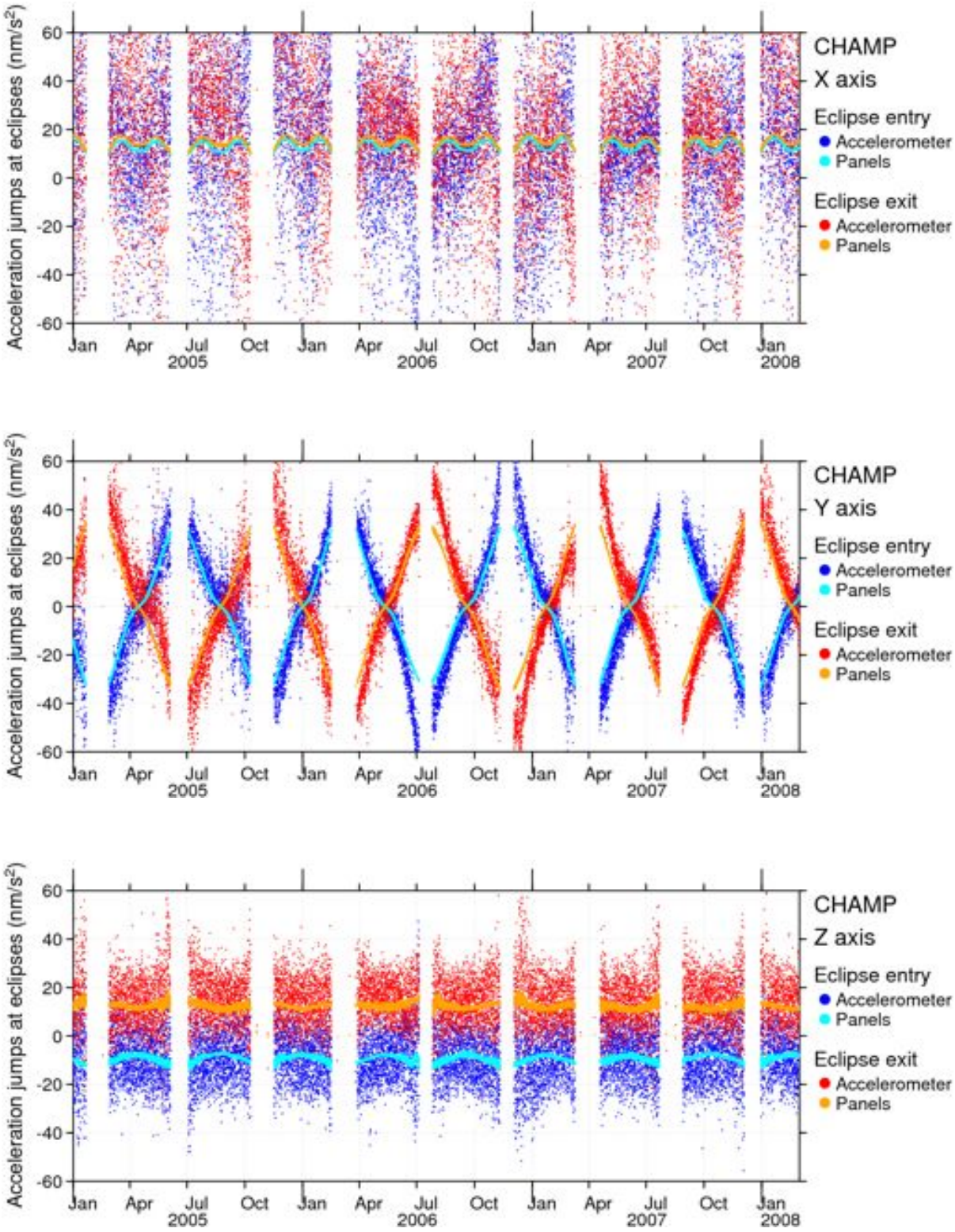

Figure 5.14 Comparison of acceleration jumps at eclipse transitions for CHAMP. The uncalibrated accelerometer data are compared with the panels solar radiation pressure model.

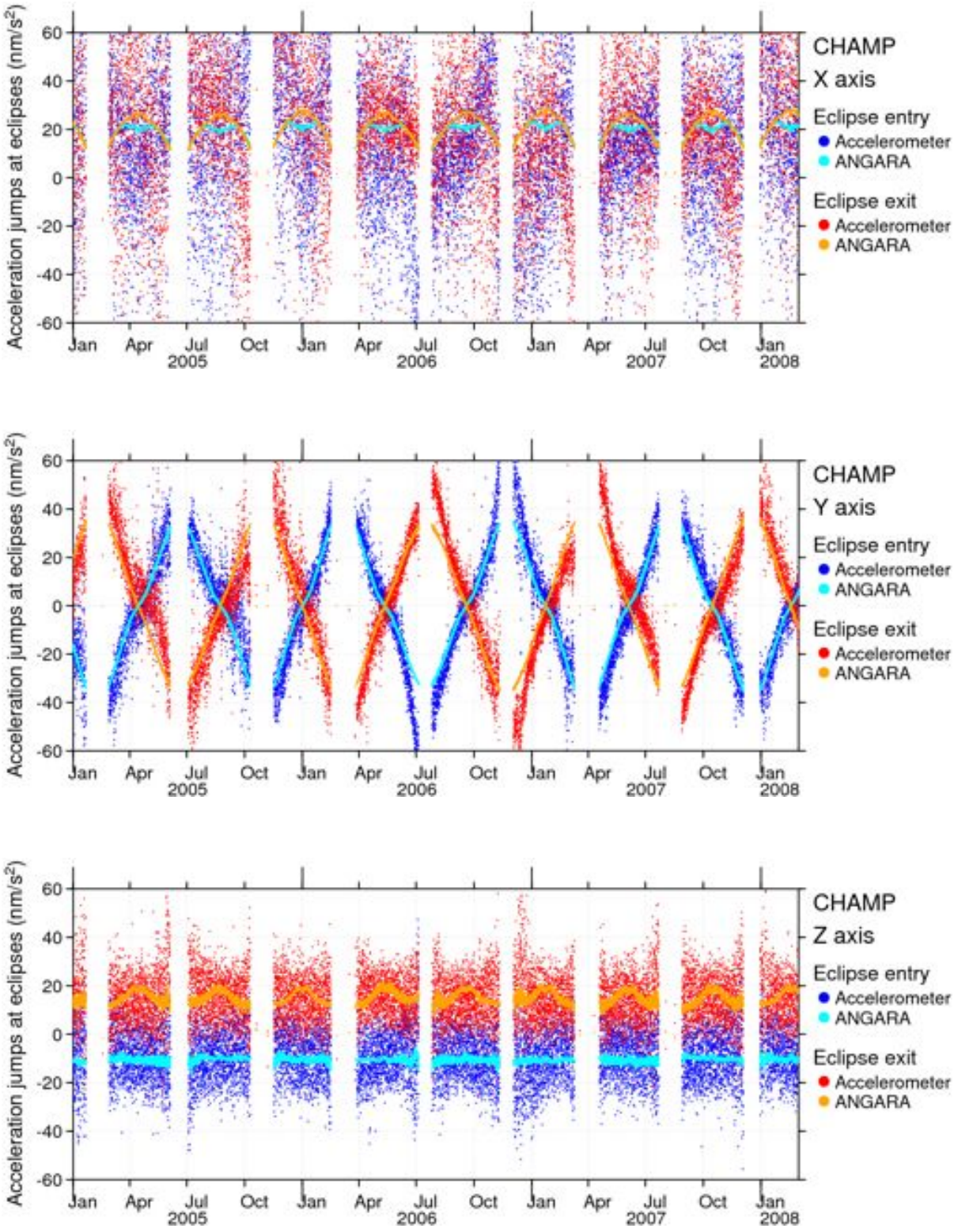

Figure 5.15 Same as the previous figure, but for the ANGARA solar radiation pressure model.

The ANGARA and panel model seem to match the GRACE data about equally well. The ANGARA acceleration jumps are slightly larger than those from the panel model. In any case, the accelerometer scale factors seem to be constant, since no drifts over time can be observed in the comparison of the data with either model. The panel model represents the curved shapes in the pattern for the Z-direction better than the ANGARA model.

The CHAMP results look much noisier than the GRACE results. It is clear that the accelerometer X-direction contains no usable information on radiation pressure during eclipse transitions, due to the high level of the drag accelerations at CHAMP's lower altitude. The Z-direction is very noisy as well, which is no surprise, because of the known problem in the instrument for this direction. For CHAMP, the Y-direction is the most interesting. Again, the ANGARA models give larger acceleration jumps than the panel model. What is most interesting however is that the point in the plots where the curves for the models cross the zero-axis, is further to the left than that point for the accelerometer data. At these points in time, the satellite is approximately in a midnight-noon orbit, so that the Y-component of the radiation pressure cancels out due to symmetry. The fact that these points do not coincide between the model and the data might indicate some problem in the model. Perhaps the geometry and optical properties of the true satellite are not as symmetric as represented by the model.

Chapter 6
Aerodynamics modelling

In the frame of the present study, improved atmospheric density models shall be derived from direct deceleration measurements on satellites. Therefore accurate methods are needed to calculate the aerodynamic and radiation forces acting on these satellites.

This chapter starts with a survey that gives an overview over the different methods for the modelling of satellite surfaces and for the calculation of aerodynamic and radiation forces.

The complexity level of the methods varies from very simple to very detailed models and algorithms. This survey is a documentation of the state of the art of aerodynamic and radiation force algorithms and a selection of the method best suited for the calculations to be carried in frame of this study.

At the end of the chapter, the selected models and calculations will be described in detail.

6.1 The high altitude atmosphere and the satellite flow regimes

The aerodynamic actions on a body depend generally on:

- Physical properties of environment through which the body is moving
- Geometry and physical surface conditions of the body
- Velocity of body relative to environment
- Orientation of body relative to velocity vector
- Behaviour of the resulting flow around the body

The flow behaviour and the appropriate analysis methods depend on flow regimes, which are characterized by fluid dynamic similarity parameters like Mach- and Reynolds number or speed ratio and Knudsen number.

In order to determine the satellites flow regime [*Bird*, 1994; *Koppenwallner*, 1989] we have to relate characteristic quantities of the flying objects to quantities in the ambient atmosphere. The relevant quantities of satellite and atmosphere are summarized in Figure 6.1 and in the following lists:

- Satellite quantities:
  - Length L
  - Velocity V
- Atmospheric quantities:
  - Mass- and particle number density ρ and n

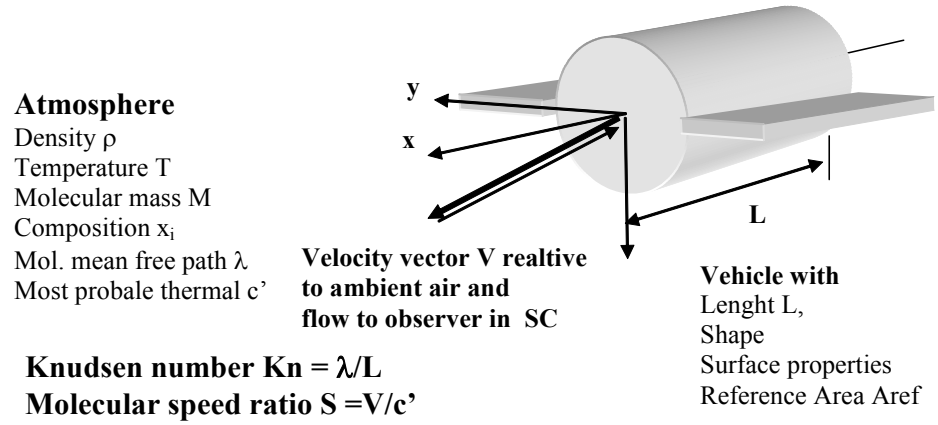

Figure 6.1 Important vehicle and atmospheric quantities

  - Temperature T
  - Molecular mass M
  - Composition x_i
- Related atmospheric quantities like
  - Molecular mean free path λ:

$$\lambda = \frac{1}{\sqrt{2}} \frac{1}{n} \frac{1}{\pi d_M^2} \tag{6.1}$$

  - Mean thermal speed c':

$$c' = \sqrt{2RT} \tag{6.2}$$

Figure 6.1 also shows that the aerodynamic reference is usually fixed to the body. Thus an observer on the body is approached by a flow with direction opposite to the flight velocity vector.

6.1.1 The high altitude atmosphere

Figures 6.2 and 6.3 show with demonstrative examples the strong property variation of the high atmosphere according to the CIRA-72 model [*Jacchia*, 1972] (see also Chapter 2, and specifically Section 2.5.1). Figure 6.2 shows the strong density and temperature variation with the solar cycle. Figure 6.3 shows the mean molecular mass and its strong decrease with altitude, which is caused by the relative increase of atomic oxygen and components with low molecular mass.

Of importance for the aerodynamic flow regimes are the mean free path (Figure 6.4) and temperature in connection with the molecular mass M. These quantities determine the characteristic similarity parameters and therefore also the flow behaviour.

One basic assumption underlying all aerodynamic models is, that the vehicle is flying through a neutral atmosphere, which is in thermal equilibrium. As aerodynamics is treated from an observation point on the vehicle, atmospheric winds are only components of the velocity vector.

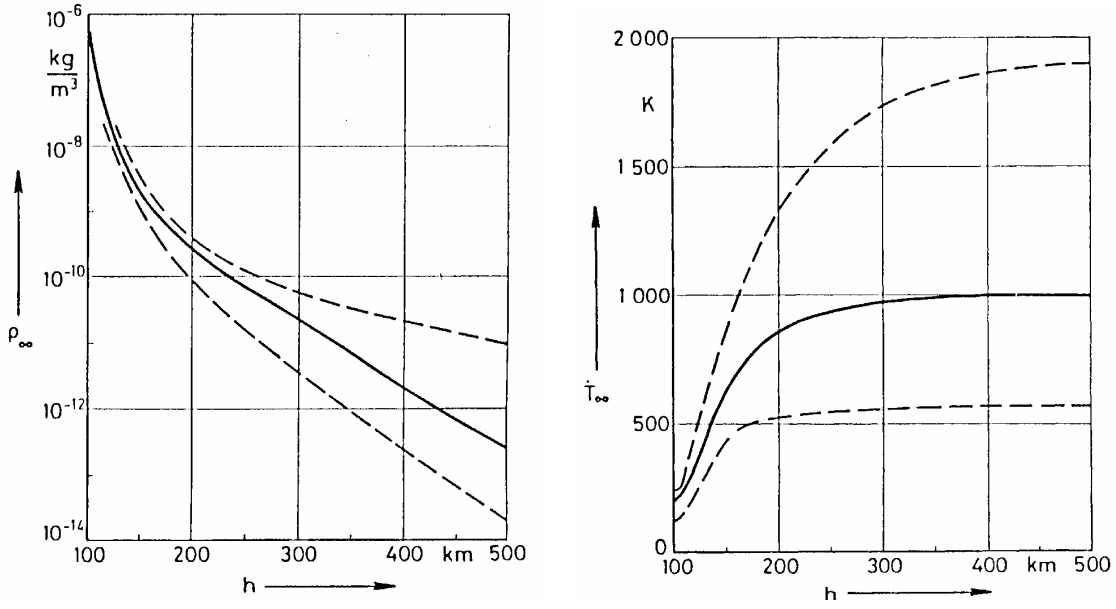

Figure 6.2 Density (left) and temperature (right) versus altitude.

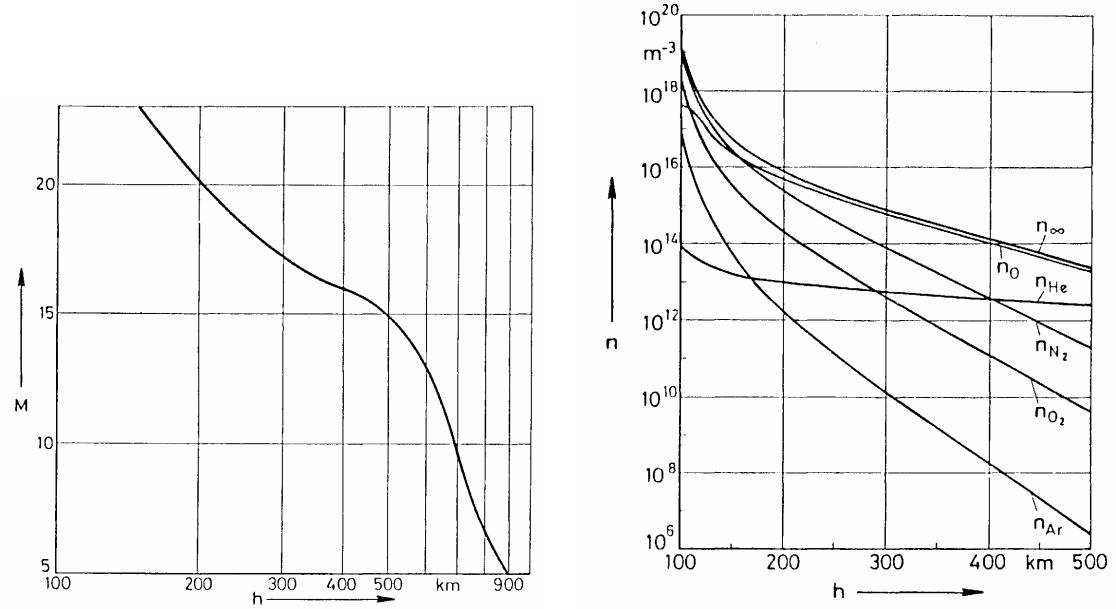

Figure 6.3 Mean molecular mass (left) and mean atmospheric composition (right) versus altitude.

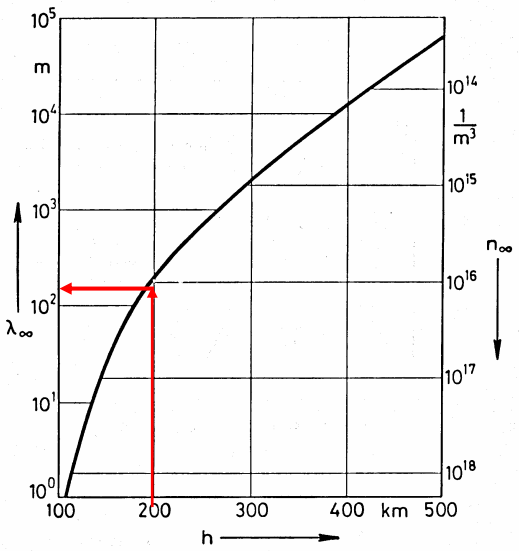

Figure 6.4 Mean free path and number density versus altitude

6.1.2 Knudsen number, molecular speed ratio and flow regimes

The Knudsen number and free molecular flow

The Knudsen number relates the vehicle size given by a characteristic length L to the mean free path of the atmospheric particles λ and is defined as:

$$Kn = \frac{\lambda}{L} \tag{6.3}$$

It is of importance that we are only interested in satellites orbiting above 200 km altitude, with a mean free path of $\lambda > 240$ m (see Figure 6.4). For all vehicles with $L < 24$ m we reach the condition $Kn > 10$ above 200 km altitude.

For $Kn \gg 1$ we have a limiting case of flow in which the non dimensional aerodynamic coefficients C_F and C_M are independent from the Knudsen number.

Due to $Kn \gg 1$ the atmospheric free stream molecules reach the body without collision with body reflected molecules. This type of flow is usually named *free molecular flow*. An observer In the flow field of the body can in this case only discriminate the following two type of particles

1. Atoms or molecules arriving from the undisturbed atmosphere (free stream).
2. Atoms or molecules arriving from the vehicles surface

Molecular speed ratio

The molecular speed ratio S relates the vehicle velocity V to the mean thermal speed c' of the undisturbed atmosphere and is defined as:

$$S = \frac{V}{\sqrt{2RT}} \tag{6.4}$$

with R the specific gas constant;

For free molecular flow, the molecular speed ratio has a similar importance as the Mach-number in continuum flow. The typical values and variation of S is shown in Figure 6.5 and can be derived from the following inputs:

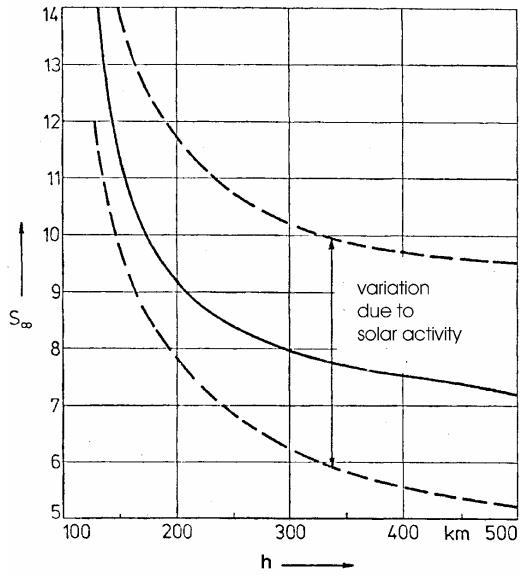

Figure 6.5 Variation of molecular speed ratio S for spacecraft in a circular orbit.

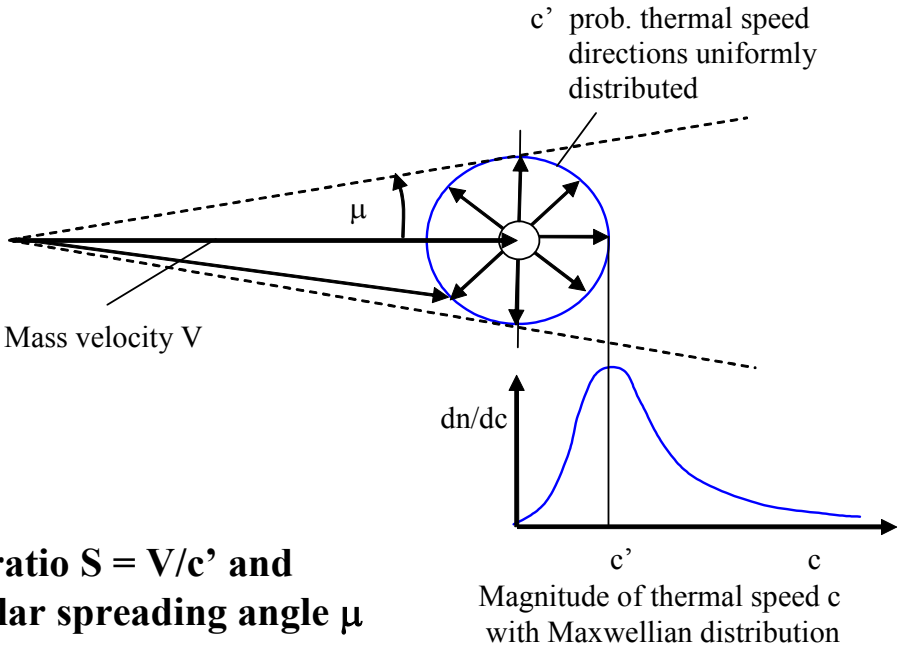

Figure 6.6 Speed ratio S and molecular spreading.

- Average satellite speed of 7600 m/s
- Atmosphere temperature and molecular mass from Figures 6.2 and 6.3.

Figure 6.5 shows that for orbits between 200 and 500 km, we can expect a speed ratio variation between $5 < S < 12$. The molecular speed ratio S considers that the vehicle is moving with velocity V in an environment of gas particles, which have:

- Velocity directions randomly distributed in space
- Velocity magnitudes c given by the Maxwellian distribution function, with c' as the most probable value.

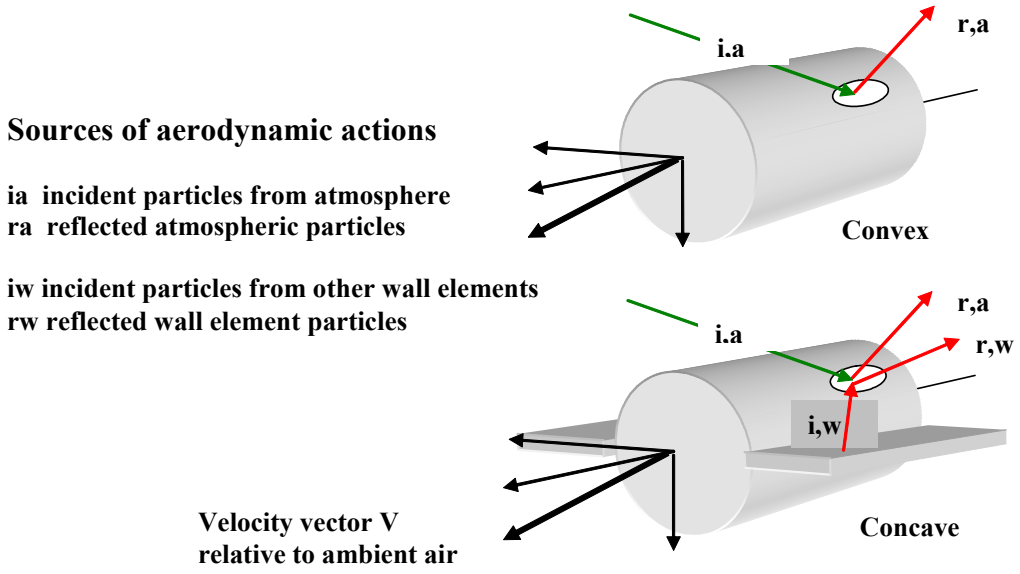

Figure 6.7 The sources of action on a surface element in free molecular flow.

Figure 6.6 explains this and the concept of a molecular Mach angle μ, which defines a mean spreading angle of molecules approaching the vehicle.

In analogy to the use of the Mach number in continuum flow, we can also define velocity flow regimes with the speed ratio S [*Schaaf and Chambré*, 1961], namely:

- Subsonic or sub-thermal flow: $S < 1; V < c'$
- Supersonic or super-thermal flow : $S > 1; V > c'$
- Hypersonic or hyper-thermal flow: $S >> 1; V >> c'$
- Ultimate hyper-thermal: $S = \infty; V = \infty$, or $c' = 0$

For $S = \infty$, we again approach a limiting flow case namely *speed ratio independence*. Speed ratio independence means that all particles approach the vehicle with uniform parallel velocity directions. As a result, the aerodynamic coefficients become independent of the speed ratio S. It must however be pointed out that the speed ratio value S, at which this limiting case is approached, depends strongly on the body shape.

6.2 Important phenomena in free molecular flow

6.2.1 The force contributions due to incident and reflected fluxes

It is common practice [*Bird*, 1994; *Schaaf and Chambré*, 1961; *Kogan*, 1969] to split aerodynamic action on a surface element into a contribution due to incidence i and a contribution due to reflection r. On convex body shapes all incident molecules arrive directly from the ambient air and leave after collision into the atmosphere. Concave surface elements will also be impinged by molecules reflected from wall elements, which can be mutually viewed. Figure 6.7 explains this situation.

The local forces on a surface element dS are usually split up into a component normal to the surface, namely surface pressure p, and a tangential component τ,

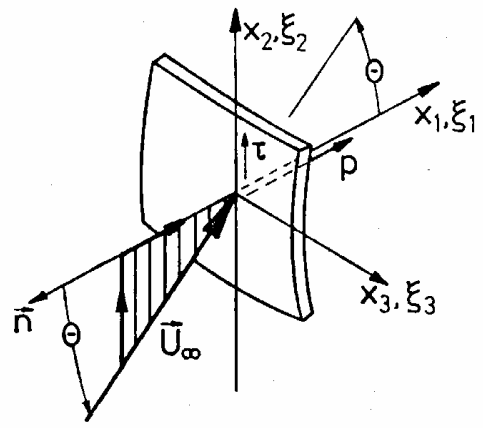

Figure 6.8 The sources of action on a surface element in free molecular flow.

located in the incidence plane. Figure 6.8 explains the local coordinate system of a surface element dS with incidence angle θ and shows directions of the local pressure p and shear stress τ.

The local pressure and shear stress with contribution from incident and from reflected flux can be expressed as follows:

Surface pressure:

$$p = p_i + p_r \tag{6.5}$$

Surface shear stress:

$$\tau = \tau_i - \tau_r \tag{6.6}$$

Pressure and shear stress are a result of normal and tangential momentum exchange with the surface and the resulting body action is obtained as balance between impinging and reemitted momentum flux.

p_i and τ_i are a result of normal and tangential momentum of impinging particles. p_r and τ_r are a result of normal and tangential momentum of the reemitted particles.

This necessary split up separates satellite aerodynamic analysis into two different areas:

a. The well established area of gas kinetics to determine incident fluxes.

b. The area of gas-surface physics, which determines the interaction of high speed gas particles with a surface.

Form a gas kinetic point of view [*Patterson*, 1956] case b is solved, if the velocity distribution function fr of the reflected particles is given as function of incident velocity distribution fi and the state of the surface.

According to kinetic theory, the momentum flux due to incident and reflected particles is given by moments over the corresponding velocity distribution function f [*Kogan*, 1969; *Patterson*, 1956].

The resulting moments for convex bodies are given below.

$$p_i = \int_{-\infty}^{+\infty}\int_{-\infty}^{+\infty}\int_{0}^{+\infty} m\xi_1\xi_1 \cdot f_i d\xi_1 d\xi_2 d\xi_3; \quad \tau_i = \int_{-\infty}^{+\infty}\int_{-\infty}^{+\infty}\int_{0}^{+\infty} m\xi_2\xi_1 \cdot f_i d\xi_1 d\xi_2 d\xi_3 \tag{6.7}$$

$$p_r = \int_{-\infty}^{+\infty}\int_{-\infty}^{+\infty}\int_{0}^{+\infty} m\xi_1\xi_1 \cdot frd\xi_1 d\xi_2 d\xi_3; \quad \tau_r = \int_{-\infty}^{+\infty}\int_{-\infty}^{+\infty}\int_{0}^{+\infty} m\xi_2\xi_1 \cdot f_r d\xi_1 d\xi_2 d\xi_3 \quad (6.8)$$

For incident particles the function f_i is the velocity distribution of the atmospheric particles, which, due to the assumption of thermal equilibrium, is Maxwellian. For a flowing gas this distribution is given below in rectangular velocity coordinates ξ_1, ξ_2, ξ_3.

$$f(\xi_1, \xi_2, \xi_3) = \frac{dn}{d\xi_1 d\xi_2 d\xi_3} = \frac{1}{\pi^{3/2}} \frac{n}{c'^3} \exp -\frac{1}{c'^2}[(\xi_1 - V_1)^2 + (\xi_2 - V_2)^2 + (\xi_3 - V_3)^2] \quad (6.9)$$

The velocity distribution f_r of reflected particles depends on surface material, gaseous interface layer on the surface and on the incidence direction. The relation between f_i and f_r is unknown beforehand and has to be solved by models and experimental input data.

Sentman [1961] used, in an identical approach, a differently located coordinate system and obtained moment integrals for resulting drag and lift contributions of local flat surface elements. Therefore, his results are also exact within the physical assumptions of kinetic theory for panel elements and diffuse reflection. After coordinate transformation, Sentman's solutions give identical results as the moment integrals (6.7) and (6.8).

6.3 Gas surface interaction (GSI) and satellite aerodynamics

6.3.1 GSI and the modelling levels

The limited knowledge of the actual gas surface interaction at orbital conditions is one of the mayor error sources in satellite drag prediction. Extensive reviews on GSI and satellite aerodynamics have been prepared by Frank Hurlbut [*Hurlbut*, 1985, 1989, 1994]. The principal question of gas-surface interaction can be reduced to the scattering of a molecular beam from a surface element as shown in Figure 6.9. This interaction is usually described by models which rely on experimental verification and input data.

GSI models and also the experimental verification approach can be divided into 3 levels:

- Level 1 Micro level for experiments and models: This approach is based on a molecular description with the aim to provide the velocity distribution of reflected particles as a result. The corresponding experiments need molecular beam facilities and diagnostics for the reflected particle flux in the whole view angle field.
- Level 2: Local action level for experiments and models: In this case, resulting surface actions due to an impinging and reflected molecular beam are investigated and modelled. Surface actions are normal force, tangential force and the energy flux.
- Level 3: Integral action for experiments and models: In this case, complete bodies are tested in wind tunnels or lab experiments (e.g. heated wires) with the aim to deduce from drag- ,lift-force or from heating, the parameters needed in GSI models.

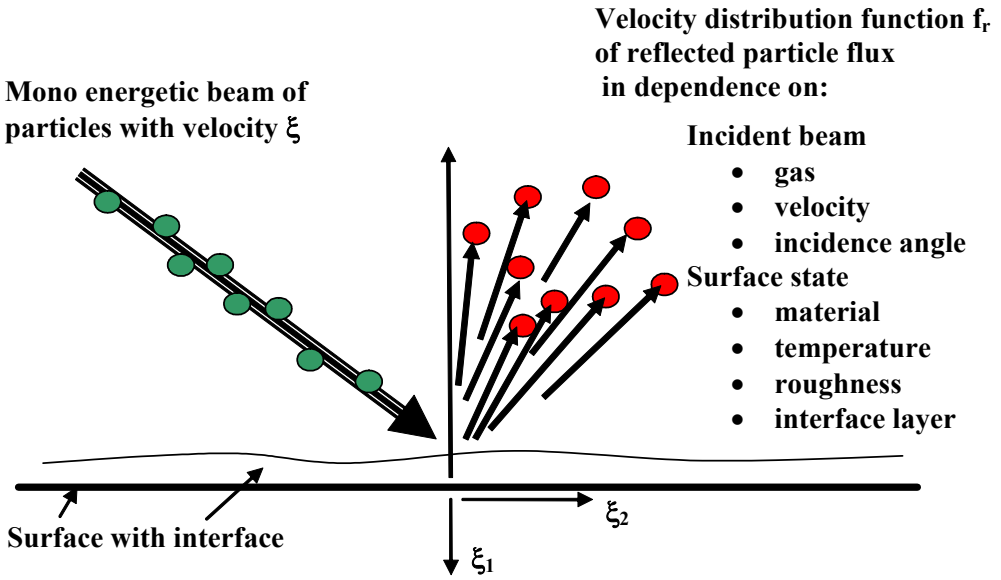

Figure 6.9 The basic question of gas-surface interaction.

6.3.2 Some relevant GSI models

The Maxwell model

This model [*Schaaf and Chambré*, 1961] assumes that one fraction σ of the incident flux is reflected diffusely according to wall temperature T_w and the remaining fraction $1-\sigma$ is reflected specularly. The model is explained in Figure 6.10

- σ is the fraction of diffuse reflected flux;
- $1-\sigma$ is the fraction of specular reflected flux.
- $\sigma = 1$ gives complete diffuse reflection
- $\sigma = 0$ gives complete specular reflection.
- $0 < \sigma < 1$, represent intermediate cases with partially diffuse, partially specular reflection.

This Maxwell model fulfills the level 1 requirement, as it provides the distribution function of reflected particles. The diffuse reflected particle fraction has the distribution function according to wall condition (n_w,T_w). The specular reflected particle fraction keeps the distribution function of incidence with modification of $\xi_{1,r} = -\xi_{1,i}$. In principle, the model needs only one empirical input parameter σ.

The modified Maxwell model

There exists also a modified Maxwell model, which assumes that the diffusely reflected fraction has a thermal velocity based on a temperature T_R, which might be different than T_w. This means that the diffusely emitted particles have been accommodated at the wall to temperature T_r.

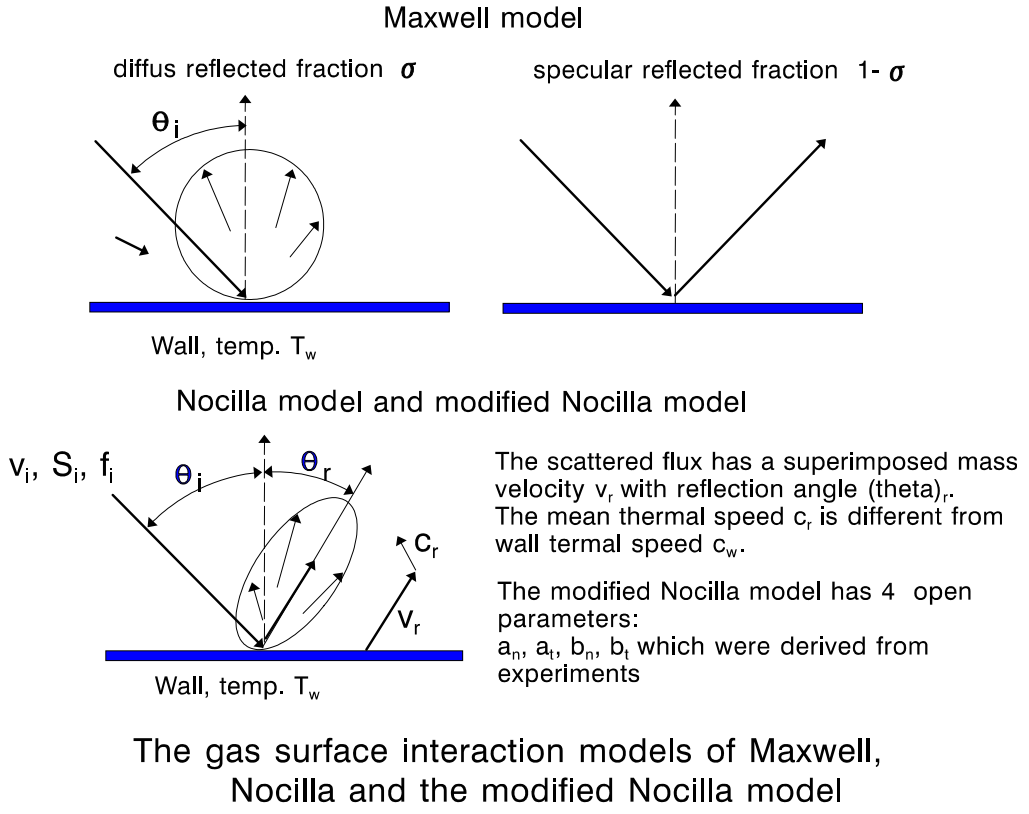

Figure 6.10 GSI models of Maxwell and Nocilla.

Schaaf-Chambré model

This model by *Schaaf and Chambré* [1961] considers the momentum and energy exchange between molecules and the surface and belongs therefore to the level 2. It needs the following three exchange coefficients, each with a value between zero and one:

- σ_N is the coefficient for normal momentum exchange
- σ_T is the coefficient for tangential momentum exchange
- σ_E is the coefficient for energy exchange (sometimes also denoted by α_E)

The definition of these coefficients is as follows

$$\sigma_N = \frac{p_i - p_r}{p_i - p_w}; \quad \sigma_T = \frac{\tau_i - \tau_r}{\tau_i - \tau_w}; \quad \sigma_E = \frac{e_i - e_r}{e_i - e_w} \tag{6.10}$$

Where the index r denotes the actual reflection, w the diffuse reflection. For $\sigma_N = \sigma_T = \sigma_E$, the Schaaf-Chambré model provides the same local forces as the Maxwell model with identical σ.

The original Nocilla model

This model is explained in Figure 6.10 as well. The model and its extensions [*Nocilla*, 1963, 1972] describe the reflected flux with lobe structure and represent the physically most relevant Level 1 models. The reflected flux with lobe like structure is given by a Maxwell distribution imposed on a macroscopic velocity v_r at an angle θ_r against the surface normal. The model needs 4 input parameters in total. The advantages of this model are its physical relevance, its simple

mathematical treatment and computational realization. The disadvantages are the 4 input parameters, which have to be determined by experiment, or just selected by the user. The model allows also the limiting case a completely diffuse reflection

The Hurlbut/Sherman/Nocilla HSN model

Based on experimental data, Hurlbut and Sherman [*Hurlbut*, 1989] improved the Nocilla model and reduced the input parameters from 4 to 3. They give the following dependence between incident and reflected flux:

$$\theta_r = -\theta_i \tag{6.11}$$

$$S_r(\theta_i) = S_{r_0}\frac{2\theta_i}{\pi} \tag{6.12}$$

$$\sigma_e(\theta_i) = \sigma_{e_0}\Big(1 - \frac{2\theta_i}{\pi}\Big) \tag{6.13}$$

$$S_r < S \tag{6.14}$$

Hurlbut showed that the parameters defined in equations (6.11)-(6.14) can be derived from the Schaaf/Chambré accommodation coefficients defined in equation (6.10).

Nocilla/Musanov /Freedländer model

In principle, this is a Nocilla model with the original Nocilla parameters derived from momentum exchange measurements. The advantage of this model is the experimental data base. Freedländer investigated the momentum exchange on large set of materials used on spacecraft and related four exchange coefficients at, an, bn and bt to the Nocilla parameters. This model is also used in the HTG RAMSES system [*Koppenwallner*, 1999].

The Schamberg Model

Schamberg is an early approach to relate the reemitted flux to the incident flux direction. The model treats incident flow as uniform and parallel (infinite speed ratio) and it corrects thermal motion by a Joule gas approximation. The model is sketched in Figure 6.11 and relates the reflected flux with the following 3 parameters to the incidence direction.

- ν defines the mean reflection angle as a function of the incidence angle. e.g $\cos\theta_r = \cos\theta_i^{\nu}$.
- ϕ_0 is the half beam width angle containing all reemitted particles; ϕ_0 is centred at θ_r.
- V_r is the velocity of reemitted particles, which is determined by the incident velocity V_i and the energy accommodation coefficient α_E, as defined in equation (6.10).

$$\frac{V_r}{V_i} = \sqrt{\frac{e_r}{e_i}} = \sqrt{1 + \alpha_E(\frac{e_W}{e_i} - 1)} \tag{6.15}$$

with

$$\frac{e_W}{e_i} = \frac{T_w}{T_{kin,i}} \tag{6.16}$$

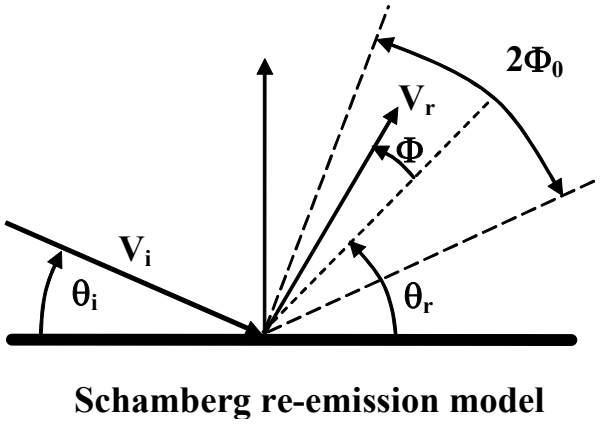

Figure 6.11 The Schamberg re-emission model.

and

$$e_i = \frac{3}{2} R T_{kin} = \frac{1}{2} V_i^2 \tag{6.17}$$

one obtains:

$$V_r = V_i \sqrt{1 + \alpha_E \left(\frac{3RT_W}{V_i^2} - 1 \right)} \tag{6.18}$$

Sutton [2009] uses a combination of Sentman aerodynamics with Schamberg gas surface interaction model and gives in his recent publication the following different relation between V_r and V_i:

$$V_r = V_i \sqrt{\frac{2}{3} \left[1 + \alpha_E \left(\frac{3RT_W}{V_i^2} - 1 \right) \right]} \tag{6.19}$$

The Model of Cook

The Cook method has been widely used by groups deriving atmospheric density from satellite decay observations. Cook used the Schamberg model in two limiting cases and derived simple formulae for satellite drag prediction, which are based on flow projected flat surface areas and speed ratio $S = \infty$.

- Case a): Diffuse angular type reflection pattern with identical V_r for all particles. In the Schamberg model this corresponds to $\theta_r = 90^\circ$ and $\phi = 90^\circ$ and Cook names this case accommodated diffuse reflection.
- Case b): Specular reflection pattern with identical V_r for all particles. In the Schamberg model this corresponds to $\theta_r = \theta_i$ and $\phi = 0^\circ$ and Cook names this case accommodated specular reflection.

In both cases V_r is related to V_i and to the energy accommodation coefficient by equation (6.18). Figure 6.12 sketches the Cook reflection patterns a) and b) as a function of the energy accommodation coefficient.

Cook also uses the simple surface lattice model, which predicts the thermal accommodation as function of mass ratio μ between incident and wall particles:

$$\alpha_E = \frac{2\mu}{(1+\mu)^2} \tag{6.20}$$

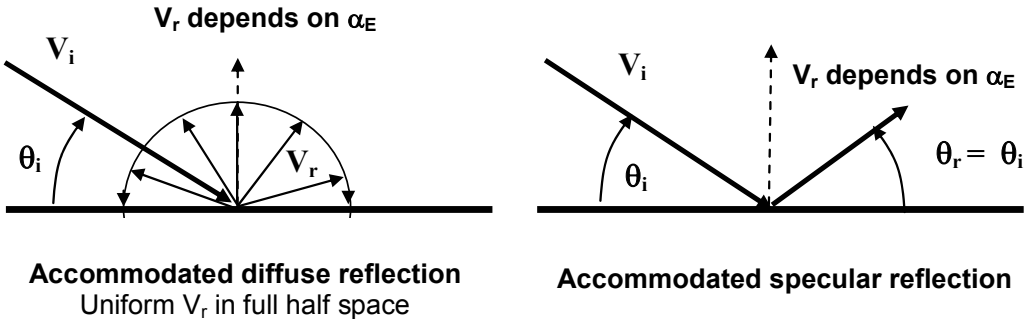

Figure 6.12 Cook's accommodated diffuse and specular reflection.

Cercignani/ Lampis model with scattering kernel

The scattering kernel gives the probability that an impinging molecule is re-emitted with velocity c. With this approach, re-emission models can be constructed, which can approximate the results of experiments. The model was tested in some cases and could reproduce experiments by proper parameter adjustment.

6.3.3 Experimental investigations

Numerous experiments have been conducted in the past in order to quantify the input parameters for GSI models. Experiments on technical surfaces and moderate incidence speed usually confirm an almost diffuse or lobe-like reflection which can be described by Maxwell or modified Nocilla models.

Worth mentioning in this context are the excellent wind tunnel experiments of Legge [*Legge et al.*, 1991], who determined the thermal and momentum accommodation coefficients on technical surfaces. The experiment showed that the coefficients are on average smaller than 1. These experiments have been conducted with incidence speed of $V < 2000$ m/s and are therefore not representative for orbital conditions.

Only a very limited set of experiments simulates incidence speeds representative for satellites. Worth mentioning are *Musanov et al.* [1985], *Collins and Knox* [1994], *Cook and Hoffbauer* [1997], *Cook et al.* [1995].

Within the frame of an ESOC contract [*Johannsmeier et al.*, 1989], HTG analysed the drag coefficient of several orbiting satellites and compared the analysis results with drag coefficients determined by ESOC from decay observations. Figure 6.13 shows, as an example, the results of KOSMOS 1870, which was of interest due to its aligned flight orientation and due to its large solar arrays. Reasonable agreement is obtained with the Schaaf-Chambré model using $\sigma_T = 1$ and $0.5 < \sigma_N < 1$, which is a reflection close to diffuse. Bowman and Moe [*Moe et al.*, 1998; *Bowman and Moe*, 2005; *Moe and Bowman*, 2005] used satellite orbit decay observations as inputs for improved drag and gas surface interaction modelling. Gas surface interaction is one important research field of rarefied gas dynamics. The published proceedings of the 25 biannual symposia contain more than 400 contributions on GSI and reflect therefore the scientific effort and the still limited progress during the last 40 years.

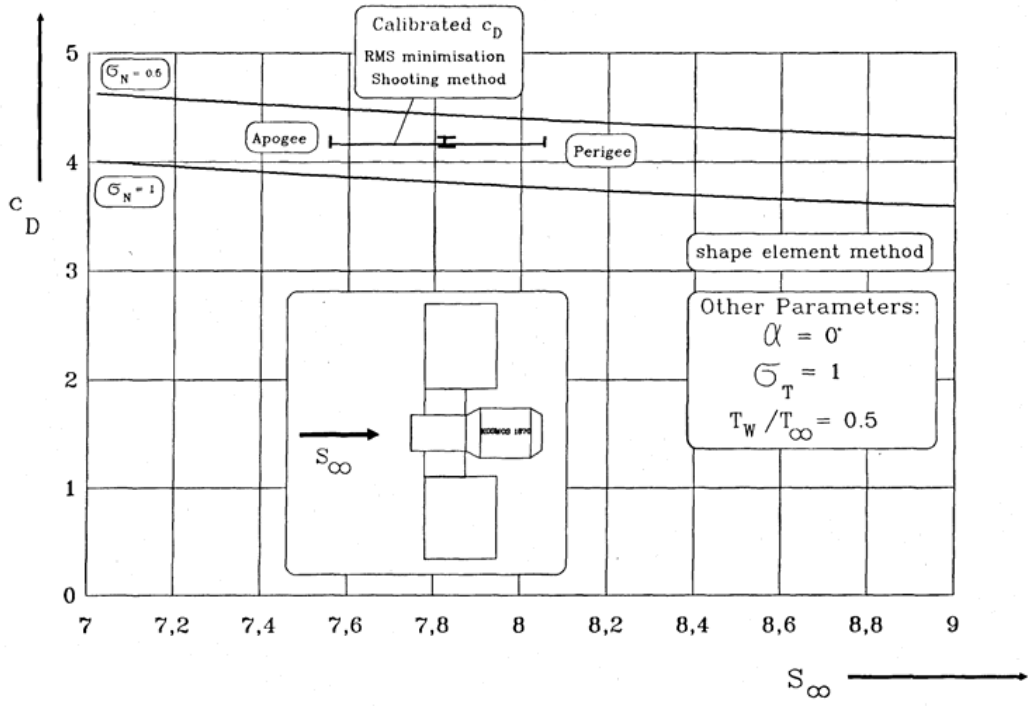

Figure 6.13 KOSMOS 1870 drag coefficient, flight deduced value and CFD analysis.

6.3.4 The use of GSI models in aerodynamic analysis methods

GSI models are used in the aerodynamic analysis to determine the local force contributions due to re-emission. Therefore each aerodynamic analysis method has to be adopted to the specific GSI model to be used.

All gas surface interaction models of level 2, which relay on the resulting action on surface elements, can only be used for convex shapes, where no information on the scattered flux is required. Concave shapes can only be treated by simplification of the aerodynamic analysis.

GSI models of level 1, which provide velocity distribution function of reflected molecules, have the advantage that they can be used for all body shapes and in all type of analysis methods e.g local panel methods and Test Particle Methods and even DSMC methods.

6.4 The aerodynamic analysis methods

The aerodynamic analysis is usually conducted in the following two steps:

1. Calculation of local pressure and sheer stress
2. Integration of local forces over surface in order to obtain the overall forces and moments.

The step 2 integration can only for a very limited range of shape elements be conducted analytically. For most practical applications the integration has to be done numerically. Therefore a panelized model of the spacecraft is an important prerequisite for accurate aerodynamic analysis.

6.4.1 Local pressure and shear stress according to kinetic theory

As explained in section 3 the local surface actions are determined by moments of the requested quantity over the distribution function. This triple integrals have been solved for convex shapes and the results are given with usual nomenclature (e.g. [*Bird*, 1994; *Kogan*, 1969]) in this section.

As GSI imposes the dominant error source in the force analysis of satellites the contributions of incident and reflected particles are strictly separated in the following. This separation should during the course of the project facilitate sensitivity analysis of drag on GSI uncertainty.

The following moment integral solutions are based on the Maxwell gas surface interaction model.

Pressure contribution of incident particles

$$c_{p_i} = \frac{p_i}{q_\infty} = \frac{1}{\sqrt{\pi} s_\infty^2} \Pi(S_N) \tag{6.21}$$

Pressure contribution of reflected particles according to the Maxwell model (specular and diffuse components):

$$c_{p_r} = \frac{p_r}{q_\infty} = \frac{1}{S_\infty^2} \left(\frac{1-\sigma}{\sqrt{\pi}} \Pi(S_N) + \frac{\sigma}{2} \sqrt{\frac{T_w}{T_\infty}} * \chi(S_N) \right) \tag{6.22}$$

$$c_p = \frac{p}{q_\infty} = \frac{1}{S_\infty^2} \left(\frac{1}{\sqrt{\pi}} \Pi(S_N) + \frac{1-\sigma}{\sqrt{\pi}} \Pi(S_N) + \frac{\sigma}{2} \sqrt{\frac{T_w}{T_\infty}} * \chi(S_N) \right) \tag{6.23}$$

Local shear stress due to incident particles:

$$c_{\tau_i} = \frac{\tau_i}{q_\infty} = \sin(\theta) * \frac{1}{\sqrt{pi}} \frac{\chi(S_N)}{S_\infty} \tag{6.24}$$

Local shear stess due to reflected particles:

$$c_{\tau_r} = \frac{\tau_r}{q_\infty} = 0 - (1-\sigma) * \sin(\theta) * \frac{1}{\sqrt{\pi}} \frac{\chi(S_N)}{S_\infty} \tag{6.25}$$

$$c_\tau = \frac{\tau}{q_\infty} = \sin(\theta) * \frac{1}{\sqrt{\pi}} \frac{\chi(S_N)}{S_\infty} [1 - (1-\sigma)] \tag{6.26}$$

with q_∞ representing the dynamic free stream pressure:

$$q_\infty = \frac{1}{2} \rho_\infty V_\infty^2 \quad , \tag{6.27}$$

S_N designating the normal component of S_∞:

$$S_N = S_\infty \cos(\theta) \quad , \tag{6.28}$$

the particle flux function $\chi(S_N)$:

$$\chi(S_N) = e^{-S_N^2} + \sqrt{\pi} S_N \Big(1 + \mathrm{erf}(S_N) \Big) \quad , \tag{6.29}$$

and the pressure function $\Pi(S_N)$:

$$\Pi(S_N) = S_N e^{-S_N^2} + \sqrt{\pi} \Big(\frac{1}{2} + S_N^2 \Big) \Big(1 + \mathrm{erf}(S_N) \Big). \tag{6.30}$$

As already mentioned, the integration of the exact local force coefficients over the surface of general body shapes is only possible for very limited shapes at zero angles of attack. A summery list of resulting drag formula for shapes like e.g. plates, sphere, cylinder, cones can be found in [*Koppenwallner*, 1999].

6.4.2 Hyper-thermal flow and approximations to local surface forces

These approximations can be derived from the exact expressions as asymptotic solutions. In the exact formula the local surface element dS and its exposure to the flow are characterized by

- The free stream speed ratio S_∞.
- The normal component of S to the surface element given by

The hyper-thermal flow of blunt bodies given by: $S_\infty >> 1$, $S_\infty \cos(\theta) > 1$

The approximations are derived by use of the limiting values of the error function in the particle flux and pressure functions. The expressions for pressure and shear stress reduce to the following simple formula:

$$c_p = \frac{p}{q_\infty} = 2\cos^2(\theta) + 2(1-\sigma)\cos^2(\theta) + \sigma_N\sqrt{\pi}\frac{\cos(\theta)}{S_\infty}\sqrt{\frac{T_W}{T_\infty}} \tag{6.31}$$

$$c_\tau = \frac{\tau}{q_\infty} = \sin(\theta)\cos(\theta)\big[1-(1-\sigma)\big] \tag{6.32}$$

These expressions can be integrated over many body shapes and served therefore as basis for the derivation of simple drag formula [*Moe et al.*, 1998].

For blunt body shape like sphere, blunt cones or cylinder in cross flow these equations give already for $S > 5$ excellent approximations for the drag [*Koppenwallner*, 1989, 1999].

The approximations fail however completely for drag prediction of slender bodies like a plate parallel or slightly inclined to the flow. In these cases the second basic assumption of $S_\infty \cos(\theta) > 1$ is usually violated. Therefore the use of hyper-thermal approximations has to be carefully checked concerning its application limit.

The hyper-thermal flow of slender bodies given by : $S_\infty >> 1$

The derivation is based on a linear approximation of the error function at its zero passage. For particle flux, pressure function and the local coefficients results then:

$$\chi(S_N) = 1 + \sqrt{\pi}S_N \tag{6.33}$$

$$\Pi(S_N) = \frac{1}{2}\sqrt{\pi} + 2S_N \tag{6.34}$$

$$c_p = \frac{p}{q_\infty} = \frac{1}{S_\infty^2}\left(\frac{1}{\sqrt{\pi}}\Big(\frac{\sqrt{\pi}}{2}+2S_N\Big) + \frac{1-\sigma_N}{\sqrt{\pi}}\Big(\frac{\sqrt{\pi}}{2}+2S_N\Big) + \frac{\sigma_N}{2}\sqrt{\frac{T_w}{T_\infty}}\Big(1+\sqrt{\pi}S_N\Big)\right) \tag{6.35}$$

$$c_\tau = \frac{\tau}{q_\infty} = \sin(\theta) * \frac{1}{\sqrt{\pi}}\frac{1+\sqrt{\pi}S_N}{S_\infty}\big[1-(1-\sigma)\big] \tag{6.36}$$

These expressions give linear approximations for small positive or negative incidence. For surfaces parallel to flow with $S_N = 0$ the following exact formula result:

$$c_p = \frac{p}{q_\infty} = \frac{1}{2S_\infty^2}\left(1+(1-\sigma)+\sigma\sqrt{\frac{T_w}{T_\infty}}\right) \tag{6.37}$$

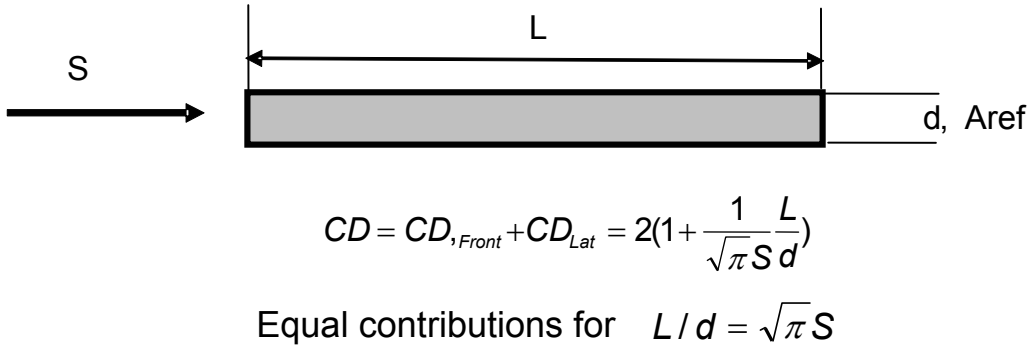

Figure 6.14 Drag contributions of front and flow aligned surfaces of a flat plate

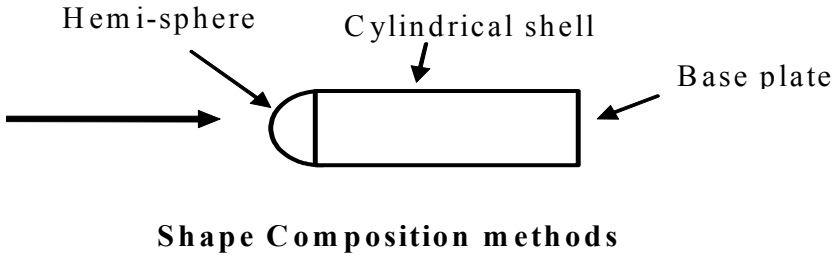

Figure 6.15 Shape composition methods

and

$$c_\tau = \frac{\tau}{q_\infty} = \frac{1}{\sqrt{\pi}}\frac{1}{S_\infty}\left[1 - (1-\sigma)\right] \tag{6.38}$$

The importance of blunt and slender body hyper-thermal flow is best explained by a flat plate with finite thickness as shown in Figure 6.14. Drag of the parallel flow aligned surface become equal to the front rea drag for $L/d = \sqrt{\pi}S$.

6.5 Methods for integral forces and moments of satellites

We have to distinguish between convex and concave shapes.

6.5.1 Methods for convex shape aerodynamics

For convex shapes the local aerodynamics is applicable and therefore shape composition methods and panel methods can be applied e.g. [*Johannsmeier and Koppenwallner*, 1990; *Bruinsma and Biancale*, 2003].

The shape element composition methods

In this case the satellite is reconstructed by shape elements as shown in Figure 6.15, and the local aerodynamic coefficients of the elements are summed up in order to get the overall aerodynamic forces. Shape composition is a simple and often used procedure but usually limited to drag calculation. Only with special procedures the calculation of lift coefficients can be included [*Johannsmeier and Koppenwallner*, 1990].

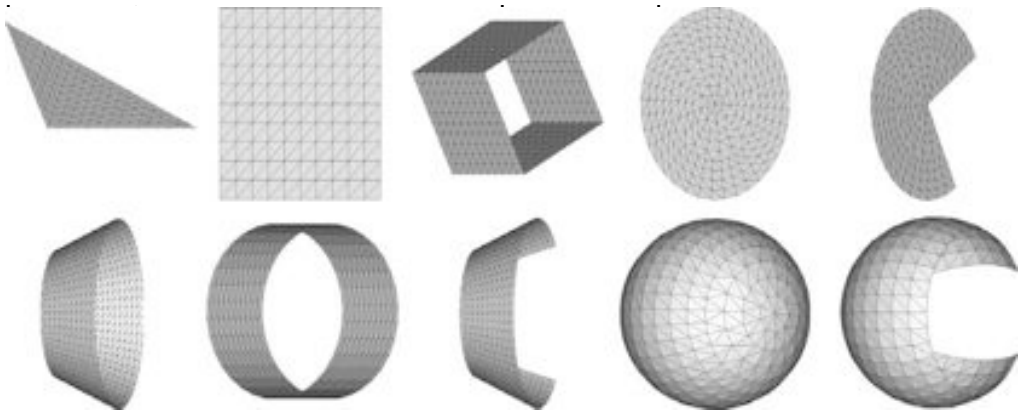

Figure 6.16 Typical panelized primitives for satellite shape construction

The flat panel methods

For satellite shapes composed of flat surface panels the formula of *Cook* [1965] and *Sentman* [1961] can be applied to calculate the overall drag and lift coefficient. In both cases the total force coefficient is given by summation of all individual panel contributions. As Cooks drag formula is based on hypersonic blunt body flow, surfaces parallel to the flow will not contribute to the drag force. This has to be considered when studying publications based on Cooks method e.g. [*Bruinsma and Biancale*, 2003].

The Sentman panel formulae are derived for diffuse reemission with temperature ratio T_r/T_i. Thus the diffusive Sentman formulae are equivalent to standard gas kinetic formulae with T_W/T_∞ replaced by T_r/T_i and diffuse re-emission with $\sigma = 1$ (equ.13 - 28). In Sentman's formulation, T_i corresponds to the free stream atmospheric static temparature T_∞. In order to determine in the original Sentman formulation the diffuse reflection temperature T_r, a relation between T_r and the energy accommodation coefficient α_E, as postulated by Cook's version of the Schamberg model, has been introduced by Moe and Moe [*Moe and Moe*, 2005].

$$\frac{V_r}{V_i} = \frac{2}{3}\left[1 + \alpha_E\left(\frac{T_w}{T_i} - 1\right)\right] \tag{6.39}$$

In this formula, T_i corresponds however to the incident kinetic temperature $T_{kin,I}$ given by equation (18). Thus care is necessary in order to avoid correct interpretations of T_i. According to our derivation V_r/V_i by equation 37 replaces in the Sentman formula the following term in the force contribution of re-emitted particles:

$$\text{Sentman} \quad \sqrt{\frac{T_r}{T_i}}\frac{1}{S} \quad \text{replacedby} \quad \frac{V_r}{V_i} \tag{6.40}$$

With this replacement in the Sentman formulation, force formula as given by Moe are obtained.

Panellized surface methods

In this method the surface of first and second order geometries is reproduced by partition into small triangular panels. The degree of partition determines the

accuracy of shape reproduction. For each panel element the local pressure and shear stress are calculated with free molecular formula. Typical examples of such methods are the RAMSES an ANGARA code of HTG [*Koppenwallner et al.*, 1994, 1995; *Fritsche et al.*, 1998]. Figure 6.16 shows some panellized primitives, which can be used to compose a complete satellite. The integral force and moments are obtained by numerical integration of local panel forces and moments over the whole surface.

$$\vec{F}_{aero} = q_\infty \int_S (c_p \vec{n} + c_\tau \vec{t}) dS \tag{6.41}$$

$$\vec{M}_{aero} = q_\infty \int_S (\vec{r} \times c_p \vec{n} + \vec{r} \times c_\tau \vec{t}) dS \tag{6.42}$$

In case exact local force formulas are applied, the numerical accuracy of this method depends only on the triangulation fineness. The actual accuracy of aerodynamic force prediction is however restricted by the validity of the gas surface interaction model and its input parameters.

6.5.2 Methods for concave shape aerodynamics

The general problem of concave shapes has already been addressed in Section 6.2. The basic gas kinetic problems are:

- The molecular shielding of local incident fluxes by surface elements which are within sight of view.
- The impinging fluxes of remitted molecules from surface elements within sight of view.

These problems have been addressed in many standard text books (e.g [*Kogan*, 1969; *Bird*, 1994]) and for special cases, like concave corner flow, analytical solutions have been derived e.g. [*Koppenwallner*, 1982; *Koppenwallner and Wuest*, 1979; *Koppenwallner*, 1985].

Due to finite speed ratio, this problem is even more complicated as radiation exchange between concave surface elements, and requires the solution of an integral equation, which can only be achieved by iterative numerical procedures. Therefore the following two approaches are available for concave SC aerodynamics.

- Approximate methods with panellized SC geometry
- Monte Carlo test particle methods with panellized SC geometry

Approximate methods with panellized concave SC geometry

These methods are in principle based on a molecular shadow analysis. The molecular shadow is determined by a speed ratio $S = \infty$ flow. Shadowed regimes are free from particles and shadowed surface panels experience therefore no aerodynamic forces. The local force calculation is performed on the following basis:

- Not shadowed areas: p and τ based on convex pressure shear stress formula;
- Shadowed areas: $p = \tau = 0$

If the geometry is represented by panellized surface elements the shadow analysis has to be conducted on panel versus panel level and can result in time consuming analysis.

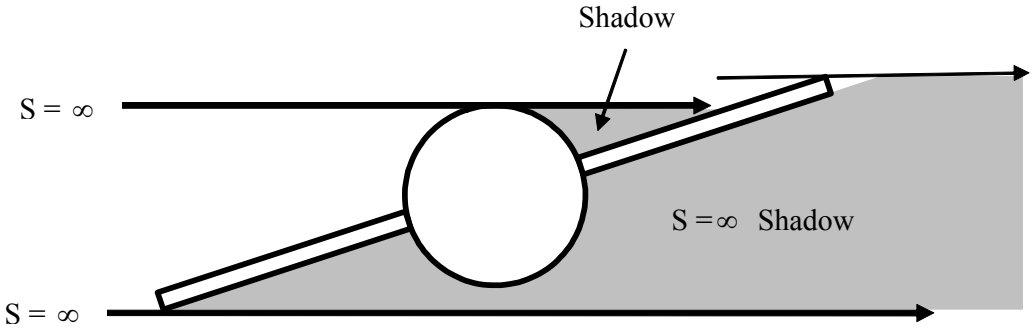

The shadow model based on infinite speed ratio flow

Figure 6.17 Explanation of infinite speed ratio shadow model

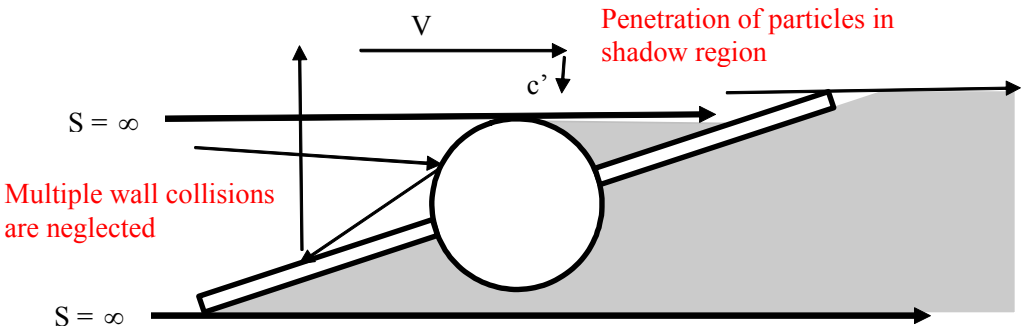

Convex body with 4 separate wall elements
Surfaces 2 and 3 may be treated as shadowed

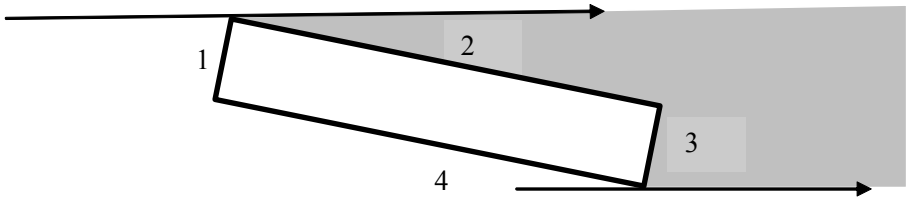

Errors of infinite speed ratio shadow models

Figure 6.18 Explanation of infinite speed ratio shadow model

Neglecting the thermal flow component, which allows particles at finite speed ratio flow to penetrate into the $S = \infty$ shadow, produces the following errors:

- Partial shielding of surface elements in concave regions is neglected
- Multiple wall collisions of particles are not considered.
- Unrealistic simplification, when applied to convex shapes

Figure 6.18 explains these error sources.

Infinite speed ratio shadow analysis is e.g. implemented as an option in the analysis methods of RAMSES and ANGARA.

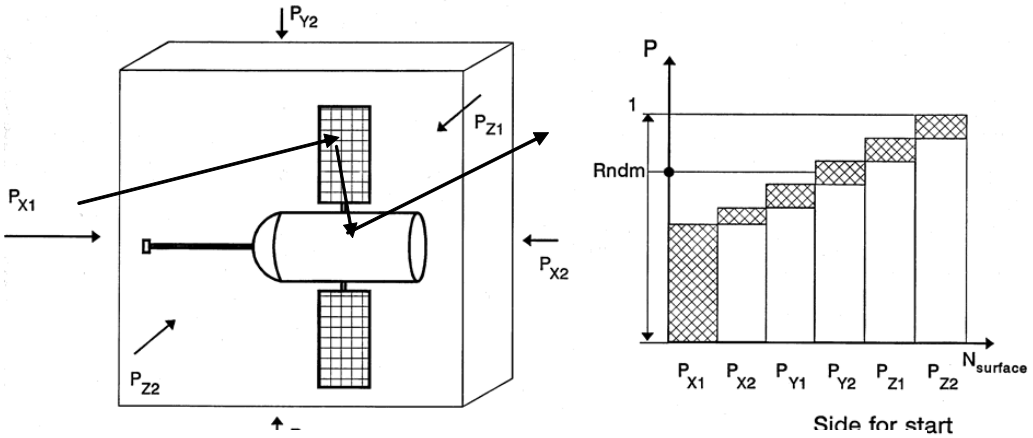

Figure 6.19 The Monte Carlo test particle method (TPM).

The Test Particle Methods (TPM) for finite speed ratio flow

The principle of these methods is e.g. explained by *Bird* [1994] in his text book. TPM is in principle restricted to free molecular flow. TPM simulates the flow by tracing individual test particles on its passage through a control volume surrounding the SC. For each particle, the resulting actions on a surface are recorded. Reflection of the particles follows the selected gas surface interaction model and each particle is traced till it leaves the control volume. Figure 6.19 explains the principle of the TPM method, used in RAMSES [*Koppenwallner et al.*, 1995] or ANGARA [*Fritsche et al.*, 1998]. The test particle flow into the control volume through the six control surfaces is uniformly distributed on each surface. The initial velocities of started test particles are determined by a random number generator according to the velocity distribution valid on the selected surface.

For the two limiting flow cases of $S = \infty$ and $S = 0$ this means e.g: For $S = \infty$, there is only particle inflow through the front control surface. In Figure 6.19, the inflow probability through control surfaces are $P_{X1} = 1$; $P_{X2} = P_{Y1} = P_{Y2} = P_{Z1} = P_{Z2} = 0$.

For $S = 0$, the inflow probability for all surfaces is equal: $P_{X1} = P_{X2} = P_{Y1} = P_{Y2} = P_{Z1} = P_{Z2} = \frac{1}{6}$.

In order to reduce the statistical error of the results, large numbers of test particles or particle hits to the surface (e.g 100000) have to be traced. Codes like RAMSES and ANGARA allow a direct control of the statistical error by continuous particle tracing till the statistical error reaches a prescribed minimum value.

Figures 5.3 and 5.4 showed, as examples, the panellized models of the CHAMP and GRACE satellites generated by the ANGARA code, whose aerodynamic behaviour was analyzed with this code using the test particle method.

6.6 Conclusions on aerodynamic analysis methods

Numerical analysis of aerodynamic forces and moments on satellites can be conducted on several levels. There exist simple formula and methods which allow fast drag estimates for simple shapes. If the satellite shape is complicated the geometry shall be represented by panellized surfaces and local free molecular

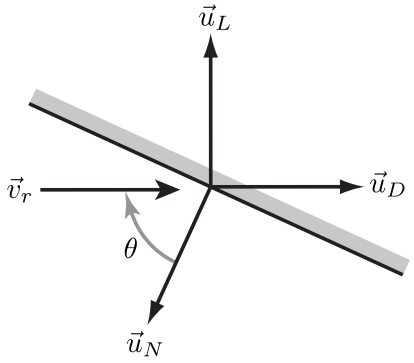

Figure 6.20 Relation of the velocity vector, panel unit normal vector, and the drag and lift unit vectors used in the aerodynamic calculations for a single panel.

panel methods can be used. By a simple shadow method can this approach be extended to treat also concave corner effects. Shadow models neglect however the influence of multiple wall collisions.

A gas kinetic correct analysis of complex concave shapes can in principle only be achieved by numerical Monte Carlo Test Particle Methods.

The mayor error source in aero force prediction results due to uncertainties in the gas surface interaction process. The influence of these uncertainties on the resulting aero forces is strongly shape dependent. Therefore a sensitivity of the SC shape on gas surface interaction parameters shall be investigated.

It is also proposed to split the resulting aerodynamic forces up into a contribution due to impinging molecules, which are not GSI dependent, and into the force contribution due to particle reflection, which is strongly dependent on gas surface interaction.

The code systems like RAMSES and ANGARA provide detailed physical modelling of the spacecraft covering panellized surface geometry and the surface properties. The code includes as analysis modules integrating panel methods, with and without shadow analysis, and Test Particle Methods. Also the most relevant gas surface interaction models are implemented in the force analysis. The code system is therefore best suited for aerodynamic force calculations within the study. It should be noted that similar universal codes are not available in Europe.

6.7 Implementations of aerodynamic models in the data processing

6.7.1 Aerodynamics of a single panel, part 1: Sentman

For the aerodynamics of a single panel, Sentman's equations [*Sentman*, 1961; *Moe et al.*, 2004] are used as the primary model. The calculation procedure starts with some geometry, of which the symbols are explained in Figure 6.20. The unit vector in the drag direction $\vec{u}_D$ is determined from the relative velocity vector.

$$\vec{u}_D = \frac{\vec{v}_r}{|\vec{v}_r|} \tag{6.43}$$

The lift unit vector $\vec{u}_L$ is perpendicular to $\vec{u}_D$ and in the plane spanned by the panel normal unit vector $\vec{u}_N$ and $\vec{u}_D$.

$$\vec{u}_L = \vec{u}_D \times (\vec{u}_D) \times \vec{u}_N) \tag{6.44}$$

Sentman's equations make use of the cosine γ of the angle between the inward normal and the drag vector, and of the cosine l of the angle between the inward normal and the lift vector. These are easily determined using their inner products.

$$\gamma = \cos(\theta) = -\vec{u}_D \cdot \vec{u}_N, \quad l = -\vec{u}_L \cdot \vec{u}_N \tag{6.45}$$

The minus signs appear because we define $\vec{u}_N$ as the panel outward normal.

The computation continues with the properties of the gas before and after its interaction with the surface. The speed ratio S is computed as before in (5.9):

$$S = \frac{v_r}{\sqrt{\frac{2RT}{m}}} \tag{6.46}$$

The kinetic temperature of the incoming particles T_{in} can be calculated as

$$T_{in} = \frac{m v_r^2}{3R} \tag{6.47}$$

where m is the molecular mass of the incident gas atoms, v_r is the relative velocity of the gas with respect to the panel and R is the universal gas constant. The composition of the atmosphere, which determines the value of m is taken from the NRLMSISE-00 empirical model.

The value of T_{in} is used in the computation of the most probable velocity of the re-admitted molecules v_{out}

$$v_{out} = v_r \sqrt{\frac{2}{3}\left[1 + \alpha_E\left(\frac{T_{wall}}{T_{in}} - 1\right)\right]} \tag{6.48}$$

which is also determined by the accommodation coefficient α_E and the panel's wall temperature T_{wall}. A wall temperature of $T_{wall} = 273$ K has been assumed.

The accommodation coefficient α_E is a key variable in this satellite aerodynamic model. It is defined as the ratio of the energy exchange that takes place between the particles and the surface to the maximum energy transfer that could take place. Values of α_E can be found either by theory or experiment (see *Cook* [1965], *Moe et al.* [2004], *Moe and Moe* [2005] and references therein), although the experimental results for conditions encountered in Earth's orbit are still sparse and uncertain. For that reason, various fixed values, in the range of 0.6 to 1.0 have been tried.

A number of substitution variables can be used in order to come to a compact representation of the drag and lift coefficient equations, of which a full derivation is available in the report by *Sentman* [1961].

$$G = \frac{1}{2S^2}, \quad P = \frac{1}{S}\exp(-\gamma^2 S^2), \quad Q = 1 + G, \quad Z = 1 + \operatorname{erf}(\gamma S) \tag{6.49}$$

$$(C_D A) = \left(\frac{P}{\sqrt{\pi}} + \gamma Q Z + \frac{\gamma}{2}\frac{v_{out}}{v_r}(\gamma\sqrt{\pi}Z + P)\right)A \tag{6.50}$$

$$(C_L A) = \left((lGZ) + \frac{l}{2}\frac{v_{out}}{v_r}(\gamma\sqrt{\pi}Z + P)\right)A \tag{6.51}$$

To clarify, the area A on the right side of these equations represents the true panel area, as listed in Tables 5.2 and 5.3, while the products $(C_D A)$ and $(C_L A)$ are computed as single entities, representing the drag and lift force divided by $\frac{1}{2}\rho v_r^2$.

Now, $(\vec{C}_F A)$ for a panel can be computed by multiplying the drag and lift coefficients with the flow-projected panel area, which is $A\gamma$, and summing the contributions vectorially.

$$(\vec{C}_F A) = (C_D A)\vec{u}_D + (C_L A)\vec{u}_L \tag{6.52}$$

6.7.2 Aerodynamics for a single panel, part 2: Cook

An alternative, more simple set of expressions for the drag and lift coefficients, attributed to *Cook* [1965], has been used extensively in the literature on CHAMP and GRACE data processing [*Bruinsma and Biancale*, 2003; *Bruinsma et al.*, 2004; *Sutton et al.*, 2005]. *Sutton et al.* [2007] provides equations for both the drag and lift coefficients, which have been implemented in order to be able to compare the results. The equivalent equations to (6.50) and (6.51) are:

$$(C_D A) = \left(2 + \gamma\frac{4}{3}\sqrt{1 + \alpha_E\left(\frac{T_{wall}}{T_{in}} - 1\right)}\right) A\gamma \tag{6.53}$$

$$(C_L A) = \left(l\frac{4}{3}\sqrt{1 + \alpha_E\left(\frac{T_{wall}}{T_{in}} - 1\right)}\right) A\gamma \tag{6.54}$$

The values for C_D and C_L should be set to zero if the backside of the panel is explosed to the flow, that is if $\gamma < 0$.

6.7.3 Mixed composition atmosphere

The next step in the force model calculations is to model the characteristics of the space environment in a way that is as realistic as possible. This section will discuss how the mixed composition of the atmosphere has been taken into account in aerodynamic calculations.

The values for the aerodynamic force coefficients times area $(\vec{C}_F A)$ found so far, both from the ANGARA model and the panel model, are a function of the molecular mass m of the gas. In reality, the atmosphere consists of a mixed composition. At the altitude of CHAMP and GRACE, atomic oxygen is the dominant constituent, but major fractions of Nitrogen and Helium can also be present. The force coefficient is a non-linear function of the molecular mass, so a summation is used to account for the different contributions of the M atmospheric species with index j.

$$(\vec{C}_F A) = \sum_{j=1}^{M} \frac{\rho_j}{\rho}(\vec{C}_F A)_j \tag{6.55}$$

The contributions for each of the species is weighted using its fractional mass density ρ_j/ρ, of which the value is taken from the NRLMSISE-00 empirical density model. This empirical model was chosen because it incorporates a large database of mass spectrometer data, and should therefore return more accurate information on the atmospheric composition than models that are based mainly on satellite drag data.

The aerodynamic calculation can now be completed. For ANGARA, equation (6.55) can be substituted into (5.5):

$$\ddot{\vec{r}}_a = \frac{1}{m}\left[\sum_{j=1}^{M} \frac{\rho_j}{\rho}(\vec{C}_F A)_j\right]\frac{1}{2}\rho v_r^2 \tag{6.56}$$

For the panels, a double summation is required, both over the atmospheric species j, as in (6.55) and over the panels i, as in (5.11). The result is again substituted into (5.5).

$$\ddot{\vec{r}}_a = \frac{1}{m}\left[\sum_{i=1}^{N}\sum_{j=1}^{M}\frac{\rho_j}{\rho}(\vec{C}_F A)_{i,j}\right]\frac{1}{2}\rho v_r^2 \tag{6.57}$$

6.8 Aerodynamic modelling sensitivity analysis

Aerodynamic models for free molecular flow can depend on a number of input parameters, such as the relative velocity, the energy accommodation coefficient, and the temperatures and molecular masses of the wall and the atmosphere. In this section, the equations for drag and lift on a flat plate by *Sentman* [1961] are used to analyze several of these dependencies. The main assumption made by Sentman was that the distribution of reflected particles was strictly specular. With this assumption, his theory is exact, and the accuracy of the aerodynamic model is strictly based on the accuracy of the input parameters.

The sensitivity analysis will start by using a simple 1 m^2 surface element, to gain more insight in the differences between the various models and the effect of parameters, before moving on to the more complicated geometries of the CHAMP and GRACE satellites.

6.8.1 Aerodynamic model

The first set of three test cases, displayed in Figure 6.21, compares the results for the ANGARA model with those for the panel model using the equation of *Sentman* [1961] and *Cook* [1965]. Since the ANGARA model in this case uses complete energy accommodation (α is fixed to 1), the results match well with those of the other two models. The Sentman model allows a variable α, but always assumes a complete diffuse re-emission of the particles. In ANGARA, which uses Maxwell's GSI model, the degree of diffuse or specular re-emission σ can be selected during the model generation. In this work, the completely diffuse case has been selected, to allow for a good comparison with Sentman's model.

The three models show very similar results for the drag component, except for the Cook model, around $\theta = 90^\circ$, where the influence of the random thermal motion of the gas is important. Since CHAMP and GRACE have several large panels that are parallel to the flow, this subtle difference is very important for density derivation.

The lift component for the three models shows larger differences over the full range of incidence angles, with the ANGARA modelling resulting in significantly higher lift values than Sentman and Cook.

6.8.2 Choice of energy accommodation coefficient

The discussion in the introduction shows that further investigation of the influence of the accommodation coefficient α is justified.

Moe and Moe [2005] have looked for specifying suitable fixed values of the accommodation coefficient as a function of specific altitude ranges, based on data from several satellites. It is therefore of significant interest to also analyze the relation between fixed α values and the drag and lift coefficients.

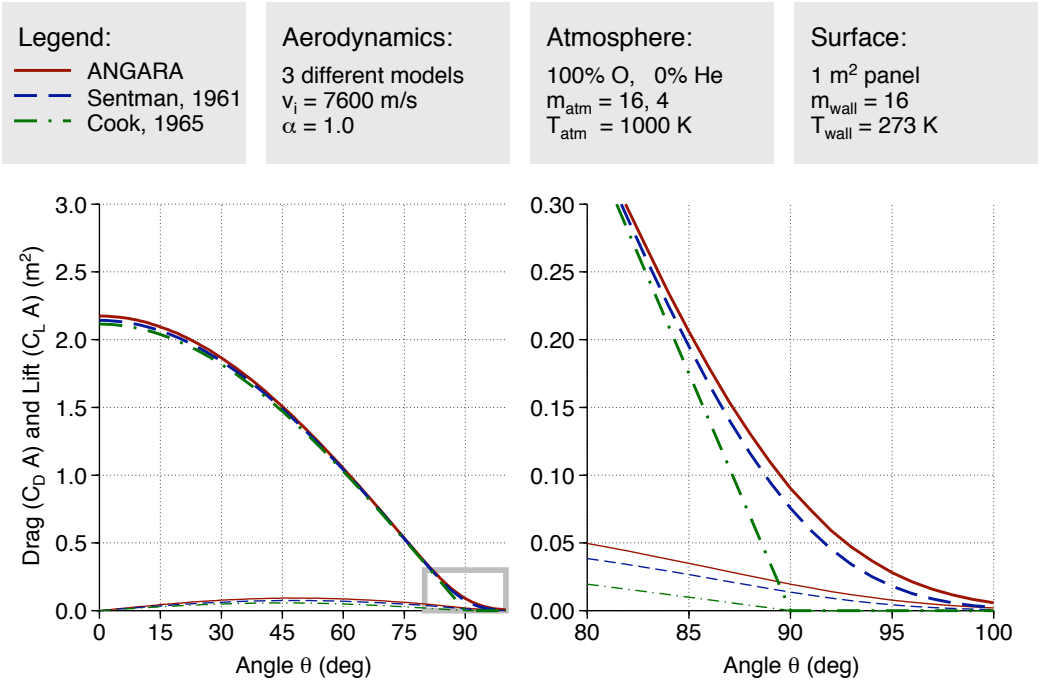

Figure 6.21 Comparison of aerodynamic drag (*thick lines*) and lift (*thin lines*) coefficients times projected area, computed using the ANGARA software and according to the equations of *Sentman* [1961] and *Cook* [1965], of a one-sided 1 m^2 panel. The gray box in the left plot is magnified in the plot on the right.

Panel

Figure 6.22 shows how the drag and lift coefficients of a flat panel change as a function of the angle θ for three different fixed values of α. In general, smaller values of α indicate that the particles have a larger remaining fraction of their original kinetic energy when they leave the satellite surface, which, in combination with diffuse reflection, leads to significantly larger values of the drag and lift coefficients. The effect on drag is largest at perpendicular incidence angles, and disappears for grazing incidence angles, while the effect on lift is large over the whole range of incidence angles.

CHAMP and GRACE

Figures 6.23 and 6.24 show the same figures, but for the complete panel models of CHAMP and GRACE, respectively. The values in these figures are based on a summation of values from Figure 6.22, with the values for each panel determined by their angle θ_i, and weighted according to the panel areas A_i.

The main feature in these curves is caused by changes in the area, as the satellite's side-slip angle β increases. At $\beta = 0°$, the flow-projected area is at a minimum, but when $\beta = 90°$, the flow hits the side of the satellite, and the flow-projected area is significantly larger. CHAMP has a smaller minimum area and a larger maximum area, compared to GRACE, which is visible in these plots. Because of the satellite's attitude control, the value of the side-slip angle β is usually quite small, except during special manoeuvres. This is why a zoomed-in view is provided in the right-hand panels of these figures.

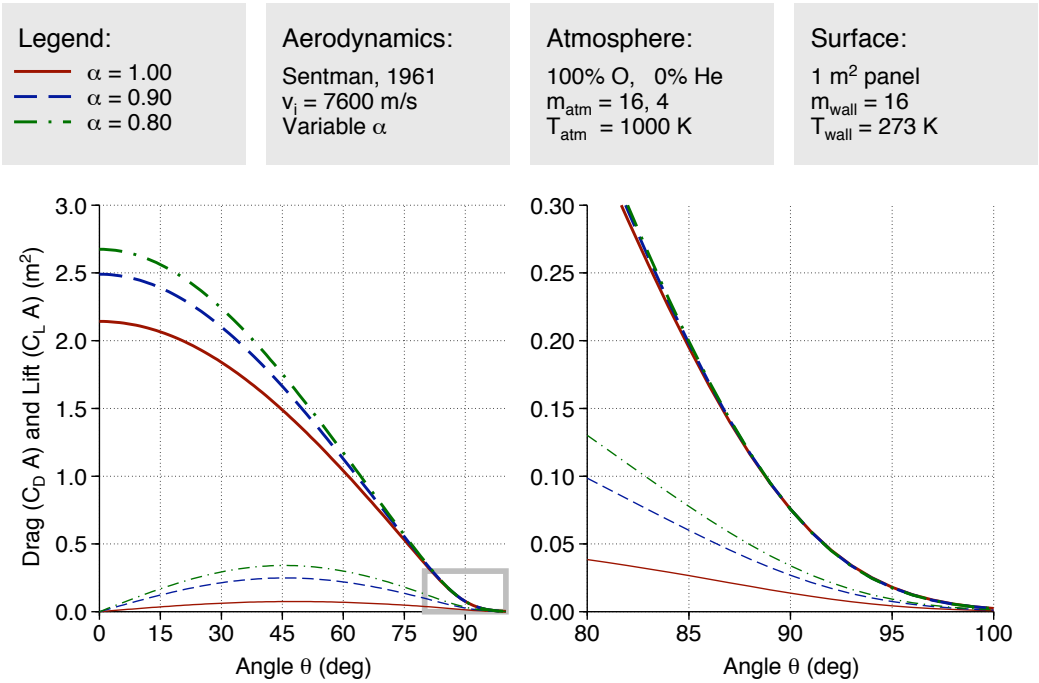

Figure 6.22 Comparison of drag and lift on a 1 m^2 surface element (a one-sided flat panel) using three fixed values of the accommodation coefficient.The determining parameters for the aerodynamic model for this and the following plots are listed in the legends. These values are typical average values for the height range of 250-450 km.

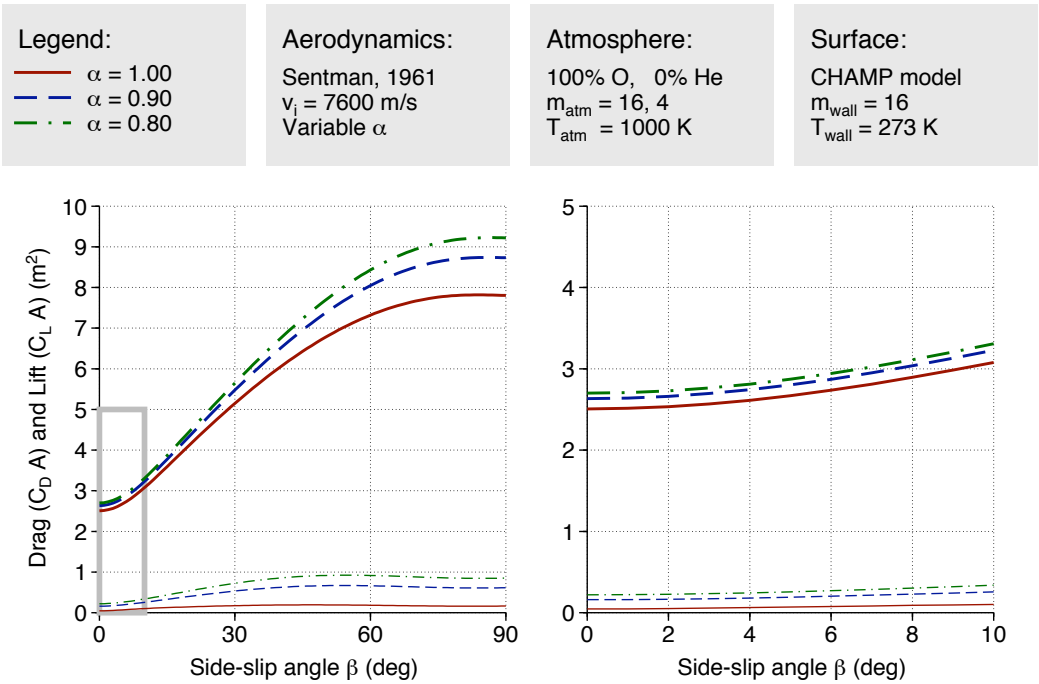

Figure 6.23 As the previous figure, but for the CHAMP panel model.

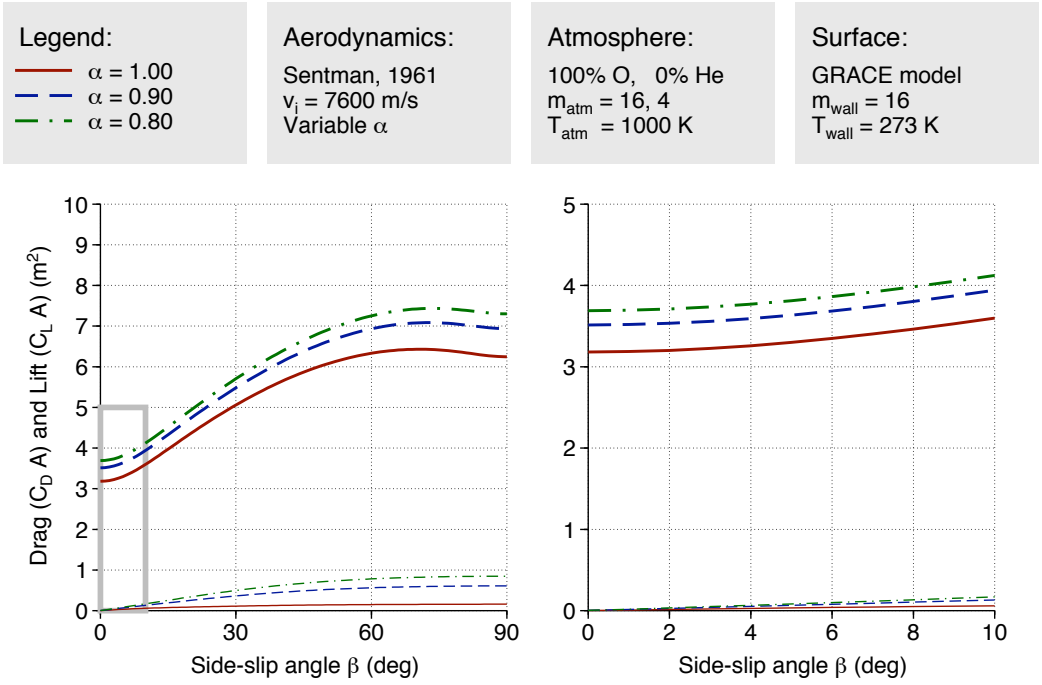

Figure 6.24 As the previous figure, but for the GRACE panel model.

6.8.3 Atmospheric composition dependency

The effect of atmospheric composition on the drag and lift calculations with Sentman's model is now investigated. Initially, three theoretical cases are defined:

- A pure atomic oxygen atmosphere,
- A pure helium atmosphere,
- An intermediate case with 20% helium and 80% oxygen.

Note that an atmosphere with pure helium is an extreme case which will not be encountered at the altitudes of CHAMP, GRACE and Swarm. The pure oxygen atmosphere is a nice simplification of the situation for these satellites for which atomic oxygen is always the dominant constituent. In reality, there is a fluctuation in the concentration of other species, such as N2 and He, which can easily reach 15%, and up to peaks of 30-50% during certain circumstances.

Panel

Figure 6.25 shows the results for the flat one-sided plate. The figure shows the situation where α is set to a fixed value of 0.9, so that only the effect on the random thermal motion of the atoms is of influence on the drag and lift magnitude.

CHAMP and GRACE

Figures 6.26 and 6.27 show the results of the same computations, but now for the entire CHAMP and GRACE panel models, respectively.

Of special interest here is the comparison at small β angles of the cases with a pure oxygen atmosphere and a mixed oxygen/helium atmosphere. It can be seen in Figure 6.26 that the drag coefficient for the mixed atmosphere case is ap-

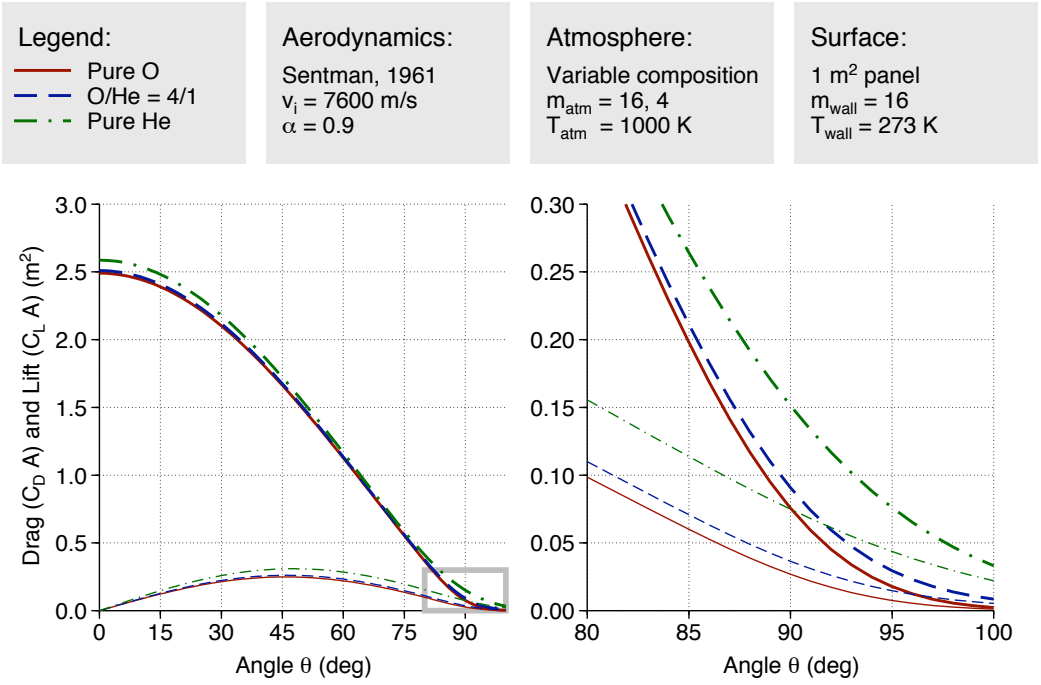

Figure 6.25 Comparison of drag and lift on a 1 m^2 surface element (a one-sided flat panel) for three different atmospheric compositions.

proximately 10% higher than the pure oxygen case, leading to 10% lower density observations.

The effect of composition on the sideways-force, shown in the bottom-right frame of these figures, is of interest for the wind determination. It can be seen that the sensitivity is much higher in the forward-flying configuration, compared to the sideways-flying configuration. There is a maximum at an angle of about 15 degrees, and a minimum at 75 degrees.

Note that the mixed-composition case will be more prevalent at higher altitudes and at low solar activity. Therefore GRACE and the higher Swarm satellite will see larger variations in the molecular mass than CHAMP and the lower Swarm pair, respectively.

6.8.4 Temperature dependency

The atmospheric temperature enters the drag and lift coefficient calculations in the determination of the speed ratio. At higher temperatures, the atmospheric molecules and atoms have a higher thermal velocity, and are more likely to hit the spacecraft surfaces at grazing incidences. The sensitivity to temperature variations is initially investigated by using 500 K, 1000 K and 1500 K as test cases. The error in the temperature output from empirical models such as NRLMSISE-00, which is used as input in the processing, is unknown. Given that density errors from that model are of the order of tens of percents, perhaps temperature errors of the order of hundreds of Kelvin can be expected.

Panel

Figure 6.28 shows the effect of the atmospheric temperature on the magnitude of the drag and lift for the single panel. The effect on drag is small overall, ex-

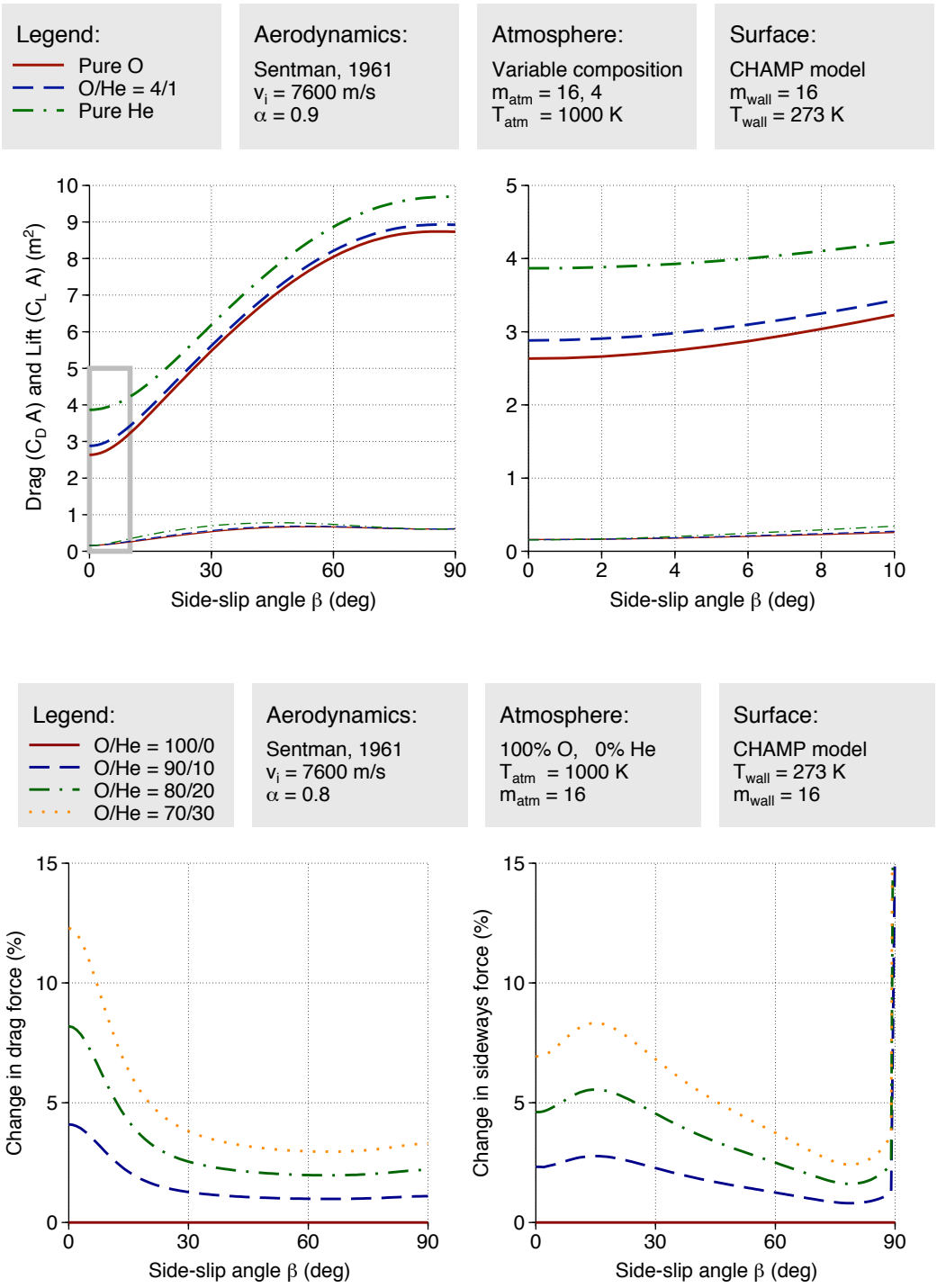

Figure 6.26 Relative sensitivity to atmospheric composition of the CHAMP aerodynamic model.

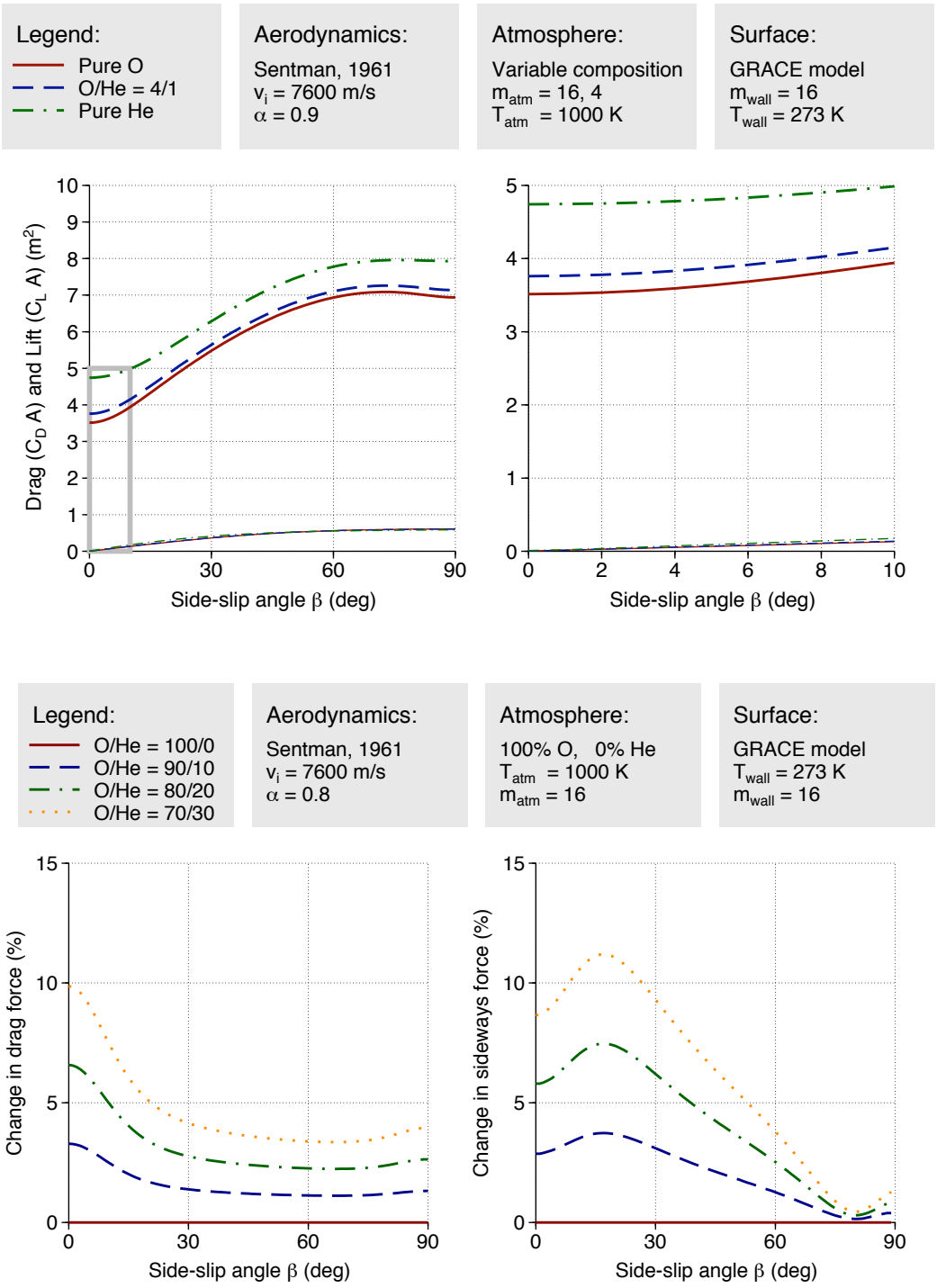

Figure 6.27 Relative sensitivity to atmospheric composition of the GRACE aerodynamic model.

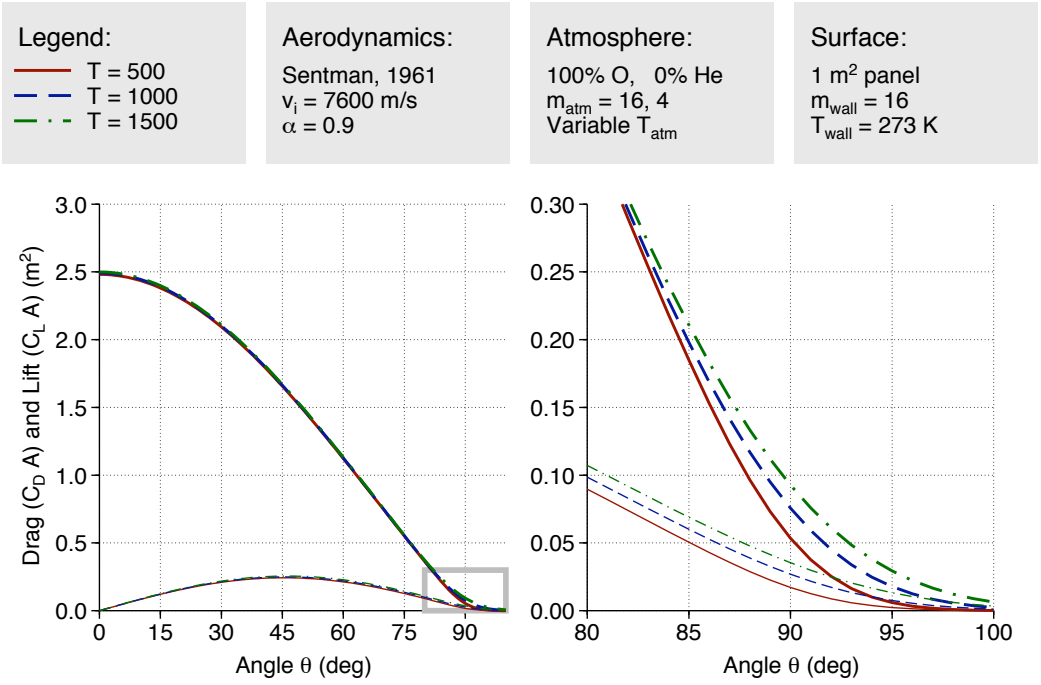

Figure 6.28 Comparison of drag and lift on a 1 m^2 surface element (a one-sided flat panel) for three different atmospheric temperatures.

cept at grazing incidences, where the random thermal motion of the gas becomes important. The effect on lift is significantly larger than on drag at all incidence angles.

CHAMP and GRACE

It is already clear from the analysis of the panel, that for long satellites with a small frontal area, such as CHAMP, GRACE and Swarm, the density and wind determination will be much more sensitive to temperature model errors than for a relatively short satellite with a large frontal area. This is confirmed by Figures 6.29 and 6.30. For small side-slip angles, an increase (or decrease) with respect to the 1000 K reference value leads to an increase (or decrease) of about 10% in the drag coefficient, and an equivalent decrease (or increase) in the accelerometer-derived density. This sensitivity is also a function of the accommodation coefficient. If CHAMP would be flying sideways, the sensitivty of the drag force to temperature errors is reduced by about a factor of four. GRACE is less sensitive than CHAMP in its nominal configuration, but a bit more when it would be flying sideways. Note that there is also a sensitivity of a few percent in the sideways force (the component of the aerodynamic acceleration in the body-fixed XY-plane that is perpendicular to drag). This sensitivity disappears in the sideways flying configuration. There is a maximum at a side-slip angle of about 10 degrees, and a minimum at about 80 degrees for CHAMP. For GRACE, the effect of temperature on the sideways force changes its sign at about 70 degrees sideslip.

Effect of wall temperature

Variations in the satellite wall temperature can be assumed to be much smaller than that of the atmospheric temperature. The wall temperature enters the drag

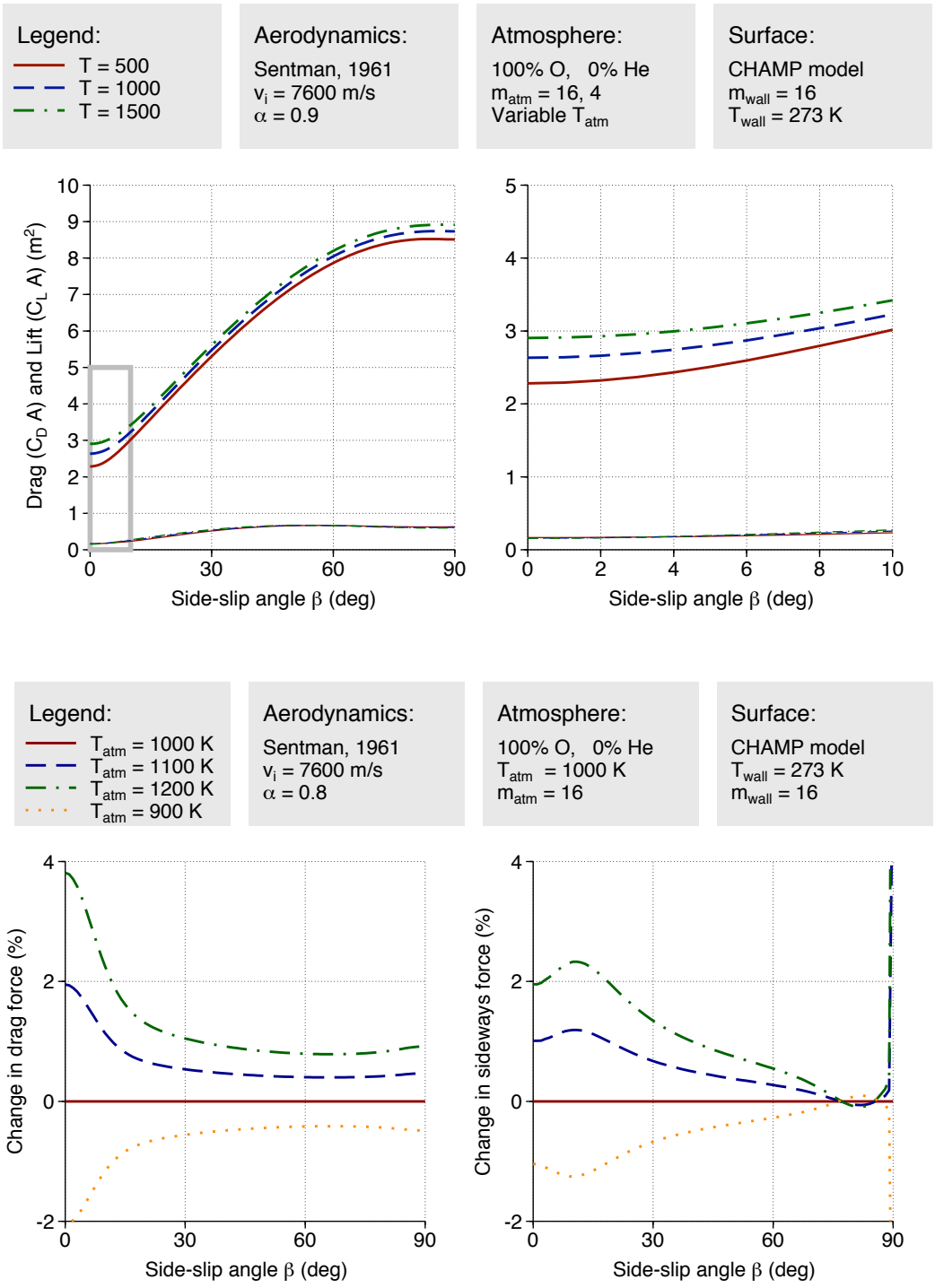

Figure 6.29 Sensitivity to atmospheric temperature of the CHAMP aerodynamic model. The absolute drag and lift coefficients times area are shown at the top, while the relative changes in the drag and sideways force with respect to a reference are shown in the bottom panels.

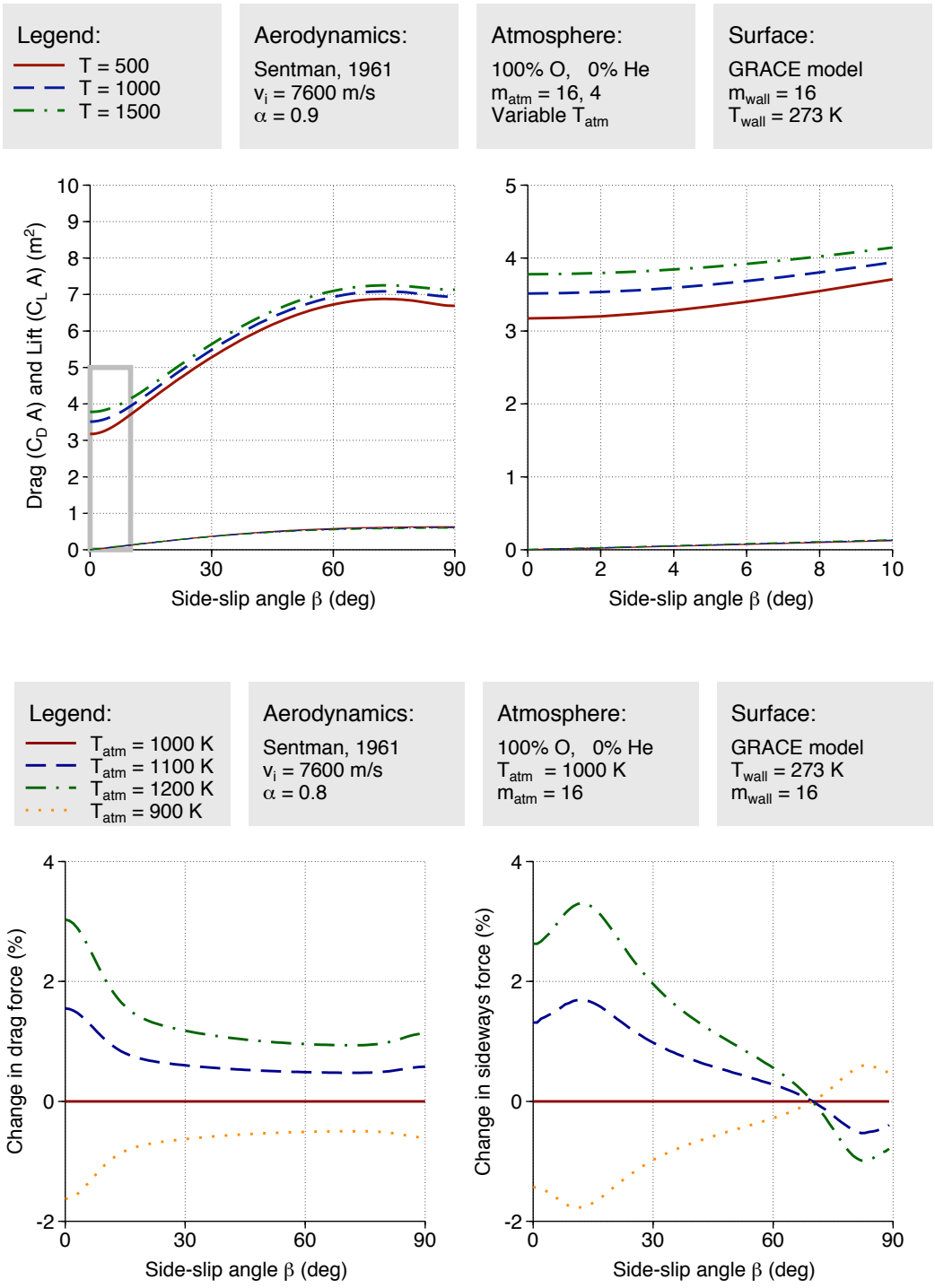

Figure 6.30 Sensitivity to atmospheric temperature of the GRACE aerodynamic model. The absolute drag and lift coefficients times area are shown at the top, while the relative changes in the drag and sideways force with respect to a reference are shown in the bottom panels.

and lift coefficient equations in the ratio T_{wall}/T_{in}, where the kinetic temperature of the gas $T_{in} = mv_r^2/3R$ is a very large number. Therefore, errors in the wall temperature do not have a large effect on the drag and lift results, and they are not further analysed here.

Chapter 7

Accelerometer calibration using GPS tracking data

7.1 Calibration approach

7.1.1 Single satellite approach

This section describes the method to calibrate an accelerometer using GPS based orbit determination. This method uses the accelerometer data instead of the usual non-gravitational force models in the orbit propagation step of the orbit determination. A scale factor and bias for each accelerometer axis are estimated from the GPS observations. The applied method is implemented in the GPS High precision Orbit determination Software Tools (GHOST) [*Montenbruck et al.*, 2005]. First an overview of the standard orbit determination technique as implemented in the reduced dynamic batch least-squares program GHOST is given. After that, the extension of GHOST to accommodate accelerometer observations is discussed. Finally, the practical implementation is discussed.

Least-squares orbit determination with piecewise constant empirical accelerations

During the precise orbit determination process, the parameters of interest are iteratively adjusted by correcting their a priori values with the solution of a least-squares system, built with all selected observations. These are undifferenced dual frequency code and phase GPS measurements. Because of the dispersive nature of the ionosphere, a linear combination of dual frequency measurements is used to eliminate ionospheric path delays. The observations are modelled based on known GPS satellite positions and clock offsets, using precise ephemeris and clock products, determined by the International GNSS Service (IGS), or the Center for Orbit Determination (CODE) in Bern, Switzerland when high rate 30 s clock products are considered. The GPS data are edited using an a priori orbit determined from a dynamical smoothing of pseudo-range-based single point position solutions. This processing scheme is presented in Figure 7.1.

During each iteration, the equations of motion of the satellite are numerically integrated from the reference epoch to the subsequent observation epochs, to obtain the residuals between the observations and the modelled measurements. At the same time the partial derivatives of the state vector with respect to the dynamical trajectory parameters are obtained from the integration of the associated variational equations [*Montenbruck and Gill*, 2000]. The gravitational and non-

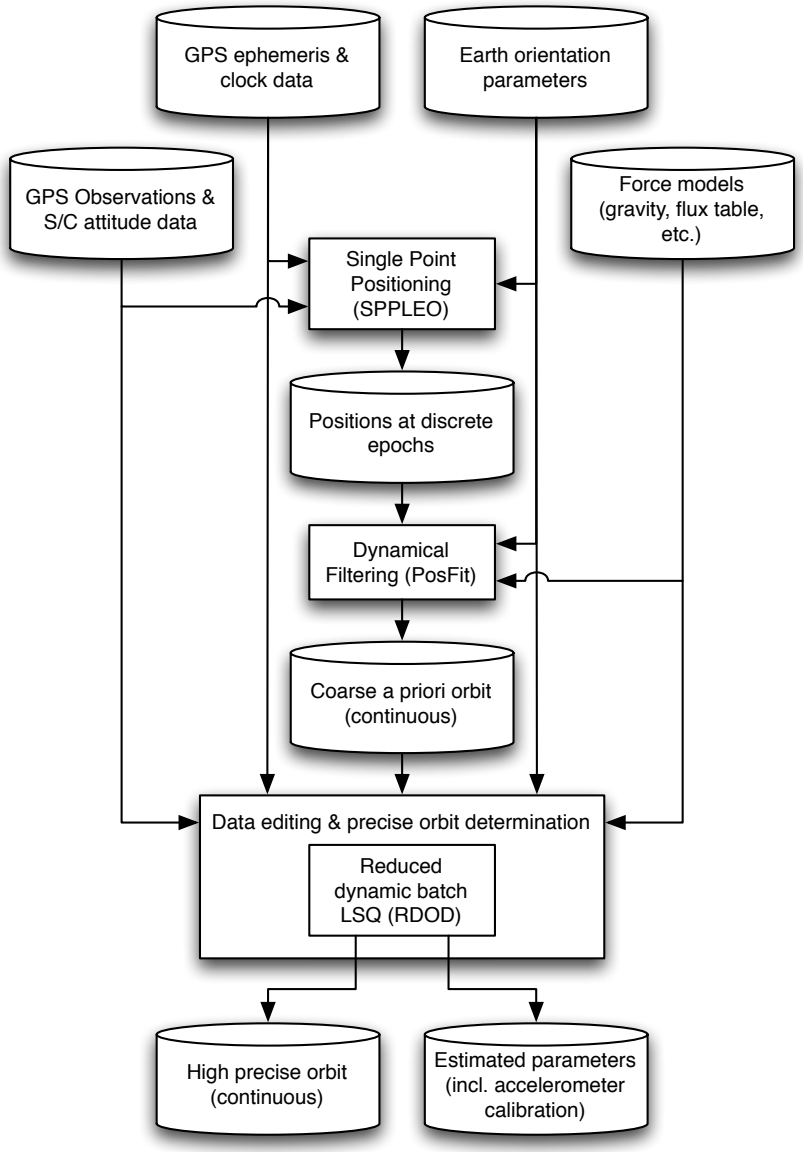

Figure 7.1 Processing scheme for GPS based precise orbit determination of LEO satellites using the GHOST software

gravitational forces are modelled following the general discussion in *Montenbruck et al.* [2005].

The estimation parameters consist of the receiver clock offset at each measurement epoch and a carrier-phase bias for each continuous single GPS satellite pass, and dynamical trajectory parameters, which are the spacecraft state vector containing the spacecraft position and velocity at the reference epoch and empirical accelerations, to compensate for deficiencies in the employed dynamical force models. During normal orbit determination, force model coefficients scaling the solar radiation pressure and atmospheric drag models are estimated as well. When accelerometer measurements are used instead of non-gravitational force models, the accelerometer calibration parameters are estimated instead, as described in the next section.

Empirical accelerations are estimated as piecewise constant parameters in radial, transverse (along-track) and normal (cross-track) direction (RTN) in inde-

pendent intervals of 600 s. This interval length is found to be the most suitable for CHAMP- and GRACE-type orbits and is a compromise between computational effort and a sufficient sampling of the characteristic time scales of the dynamical model deficiencies [*Montenbruck et al.*, 2005]. The empirical accelerations are characterized by an expectation value of zero and an a priori variance which constrains them [*Jäggi et al.*, 2006].

Accelerometer calibration

The SuperSTAR accelerometers on board the GRACE spacecraft, manufactured by ONERA, are successors of the STAR accelerometer flying on CHAMP [*Touboul et al.*, 2004]. The instrument principle relies on the measurement of changes in electrostatic forces needed to maintain a proof mass in the center of a cage. The center of mass of the proof mass is placed as close as possible to the center of mass of the spacecraft. Both proof mass and spacecraft are therefore influenced by the same gravitational forces. The non-gravitational forces act only on the spacecraft and consequently on the instrument cage, inducing a movement of the proof mass which is measured by capacitive detectors.

Because the voltages required to suspend the proof mass in a laboratory environment are different from those in orbit, the instrument calibration parameters are not known precisely at the time of launch. This leads to the necessity to determine calibration parameters when processing the accelerometer observations for e.g. gravity field determination, atmospheric density retrieval [*Bruinsma et al.*, 2004] or precise orbit determination [*Kang et al.*, 2006].

The calibration equation is formulated as:

$$\vec{a}_{cal} = \vec{S} \cdot \vec{a}_{obs} + \vec{B} \tag{7.1}$$

with $\vec{a}$ a three-dimensional vector with the accelerometer observations in the Spacecraft Reference Frame (XYZ_{SRF}) for the GRACE satellites and the Spacecraft Frame ($XYZ_{S/C}$) for CHAMP (see Figure 4.9). $\vec{S}$ represents a 3×3 diagonal matrix containing a scale factor in each direction, thus assuming no cross-couplings between accelerometer axes, and $\vec{B}$ the bias vector. The bias factor refers the observations to the correct absolute reference level, while the scale factor adjusts the amplitude of the measured variations. Because the GRACE and CHAMP satellites fly in a near-circular orbit, the described reference frames agree within a few degrees with the radial/transverse/normal frame in which the empirical accelerations are defined.

Note that the above equation is the same as the one that can be found in the documentation for GRACE [*Bettadpur*, 2004], but the definition on the CHAMP product is different [*Förste*, 2002]. It goes without saying that the application of biases and scale factors should conform with the way they are determined, so equation (7.1) will be used throughout the project.

When using the accelerometer observations for orbit determination the calibrated measurements are directly inserted into the equation of motion and the scale and bias factors are estimated in the least-squares adjustment procedure. The non-gravitational force models are no longer considered in the calculation of the accelerations experienced by the spacecraft. Empirical accelerations are still estimated, but with a reduced a priori variance, as drag and solar radiation pressure models imply a higher amount of uncertainty compared to the direct measurements of them with an accelerometer. The spacecraft equations of motion are

defined and integrated in an inertial reference system, within GHOST realized by EME2000 (mean equator and equinox of J2000). Therefore the measured accelerations are transformed from the considered frame to the inertial reference frame with attitude information obtained from star camera observations, provided as quaternions. The variational equations are updated accordingly taking into account the proper transformation matrices.

When estimating the scale and bias factors in the reference frame directions, the parameters in Y and Z direction are closely correlated with the initial state vector. Furthermore the Y direction (out of plane) is the weakest bounded by the dynamics. Therefore the scale and bias factors in Y and Z direction are tightly constrained to their a priori values, leading to the necessity of good a priori values, especially for the bias factor. As mentioned above, the bias shifts the observations to the correct mean value. The determination of an a priori bias factor is composed of two parts, given by the following equation:

$$\vec{B}_{a\ priori} = -\vec{S}_{a\ priori}\ mean(\vec{a}_{meas}) + mean(\vec{a}_{model}) \tag{7.2}$$

First the mean value of the accelerometer measurements $\vec{a}_{meas}$ is determined, and subtracted from the observations, which shifts them to fluctuate around zero. These corrected measurements are used as accelerometer observations in the POD process. Second, the a priori bias factor is set to the mean value of the modelled non-gravitational and empirical accelerations $\vec{a}_{model}$, calculated and estimated with the standard reduced dynamic technique described above. This shifts the accelerometer observations, corrected for their mean, to a magnitude which is expected to be close to the correct value. The a priori scale factor is set to the advertised values [*Bettadpur*, 2004; *Förste*, 2002].

Practical implementation of accelerometer calibration

In the current implementation, the satellite data are processed in batches of 24 hours. Each day, one scale and bias factor are estimated per instrument axis, according to equation (7.1). This results in a daily set of calibration factors in the Spacecraft Reference Frame (GRACE) or the Spacecraft Frame (CHAMP).

Empirical accelerations are estimated in batches of 600 seconds, with a priori standard deviations of 5 nm/s^2 in radial direction, and 10 nm/s^2 in along track and cross track direction.

The radial component of the CHAMP accelerometer instrument provides erroneous data due to an unforeseen techinical malfunction. For this reason, the data from this accelerometer component should not be used for scientific studies. The correction to the erroneous CHAMP accelerometer data in Z direction included in the accelerometer files is of poor quality and does not lead to meaningful total accelerations. Therefore, an iterative procedure is followed, where the accelerations acting on the spacecraft are modelled with the ANGARA software, making use of density retrieved out of the calibrated accelerometer measurements in X-direction. The Z-component of the accelerometer data is then replaced by the modelled values, and the calibration is repeated with this corrected data set. This approach results in more stable calibration parameters in the two other directions.

7.1.2 Multi-satellite approach

The Filter for Relative Navigation of Satellites [*Kroes et al.*, 2005] is a tool for the relative navigation of formation flying satellites with a smoothed Kalman filter

resolving the double difference carrier phase ambiguities. This method results in an overall 1-dimensional relative position precision under the 1 mm level, which is more than an order of magnitude more precise than the absolute positions. The filter processes single difference GPS pseudorange and phase observations and uses (pseudo) relative spacecraft dynamics to propagate the relative states over the observation epochs. In the approach presented here, no non-gravitational force models will be applied. All differential non-gravitational accelerations are then absorbed by the estimated empirical accelerations. This allows for an offline determination of the scale factor and a differential bias for the accelerometer onboard the two considered satellites, from these differential empirical accelerations.

$$\Delta\vec{a}_{emp} = \vec{S}_1 \cdot \vec{a}_{obs,1} - \vec{S}_2 \cdot \vec{a}_{obs,2} + \Delta\vec{B} \tag{7.3}$$

7.2 Single satellite calibration

7.2.1 Calibration parameters with varying scale factor

The accelerometer data of the CHAMP and GRACE satellites is processed, applying the same settings for the calibration parameters, which result in high-quality orbits [*Van Helleputte and Visser*, 2008]. These amount to an a priori standard deviation for the scale factors of 0.1 for S_X and 0.01 for S_Y and S_Z and for the bias 100 nm/s^2 for B_X and 1 nm/s^2 for B_Y and B_Z, with X, Y, Z the spacecraft reference frame. The a priori bias in each direction is found by summing the mean of the accelerometer data and the mean of the GHOST [*Montenbruck et al.*, 2005] modelled non-gravitational accelerations in the respective direction. The a priori scale factor is set to the advertised values, which are listed in Table 7.1 [*Bettadpur*, 2004; *Förste*, 2002]. The malfunctioning of the Z direction of the accelerometer on board of CHAMP is accounted for with modelled accelerations provided in the accelerometer data files [*Förste and Choi*, 2005]. The CoG offset is considered to be small and is not co-estimated in the orbit determination.

The 3D precision of the determined orbits with respect to external orbits determined without accelerometer data are below 4 cm for the GRACE satellites, and below 6 cm for CHAMP. The GRACE reference orbits are computed at JPL and are part of the L1B products, CHAMP reference orbits were determined at DEOS with the GEODYN software.

In Figure 7.2 the scale factor in X-direction and the bias parameters in X-, Y- and Z-direction (of the SRF) are presented for the GRACE B satellite. The scales in the other two directions are not included because these show little variation with respect to the a priori values, because of the applied constraints. The solid lines show the advertised values [*Bettadpur*, 2004], where it has to be mentioned that their period of applicability is stated to be limited until November 1st, 2003.

	CHAMP	GRACE A	GRACE B
S_X	0.833	0.96	0.96
S_Y	0.875	0.98	0.97
S_Z	1.0	0.94	0.92

Table 7.1 A priori scale factors

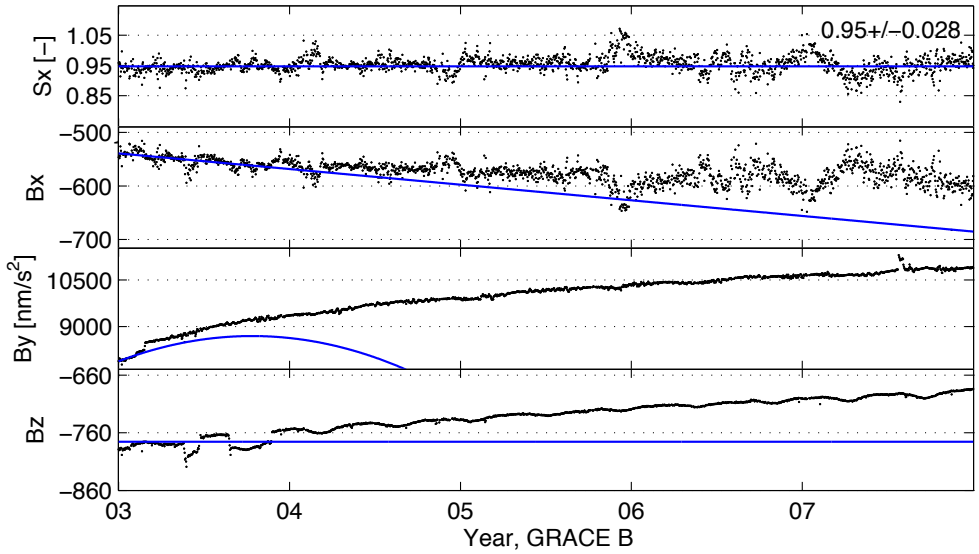

Figure 7.2 Scale (X-direction) and bias factors in the SRF frame for GRACE B, compared to advertised values (solid line)

However, it is clear that the user of the accelerometer data has to calibrate the accelerometer measurements. What is immediately apparent when inspecting the figure is the strong anti-correlation between scale and bias parameters. This makes it not straightforward to address instrument behavior. The standard deviation of the scale factor here amounts to 0.028, where a more constant value is expected. Apparently, this technique scales the non-gravitational force acting on the spacecraft rather than the instrument measurements.

7.2.2 A constant scale factor

Because of the strong correlation between scale and bias, and because a comparison of the data with non-gravitational force models (e.g. eclipse transitions) indicates that the scale is not expected to show large variations, another approach is proposed, where the scale factor in all three directions is kept constant. The scale factors are set equal to the advertised values, the result of an earlier calibration, which were listed in Table 7.1. The a priori standard deviation of the bias parameters is the same as described above, so the value in the X-direction is a hundred times larger than in the other two directions. The resulting bias values are now much smoother, illustrated in Figure 7.3 with the bias parameter in flight direction for the CHAMP and GRACE spacecraft. All sequences show a clear trend, and distinct jumps in the bias values are now visible. The outlier points may be attributed to maneuvers or data gaps in the GPS or attitude data. Identification of the features visible in this plot is subject of further research, but an initial comparison shows that it is likely that these can be associated with on-board software updates, switching between the redundant chains of on-board hardware, resets and on board temperature variations. In the case of the CHAMP time series, the jumps and irregularities were recognized by the CHAMP project team, who needed to include these in their bias function to get reasonable results (H. Lühr, GFZ, private communication) and events during the first two years of the mission are mentioned in [*Perosanz*, 2003]. The calibration parameters determined with this method are applied for the density and wind retrieval.

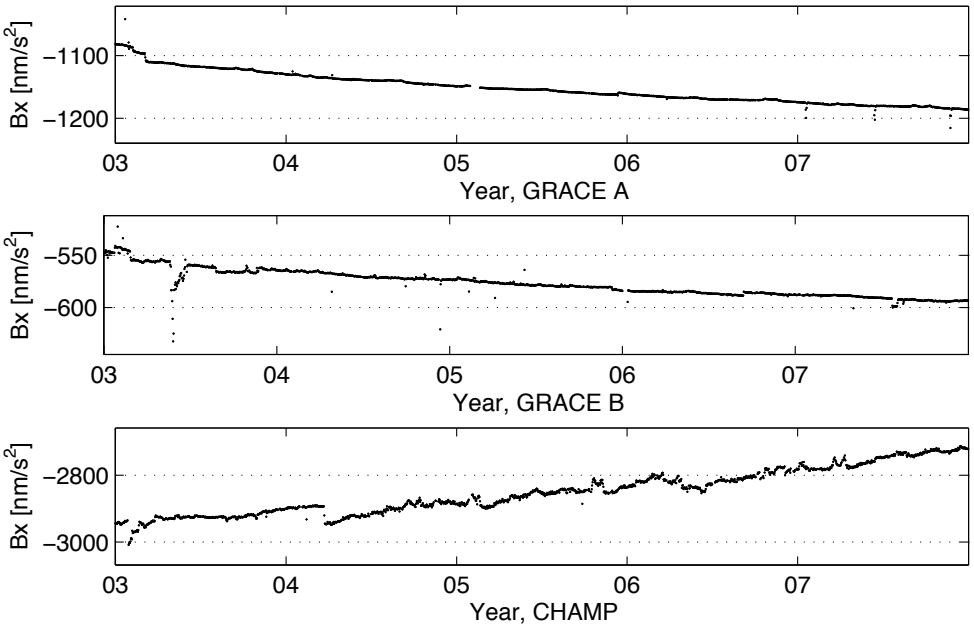

Figure 7.3 Bias in X-direction for GRACE and CHAMP, estimated with a constant scale factor

	(1)	(2)
S_X [-]	0.97 ± 0.024	0.95 ± 0.015
S_Y [-]	1.04 ± 0.138	1.05 ± 0.149
S_Z [-]	1.47 ± 1.07	1.0 ± 0.536
B_X [nm/s^2]	-569 ± 11	-559 ± 7
B_Y [nm/s^2]	9800 ± 1301	9904 ± 1408
B_Z [nm/s^2]	-1105 ± 927	-702 ± 462
rms 3D [cm]	5.81	9.39

Table 7.2 Unconstrained estimation, (1) with empirical accelerations, (2) without

7.2.3 Unconstrained estimation

The approach presented in Section 7.1.1 relies heavily on a priori bias and scale factors. Also, as seen above, better bias factors are obtained when keeping the scale factor constant. Therefore the question arose how stable an unconstrained estimation would be. If the accelerometer signal is strong, an unconstrained estimation without co-estimating empirical accelerations resulted in a stable scale factor in X-direction (along-track). When estimating empirical accelerations, results got worse. Also in the other two directions an unconstrained estimation did not lead to good scale factors, although the ones obtained by this approach can still serve as a first guess when no information is available. The results are listed in Table 7.2. Repeating this approach for the scale factor in X-direction for the whole period available shows that only in the case of a strong signal a good result is obtained, see Figure 7.4, where also the formal error of this component and the standard deviation of the accelerometer signal, a measure for its strength, are included.

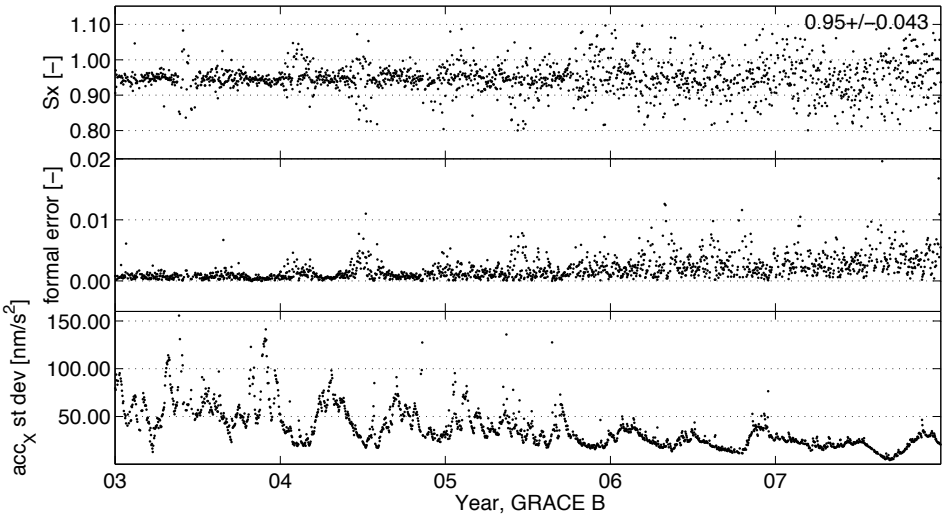

Figure 7.4 Scale factor in X direction, obtained with unconstrained estimation, and associated formal error and standard deviation of the accelerometer signal

7.2.4 Other tests

Variation of the orbit determination arc length

Three tests with a different arc length are conducted (with CHAMP data for the period of day of year 200-365 in 2003): an arc length of half a day, 2 days, and equal to an integer number of orbital revolutions, this number the closest to a full day. The last test resulted in no significant differences in estimated scale and bias parameters compared to the standard one day processing. Setting the arc equal to half a day or two days has a bigger impact on the calibration parameters. These are compared in Table 7.3 for the considered period. A shorter arc results in a larger deviation in X-direction, and a smaller deviation for a larger arc. In Y direction, the estimated scale factor deviates less from the a priori value for a short arc, where for a longer arc the estimated value deviates more from the a priori scale. Preliminary wind speed calculations suggested a lower cross-track scale factor than the currently applied values. This together with the (slightly) more stable estimation in X-direction pleads in favor of the longer arc estimation. Because the small impact in flight direction however, the remaining uncertainty in cross-track direction and the longer run-time, this approach is not applied to a larger data set.

	1/2 day	1 day	2 days
S_X [-]	0.85 ± 0.03	0.85 ± 0.02	0.85 ± 0.02
S_Y [-]	0.83 ± 0.02	0.78 ± 0.03	0.73 ± 0.05
S_Z [-]	1.0	1.0	1.0
B_X [nm/s^2]	-2979 ± 84	-2982 ± 75	-2980 ± 62
B_Y [nm/s^2]	239 ± 18	225 ± 18	208 ± 20
B_Z [nm/s^2]	9 ± 5	7 ± 5	4 ± 4

Table 7.3 Calibration parameters for varying orbit arc lengths

		mean [nm/s^2]	stand deviation [nm/s^2]
CHAMP	along-track	0.06 ± 0.1	10.9± 2.4
	cross-track	0.35 ± 0.6	28.0 ± 2.3
GRACE A	along-track	0.04 ± 0	4.4± 1.4
	cross-track	-1.04 ± 0.2	7.3 ± 1.5

Table 7.4 Variation of the estimated empirical accelerations

	CHAMP	GRACE A
S_X [-]	0.84 ± 0.03	096 ± 0.015
S_Y [-]	0.52 ± 0.19	0.95 ± 0.093
S_Z [-]	1.05 ± 0.38	0.95 ± 0.047
B_X [nm/s^2]	-2964 ± 95	-1113 ± 22
B_Y [nm/s^2]	135 ± 68	26948 ± 2644
B_Z [nm/s^2]	11 ± 61	-504 ± 26

Table 7.5 Calibration parameters for CHAMP and GRACE without estimating empirical accelerations

Influence of the estimation of empirical accelerations

In the standard processing, empirical accelerations are still estimated to account for deficiencies in the gravitational force models and in the case of CHAMP to account for accelerations due to maneuver events, which are not included in the accelerometer data (whereas these are present in the GRACE accelerometer data). Because drag and solar radiation pressure models imply a higher amount of uncertainty compared to the direct measurements of them with an accelerometer, the a priori standard deviation of the along-track empirical accelerations is reduced to a value of 10 nm/s^2, compared to about 30 nm/s^2 in a standard reduced dynamic orbit determination. As a result, the remaining estimated empirical accelerations in along-track direction are small, where in cross-track direction their pattern remains largely unaffected (comparing the case with and without applied accelerometer data). However, the estimated empirical accelerations do not show a significant mean value, which indicates that their estimation does not affect the estimation of the accelerometer bias calibration factor. Table 7.4 summarizes the mean and standard deviation of the remaining empirical accelerations for CHAMP and GRACE A (for the year 2003), where the difference in magnitude of the empirical accelerations is clearly visible.

A test is done without estimating empirical accelerations, for CHAMP and GRACE A in the year 2003, where only the initial state vector and bias and scale factors in three directions are estimated. The resulting calibration parameters are presented in Table 7.5. The values in X-direction show little variation compared to the case including empirical accelerations, where the parameters in Y- and Z-direction show a larger variation, and in the case of CHAMP this variation becomes high. The resulting orbit precision with respect to reference orbits now amount to about 10 cm for GRACE orbits and around 30 cm for CHAMP orbits. All this supports the difference in magnitude of the remaining empirical accelerations presented in Table 7.4, and consequently the fact that maneuvers, which occur frequently, are not included in the CHAMP accelerometer data.

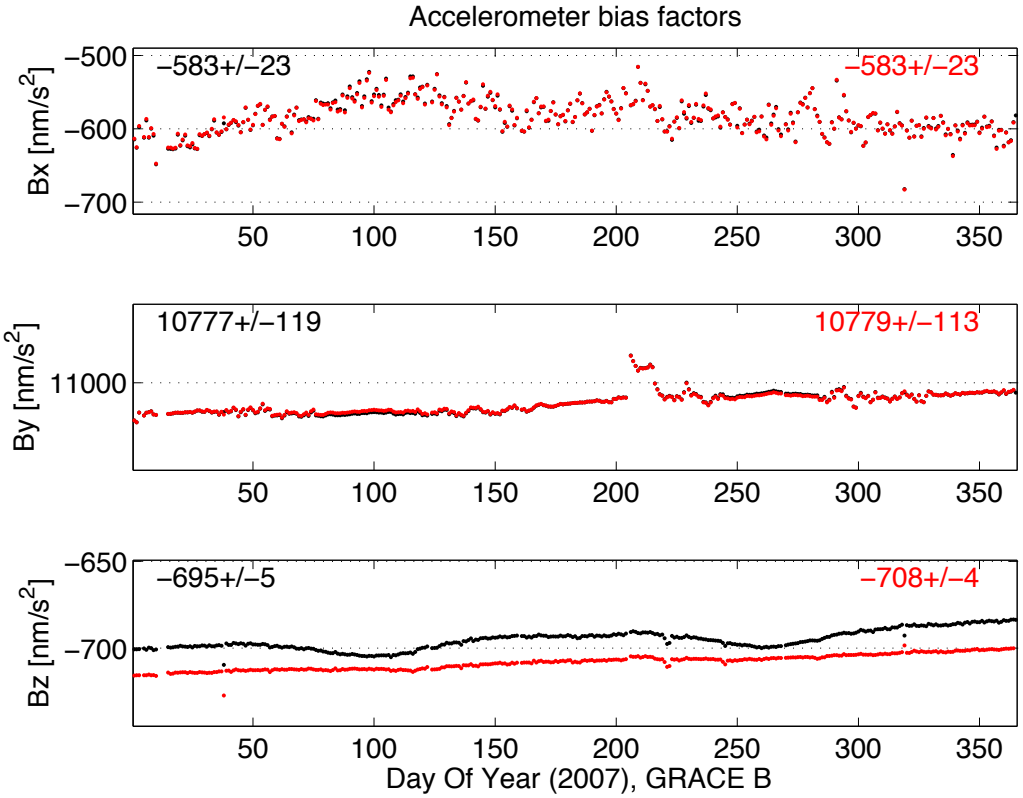

Figure 7.5 A priori bias factor obtained with different a priori models, red including albedo radiation, black only drag and solar radiation pressure

Improved a priori force models

The non-gravitational force models, implemented in the GHOST software and applied to determine an a priori bias factor, as described in Section 7.1.1, only consist of drag and direct solar radiation. Because in radial direction (instrument Z-axis) the bias factor is tightly constrained to its a priori value, the calibration is repeated for a selected period for GRACE B with an a priori model including albedo radiation. The results are presented in Figure 7.5 and the effect in radial direction is now visible, however there is (almost) no effect on the bias in the other two directions. Therefore all the data available is not reprocessed in this way.

7.3 Multi-satellite calibration

The Filter for Relative Navigation of Satellites [*Kroes et al.*, 2005] is a tool for the relative navigation of formation flying satellites with a smoothed Kalman filter resolving the double difference carrier phase ambiguities, resulting in a overall 1-dimensional relative position precision under the 1 mm level. The filter processes single difference GRACE GPS pseudorange and phase observations and uses (pseudo) relative spacecraft dynamics to propagate the relative states over the observation epochs. Here, no non-gravitational force models are applied. All differential non-gravitational accelerations are then supposed to be absorbed by the estimated empirical accelerations, which are estimated every 10 seconds and propagated over time using a Gauss-Markov process model with an autocorrelation time of 600 s. The analysis presented here focuses on the along-track ac-

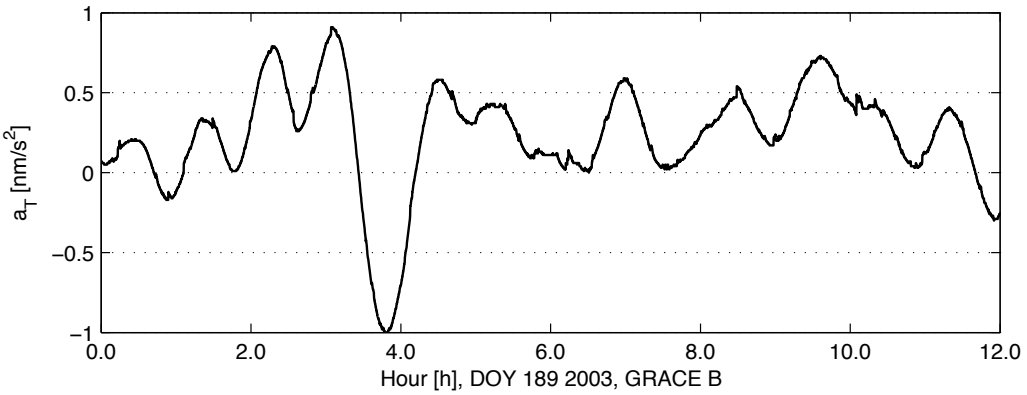

Figure 7.6 Along-track differential empirical accelerations, reference case

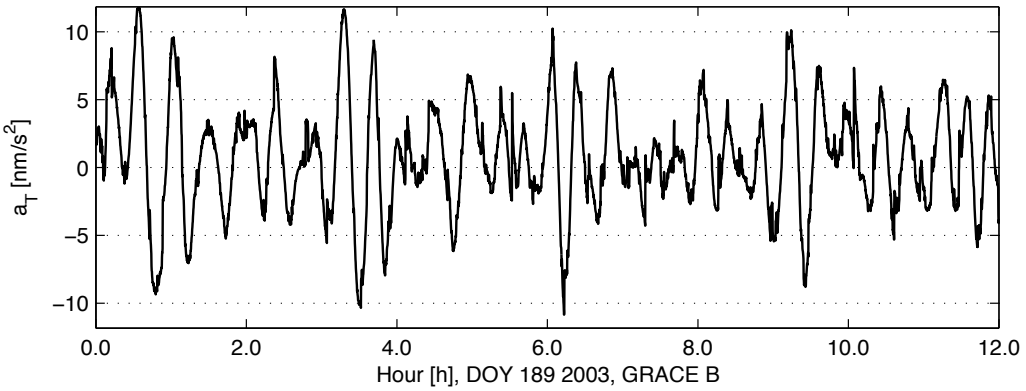

Figure 7.7 Along-track differential empirical accelerations, no non-gravitational force modelling

celerations alone, as these are the best determined. The radial accelerations are constrained to zero in the filter, and the cross-track accelerations are less observable.

Figure 7.6 shows the along-track empirical accelerations when non-gravitational force models are still applied, as a reference. It is clearly visible that the estimated differential accelerations are very small. The fit of the relative position with respect to the KBR data is 0.90 mm.

In Figure 7.7 the along-track accelerations are presented when no non-gravitational force models are applied. Now the a priori and steady state standard deviation are increased, to account for the anticipated larger deficiencies due to the not modelled non-gravitaitonal forces. The resulting empirical accelerations are larger in amplitude than in the reference case, and the frequency is also higher. The fit with respect the KBR data is a bit worse, around 1.6 mm.

When comparing them with respect to the difference of the accelerometer measurements of GRACE B minus the measurements of GRACE A (in the X-direction of the instrument frame) the agreement is quite low, see Figure 7.8. Here the mean value of the differential acceleration measurements is subtracted to facilitate comparison. The empirical accelerations have a clear sinusoidal pattern, while the differential accelerometer measurements show a different pattern. Also spikes are present in the latter, which are contributed to eclipse transitions, and these short term variations are not caught at all by the empirical accelerations. This is confirmed when zooming in to a timeframe of an hour, see Figure 7.9.

When looking at the spectrum of both sequences in Figure 7.10, the difference

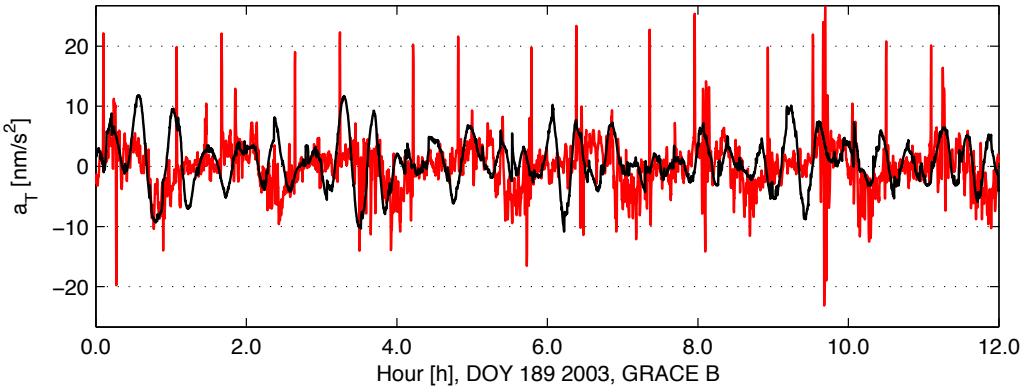

Figure 7.8 Along-track differential empirical accelerations (black) and differential accelerometer measurements (red)

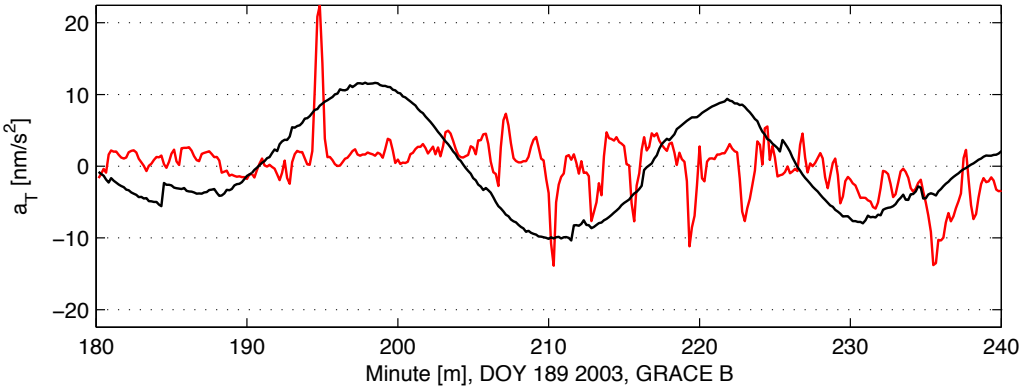

Figure 7.9 Along-track differential empirical accelerations (black) and differential accelerometer measurements (red)

between both is clear. The differential empirical accelerations still have a once per revolution and 2 per revolution peak, agreeing with the sinusoidal pattern visible in the above figures, while the differential accelerometer measurements have peaks at higher frequencies, around 10^{-3} Hz.

As a final test, the autocorrelation time is decreased to 10 s to see whether this has an influence on the differential empirical accelerations. As Figure 7.11 reveals, this is not the case. The same pattern as in Figure 7.7 is visible, so in the case of relative navigation the autocorrelation time has no big influence on the estimated empirical accelerations.

The differential empirical accelerations estimated by a relative filter can not be applied for the calibration of differential accelerometer measurements. Apparently the empirical accelerations do not represent true differential non-gravitational forces and reflect more their stochastic properties of a means for the filter to converge more easily.

Although the above shows that this technique doesn't lead to a useful calibration, it has to be mentioned that the empirical accelerations are estimated along the orbit, while the accelerometer measurements are taken in the instrument frame, where the X-axis is not aligned perfectly with the along-track direction. Because the deviation is small for the GRACE satellites, not much benefit is expected from aligning the differential accelerometer measurements to the along-track frame. Furthermore, it can be checked whether low-pass filtered differential accelerometer measurements agree better with the estimated empirical accelera-

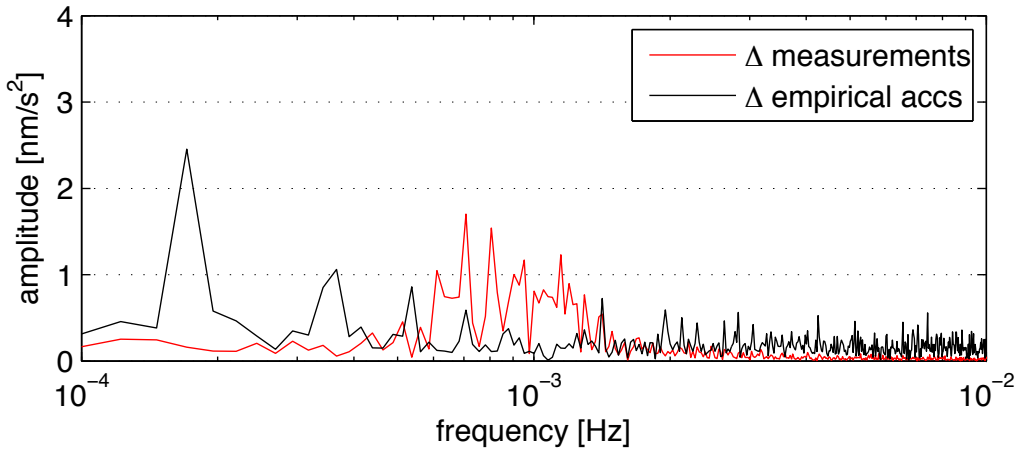

Figure 7.10 Spectral analysis of the along-track differential empirical accelerations (black) and differential accelerometer measurements (red)

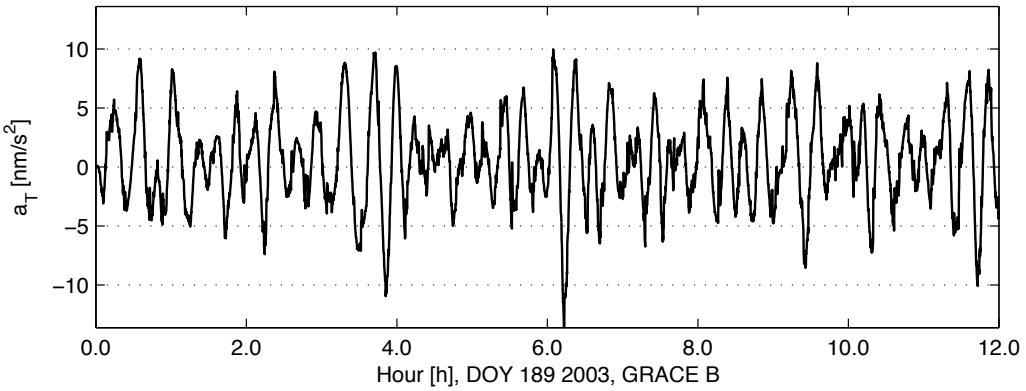

Figure 7.11 Along-track differential empirical accelerations, 10 s autocorrelation time

tions, as these don't show high frequency variations. Again no big improvement is expected, as the patterns of both sequences are clearly different.

The conclusion is that the multi-satellite calibration by differential empirical accelerations proves unreliable.

7.4 Implementation of calibration in the data processing

Since the calibration is based upon orbit determination runs that use GPS data over daily arcs, the result is a time series of daily bias and scale factor values. Over the course of the project, several versions of the calibration data have become available, and these were post-processed in different ways, to get the most out of the data. These have been given identifiers, such as R02, R03, etc., so that they can be distinguished in the project's database. Table 7.6 gives a description of the evolution each of these calibration time series. Figure 7.12 gives a detailed view of two of the bias time series for CHAMP, with known satellite events and eclipse-free periods superimposed.

ID	Description
R01	First generation calibration time series, based on the nominal precise orbit determination configuration, and with estimation of both biases and scale factors - no longer used in the data processing.
R02	Second generation calibration time series - with constant scale factor assumed, and radial accelerations from models applied for CHAMP to replace the malfunctioning accelerometer component for consistent orbital dynamics.
R03	Derived from R02, but with Y-axis calibration biases derived from non-gravitational force models, where density estimates from the X-axis data are used to model the Y-axis aerodynamic acceleration. The X-axis and Z-axis calibration values are copied from the R02 series. This approach resulted in much improved crosswind products from CHAMP data.
R02B	Derived from R02, with a smoothing and editing algorithm applied. These values are applied using piecewise-linear interpolation, instead of the piecewise-constant method of the earlier calibration data.
R03B	Derived from R02B, but with Y-axis calibration biases again derived off-line from non-gravitational force models. Subsequently, the smoothing and editing is applied again. These biases are also interpolated using a piecewise-linear variation between the daily values.

Table 7.6 Descriptions of the identifiers used for the calibration time series used in the accelerometer data processing.

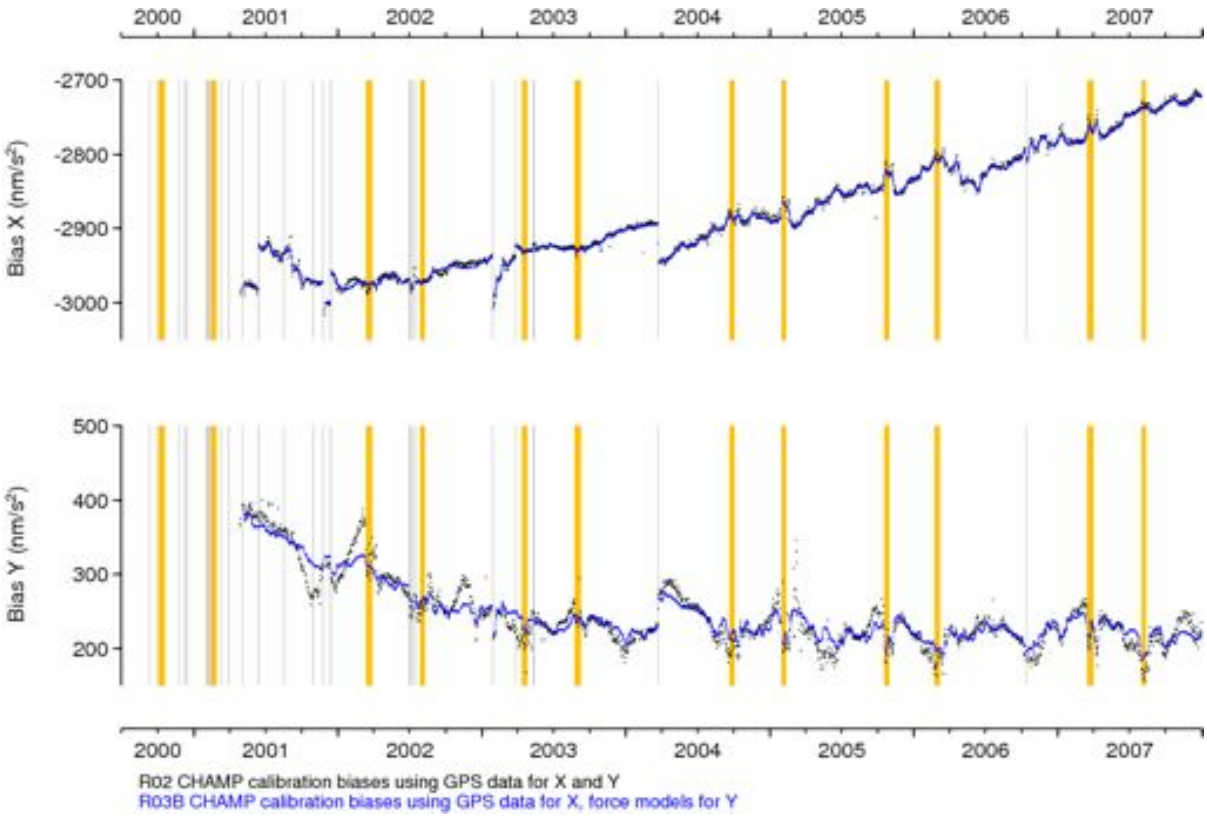

Figure 7.12 Comparison of calibration time series. Vertical grey lines indicate known satellite events, such as resets, software updates and switches of redundant electronics. The yellow/orange areas indicate periods without eclipses.

Chapter 8
Density and wind determination processing

8.1 Introduction

In the density and wind determination processing, the pre-processed data products of Chapter 4 are used and combined with inputs from Chapter 7 (calibration) and Chapters 5 and 6 (force modelling) in order to derive density and wind data from the accelerometer observations.

This chapter will start with an overview flowchart, which outlines the complete data processing chain from preprocessed products to accelerometer-derived density and wind products. In the remainder of the chapter, all the intermediate and end products, and the algorithms to generate them, are described in detail.

8.2 Processing flow chart

A flow chart for the data processing is shown in Figure 8.1. The figure consists of two sections, one resulting in the DENS_DIRECT products and another, omitting redundant detail, for the DENSWIND_ITERATIVE products. The products that resulted from the preprocessing of Chapter 4 are shown in a darker shade at the top of the flow chart. In the first step of the processing, these products are used as inputs for the computation of radiation pressure forces (RADPRESS) and the relative velocity of the atmosphere with respect to the satellite due to its orbit velocity and the Earth's corotation (WINDMODEL_SC_ORBITCOROTATION). Empirical model results for density (the DENSMODEL products) and winds (WINDMODEL_LOCAL and WINDMODEL_SC) are computed as well at this stage. Their results can both be used for comparisons with the accelerometer-derived results (presented in Chapter 9), but they are also used in the processing itself. For instance, the along-track component of HWM-93 and HWM07 winds can optionally be used in the density derivation, and the temperature and composition from NRLMSISE-00 are required for aerodynamic model calculations (see Section 6.7.1).

In a separate chain of processing, the accelerometer data are calibrated, by using the scale factor and bias results of Chapter 7. The computed radiation pressure accelerations can then be subtracted from the resulting calibrated accelerations, with the intention of leaving only the aerodynamic accelerations in the ACCEL_NORADPRESS products.

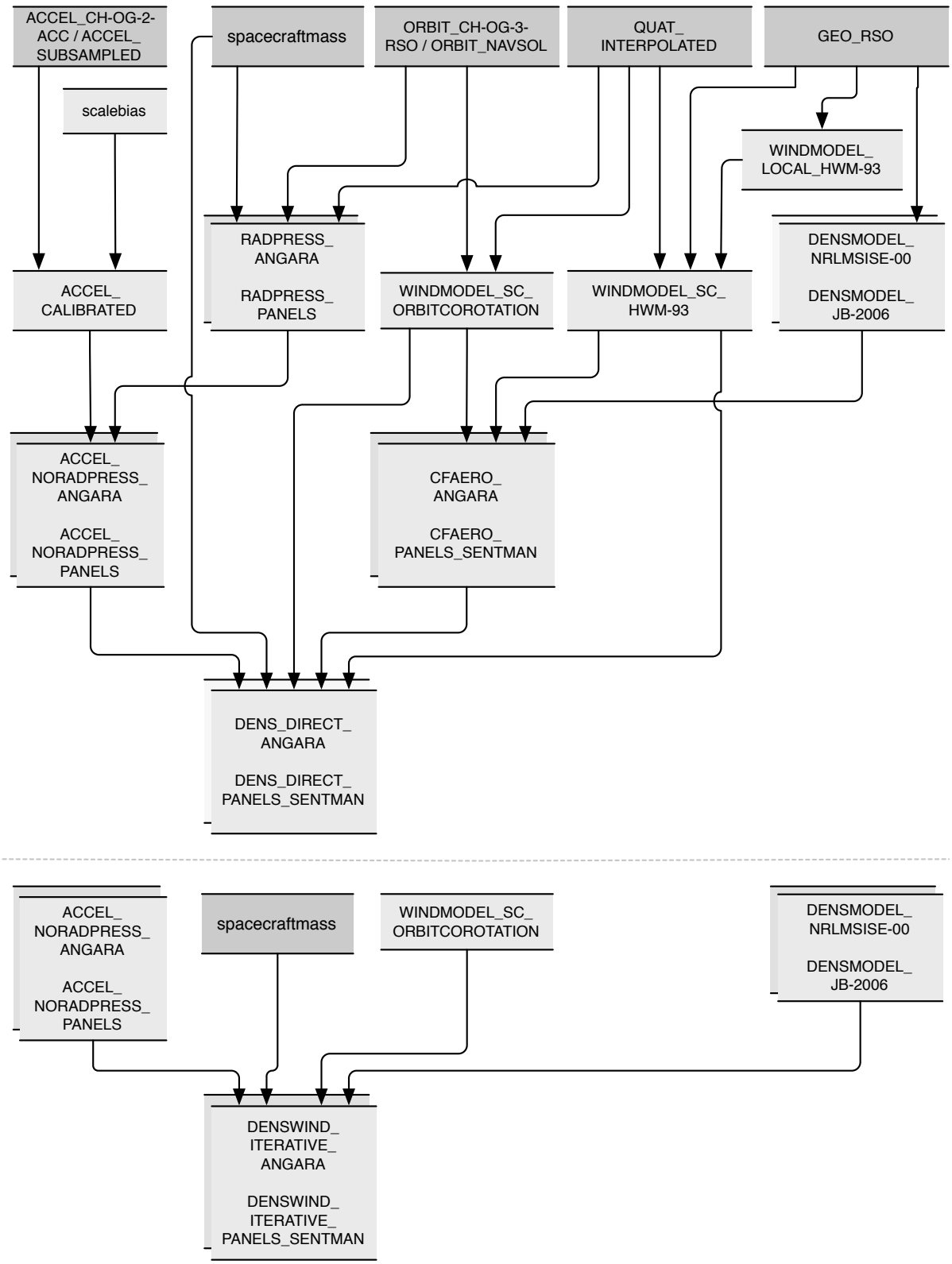

Figure 8.1 Flow charts of the data products used to produce density and wind products from the preprocessed products. Top: full flowchart for the DENS_DIRECT products. Bottom: Simplified flowchart for the DENSWIND_ITERATIVE products.

The distinction between the DENS_DIRECT and DENSWIND_ITERATIVE methods comes into play at this point. In the DENS_DIRECT method, there are two approaches for approximating the wind direction in the aerodynamic calculations. Either they are assumed to be only caused by the orbital velocity and atmospheric corotation, or the HWM-93 wind results are added to these effects as well. For both cases, the aerodynamic force coefficients times area $(\vec{C}_F A)_s$ are determined and stored in the CFAERO products, which are used to solve the drag equation directly.

For the DENSWIND_ITERATIVE products, the density and wind in the Y-direction of the body-fixed frame are estimated together. Since this wind direction and velocity have an influence on the value of $(\vec{C}_F A)_s$, they are calculated iteratively until the aerodynamic acceleration direction in the body-fixed X-Y plane matches the direction of the aerodynamic acceleration derived from the accelerometer. This will be further explained in later sections.

8.3 Acceleration products

The acceleration products form the core of the data processing. The measured and calibrated accelerations are of course the primary data source. Several types of modelled accelerations are used to be able to separate non-gravitational force contributions. Finally, simulated accelerations are constructed from the non-gravitational force models, in order to be able to compare the data and models in terms of accelerations.

8.3.1 Calibrated accelerations: ACCEL_CALIBRATED

The calibrated non gravitational accelerations $\ddot{\vec{r}}_{\text{cal}}$ are determined by applying the calibration factors from Chapter 7 to the ACCEL_CH-OG-2-ACC for CHAMP and to ACCEL_SUBSAMPLED for GRACE. The fields of this product are:

1. Linear acceleration in S/C X-direction (m/s^2)
2. Linear acceleration in S/C Y-direction (m/s^2)
3. Linear acceleration in S/C Z-direction (m/s^2)

Figures 8.2 and 8.3 show a year's worth of the calibrated accelerometer data for CHAMP and GRACE, respectively. The medium-to-low solar activity year 2005 was chosen to illustrate several features in the data that come in to play when deriving densities and winds. The most immediately noticable features are the long stretched curves, which are due to the acceleration jumps at eclipses, for which the geometry changes over the year.

The aerodynamic acceleration variations are visible as a vertical stripy pattern, which is most pronounced in the X-direction. In fact, the radiation pressure pattern is almost completely obscured for the CHAMP X-direction plot. A 'noisy' behaviour around the poles (at 90 and 270 degrees argument of latitude) is also visible, which is due to fast changes in the aerodynamic accelerations when the satellite crosses the auroral ovals. The GRACE data also exhibits many gray patches, which are at times when there is no data. Most of this data has been removed during the pre-processing, in the ACCEL_EDITED step (see Section 4.7.3), because of the proximity of manoeuvres. Other short anomalies, which are not always visible in the Level 1B-derived GRACE data, are believed to be due to

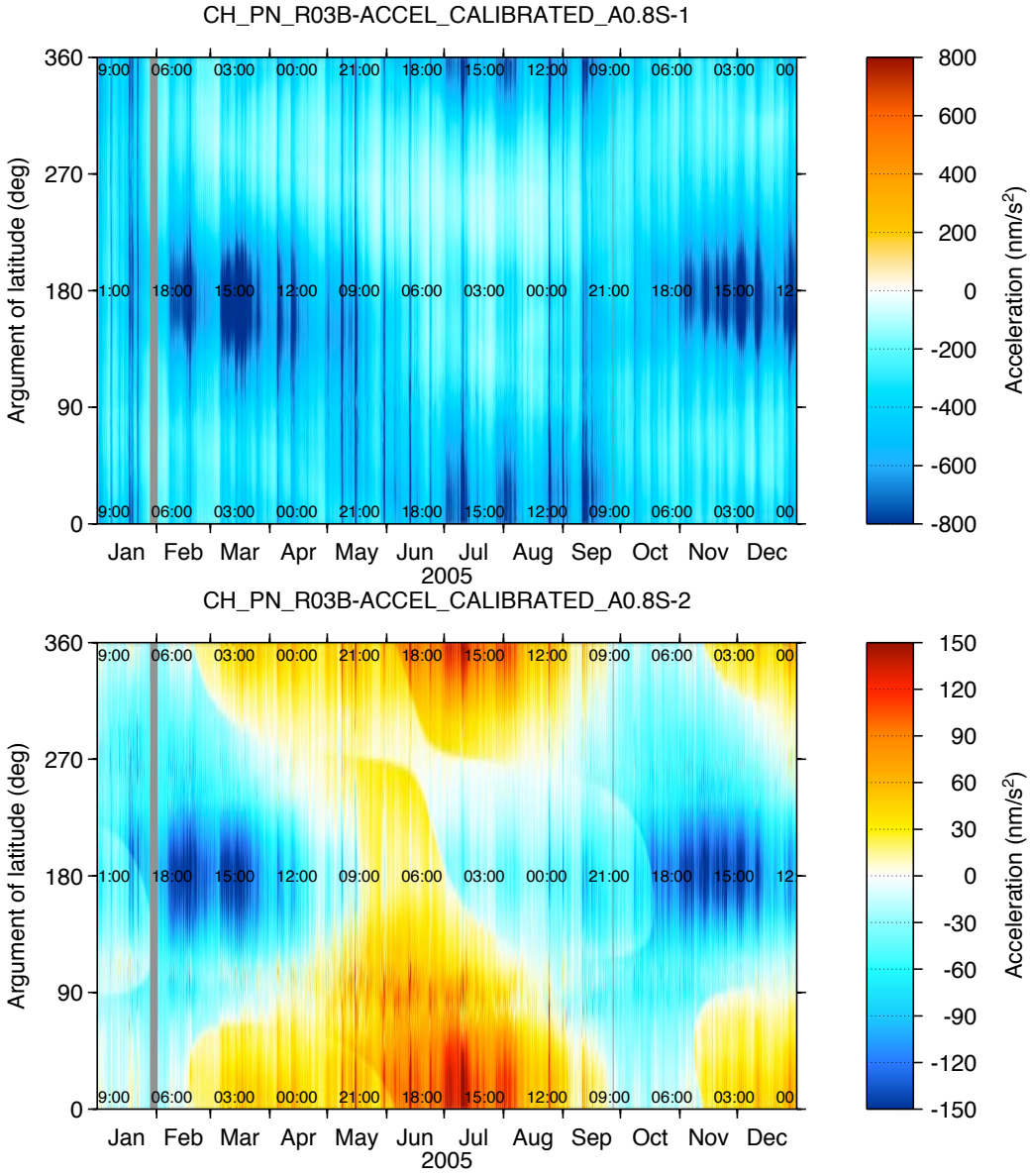

Figure 8.2 Calibrated acceleration measurements for CHAMP in the body-fixed X- (left) and Y-direction (right).

'twangs' of the satellite's thermal isolation, and switches in the circuits of on-board magnetic torquers and heaters [*Flury et al.*, 2008]. The GRACE-A satellite switched its orientation on December 11, 2005, which causes the accelerations in the X- and Y-directions to be inverted after this date.

8.3.2 Radiation pressure model output: RADPRESS_ANGARA and RADPRESS_PANELS

The RADPRESS data are computed using the equations for solar and terrestrial radiation pressure described in Chapter 5, making use of the ORBIT and QUAT_INTERPOLATED data. The acceleration vectors $\ddot{\vec{r}}_{\mathrm{srp}}$, $\ddot{\vec{r}}_{\mathrm{alb}}$ and $\ddot{\vec{r}}_{\mathrm{IR}}$ for the contributions by sunlight, Earth albedo and Earth infrared radiation, respectively, are available separately in the spacecraft body-fixed frame.

1. Solar radiation pressure acceleration along the S/C X-axis ($\mathrm{m/s^2}$)

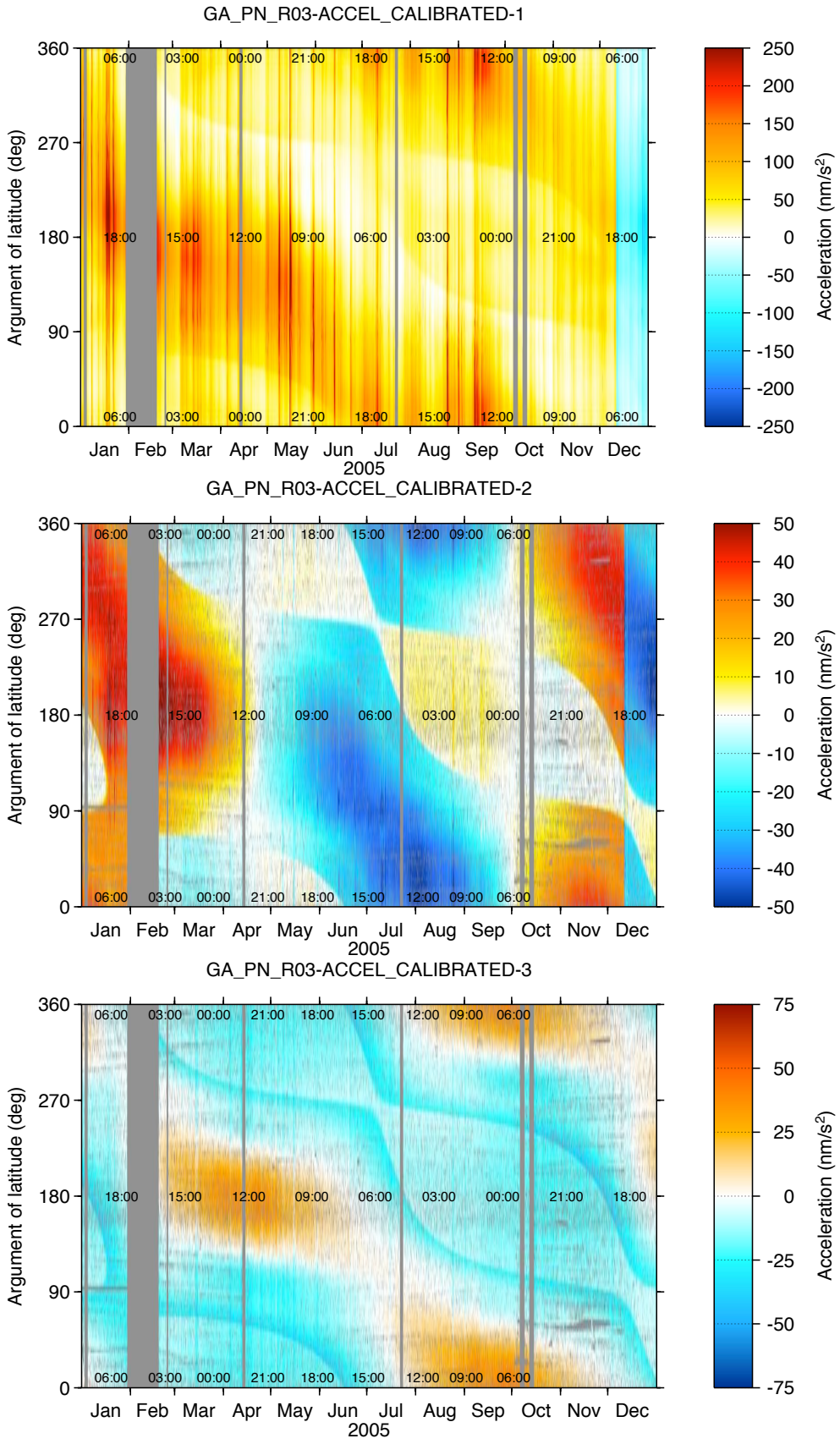

Figure 8.3 Calibrated acceleration measurements for GRACE-A in the body-fixed X- (top), Y- (centre) and Z-direction (bottom).

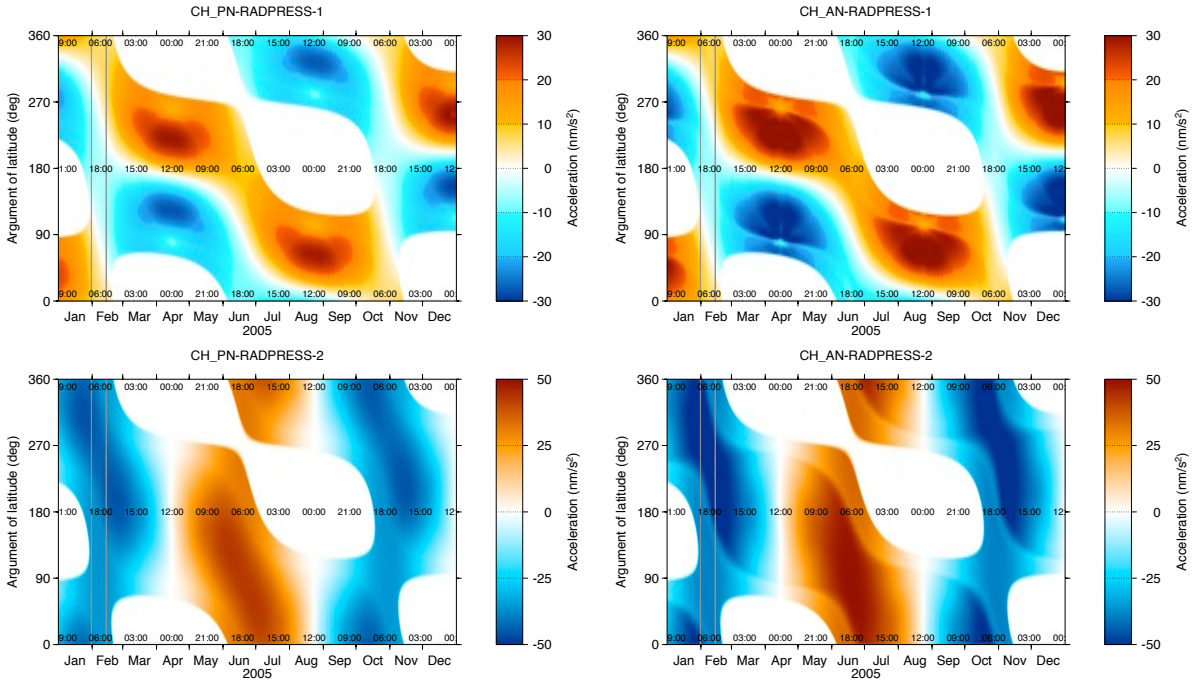

Figure 8.4 Modelled solar radiation pressure accelerations for CHAMP using the panel model (left) and the ANGARA model (right), for the X-direction (top) and Y-direction (bottom).

2. Solar radiation pressure acceleration along the S/C Y-axis (m/s^2)
3. Solar radiation pressure acceleration along the S/C Z-axis (m/s^2)
4. Earth albedo radiation pressure acceleration along the S/C X-axis (m/s^2)
5. Earth albedo radiation pressure acceleration along the S/C Y-axis (m/s^2)
6. Earth albedo radiation pressure acceleration along the S/C Z-axis (m/s^2)
7. Earth infrared radiation pressure acceleration along the S/C X-axis (m/s^2)
8. Earth infrared radiation pressure acceleration along the S/C Y-axis (m/s^2)
9. Earth infrared radiation pressure acceleration along the S/C Z-axis (m/s^2)

The modelled solar radiation pressure accelerations for CHAMP and GRACE are shown in Figures 8.4, 8.5, respectively. Earth albedo and infrared radiation pressure for GRACE only is shown in a similar manner in Figure 8.6. The distinctive eclipse patterns are visible for the solar radiation pressure accelerations. The albedo and infrared accelerations are only displayed for GRACE's Z-direction, as they can not be compared with real data for CHAMP, due to the malfunction of that axis. The albedo and infrared radiation pressure accelerations in the spacecraft X- and Y-directions have a maximum magnitude below 1 nm/s^2, so they can safely be neglected for the purposes of this project. In the Z-direction, these Earth radiation pressure accelerations show a seasonal dependence, based on the monthly maps of ERBE data. The infrared radiation pressure has a mimimum in June and July, when the satellite flies over Antarctica, at 270 degrees argument of latitude.

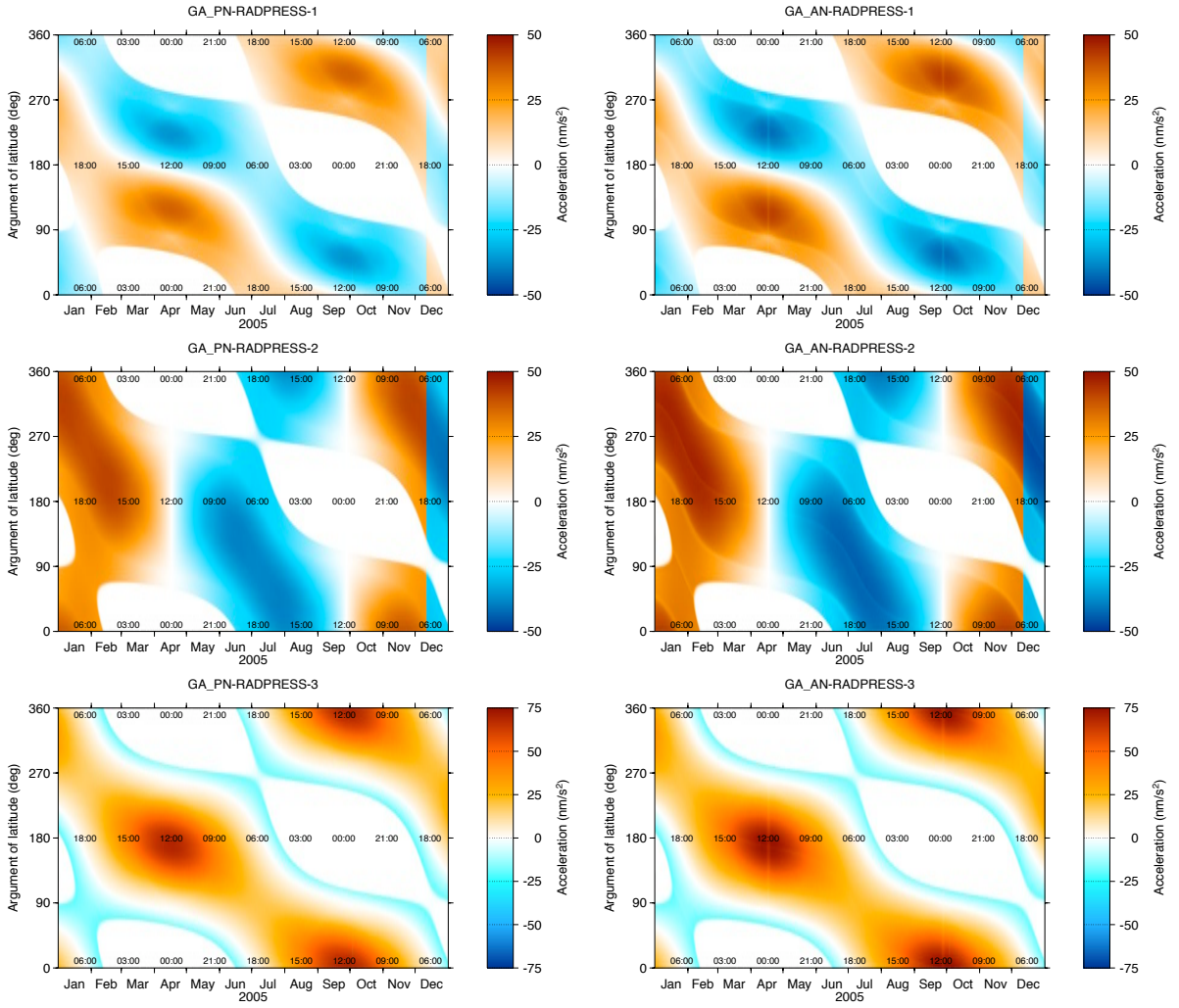

Figure 8.5 Modelled solar radiation pressure accelerations for GRACE-A in the X-, Y- and Z-directions (top to bottom), using the panel model (left) and ANGARA model (right).

8.3.3 Accelerations with radiation pressure removed: ACCEL_NORADPRESS_ANGARA and ACCEL_NORADPRESS_PANELS

THE ACCEL_NORADPRESS products are intended to represent the accelerometer data with radiation pressure contributions removed. The three vectors of the RADPRESS products are subtracted from the ACCEL_CALIBRATED products $\ddot{\vec{r}}_{\mathrm{cal}}$, resulting in the acceleration due to aerodynamics $\ddot{\vec{r}}_{\mathrm{a}}$.

$$\ddot{\vec{r}}_{\mathrm{a}} = \ddot{\vec{r}}_{\mathrm{cal}} - \ddot{\vec{r}}_{\mathrm{srp}} - \ddot{\vec{r}}_{\mathrm{alb}} - \ddot{\vec{r}}_{\mathrm{IR}} \tag{8.1}$$

Note that the assumption is made in this equation that there are no calibration errors and that other acceleration sources in the calibrated accelerometer data are negligible, compared to the aerodynamic acceleration. The following data fields are available in this product:

1. Linear acceleration in S/C X-direction ($\mathrm{m/s^2}$)
2. Linear acceleration in S/C Y-direction ($\mathrm{m/s^2}$)
3. Linear acceleration in S/C Z-direction ($\mathrm{m/s^2}$)

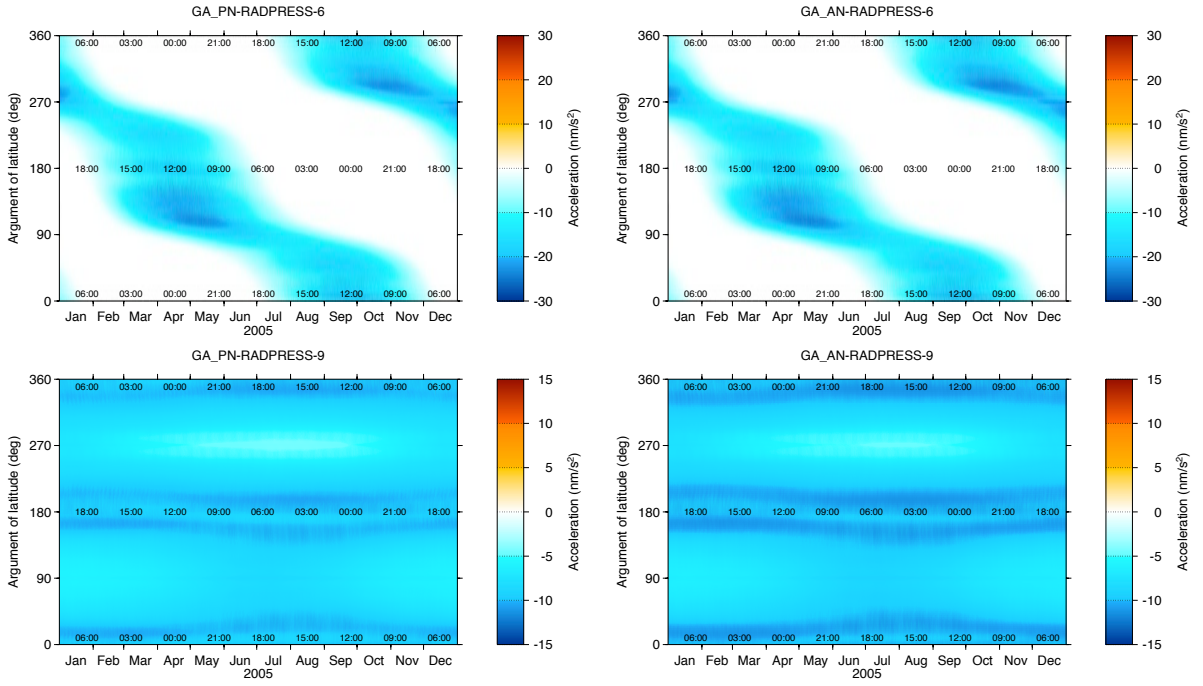

Figure 8.6 Modelled Earth albedo (top) and Earth IR (bottom) radiation pressure accelerations for GRACE-A using the panel model (left) and ANGARA model (right).

Figures 8.7 and 8.8 show the resulting accelerations for the CHAMP and GRACE-A satellites. They represent the difference between Figures 8.2 and 8.3 on the one hand and 8.4 and 8.5. The Z-components are again not shown for CHAMP, because this component does not function properly. Note that the X-component looks very similar to Figure 8.2, due to the small radiation pressure magnitude compared to the aerodynamic acceleration magnitude. For GRACE, the eclipse pattern seems nicely removed from the X-direction, but in the Y- and Z-directions, the edges of the eclipse regions clearly stand out, hinting at an uncertainty of 5-10 nm/s^2 in the radiation pressure modelling, and higher values during the semi-shadow transitions. For CHAMP, such features can not be seen in the X- and Y-axis data on this colour scale, due to the higher magnitude of the drag acclerations.

8.3.4 Modelled aerodynamic accelerations: AERO_ANGARA_DIRECT, AERO_ANGARA_NRLMSISE-00, AERO_PANELS_SENTMAN_DIRECT and AERO_PANELS_SENTMAN_NRLMSISE-00

The AERO products consist of modelled aerodynamic accelerations. They are used to be able to compare force models and accelerometer measurements. The _DIRECT versions of these products are based on the density estimates from the along-track accelerometer axis. The X-component of this product are therefore exactly identical to the X-component of the ACCEL_NORADPRESS product, but the Y- and Z-components are dependent on the aerodynamic model. The NRLMSISE-00 versions use the densities from this empirical model, and are therefore a representation of the modelled accelerations as they would be used in

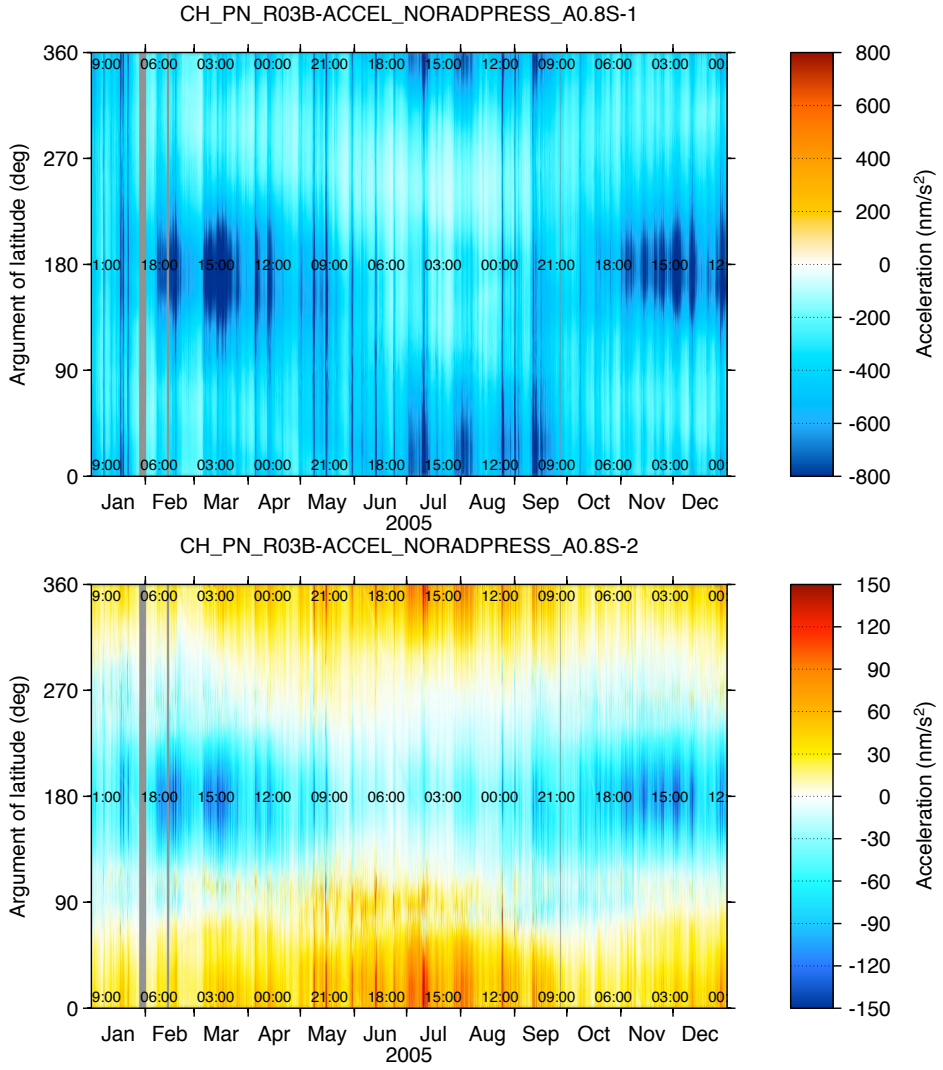

Figure 8.7 Calibrated acceleration measurements with radiation pressure model contributions removed for CHAMP in the body-fixed X- and Y-directions.

precise orbit determination of a satellite for which an accelerometer is not available. The data fields are as follows:

1. Linear acceleration in S/C X-direction (m/s^2)
2. Linear acceleration in S/C Y-direction (m/s^2)
3. Linear acceleration in S/C Z-direction (m/s^2)

Figure 8.9 shows the modelled aerodynamic accelerations for CHAMP, which can be compared with the measured accelerations in Figures 8.2 and 8.7.

8.3.5 Modelled non-gravitational accelerations: ACCEL_SIMULATED

Simulated accelerations are constructed by summing the RADPRESS and AERO products. Read the descriptions of those products for more details. For CHAMP, the Z-component of the ACCEL_SIMULATED_ANGARA_DIRECT version of this product is used in the accelerometer calibration, to replace the faulty output from the broken accelerometer Z-axis. The data fields are again as follows:

1. Linear acceleration in S/C X-direction (m/s^2)

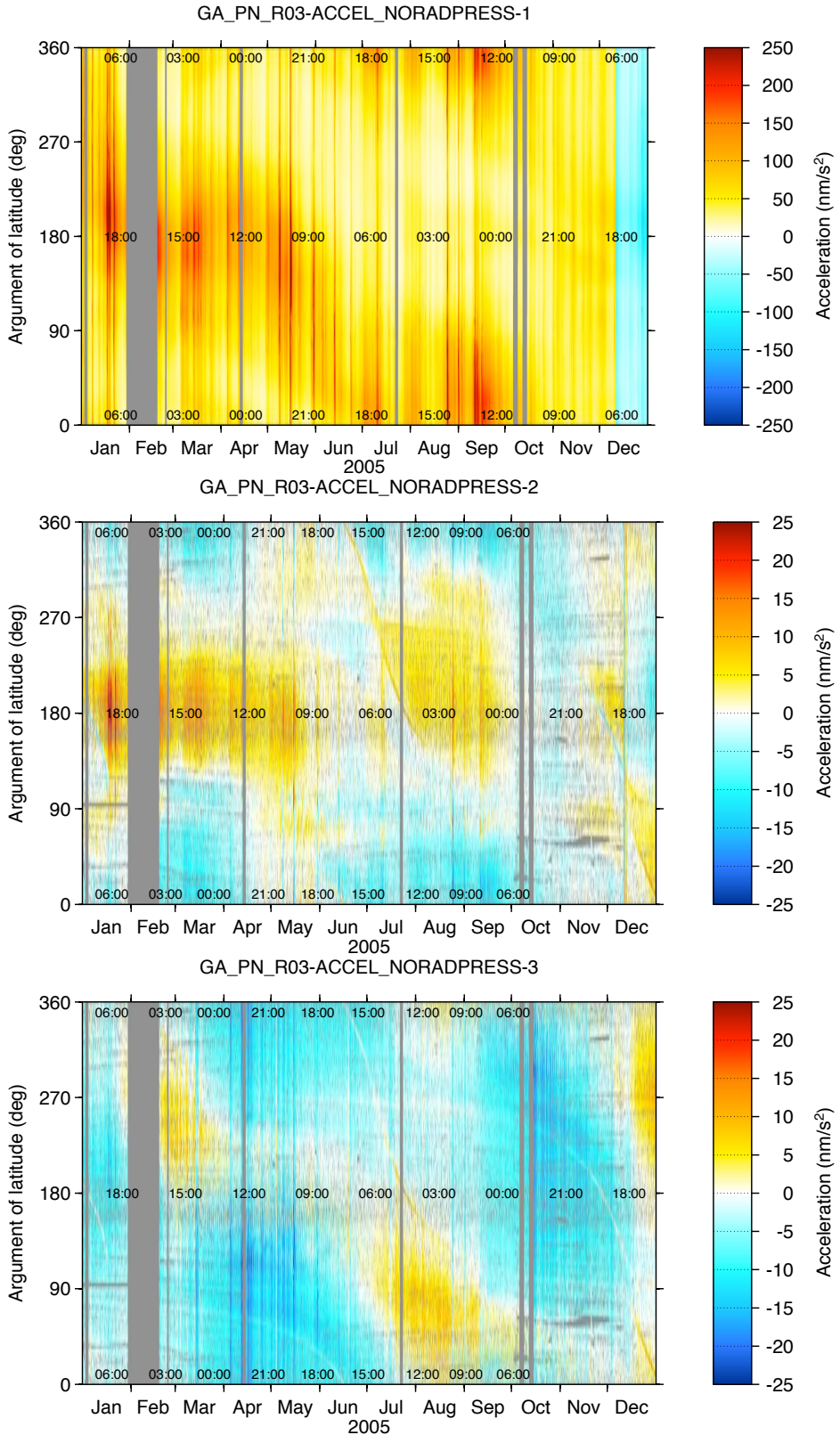

Figure 8.8 Calibrated acceleration measurements with radiation pressure model contributions removed for GRACE in the body-fixed X-, Y- and Z-directions.

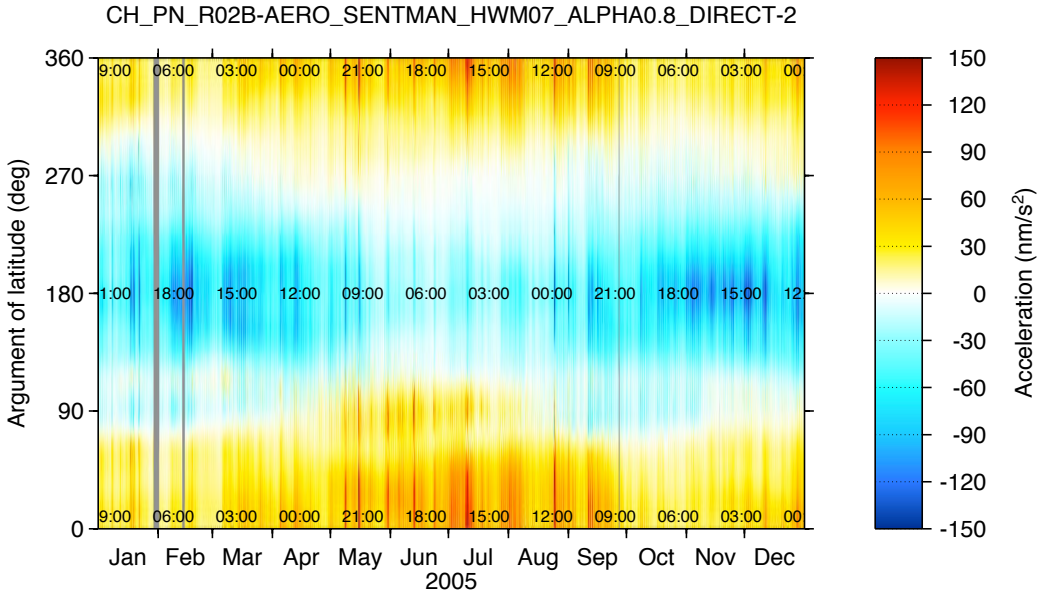

Figure 8.9 Modelled aerodynamic accelerations in the Y-direction, using the panel model with Sentman's equations and the density derived from the accelerometer X-component.

2. Linear acceleration in S/C Y-direction (m/s^2)
3. Linear acceleration in S/C Z-direction (m/s^2)

8.3.6 Aerodynamic force model coefficients: CFAERO

The aerodynamic force model coefficient products are used in the density estimation for the DENS_DIRECT products, described below. The data from these products can also be studied to get an idea of the differences between the various aerodynamic models (ANGARA, Sentman's theory for panels, etc.)

These products contain values of the vectors $(\vec{C}_F A)$, computed using the ANGARA and Sentman aerodynamic models, according to equation (6.55).

Two approaches are used for calculating the relative velocity that serves as an input to the aerodynamic model calculations. In the first one, HWM winds, from the WINDMODEL_SC_HWM-93 or WINDMODEL_SC_HWM07 products are included, by adding them to the contributions due to orbital velocity and atmospheric corotation, that were stored in the WINDMODEL_SC_ORBITCOROTATION product:

$$\vec{v}_r = \vec{w}_b^o + \vec{w}_b^c + \vec{w}_b^m \tag{8.2}$$

In the second approach, only the contributions due to the orbital velocity and atmospheric corotation are used.

$$\vec{v}_r = \vec{w}_b^o + \vec{w}_b^c \tag{8.3}$$

The following fields are available per record:

1. Aerodynamic force coefficient times area along the S/C X-axis (m^2)
2. Aerodynamic force coefficient times area along the S/C Y-axis (m^2)
3. Aerodynamic force coefficient times area along the S/C Z-axis (m^2)

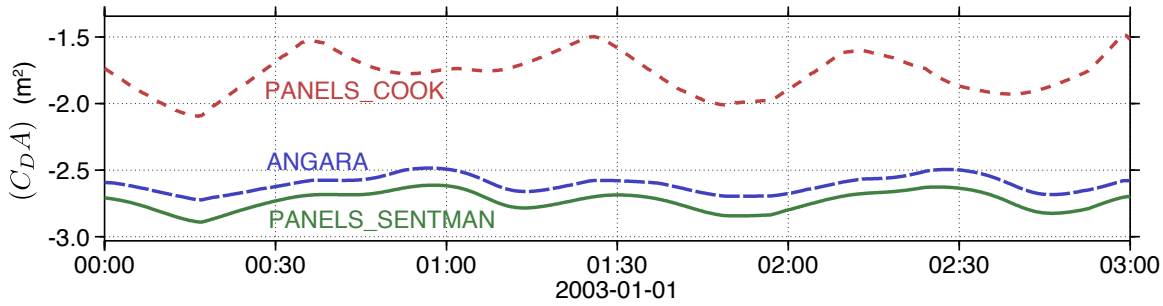

Figure 8.10 Drag component of modelled aerodynamic force coefficients for CHAMP in the S/C X-direction. The lift component is negligible in this direction.

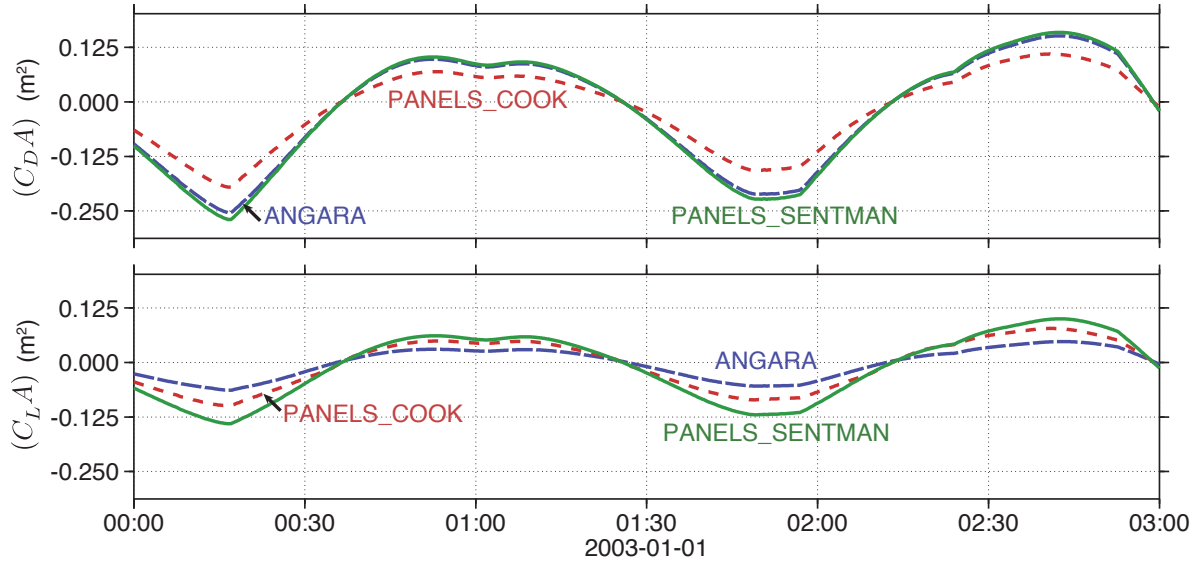

Figure 8.11 Drag (top) and lift (bottom) components of modelled aerodynamic force coefficients for CHAMP in the S/C Y-direction.

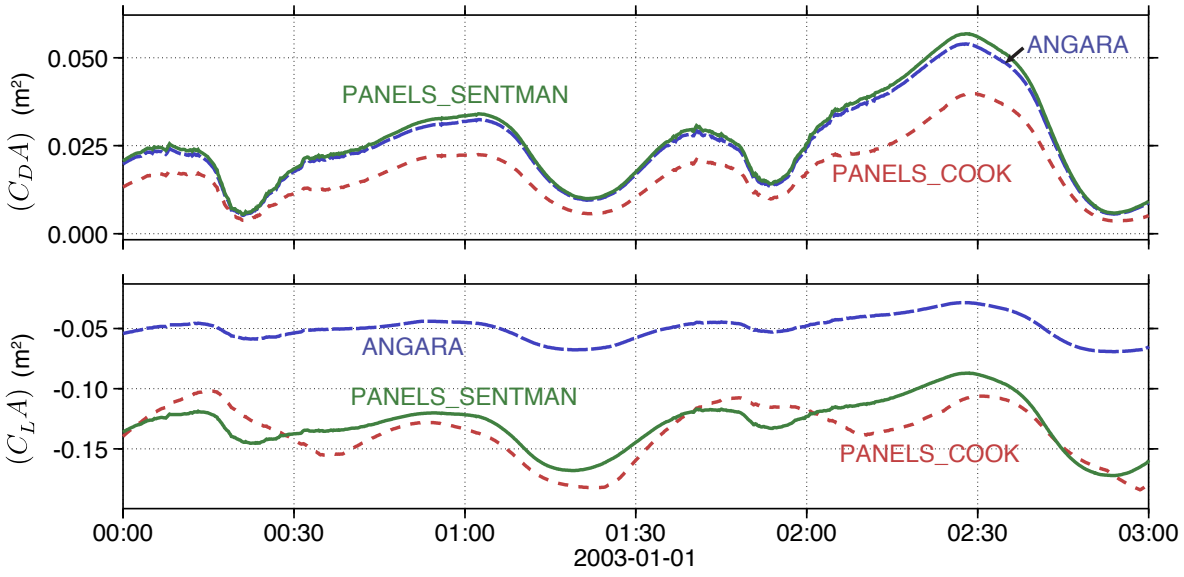

Figure 8.12 Drag (top) and lift (bottom) components of modelled aerodynamic force coefficients for CHAMP in the S/C Z-direction.

The aerodynamic force coefficient vectors (with subscript a for aerodynamics) can be decomposed in drag (subscript D) and lift and sideways force contributions (subscript L), according to

$$(\vec{C}_F A)_a = (\vec{C}_F A)_D + (\vec{C}_F A)_L \tag{8.4}$$

where drag is defined to be the component in the direction of the relative velocity $\vec{v}_r$ and lift is computed from (8.4).

Figures 8.10, 8.11 and 8.12 show these decomposed aerodynamic force coefficients in the S/C X-, Y- and Z-directions, respectively, for the ANGARA, panel/Sentman and panel/Cook aerodynamic models.

The X-component is the most important for density determination. The Cook method results in much smaller drag coefficients than the ANGARA and Sentman methods. It also exhibits a much larger variation. This can be explained by considering Figure 6.21 and taking into account that CHAMP's large solar panels, boom panels and bottom panel are oriented at an angle of attack between 80° and 100°. Sentman's theory results in much larger drag coefficients for that region, and with a smaller slope. The ANGARA results are slightly smaller, but otherwise very similar to the Sentman results. The lift and sideways forces of the panels generally result in less than 1% of the acceleration due to drag in the X-direction.

This is different in the Y- and Z-directions, where lift plus sideways forces and drag contributions are of the same order of magnitude. The Y-direction, shown in Figure 8.11, is of most importance to the wind determination. There is again a good agreement between the ANGARA and panel/Sentman models for the drag component, although for the lift component, the ANGARA result is noticeably smaller. The drag component in the Z-direction is very small, as it is proportional to the sine of the pitch angle. There is a considerable discrepancy between the lift plus sideways force components in this direction though, with the ANGARA model returning much smaller lift and sideways forces than the two panel models.

8.4 Accelerometer-derived density and wind products

A crucial problem in the derivation of density and wind from a satellite accelerometer is the fact that there are just three observations (accelerations in three directions) for four unknowns (density and wind speeds in three directions).

For near-circular orbits, wind velocities in the radial direction are small. Radiation pressure accelerations usually dominate this component, so its data is frequently ignored in density and wind studies. Since typical horizontal wind speeds of a few hundred m/s are also relatively small compared to the satellite orbital velocity of about 7700 m/s, the wind speed in the accelerometer component that is aligned with the velocity-direction can be neglected or modelled, in order to easily be able to derive density from that component. The DENS_DIRECT products allow a comparison between various choices for that approach.

However, for non-spherical satellites such as CHAMP and GRACE, the direction of the wind with respect to the spacecraft is of influence on the direction and magnitude of the aerodynamic accelerations. Ideally, one should therefore try to derive information on the wind speed and density in a combined approach. Such an approach is used in the DENSWIND_ITERATIVE products.

8.4.1 Accelerometer-derived densities using the direct algorithm: DENS_DIRECT_ANGARA and DENS_DIRECT_PANELS_SENTMAN

The DENS_DIRECT products are based on the solution of the drag equation, using the aerodynamic force coefficients from the CFAERO products as inputs. The density determination is done both with and without the inclusion of the HWM winds in the relative velocity vector $\vec{v}_r$, which is once more calculated according to (8.2) and (8.3). Another distinction is made based on the number of accelerometer axes that are used. The aerodynamic acceleration is present in all three accelerometer axes. But the effect is by far the strongest in the X-component, and only very small in the Z-component of the spacecraft body-fixed frame. The two approaches tested for this product are therefore based on an estimation from the X-component only, and one from the vector sum of the X- and Y-components. If $\vec{a}$ is the aerodynamic acceleration from the ACCEL_NORADPRESS product with components a_x, a_y and a_z, m is the spacecraft mass and $(\vec{C}_F A)$ the aerodynamic force model coefficient times area from the CFAERO product with components $(C_F A)_x$, $(C_F A)_y$ and $(C_F A)_z$, then the density ρ is computed from

$$\rho = \frac{2ma_x}{(C_F A)_x v_r^2} \tag{8.5}$$

for the X-axis approach. For the X- and Y-axis approach, the modulus of the two vector components is used instead:

$$\rho = \frac{2m(a_x^2 + a_y^2)^{\frac{1}{2}}}{\left[(C_F A)_x^2 + (C_F A)_y^2\right]^{\frac{1}{2}} v_r^2} \tag{8.6}$$

These computations results in the following data fields:

1. Density from the accelerometer component in the S/C X-direction (kg/m^3)
2. Density from the accelerometer components in the S/C X- and Y-directions (kg/m^3)

8.4.2 Accelerometer-derived densities using the iterative algorithm: DENSWIND_ITERATIVE

The DENS_DIRECT data was based on simple assumptions about the relative velocity (wind). In the DENSWIND_ITERATIVE product, a more sophisticated approach is used, in which the cross-track wind direction is solved in an iterative approach, so that the resulting modelled aerodynamic acceleration in the X-Y plane best fits with the accelerometer data. Using this cross-track wind speed, and assuming zero along-track winds, the density is then computed, resulting in the following two data fields:

1. Density from the accelerometer components in the S/C X- and Y-directions (kg/m^3)
2. Wind speed along the accelerometer component in the S/C Y-direction (m/s)

In more detail, the computation approach is as follows:

1. The relative velocity vector $\vec{v}_r$ in the body-fixed frame is computed from the orbital velocity and atmospheric corotation velocity, according to (8.3):

$$\vec{v}_r = \begin{pmatrix} v_{r,x} \\ v_{r,y} \\ v_{r,z} \end{pmatrix} = \vec{w}^o + \vec{w}^c \tag{8.7}$$

The X- and Z-components of this velocity vector will remain fixed, while the Y-component will serve as a first estimate for the iterative adjustment that follows.

2. The aerodynamic force coefficient times area $(\vec{C}_F A)$ is computed as a function f of $\vec{v}_r$ (among others). This vector is computed either using the panel model or the ANGARA model, as explained in Section 5.2.

$$(\vec{C}_F A) = f(\vec{v}_r, \ldots) \tag{8.8}$$

3. Since $(\vec{C}_F A)$ is in the direction of the modelled aerodynamic acceleration, it should be in the same direction as the observed aerodynamic acceleration $\vec{a}$ (from the ACCEL_NORADPRESS product). The Z-component of the aerodynamic acceleration can usually be neglected. Therefore, the proper cross-track velocity has been found if the sine of the angle between the acceleration and the X-axis projection on the X-Y plane is the same for model and observation. The symbol η is introduced to represent the sine of this angle, with subscripts m, o and v representing the aerodynamic model acceleration, the observed aerodynamic acceleration and the relative velocity that is used as input for the model, respectively.

$$\eta_m = \frac{(C_F A)_y}{(C_F A)_x}, \quad \eta_o = \frac{a_y}{a_x}, \quad \eta_v = \frac{v_{r,y}}{v_{r,x}} \tag{8.9}$$

For practical purposes, the absolute value of the difference d between the value of η for the model and the observation should be smaller than some convergence limit ϵ:

$$d = \eta_m - \eta_o \tag{8.10}$$

$$|d| \leq \epsilon \tag{8.11}$$

A value of $\epsilon = 10^{-7}$ was picked.

4. If convergence has not been reached, an adjustment to the Y-component of the relative velocity is made. The local slope s in the relation between η_v and η_m is calculated numerically using the aerodynamic model:

$$s = \frac{\Delta\eta_v}{\Delta\eta_m} \tag{8.12}$$

This slope is then used to bridge the gap between model and observation.

$$v_{r,y}^i = v_{r,y}^{i-1} + s\, d\, v_{r,x} \tag{8.13}$$

The new value of $\vec{v}_r$ can then be used in an iteration of steps 2, 3 and 4 until convergence is reached.

5. If convergence has been reached, density is computed using equation (8.6)

$$\rho = \frac{2m(a_x^2 + a_y^2)^{\frac{1}{2}}}{\left[(C_F A)_x^2 + (C_F A)_y^2\right]^{\frac{1}{2}} v_r^2} \tag{8.14}$$

and the wind velocity with respect to a co-rotating atmosphere in the Y-direction of the spacecraft body-fixed frame w_y is determined from $\vec{v}_r$:

$$w_y = v_{r,y} - w_y^o - w_y^c \tag{8.15}$$

8.4.3 The iterative density and wind retrieval algorithm, version 2: DENSWIND_ITERATIVE2

The DENSWIND_ITERATIVE2 product is an improvement over the DENSWIND_ITERATIVE product, as described in the previous section.

The density and wind determination algorithms for satellite accelerometer data rely on the assumption that the satellite velocity is much larger than the wind velocity. This assumption allows one to neglect the in-track component of the wind, and to solve for the perpendicular wind component and density from the two accelerometer observations along perpendicular directions. There are subtly different ways in which this assumption can be implemented in an algorithm however, which will be discussed below. An additional assumption is that the vertical component of the wind can be neglected as well. This is necessary due to the small influence of drag on the acceleration in this direction, compared to residual radiation pressure model errors.

The neglection of both the in-flight and vertical winds will of course incur an error in the density and crosswind derivation, but unless other observations can be used, it is necessary for the accelerometer processing. An analysis of the impact of the horizontal wind model in the density derivation is provided in Chapter 9. The effect of unmodelled in-track and vertical winds on the crosswind determination has been studied as part of the simulations for Swarm, presented in Chapter 12.

The algorithm used for the DENSWIND_ITERATIVE product depended on the assumption that the offset between the directions of the measured and modelled aerodynamic accelerations was due to a wind vector in the Y-direction of the spacecraft body-fixed frame. The addition of this wind vector leads to a change in the orientation and magnitude of the relative velocity vector, which makes the modelled aerodynamic acceleration match the observed one. This is a reasonable assumption to use for deriving crosswind speeds for periods with a nominal attitude behaviour of the satellite, i.e. when the X-axis is more or less parallel to the relative velocity and when the Y-axis is more or less in the horizontal plane and perpendicular to the relative velocity of the spacecraft. However, this assumption leads to a singularity when the satellite is flying sideways, so that the Y-axis is in the flight-direction. And even for intermediate angles between the relative velocity and the X-axis, the algorithm will lead to unrealistically modified relative velocity vectors.

An improved assumption to base the wind determination on would be that the length (magnitude) of the relative velocity vector is completely determined by the sum of the orbital velocity, the corotation velocity and a model for the winds. Only the direction of this vector can then be adjusted, irrespective of its original orientation in the X-Y plane of the satellite body-fixed frame, to yield a modelled force with the same direction as the measured acceleration. The Z-component of the body-fixed frame is still ignored, by setting this vector component to zero in both the model results and data.

The subtle but important change in the assumption described above allows for the derivation of a crosswind speed that is independent of the orientation of the satellite in space.

Algorithm description

Figure 8.13 gives a schematic view of the ITERATIVE2 algorithm.

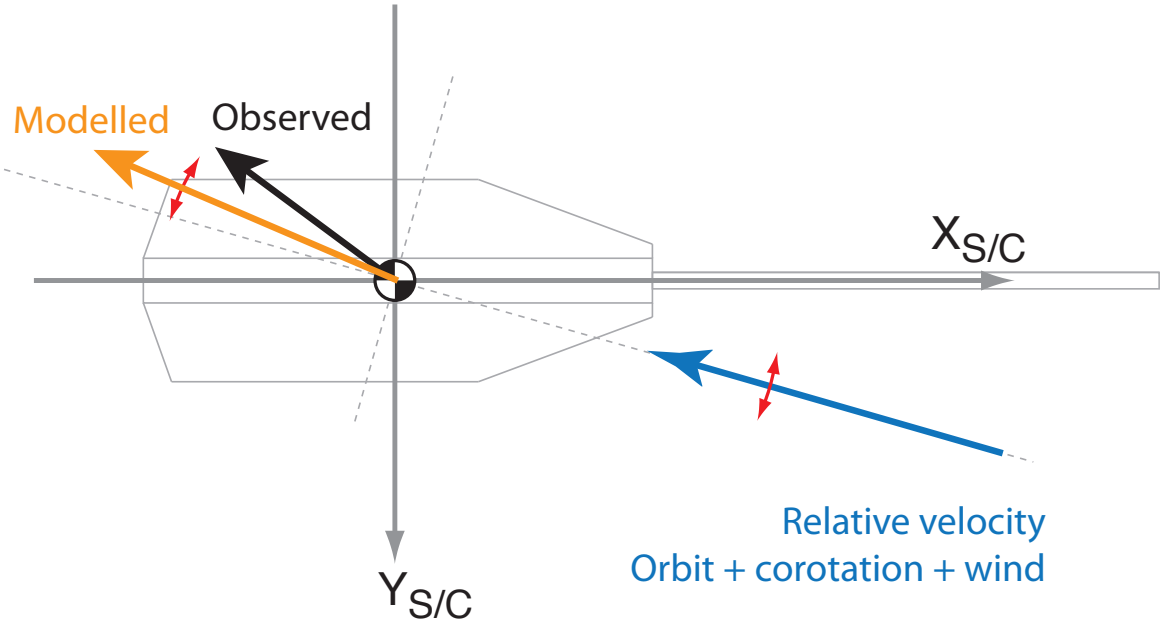

Figure 8.13 Schematic representation of the relative velocity and the modelled and measured accelerations used in the derivation of crosswinds in the DENSWIND_ITERATIVE2 algorithm.

Let $\vec{u}_o$ represent the unit vector of the observed acceleration in the XY-plane. And $\vec{v}_{r_0}$ is the initial guess for the relative velocity, composed of the orbit and atmospheric corotation velocity contributions. The horizontal winds from a HWM model are not yet added at this stage.

$$\vec{v}_{r_0} = \vec{v}_o + \vec{v}_c \tag{8.16}$$

Then $\vec{u}_{m_0}$ is the unit vector of the initial modelled acceleration, which is a complex function of the relative velocity, as well as the accommodation coefficient α, temperature T and composition $\vec{C}$, as described in Chapter 6:

$$\vec{u}_{m_0} = f(\vec{v}_{r_0}, \alpha, T, \vec{C}) \tag{8.17}$$

An iterative process can now be started, where the index i will be used to describe the iteration number. Usually only a few iterations are required.

The vector $\vec{l}_i$ is the difference between the observed and modelled acceleration direction (unit) vectors:

$$\vec{l}_i = \vec{u}_o - \vec{u}_{m_i} \tag{8.18}$$

If the magnitude of $\vec{l}$ is close enough to zero, convergence has been reached. If not, the relative velocity must be adjusted.

The adjustment is made by a rotation about the spacecraft Z-axis. Another option would be to rotate around the local vertical axis. The rotation axis is represented by a unit vector $\vec{u}_Z$.

The magnitude of the rotation is determined by local numerical differentiation. First, a vector $\delta\vec{v}$ is defined to be perpendicular to the relative velocity and the rotation axis, by using

$$\delta\vec{v} = \epsilon \frac{\vec{v}_{r_i} \times \vec{u}_Z}{|\vec{v}_{r_i} \times \vec{u}_Z|} \tag{8.19}$$

where ϵ is a very small number.

Next, two relative velocity vectors are formed, which keep the magnitude of the undadjusted relative velocity, but which are rotated slightly in both directions with respect to the relative velocity of the current iteration:

$$\vec{v}_r^{+} = |\vec{v}_{r_0}| \frac{\vec{v}_{r_i} + \delta\vec{v}}{|\vec{v}_{r_i} + \delta\vec{v}|}, \quad \vec{v}_r^{-} = |\vec{v}_{r_0}| \frac{\vec{v}_{r_i} - \delta\vec{v}}{|\vec{v}_{r_i} - \delta\vec{v}|} \tag{8.20}$$

These modified relative velocities will result in modified modelled accelerations, of which we are only interested in the direction, at the moment, so we use its unit vector:

$$\vec{u}_m^{+} = f(\vec{v}_r^{+}, \dots), \quad \vec{u}_m^{-} = f(\vec{v}_r^{-}, \dots) \tag{8.21}$$

And this in turn leads to modified difference vectors:

$$\vec{l}^{+} = \vec{u}_o - \vec{u}_m^{+}, \quad \vec{l}^{-} = \vec{u}_o - \vec{u}_m^{-} \tag{8.22}$$

Next, the slope vector $\vec{s}$ is computed, which represents the (differential) change in the rotation of the relative velocity required for a change in the length of $\vec{l}$:

$$\vec{s} = \frac{\vec{v}_r^{+} - \vec{v}_r^{-}}{l^{+} - l^{-}} \tag{8.23}$$

A new relative velocity for the iteration $i+1$ can be computed using this slope:

$$\vec{v}_{r_{i+1}} = |\vec{v}_{r_0}| \frac{\vec{v}_{r_i} - \vec{s}|\vec{l}_i|}{\left|\vec{v}_{r_i} - \vec{s}|\vec{l}_i|\right|} \tag{8.24}$$

Once the process has converged, the crosswind speed vector $\vec{v}_{cw}$ is determined by subtracting the original velocity $\vec{v}_{r_0}$, consisting of the orbit plus corotation velocity, from the relative velocity that was found in the last iteration $\vec{v}_{r_i}$.

$$\vec{v}_{cw} = \vec{v}_{r_i} - \vec{v}_{r_0} = \vec{v}_{r_i} - \vec{v}_o - \vec{v}_c \tag{8.25}$$

The density is then calculated in the same way as before:

$$\rho = \frac{2m(a_x^2 + a_y^2)^{\frac{1}{2}}}{\left[(C_F A)_x^2 + (C_F A)_y^2\right]^{\frac{1}{2}} v_{r_i}^2} \tag{8.26}$$

If modelled in-track winds, for example from one of the HWM models, are to be taken into account, the projection of this modelled wind vector $\vec{v}_m$ on the initial velocity is added to the initial velocity:

$$\vec{v}_{r_0}^{*} = \vec{v}_{r_0} + \frac{\vec{v}_m \cdot \vec{v}_{r_0}}{|\vec{v_{r_0}}|} \frac{\vec{v_{r_0}}}{|\vec{v_{r_0}}|} \tag{8.27}$$

and the projection of the modelled wind vector on the end velocity is added to the end velocity:

$$\vec{v}_{r_i}^{*} = \vec{v}_{r_i} + \frac{\vec{v}_m \cdot \vec{v}_{r_i}}{|\vec{v_{r_i}}|} \frac{\vec{v_{r_i}}}{|\vec{v_{r_i}}|} \tag{8.28}$$

These two velocities, with the asterisked superscripts, can then be substituted into equations (8.25) and (8.26), for crosswind and density results for which the in-track wind was taken from the model.

The data is stored in the following fields:

1. Density from the accelerometer components in the S/C X- and Y-directions (kg/m3)
2. Crosswind speed along the accelerometer component in the S/C X-direction (m/s)
3. Crosswind speed along the accelerometer component in the S/C Y-direction (m/s)
4. Crosswind speed along the accelerometer component in the S/C Z-direction (m/s)
5. Attack angle alpha (deg)
6. Side-slip angle beta (deg)

8.4.4 Accelerometer-derived winds in the local frame: CROSSWIND_LOCAL

To ease geophysical interpretation, the crosswind speeds from the DENSWIND_ITERATIVE2 products are converted to the local coordinate system, resulting in the following data fields:

1. Crosswind speed in the zonal (Eastward) direction (m/s)
2. Crosswind speed in the meridional (Northward) direction (m/s)
3. Crosswind speed in the vertical (Upward) direction (m/s)

Basically, the inverse transformation of Section 4.8.4 is applied to the data.

Users of this product must take care that the three vector components in this product do not represent the full 3D wind vector. In the nominal attitude configuration of CHAMP and GRACE, the vertical component is always very close to zero, the zonal component is only accurate for low and mid latitudes, and goes to zero over the poles, and the meridional component is zero for low and mid latitudes, and only represents part of the meridional winds at high latitudes.

8.4.5 Height-normalized density results: DENS_HEIGHTNORMALIZED

The effect of altitude variations over the orbit can be (partly) removed by normalizing the recovered densities to a reference altitude using a density model. The densities at satellite altitude are divided by the model density at satellite altitude and multiplied by the model density at the reference altitude. This procedure will introduce some model error in the results, especially as the reference altitude is far from the true satellite altitude. Nevertheless, high-frequency information is kept, and will be easier to interpret, once the height-variation is removed. The following data fields are available:

1. Density normalized to 475 km (kg/m3)
2. Density normalized to 450 km (kg/m3)
3. Density normalized to 425 km (kg/m3)
4. Density normalized to 400 km (kg/m3)
5. Density normalized to 375 km (kg/m3)
6. Density normalized to 350 km (kg/m3)
7. Density normalized to 325 km (kg/m3)

Chapter 9

Comparisons with density and wind models

The output of the density and wind processing, as described in Chapter 8, will be compared with the output of the density and wind models, introduced in detail in Chapter 2. The size and scope of the dataset, spanning over 5 years, and various conditions in terms of solar and geomagnetic activity, warrants a multi-facetted investigation, from detailed comparisons at relatively short to multi-year timescales in Sections 9.1, to statistical analyses over the entire dataset, presented in Section 9.2.

9.1 Comparison of time series

In this section, the data and models will be presented graphically in figures of time series data.

9.1.1 Orbit time series for forward and sideways flying CHAMP

The comparison of models and data begins with just two full orbits. On October 7 and 8, 2001, a test was performed on the CHAMP spacecraft, during which it was flown sideways, with a yaw angle of approximately 90 degrees with respect to nominal, for several hours. Figure 9.1 shows the density and wind retrieval results from that orbit, and compares it with an orbit 24 hours earlier, when the satellite was flying in its. This comparison of special interest, because in the sideways flying configuration, the satellite has a completely different aerodynamic shape with respect to the incoming particles, than in its usual, forward flying attitude mode. This is of great interest for testing the fidelity of the aerodynamic model and processing strategy. If the model and processing strategy are correct, the results should be similar, regardless of the spacecraft orientation. Any discrepancies that are observed, that can not be attributed to changes in the atmosphere within the 24 hours, indicate shortcomings in the models and algorithms used. In Figure 9.1, the accelerometer-derived winds and densities are plotted for a range of values of the accommodation coefficient, and are compared with several density models (NRLMSISE-00, JB-2008, HASDM) and wind models (HWM-93 and HWM07).

The following observations and conclusions can be made with regards to the wind results in this figure:

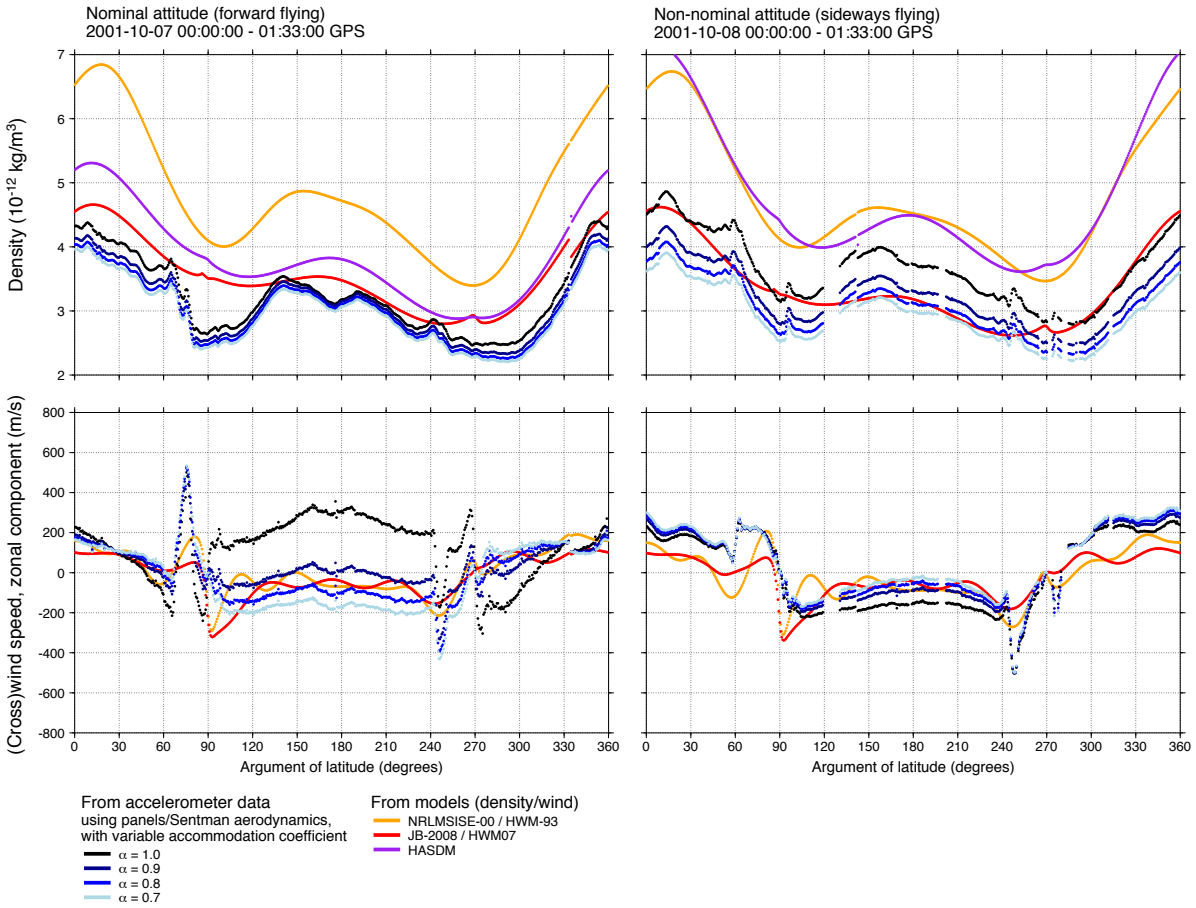

Figure 9.1 Two single orbits of density (top) and wind speed (bottom), for CHAMP in the nominal, forward flying configuration (left), and in the special, temporary, sideways flying case (right), exactly one day later.

- The three density models are not in very good agreement for these two days. There are very large day-to-day differences, probably due to the strong temporal variability of the solar EUV proxies at the considered time in the solar cycle.
- The density observations are generally somewhat lower than the density model results. In the forward-flying configuration, the choice of accommodation coefficient has only a limited influence on the magnitude of the accelerometer-derived density. For the sideways-flying configuration, this influence is much larger. This is in accordance with the results of the sensitivity analysis presented in Section 6.8.

With regards to the wind results in this figure, similar conclusions can be made:

- The winds from both HWM models are very similar for both days.
- The observed winds however shows some discrepancies. This indicates aerodynamic modelling errors, related to the changes in the satellite's aerodynamic shape.
- Note that the discrepancies in the wind results are largest for the data derived with an accommodation coefficient of 1. In the forward-flying case, this data

series is clearly not in agreement with the models. The wind data derived with lower accommodation coefficients shows a better agreement.

- The variation of the accommodation coefficient has a less pronounced effect on the wind speed derivation when the satellite is flying sideways (opposite to the effect on density). This is in accordance with the results of the sensitivity analysis presented in Section 6.8.

9.1.2 CHAMP and GRACE data overview, 2002–2007

The density and wind data shown in Figure 9.1 was for just two single orbits. By gridding the data as a function of time on the X-axis and argument of latitude along the Y-axis, and using colour to represent the density or wind magnitude, many such orbits can be represented in a single Figure. Figures 9.2 and 9.3 show such Figures for six years (2002—2007) of CHAMP and GRACE, along with corresponding model output evaluated along the tracks. Section 9.1.3 will show zoomed in views on this data, and comparisons with other models.

These Figures show the large dependence on the local solar time (which is printed at regular intervals at the equator crossings). In the density, this shows up as the diurnal bulge, which the orbital plane passes through about twice a year for the ascending tracks and twice per year for the descending tracks. In the wind plots, the local time dependence shows up as alternating periods of predominantly westward (blue) winds and eastward (red) winds.

Especially in the density plots, the depence on changes in solar EUV radiation and geomagnetic activity are apparent. The heightened EUV radiation at solar max is clearly visible in 2002, and the last quarter of 2003. Geomagnetic storms are short-lived events, and show up as vertical lines in these plots.

A good correspondence between density data and models is apparent in both Figures, even though the data shows somewhat lower values than the models. For the wind speeds, the CHAMP results show a much greater resemblance to the models than those from GRACE. Only during 2002 is there some resemblance for GRACE wind speeds. Afterwards, radiation pressure acceleration model errors take over, because of the relatively very low drag signal.

9.1.3 Detailed comparisons with empirical models during geomagnetic storms

In this Section, zoomed in views of the plots shown in Figures 9.2 and 9.3 will be presented, to illustrate the differences and similarities between models and data in more detail.

The observed density data from CHAMP and GRACE shows large overall global increases during the periods of high geomagnetic activity. Such conditions occurred for example on October 29 and October 30/31, 2003 (the “Halloween Storm”), plotted in Figure 9.4, and in early April 2005, when the orbits of both missions were co-planar, plotted in Figure 9.5.

During the former period, the global air density in the upper thermosphere increased by roughly a factor of two above values that were already high, due to the sustained high solar EUV fluxes. During this period, the highest density values observed by CHAMP and GRACE are on the dayside – and at moderate to high southern latitudes. This corresponds to the satellite passage close to the southern polar cusp – sunlit – with photo-ionisation thus enhancing ionospheric conductivity and increasing the Joule heating and momentum transfer “loads”

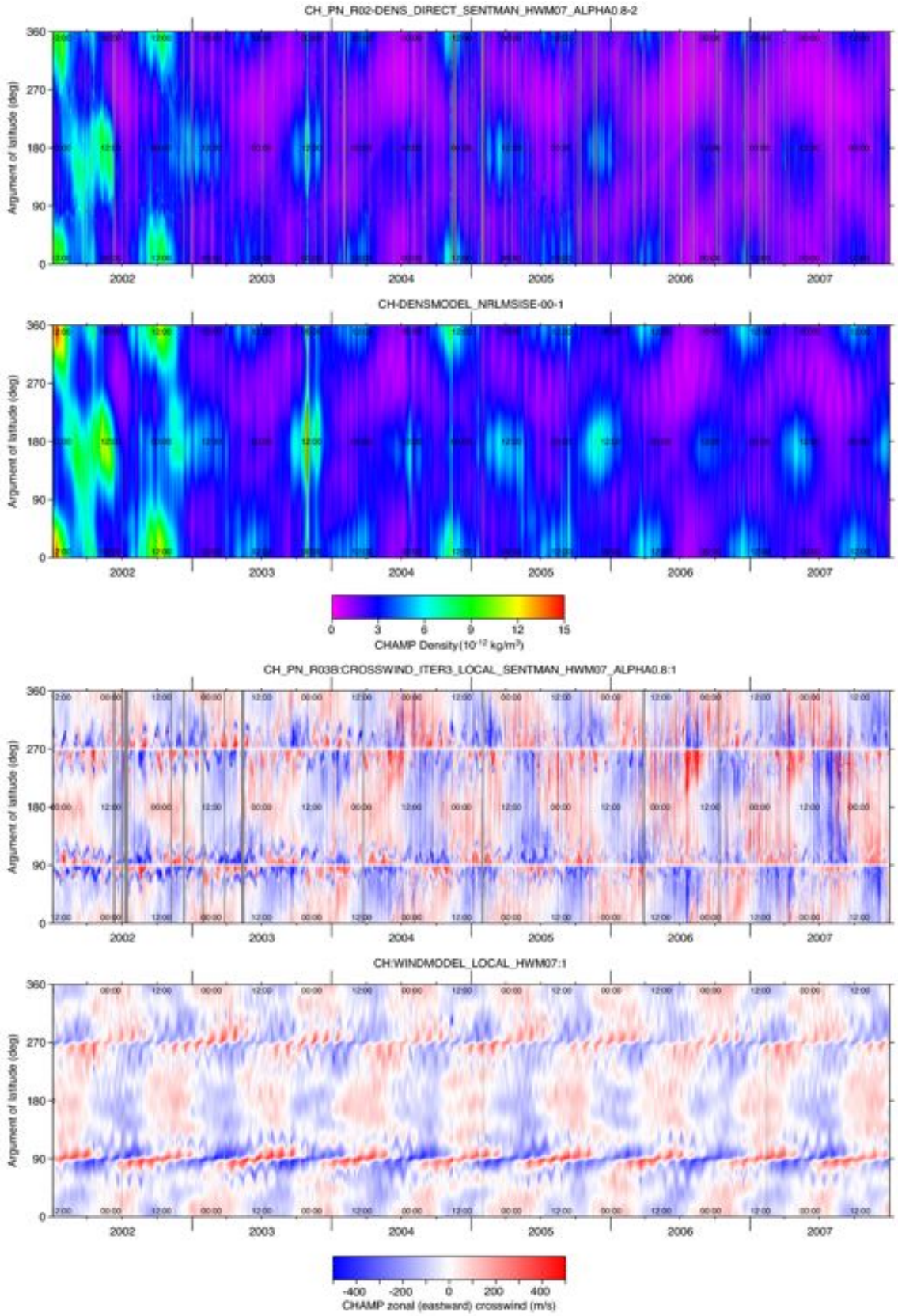

Figure 9.2 Comparisons of density (top two panels) and zonal wind (bottom two panels), derived from accelerometer data (top panel in each pair) and the NRLMSISE-00 and HWM07 models (bottom panel in each pair), along the CHAMP orbit.

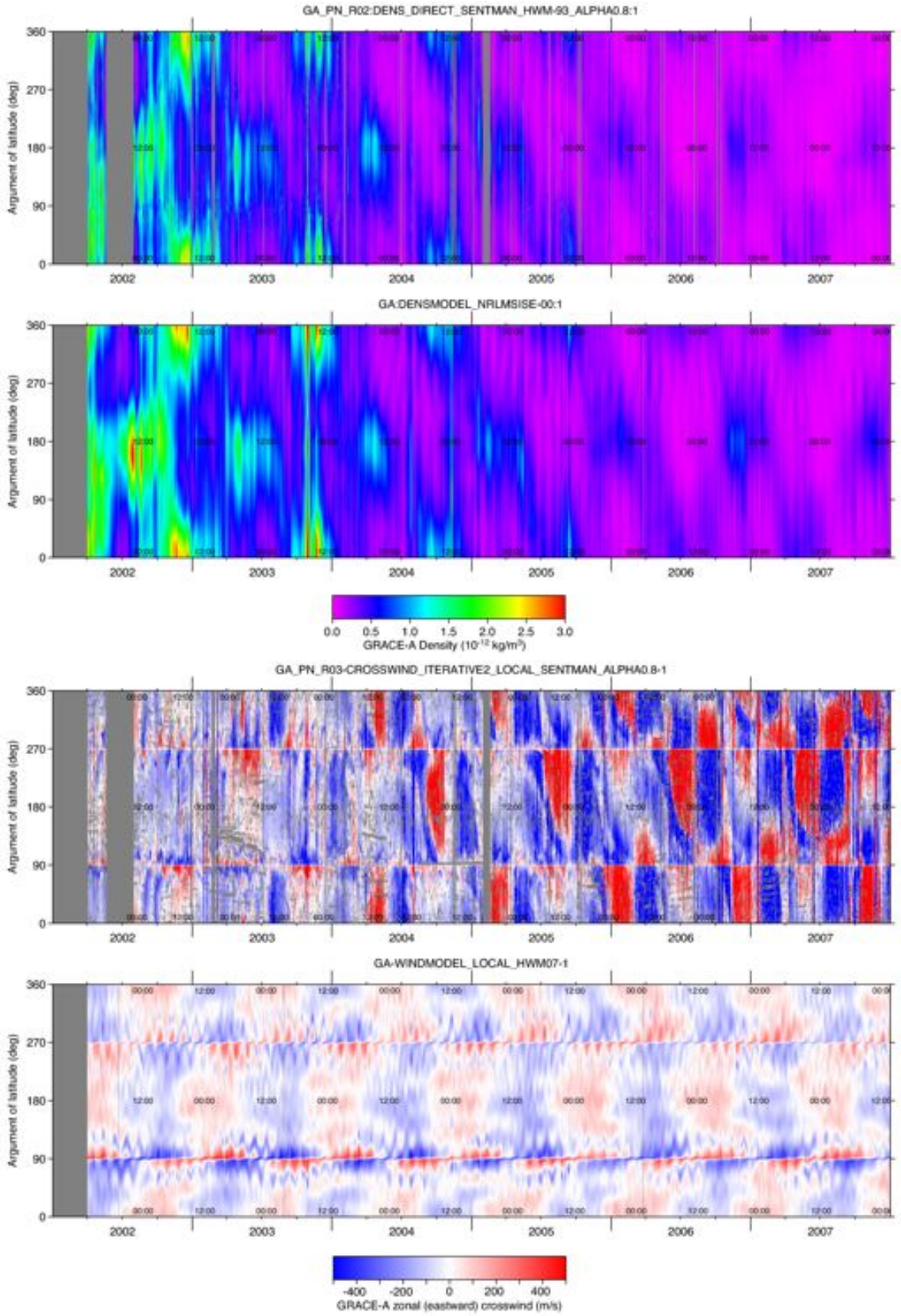

Figure 9.3 Comparisons of density (top two panels) and zonal wind (bottom two panels), derived from accelerometer data (top panel in each pair) and the NRLMSISE-00 and HWM07 models (bottom panel in each pair), along the GRACE-A orbit.

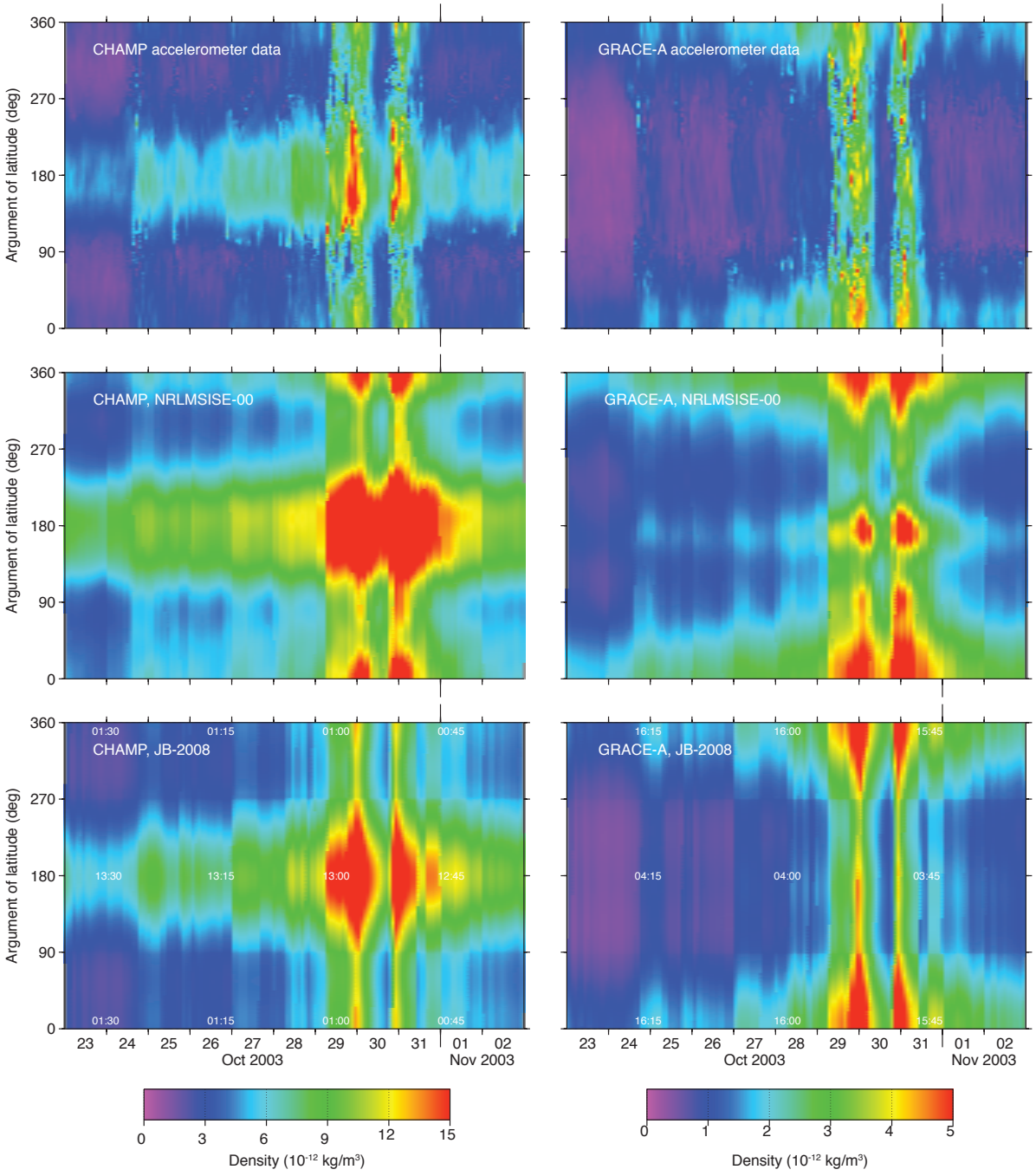

Figure 9.4 Comparisons of total neutral densities along the tracks of CHAMP (left) and GRACE-A (right), for the large October 2003 geomagnetic storm, and the days leading up to it, as computed (from top to bottom) from accelerometer data, the NLRMSISE-00 model and the JB-2008 model.

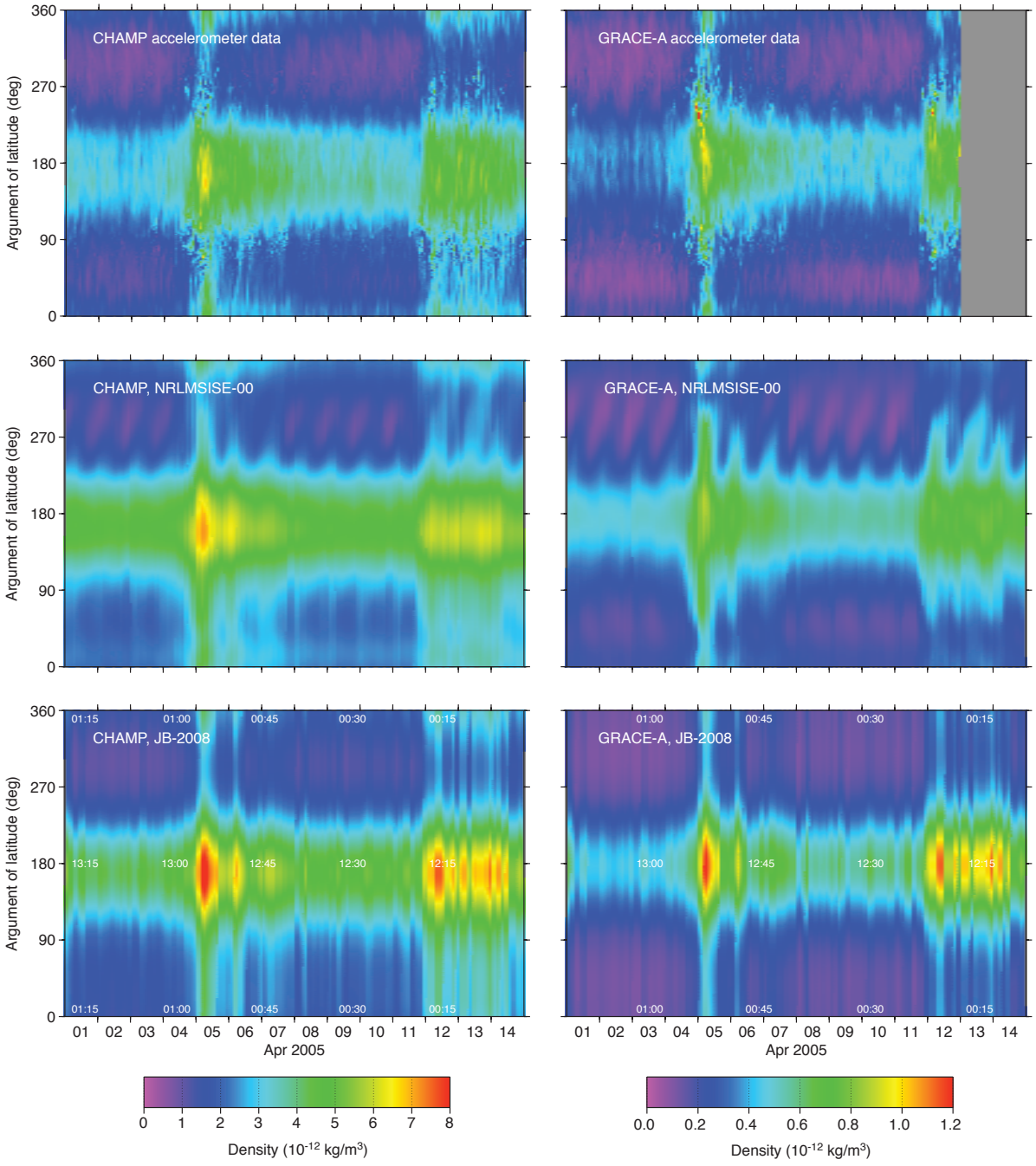

Figure 9.5 Comparisons of total neutral densities along the tracks of CHAMP (left) and GRACE-A (right), for the first 15 days of April 2005, as computed (from top to bottom) from accelerometer data, the NLRMSISE-00 model and the JB-2008 model. During these days, both missions were in nearly co-planar orbits.

of the ionosphere on the solar wind / magnetospheric drivers (the solar wind dynamo – crossing the terrestrial magnetospheric magnetic field).

9.1.4 Comparison of densities and winds with CTIPe data in January 2005

CTIPe is the most up-to-date version of the fully-coupled physical/theoretical model of thermosphere-ionosphere (see Section 2.8.3). The very latest version has been made available for providing time-dependent simulations of the thermosphere and ionosphere for comparisons with the semi-empirical models, and with data from the CHAMP and GRACE missions.

The latest version of the CTIP model, CTIPe, has very recently been adapted to follow better significant atmospheric changes during geomagnetic storms, such as the creation, transport and dissipation of Nitric Oxide. NO plays a critical role in the ionosphere, and it also has a very important role in the cooling of the thermosphere following major geomagnetic disturbances. CTIPe additionally includes atomic Hydrogen as an additional species. This may be significant during periods of low solar and geomagnetic activity, as have occurred since 2004/2005.

Data from the very latest version of CTIPe for 15 days in early January 2005 has kindly been made available by the modelling group at NOAA. There was an interesting geomagnetic disturbance during this period, allowing the comparison of physical models, empirical models and CHAMP and GRACE data, in terms of densities and wind speed, for a wide range of geomagnetic activity. The solar activity was relatively low during this period. This comparison is shown in Figures 9.6 for the densities and 9.7 for the wind speeds.

Densities in January 2005

The effects of the geomagnetic disturbance on the density around January 7 and 8 are quite clear in Figure 9.6. There is a rather higher degree of structure in the predictions of the JB-2008 model, compared to the NRLMSISE-00 plot, reflecting the higher temporal resolution of the hourly Dst index of geomagnetic activity, in contrast to the three-hourly ap index.

The CTIPe results show an even higher degree of fine detail, compared to the two empirical models, and further approaches the structure seen in the satellite data. A significant difference is in the absolute density values, where CTIPe is of the order 40% higher than either the NRLMSISE-00 or the JB-2008 model. There also seems to be a a gradient from pole to pole in the CTIPe data that is not apparent in the satellite data and empirical models. These issues could be due to CTIPe, or the way the data are interpolated and extrapolated to the satellite altitudes. This will be considered in extended work with the authors of the CTIPe model, in which different time spans will be considered as well.

Zonal wind speeds in January 2005

The zonal wind predictions by HWM-93 (see Figure 9.7) show little changes of structure, even during the disturbed period of January 7 and 8, 2005. The zonal wind predictions by HWM07 show larger and more rapid changes of the wind structure during the disturbed period. The zonal wind predictions by CTIPe show many more variations of wind structure, even during relatively quiet days in thsi period. During the disturbed period on January 7 and 8, the wind structures are more active, and the disturbances extend to much lower geographic

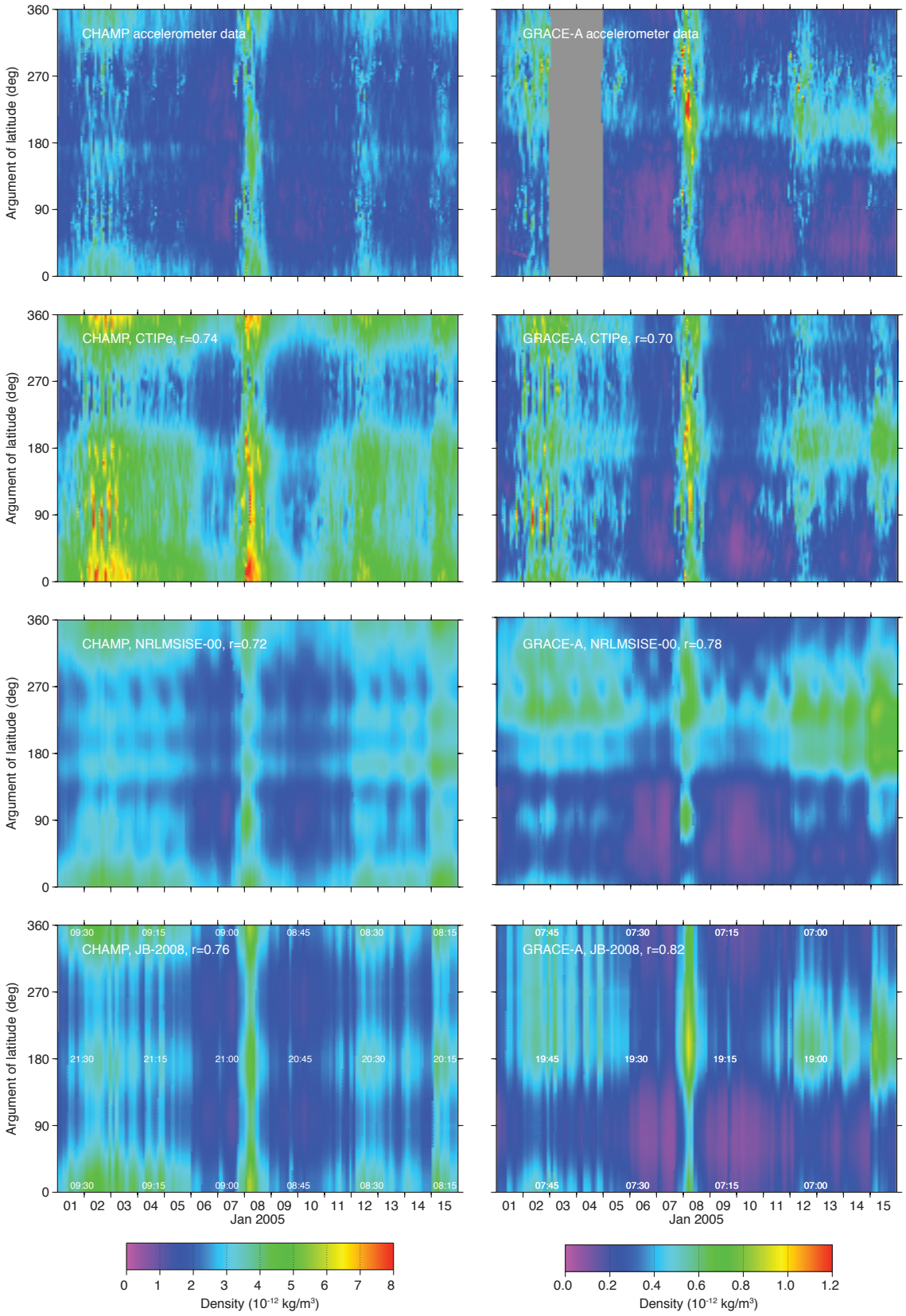

Figure 9.6 Comparisons of total neutral densities along the tracks of CHAMP (left) and GRACE-A (right), for the first 15 days of January 2005, as computed (from top to bottom) from accelerometer data, the CTIPe model, the NLRMSISE-00 model and the JB-2008 model. The linear correlation coefficient r with the data is given for each of the models.

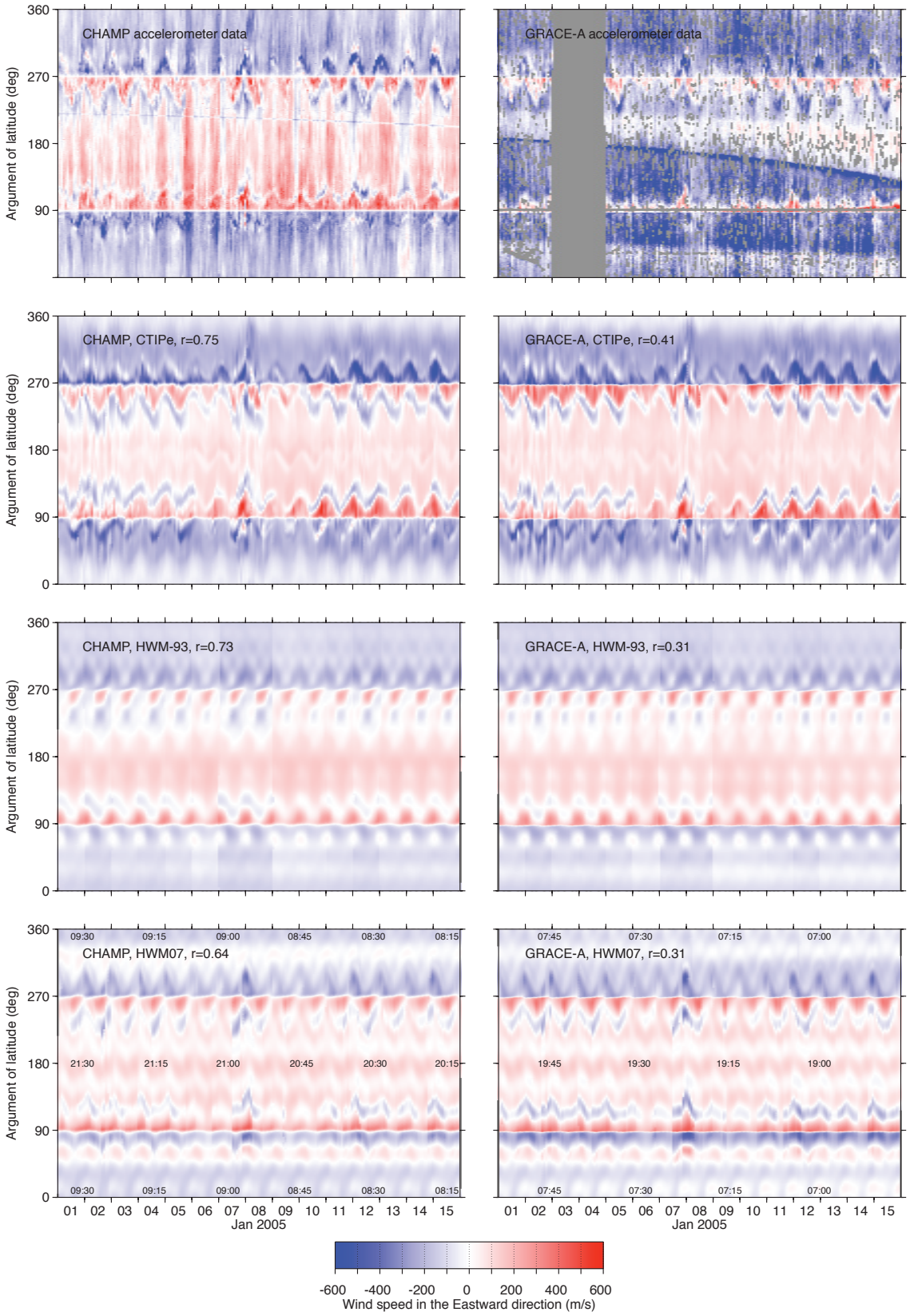

Figure 9.7 Comparisons of Eastward wind speed along the tracks of CHAMP (left) and GRACE-A (right), for the first 15 days of January 2005, as computed (from top to bottom) from accelerometer data, the CTIPe model, the HWM-93 model and the HWM07 model. The linear correlation coefficient r with the data is given for each of the models.

(and geomagnetic latitudes), than those displayed by the HWM-93 and HWM07 models. The CTIPe winds generally show larger amplitudes, closer to the results from the CHAMP accelerometer.

The GRACE accelerometer wind results clearly suffer from large radiation-pressure model induced wind errors, due to the very low drag signal. The radiation pressure error causes the plot to show predominantly high westwards winds, even though each of the models shows that over the descending tracks, the winds should be predominantly eastward. The large dark curved section in the GRACE wind plot is caused by additionally large errors due to incorrect eclipse transition timing in the radiation pressure model.

The zonal wind observations from CHAMP show more variations of structure, particularly during the disturbed periods, than any of the models. However, the general correspondence between the CHAMP winds and and those of CTIPe appears remarkably good. The low latitude extension of wind disturbances on January 7 and 8 is precisely what is seen in the CTIPe modelling – but this is not observed in the HWM-93 and HWM07 models.

9.2 Statistical evaluation

After the rather qualitative comparisons of density and wind models with the CHAMP- and GRACE-derived data in the previous Sections, this Section will be used to present a statistical evaluation of data/model density ratios. Due to the very large range of density values encountered, it is useful to provide performance statistics in terms of these dimensionless ratios.

Section 9.2.1 will show some histograms of these ratios, and demonstrate the largely log-normal distribution. Next, in Section 9.2.3, the mean and standard deviation of the data/model ratios for complete data sets are examined, for a more detailed look at the relative quality of different density models, and the effect of different processing choices on the agreement of data with models. Finally, a finer grained look at the data will be given in Section 9.2.2, where the data are first binned according to several variables, before the statistics are examined.

9.2.1 Histograms and the log-normal distribution of data/model ratios

In this section, the accelerometer data are compared with NRLMSISE-00 model data (see Section 2.3.3) and HASDM model data (see Section 2.7), along the CHAMP and GRACE tracks. The HASDM density data along the satellite tracks was kindly provided by Bruce Bowman.

The comparison is made by computing the accelerometer-derived data over model density ratios for a long time span, so that a wide range of conditions are sampled. These ratios are then plotted in a histogram. Four such histograms are presented in Figure 9.8. It turns out that the data/model ratios fit reasonably well with a log-normal distribution [*Bezděk*, 2007; *Limpert et al.*, 2001], which is to be expected because of the largely multiplicative nature of the equations governing both the density models (Chapter 2) and the data reduction from accelerometry (Chapter 8). This is why the log-normal mean and standard deviation of the data are computed, and the accompanying log-normal distribution plotted in the Figure as a solid black line. The comparison with HASDM results in much narrower histograms, corresponding to lower standard deviations, than the comparison with the standard empirical model NRLMSISE-00. HASDM data are currently

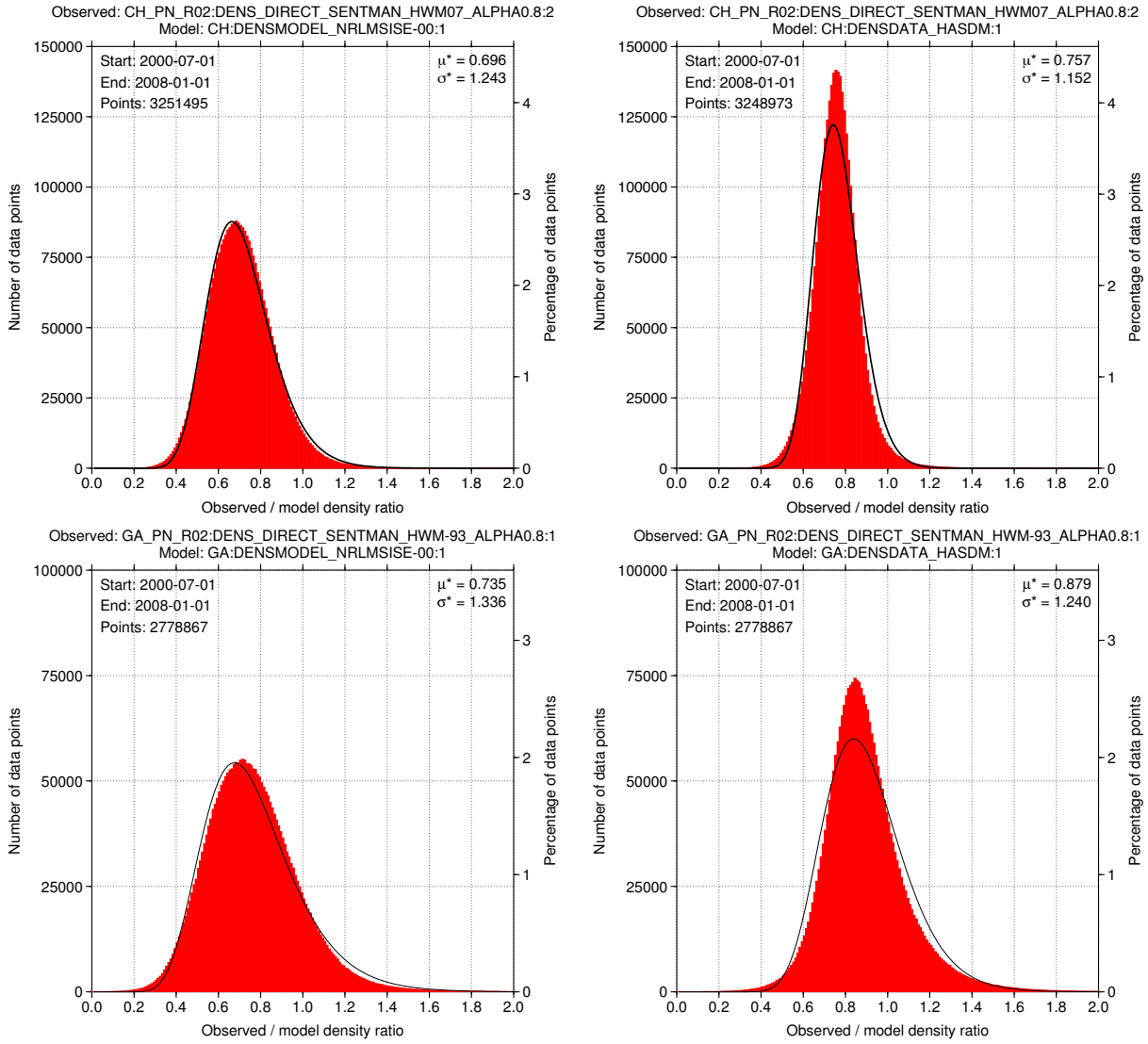

Figure 9.8 Distribution of data/model density ratios over 0.01-wide bins, for CHAMP (top) and GRACE-A (bottom). The NRLMSISE-00 model is used in the left panel, and the HASDM calibrated model in the right panel. The thin black lines show the log-normal distribution using the mean and standard deviation computed from all data.

the most accurate independent source of density data available for comparison with the CHAMP and GRACE data.

These (multiplicative) standard deviations contain both contributions of errors in the models and errors in the accelerometer-derived densities. Since the accelerometer has a much higher spatial and temporal resolution than the model, a significant part of the standard deviation must be due to the model error. The standard deviation gives an upper bound of the accuracy of both data sets. When comparing different versions of the accelerometer data with the HASDM data, a lower standard deviation will indicate that the data processing is more accurate.

The ratio of data over NRLMSISE-00 clearly results in a better fit with a perfect log-normal distribution than the ratio of data over HASDM values. This could perhaps be partly related to outliers in the accelerometer-derived density data skewing the statistics, which is less apparent for the less accurate model, but this remains to be further investigated.

9.2.2 Statistics for geomagnetic coordinate and activity level bins

In order to investigate the statistics of data/model density ratios in more detail, the measurements have been binned according to several variables, after which the log-normal mean and standard deviation have been determined for all the data in each bin. Figures 9.9 and 9.10 shows the results of this analysis, for HASDM and NRLMSISE-00, respectively. The binning and computation of statistics has been performed both in a two-dimensional fashion, which is represented in the coloured parts of the plot, and aggregated in one dimension, shown in the black and white and gray plots.

The top half of each of the figures shows the binned statistics as a function of the $F_{10.7}$ solar activity proxy and Kp geomagnetic activity index. Higher values of these two variables tend to cause larger densities and therefore larger drag signals, which should aid in more accurate density retrieval and modelling. This is confirmed by the lower standard deviations of the ratios at high $F_{10.7}$. The data/HASDM ratios show a relatively constant mean, as a function of these conditions, while the data/NRLMSISE-00 ratios are more erratic. This is an indication that the drag data from the calibration objects used in the HASDM model calibration, agrees reasonably well under all conditions with the CHAMP and GRACE data. On the other hand, the $F_{10.7}$ proxy that drives the NRLMSISE-00 model dependence on solar EUV variation is clearly not so well-correlated with the observed density changes.

The log-normal standard deviation increases with increased Kp, even though higher densities are expected under high Kp conditions, similar to the high $F_{10.7}$ conditions. This can be explained because rapid variations in the thermosphere occur during geomagnetic storms at high Kp, which leads to errors in the models, which are not capable of fully reproducing these variations, and to errors in the data, mainly because of higher in-track wind velocities. The log-normal standard deviation for the data/HASDM ratios rises from values as low as about 10% at low geomagnetic activity (and high EUV energy input), to as high as 30% to 50% during the most severe storm conditions.

The bottom halves of Figures 9.9 and 9.10 are used to investigate the offset (in terms of the log-normal mean) and accuracy (in terms of the log-normal standard deviation) as a function of the geomagnetic local solar time and latitude. Both the data/HASDM and data/NRLMSISE-00 figures show that the standard deviation is lowest (most accurate) on the low-latitude dayside and less accurate on the night side and near the poles. Of course, the diurnal bulge causes a greater drag signal on the dayside. In addition, more thermospheric variability is expected near the poles and on the night-side. Therefore these features are as expected.

One additional feature that stands out is the change in mean value of the data/HASDM ratio for GRACE as a function of latitude. The mean data/model ratio is about 15% higher over the poles compared to the equator. This is not the case for the data/NRLMSISE-00 ratios, or for the CHAMP data, which could indicate that this is due to a problem in the HASDM model at higher altitudes. A further investigation has shown that this polar/equatorial difference in in the mean GRACE data/HASDM ratios is prevalent at low solar activity, where the drag signal is low. Under these conditions it would be more difficult to get accurate calibration drag data for HASDM, which could explain this error.

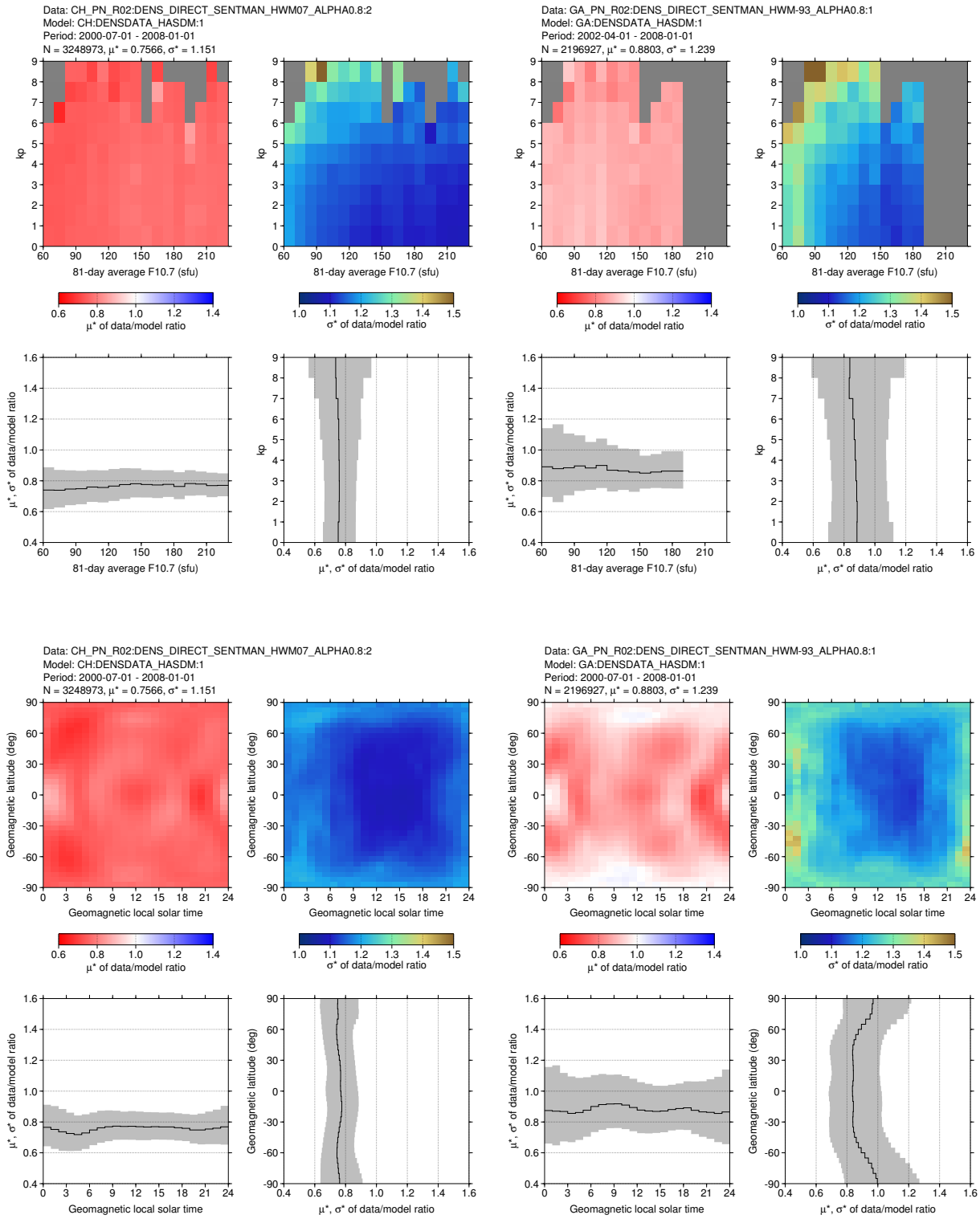

Figure 9.9 Log-normal statistics of data/HASDM density ratios for CHAMP (left half) and GRACE (right half), grouped in $\bar{F}_{10.7}$ and k_p bins (top half) and geomagnetic local solar time and geomagnetic latitude bins (bottom half).

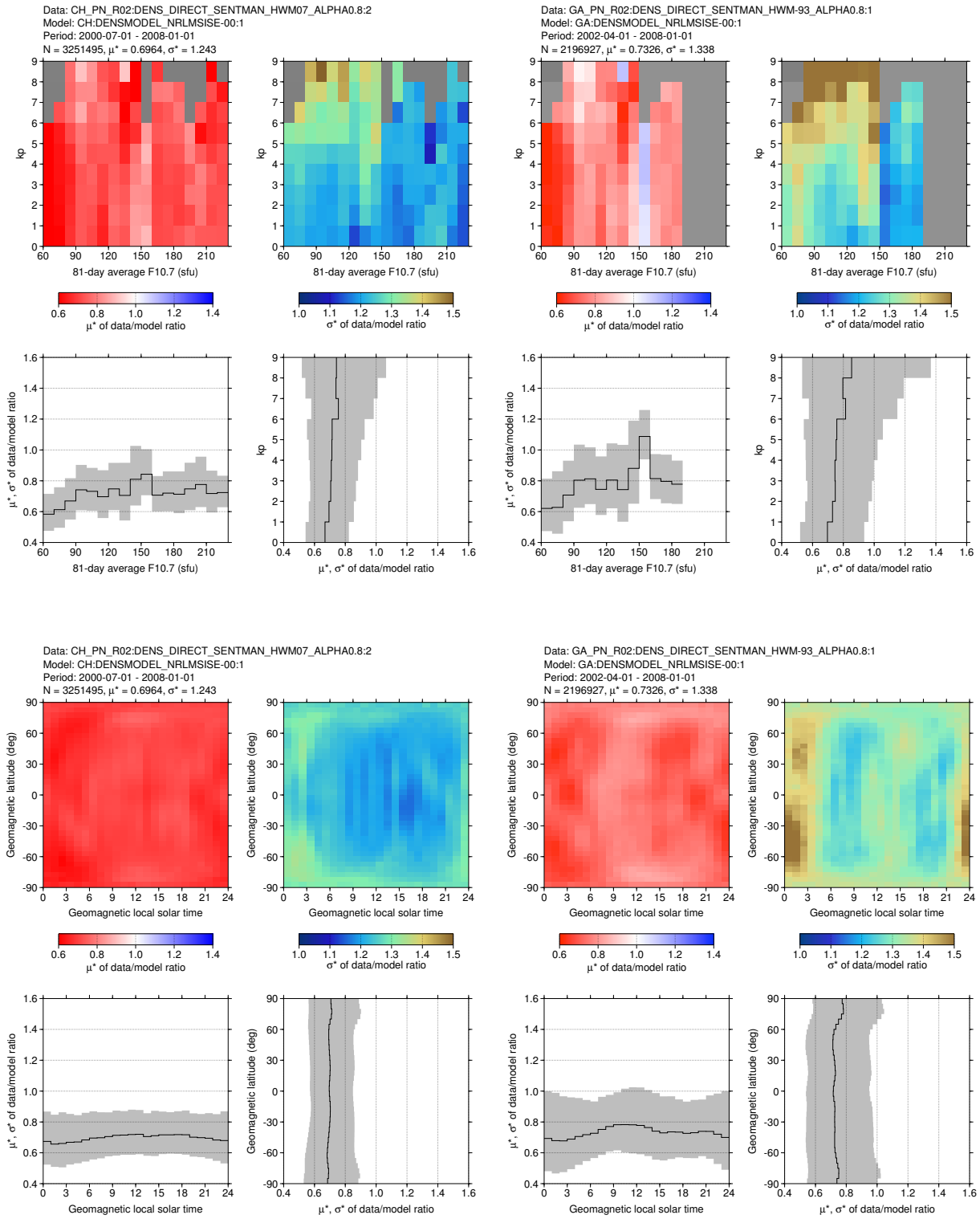

Figure 9.10 Log-normal statistics of data/NRLMSISE-00 density ratios for CHAMP (left half) and GRACE (right half), grouped in $\bar{F}_{10.7}$ and k_p bins (top half) and geomagnetic local solar time and geomagnetic latitude bins (bottom half).

	CHAMP			GRACE		
Model	N	$\mu*$	$\sigma*$	N	$\mu*$	$\sigma*$
CIRA-72 (Jacchia)	3247175	0.652294	1.25138	2196926	0.701686	1.35437
Jacchia-Bowman 2006	3247175	0.708987	1.22203	2196925	0.789377	1.33610
Jacchia-Bowman 2008	3247175	0.765333	1.20573	2196927	0.865635	1.31661
DTM-78	3247175	0.677565	1.32159	2196927	0.697781	1.44940
DTM-94	3247175	0.704782	1.31337	2196927	0.723216	1.46576
MSIS-86	3247175	0.694427	1.25071	2196927	0.729678	1.34689
NRLMSISE-00	3247175	0.696331	1.24340	2196927	0.732613	1.33849
HASDM	3244653	0.756588	1.15179	2196927	0.880313	1.23990

Table 9.1 Statistics (log-normal) of the accelerometer-derived over model density ratios for CHAMP and GRACE, comparing various models. The processing for CHAMP made use of panels, Sentman aerodynamics with $\alpha_E = 0.8$, HWM07, R02 calibration, and the direct algorithm using both X- and Y-axes of the accelerometer. The GRACE processing used panels, Sentman aerodynamics with $\alpha_E = 0.8$, HWM-93, R02 calibration, and the direct algorithm using the X-axis only.

9.2.3 Evaluation of empirical density models

So far, we have only looked at the HASDM and NRLMSISE-00 models. Table 9.1 lists the log-normal means and standard deviations for the data/model ratios for several other models as well. The two DTM models evaluated here clearly do not provide the same level of consistency with the data as the other models. When looking at the progression from CIRA-72 to MSIS-86 (CIRA-86) to NRLMSISE-00 and the Jacchia-Bowman models (proposed for CIRA-2008), it is clear that in terms of absolute densities, there has been only very little progression until very recently. The first three models mentioned above result in about the same level of consistency with the CHAMP and GRACE data. The JB-2006 model was already a good step forward, and the JB-2008 model even more so.

9.2.4 Evaluation of processing choices

The data has also been used to investigate several processing choices. For this investigation, all CHAMP data has been processed using a large number of combinations of different models and parameters. The data analysis for CHAMP is based on the period between January 1, 2001 to December 31, 2007. For GRACE, the data period started on January 1, 2003 instead. January 1, 2003 is also the starting date for the comparison of the calibration parameters for CHAMP, since the R01 parameters were never computed for 2002 and earlier.

The results of the comparisons are available in Tables 9.2 and 9.3 for CHAMP and GRACE-A, respectively.

To reduce processing time, the time step was set to 60 seconds, so that every sixth measurement was used (if available). It is not expected that this significantly changes the statistics with respect to an analysis of the full database of 10 second measurements. Around 3 million data points are compared for CHAMP. For GRACE, about 2.5 million measurements are used for those algorithms which use the X-axis only, while a little under 2 million measurements are available when the Y-axis data are used as well. This is due to the editing of Y-axis data around attitude thruster activation times.

Aerodynamics	Rad. press.	Cal.	Algorithm	Winds	N	$\mu*$	$\sigma*$
Calibration scheme (2003–2007 only)							
Sentman (α =0.8)	Panels	R01	Direct – XY	HWM07	2422357	0.75105	1.16655
Sentman (α =0.8)	Panels	R02	Direct – XY	HWM07	2439498	0.75141	1.16129
Sentman (α =0.8)	Panels	R02B	Direct – XY	HWM07	2581424	0.75123	1.16198
Sentman (α =0.8)	Panels	R03	Direct – XY	HWM07	2439498	0.75012	1.16182
Sentman (α =0.8)	Panels	R03B	Direct – XY	HWM07	2574945	0.75019	1.16251
Algorithm							
Sentman (α =0.8)	Panels	R02	Direct – X	HWM07	3248874	0.75499	1.15308
Sentman (α =0.8)	Panels	R02	Direct – XY	HWM07	3248973	0.75661	1.15176
Sentman (α =0.8)	Panels	R02	Iter3 – XY	HWM07	3248973	0.74714	1.15957
Sentman (α =0.8)	Panels	R03	Direct – X	HWM07	3248878	0.75496	1.15314
Sentman (α =0.8)	Panels	R03	Direct – XY	HWM07	3248973	0.75531	1.15221
Sentman (α =0.8)	Panels	R03	Iter3 – XY	HWM07	3248973	0.75298	1.15344
Radiation pressure force model							
ANGARA (α =0.8)	ANGARA	R02	Direct – X	HWM07	3240636	0.85022	1.15238
ANGARA (α =0.8)	ANGARA	R02	Direct – XY	HWM07	3240636	0.85882	1.15030
ANGARA (α =0.8)	Panels	R02	Direct – X	HWM07	3247835	0.85052	1.15154
ANGARA (α =0.8)	Panels	R02	Direct – XY	HWM07	3247835	0.85339	1.15125
Aerodynamic force model							
Sentman (α =0.8)	Panels	R02	Direct – XY	HWM07	3248973	0.75661	1.15176
Sentman (α =1.0)	Panels	R02	Direct – XY	HWM07	3248973	0.82370	1.15144
ANGARA (α =0.8)	Panels	R02	Direct – XY	HWM07	3247835	0.85339	1.15125
ANGARA (α =1.0)	Panels	R02	Direct – XY	HWM07	3247835	0.80488	1.15140
Cook (α =0.8)	Panels	R02	Direct – XY	HWM07	3248973	1.05511	1.17134
Cook (α =1.0)	Panels	R02	Direct – XY	HWM07	3248973	1.17838	1.17523
Sphere (C_DA =2.5m^2)	Panels	R02	Direct – XY	HWM07	3127592	0.88643	1.16617
Sphere (C_DA =3.0m^2)	Panels	R02	Direct – XY	HWM07	3127592	0.73869	1.16617
Wind model							
Sentman (α =0.8)	Panels	R02	Direct – X	None	3248882	0.75554	1.15498
Sentman (α =0.8)	Panels	R02	Direct – XY	None	3248973	0.75716	1.15363
Sentman (α =0.8)	Panels	R02	Direct – X	HWM-93	3248846	0.75492	1.15288
Sentman (α =0.8)	Panels	R02	Direct – XY	HWM-93	3248973	0.75650	1.15151
Sentman (α =0.8)	Panels	R02	Direct – X	HWM07	3248874	0.75499	1.15308
Sentman (α =0.8)	Panels	R02	Direct – XY	HWM07	3248973	0.75661	1.15176

Table 9.2 Statistics (log-normal) of the accelerometer-derived over HASDM density ratios for CHAMP, comparing various processing choices. All available data, from 2001 to 2007, was used for the evaluation, except for the comparison of calibration factors, since the R01 calibrations were only available for the period from 2003 to 2008.

Aerodynamics	Rad. press.	Cal.	Algorithm	Winds	N	$\mu*$	$\sigma*$
			Algorithm				
Sentman (α=0.8)	Panels	R02	Direct – XY	HWM-93	1984654	0.939	1.308
Sentman (α=0.8)	Panels	R02	Iterative2 – XY	HWM-93	1984654	0.970	1.314
			Aerodynamic force model				
Sphere (C_DA=3.0 m^2)	Panels	R02	Direct – X	HWM-93	2507773	1.097	1.252
Cook (α=1.0)	Panels	R02	Direct – X	HWM-93	2507773	1.392	1.268
Cook (α=0.8)	Panels	R02	Direct – X	HWM-93	2507773	1.164	1.265
Sentman (α=1.0)	Panels	R02	Direct – X	HWM-93	2507773	1.018	1.247
Sentman (α=0.8)	Panels	R02	Direct – X	HWM-93	2507773	0.881	1.248
			Wind model (all data)				
Sentman (α=0.8)	Panels	R02	Direct – X	None	2507774	0.881	1.250
Sentman (α=0.8)	Panels	R02	Direct – X	HWM-93	2507773	0.881	1.248

Table 9.3 Statistics (log-normal) of the accelerometer-derived over HASDM density ratios for GRACE-A, comparing various processing choices. All statistics are for data from the period January 1, 2003 to December 31, 2007. A 60-second time-step was used instead of the nominal 10-second time-step of the data, in order to reduce computation time.

In general, when comparing these two tables, it is clear that the standard deviations for GRACE are much higher than for CHAMP. It is not clear how much of this is due to an increasing error in the HASDM data with altitude, or with larger error sources (relative to the drag signal) in the accelerometer data and processing for GRACE. Both effects are expected to contribute.

Calibration strategy

The calibration strategy is investigated only for CHAMP. See Section 7.4 for details on the various calibration time series, and their identifiers. The R01 calibration parameters, which were used in the dataset at the time of the second progress meeting in Potsdam, are compared with the R02 calibration parameters, for which the scale factor is held fixed. In the R03 Note that this comparison is made for a different time interval than the other comparisons for CHAMP: Since R01 calibration parameters are not available before January 1, 2003, data from 2002 is omitted. The standard deviation of the density data compared to HASDM is lower using the newer R02 and R03 calibrations, compared to R01. This confirms our finding that the accelerometer scale factor is constant, or varies only very little.

There is no such apparent improvement when moving from R02 to R03. The difference is small, but in favour of R02. The main difference between these time series is in the cross-track component, to arrive at more accurate wind speeds, so it is no surprise that the difference is so small.

The smoothing and editing of the calibration time series, introduced in the R02B and R03B calibration series, does not make much of a difference in the statistics either. The standard deviations are slightly worse, but this could be because more data is available, since small gaps in the calibration time series are now interpolated as part of the smoothing algorithm.

Iterative approach versus direct approach

The direct and iterative density determination procedures are compared as well (see Chapter 8) for details on the two approaches. In general, the differences are rather small. The iterative algorithm seems to lead to slightly worse results compared with the direct one, when using the R02 calibration parameters, both for CHAMP and GRACE. The R03 calibration, in which the cross-track data is improved, reduces this small difference.

When looking at the use of the X-axis only, or the X- and Y-axes for the direct approach, the dual-axis approach gives better results for CHAMP, while for GRACE the single-axis approach works better. A possible explanation for this difference is that this is due to the higher level of error in the accelerometer Y-axis data for GRACE, due to the higher altitude. At the higher altitude, the drag signal is lower, so that any unmodelled or badly modelled other forces have a larger relative contribution.

Radiation pressure models

The panel and ANGARA radiation pressure models were compared for CHAMP only. The differences are very small, and no firm conclusions can be drawn from these numbers.

Comparison of aerodynamic models

Density results using four different aerodynamic models have been compared with the HASDM data. For CHAMP, each of these models has been tested with two different settings for one of the key model parameters. For GRACE, the choices are somewhat more limited due to constraints on the processing time. To summarize the choices:

- The sphere, or fixed model assumes a fixed drag coefficient and area, and no lift. Values of 2.5 m^2 and 3.0 m^2 for the product of drag coefficient and area have been tried.
- The Cook model was used in the processing with values for the accommodation coefficient of 1.0 and 0.8.
- The Sentman model was used with the same accommodation coefficient choices.
- The ANGARA model has only been tested for CHAMP. Values of the Maxwell coefficient of 1.0 and 0.8 were tried.

Judging from the standard deviations in the tables, the Cook model results in the worst fits with HASDM. The Sentman [*Sentman*, 1961] and ANGARA [*Fritsche et al.*, 1998] models perform about equally well, with a slight advantage for ANGARA, in terms of standard deviation, and the fixed model scores in between. The improved physical representation of Sentman and ANGARA over Cook is thus confirmed. The fact that the fixed aerodynamics scores better than Cook's is further evidence that the wrong aerodynamics assumptions were used in most publications about CHAMP and GRACE data processing before 2008 (e.g. [*Bruinsma and Biancale*, 2003; *Sutton et al.*, 2007]). The model parameters, such as the accommodation coefficient α, while significantly affecting the mean, do not have much impact on the standard deviation, although the influence is a bit larger in the case of Cook's model, especially for CHAMP.

Horizontal wind models

The density data has been processed with horizontal winds assumed zero, and with the HWM-93 model or HWM07 model applied. HWM07 was only tested for CHAMP. In the processing algorithm, the output of the wind models is added to the relative velocity vector, which enters in quadratic form in the density derivation equations. The wind has an indirect effect as well, since the drag coefficient is a function of the relative velocity vector. The use of a wind model results in only very slightly lower standard deviations. There is no effect on the mean. Also, no firm distinction can be made between the HWM-93 model and HWM07 model. The use of a wind model therefore has a fairly modest positive effect on the density derivation results.

Log-normal mean of the ratios and offsets between data and models

The offsets in the mean of the density ratios of data over model were a major concern during the discussions at the second progress meeting in Potsdam. Tables 9.2 and 9.3 show that a wide range of mean values are possible, depending on the choice of the aerodynamic model and aerodynamic parameters made during the processing.

It has to be remarked that the ideal ratio of 1.0 in the data over HASDM ratio does not necessarily mean that the data represent (on average) the true situation. HASDM is based on the analysis of orbital decay due to drag of a large number of calibration satellites, and the ballistic coefficients for these objects is based on an analysis using an empirical model. This empirical model in turn likely contains a bias with respect to the truth. In addition, biases between data and models can be introduced due to incorrect aerodynamic modelling, misrepresentation of physical phenomenon, etc. They can therefore be functions of parameters such as the altitude, composition, temperature, and related parameters such as the level of EUV input, magnetic activity, etc. Such variations will not show up in the single mean values of these Tables.

Because of these reasons, the mean values will not be interpreted here in much depth. There are just a few observations that can be made, without the risk of having to delve too deeply into all the complicated (and sometimes controversial) matters that surround the determination of absolute densities.

- The ratios for GRACE are generally higher than for CHAMP, even if consistent processing choices have been made. This indicates an important inconsistency in the modelling somewhere, most likely either in the aerodynamic model or in the height variation of the HASDM model.
- The choice of the use of a wind model in the processing does not affect the mean.
- The dual-axis approaches result in slightly higher mean values than the single-axis direct approach.
- The ANGARA model results in a higher mean (and closer to one) than the Sentman panel model for CHAMP, while the standard deviations are identical.
- Lowering the energy accommodation coefficient α results in a lower mean, even though the standard deviation remains about the same.

- Lowering the Maxwell coefficient σ used in the ANGARA model results in a higher mean, even though the standard deviation remains about the same.

Chapter 10

Calibration of empirical density models

In this work package, the NRTDM density calibration software is adapted to accept accelerometer-derived density data. The NRTDM software was originally set up to adjust empirical density models based on Two-Line Element-derived density data. A full description can be found in the final report *Doornbos* [2006], and results of that study were also published in *Doornbos* [2007], *Doornbos et al.* [2007] and *Doornbos et al.* [2008].

In Section 10.1, the methods by which the empirical models are adjusted is reviewed. Section 10.2 will present the results of the calibration using accelerometer-derived density data.

10.1 Parameterization methods for density model calibration

The process of density model calibration involves the estimation of a set of calibration parameters. The estimation is based on a least-squares adjustment, using the Levenberg-Marquardt algorithm [*Moré et al.*, 1980; *Bevington and Robinson*, 2003; *Press et al.*, 2007], in order to minimize the difference between TLE-derived observed density values and their equivalent values computed using the parameterized model. The next paragraphs will discuss the two ways of parameterizing the density model which have been tested.

10.1.1 Height-dependent model density scale factors

The first parameterization method uses height-dependent scale factors. If the unadjusted empirical model density is designated ρ_m, then the adjusted model is calculated by multiplying this value with a scale factor f:

$$\rho_{adj} = f(h, \phi, \lambda_\odot) \cdot \rho_m \tag{10.1}$$

The scale factor f can be a function in 3-dimensional space, expressed in height h above the Earth's surface, latitude ϕ and local solar time $\lambda_\odot$.

The height variation of f is accomplished by a piecewise-linear interpolation between a set of N_{f_h} scale factors f_{h_i} at predefined reference heights h_i. Above and below the bottom-most and top-most reference height (h_1 and h_N, respectively),

the scale factor is kept constant. This is illustrated in Figure 10.1.

$$f = \begin{cases} f_{h_1} & \text{if } h < h_1 \\ f_{h_i} + \frac{h-h_i}{h_{i+1}-h_i}(f_{h_{i+1}} - f_{h_i}) & \text{if } h_i \leq h \leq h_{i+1} \text{ for } i = 1, ..., N_{f_h} - 1 \\ f_{h_N} & \text{if } h > h_N \end{cases} \tag{10.2}$$

If N_{f_h} equals one, there is no height-dependence in the correction, and the value of h_1 is irrelevant.

This scheme is a simple improvement over the method used by *Yurasov et al.* [2005*b*], in which a two-parameter correction corresponding to a scale factor with a slope in height was estimated. In their method, the density multiplication factor will reach unrealistic values at low and high altitudes. Therefore, such an adjustment will certainly result in invalid density values above and below the perigee height range of the calibration data, even though the original unadjusted model could still be valid there. In (10.2), this behaviour is avoided if the heights h_i are set within the height span of the calibration data.

The height levels introduced above offer the possibility for adding spatial resolution of the density correction function in the vertical direction. In order to accomodate spatial variations in the horizontal plane, each height-dependent scale factor f_{h_i} can be expanded in a set of spherical harmonics in latitude ϕ and local solar time $\lambda_\odot$. In analogy to the Fourier-series expansion for two-dimensional datasets, spatial features in the horizontal plane around the Earth can be represented using the equation:

$$f_{h_i} = C_{00}^{h_i} + \sum_{n=1}^{N_{h_i}} \left[\sum_{m=0}^{n} C_{nm}^{h_i} P_{nm}(\sin\phi)\cos(m\lambda_\odot) + \sum_{m=1}^{n} S_{nm}^{h_i} P_{nm}(\sin\phi)\sin(m\lambda_\odot) \right] \tag{10.3}$$

The coefficients $C_{nm}^{h_i}$ and $S_{nm}^{h_i}$ are the model parameters that are to be estimated using the density observations, while P_{nm} are the associated Legendre functions of degree n and order m. The low degree and order spherical harmonic coefficients have a clear physical interpretation: C_{00} is a global scale factor. Its default value should be set to one. The higher degree and order coefficients are the ones that allow for variation in the horizontal plane. Their default value is zero. The three components of degree and order 1 allow for an offset with respect to the geocenter: C_{11} for the X-direction, S_{11} for Y and C_{10} for Z. Zonal coefficients, where $m = 0$, can represent variations in latitude only: C_{20} introduces a flattening (ellipsoidal instead of spherical shape) and C_{30} a hemispherical asymmetry with respect to the equator (pear-shape).

Figure 10.1 illustrates this calibration scheme where a linear interpolation is used between two height levels, at 300 and 500 km altitude. At the lower level, a spherical harmonic expansion up to degree and order 1 is used, while at the higher level, the expansion is to degree and order 2. Using such low order spherical harmonics, the shape, position and amplitude of the diurnal density bulge can be easily modified. If sufficient data are available, higher order spherical harmonics could be used to represent shorter wavelength density fluctuations, but this has not been tested during this study.

10.1.2 CIRA-72 temperature corrections

A second tested parameterization method involves the use of CIRA-72 temperature corrections. The scheme is based on the Dynamic Calibration Atmosphere

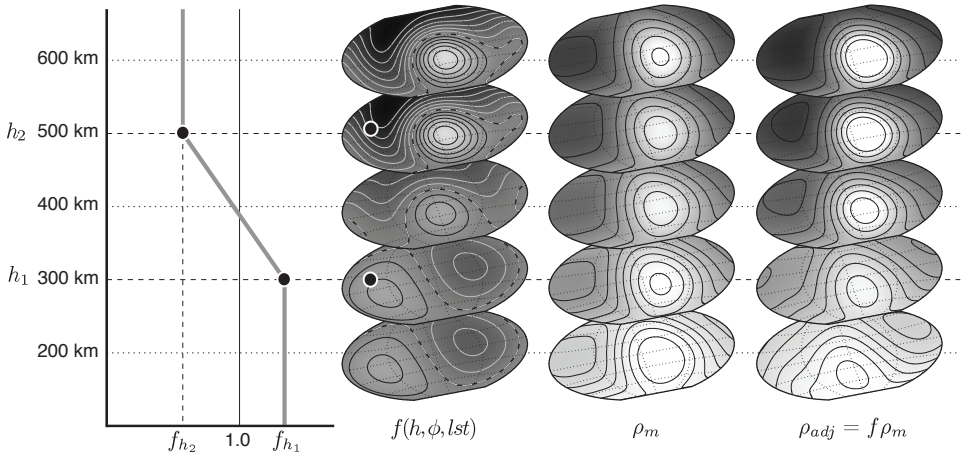

Figure 10.1 Illustration of the height-dependent scale factor calibration scheme, using two height levels, at 300 and 500 km, with spherical harmonic expansions up to degree and order 1 and 2, at each height level, respectively.

(DCA) [*Bowman and Storz*, 2002; *Casali and Barker*, 2002] used in the HASDM project [*Storz et al.*, 2005]. In order to explain the scheme, it is necessary to read the short introduction to the way the CIRA-72 model computes temperatures and densities, given in Section 2.5.1. A full description and source code of the model are available in *Jacchia* [1972].

As explained in Section 2.5.1, vertical density profiles at a given location are computed by integrating the hydrostatic and diffusion equations from the lower boundary conditions, based on a temperature profile that is a function of two temperatures T_x and T_∞.

In this second calibration scheme, two corrections to these temperatures, ΔT_x and ΔT_∞, are both expanded in spherical harmonics, in a similar manner as the height-dependent scale factors of (10.3). A set of spherical harmonic coefficients of these temperature corrections, $C_{nm}^{T_x}$, $S_{nm}^{T_x}$, $C_{nm}^{T_\infty}$ and $S_{nm}^{T_\infty}$, can then be estimated during the calibration procedure.

The resulting corrections ΔT_∞ and ΔT_x are then added to the equations (2.9) and (2.10), as follows:

$$T_\infty = T_c\, D + \Delta T_G + \Delta T_\infty \tag{10.4}$$

$$T_x = a + bT_\infty + c\, \exp(kT_\infty) + \Delta T_x \tag{10.5}$$

The complete temperature profile and local densities are then computed using the standard model formulations, as explained in Section 2.5.1. Figure 10.2 illustrates the influence of the calibration parameters on the temperature and density profiles of the CIRA-72 model.

10.1.3 Pros and cons of the two calibration methods

A theoretical disadvantage of the temperature correction method is that adjustments can only be made with two degrees of freedom in the vertical. A benefit of the temperature calibration scheme over the scale factor scheme is that the estimated parameters have a physical meaning in the model. The scale factors apply only to the total neutral density. Therefore, the temperature and composition results of the original model remain unaffected by the scale factors, and are

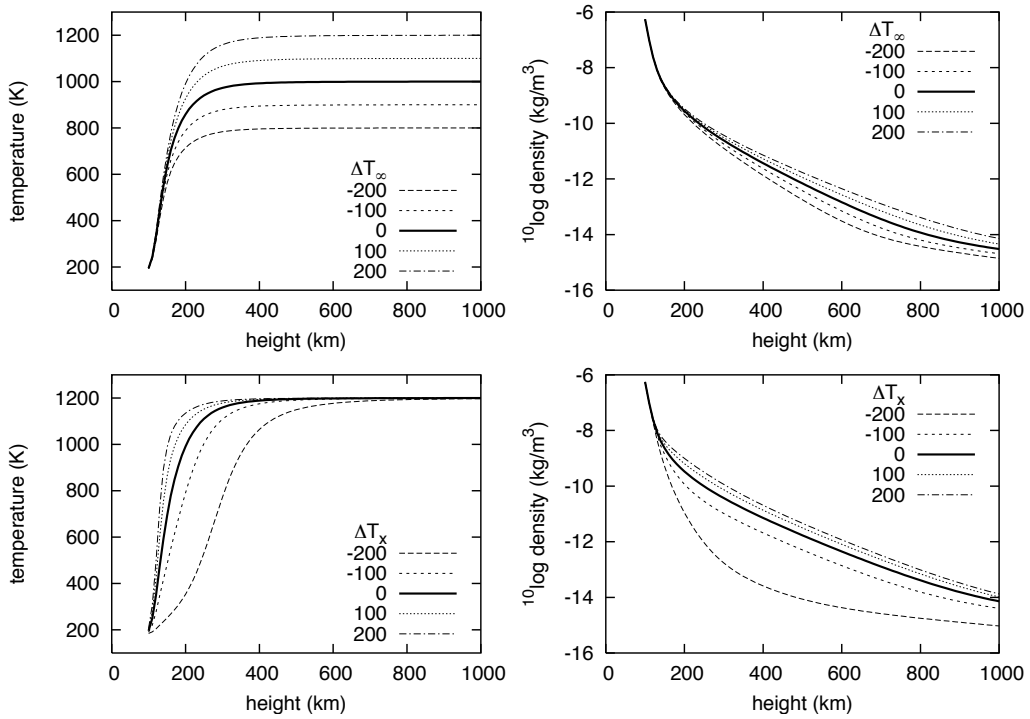

Figure 10.2 Vertical profiles of density and temperature for various values of the calibration corrections for the inflection point and exospheric temperatures.

no longer physically coherent with the scaled total density. In contrast, the corrected temperatures are at the basis of the CIRA-72 model, in which density and composition are computed based on physical principles from these temperatures.

Note however that the value of the corrected temperature at 125 km should not be interpreted as representing the true temperature at this altitude. The uncorrected temperature parameter is closely tied to the lower boundary conditions of the CIRA-72 model, and its correction will be extrapolated from drag data above 200 km through the temperature-density relations of the model, both of which will introduce considerable uncertainties.

10.2 Calibration results

The calibration results will be presented in two parts. First, the time series of model calibration parameters will be studied, and then the calibrated models are evaluated along the CHAMP and GRACE satellite tracks, and compared with their input data and with independent density data.

10.2.1 Time series of calibration parameters

The most simple calibration possible is the application of a single scale factor (C_{00}), at a single height level. This scale factor, estimated from the accelerometer data, is then applied to all the density model output. Such a calibration has been performed twice, one time using data from only the CHAMP satellite and one time using only the GRACE satellite data. In this case, the CH_PN_R03 and GA_PN_R03 categories have been used, and the DENSWIND_ITER3_SENTMAN_ALPHA0.9 products from those categories were

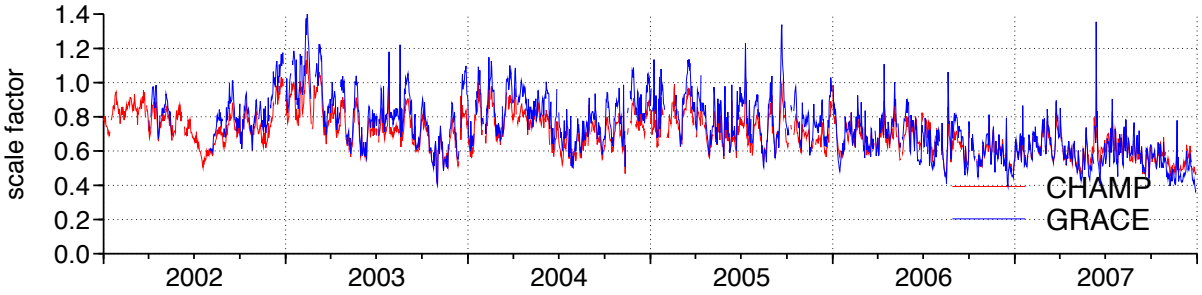

Figure 10.3 Estimated density model scale factors (C_{00}) for the NRLMSISE-00 model, comparing the CHAMP data (red line) and GRACE data (blue line) density data, used separately.

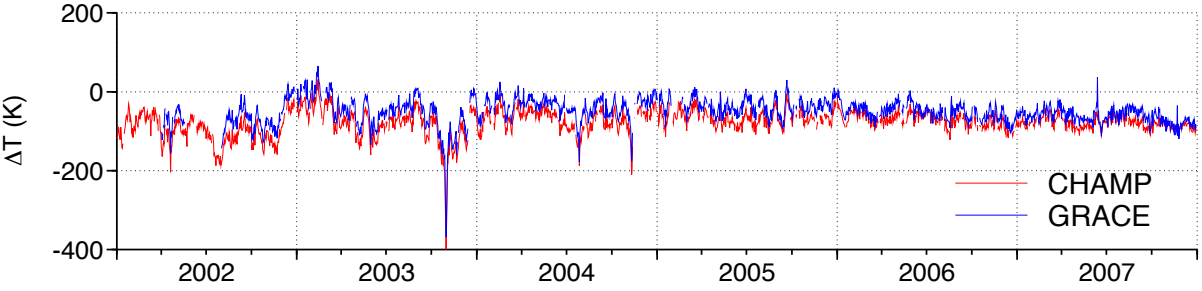

Figure 10.4 Estimated CIRA-72 exospheric temperature adjustments ($C_{00}^{T_\infty}$) comparing the CHAMP data (red line) and GRACE data (blue line), used separately.

chosen. These products contain density error estimates, which were used for weighting the data. The density model scale factors for the NRLMSISE-00 model were estimated on a daily basis.

The resulting time series is visible in Figure 10.3. It is clear that the scale factor time series for both satellites are very similar, even though the satellites are at different altitudes, and their local solar time coverage changes continually. This result is in line with the findings from the TLE-derived densities in *Doornbos* [2006]. It indicates that there is a large global, time-varying error, which is largely due to the incorrect representation of solar EUV heating (through the $F_{10.7}$ proxy) in the empirical models.

The GRACE-derived scale factors are a little higher than those from CHAMP, in the earlier years. However, for both satellites, the scale factors are generally below one, indicating that the NRLMSISE-00 model is scaled down, and was originally predicting densities that were too high. At high solar activity, there are large variations at approximately the solar rotation rate, indicating that the model calibration compensates for inaccurate representation of the solar EUV radiation energy input in the thermosphere. At low solar activity, the scale factor becomes lower and lower. This might be related to the long-term thermospheric cooling trend, which in other analyses was shown to be strongest at solar minimum [*Emmert et al.*, 2008*a*].

A similar analysis can be made using the CIRA-72 temperature adjustments. Those results are visible in Figure 10.4. The discrepancy between the modelled and observed densities translate into an exospheric temperature that is about 100 K lower, than predicted by Jacchia's temperature equations (2.8) and (2.9), based on $F_{10.7}$ and a_P. Note that this mean offset could be related to errors in the accelerometer processing, such as the panel areas, accommodation coefficient, etc., as well as to errors in the a priori models. Note that an offset of the same mag-

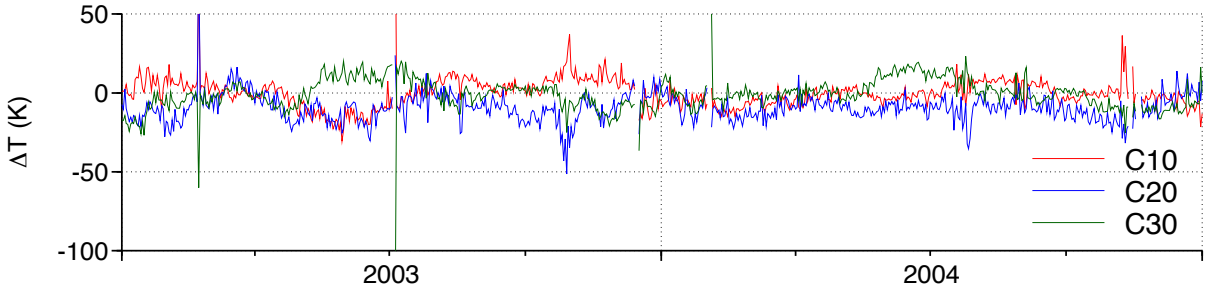

Figure 10.5 Estimated zonal components ($C_{10}^{T_\infty}$, $C_{20}^{T_\infty}$ and $C_{30}^{T_\infty}$) of the CIRA-72 exospheric termperature adjustment, using the CHAMP and GRACE data combined.

nitude is visible both at high solar activity (2002) and at low solar activity (2007). This is in contradiction to the conclusions of [*Emmert et al.*, 2008*a*], which showed a larger temperature difference between data and models at solar minimum than at solar maximum. However, their analysis was based on the NRLMSISE-00 model, not the CIRA-72 model, and they used TLE-derived drag data over a much longer time span, spanning multiple solar cycles.

There is a large variation of the temperature about this mean of about 50-100 K at high solar activity. This variability decreases at low solar activity. There is a significant peak of up to -400K around the time of the October 2003 storms, suggesting that the CIRA-72 model was overestimating the temperature change due to the sudden large additional energy input at that time.

Figure 10.5 shows the exospheric temperature change time series for the CIRA-72 adjustment at the first, second and third order zonal components. Contrary to the previous plots, these values were estimated from the combined processing of CHAMP and GRACE data. The C_{10} and C_{30} components represents a North-South shift, the C_{20} component a shift from the poles to the equator or vice versa. The temperature corrections have an amplitude of about 20–30 K. Large peaks are visible around the October 2003 storm and other solar and geomagnetic activity related events. There are also some clear outliers, which should be investigated. But most of the variation in these time series seems to be at longer wavelengths, such as at the annual and semi-annual periods. This indicates that the calibration adjusts for inadequate representation of seasonal and local solar time variations in the original CIRA-72 model.

10.2.2 Evaluation of calibrated densities along CHAMP and GRACE trajectories

The evaluation of calibration results is done by making use of the scale-factor approach only, where NRLMSISE-00 is used as the a priori model. The calibrations are done by estimating only a single scale factor (C_{00}), or a series of four zonal harmonics (C_{00}, C_{10}, C_{20}, C_{30}), over intervals of 3 hours and one day. Due to the limited altitude range of the accelerometer measurements, all adjustments are made without taking into account height variations.

Figure 10.6 gives an illustration of what the calibrated data looks like, compared to the original densities, and the uncalibrated model.

For both CHAMP and GRACE-A, the various calibrated models are evaluated using statistics of the data along the satellite tracks. The data over calibrated model density ratios are computed, and the log-normal mean and standard devi-

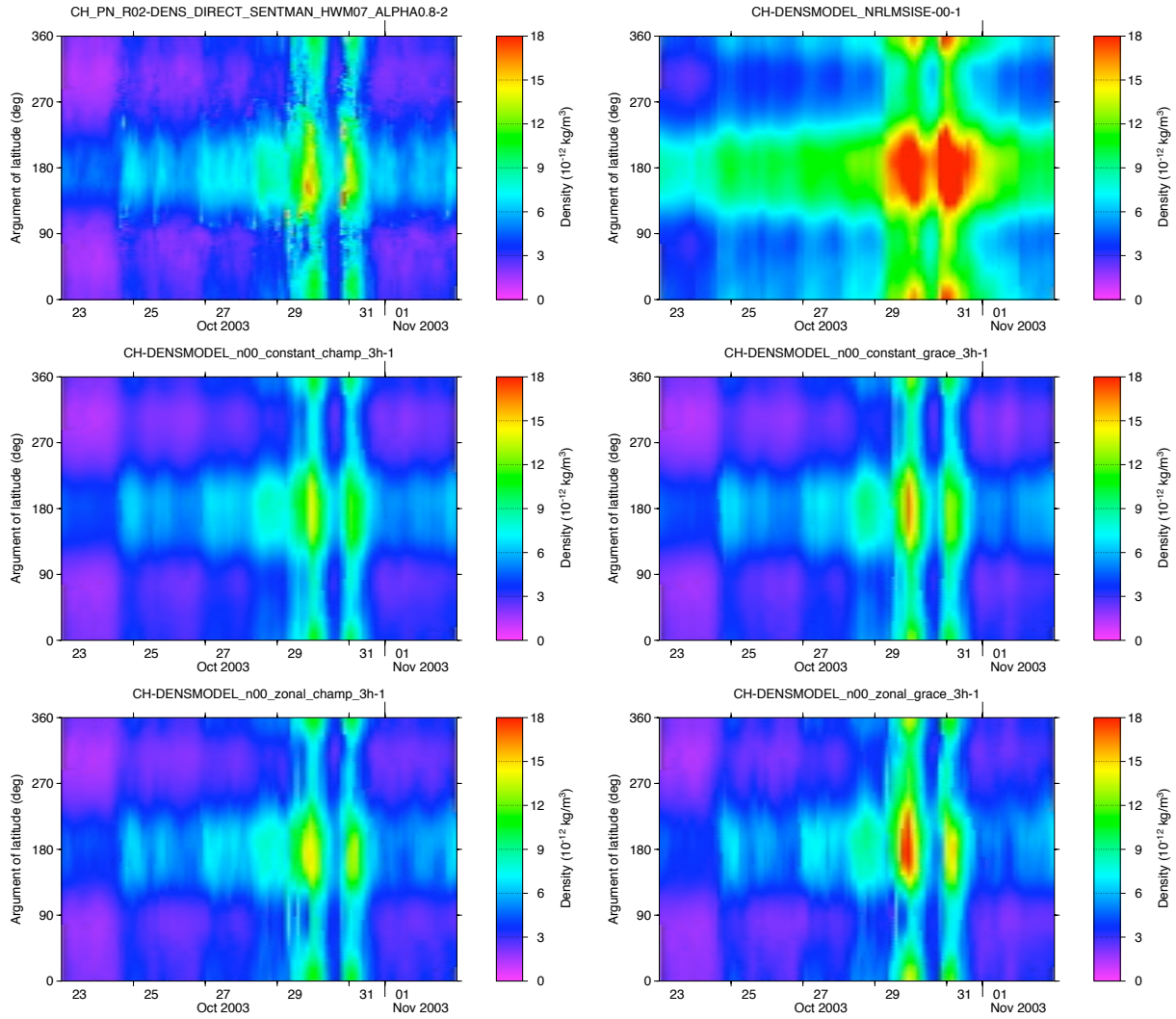

Figure 10.6 Comparison of calibrated densities along CHAMP tracks, for the period around the October 2003 geomagnetic storm. The top row contains the accelerometer-derived CHAMP density data (left), and the uncalibrated NRLMSISE-00 model output (right). The other rows contain calibrated model results using only a constant scale factor (second row), and one using the additional zonal harmonics (third row). In these rows, the CHAMP data itself was used for the panels in the left column, and independent GRACE data for the panels in the right column. A 3-hourly calibration interval was used.

base model	cal. data	parameters	interval	N	$\mu*$	$\sigma*$
NRLMSISE-00	–	–	–	3082484	0.742	1.250
HASDM	–	–	–	3082484	0.770	1.141
NRLMSISE-00	CHAMP data	C_{00}	daily	3082439	1.007	1.151
NRLMSISE-00	CHAMP data	C_{00}	3-hourly	3082433	1.002	1.139
NRLMSISE-00	CHAMP data	C_{00}, C_{10}, C_{20}, C_{30}	daily	3082453	1.004	1.144
NRLMSISE-00	CHAMP data	C_{00}, C_{10}, C_{20}, C_{30}	3-hourly	3082430	0.996	1.119
NRLMSISE-00	GRACE-A data	C_{00}	daily	2987384	0.928	1.168
NRLMSISE-00	GRACE-A data	C_{00}	3-hourly	2981968	0.922	1.159
NRLMSISE-00	GRACE-A data	C_{00}, C_{10}, C_{20}, C_{30}	daily	2987384	0.918	1.168
NRLMSISE-00	GRACE-A data	C_{00}, C_{10}, C_{20}, C_{30}	3-hourly	2980880	0.906	1.155

Table 10.1 Log-normal statistics of data/model density ratios, evaluated along the CHAMP orbit, over the year 2003.

base model	cal. data	parameters	interval	N	$\mu*$	$\sigma*$
NRLMSISE-00	–	–	–	2997772	0.801	1.325
HASDM	–	–	–	2997772	0.867	1.184
NRLMSISE-00	GRACE-A data	C_{00}, C_{10}, C_{20}, C_{30}	daily	2997711	0.993	1.187
NRLMSISE-00	GRACE-A data	C_{00}, C_{10}, C_{20}, C_{30}	3-hourly	2996623	0.980	1.155
NRLMSISE-00	CHAMP data	C_{00}	daily	2980444	1.089	1.207
NRLMSISE-00	CHAMP data	C_{00}	3-hourly	2979356	1.084	1.193
NRLMSISE-00	CHAMP data	C_{00}, C_{10}, C_{20}, C_{30}	daily	2989101	1.086	1.200
NRLMSISE-00	CHAMP data	C_{00}, C_{10}, C_{20}, C_{30}	3-hourly	2979356	1.077	1.178

Table 10.2 Log-normal statistics of data/model density ratios, evaluated along the GRACE-A orbit, over the year 2003.

ation of these ratios are computed (as explained in Section 9.2), and presented in Tables 10.1 and 10.2. Only data for the year 2003 was used for this evaluation.

These tables contain three sections. The top section shows the statistics for NRLMSISE-00 and HASDM, that were evaluated in Chapter 9 as well, although that was for a different time period. These data, especially the uncalibrated NRLMSISE-00 statistics, serve as a reference for the improvement that the calibration can bring. The evaluation of the HASDM model was included as well, in order to be able to compare whether the calibration with accelerometer data from just one mission can compete with the calibration using many radar-tracked calibration objects.

The second section contains the results of the calibration using data from the same satellite as is used in the evaluation. This is of course not a fair evaluation of the benefits of the calibration, but these statistics are included in order to evaluate the limits of the parameterization that are used. For example, the log-normal means of the data/model density ratios is within 1 percent for CHAMP and within 2 percent for GRACE. These numbers are not exactly equal to one, probably because of the fact that the data are weighted in the calibration, and not in the evaluation. The standard deviations decrease significantly with the introduction of additional calibration parameters, as expected. However, only in

the case of the estimation of four zonal harmonic parameters over 3-hourly time intervals, do the calibrated models outperform HASDM. And this is when the same data are used for calibration and evaluation, while the HASDM calibration is done with independent data. This result serves as an excellent example of the validity of the HASDM data.

The third section in these two tables shows the results for the calibration with independent data. As expected, these are somewhat worse than in the case where the same data are used both for evaluation and calibration. Still, a very significant improvement over the uncalibrated NRLMSISE-00 model is seen.

In the case of the evaluation along the GRACE-A track, the calibrated model using only CHAMP data results in a lower standard deviation than the HASDM model, which is calibrated using many radar-tracked objects. This demonstrates the validity of the CHAMP data for thermospheric density modelling.

The GRACE-calibrated model, evaluated along the CHAMP trajectory does not exceed the performance of HASDM. This could indicate that improvements to the GRACE density data processing are possible.

It would be interesting to evaluate the performance of CHAMP and GRACE calibrated models in the orbit determination of higher altitude satellites, such as ERS-2, Envisat and Cryosat-2. Perhaps the higher altitude GRACE data will bring in more value there. Another exciting possibility for future investigations is the calibration of density models using combined data from accelerometers and TLE data. As recommended by an earlier feasibility study for ESA/ESOC [*Doornbos*, 2004; *Doornbos et al.*, 2005], these two data types could complement each other. The accelerometer data provides high temporal and spatial resolution along a narrow satellite track, while TLE-derived densities could provide global spatial coverage, if enough calibration objects are available, albeit at a much lower temporal resolution. The cross-calibration of such data sets would be an interesting investigation by itself.

Chapter 11
Geophysical Interpretation

Within this Chapter we perform some validity checks of the density and wind processing results. It is closely related to the comparison with existing empirical density and wind models as it was outlined in Chapter 9, but in distinction to that we try now to find some self-consistent means to check the correctness and plausibility of the density and wind estimations obtained. For this task, we partially have to make use of the mentioned empirical models and we will try to interpret the preliminary results in a geophysical context.

The data analyses of this Chapter rely on the broad lay-out and well-organized data product storage and retrieval system of this project. It makes ample use of its various data products. Most data sets of the CHAMP and GRACE missions stored there have a standard time resolution of 10 sec. They constitute therefore, depending on the period lengths considered, quite large data files in terms of memory allocation.

The download and ingestion of the ASCII data files appeared as a first "bottleneck" of the analysis procedures because of their relatively long processing times. Nevertheless, the fact that all relevant data files of the storage system are given as continuous and equidistant time series with the same 10-sec cadence (where data gaps are marked by specific "fill values"), proved to be very convenient for an efficient reading of the ASCII data tables. The data files that have been selected for further local use within the frame of these geophysical efforts have then been converted into binary files using the CDF storage routines of IDL (.cdf data files). This was done for the benefit of less memory consumption and faster Input/Output processing times at the local computer network.

Several "handy" interval lengths of the data files to be investigated were tested that reached from one-day files over one-month series up to one-year packages. We use mainly (if not otherwise stated explicitely) the first field from the CH/GA/GB_PN_R02:DENS_DIRECT_SENTMAN_ALPHA0.8 products for the thermospheric density analyses (in Sect. 11.1), which depends only on the along-track accelerometer (x-axis) measurements. For the thermospheric wind studies (in Sect. 11.2) we preferably used the CH/GA/GB_PN_R03:DENSWIND_ITERATIVE2_SENTMAN_ALPHA0.8 products because of the more advanced calibration level ("R03", see Section 7.4) that appeared to be crucial for the use of the sensitive cross-track component and the particular data analysis technique of iterative estimations.

Both Fortran and IDL-programs have been used for the data analyses of these geophysical tests.

11.1 Thermospheric Mass Density

For the geophysical analyses in this and the subsequent sections, we use data of a seven-year interval (2001-2007) that comprises all solar activity levels from the maximum year of the 23rd cycle 2001/2002 over the years of declining solar EUV activity but with enhanced geomagnetic activity, including a series of extreme geomagnetic storms ("superstorms") in particular in 2003, up to the solar minimum years 2006/2007.

As for CHAMP, an (at least) five-year period has some "practical" benefits. The orbital precession rate of CHAMP is 15° within an 11-day period which is equivalent to a full local time (LT) coverage for both ascending and descending wings of the orbits within ≈262 days. We can therefore achieve almost exactly 7 full LT coverages within a five-year period, which covers also different seasons sufficiently well for the various local time ranges. The GRACE satellites with their slower precession rate, however, perform only about $5\frac{2}{3}$ full LT coverages within five years, i.e. one full coverage in ≈322 days, which leads to an interference between seasonal and local time dependences.

11.1.1 Comparison of ascending and descending orbits

A first evident test of the validity of density estimations obtained with the various approaches of this study, is the comparison of the measurements from ascending and descending orbits during the same local times. As mentionend above, due to the orbital constraints of CHAMP with its near-polar circular orbit and an inclination of about 87°, the different branches of the orbit within one and the same local time slice are about 4 months apart (more exactly: ∼131 days). The altitude variations (orbit ellipticity and the decay rate) are quite small and are neglected for the first approach (for some refinement in this regard, see below).

Figure 11.1 shows an example of such a comparison of the descending (upper panel) and ascending (lower panel) orbital branches for the year 2003. The measured quantity is in this specific case derived from the "Dens_Direct_ANGARA" retrieval method, where the density is estimated from the accelerometer measurements in the S/C x-direction while neglecting any possible neutral wind influence in this along-track direction. The densities are drawn in a linear scale versus local time and color-coded with the actual values of the F10.7 solar index, which stands as proxy for the solar EUV radiation intensity. The time interval from Jan 15 to Oct 03, 2003, was chosen such that each local time moment is covered by both ascending and descending orbits (262 days) as CHAMP's orbital plane is precessing during this time once through the full 360° local time azimuth.

The predominant density variation as shown in Figure 11.1 is that of the diurnal variation with a more-or-less sinosoidal behaviour. Despite of the density modulations, that are mainly due to varying solar activity (see below), the upper and lower smoothed envelopes reveal maximum and minimum values at about 14 MLT and in the early morning sector at about 04 MLT, respectively. This is at least true for the descending orbits in the upper panel. It is in accordance with the generally accepted view of diurnal thermospheric density variations which is well-known for long time (see, e.g., *Jacchia and Slowey* [1968]). The diurnal density variation of the ascending orbits (lower panel) for this time interval seems to have somehow phase shifted maximum and minimum values at sunset time (≈18 MLT) and during sunrise (≈06 MLT), respectively.

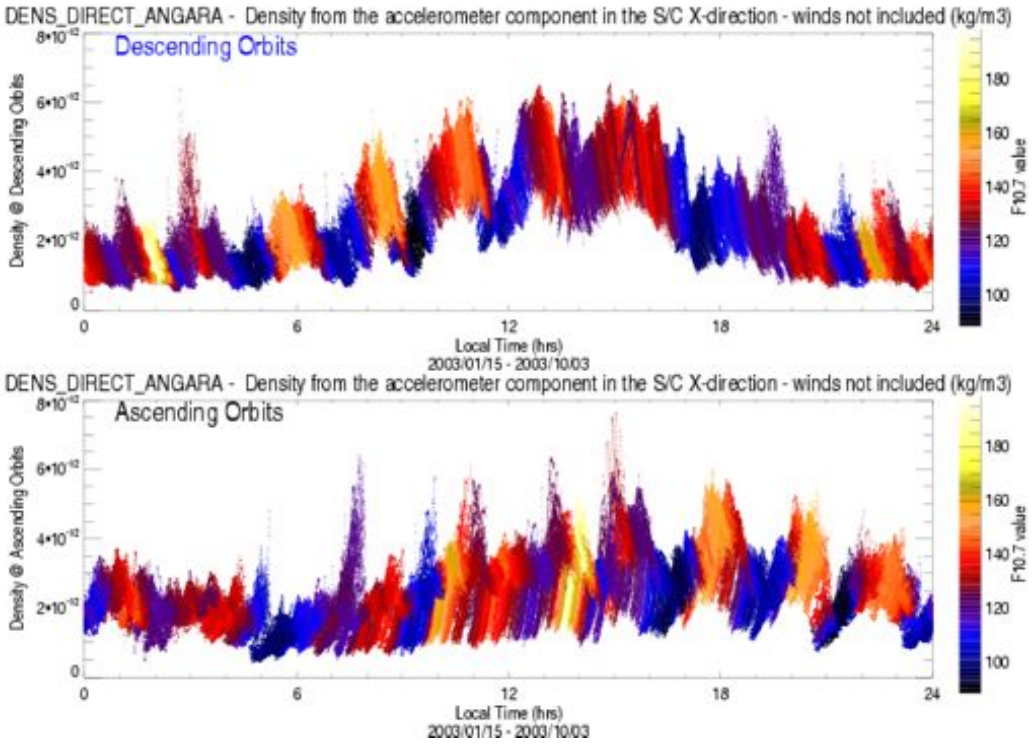

Figure 11.1 CHAMP density variations at low- to mid-latitudes ($\pm 60°$) for descending (top panel) and ascending (bottom) orbits of a 262-days-interval in 2003 separately, color-coded with the actual F10.7 index values.

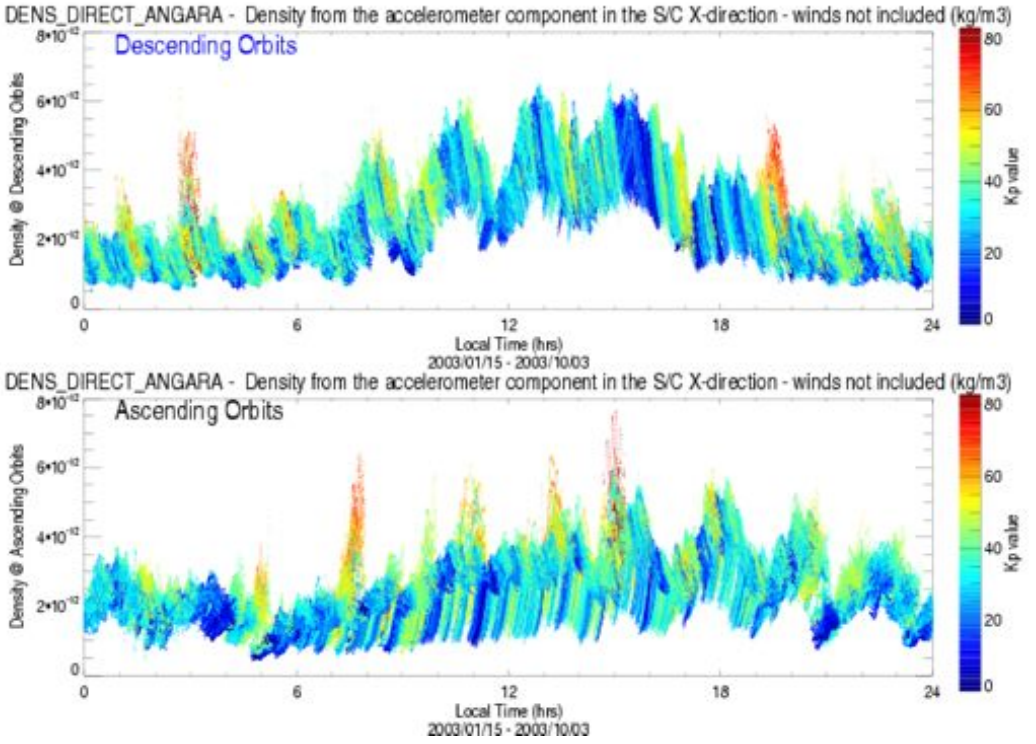

Figure 11.2 The same density variation as in Figure 11.1, but color-coded with the planetary geomagnetic Kp index (color scale multiplied with 10).

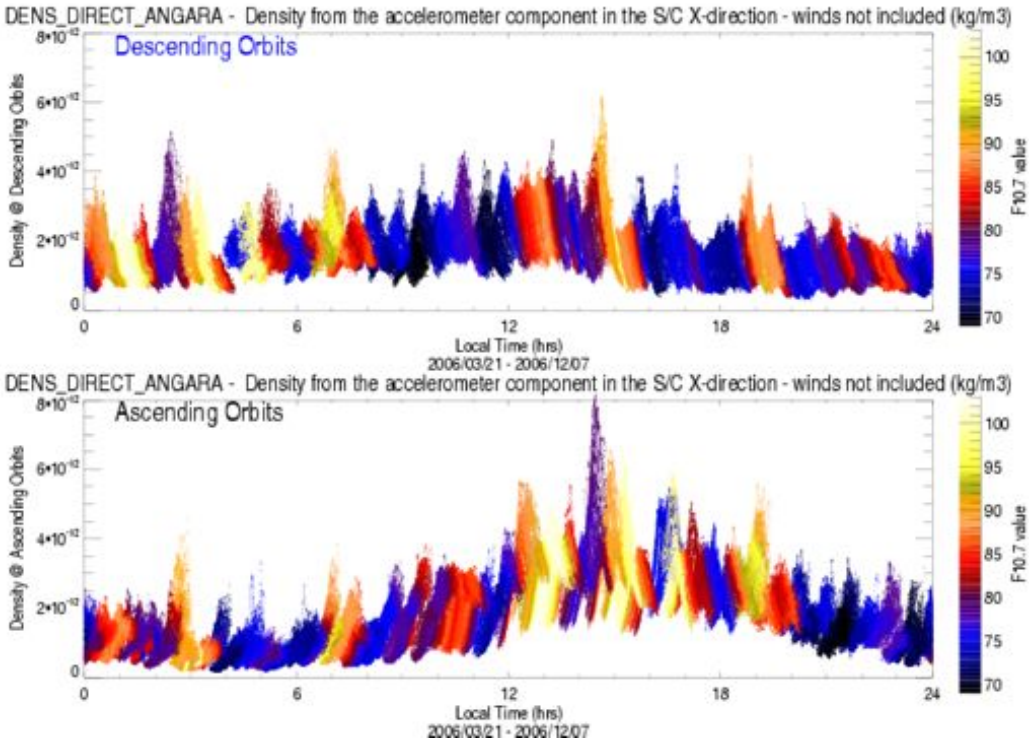

Figure 11.3 The same density variation versus local time in dependence on the solar activity index F10.7 as in Figure 11.1, but for the low solar activity year 2006. The same ordinate scale length is used for direct comparison.

The density variation shows also a distinct modulation with an amplitude of about factor two. The modulation is clearly correlated with the solar activity index F10.7, which is used as a proxy for the solar EUV radiation intensity. The intervals of enhanced mass density ("bulges") during certain local time intervals can be mostly identified as periods of enhanced F10.7 values; the time intervals in between ("valleys") are characterized by low F10.7 values with the blue end of the color scale. The year 2003 on the declining solar cycle was characterized by an on average medium solar activity level of about $F_{10.7} \approx 130$ with large-amplitude regular variations of the F10.7 flux that followed the 27-day solar rotation period (for the pecularities of the solar flux variation see, for example, *Vellante et al.* [2007]). At the same time, we observed very intense geomagnetic activity throughout the year 2003, which culminated in the occurence of so-called superstorms at the end of October and in November 2003. The density modulations clearly follow the variations in F10.7.

There are short intervals with even larger excursions to even more severe density enhancements which are related to geomagnetic disturbance periods. This is also illustrated in Figure 11.2 which shows the same density variation as Figure 11.1, but this time color-coded with the planetary geomagnetic Kp index. The geomagnetic activity is much more fine-structured and not related to the factor-two amplitude modulation. There are, however, short intervals of high-density excursions, indicated by the reddish colors of the upper end of the color scale as, e.g., near 07:30 LT of the ascending orbits (lower panel), corresponding to the peak near 19:30 LT of the descending orbits (upper panel), that belong to one and the same geomagnetic disturbance period.

The large-amplitude modulations due to the solar flux variations together

with different geomagnetic activity levels and possible seasonal density variations during the different times of the ascending and descending orbital branches complicate the direct comparison. The largest effects during the year 2003 are obviously caused by the large solar flux variations. One has to find some proper mean to overcome these difficulties and to find an objective measure to reduce these variations to a common reference level.

The study of *Liu et al.* [2005] discusses the correlation between the mass density variation and the solar EUV radiation. They find an approximate linear correlation in their case study of the year 2002 (high solar activity) with relatively high correlation coefficients of the order of 0.7. These correlations were derived separately for quiet and moderate geomagnetic conditions as well as for both dayside and nightside sectors (Figure 7 in *Liu et al.* [2005]). The CHAMP accelerometer measurements used for the analysis were confined to a latitude range of $\pm 30^\circ$ magnetic latitude. The effect of F10.7 on the mass density variation is shown to be stronger on the dayside than on the nightside:

$$\begin{aligned} \rho &= 0.08\, F_{10.7} - 5.31 \quad (daytime) \\ \rho &= 0.05\, F_{10.7} - 3.45 \quad (nighttime) \end{aligned} \tag{11.1}$$

with ρ given in $[10^{-12}\, kg\, m^{-3}]$ and $F_{10.7}$ in the usual units of the solar EUV index. The linear relations in equation (11.1) are valid for geomagnetically quiet conditions (Kp = 0...2) and, as written above, they were derived from the CHAMP accelerometer data set of the high solar activity year 2002.

These simple relations (equation 11.1) could be applied to the data set of our study to reduce the mass density variations, caused by the solar EUV (with its proxy, the F10.7 radiation index), to a common median solar activity level. Such linear relations or, possibly, more complicated relations could be estimated from our complete data set, considering also further dependencies like height and seasonal variations.

An alternative possibility would be the use of existing empirical models to reduce the solar flux dependence of the mass density variations to a common reference according to, e.g., the observed $F_{10.7}$-values to the common level of $F_{10.7} = 130$:

$$\rho_{130}^{obs} = \rho_{F10.7}^{obs} \frac{\rho_{130}^{model}}{\rho_{F10.7}^{model}} \tag{11.2}$$

For this kind of referencing, any empirical thermospheric density model could be used that has an explicit solar EUV index as one of the input parameters. This is the case for all models of common use (see Chapter 9).

Figure 11.3 shows the same density variation versus local time in dependence on the solar activity index F10.7 as in Figure 11.1, but for the low solar activity year 2006. The same ordinate scale length has been used for both plots to ease the direct comparison. The low solar activity level is accompanied by relatively small variations of the F10.7 index, as can be seen by a much smaller or even negligible amplitude modulation compared with the color-scaled solar EUV variation. The variations with the geomagnetic activity are much more prominent, which can be seen by the spiky, short time enhancements as, e.g., at ≈14:30 LT and correspondingly at ≈02:30 LT. Considering intervals outside the geomagnetic disturbances, direct comparisons of latitudinal density profiles during ascending and descending orbital branches could be more reliable, i.e. less disturbed by solar EUV activity changes.

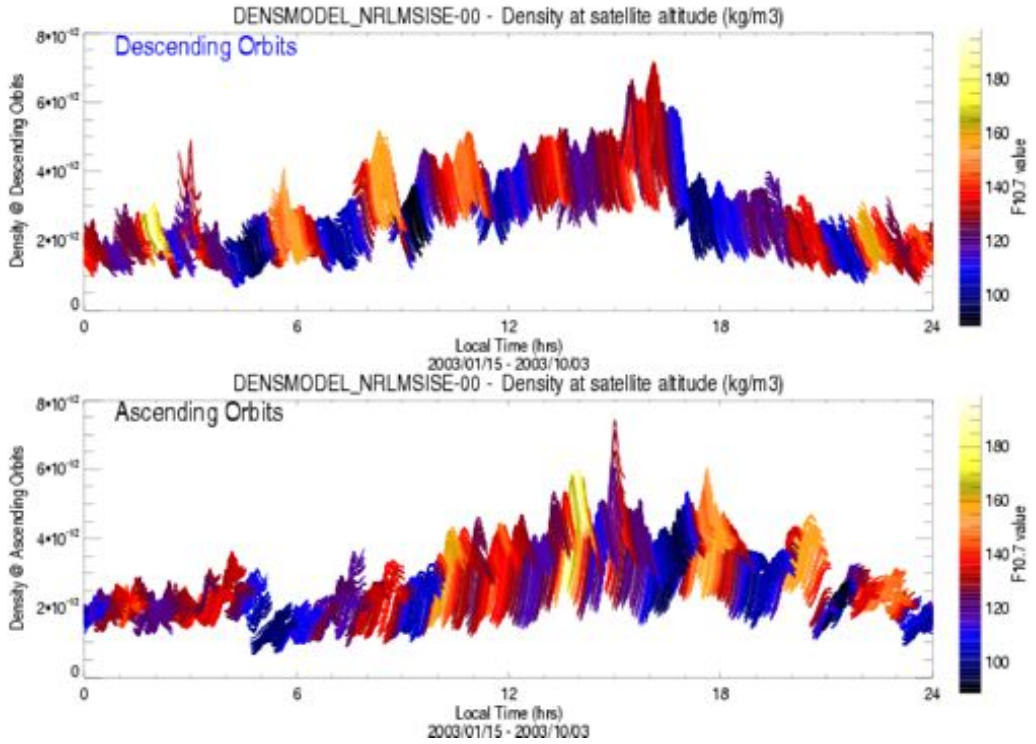

Figure 11.4 NRLMSISE-00 density variations at low- to mid-latitudes ($\pm 60^{\circ}$) for descending (top panel) and ascending (bottom) orbits of a 262-days-interval in 2003 separately, color-coded with the actual F10.7 index values, using the same orbits as CHAMP as well as the same solar and geophysical conditions as shown in Figure 11.1.

The mass density variation with the height of the S/C is also noticable, but obviously less important in case of the near-circular CHAMP orbit. This modulation can be corrected for a common reference height level according to the relation:

$$\rho^{obs}_{400\ km} \;=\; \rho^{obs}_{S/C}\ \frac{\rho^{model}_{400\ km}}{\rho^{model}_{S/C}} \tag{11.3}$$

Figure 11.4 is a pendant to Figure 11.1, but in difference to that the mass density values are generated with the empirical thermosphere model NRLMSISE-00, using the same set of orbits with its orbital elements and the same solar and geomagnetic index values as input to the model. The data points are color-coded with the actual F10.7 index values as in Figure 11.1.

The density variation shows the expected diurnal variation with maximum and minimum values in the afternoon and after midnight, respectively. The step-like variation near $\sim$05 LT of the ascending orbits (lower panel) and correspondingly $\sim$17 LT for the descending orbits (upper panel) are the moments of the start- and end-point of the 262-days-interval. They refer to different seasons of the year which might be the cause for the dicontinuous behaviour during these local times. The modulation with the F10.7 value is also visible, but its amplitudes are diminished for the NRLMSISE-00 model runs (Figure 11.4) in comparison with the CHAMP measurements (Figure 11.1). This might be an indication that the F10.7 dependence of the model is less dynamic than the accelerometer observations, at least with respect to the analysis method used in this case.

11.1.2 The day-to-night mass density ratio

The mass density ratio between the central hours around the maximum and minimum values during daytime and nighttime, respectively, are thought to be relatively constant for the full range of various different solar EUV flux intensities. This might not be true for moderate to strong geomagnetic conditions, during which this ratio becomes smaller as a rule, depending on strong density enhancements during nighttime.

The day-to-night mass density ratio can therefore be used for a further testing of the validity of the density estimations from the accelerometer measurements, if one confines to periods of low geomagnetic activity.

The physical idea behind this reasoning is the consideration of the thermal structure of the Earth's thermosphere. The thermal balance in the thermosphere is governed by the heat conduction equation that comprises various heating sources and losses as well as the heat transport by thermal conduction, which is a function of the neutral temperature itself, thermal advection and convection terms. The Earth's thermosphere is heated primarily due to the absorption of solar extreme ultraviolet (EUV) radiation by the atmospheric constituents. Additionally, at high latitudes and in particular during geomagnetic disturbed periods, other heating sources become important as collisions between charged particles and neutral constituents, the so-called Joule heating, and direct and indirect heating by solar wind influences as energetic particle precipitations in the auroral zone that are mediated through the magnetosphere. The main heat loss is due to emissions in the infrared (IR). Radiative loss by IR occurs when atmospheric constituents are present which have transition levels in the infrared range of the spectrum as it is the case for atomic oxygen in the terrestrial thermosphere [*Bauer*, 1973].

The solution of the time-dependent heat balance equation leads to a time variation of the thermospheric temperature, characterized by the so-called exospheric temperature T_∞, having a maximum which occurs several hours later than that of the maximum EUV heat input (midday), due to the thermal inertia of the atmosphere. The solution of the heat balance equation with realistic inputs leads to a T_∞ maximum at about 17:00 LT (see, e.g., *Bauer and Lammer* [2004], Figure 2.5]). The thermospheric density maximum, on the other hand, occurs around 14:00 LT as it is known for many years from satellite drag observations since the early days of the space era and consequently a temperature maximum was inferred for the same time from atmospheric model considerations [*Jacchia and Slowey*, 1968]. This problem has been termed the diurnal phase anomaly between atmospheric density and temperature by *Chandra and Stubbe* [1970].

At the equator during nighttime conditions, the mass density often shows a secondary maximum around midnight. It was termed the 'Midnight Density Maximum (MDM)' acording to *Arduini et al.* [1997], in reminiscence of the 'Midnight Temperature Maximum (MTM)' observed by *Spencer et al.* [1979].

Nevertheless, the day-night temperature ratio between maximum and minimum temperatures has been shown to be relatively constant (though, also there is a difference between estimates derived from satellite drag observations that range from 1.5 to 2.0 and the theoretical model prediction that gets about 1.3 [*Bauer*, 1973; *Bauer and Lammer*, 2004]), independent of the solar cycle variations of solar EUV flux.

A constant day-night temperature ratio implies that the density ratio should be constant as well at a given height level, but contrary to the thermospheric temperature, which levels out to a height-independent T_∞ above about $\sim$250 km,

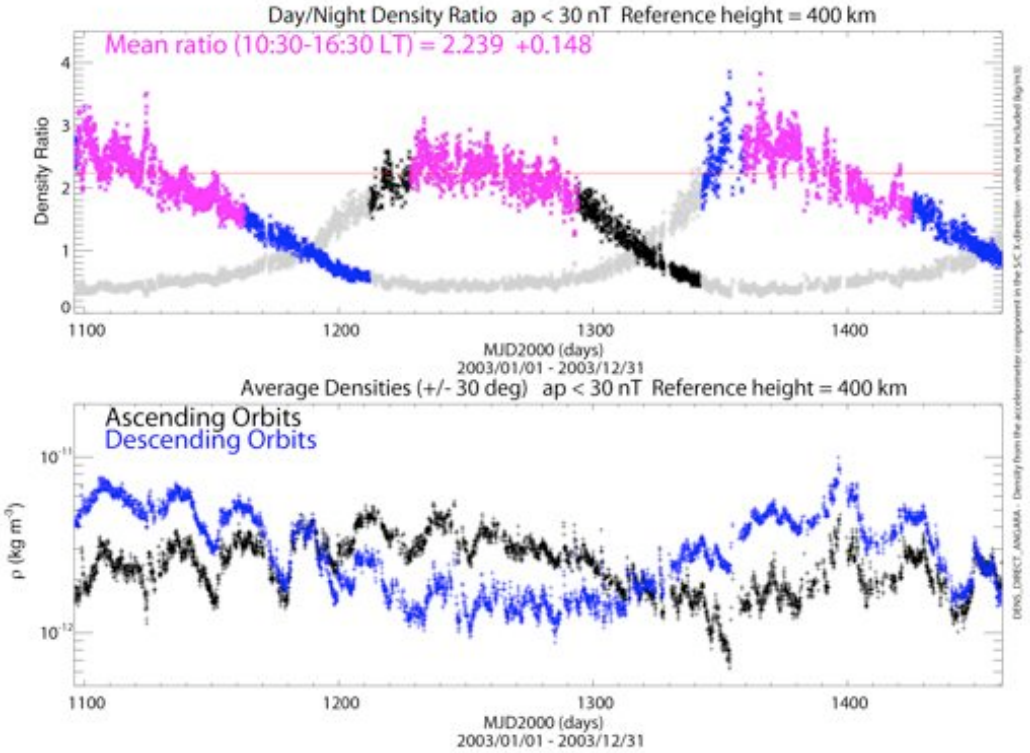

Figure 11.5 Illustration of the estimation of the mean day/night mass density ratio for CHAMP measurements (using "DENS_DIRECT" with the ANGARA force model) during geomagnetically quiet conditions (ap $<$ 30 nT) in the year 2003. The lower panel shows the direct orbit-by-orbit density averages between $\pm 30^\circ$ latitude for ascending (black points) and descending (blue) orbits. The upper panel shows the day-to-night mass density ratio in black and blue for equator crossings of the S/C orbit between 06 LT and 18 LT during the ascending and descending orbits, respectively, and the inverse values (in grey) for the nighttime orbital parts between 18 LT and 06 LT. Data points of the local time interval between 10:30 LT and 16:30 LT, which were used for the determination of the day-night ratio, are highlighted in magenta color. The mean ratio and its mean square deviation, finally, is indicated in the upper left corner of the upper panel.

the day-night density ratio should be different at different altitudes according to the barometric law:

$$\rho \;=\; \rho_0 \;\exp\left(-\frac{z}{H}\right) \tag{11.4}$$

where $H = k_B T/mg$ is the atmospheric scale height with k_B as the Boltzmann's constant, m the constituent's mass, and g the Earth's gravity acceleration.

The mass density ratio was taken between the central hours around the daytime diurnal maximum (10:30–16:30 LT) and the nighttime minimum values (22:30–04:30 LT) of the thermospheric mass density. As a measure of global geomagnetic activity we used the ap index, selecting only those data that were obtained during intervals below a certain threshold (ap $<$ 30 nT or even ap $<$ 15 nT).

Figure 11.5 shows as a first example the ratio (upper panels) and the orbit-by-orbit density averages between $\pm 30^\circ$ latitude for ascending (black points) and descending (blue) orbits for the year 2003 in the lower panels. The mean ratio and its mean square deviation is indicated within each of these Figures and as a summary in the Table 11.1 (second column) below for several years of the 23rd solar cycle. The Table lists also the corresponding values of NRLMSISE-00 model values illustrated in the subsequent section, where the same set of orbital values

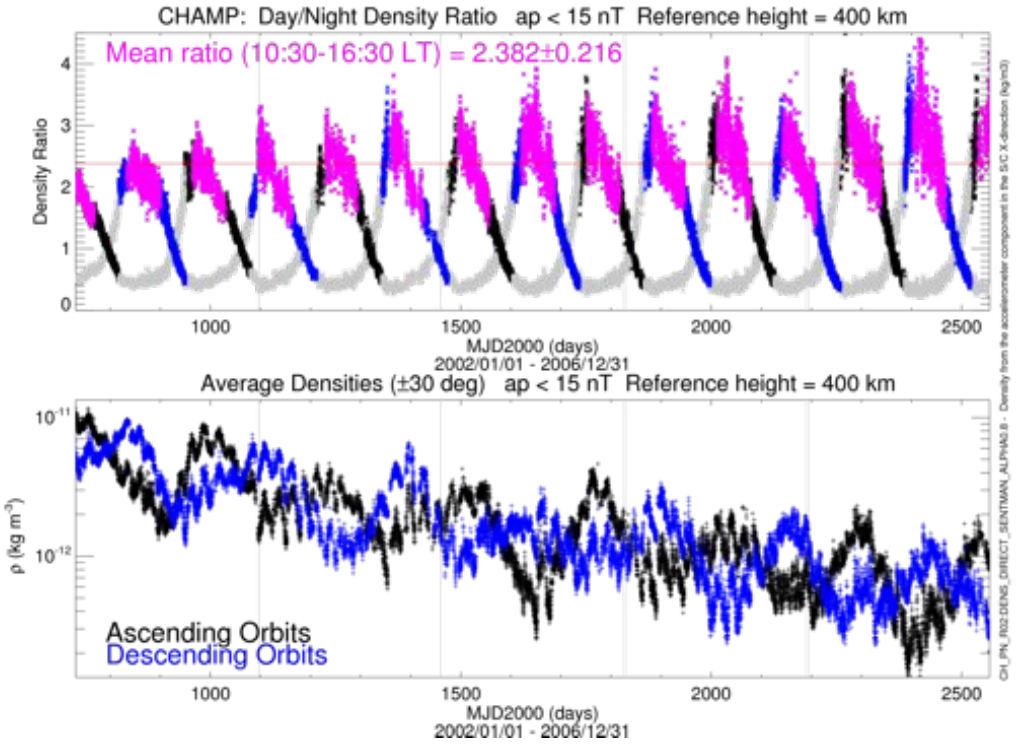

Figure 11.6 This Figure is a repetition of Figure 11.5, but now for a much longer time interval and using a different S/C surface model product with the R03 calibrations. It shows an illustration of the mean day/night mass density ratio estimation for CHAMP measurements (upper panel), using "DENS_DIRECT" with the Sentman panel force model and $\alpha = 0.8$ during geomagnetically quiet conditions (ap $<$ 15 nT) for the years 2002–2006. The density measurements are normalized to an altitude of 400 km by means of the NRLMSISE-00 model (see text).

and the same solar and geomagnetic conditions have been used for the estimation of the day/night mass density ratio.

The yearly mean values have been obtained from mean averages of the low-latitude orbit passes across the equator during daytime and nighttime hours of the time intervals indicated, using only geomagnetically quiet conditions (ap $<$ 30 nT). The CHAMP values are derived in this case trom the "DENS_DIRECT" calculations that make use of the ANGARA force model. The CHAMP mass density ratio values are generally larger by up to ∼10% than the corresponding model values derived from NRLMSISE-00. Exceptions are the years 2001 and 2007 with relatively high model mass density ratio values. The standard mean square deviation of the ratio values during all the years is also generally larger for the S/C observations in comparison with the model values.

The mass density estimations were scaled here to a common reference height (see last column in Table 11.1) close to the actual height according to equation (11.3). This was important in particular for the years 2001 and 2002, where the orbital ellipticity was obviously much larger than during later years, which resulted in more evident overestimations of the ratio values. The scaling proved to be quite sensitive to the actual height difference to be bridged by the scaling; tests with larger height distances resulted in overstimated ratio values. The larger values in 2001 and 2007 for the NRLMSISE-00 model mass density ratio values (third column in Table 11.1) are probably due to this error; the distances of the actual S/C altitude to the reference level height is somehow larger for these intervals.

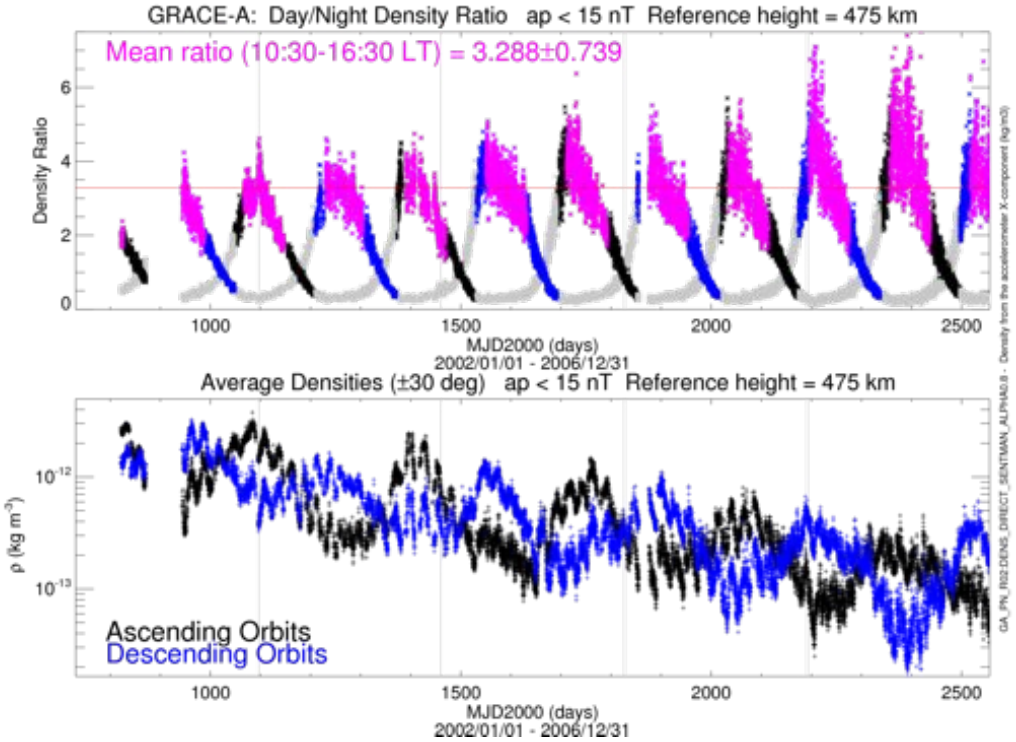

Figure 11.7 The same logarithmic density variation and day/night density ratio as in Figure 11.6, but now for GRACE-A during the same 5-year interval 2002–2006 and normalized to 475 km.

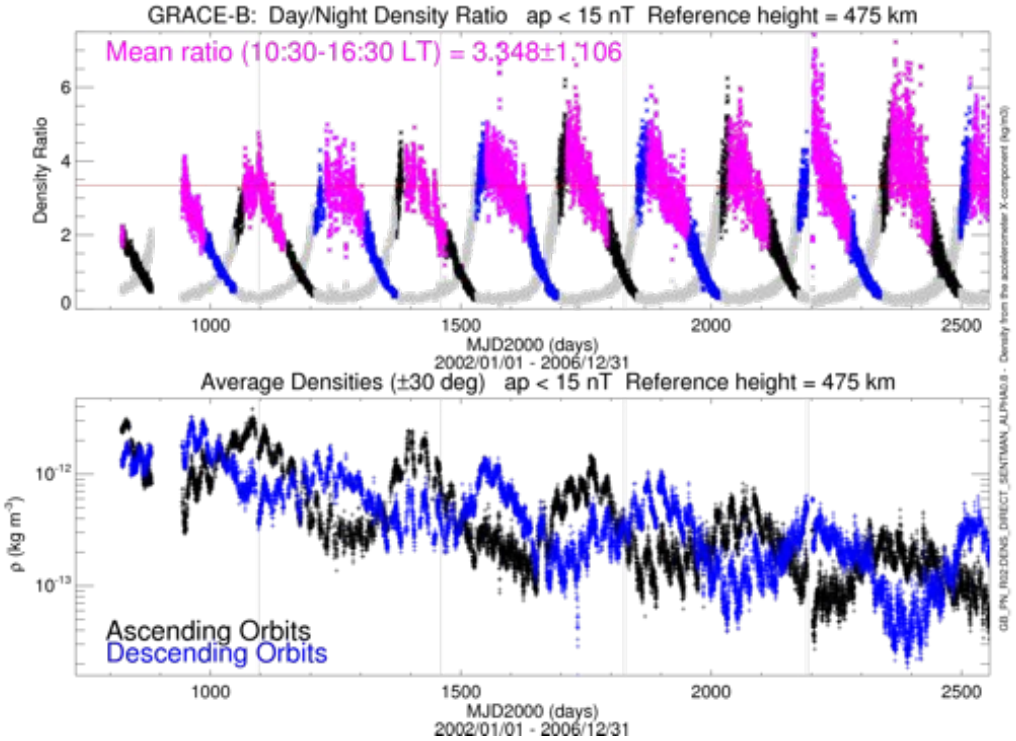

Figure 11.8 The same logarithmic density variation and day/night density ratio as in Figure 11.6, but now for GRACE-B (2002–2006) and normalized to 475 km height as in the previous Figure 11.7.

Year	Day/Night ratio CHAMP	Day/Night ratio NRLMSISE-00	Reference height [km]
2001 (no S/C data yet)		2.441 ± 0.186	425
2002	2.271 ± 0.109	2.160 ± 0.083	425
2003	2.239 ± 0.148	2.096 ± 0.069	400
2004	2.337 ± 0.204	2.278 ± 0.122	400
2005	2.307 ± 0.162	2.240 ± 0.074	375
2006	2.354 ± 0.194	2.311 ± 0.131	375
2007 (first half only)	2.305 ± 0.189	2.344 ± 0.141	375

Table 11.1 Yearly values of the day/night mass density ratio according to CHAMP measurements (using "DENS_DIRECT" with the ANGARA force model), compared with corresponding model values of the NRLMSISE-00 model, where the same set of orbital values and the same solar and geomagnetic conditions have been used. Mass density ratios listed here were calculated between $\pm 30^\circ$ latitude, for local time intervals from 10:30 LT to 16:30 LT, and during geomagnetically quiet conditions (ap $<$ 30 nT). The mass density estimations have been scaled to a common reference height that is given in the last column.

The mass density ratio appears therefore to be susceptible to the empirical model scale height or the day/night mass density ratio itself is height dependent.

Figures 11.6–11.8 show the ratio (upper panels) and the orbit-by-orbit density averages between $\pm 30^\circ$ latitude for ascending (black points) and descending (blue) orbits of the years 2002–2006 in the lower panels. The day/night mass density ratio equals to unity at about 07:30 LT and 19:30 LT, where the two lines of the upper panels have their crossing points. The daytime hours (06:00–18:00 LT) are drawn as black asterisks for the ascending orbit parts and blue ones for the descending. The nighttime intervals are supplemented with light grey symbols.

The intervals of daytime hours between 10:30 LT and 16:30 LT (indicated with asterisks in magenta colour) are actually used for the estimation of the mean mass density ratio, as noted in the upper left corner. There appears to be a steady increase of this mean ratio with time as deduced from the CHAMP density estimations for the years 2002–2006 as shown in Figure 11.6, upper panel, as well as a steady increase of the variance range of this parameter over the years shown, i.e., with decreasing solar activity.

The mean ratio level of about $\sim$2.4 is relatively high in comparison with similar estimations as, e.g., in the paper of *Liu et al.* [2005]. The results of *Liu et al.* [2005] were obtained for high solar activity only. We will come back again to this phenomenon in Section 11.1.3, Figure 11.16.

The same trend over the years of decreasing solar activity is visible in Figures 11.7 and 11.8 for the S/C GRACE-A and GRACE-B, respectively, though on a considerably higher level of the ratio values. The mean ratio level at the higher altitudes of the GRACE satellites (475 km reference height) is at about $\sim$3.3 with a much larger variance (cf. also Figure 11.16 later).

For the interpretation of these observational facts, we are puzzled by the ambiguity, that they could either be due to a real geophysical phenomenon or they could indicate some weakness in our accelerometer calibration and/or density estimation algorithms of the force models (or both simultaneously). Within a geophysical interpretation, there seems to be an anticorrelation of the mass density ratio with solar activity and a positive correlation with the satellite height.

The lower panels of Figures 11.6–11.8 show the steady decline of the average

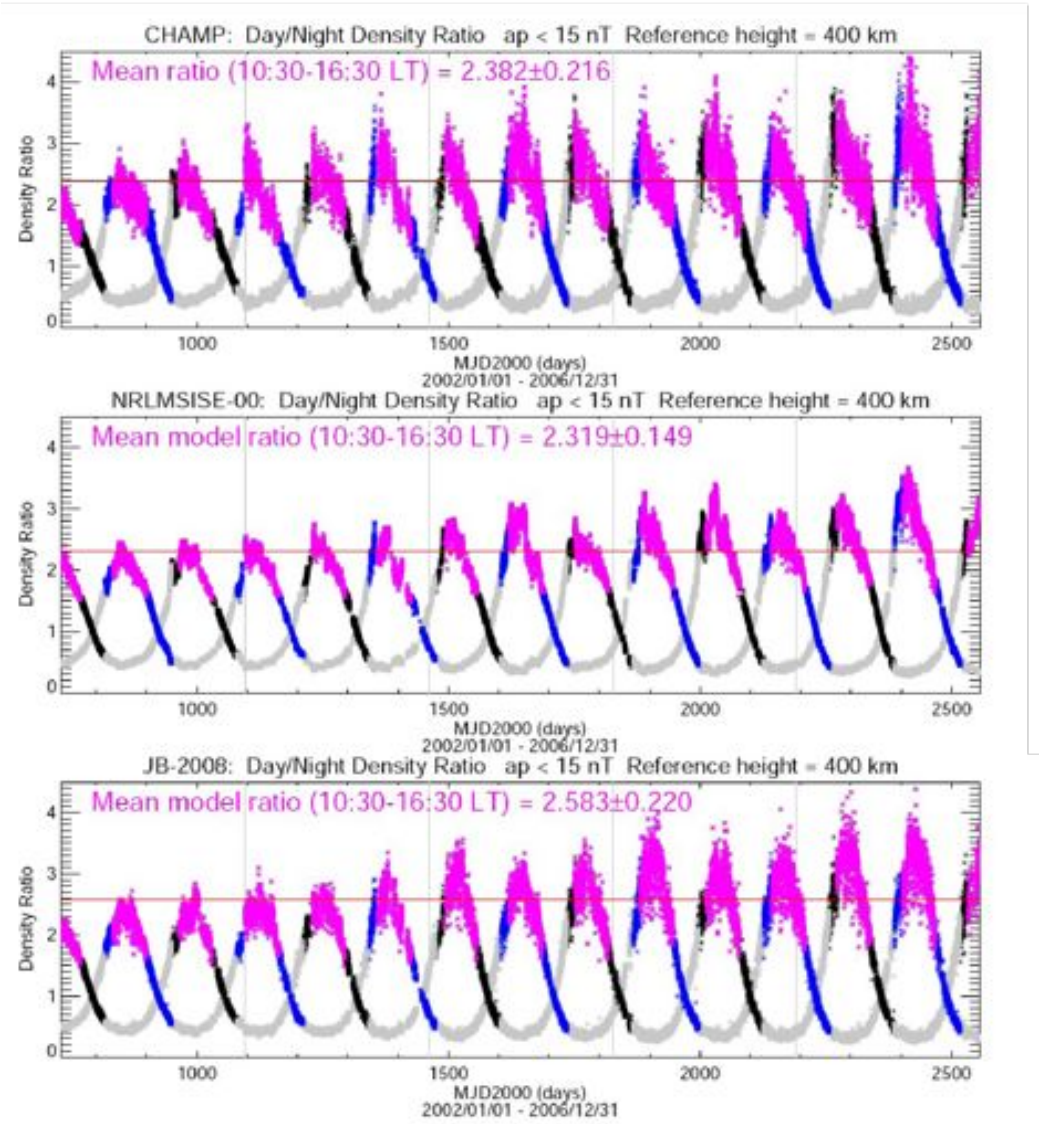

Figure 11.9 This plot shows the day/night mass density ratio of the CHAMP measurements from the years 2002–2006, normalized to 400 km height and confined to $< \pm 30^\circ$ latitude, in comparison with two empirical models. The upper panel repeats the day/night ratio as shown in the upper panel of Figure 11.6, the middle panel is a comparison with the corresponding NRLMSISE-00 model values at the same points along the S/C orbit, while the lower panel compares it with the latest Jacchia-Bowman model (JB-2008). The mean ratio and its mean square deviation for each data set is indicated in the upper left corner of each panel. Here, periods with daytime hours between 10:30 LT and 16:30 LT over the corresponding nighttime values between 22:30 LT and 04:30 LT have been used for the ratios as indicated by the magenta color.

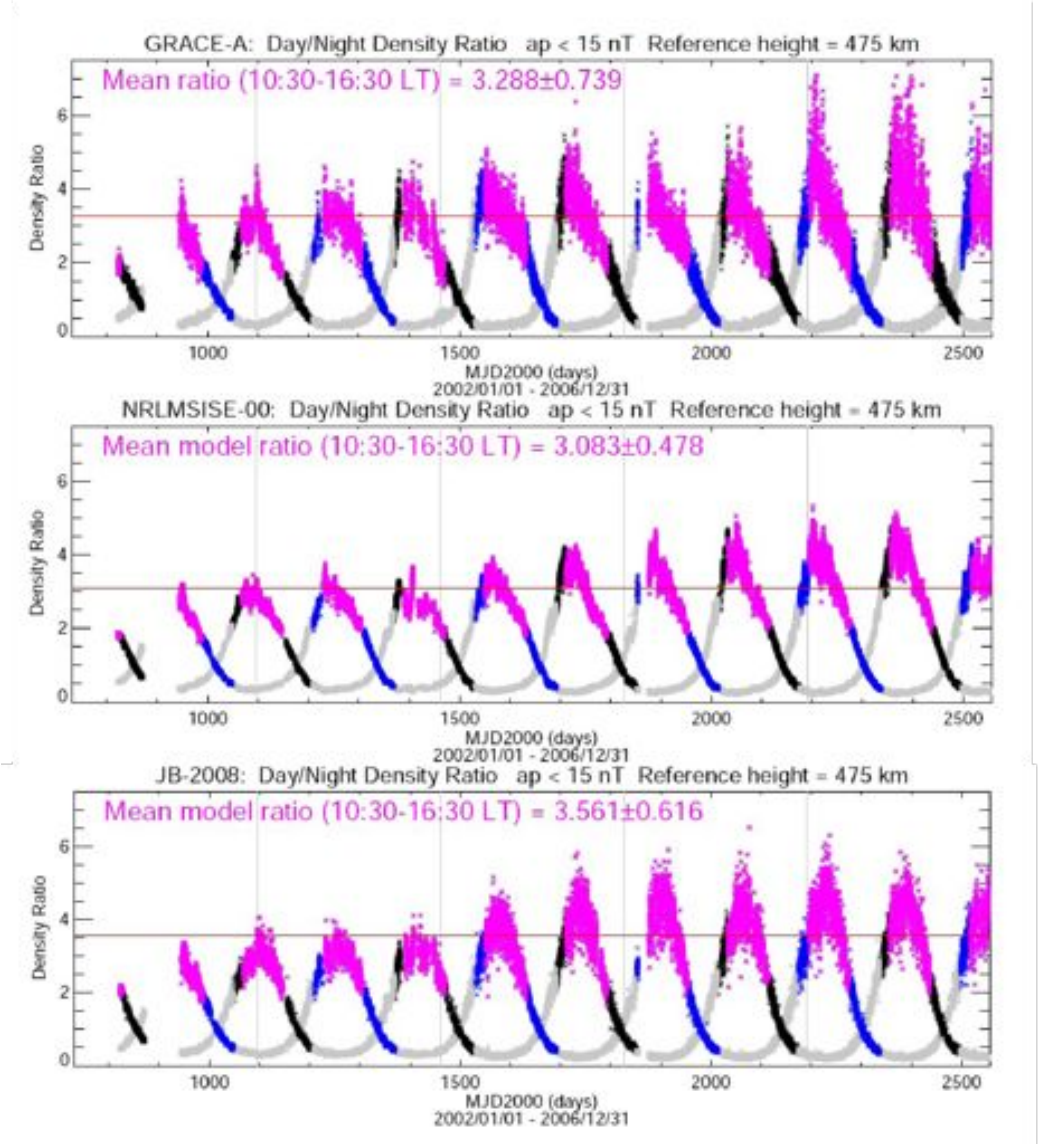

Figure 11.10 These are the same day/night mass density ratio comparisons as in Figure 11.9, but now for GRACE-A (2002–2006) and normalized to 475 km height as in Figure 11.7.

density at low ($< \pm 30°$) geographic latitudes with the decreasing solar activity over the years 2002–2006. Superposed on this longer trend, the precession period of 262 days (322 days) with sinusoidal variations of the average mass density along the ascending (black lines) and descending orbital wings (blue) can be observed in case of CHAMP (GRACE). Even shorter regular variations with periods of about 27 days are clearly visible throughout the whole time interval. They are the result of the periodical change of solar flux values with the solar rotation period. Stronger activity regions at the sun's surface re-appear with this periodicity and the resulting mass density variations indicate a strong correlation with solar EUV and X-ray fluxes, the topic of the subsequent section.

Figures 11.9 and 11.10 show a comparison of the measured day/night mass density ratio of the CHAMP and GRACE-A satellites, respectively, with corresponding values obtained from empirical neutral density models like the NRLMSISE-00 (middle panels) and the latest Jaccia-Bowman model (JB-2008, lower panels). The model values are taken at the same points along the S/C

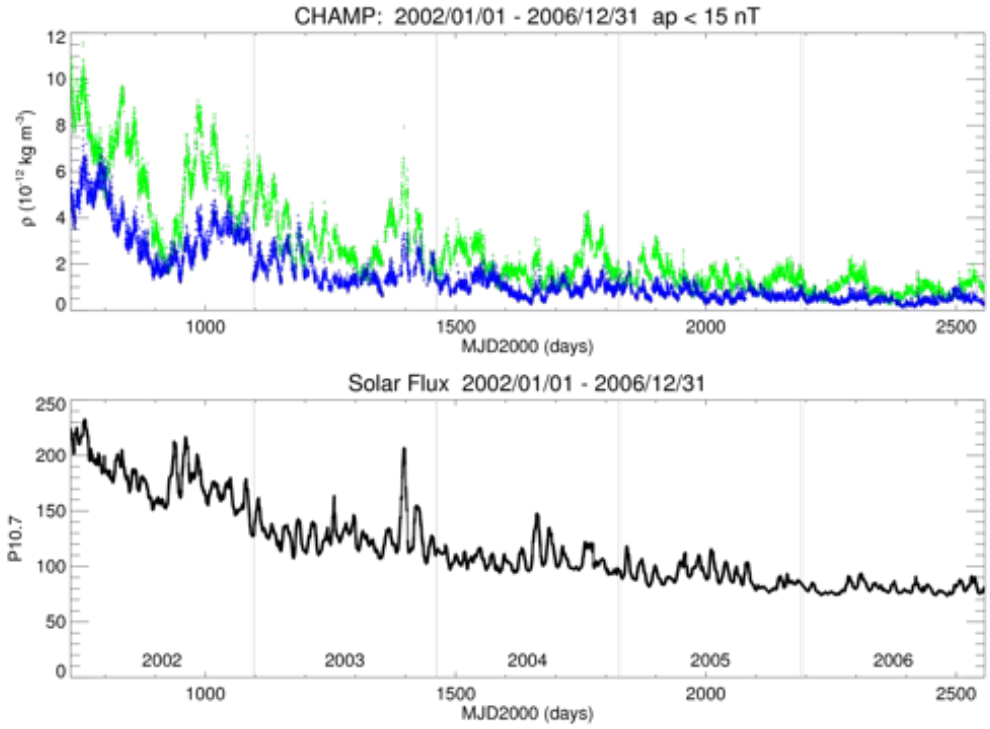

Figure 11.11 Comparison of density estimations (using "DENS_DIRECT" of the Sentman's panel force model with $\alpha = 0.8$) along two opposite local times during daytime hours between ∼07:30–19:30 LT (green) and nighttime hours between ∼19:30–07:30 LT (blue) for CHAMP orbits at low- to mid-latitudes ($\pm 30°$) versus Modified Julian Day, referenced to Jan 1st, 2000 (MJD2000). The data are filtered for quiet geomagnetic conditions (ap < 15 nT) (upper panel). The lower panel shows the solar radiation index $P_{10.7}$ (see text) which indicates the steady decline of the solar EUV activity in parallel to the average low-latitude thermospheric density over the five-years-interval 2002-2006.

orbits and for the same geographic and geomagnetic selection criteria as used in the upper panels.

The day/night mass density ratios obtained with the empirical models confirm the principle behaviour for both S/C, perhaps with the exception of the large scatter in the S/C data in particular during lower solar activity in the later years. The NRLMSISE-00 model data show the least scatter in the diurnal variation, while the Jaccia-Bowman model 2008 is closer to the observations with respect to the scatter in the day/night mass density ratio both for CHAMP (Figure 11.9) and GRACE (Figure 11.10. But the scatter in the observations (upper panels) is largest in any case, in particular for high solar activity in the GRACE data. Additionally, they show a certain regular local time variation (see below, Section 11.1.4).

11.1.3 Solar activity dependence

The upper panels of Figures 11.11 and 11.12 are in principle repetitions of the mass density variation plots in the lower panels of Figures 11.6 and 11.7 for CHAMP and GRACE-A, respectively, but now drawn with a linear scale. The corresponding plot for GRACE-B is omitted here, because it is quite similar to that of GRACE-A in Figure 11.12. For comparison, the mass density variations are put into the context of the solar EUV flux variations shown in the lower panels, represented by the proxy index $P_{10.7} = (F_{10.7} + \overline{F}_{10.7})/2$. The index $P_{10.7}$ was introduced

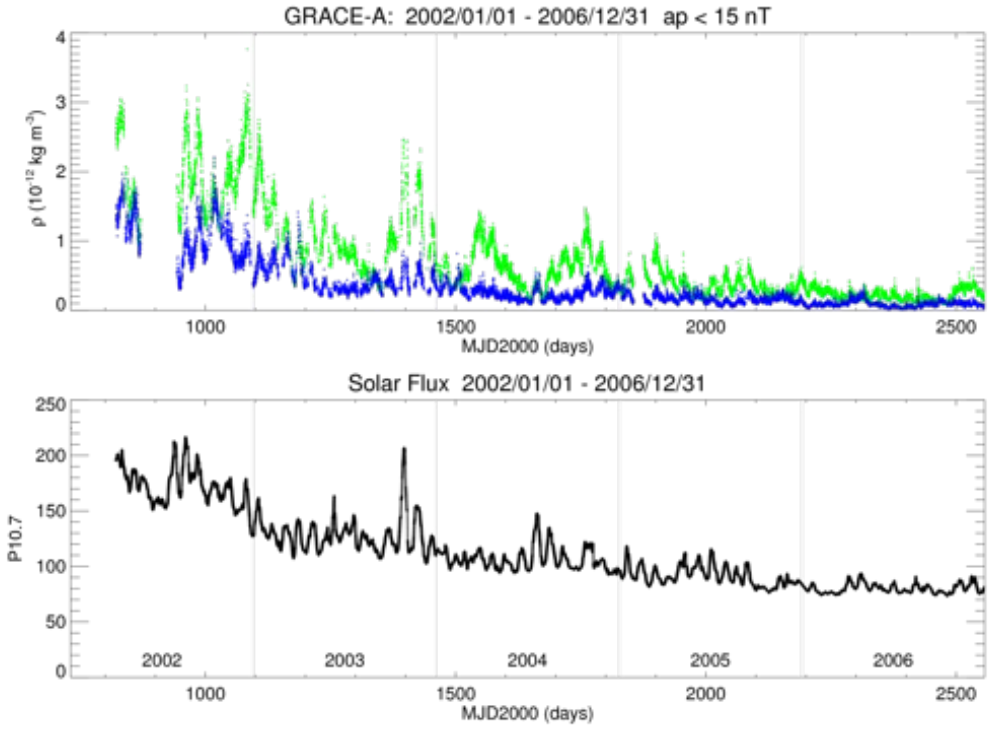

Figure 11.12 The same density variation versus time in dependence on the solar activity index $P_{10.7}$ as in Figure 11.11 during the years 2002-2006, but for GRACE-A. The reference height used here is 475 km. The corresponding plot for GRACE-B (not shown) is very similar.

by *Richards et al.* [1994] and is considered a better proxy for the solar EUV than the daily $F_{10.7}$ for studies of this kind. It combines the short-term daily variations with their centered 81-day (i.e., three solar rotations) arithmetic averages, so that the variation of $P_{10.7}$ is much smoother than $F_{10.7}$. Both proxies are measured in units of $[10^{-22} Wm^{-2} Hz^{-1}]$. Here, the green line in the upper panels show daytime mass density values obtained between 07:30–19:30 LT, while the blue lines show the corresponding nighttime values for local times between 19:30–07:30 LT. The strong positive correlation between the mass density variation and the solar flux level is obvious and will be shown explicitely in Figures 11.13 and 11.14 as well as in Table 11.2 below.

In the linear presentation of the upper panels in Figures 11.11 and 11.12, the modulation with solar EUV flux variations in the periodicity of the solar rotation period is well visible during the years of high and moderate solar activity 2002-2004, while it is quite faint in 2006 due to missing active regions at the quiet sun.

The larger periods with quasi-semiannual maxima in spring and autumn (as, e.g., in 2004) can be noticed in the daytime mass density variations (green lines, upper panels), which are not seen in the $P_{10.7}$ variations (lower panels). They are mainly due to the above-mentioned periodicity with the satellite's precession periods through all local times (both for CHAMP and GRACE in Figures 11.11 and 11.12, respectively). Nevertheless, a semi-annual mass density variation might be present as will be shown subsequently (cf. section 11.1.5 and Figures 11.19–11.20). They are probably due to the known larger geomagnetic activities during equinox periods, which seem to appear as enhanced thermospheric densities despite of the selection criterion with ap $<$ 15 nT. In any case, the specific orbit constraints are responsible for some ambiguities with respect to local time and

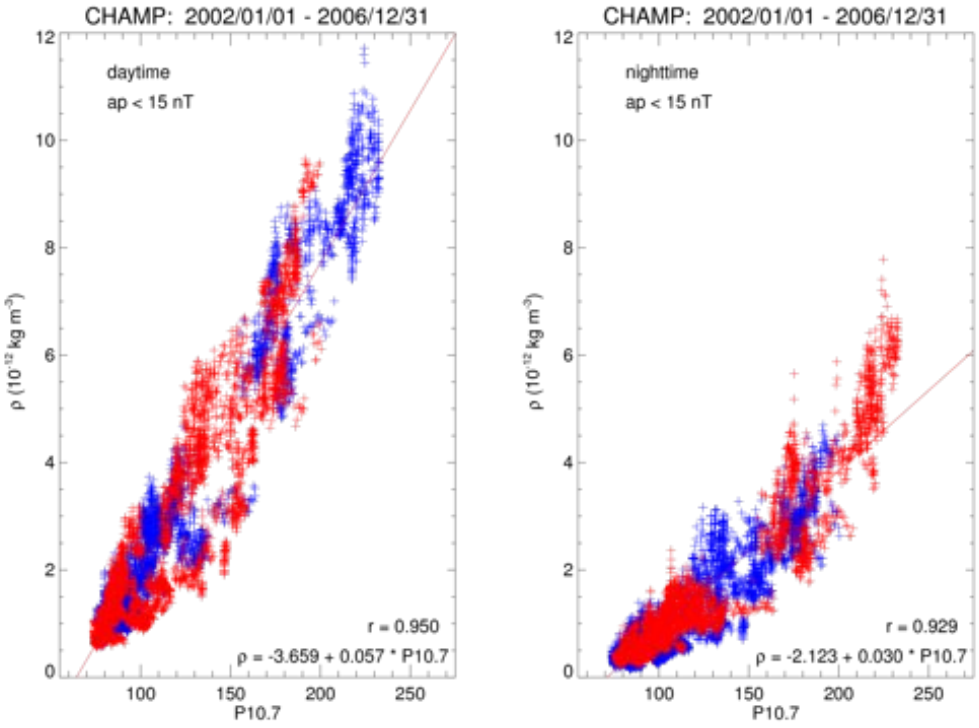

Figure 11.13 Distribution of the CHAMP thermospheric mass density, scaled to a reference height of 400 km, versus the solar EUV activity index $P_{10.7}$ (see text). Data of the years 2002–2006 were filtered for quiet geomagnetic conditions (ap $<$ 15 nT) and sorted for daytime (left panel) and nighttime (right panel) conditions. The least-square fit of the linear correlation is indicated with the red line and the numbers are noted for each case in the lower right corner of each panel together with the corresponding correlation coefficient "r" (cf. also Table 11.2).

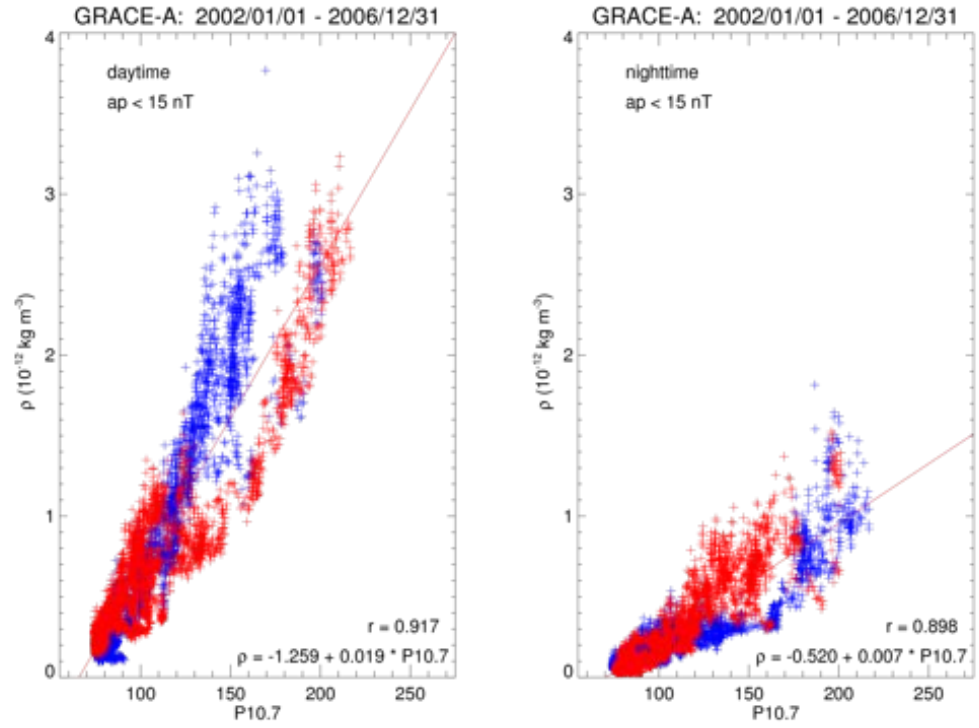

Figure 11.14 The same mass density distribution versus local solar EUV activity index $P_{10.7}$ as in Figure 11.13, but for GRACE-A. The reference height is 475 km in this case.

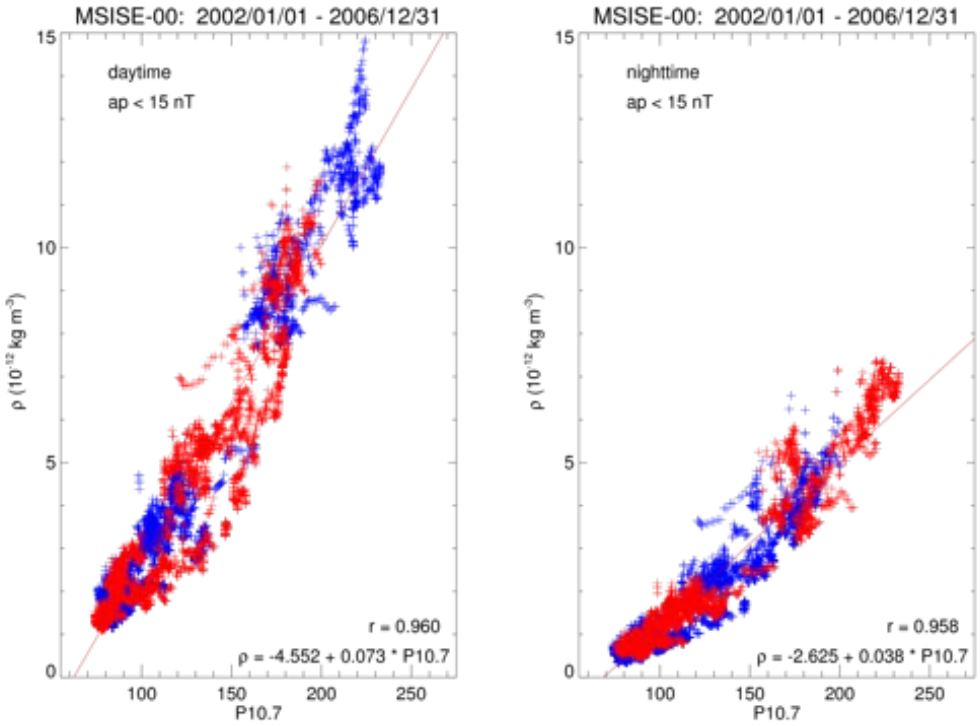

Figure 11.15 The same mass density distribution of the CHAMP data versus the solar EUV activity index $P_{10.7}$ as in Figure 11.13, but here empirical model values of NRLMSISE-00 are used instead, but at the same points along the orbit and under the same selection criteria as there. The reference height is again 400 km.

seasonal dependencies. An "thought" upper and lower envelope of the daytime and nighttime curves in Figures 11.11 and 11.12 reflect the long-term trend of mass density decrease with decreasing solar activity, while the overlaid mid-term periodicity (with a period of 262 days in case of CHAMP) are actually local time variations of the density. Those are easier seen in the logarithmic presentations of Figures 11.6–11.8, lower panels, which display ascending and descending orbital wings explicitely.

Superposed on these trends, some "spiky" periods of mass density variation with large enhancements can be observed. They represent some particular active periods, like the intervals of the so-called "superstorms" in October and November 2003. These events are also characterized by extreme EUV fluxes and are clearly reflected in the mass density peaks during both daytime and nighttime.

To separate solar EUV dependent variations, represented by its proxies, the $F_{10.7}$ or the composite $P_{10.7}$ flux indices, from the mass density changes of different origin (as, e.g., seasonal variations), existing empirical models could be used, as outlined already in equation (11.2).

An alternative possibility is the use of our own data sets to deduce linear relations or, possibly, more complicated relations from the the observations itselves. This will be done in the following.

Figures 11.13–11.14 show the correlation between the mass density observations versus the $P_{10.7} = (F_{10.7} + \overline{F}_{10.7})/2$ solar EUV radiation index as a scatter plot. We used again filtered (ap < 15 nT), height-scaled to the respective reference height, and averaged low-latitude ($< \pm 30°$) data for these analyses. The straight red line represents a linear regression of all these data points over the full

EUV index	S/C (model)	Daytime coeff.	Daytime const	Daytime r	Nighttime coeff.	Nighttime const	Nighttime r	Reference
$F_{10.7}$	CHAMP	0.08	-5.31	0.72	0.05	-3.45	0.72	*Liu et al.* [2005], Kp = 0-2
$F_{10.7}$	CHAMP	0.051	-3.035	0.921	0.027	-1.805	0.902	400 km, ap $<$ 15 nT
	NRLMSISE-00	0.066	-3.754	0.929	0.035	-2.243	0.935	400 km, same as CHAMP
	JB-2008	0.062	-3.505	0.909	0.032	-2.112	0.905	400 km, same as CHAMP
	GRACE-A	0.016	-0.983	0.894	0.006	-0.413	0.875	475 km, ap $<$ 15 nT
	GRACE-B	0.016	-0.972	0.891	0.006	-0.400	0.870	475 km, ap $<$ 15 nT
	NRLMSISE-00	0.019	-1.137	0.928	0.009	-0.571	0.928	475 km, same as GRACE-A
	NRLMSISE-00	0.019	-1.133	0.926	0.008	-0.567	0.928	475 km, same as GRACE-B
	JB-2008	0.016	-0.873	0.851	0.007	-0.425	0.844	475 km, same as GRACE-A
$P_{10.7}$	CHAMP	0.057	-3.647	0.949	0.030	-2.119	0.927	400 km, ap $<$ 15 nT
	NRLMSISE-00	0.073	-4.552	0.960	0.038	-2.625	0.958	400 km, same as CHAMP
	JB-2008	0.068	-4.194	0.933	0.035	-2.460	0.927	400 km, same as CHAMP
	GRACE-A	0.019	-1.259	0.917	0.007	-0.520	0.898	475 km, ap $<$ 15 nT
	GRACE-B	0.019	-1.243	0.913	0.007	-0.504	0.893	475 km, ap $<$ 15 nT
	NRLMSISE-00	0.022	-1.462	0.951	0.010	-0.707	0.945	475 km, same as GRACE-A
	NRLMSISE-00	0.022	-1.457	0.951	0.010	-0.702	0.946	475 km, same as GRACE-B
	JB-2008	0.019	-1.131	0.866	0.008	-0.533	0.862	475 km, same as GRACE-A

Table 11.2 Approximative linear relationships between the measured thermospheric mass density values ρ at the given reference height levels (indicated in the last column) and the solar EUV flux variations. These comprise the linear slope ("coeff.") and the constant ("const") term of the least-square approximation with a correlation coefficient "r" for both daytime (columns 3–5) and nighttime (columns 6–8) conditions. The data were filtered for low geomagnetic conditions (ap $<$ 15 nT) and they represent low latitudes ($< \pm 30^\circ$) only for the years 2002–2006. Here, ρ is measured in $[10^{-12}\, kg\, m^{-3}]$ and the solar fluxes are estimated with their proxies $F_{10.7}$ and $P_{10.7} = (F_{10.7} + \overline{F}_{10.7})/2$ in the usual units of the solar EUV index. The latter dependencies are illustrated in Figure 11.16 for CHAMP and GRACE-A (GRACE-B is similar to GRACE-A in this respect). The first data line is taken from the cited paper. They used CHAMP data from the accelerometer data set of the high solar activity year 2002, filtered for different geomagnetic activity conditions; the numbers here are for quiet geomagnetic conditions only (Kp=0-2).

range of solar activity levels. The corresponding numbers for the least-square approximations are shown in the lower bottom right of each plot and are summarized in Table 11.2 for all S/C during both daytime and nighttime intervals as well as for both $F_{10.7}$ and $P_{10.7}$ indices.

The Figures 11.13–11.14 reveal a quite strong linear relationship between the mass densities and the solar EUV flux indices with correlation coefficients close to 0.9 or higher. The correlations are slightly better for the composite index $P_{10.7}$ than for the daily value $F_{10.7}$ (see Table 11.2). For solar EUV fluxes above about $P_{10.7} >\sim 200$ in case of CHAMP and $P_{10.7} >\sim 150$ in case of GRACE, the data scatter shows some indications of possibly larger slopes both during daytime and nighttime.

The daytime slopes are a factor of 2.0 larger than the nighttime ones in case of CHAMP and by a factor of about 2.5 in case of the GRACE satellites. The difference of the slopes between the different satellite missions which operate at different heights is even larger. It is of the order of factor 3.0 for daytime conditions and factor 4.0 for nighttime (see Table 11.2).

In the daytime plots of the two GRACE satellites (Figure 11.14, left panel, GRACE-B is similar, but not shown here), there are indications of a splitting into two separate branches of the distribution with different slopes. This behaviour is probably due to a different seasonal coverage during the ascending and descending orbits, because of the interference between local time and seasonal variations for the GRACE satellites.

The scaling of the thermospheric density values to a common solar activity level of $P_{10.7} = 130$ will be done subsequently according to the following relation:

$$\rho_{130}^{obs} \;=\; \rho_{P10.7}^{obs}\,\frac{130 \cdot coeff + const}{P_{10.7} \cdot coeff + const} \tag{11.5}$$

It will be used, e.g., in section 11.1.5 for the generation of Figures 11.19–11.20.

11.1.4 Local Time dependence of the mass density ratio

In this section we will first consider again the dependencies of the day/night mass density ratio on the solar EUV flux proxy $P_{10.7}$, which was mentioned already in section 11.1.2 with regard to the upper panels of Figures 11.6–11.8.

Figure 11.16 shows scatter plots of the day/night mass density ratio drawn versus the $P_{10.7}$ index for both ascending (blue) and descending (red data points) orbital wings for the CHAMP and GRACE-A S/C (GRACE-B is similar and therefore not shown here). The data points selected represent quiet geomagnetic conditions (ap < 15 nT) and low latitude ($< \pm 30°$) averages of height-corrected mass density ratios. There are no significant differences in the distribution of these data points between the ascending and descending orbits.

The pattern of the distributions for CHAMP on the one side and the GRACE satellites on the other (Figure 11.16) are quite similar, but the latter density ratio values show systematically higher values, i.e., on average about 2.3 for CHAMP versus 3.3 for GRACE. The scatter of the data points is large for low solar activity levels and becomes smaller with increasing $P_{10.7}$ index values (the same principal distribution is obtained for the $F_{10.7}$ proxy of solar EUV flux intensities – not shown here). This trend was already seen in Figures 11.6–11.8 as temporal change of the ratio variances during the solar cycle decline. The causes for this solar EUV flux dependency is not clear. It seems to have a geophysical background rather than errors in the data processing. This phenomenon needs further studies, maybe first of all by global theoretical physical-numerical simulations.

Figures 11.17–11.18 illustrate the local time variation of the day/night mass density ratio for all three satellites, respectively. Again, the scatter plot with the two different colours represent ascending (blue) and descending (red) orbits separately. The four panels of the Figures stand for the four different seasons, sampled over the years 2002-2006 and sorted accordingly in time intervals of $\sim$91 days around the equinoxes (left panels) and solstices (right).

The day/night mass density ratios are obtained under the same selection criteria as in the previous Figure 11.16, i.e., they represent quiet geomagnetic conditions (ap < 15 nT) and low latitude ($< \pm 30°$) averages of the height-corrected mass density ratios. This time there are some differences in the distribution of these data points between the ascending and descending orbits in case of the GRACE satellites (Figure 11.18, GRACE-B is similar, not shown here). This is due to the slow precession rate of GRACE; the local time coverage during each season is not equally distributed between ascending (blue) and descending (red) orbital wings.

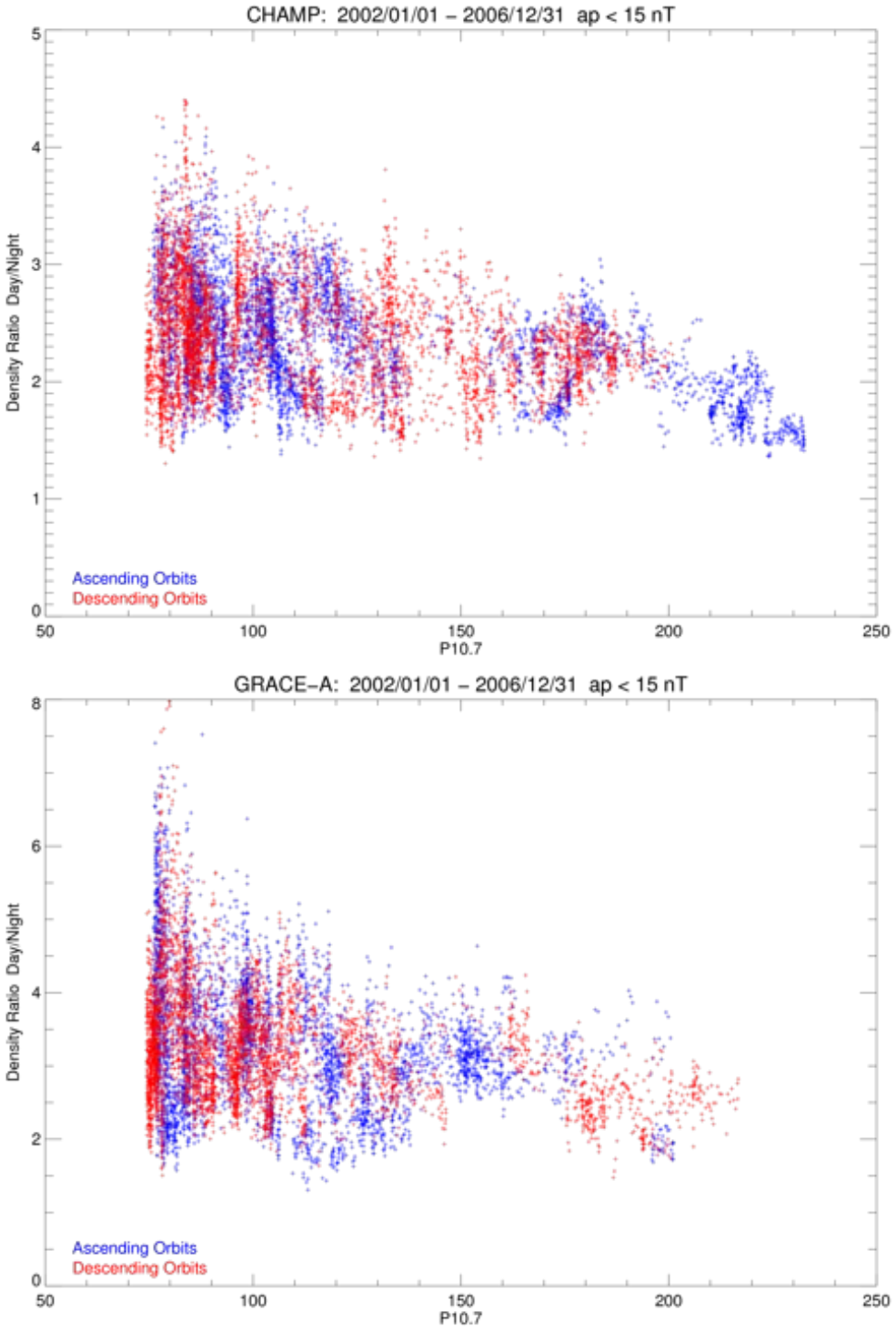

Figure 11.16 The day/night mass density ratio is drawn here versus the solar EUV activity index $P_{10.7}$ for both ascending (blue dots) and descending (red dots) dayside orbits of the years 2002–2006. The data are filtered for relatively quiet geomagnetic conditions (ap $<$ 15 nT). The average densities of the two opposite (in LT) orbit parts are obtained between $\pm 30^{\circ}$ geographic latitide. The reference height for CHAMP is 400 km (upper panel) and 475 km for GRACE-A (lower panel).

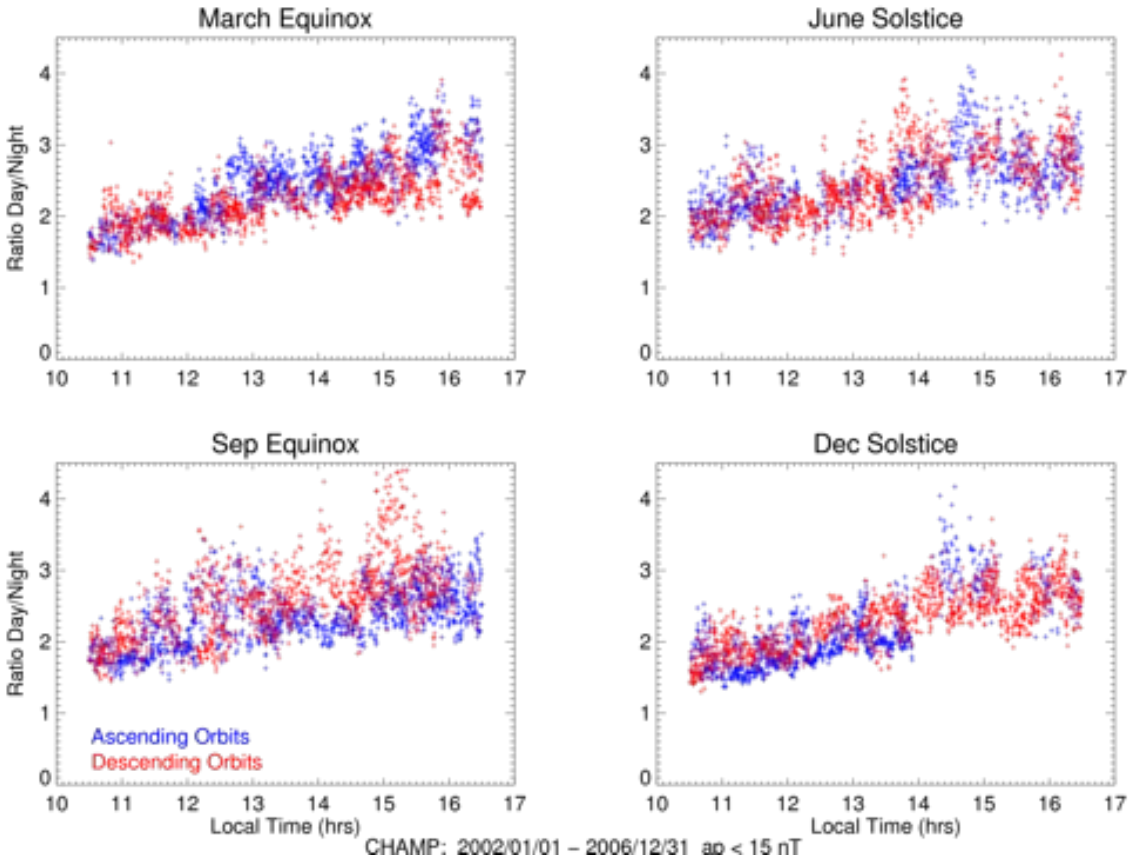

Figure 11.17 This plot shows the local time dependence of the day/night mass density ratio separately for the four seasons and indicating both ascending (blue dots) and descending (red dots) dayside orbits. Five years (2002-2006) of averaged low-latitude ($\pm 30^\circ$) CHAMP data are used which were converted to the common reference height of 400 km.

Apart from that separation of different populations in the GRACE data, there are no significant differences between the different seasons. During all seasons, there is a very clear diurnal trend of increasing mass density ratios with local time. The ratio maximizes in all cases during the afternoon hours and in some cases as, e.g., the March equinox of the CHAMP data (Figure 11.17, upper left panel) the scatter of the data points increases also with local time. It should be kept in mind, that the calculated ratios result from measurements of one and the same orbits which are almost exactly 12 hrs apart in local time. The afternoon maximum results therefore from the interplay between the minimum densities in the early morning hours and high densities in the aftenoon hours. The smaller morning ratios are the result of increasing densities during the morning hours over still higher densities in the pre-midnight hours.

11.1.5 Seasonal mass density variations

Finally we consider the seasonal variations of the thermosperic mass density as obtained from accelerometer data of CHAMP (Figure 11.19) and GRACE (Figure 11.20, GRACE-B is similar – see Table 11.3) in the result of the calibration efforts and force model processings of our project. The density data are shown separately for daytime (upper panels with green data points) and nighttime (lower panel, blue data points) conditions. They are height-corrected according to equa-

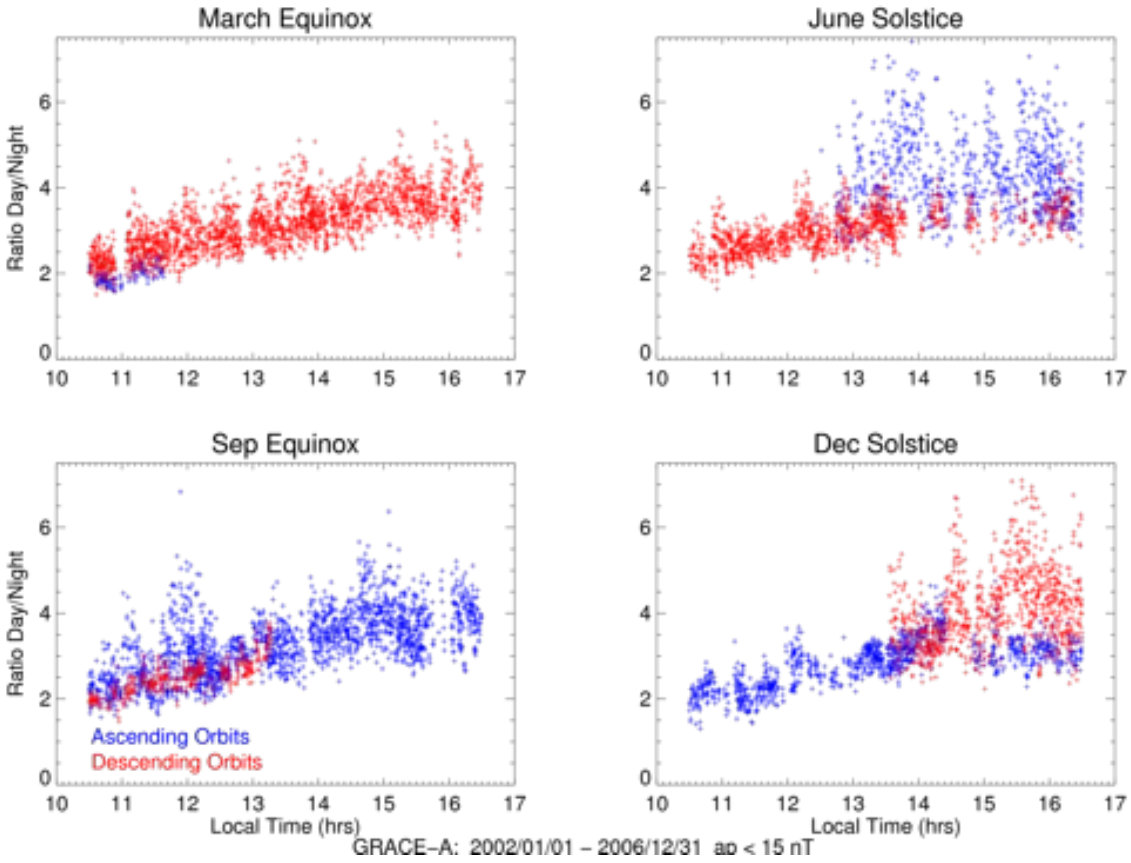

Figure 11.18 The same mass density ratio dependence versus LT for the four seasons separately as in Figure 11.17, but for the GRACE-A. The reference height is 475 km.

tion 11.3 and adjusted to a common solar activity level according to equation 11.5 with a reference of $P_{10.7} = 130$.

The continuous red curves in Figures 11.19 and 11.20 show the fitting of the data points with respect to sinusoidal annual and semi-annual terms according to:

$$\rho(t) = const + a_1 \cos(2\pi/365 \cdot t + \phi_1) + a_2 \cos(4\pi/365 \cdot t + \phi_2) \qquad (11.6)$$

Here, t stands for "Day Of Year" (DOY) and ρ is measured in $[10^{-12}\, kg\, m^{-3}]$. The phases ϕ_1 and ϕ_2 are measured in [rad]. The number values of the fitting are summarized in Table 11.3 for all three satellites (as plotted in Figures 11.19 and 11.20). The dashed red line in Figure 11.19 shows similar results of a presentation of H. Lühr, S. Müller, and S. Rentz (private communication), given at the COSPAR meeting in Montrèal in July this year. They used also CHAMP data (with a different, previous calibration) of the years 2002–2005; the numerical values of their fitting is also listed in Table 11.3, first line. Their constant term is systematically larger, but the sinusoidal variations are about the same.

The fitting reveals a clear seasonal, semi-annual variation with maxima at the equinoxes, in addition to an annual variation with a minimum around the June solstice. The daytime and nighttime variations are about in phase with the difference in magnitude of ≈2.3 (CHAMP) and ≈3.3 (GRACE) that corresponds to the average mass density ratios according to the discussion in the previous section 11.1.4.

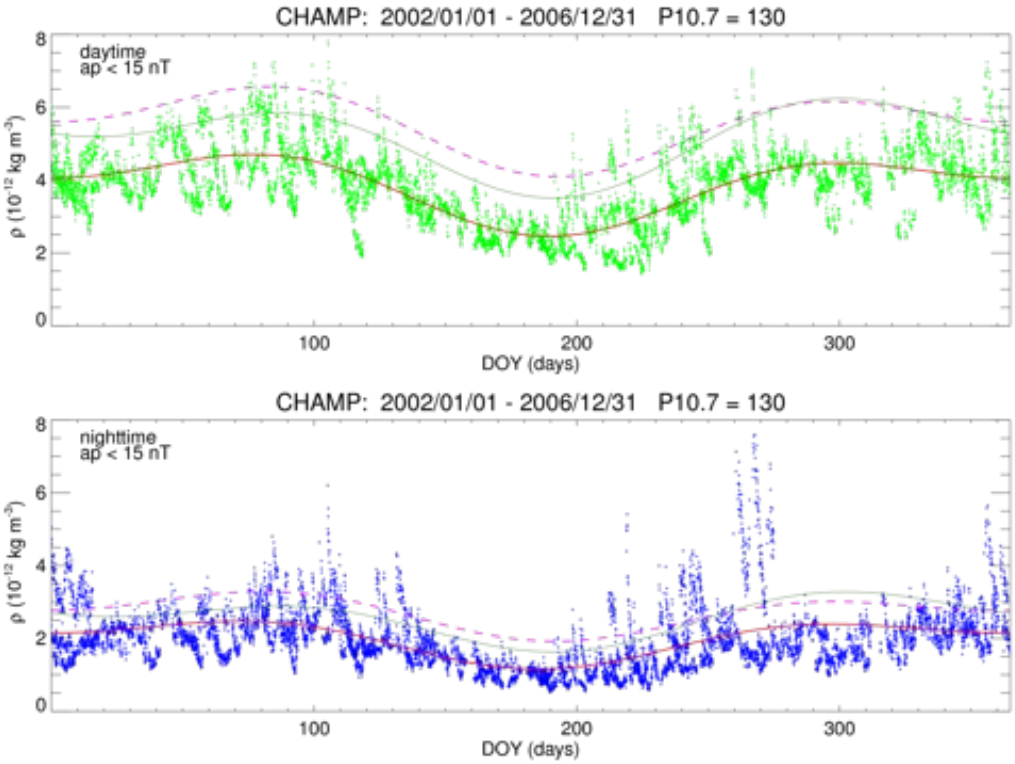

Figure 11.19 Seasonal variation of the thermospheric density for daytime (upper panel) and nighttime conditions (lower panel). The CHAMP measurements are scaled to both a common height level (400 km) and a common solar activity level of $P_{10.7} = 130$ according to (11.5) and the linear regression coefficient which was found in Figure 11.13. The data set comprises five years (2002-2006) and is based on the "DENS_DIRECT" calculations with the Sentman panel force model and $\alpha = 0.8$ during geomagnetically quiet conditions (ap $<$ 15 nT). The red dashed line shows a least-square fitting of the annual and semi-annual variations as obtained in a work of H. Lühr, S. Müller, and S. Rentz that was presented at the 37th COSPAR meeting in Montrèal recently and is based on CHAMP data for the years 2002-2005. The full red line show the corresponding least-square fit for the present data set (see Table 11.3). Finally, the full dark green lines show the corresponding least-square fits for the NRLMSISE-00 model runs, using the same data points in space and time as the original CHAMP observations. The fit values are also listed in Table 11.3.

The scatter of the data points around the fitted curves are generally largest during the equinoctial maxima; some extreme outliers as, e.g., in the lower, nighttime panel of the CHAMP observations in Figure 11.19 around DOY≈270, are obviously due to the extreme storm events.

11.2 Thermospheric cross-track wind

11.2.1 The low-latitude zonal thermospheric wind

The Earth's thermosphere is heated primarily due to the absorption of solar extreme ultraviolet (EUV) radiation by the atmospheric constituents. In a most simplistic view one would expect an uprise of the neutral air within the upper atmosphere close to the subsolar point, a divergent flow (wind) around the globe, somehow influenced by the action of the Coriolis and centrifugal forces, resulting in a converging flow at the nightside. At low latitudes, this would mean, that we

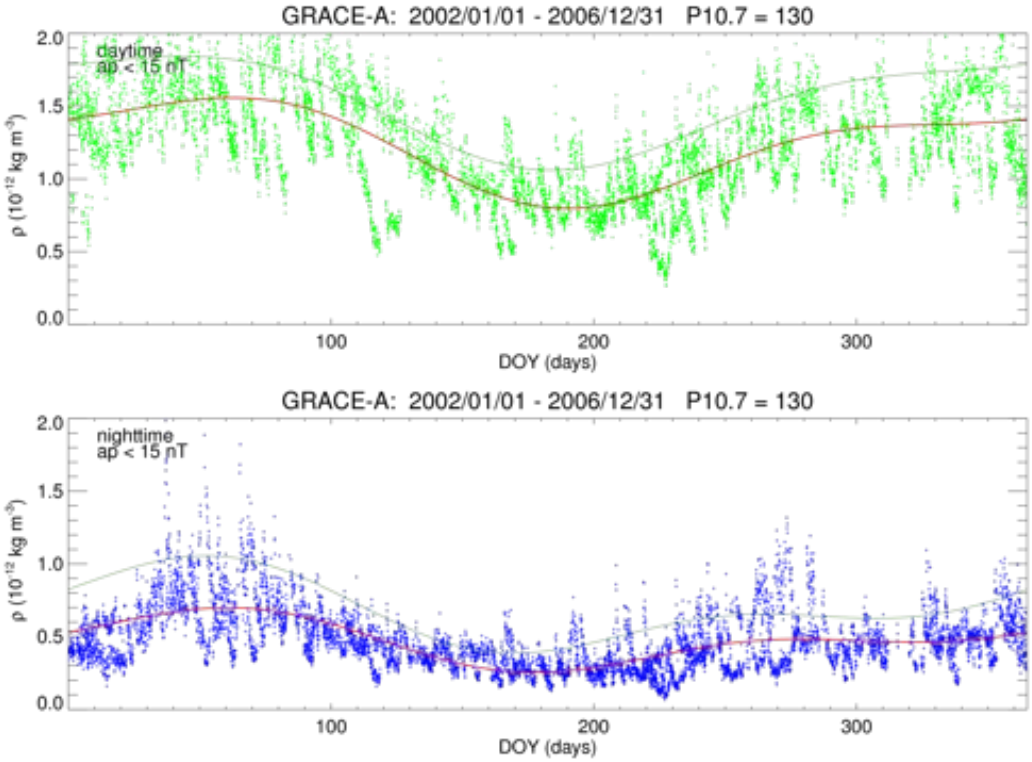

Figure 11.20 The same seasonal variation of thermospheric density as in Figure 11.19, but now for GRACE-A, referenced to an altitude of 475 km together with the fitted annual and semi-annual variations (red curve, see Table 11.3).

S/C	Daytime const	a_1	ϕ_1	a_2	ϕ_2	Nighttime const	a_1	ϕ_1	a_2	ϕ_2
CHAMP$^{(\star)}$	5.561	0.783	-6.666	-0.7032	6.066	2.721	0.4483	-0.4159	-0.369	-0.1633
CHAMP	3.855	0.810	-6.526	-0.589	6.119	1.994	0.496	-0.128	-0.338	-0.052
NRLMSISE-00	5.144	0.868	-6.239	-0.785	5.889	2.571	0.527	0.162	-0.445	-0.484
JB-2008	4.808	0.957	-6.648	-0.788	5.949	2.339	0.479	-0.082	-0.343	-0.327
GRACE-A	1.238	0.324	-6.642	-0.131	6.312	0.475	0.156	-0.496	-0.100	0.610
GRACE-B	1.240	0.325	-6.624	-0.123	6.307	0.467	0.154	-0.479	-0.086	0.704
NRLMSISE-00$^{(A)}$	1.525	0.367	-6.446	-0.104	6.466	0.692	0.243	-0.511	-0.147	1.007
NRLMSISE-00$^{(B)}$	1.523	0.364	-6.443	-0.106	6.439	0.687	0.237	-0.496	-0.139	0.990
JB-2008$^{(A)}$	1.310	0.340	-6.599	-0.117	5.908	0.499	0.154	-0.481	-0.049	0.944

Table 11.3 Annual variations of the scaled mass density measurements at low latitudes $< \pm 30^\circ$ for both daytime hours (columns 2–6, and shown in Figures 11.19 and 11.20, upper panel) and nighttime hours (columns 7–11 and the Figure's lower panels). The scaling is done with respect to a common height level (400 km for CHAMP and 475 km for the GRACE satellites) as well as with respect to a common solar activity reference level of $P_{10.7} = 130$. The fitting is done with respect to annual and semi-annual variation terms: $\rho(DOY) =$const$+a_1 \cos(2\pi/365 \cdot DOY + \phi_1) + a_2 \cos(4\pi/365 \cdot DOY + \phi_2)$, where ρ is measured in $[10^{-12} kg\, m^{-3}]$ and DOY is 'day of year' [in days]. The first data line $(\star)$ is deduced from CHAMP observations of the years 2002–2005, as presented at the 37th COSPAR meeting in Montrèal by Lühr et al. (private communication). Additionally, empirical models runs for NRLMSISE-00 and JB-2008 at CHAMP locations were performed.

observe an eastward wind in the afternoon to midnight sector and a westward wind after midnight on the dawn side prior to midday. It is known for a long time since shortly after the advent of the space era (see, e.g., *Jacchia* [1971*a*; *Bauer* [1973]) that the global thermospheric density maximum is time shifted with respect to the subsolar point by about two hours and the temperature and pressure maxima are even further shifted.

The thermal balance in the thermosphere is governed by the heat conduction equation that comprises various heating sources and losses as well as the heat transport by thermal conduction, which is a function of the neutral temperature itself, thermal advection and convection terms. The main heat loss is due to emissions in the infrared (IR). Radiative loss by IR occurs when atmospheric constituents are present which have transition levels in the infrared range of the spectrum as it is the case for atomic oxygen in the terrestrial thermosphere [*Bauer*, 1973]. The solution of the time-dependent heat balance equation leads to a time variation of the thermospheric temperature, characterized by the so-called exospheric temperature T_∞, having a maximum which occurs several hours later than that of the maximum EUV heat input (midday), due to the thermal inertia of the atmosphere.

The solution of the heat balance equation with realistic inputs leads to a T_∞ maximum at about 17:00 LT (see, e.g., Figure 2.5 in *Bauer and Lammer* [2004]). The thermospheric density maximum, on the other hand, occurs around 14:00 LT as is known from satellite drag observations since the early days of the space era. Consequently, a temperature maximum was inferred for the same time from atmospheric model considerations [*Jacchia and Slowey*, 1968]. This problem has been termed the diurnal phase anomaly between atmospheric density and temperature by *Chandra and Stubbe* [1970]. The thermospheric pressure bulge as the main driver of the low- to mid-latitude winds, finally, should be found somewhere in between the density and temperature maxima, as both components contribute to this quantity.

Additionally, at high latitudes and in particular during geomagnetic disturbed periods, other heating sources become important as collisions between charged particles and neutral constituents, the so-called Joule heating, and direct and indirect heating by solar wind influences as energetic particle precipitations in the auroral zone that are mediated through the magnetosphere. The high-latitude wind circulation will be dealt with further below in Section 11.2.4.

Figure 11.21 shows the CHAMP cross-track wind determinations obtained from the calibration results CH_PN_R03. Here, we use the data product **"DENSWIND_ITERATIVE2_SENTMAN_ALPHA0.8"** and calculated averaged zonal wind velocities between $\pm 30^\circ$ geographic latitude both for ascending (blue points) and descending (red) orbits independently. Each data point of this scatter plot represents one passage of the low latitude region near the geographic equator. The lower panel of Figure 11.21 uses the same data points as plotted in the upper panel, but now it shows the local time (LT) variation of the geographic eastward zonal wind velocity for both ascending and descending orbits.

Here, the diurnal variation of both ascending (blue) and descending (red dots) low latitude orbital averages of the zonal wind determinations show a congruent and reasonable behaviour with a westward directed wind from shortly prior to sunrise until about 15:30 LT, and eastward wind during the late afternoon and nighttime hours. The amplitudes show a quasi-sinusoidal variation in the range of $\approx \pm 150$m/s.

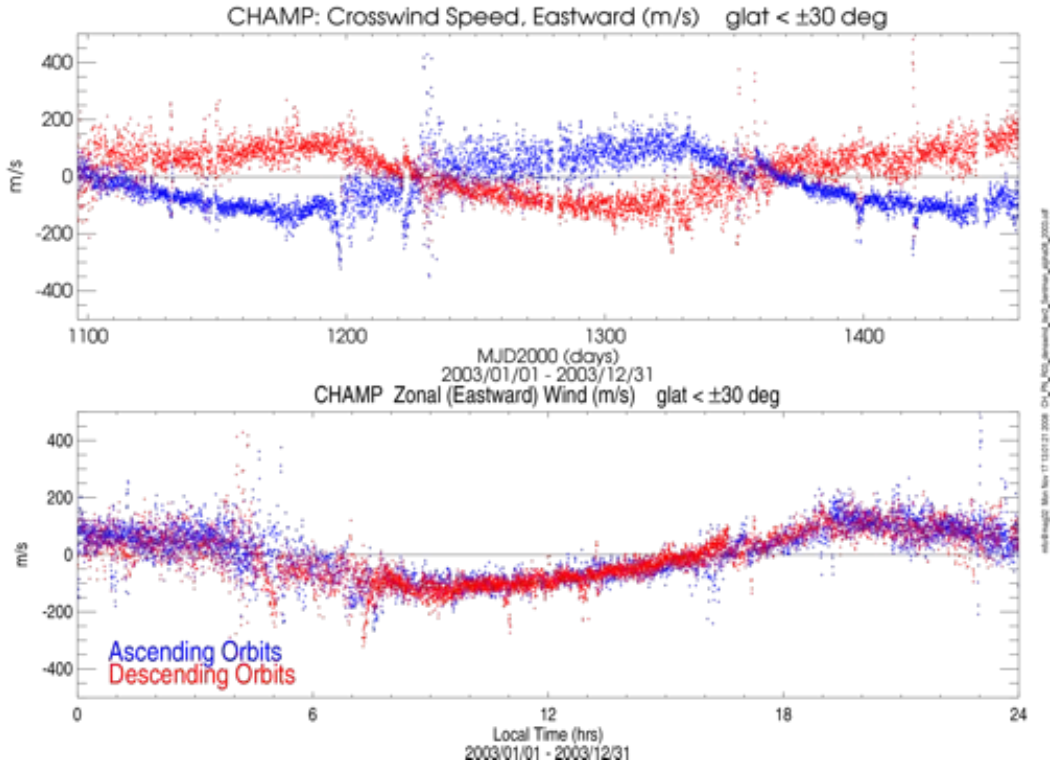

Figure 11.21 Scatter plot of the eastward cross-track zonal wind velocities at low geographic latitudes, averaged between $\pm 30^{\circ}$, for ascending (blue points) and descending (red) orbits. The upper panel shows orbit by orbit the variation versus MJD for the full year 2003; in the lower panel the same values are plotted versus Local Time, projected into geographic eastward direction. Here, we use the calibration runs labeled **CH_PN_R03** with the product "DENSWIND_ITERATIVE2_SENTMAN_ALPHA0.8".

Figure 11.22 shows the same scatter plots as Figure 11.21, but now for the GRACE, obtained from the analog data products of GA_PN_R03 with the DENSWIND_ITERATIVE2_SENTMAN_ALPHA0.8 runs. These wind determinations are more difficult because of the smaller signal strength at the higher altitudes of about 500 km. Further, the calibration has certainly a larger influence on the wind results than on the density (drag) estimations. It is clear, that the R03 calibrations for the GRACE satellites are not yet optimal; the average behaviour of the scatter curves look still quite messy at this stage. This concerns in particular the nighttime and sunrise/sunset intervals, which show a large scatter and frequent sign changes. The daytime interval between about 07 LT and 15 LT is more reasonable with maximum amplitudes of 200m/s of westward wind during prenoon and a wind reversal to eastward wind at about 14 LT. The GRACE orbit modelling and calibration certainly needs still some improvement.

11.2.2 The afternoon wind reversal - an independent check

Figure 11.23 shows the comparison of the low-latitude wind estimations (PN_R03 calibration) for CHAMP in 2003 with the corresponding values obtained from the most advanced empirical wind model HWM-07 [*Drob et al.*, 2008], including the upper thermospheric storm-induced disturbance winds as modelled in the DWM07 model [*Emmert et al.*, 2008*b*], which is considered here as an integral part of the HWM-07. The upper panel of Figure 11.23 is a repetition of

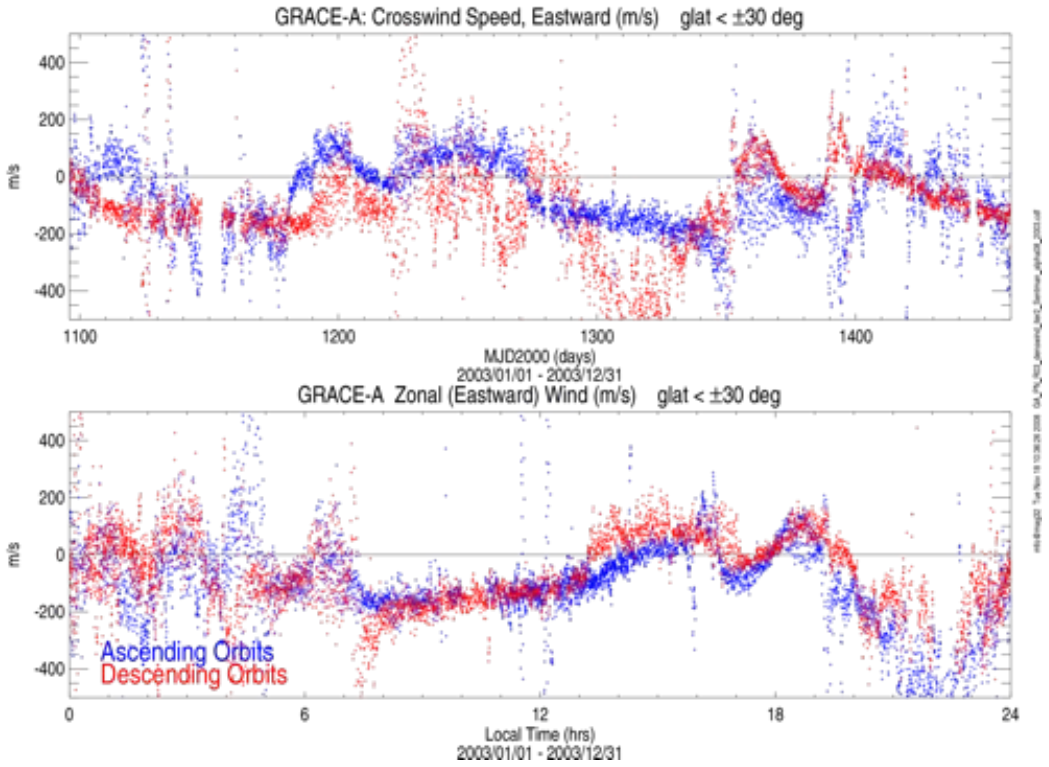

Figure 11.22 The same scatter plot of the averaged y-component zonal wind velocities at low geographic latitudes as in Figure 11.21, but now for both GRACE-A (GRACE-B shows a similar behaviour). Here, we use the same calibration approach as in the previous Figure 11.21, namely **GA/GB_PN_R03** data with the product "DENSWIND_ITERATIVE2_SENTMAN_ALPHA0.8"

the lower panel in Figure 11.21, while the lower panel shows the direct comparison of hourly averages with the state-of-the-art empirical thermospheric wind model. The model values are sampled in the same manner as hourly averages of the orbit-by-orbit averages at the same positions along the orbit trajectory and for the same geophysical conditions as the corresponding data set of the CHAMP orbits, separated into ascending (black curves) and descending (green) low-latitude equator crossings. The average variances are indicated by the vertical bars for each individual hour and each curve, where the width of the bar corresponds to $\pm 1\sigma$.

The correspondence between the ascending and descending curves on the one hand, and the derived low-latitude diurnal wind variations with the HWM-07 model variations is quite impressive already, although some noticeable differences are evident. Corresponding plots for other yearly overviews of the CHAMP results can be found below in Section 11.1.3 (Figures 11.26 to 11.29). The different yearly plots are mainly different with regard to the width of the scatter, but the diurnal variation and its differences with respect to HWM07 are about the same for all plots (to slightly different degrees). The main differences of the R03 zonal wind results to the HWM07 "climatological" modelling can be summarized as follows:

- the dusk transition through zero is about 17:30 LT for HWM07, but generally about two hours earlier in our R03 data set;
- there is the general tendency for "more eastward" wind amplitudes of the R03 CHAMP data in the afternoon to nighttime hours (≈14–22 LT) and

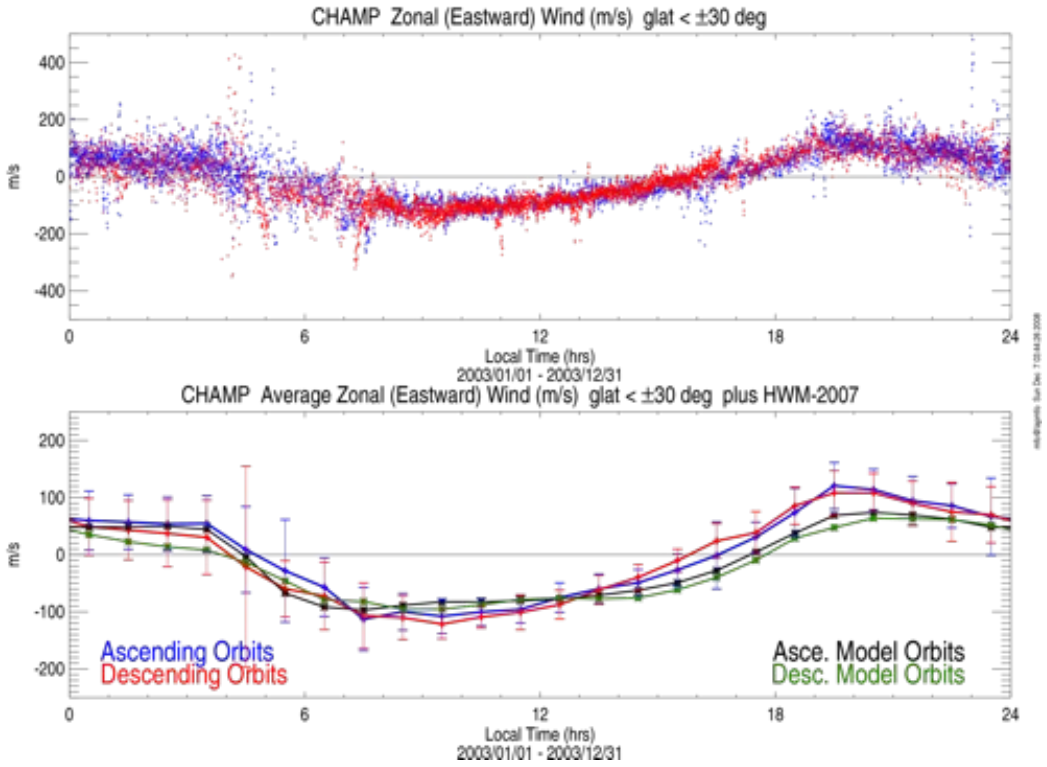

Figure 11.23 Comparison of the diurnal variation of eastward zonal wind velocities at low geographic latitudes, averaged between $\pm 30^{\circ}$, with corresponding values obtained from the empirical neutral wind model HWM-07 [*Drob et al.*, 2008; *Emmert et al.*, 2008*b*]. The upper panel shows the same scatter plot of the averaged eastward zonal wind velocities for the year 2003, separated into ascending (blue points) and descending (red) orbits, as shown in the lower panel of Figure 11.21. The lower panel shows hourly averages for both the CHAMP zonal wind velocities and the HWM-07 model data, obtained at the same locations in space and time along the S/C path, separately for ascending (black curves) and descending (green) orbits. The (1-σ) variances are indicated by the vertical bars for each individual hour and each curve.

- a less obvious tendency for "more westward" wind amplitudes in the prenoon hours (from about sunrise 05 LT to ≈11 LT), but not for each year;
- the steeper early morning (≈05 LT) wind reversal coincides quite well for CHAMP and HWM-07 results.

The afternoon to midnight differences (possible overestimation of the R03 CHAMP results with respect to the HWM-07 results) is generally present for each year, while the prenoon effect is more rarely seen (e.g., in 2002: 07-10 LT, in 2005: 05-09 LT, and in 2007: 05-11 LT).

The prenoon differences seem to be related to another effect: one can have the impression that periods of larger scatter (larger variance) are not simply a larger Gaussian (symmetric) scatter, but they are mostly connected with a shift of the mean values to one side preferably.

The opposite prenoon-to-afternoon differences between R03 CHAMP data and HWM-07 model values seem to be related to the solar illumination of the S/C; there seems to be a slightly larger force away from the sun in the CHAMP data. But this overshoot is stronger for the afternoon to nighttime side compared with the prenoon effects - and it seems to extend even into the dark, non-illuminated

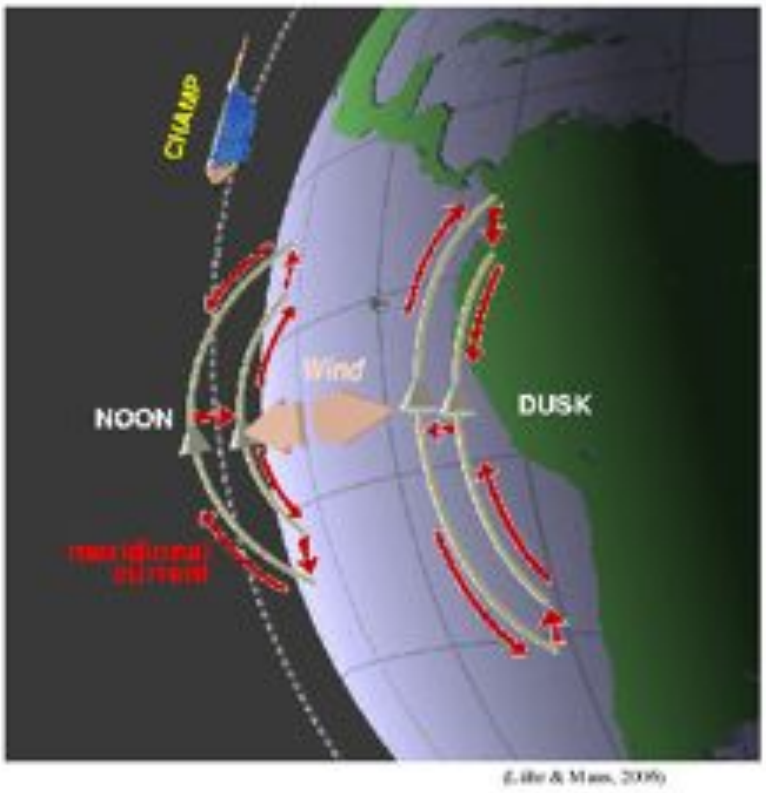

Figure 11.24 Schematic illustration of the dayside F-region dynamo over the magnetic dip-equator driven by thermospheric neutral winds. Meridional current systems with opposite sense are set up in the noon and dusk sector (from *Lühr and Maus* [2006], Figure 2).

periods near midnight. Could this difference be related to an error in the estimation of the IR backscatter effects of the S/C panel modelling?

The significant difference between the west-to-east wind reversal times of about two hours between the (preliminary) R03 CHAMP estimations and the HWM-07 model results is a challenging item. There is an interesting opportunity for an independent check of the wind reversal time, which results from the F-region dynamo theory, that was originally proposed by *Rishbeth* [1971*a*] and further outlined in the paper of *Rishbeth* [1971*b*]. The dayside F-region dynamo causes a closed meridional current system within the upper atmosphere in the ionospheric E- and F-layers as shown schematically in Figure 11.24, which is taken from *Lühr and Maus* [2006], Figure 2.

The F-region dynamo is driven by the thermospheric zonal wind component. The current system then consists of field-aligned loop currents between the E- and F-region, a Pedersen closure current in the E-region of low- to mid-latitudes, and a vertical current above the geomagnetic dip-equator. The latter causes a magnetic disturbance field, which is measured in the azimuthal direction (S/C y-component) by means of the flux gate magnetometer (FGM) on board CHAMP during traversing this current sheet. Other current systems of that region, like the Equatorial Electrojet (EEJ), the pressure-gradient or the gravity driven currents, are manifested in different components and/or in the magnitude of the geomagnetic disturbance vector.

The FGM measurements onboard the S/C provide therefore an unique and

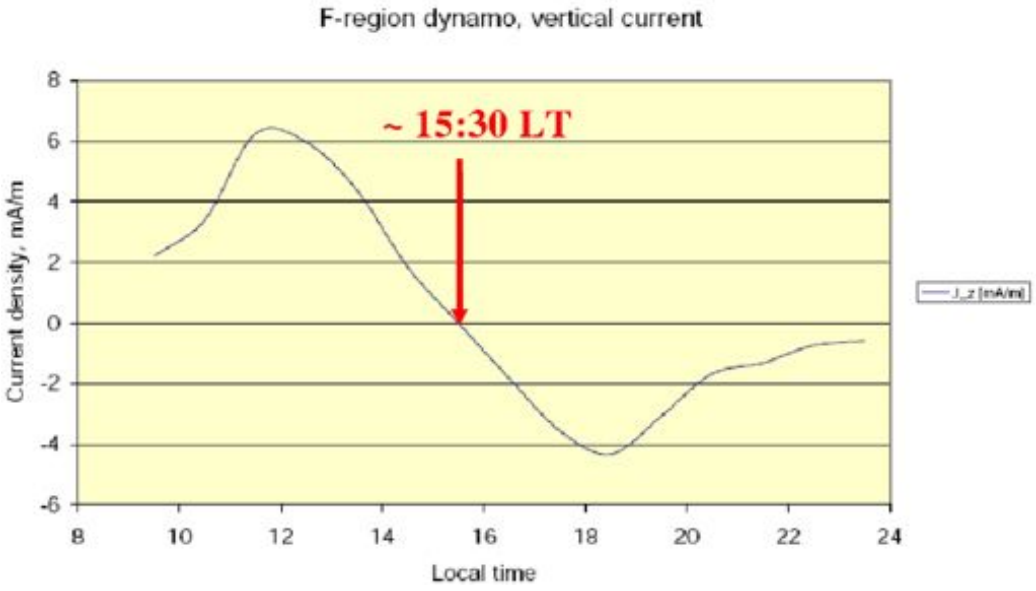

Figure 11.25 Local Time variation of the vertical current density (mA/m) at about 400 km altitude driven by the F-region dynamo. These are long-term averages as derived from CHAMP FGM measurements of the years 2001 to 2005 (*Lühr et al.* [Dec 2008], Figure 2.7).

independent opportunity to check the thermospheric zonal wind orientation in a statistical average sense. Figure 11.25, adapted from *Lühr et al.* [Dec 2008], Figure 2.7, shows the local time variation of the typical current density, that is driven by the dayside F region dynamo, as observed by CHAMP, averaged over the years 2001 to 2005. The current density shows clear peaks of opposite sign at noon and near sunset local time. This is indicative for a change in zonal wind direction from westward during daytime to eastward during evening/nighttime hours. Toward nighttime hours, the current fades slowly away, probably because the ionospheric conductivity becomes progressively smaller there [*Lühr and Maus*, 2006].

The zero transition on average should mark the transition from a westward directed thermospheric zonal wind around noon to an eastward wind prior to sunset. According to this long-term average, this wind reversal occurs at ≈15:30 LT, which coincides quite well with the preliminary findings of our R03 calibration CHAMP data, as shown for several yearly averages of the diurnal zonal wind variation in Figure 11.23 and later in Figures 11.26 to 11.29.

11.2.3 Solar activity dependence

Solar activity dependences of the thermospheric wind determinations are obvious, when looking at the scatter plots of Figures 11.26 for high solar activity in 2002, Figures 11.23 and 11.27 for moderate activity in 2003/2004 and finally Figures 11.28 and 11.29 for low solar activity in 2005/2007. The lower densities for declining solar activity (and at higher altitudes as for the GRACE data) are unfavourable for the wind derivation. The scatter of the data increases steadily with declining solar activity. On the other hand, the amplitudes and phases of the yearly averages do not seem to show obvious differences, at least they cannot be noticed at a first glance. A detailed analysis has to be done with the full data set when good calibrations are available throughout.

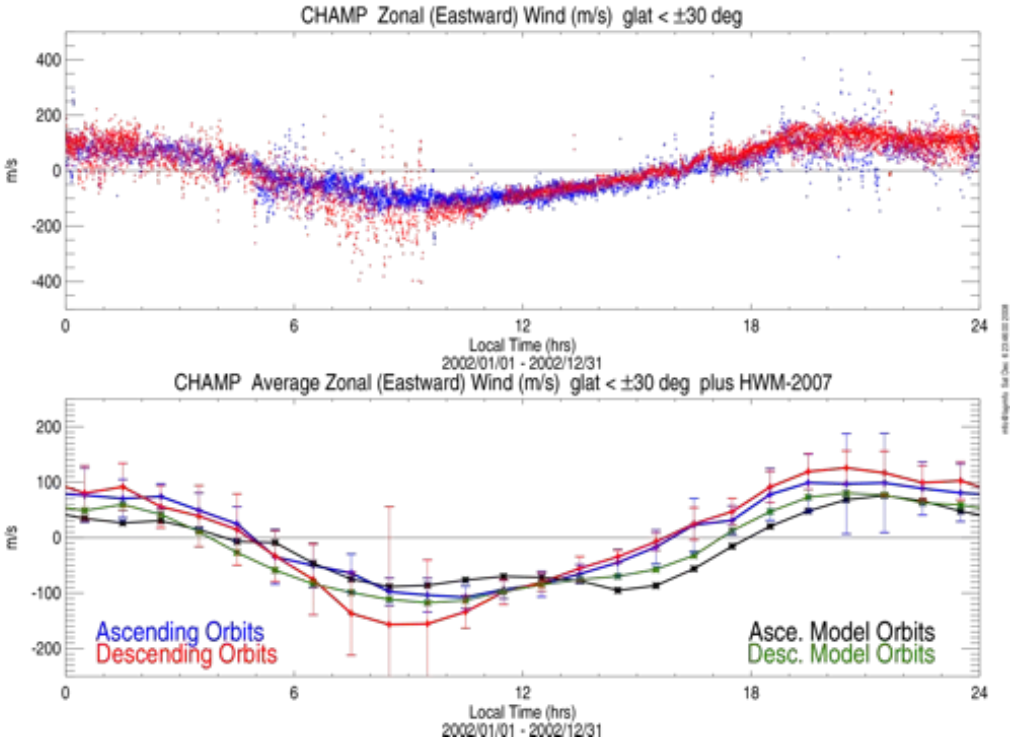

Figure 11.26 Same diurnal variation of the zonal (Eastward) CHAMP wind velocities as shown in Figure 11.23 in comparison with the HWM-07 model, but for the year of high solar activity 2002.

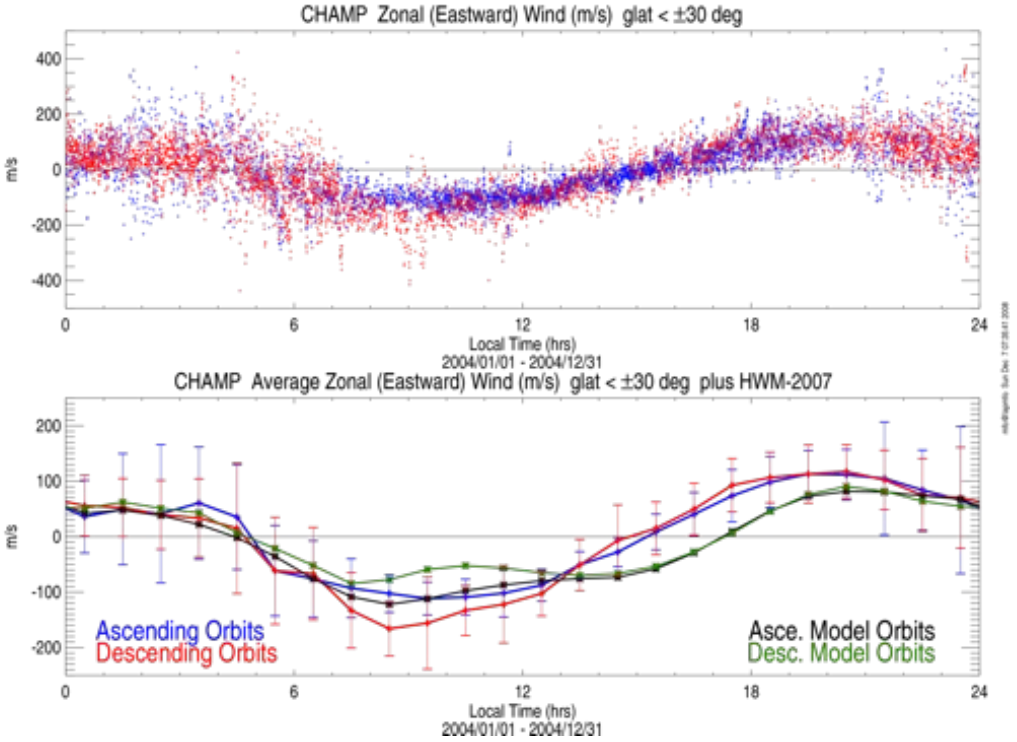

Figure 11.27 Same diurnal variation of the zonal (Eastward) CHAMP wind velocities as shown in Figure 11.23 in comparison with the HWM-07 model, but for moderate solar activity in 2004.

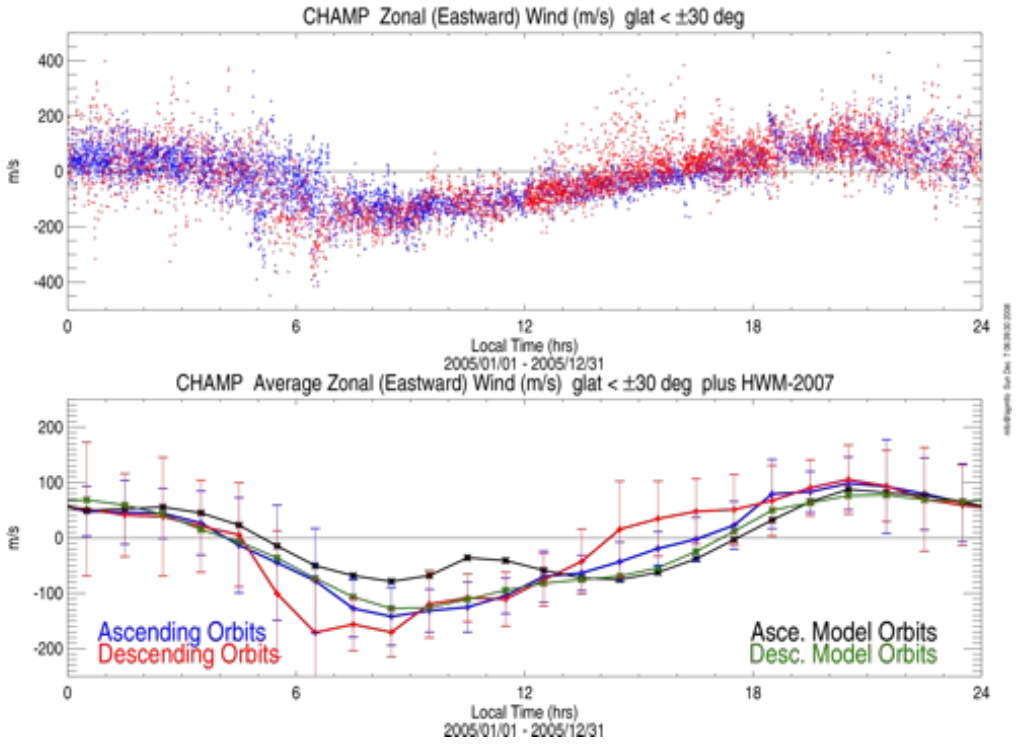

Figure 11.28 Same diurnal variation of the zonal (Eastward) CHAMP wind velocities as shown in Figure 11.23 in comparison with the HWM-07 model, but for low solar activity in 2005.

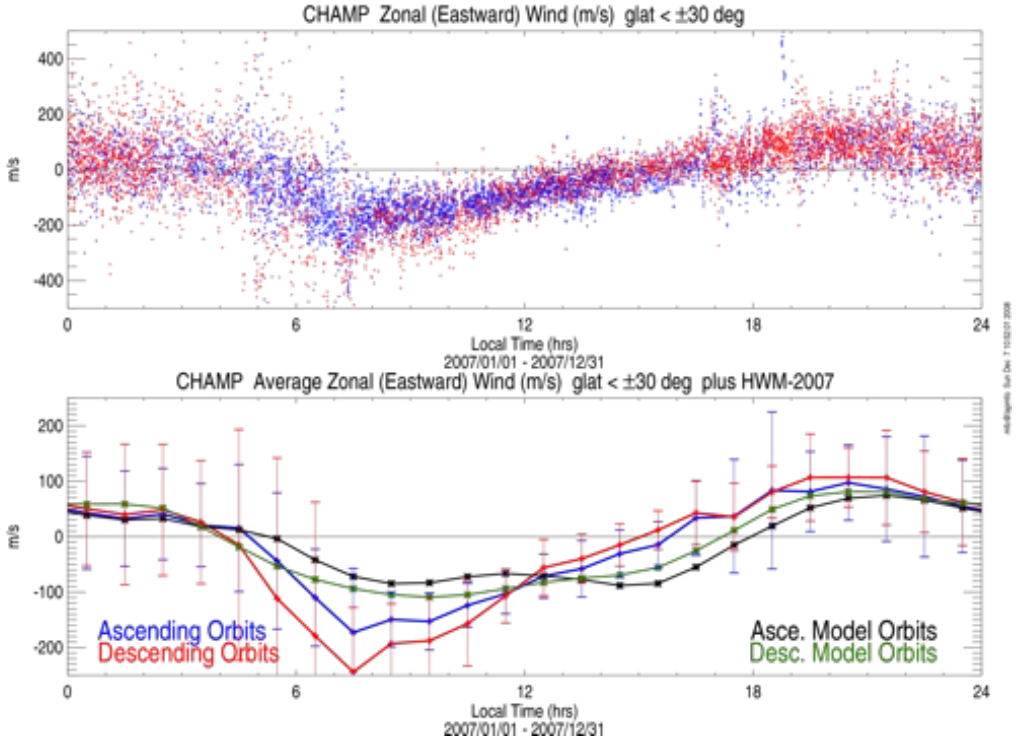

Figure 11.29 Same diurnal variation of the zonal (Eastward) CHAMP wind velocities as shown in Figure 11.23 in comparison with the HWM-07 model, but for low solar activity in 2007.

Slight differences in the local-time behaviour, which can be noticed for instance around prenoon hours, are most likely a seasonal effect. Each annual mean diurnal zonal wind variation curve is composed from different intervals of the year, i.e. there are different mixtures of local time and seasonal variations, which are unresolvable by this simple statistical method used here.

Further, there seems to be a daytime modulation with a secondary minimum near the local noon, mainly seen in the HWM-07 model data, and hardly seen (if it is even a real effect) in the R03 CHAMP data. The exact position of this secondary minimum might depend on season. The differences in local-time behaviour of this minimum might be related to larger ion drag during periods of higher plasma density near noon-time at low latitudes, but this is only a likely suspicion, disregarding the complexity of the whole dynamic system.

11.2.4 High-Latitude thermospheric wind pattern

At high latitudes the thermospheric wind is governed more directly by the geomagnetic co-ordinate system. To state it more precisely, the neutral air parcels are subjected to forces which obey both geographic coordinates, like the Coriolis and the centrifugal forces as well as the dayside heating source by EUV radiation, and geomagnetic coordinates as, e.g., high-latitude particle precipitaions, Joule heating, and electrodynamic forces. The strong geomagnetic control of the high-latitude thermosphere dynamics has been shown since the early satellite observations of thermospheric neutral air motion (e.g., *Hays et al.* [1984], *Killeen et al.* [1986], and *Richmond et al.* [2003]).

The larger displacement of the geographic and geomagnetic poles in the South in comparison with the North Hemisphere might cause some differences between the hemispheres in the high-latitude thermospheric circulation pattern and their variances as discussed in the paper of *Förster et al.* [2008].

Figure 11.30 shows the preliminary average thermospheric wind circulation results of the R03 calibration for CHAMP data of the year 2003 without sorting them for any solar wind and IMF dependence. The full-vector patterns are derived for both the North (upper panel) and South Hemisphere (lower panel) from the cross-track wind component measurements by assembling them in a statistical approach to get the full horizontal wind pattern over the high-latitude circumpolar regions in orthogonal Solar Magnetic (SM) coordinates.

For a particular point in space we combine measurements from different orbits that cross this point at various distinct time moments which are distributed over the whole time interval of measurements in 2003. The reconstruction of the full horizontal wind vector at this point is done with a Singular Value Decomposition (SVD) method which combines the n individual component measurements V_{yi} of a given bin with their known directions $\vec{k}_i$ in the horizontal plane to a best-fit wind vector $\vec{V}$ estimation at the bin location that is obtained by minimizing δf in:

$$\sum_{i=1}^{n} \left(V_{yi} - \vec{k}_i \vec{V} \right)^2 \; = \; \delta f \tag{11.7}$$

This vector estimation is done for each bin of the 2-D grid independently. The method is explained in more detail in the paper of *Förster et al.* [2008], where it was applied to the same CHAMP data interval of the year 2003. But a different set of wind estimates had been used there, based on a simplified method for their derivation [*Liu et al.*, 2006].

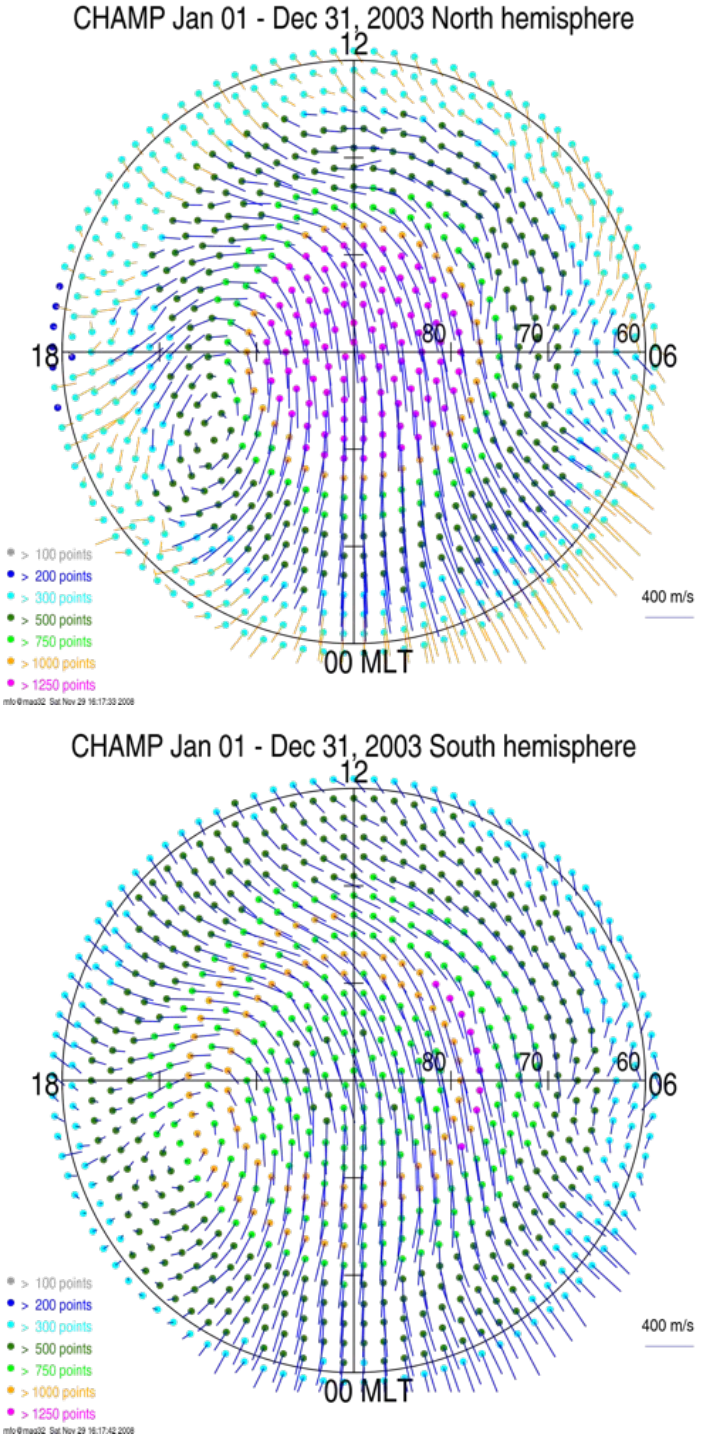

Figure 11.30 Thermospheric wind circulation pattern obtained from the cross-track accelerometer measurements of CHAMP (R03 calibration, see text) during the year 2003 for both North (upper panel) and South Hemisphere (lower panel), averaged over all solar wind and IMF conditions (cf. *Förster et al.* [2008], Figure 1). The wind direction is shown by small vectors at each bin's position within the MLT/magnetic latitude dials with an outer border at $60°$. The blue/yellow lines indicate the magnitude with the scale given at the lower right; the number of data points in each bin is colour-coded with the scale at the lower left.

In Figure 11.30, the average wind direction is shown by small blue vectors with the origin in the dots at the bin's position within the MLT versus magnetic latitude dials; their lengths indicate the magnitude. A scale is given on the lower right side of the plot. The number of data points in each bin is colour-coded in the dots, with respect to the scale at the lower left. The outer border of the circular plots is at 60° magnetic latitude and the numbers at the outer border indicate the magnetic local time (MLT) with high noon at the top and the dawn and dusk at the right and left side, respectively.

Both dial plots in Figure 11.30 show the neutral thermospheric air circulation at the S/C orbital height level of about 400 km across the high-latitude circumpolar regions. The patterns are dominated by a cross-polar bulk flow from the dayside afternoon to the nightside, which is partly driven by the dayside EUV heating from the solar radiation. The flow velocities are strongest within the polar cap region at magnetic latitudes $>\approx 80^\circ$ and the cross-polar circulation is modified by auroral and polar energy input and electrodynamic forces, which are driven by the solar wind - magnetopause coupling processes, in particular due to the magnetic reconnection with the IMF.

At the duskside, a large circular vortex motion can be recognized, while on the dawnside a smaller deflection of the laminar stream takes place. Beside the solar wind and IMF drivers, the interplay of thermodynamic and electrodynamic processes as well as of the Coriolis and centrifugal forces causes these dawn-dusk differences of typical large-scale high-latitude circulation patterns.

Similar patterns of the yearly average high-latitude thermospheric wind circulation of the year 2003 have been obtained in the paper of *Förster et al.* [2008], Figure 1, as mentioned above already. The strong IMF control of the high-latitude circulation pattern, in particular its dependence on the IMF B_y and B_z components, has been demonstrated there and can be revealed also with the R03 calibration data set (not shown here). It confirms earlier findings (as, e.g., those of the AE-C and DE satellites in the early 80-ies [*Hays et al.*, 1984] [*Killeen et al.*, 1986]), but puts it now on a much broader statistical base and allows more detailed insights into the high-latitude coupling processes between the neutral and the plasma components.

11.2.5 The attitude calibration manoeuvre in June 2004

An attitude calibration manoeuvre was performed with the CHAMP satellite during the period 21-29 June 2004. The purpose of this campaign was to determine the attitude control characteristic, when small angular offsets are commanded [*Lühr and Falck*, 2004]. Here, we will inspect the various slight offsets from the nominal attitude to learn, whether they have any apparent influence on the results of our data retrieval of density and cross-wind estimations.

The two attitude components of interest - the pitch and the yaw - were tested; a bias in roll will have no effect on the drag. In a first series, set-points were varied in the pitch direction. This angle was changed from $+2^\circ$ in steps of one degree down to -2°. Each angular offset was applied for about 12 hours continuously. For reference CHAMP was flying between subsequent periods of biased attitude for about 12 hours in the nominal attitude mode. The same sequence of angular offsets were applied to the yaw direction during a subsequent series (cf. the Table in Figure 11.33).

The switching of the set-points was always performed at an ascending equator crossing, which occured during this campaign on the night side ($\sim$03:20 LT).

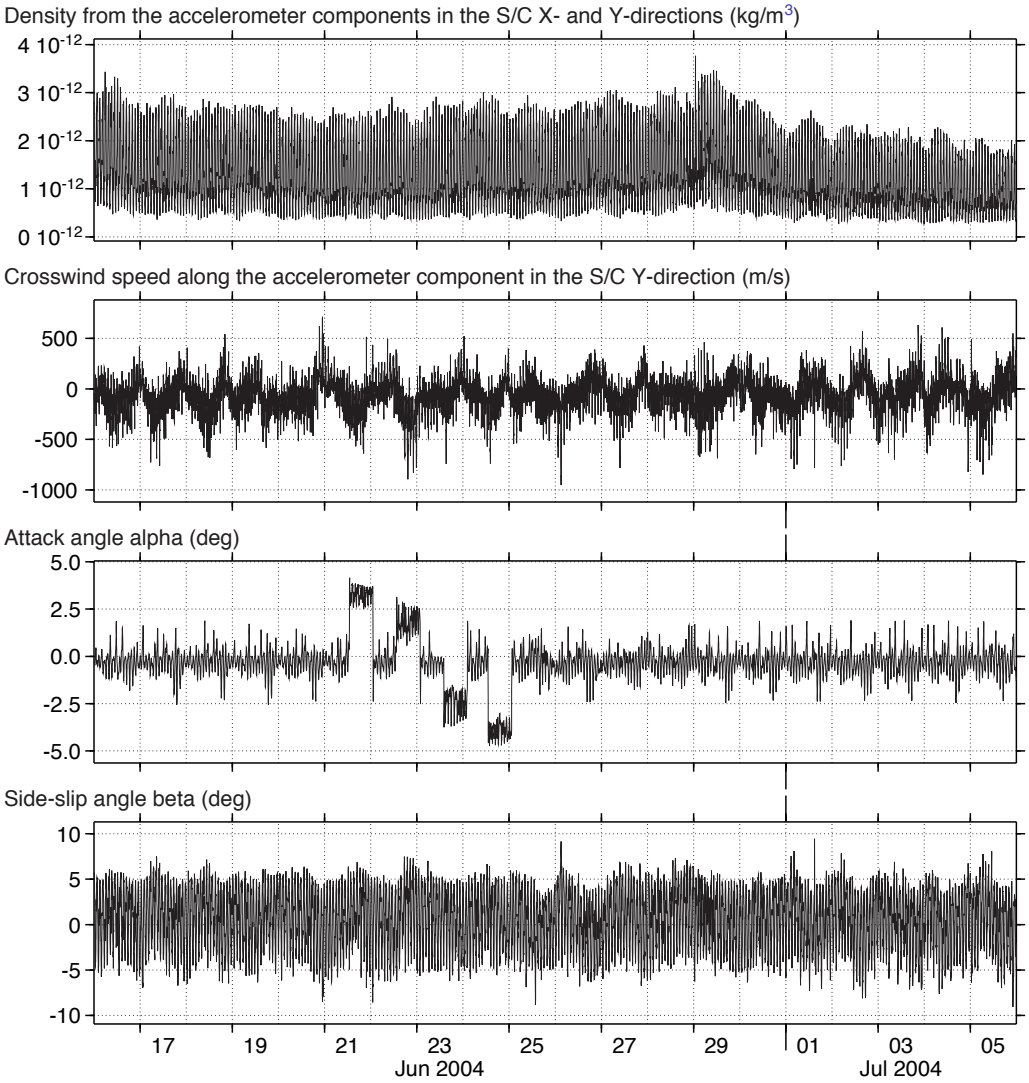

Figure 11.31 Overview of some CHAMP measurements along the orbit during a 20-day interval in June 2004, which comprises the attitude calibration campaign of June 21-29, 2004 [*Lühr and Falck*, 2004]. The panels show (from top to bottom) the density estimation, the cross-wind speed in the S/C y-component, the angle of attack α [deg] and the sideslip angle β [deg]. The pitch angle manoeuvres, which can be noticed in the third panel, appear to be somehow exaggerated with respect to the intended campaign values (cf. Table in Figure 11.33 and text); the yaw angle manoeuvres are hardly seen in the sideslip angle variations (fourth panel).

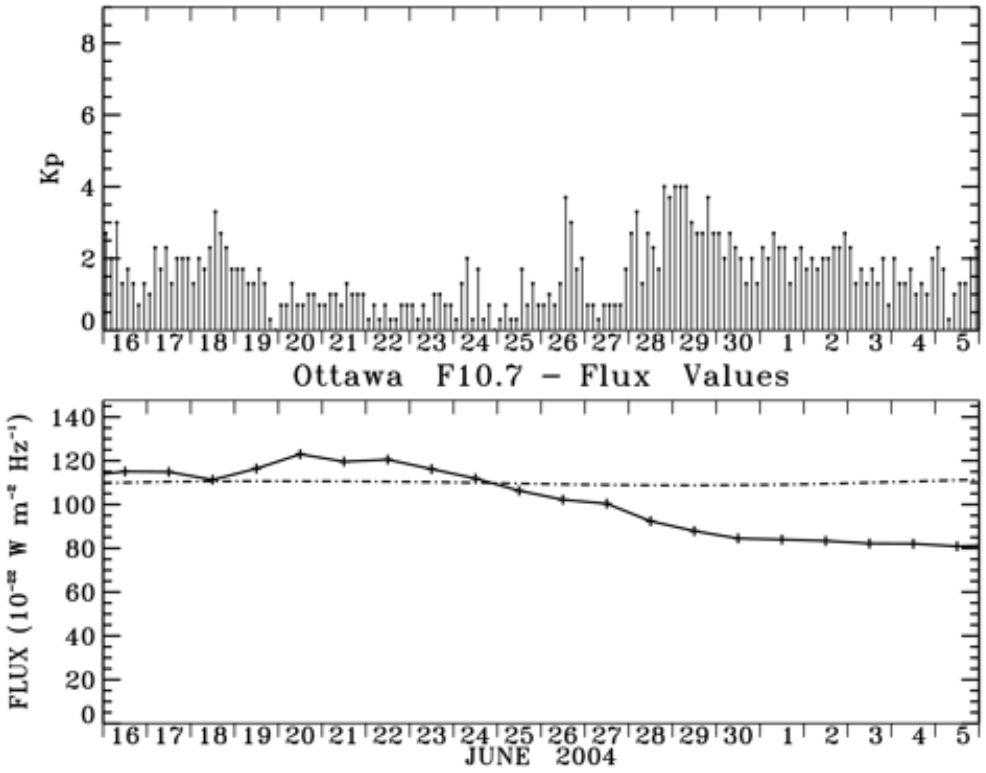

Figure 11.32 Geomagnetic and solar conditions during the same 20-day intervall in June 2004 as shown in Figure 11.31 with the Kp values (upper panel) and the $F_{10.7}$ values with the daily variations (full line) and the 3-months averages (dot-dashed) in the lower panel.

Table 1: Time-tagged command sequence for the attitude calibration campaign.

Interval	Begin	End	Set-point pitch	Set-point yaw
1	21 Jun 2004, 12:51:19	22 Jun 2004, 01:08:20	+2	0
2	22 Jun 2004, 01:08:20	22 Jun 2004, 13:25:21	0	0
3	22 Jun 2004, 13:25:21	23 Jun 2004, 01:42:21	+1	0
4	23 Jun 2004, 01:42:21	23 Jun 2004, 13:59:22	0	0
5	23 Jun 2004, 13:59:22	24 Jun 2004, 02:16:22	-1	0
6	24 Jun 2004, 02:16:22	24 Jun 2004, 13:01:14	0	0
7	24 Jun 2004, 13:01:14	25 Jun 2004, 01:18:14	-2	0
8	25 Jun 2004, 01:18:14	25 Jun 2004, 13:35:14	0	0
9	25 Jun 2004, 13:35:14	26 Jun 2004, 01:52:14	0	+2
10	26 Jun 2004, 01:52:14	26 Jun 2004, 12:37:06	0	0
11	26 Jun 2004, 12:37:06	27 Jun 2004, 00:54:05	0	+1
12	27 Jun 2004, 00:54:05	27 Jun 2004, 13:11:04	0	0
13	27 Jun 2004, 13:11:04	28 Jun 2004, 01:28:02	0	-1
14	28 Jun 2004, 01:28:02	28 Jun 2004, 12:12:54	0	0
15	28 Jun 2004, 12:12:54	29 Jun 2004, 00:29:52	0	-2

Figure 11.33 Time-tagged command sequence for the attitude calibration campaign of June 21-29, 2004 (from *Lühr and Falck* [2004], Table 1).

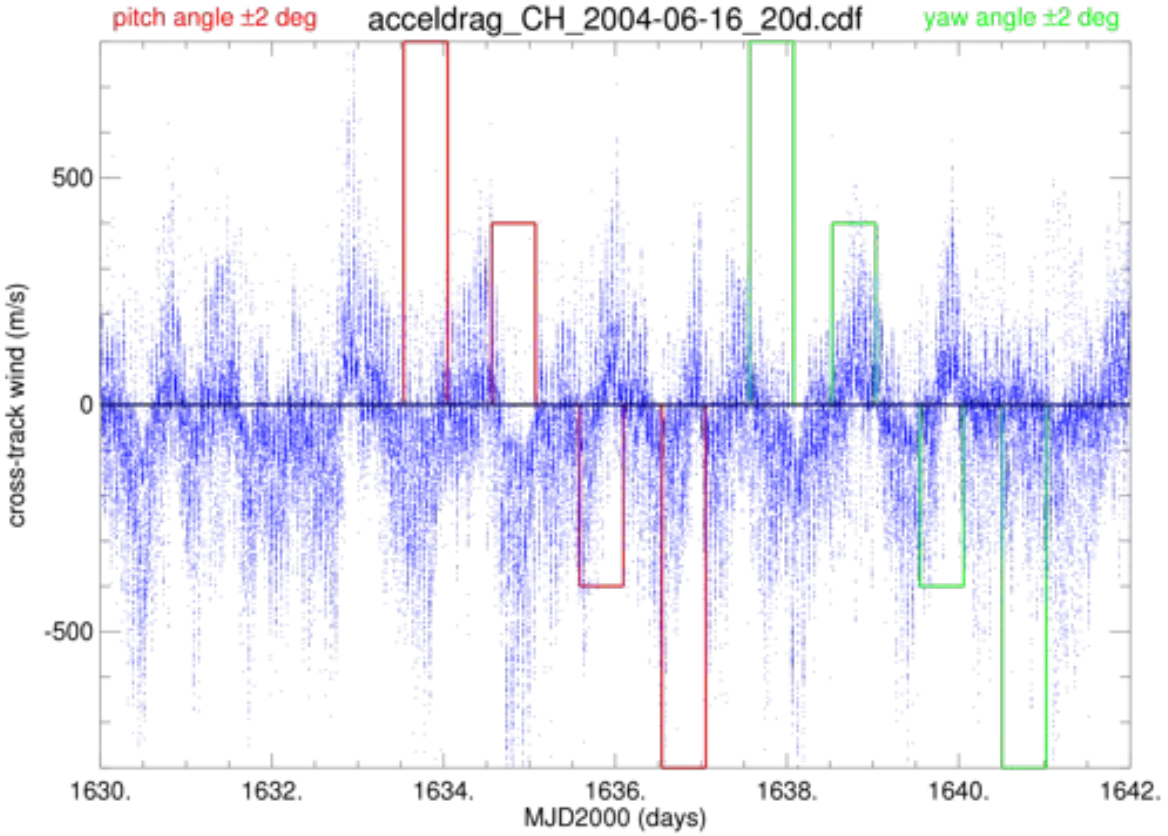

Figure 11.34 Cross-track wind along the S/C y coordinate for all full CHAMP orbits versus UT during a 12-day intervall in June 2004 which comprises the attitude calibration manoeuvre period. At low latitudes, positive values correspond to an eastward directed thermospheric wind component. Steplike pitch angle variations are indicated by a red colour line; the yaw angle manoeuvres are shown as a green line. The precise timings are listed in the Table of Figure 11.33.

Therefore both the offset and aligned attitude intervals were sampled always over integer numbers of orbit intervals. To avoid confusion with possible regional influences on the attitude behaviour, the nominal attitude mode has always been run during the first half of an UT-day, and the biased mode during the second half [*Lühr and Falck*, 2004].

The results of the estimated density, cross-track wind, and the angles of attack and side-slip (with respect to the bulk air flow around the S/C) for a 20-day interval in June/July 2004 that comprises the attitude manoeuvres are shown in Figure 11.31, which was downloaded from the project web page. Here, we use the same data product and calibration run as before - the "Denswind_iterative_Sentman" method applied to the panel model with an alpha-parameter of 0.8 and using the "R03" calibration.

At first glance, there seems to be no correlation of the density and cross-track wind estimations with the attitude offset periods. The third panel shows clearly the pitch angle offsets of the campaign, which are larger than the offset position values as listed in the Table of Figure 11.33. They attain values up to $\pm 4^\circ$ or even slightly more for the periods with $\pm 2^\circ$ offset in pitch angle and up to $\pm 3^\circ$ for the $\pm 1^\circ$ offsets. The reason for this deviation is the overreaction of the attitude to the bias in pitch. Corresponding plots of the deflection angles about the roll, pitch,

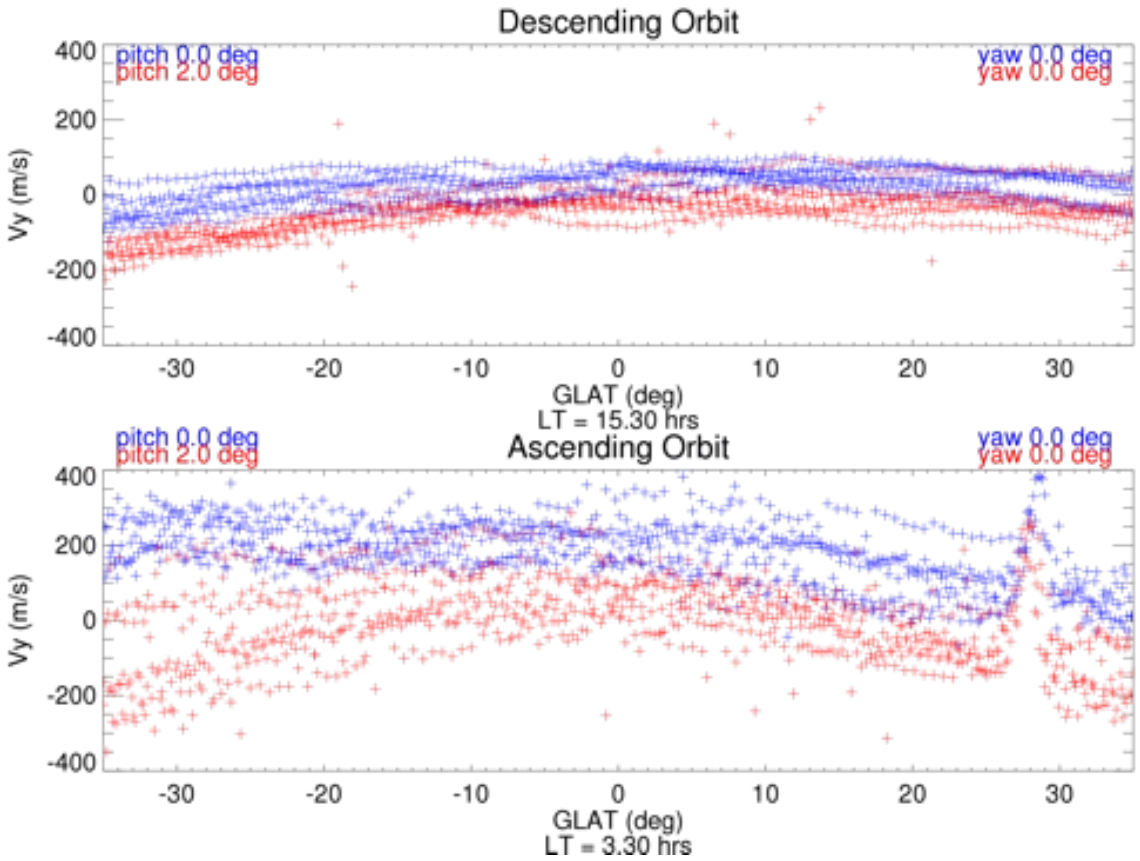

Figure 11.35 Cross-track wind along the S/C y coordinate for all full CHAMP orbits versus UT during a 12-day intervall in June 2004 which comprises the attitude calibration manoeuvre period. At low latitudes, positive values correspond to an eastward directed thermospheric wind component. Steplike yaw angle variations are indicated by a cyan colour line in the upper panel; the pitch angle manoeuvres are shown as a red line in the lower panel. The precise timings are listed in the Table of Figure 11.33.

and yaw axes, which are shown for all the intervals within the documentation of the experiments [*Lühr and Falck*, 2004], clearly show that frequent thruster activity is required in order to keep the S/C in this unstable attitude control band.

The biases of the yaw deflections (fourth panel of Figure 11.31) behave differently. These deflection angles are hardly visible - except of slight dents toward more negative values on the second half of June 25 and 26 and toward more positive values on June 28 - due to the large variability of the sideslip angle, which indicates the regularly varying co-rotation wind (along the polar circular orbit) and the larger wind amplitudes at high latitudes. Surprisingly, these yaw excursions go into the opposite direction of the commanded yaw offsets. For an unknown reason, CHAMP shows a stable behaviour for deflections about the yaw axis. Therefore the S/C tends to compensate for the imposed yaw biases with deflections in the opposite direction.

The geomagnetic and solar conditions as shown in Figure 11.32 were fairly quiet throughout the whole interval, except of a moderate disturbance on the last day of the campaign. The smooth variations of the density measurements with a slight increase on June 29 confirm this quiet-time behaviour. Both density and cross-track wind estimations show however a variation with a predominantly diurnal mode, i.e. the sampling along the various orbits which are spaced from

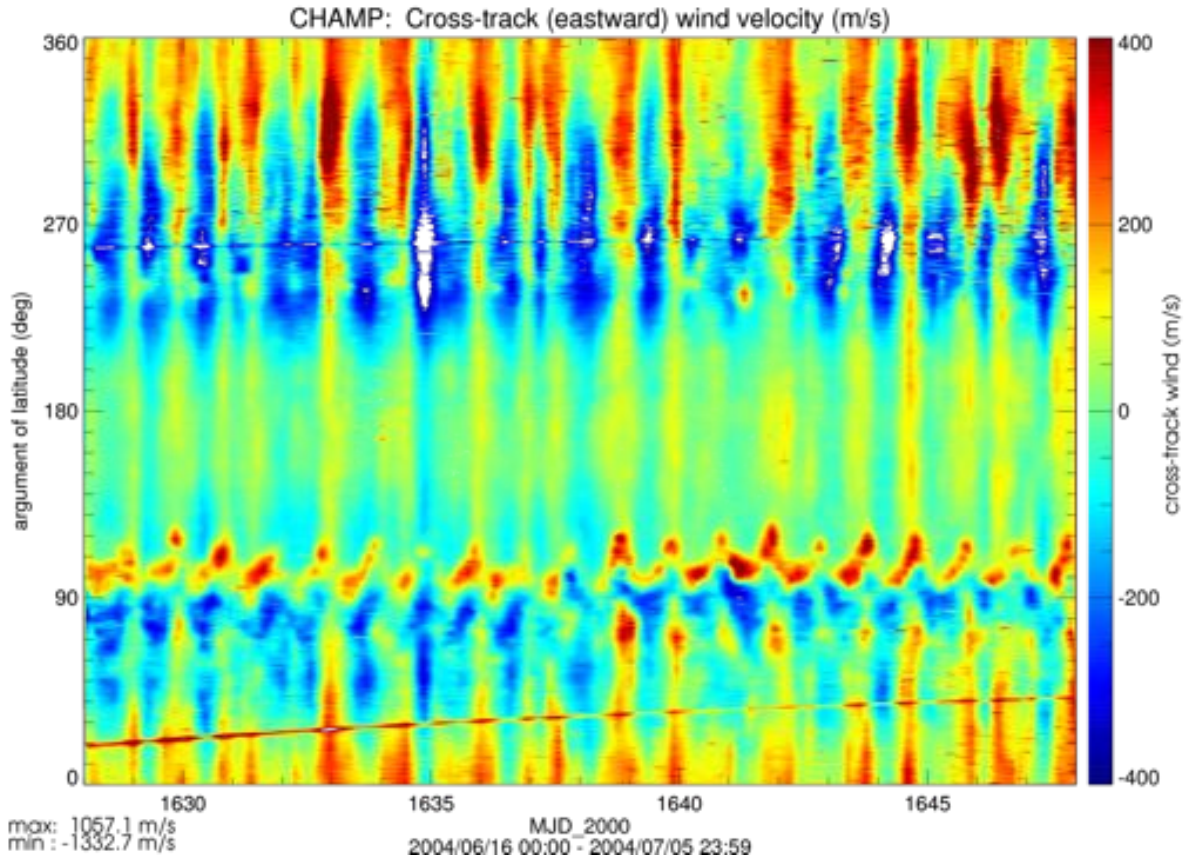

Figure 11.36 Cross-track wind along the S/C y coordinate for all full CHAMP orbits during a 20-day intervall including the attitude calibration campaign as shown in Figure 11.31, but now drawn as false-colour plot over UT (or the Modified Julian Day, MJD) and the argument of latitude of the S/C [deg] along its near-circular orbit. Equator crossings are at 0° (ascending orbit at ∼03:20 LT) and 180° (descending at ∼15:20 LT); passages close to the North and South pole occur at 90°and 270° respectively.

orbit-to-orbit by about 24° in longitude once per day around the whole globe, reveal an UT- or azimuthal variation with a periodicity of global scale.

Figure 11.34 shows the variation of the cross-track wind measurements along the CHAMP orbits during a 12-day interval which comprises the attitude calibration manoeuvre days. Overlaid on this are the steplike pitch angle (in red) and yaw angle (green lines) experiment times. Again, any obvious correlation between the cross-track wind estimations of this R03 calibration run and the neutral wind variation is not discernible. The large wind amplitudes on June 21 (DOY 1633) with a relativly sharp increase toward positive values (eastward wind at low latitudes for ascending orbits and westward for descending), which were at first glance suspected to be somehow artificial, finally appeared to be obviously of natural origin, as the closer inspection of various parameters of the whole calculation chain revealed. The sharp increase starts prior to midnight and the same is true for the decline at the end of this day, so that any relation to the calibration procedure (which is done on a daily basis) can be ruled out.

The direct comparison of measurements for ascending and descending orbits at low geographic latitudes for measurements both during the pitch angle manoeuvre (in red) and during the reference interval (in blue) as shown in Figure 11.35 seems to be of low value because of the dominating diurnal (global)

oscillation mode. Such low-latitude comparisons were done for all manoeuvre intervals and for different reference intervals, including a 24-hour shift for the first and last interval (not shown here), but they give no hint on any non-regular behaviour of the processing scheme.

But Figure 11.35 shows another phenomenon, which deserves clarification: the peak-like increase of the eastward wind along the orbital track close to 30° north with an amplitude of about 500 m/s above the background zonal wind.

To elucidate its origin, Figure 11.36 shows a global plot of the cross-track thermospheric wind measurements along the CHAMP orbit for the whole 20-day interval of June/July 2004 as in Figure 11.31. This colour plot shows the cross-track wind magnitude over UT (MJD_2000) and the argument of latitude, which is measured from the ascending node along the orbit in degrees of the circular orbit. The passages close to the North- and South pole take place near 90° and 270°, respectively, while the equator crossing of the descending orbital part is located at 180°.

The peak-like cross-track wind increase is seen in this colour plot as a trace at low- to mid-latitudes in the ascending part of the orbit (20° to 40° argument of latitude), which was on the early morning side (∼03:30 LT). Another trace can be noticed close to the South pole passage at ∼260°. These traces are located near the sun's terminator line along the S/C orbit, where the solar zenith angle is in the range of 108° – 110°. This is obviously either an incomplete solar illumination correction or an overshoot of this correction. In the case of this interval in June 2004 on the early morning (ascending) part of the orbit, this has a width of about 3° or 330 km of the orbit, which translates in about 43 sec of incorrect timing of the solar eclipse.

With respect to the CHAMP attitude calibration manoeuvre of June 2004, however, no obvious influences of the offset in S/C attitude could be found in the calculation results of density and cross-track wind.

Chapter 12
Simulations for Swarm

In this Chapter, the data relevant for density and wind retrieval from the future Swarm constellation is simulated and analyzed. The goals of these analyses are as follows:

- To determine the accuracy at which the Swarm accelerometers can be calibrated, if using the same techniques used for CHAMP and GRACE and when making use of data from the constellation of three identical satellites;
- To investigate the expected accuracy of the Swarm density and wind data products.

The last item, the accuracy of density and wind data products, depends partly on the strength of the acceleration signal, and therefore on the satellite altitude and the level of solar activity. Therefore, orbit, attitude and accelerometer data for the entire mission was generated for analysis.

For the first item, the investigation of calibration accuracy, simulated GPS tracking data are required as well. The calibration accuracy likely also depends on the signal strength and constellation geometry, which change over time. However, doing the calibration simulation over a very long time period is not feasible, and therefore only a single day has been selected. The selected day was chosen to be near the beginning of the mission, and to contain a geomagnetic storm during part of the day, in order to make an interesting and representative test case.

12.1 Producing simulated measurements

Each of the types of simulated data will be discussed in some detail in the next subsections: The initial, long-term orbit data in Section 12.1.1, attitude quaternions in Section 12.1.2, accelerometer data in 12.1.3 and finally, the GPS tracking data in Section 12.1.4.

12.1.1 Simulated orbit data

The starting point for the simulated orbit data is the constellation #4 from the report on the Swarm magnetic field inversion analysis [*Olsen et al.*, 2007].

The orbital data that was generated for this report was obtained from its authors, but it was found that the velocity component in these files was initially not physically correct, due to a bug in the code used for the orbit generation [*Olsen*, personal communication, 2008]. Eventually, this bug was fixed and new orbit

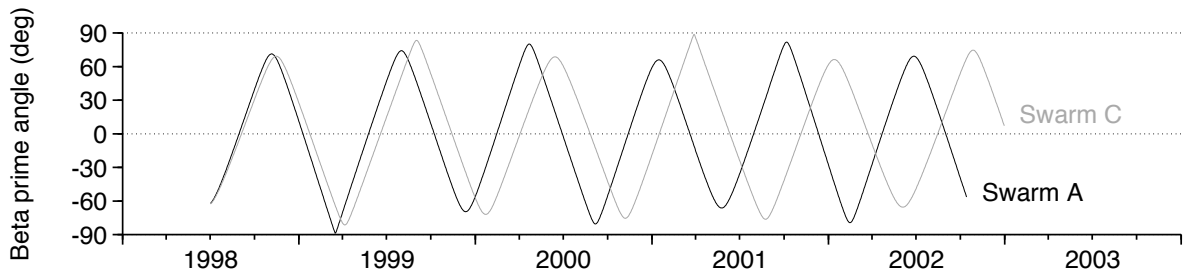

Figure 12.1 Time series for the simulated orbits of Swarm A and Swarm C of beta prime, which is the angle between the orbital plane and the sun-satellite vector.

files were generated, but in the meantime, it was decided that in order to proceed, it was required to independently propagate the orbits from the specified initial conditions, using the GEODYN software [*Rowlands et al.*, 1995].

In the simulation, a start date and time of July 30, 1998 at 00:00:00 UTC is chosen, which is approximately one solar cycle before the expected launch date. Because of this simulated launch date, the measured solar and geomagnetic activity of the previous solar cycle can be used as a simulation for the next one.

Force models

The EIGEN-CG03C gravity field [*Förste et al.*, 2005*b*] model was used for the orbit computations in GEODYN. The MSIS-86 model was used for the atmospheric density, and a cannonball representation with a $C_D = 2.29$, a $C_R = 1.5$, area $A = 0.95$ m^2 and mass $m = 500$ kg were used. The value of C_D was chosen to conform with the ballistic coefficient of $B = 230$ kg/m^2 used by *Olsen et al.* [2007], even though this value is likely much lower than what is realistic for a satellite shaped such as Swarm. A value in this range was chosen by *Olsen et al.* [2007] based on orbital analyses of Swarm with empirical atmospheric density models, such as MSIS. This lower than physical value of C_D is obtained in such an analysis, because of the likely overestimation of density by the model. Since the same or a similar density model is used in the orbit propagation for our analysis, we have stuck to roughly the same values for the satellite model.

Orbital elements

At the start epoch, all three satellites are assumed to have been launched into orbits with an eccentricity of 0, and an argument of perigee of 0°. Swarm A and Swarm B are at an initial altitude of about 450 km, while Swarm C is 80 km higher, at 530 km, leading to semi-major axis values of 6821.2 and 6901.2 km, respectively. The inclination for Swarm A and B is 87.4°, while for Swarm C it is 88.0 °.

The lower pair is flying close together, with a mean anomaly at epoch of 0° for both satellites and the right-ascension of the ascending node at 0° for Swarm A and -1.4° (or 358.6°) for Swarm B.

The initial right ascension at the ascending node of the higher satellite, Swarm C, is 0°, so that at the start of the mission, it is orbiting in nearly the same orbital plane as the lower pair. However, due to the different altitudes, the satellites experience different orbital drifts, causing a slowly changing angle between the orbital planes. The variation in the beta prime angle (the angle between the orbit plane and the sun-satellite vector) is shown in Figure 12.1. The figure shows that

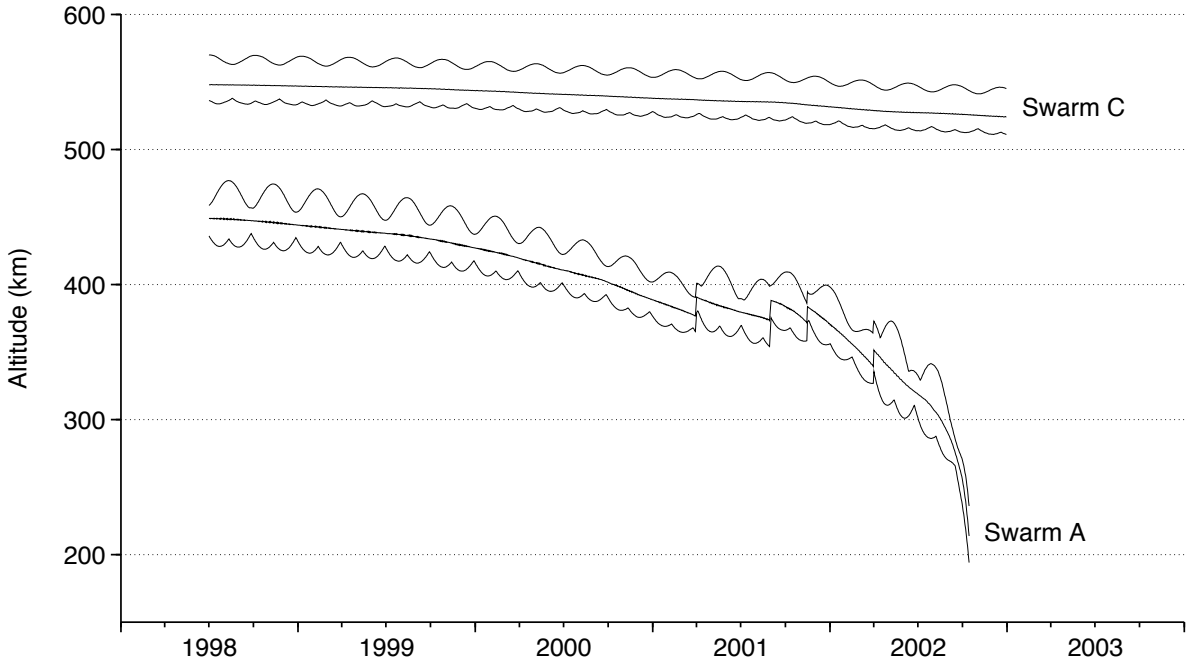

Figure 12.2 Evolution of the altitude of Swarm A/B (bottom curve) and Swarm C (top curve) in the simulated orbits.

at the end of the mission, the drift is nearly 180°. At the beginning and end of the mission, the satellites will therefore provide a sampling of the atmosphere which is most suitable for studying variations with altitude, since they will slice the atmosphere at roughly the same local solar time. Halfway through the mission the sampling will be more suitable for studying variations with local solar time.

Manoeuvres

The angular offset between the orbital planes of Swarm A and B of 1.4° is expected to be maintained using manoeuvres, for the duration of the mission. The maximum time difference between these two satellites when crossing the equator is specified at 10 seconds. Since the distance between those satellites remains so small, only one of them, Swarm A, is simulated for the entire mission duration. The orbit of Swarm B is only generated for the single day that was selected for the analysis of calibration parameter estimation.

The orbit of Swarm A includes the orbit raising manoeuvres at the times that are given by *Olsen et al.* [2007]: Increases of 15 km were made on April 1, 2001 and September 1, 2001. Additional boosts of 12 km were provided on November 15, 2001 and April 1, 2002. The evolution of the orbital altitude range covered by the satellites is plotted in Figure 12.2.

In this simulation, the perigee altitude of Swarm A get below 200 km for the first time in mid-October, 2002, after which the computation is stopped. Swarm C is then still at an altitude of around 525 km, having decayed no more than about 25 km.

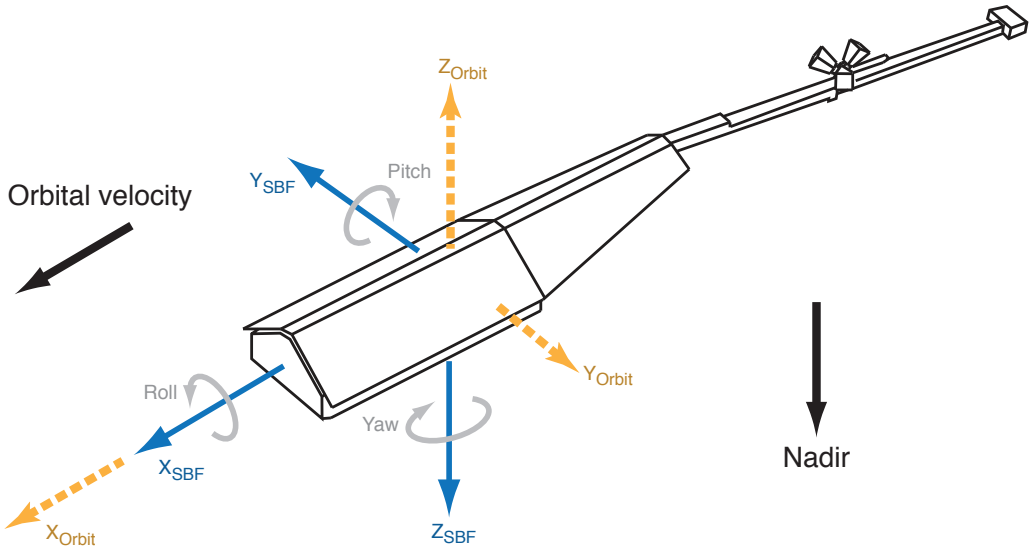

Figure 12.3 Orientation of the spacecraft body-fixed frame and of the orbit-fixed frame (along-track, cross-track and radial). The orientation of the orbit-fixed axes is shown for the nominal attitude, with all Euler angles at zero. Compare with the orientation of the axes of CHAMP and GRACE in Figure 4.9.

Truth orbits for accelerometer calibration tests

The above mentioned orbit generation is run for the entire duration of the simulated mission, from July 1998 to October 2002. For the accelerometer calibration tests, an additional set of orbits is generated for just the days around July 30, 1999, which is the selected test day for this investigation. For these much shorter orbit arcs, the setup is as described above, with the following exceptions:

- The initial state vectors for Swarm A and C are simply obtained from the above-mentioned long-term orbit generation, for the epoch in question.
- An additional run for Swarm B is added, for which the state is identical to Swarm A, except for a shift of -1.4° in the right ascension of the ascending node.
- The simple cannonball non-gravitational force models are switched off, and are replaced with the simulated accelerometer data (see Section 12.1.3).
- The simulated attitude quaternions (see Section 12.1.2) are used, so that the accelerometer data, which is given in the satellite body-fixed frame, can be converted to the inertial frame for integration.

12.1.2 Simulated attitude quaternions

The simulated attitude quaternions for the Swarm satellites are based on those for CHAMP. Figure 12.3 shows the nominal orientation of the body-fixed frame with respect to nadir and the inertial velocity vector. The orientation of the satellite is the same as for CHAMP (see Figure 4.9), when taking into account that CHAMP flies with its boom in the forward direction, while Swarm has its boom pointed backwards, in the opposite direction of the flight direction.

The CHAMP attitude deadband is about 2 degrees around each axis, while for Swarm this number will be 4 degrees [*Bock*, personal communication, 2008]. The starting point for this simulation are the Euler angles between the CHAMP

Figure 12.4 The coloured areas, assigned to the surfaces in the Swarm satellite drawings. These coloured areas were measured in the Photoshop Extended CS3 software, in order to generate the approximate panel area data for a preliminary panelized satellite model.

body-fixed frame and the orbit-fixed frame, in the CH:EULER_INTERPOLATED product (see Section 4.6.3).

These Euler angles are multiplied by two and copied with different time offsets of 1825 days (roughly 5 years), 1855 days and 1885 days for Swarm A, B and C, respectively. The time offsets are used first of all to make the CHAMP data overlap with the Swarm simulation period. Additional offsets for the three satellites are introduced to make it seem that the satellites are steered in attitude independently.

The simulated Swarm trajectories are used to convert the resulting Euler angles back to quaternions, which are compatible with the Swarm orbit and with the software used in the further processing.

12.1.3 Simulated accelerometer measurements

The simulated accelerometer observations were generated using the orbits and quaternions described above, in combination with a panel model of the satellite geometry and the algorithms that were written for the CHAMP and GRACE data processing, as described in the Task 2 report. The steps will be described below.

Swarm panel model

A preliminary panel model for Swarm was generated, using a quick-and-dirty approach, by making use of drawings of the outer surfaces, provided by ESA [*Ralf Bock*, personal communication, 2008]. The PDF files of the drawings were opened in Adobe Photoshop Extended CS3, in which they were rasterized. The measurements function of this software allows one to assign a physical dimension (in mm, for example) to the size of a pixel, after which different areas in the drawing can be measured by making selections. Figure 12.4 shows coloured areas which were measured in this way.

The resulting panel model is provided in Table 12.1. The optical properties of the panel materials were copied from the equivalent panels in the CHAMP and GRACE models. This panel is suitable for simulations, but it is needless to say that a more accurate model should be provided for the real Swarm data processing in the future, based on drawings of the completed satellite design, and optical properties provided by the manufacturer and/or obtained in a test facility. A model can then also be build using the ANGARA software, either for replacement, validation or fine-tuning of a panel model.

i	Description	Area (m^2)	Outward normal			Visible refl.		IR refl.		Material
			X_{SBF}	Y_{SBF}	Z_{SBF}	spec.	diff.	spec.	diff.	
1	Front	0.95	1.0000	0.0000	0.0000	0.40	0.26	0.23	0.15	SiOx/Kapton
2	Back	0.36	-1.0000	0.0000	0.0000	0.40	0.26	0.23	0.15	SiOx/Kapton
3	Left	1.42	0.0000	-1.0000	0.0000	0.40	0.26	0.23	0.15	SiOx/Kapton
4	Right	1.42	0.0000	1.0000	0.0000	0.40	0.26	0.23	0.15	SiOx/Kapton
5	Top	0.83	0.0000	0.0000	-1.0000	0.05	0.30	0.03	0.16	Si glass
6	Bottom	1.60	0.0000	0.0000	1.0000	0.68	0.20	0.19	0.06	Teflon
7	Bottom/back	3.40	-0.1381	0.0000	0.9904	0.40	0.26	0.23	0.15	SiOx/Kapton
8	Left SA	3.40	0.0000	-0.5878	-0.8090	0.05	0.30	0.03	0.16	Si glass
9	Right SA	3.40	0.0000	0.5878	-0.8090	0.05	0.30	0.03	0.16	Si glass
10	Left SA inside	0.97	0.0000	0.5878	0.8090	0.40	0.26	0.23	0.15	SiOx/Kapton
11	Right SA inside	0.97	0.0000	-0.5878	0.8090	0.40	0.26	0.23	0.15	SiOx/Kapton
12	Boom top	0.29	-0.2334	0.0000	-0.9724	0.40	0.26	0.23	0.15	SiOx/Kapton
13	Boom bottom	0.29	0.2334	0.0000	0.9724	0.40	0.26	0.23	0.15	SiOx/Kapton

Table 12.1 The Swarm preliminary panel model properties. This model is for simulation purposes only, and not intended for use with real data. Materials and optical properties are taken from CHAMP and GRACE sources and most likely will not apply directly to Swarm.

Generating accelerometer data

The Swarm simulated accelerometer data are generated using the software written earlier for the CHAMP and GRACE data processing.

The following steps are followed:

- The solar and Earth radiation pressure accelerations are calculated in the satellite body-fixed frame, based on the simulated orbit and quaternions, making use of the panel model.
- The simulated orbit data product, generated with GEODYN (see Section 12.1.1) is converted to longitude, latitude and altitude.
- The simulated density is provided by the NRLMSISE-00 model.
- The simulated wind speeds are derived from the HWM-93 model.
- The HWM-93 winds are converted to the satellite body-fixed frame.
- The relative velocities due to the orbital velocity and atmosphere corotation are calculated in the satellite body-fixed frame.
- The panel model is used in conjunction with the relative velocity components, and the composition from the NRLMSISE-00 model, to generate the aerodynamic force coefficient vectors.
- The aerodynamic forces are calculated from the force coefficient vectors and the modelled densities and relative velocity components.
- The aerodynamic and radiation pressure forces are summed, to arrive at the total non-gravitational accelerations.
- For the investigation of accelerometer calibration, Guassian noise is applied to the accelerations, and biases and scale factors are applied as well.

Figures 12.6 and 12.7 show the daily mean, minimum and maximum accelerations on the Swarm satellites for the simulated duration of the mission. More detailed views of the acceleration signal in the X- and Y-directions for the first year for Swarm A are plotted in Figures 12.8 and 12.9, as examples. The stripy

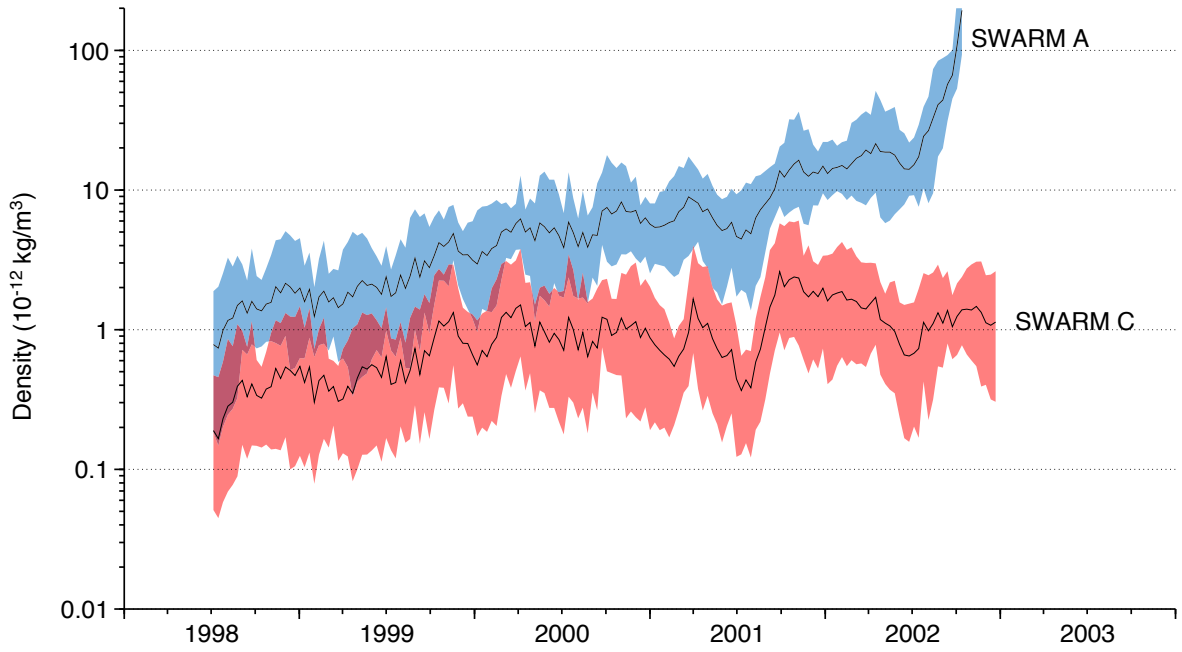

Figure 12.5 10-day mean values (black lines), and range between minimum and maximum values (shaded areas) of NRLMSISE-00 densities along the Swarm A and Swarm C orbits, plotted against a logarithmic Y-axis scale.

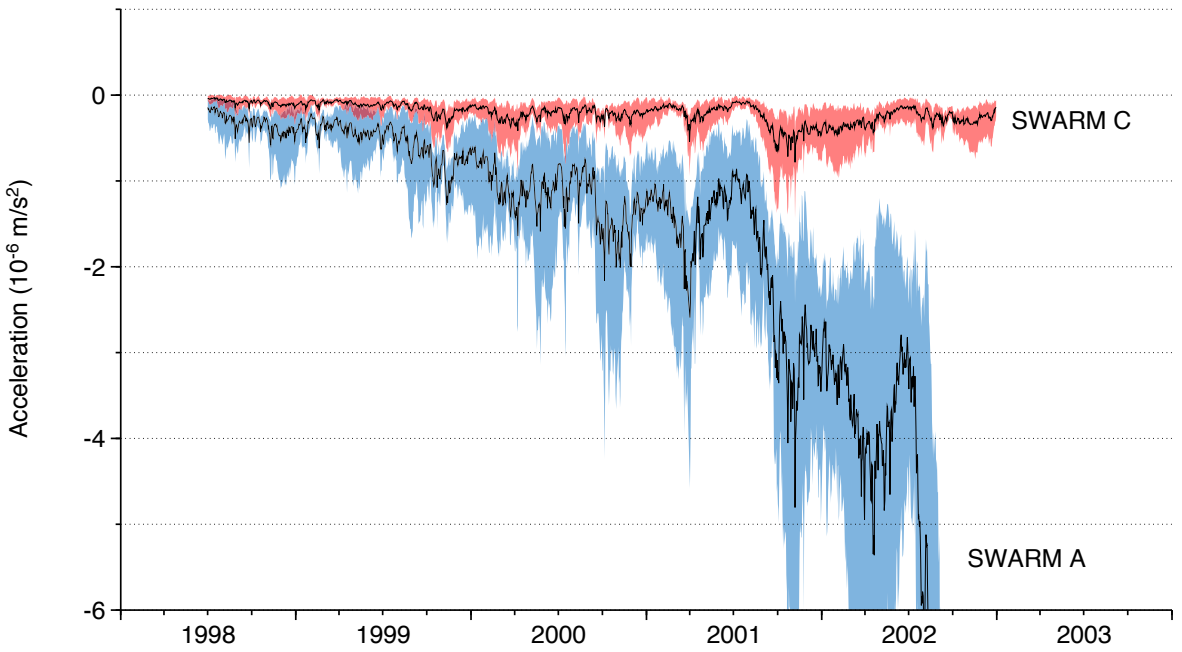

Figure 12.6 Daily mean values (black lines), and range between minimum and maximum values (shaded areas) of the simulated non-gravitational accelerations for Swarm A and Swarm C, in the SBF X-direction.

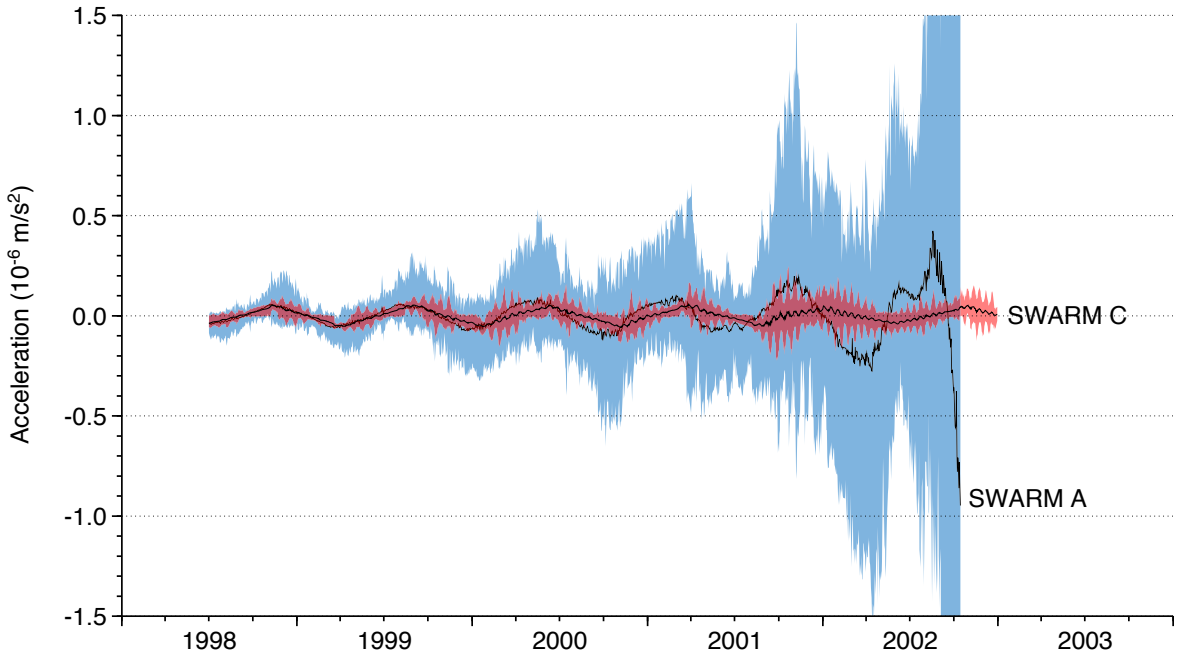

Figure 12.7 Daily mean values (black lines), and range between minimum and maximum values (shaded areas) of the simulated non-gravitational accelerations for Swarm A and Swarm C, in the SBF Y-direction.

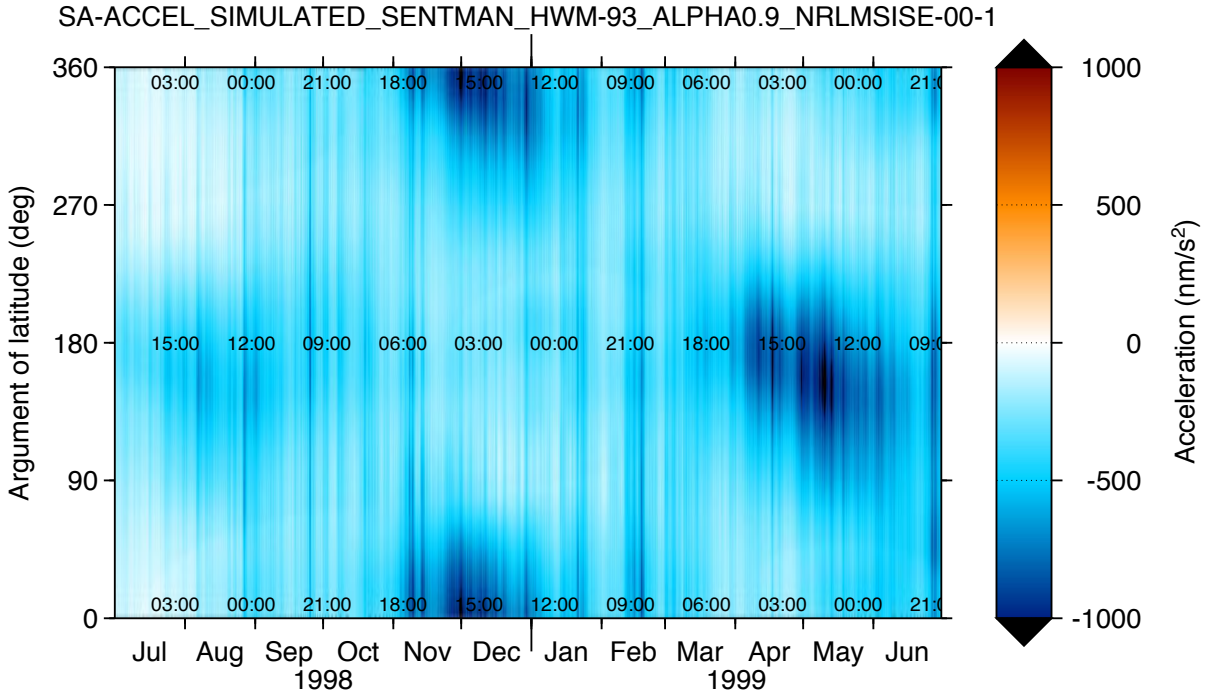

Figure 12.8 Simulated non-gravitational accelerations for Swarm A, in the SBF X-direction, during the first year of the simulation.

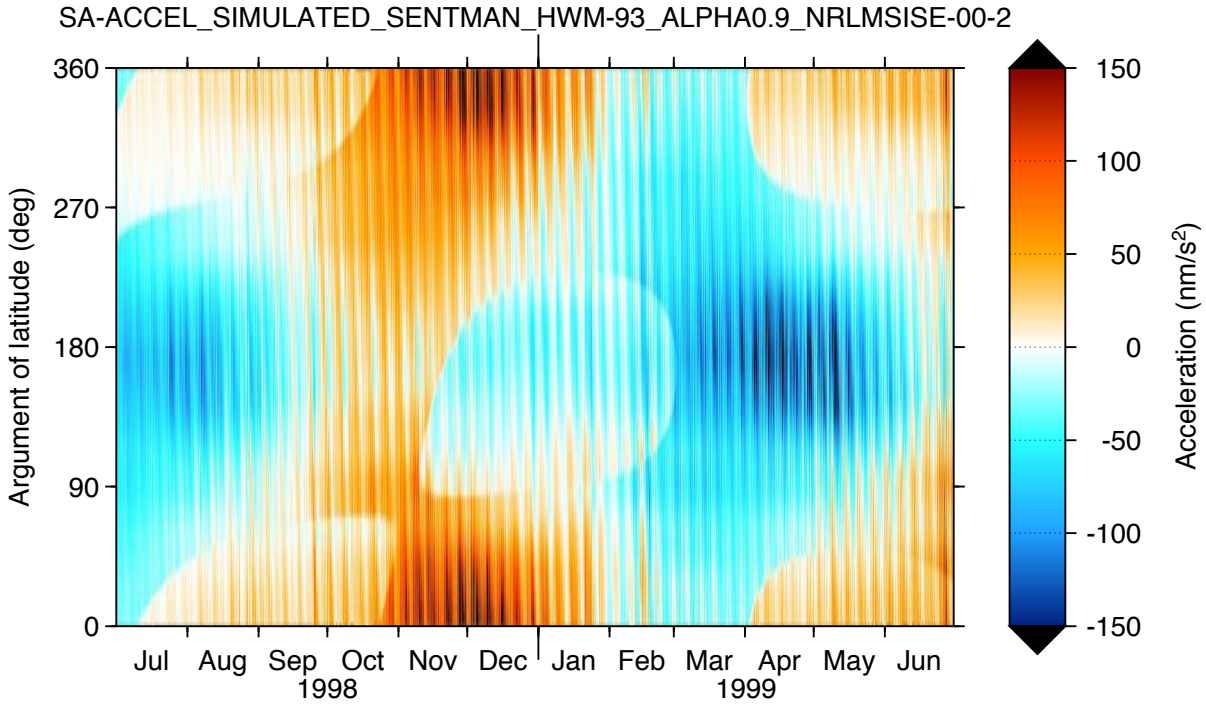

Figure 12.9 Simulated non-gravitational accelerations for Swarm A, in the SBF Y-direction, during the first year of the simulation.

Satellite	a (m)	e	i (deg)	Ω (deg)	ω (deg)	M (deg)
Swarm1	6791735.4	0.00072	87.40	217.35	122.78	345.13
Swarm2	6791735.7	0.00072	87.40	215.95	122.52	345.39
Swarm3	6911651.5	0.00175	88.01	257.05	65.83	148.74

Table 12.2 Osculating Kepler elements for the three Swarm satellites (30 July 1999, 0:00:00).

pattern, with a period of several days, that is visible in the detailed Figure for the Y-axis accelerations, is likely due to the periodicity of the attitude data that was used as an input. Since the attitude data are copied from CHAMP, it has a different periodicity than the orbital periodicity of the simulated Swarm satellite.

12.1.4 Simulated GPS tracking data

The simulated GPS tracking observations consist of one-way Satellite-to-Satellite Tracking (SST) range measurements between the GPS and Swarm satellites, and of one-way range measurements between the GPS satellites and a network of ground stations. The time interval of the observations is 10 s. An elevation cut-off of 0 deg was used for the SST observations and 10 deg for the observations take by the ground stations. The network of ground stations consists of a selection of 50 existing IGS stations (Figure 12.10) for which the station coordinates were taken from ITRF2000 [*Altamimi et al.*, 2002]. The orbital motion of the GPS satellites was taken from the final IGS GPS ephemeris solution [*Dow et al.*, 2005]. For the selected day, 30 July 1999, a total of 27 GPS satellites was operational. The initial conditions for the Swarm satellite orbits are displayed in Table 12.1.4

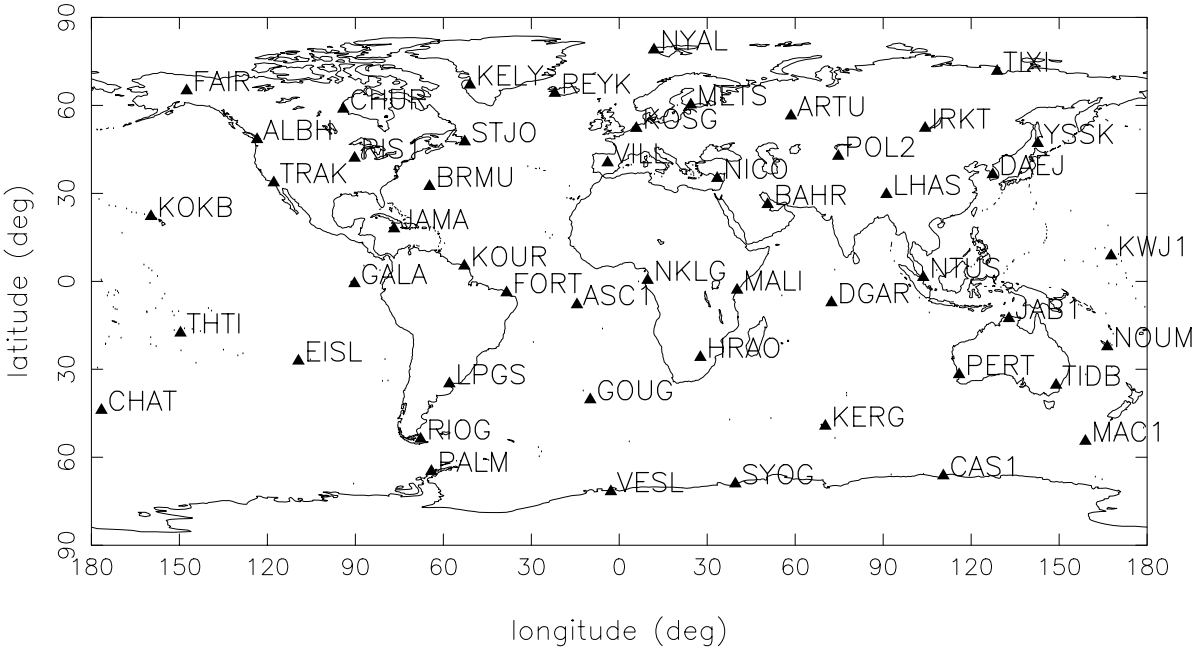

Figure 12.10 Network of GPS ground stations

Furthermore, the model of the real world included dynamic force models. The static gravity field model consisted of the EIGEN-CG03C [*Förste et al.*, 2005*a*], truncated at degree and order 35. For the ocean tides, the PGS7751e model was used, which includes resonances from CHAMP orbital analysis [*Lemoine et al.*, 2003]. More details about the real world model are displayed in Table 12.3. In addition, more background information about the simulation software system can be found in [*Van den IJssel and Visser*, 2003, 2004] and also [*Visser and Van den IJssel*, 2000].

12.2 Accelerometer calibration - simulated configurations

The estimation of accelerometer calibration parameters (i.e. biases and scale factors) by precise orbit determination (POD) has been tested extensively with real data from the CHAMP and GRACE missions [*Reigber et al.*, 1999; *Tapley et al.*, 2004]. In addition, the concept of estimating non-gravitational accelerations by POD has been investigated as well showing that this approach is capable of resolving the non-gravitational accelerations at long wavelengths, typically with periods of 15 min or spatial resolution $>$ 6000 km [*IJssel and Visser*, 2007].

This Chapter starts with a brief overview of the methods used in the simulation study (Section 12.2.1). For the selected day, 30 July 1999, an assessment was made of the possibilities for single- and multi-satellite accelerometer calibration and estimation of non-gravitational accelerations. The simulations are based on the same tools and methods outlined in [*Van den IJssel and Visser*, 2003, 2004]. The tools were extended with the possibility to do multi-satellite analysis (see Section 12.2.1). More details about the incorporation of error sources can be found in Section 12.2.2. Finally, results are described and discussed in Sections 12.2.3 and 12.2.4.

Dynamic models	
Gravity model	EIGEN-CG03C [*Förste et al.*, 2005*a*]
Tidal gravity	Wahr solid earth tides; background ocean tides: PGS7751e
Third body attraction	Sun, Moon, Mercury, Venus, Mars, Jupiter, Saturn, Neptune, according to JPL DE200 ephemeris
Reference frame	
Polar motion	Earth orientation and length of day from IERS EOP 90 C 04 solution
Coordinate system	J2000; precession IAU 1976 (Lieske model); nutation IAU 1980 (Wahr model)
Station coordinates	ITRF2000 solution of selected ground stations [*Altamimi et al.*, 2002]
Measurement models	
Speed of light	c = 299792.458 km s^{-1}
Tropospheric corrections	model according to A. Niell [*Niell*, 1996]
Satellite models	
Swarm	Mass: 500 kg; Cross-sectional area (perpendicular to flight direction): 0.95 m^2
GPS	Relevant models depending on satellite type Ephemeris from final IGS solution [*Dow et al.*, 2005]

Table 12.3 Modelling the real world

12.2.1 Methodology

The following sections contain a brief description of the methods used in the simulations to estimate accelerometer calibration parameters and non-gravitational accelerations. For more details is referred to the Task 1-3 reports of this study.

Single-satellite

The method of estimating accelerometer calibration parameters for the GOCE accelerometers is based on a precise orbit determination [*Montenbruck and Gill*, 2000] in which these calibration parameters are introduced as additional unknowns. The method is the same as typically used for deriving the observation and least-squares normal equations for CHAMP and GRACE accelerometer calibration parameters [*Bruinsma and Biancale*, 2003; *Bruinsma et al.*, 2004; *Visser and Van den IJssel*, 2003].

First, use will be made of this standard method of estimating accelerometer biases and scale factors by POD. Accelerometer observations are modelled as:

$$a_{i,cor} = SF_i \times a_{i,obs} + b_i \tag{12.1}$$

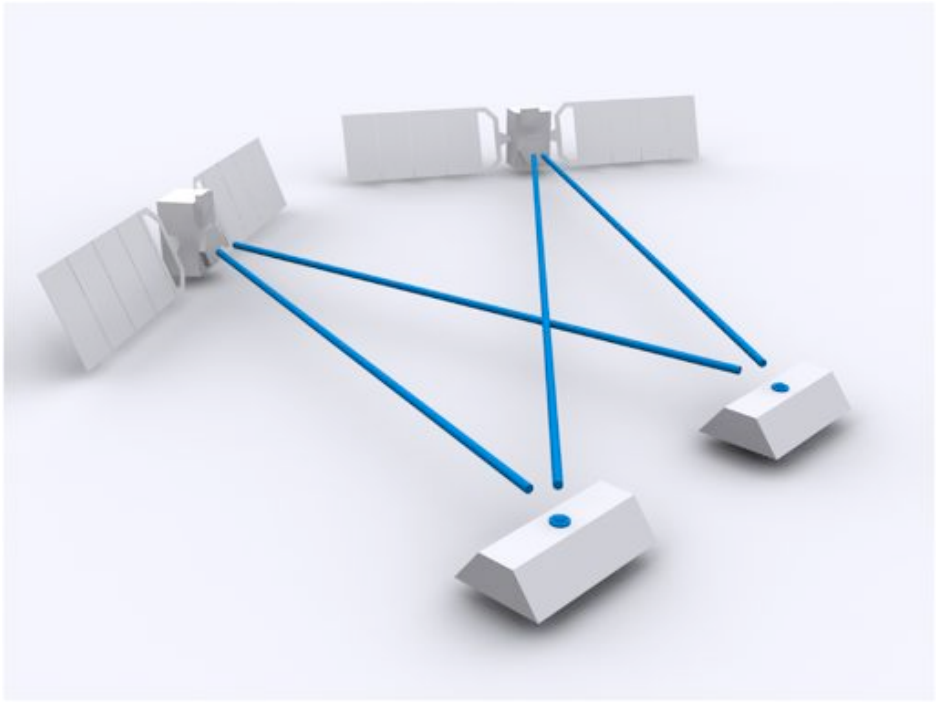

Figure 12.11 Space-borne differential GPS for two Low Earth Orbiting (LEO) satellites.

where $a_{i,obs}$ represents the observation for axis i ($i = x, y, z$), $a_{i,cor}$ represents the corrected observation, and SF_i and b_i represent the scale factor and bias, respectively.

Second, time series of non-gravitational accelerations are estimated by means of GPS-based POD as outlined in detail in e.g. [*Van den IJssel and Visser*, 2003, 2004; *IJssel and Visser*, 2007]. The single-satellite methods are based on the analysis of tripled-differenced GPS observations, thereby avoiding the need to estimate carrier-phase ambiguities and clock parameters. Use is made of the NASA/GSFC GEODYN software to compute the observation and normal equations [*Rowlands et al.*, 1995].

Multi-satellite

In addition to the single-satellite methods, a dual-satellite method has been implemented which is based on so-called space-borne differential GPS (Figure 12.11), where double differences are formed between two GPS satellites and two Swarm satellites. For such a geometry, it has been proved that a successful ambiguity resolution can be done [*Kroes et al.*, 2005] strengthening the geometric information content of the GPS tracking data.

The converged parameter solutions from the single-satellite methods are used as start values for one additional iteration allowing to estimate corrections based on the ambiguity fixed double differences. The observation equations for undifferenced GPS observations are taken from the last iteration of the single-satellite runs. The double-differencing, accumulation into normal equations and generation of new parameter solutions are done by a separate software utility in which correlations between double differences have been taken into account. In addition, redundant double differences were eliminated using the Gramm-Schmidt orthonormalization procedure [*Golub and Van Loan*, 1996].

Satellite	mean			RMS about mean		
	X	Y	Z	X	Y	Z
10-sec interval						
Swarm1	-514.66	47.84	-5.80	159.12	30.02	16.51
Swarm2	-516.84	58.20	-5.65	161.32	36.33	15.80
Swarm3	-108.99	29.43	-3.06	44.56	15.16	11.31
Swarm1-2	-2.18	10.36	0.15	12.96	32.62	21.01
Swarm1-3	405.67	-18.41	2.75	144.66	22.64	22.68
Swarm2-3	407.84	-28.77	2.60	146.48	30.18	20.65
15-min averaged						
Swarm1	-514.63	47.84	-5.80	149.99	26.97	14.89
Swarm2	-516.77	58.21	-5.66	151.28	32.97	14.95
Swarm3	-108.98	29.42	-3.05	42.39	13.21	9.90
Swarm1-2	-2.14	10.38	0.14	11.07	29.75	19.24
Swarm1-3	405.64	-18.41	2.75	135.63	18.95	20.44
Swarm2-3	407.78	-28.79	2.61	136.51	25.39	19.26

Table 12.4 Simulated non-gravitational accelerations for 30 July 1999, 0:15 - 5:45 (values in nm/s^2). Both single- and differential dual-satellite values have been included.

12.2.2 Simulation of error sources

The effect of the following error sources on the accuracy of estimated accelerometer calibration parameters and non-gravitational accelerations is assessed:
1) Sensor errors;
2) Earth's gravity field and tide model error;
3) GPS related errors.

Ad 1. For the accelerometer calibration runs, accelerometer and star tracker noise has been modelled and included. Moreoever, accelerometer observations have been corrupted by non-zero biases and scale factors unequal to 1. For reference, the signal magnitude of the simulated non-gravitational accelerations is displayed for all three Swarm satellites in Table 12.4. Also, the signal magnitudes for the differential accelerations is displayed (Swarm1-2 = Swarm2 - Swarm1, etc.). The time interval of the simulated accelerations is equal to 10 s. The values averaged over time intervals of 15 min haven been included as well for comparison with estimated non-gravitational accelerations (see Section 12.2.4).

Ad 2. Predictions for GRACE are used to corrupt the gravity field model that will be used in the POD, in other words a realistic "clone" is made of the a priori gravity field model used to simulate the original satellite orbit and GPS observations. In fact, gravity field coefficient errors are commensurate with the claimed precision of the GGM02C model [*Tapley et al.*, 2005].

In the simulation of the original satellite orbit and GPS observations, use is made of a tide model that includes resonances estimated from CHAMP tracking data. This tide model, referred to as PGS7751e [*Lemoine et al.*, 2003], was kindly

Gravity field	EIGEN-CG03C clone according to GGM02C coefficient errors
Tides	EGM96 vs. PGS7751e
Station coordinates	0.5 cm Gaussian with zero mean for all station coordinates; Helmert parameter errors: translations around a few mm, rotations around 0.01 mas, and scale factor of 0.4 ppb [*Altamimi et al.*, 2007]
Observation noise*	2 mm @ 0.1 Hz Gaussian with zero mean for for ionospheric free undifferenced observations
Star tracker	20 arcsec Gaussian with zero mean for all axes
Troposphere	0.5% of standard atmosphere for GPS observations to ground station network
GPS ephemeris error	1-cpr with RMS average of 5 cm amplitude for each axis
Antenna offset	around a few mm for each axis
Accelerometer	3 nm/s^2 at 10.0 sec Gaussian with zero mean plus biases ranging between -2400 to +800 nm/s^2 and scale factors ranging between 0.85 and 0.98

Table 12.5 Error sources

provided by the Goddard Space Flight Center and can be considered an update to the model that was estimated together with the EGM96 gravity field model [*Lemoine et al.*, 1998]. To study the effect of tide model error, POD experiments will be conducted where the EGM96 tide model is used as reference instead of the true model PGS7751e.

Ad 3. The following error sources are taken into account:

- ephemeris errors of the GPS satellites;
- GPS SST carrier phase observation noise;
- ground station coordinate errors (*);
- reference frame errors (*);
- atmospheric propagation delay errors (*).

The error sources marked with (*) are included because use will be made of differenced GPS observations and thus observations by ground stations are included.

Realistic levels for these error sources have been defined and simulated (Table 12.5) based on state-of-the-art instrument performances and processing techniques. Their effect on the accuracy of estimated parameters will be assessed.

12.2.3 Accelerometer calibration parameters

Nominally, only the following parameters are estimated for each satellite:

- Begin position and velocity (3+3=6 coefficients);
- Accelerometer bias and scale factors for X, Y and Z azis (2x3=6 coefficients).

In addition, a few cases were investigated where also one set of along-track and cross-track 1 cycle-per-orbital-revolution (cpr) empirical accelerations were estimated as well (4 additional parameters). The arc length is equal to one day for all cases.

Satellite	Observation type	Number
Single-satellite		
Swarm1	triple differences	970158
Swarm2	triple differences	968400
Swarm3	triple differences	979110
Multi-satellite		
Swarm 1-2	double differences	77217
Swarm 1-3	double differences	44140
Swarm 2-3	double differences	43797

Table 12.6 Number of double and triple differences

It has to be noted that the values for the biases and scale factors that are included in the Tables (represented by $SF_{i,r}$ and $b_{i,r}$) in the following sections are obtained from the values as defined by Equation 12.1 in the following way:

$$\begin{aligned} SF_{i,r} &= 1/SF_i \\ b_{i,r} &= -b_i/SF_i \end{aligned} \tag{12.2}$$

This choice was made to allow a direct comparison for the cases where the accelerometer observations were corrupted by scale factors unequal to 1 and biases unequal to zero (Table 12.5). In principle, when an accelerometer suffers from a scale factor which is unequal to one, the scale factor estimated in the POD is ideally equal to the inverse of this scale factor (and likewise the bias as indicated by Equation 12.2).

Single-satellite

The GPS space segment and global network of ground stations guarantee that at every time instance many triple differences can be formed (in general around 10 independent triple differences or more) resulting in a continuous and homogeneous accumulation of observations from which the selected orbital and accelerometer calibration parameters are to be estimated (Table 12.6). No data gaps were simulated, which is not unrealistic given the very reliable performance of modern space-borne GPS receivers.

Table 12.7. It can already be concluded that the accelerometer biases and scale factors can be determined best for the X axis (predominantly along-track direction): the formal errors are an order of magnitude smaller compared to those for the Y axis (cross-track direction) and Z axis (radial direction). In addition, the calibration by POD is anticipated to be less precise for Swarm3, which is flying at a higher altitude and thus experiences smaller non-gravitational accelerations (Table 12.4).

The formal errors for the estimated accelerometer calibration parameters, as derived from the inverse of the normal matrix, are displayed in

The actually estimated biases and scale factors are included in Tables 12.8-12.9 for several error sources. It can be seen that the errors of the estimated biases and scale factors are relatively small in case of GPS observation noise, tropospheric correction errors, GPS ephemeris error, station coordinate errors and reference

Satellite	bias			Scale factor		
	X	Y	Z	X	Y	Z
Swarm1	82.62	1316.01	1444.66	55.58	1797.97	9556.77
Swarm2	40.26	2134.43	831.86	91.18	1861.52	6270.31
Swarm3	130.37	2078.96	1062.46	430.80	6788.10	5539.34

Table 12.7 Formal errors for estimated biases (pm/s^2) and scale factors (part per million) for 24-hr arc (30 July 1999 0:00:00 - 31 July 1999 0:00:00) using single-satellite precise orbit determinations from triple differences. The values are scaled by assuming a triple-difference noise of 0.6 mm/s.

frame errors. For the X and Y axes, also star tracker noise and GPS antenna offset errors hardly affect the estimated biases and scale factors, whereas already a noticeable effect can be seen for the Z axis (up to 0.024 error in scale factor), which is consistent with its relatively large formal error (Table 12.7). The level of simulated dynamic model errors causes small errors for the X axis accelerometer calibration parameters, whereas errors up to 0.16 for the Y axis scale factor for Swarm3 (highest flying satellite) and -0.043 for the Z axis scale factor can be observed (Table 12.9). The dominant error source appears to be the simulated tide model error, which might be too pessimistic given the fact that an old model based on the production of the EGM96 gravity field model in 1996 was used as reference.

When corrupting the accelerometer observations by biases and scale factors, these parameters can be reconstructed very well by POD in the presence of GPS observation noise as only error source (second part of Table 12.9): the error in terms of biases is very low for the X axis (< 1 nm/s^2) and up to 5-10 nm/s^2 for the Y- and Z axes, the error in terms of scale factor is of the order of 0.001 for the X and Y axes, and 0.02 for the Z axis. When all error sources are included, only the scale factors for the X axis can be determined well (error smaller than 0.01), whereas the error for the Y and Z axes ranges up to 0.19, especially for the Y axis and for the higher flying Swarm3 satellite. In general, biases for the X axis can be determined with high accuracy, whereas the biases for the other two axes have errors up to about 40 nm/s^2. An additional computation was done where empirical 1-cpr accelerations in the along-track and cross-track direction were coestimated to absorb dynamic modelling errors. It was found that especially for the Y and Z axes this resulted in much bigger errors for the scale factors and therefore this approach was no longer pursued.

Multi-satellite

The GPS tracking geometry and the fact that the lower Swarm pair flies in tandem leads to a stable double-difference observation geometry. At each instance, a minimum number of 5 and maximum number of 12 independent double differences can be formed (Figure 12.12,left). For combinations of one lower satellite (Swarm1 or Swarm2) and the higher satellite (Swarm3), instances occur where no double differences can be formed (Figure 12.12, middle and right). The maximum number was found to be equal to 11. The distribution in time changes significantly, which is due to the difference in orbital velocity and thus rotation rate around the earth for Swarm1/Swarm2 and Swarm3.

Satellite	bias			Scale factor		
	X	Y	Z	X	Y	Z
GPS observation noise						
Swarm1	-0.02	-0.04	-0.32	1.000	1.000	1.003
Swarm2	-0.01	0.24	0.18	1.000	1.000	1.003
Swarm3	-0.02	-0.59	0.05	1.000	1.001	1.000
Star tracker noise						
Swarm1	-0.14	-6.12	-2.76	1.000	0.999	1.015
Swarm2	0.28	5.12	1.87	1.000	1.001	0.988
Swarm3	0.37	4.58	2.35	1.001	1.001	0.989
Tropospheric correction error						
Swarm1	-0.01	0.41	-0.20	1.000	1.000	0.999
Swarm2	-0.00	0.52	-0.05	1.000	1.000	0.999
Swarm3	0.01	0.02	0.06	1.000	0.999	0.999
GPS ephemeris error						
Swarm1	-0.01	0.96	-0.43	1.000	0.999	0.997
Swarm2	0.02	-0.12	-0.67	1.000	0.999	0.996
Swarm3	-0.07	-0.84	-0.41	1.000	1.001	0.999
GPS antenna offset error						
Swarm1	-0.35	-0.82	-6.57	1.000	1.000	1.024
Swarm2	-0.03	1.86	-1.73	1.000	0.999	0.996
Swarm3	0.26	0.53	2.82	1.001	0.999	0.995
Helmert parameters error						
Swarm1	0.00	-0.03	0.02	1.000	1.000	1.000
Swarm2	0.00	-0.11	0.04	1.000	1.000	1.000
Swarm3	0.00	0.04	0.01	1.000	1.000	1.000
Random station coordinate errors						
Swarm1	0.00	0.03	-0.00	1.000	1.0000	1.000
Swarm2	-0.00	0.08	-0.01	1.000	1.000	1.000
Swarm3	-0.00	0.00	-0.01	1.000	1.000	1.000

Table 12.8 Estimated biases (nm/s^2) and scale factors for 24-hr arc (30 July 1999 0:00:00 - 31 July 1999 0:00:00) using single-satellite precise orbit determinations from triple differences. Effect of individual error sources (Table 12.5). Part I.

Satellite	bias			Scale factor		
	X	*Y*	*Z*	*X*	*Y*	*Z*
Gravity field model error						
Swarm1	-0.7352	-12.3677	-8.7790	0.9996	1.0112	0.9571
Swarm2	0.1148	-17.4676	-5.8256	1.0009	1.0029	1.0121
Swarm3	0.2206	4.5954	-0.1151	1.0008	1.0481	1.0083
Tide model error						
Swarm1	-0.4548	-8.3925	-14.2801	1.0006	1.0418	0.9981
Swarm2	-0.1706	-0.9546	-11.2242	1.0007	1.0359	1.0398
Swarm3	-0.6199	-33.4045	0.3863	0.9996	1.1577	0.9760
Cases below include accelerometer errors						
True values						
Swarm1	500.00	-2000.00	-300.00	0.920	0.900	0.950
Swarm2	-1500.00	-2400.00	800.00	0.910	0.980	0.920
Swarm3	350.00	-2300.00	-600.00	0.830	0.870	0.850
Accelerometer observation errors						
Swarm1	499.04	-1999.23	-305.88	0.919	0.898	0.922
Swarm2	-1500.71	-2410.52	795.26	0.909	0.977	0.938
Swarm3	350.38	-2289.91	-592.82	0.828	0.869	0.870
All error sources						
Swarm1	497.48	-2023.59	-336.47	0.919	0.945	0.912
Swarm2	-1500.53	-2421.87	778.67	0.911	1.013	0.970
Swarm3	350.52	-2309.70	-588.64	0.830	1.064	0.840
All error sources: 1-cpr along-/cross-track emp. acc.						
Swarm1	496.87	-2033.05	-356.98	0.919	0.934	1.282
Swarm2	-1499.47	-2423.40	786.52	0.913	0.962	0.818
Swarm3	350.11	-1914.17	-580.90	0.827	-6.670	0.986

Table 12.9 Estimated biases (nm/s^2) and scale factors for 24-hr arc (30 July 1999 0:00:00 - 31 July 1999 0:00:00) using single-satellite precise orbit determinations from triple differences. Effect of individual error sources (Table 12.5). Part II.

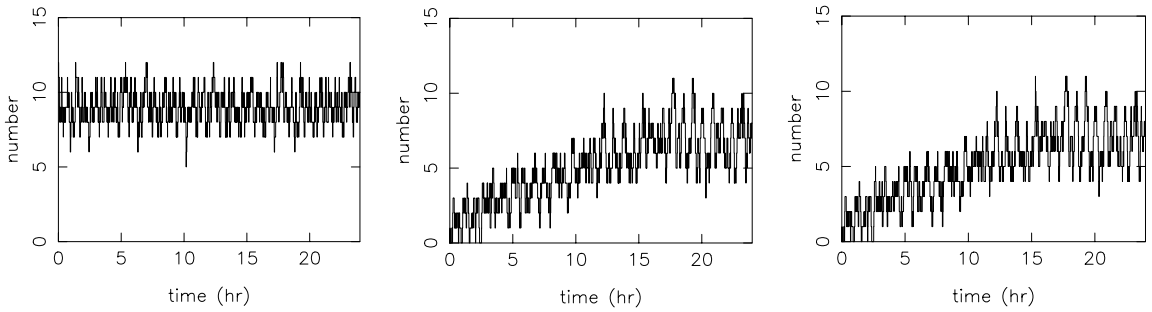

Figure 12.12 Number of GPS double differences for the Swarm pairs 1&2 (left), 1&3 (middle) and 2&3 (right). Time since 30 July 1999, 0:00.

Satellite	bias			Scale factor		
2-satellite double differences						
	X	Y	Z	X	Y	Z
Swarm1	15.24	33.27	35.52	26.34	208.01	177.36
Swarm2	14.99	28.50	23.24	25.37	138.39	112.39
2-satellite double differences						
Swarm1	3.89	47.10	68.51	2.20	113.89	223.88
Swarm3	3.14	43.42	32.44	9.07	456.46	172.03
2-satellite double differences						
Swarm2	1.36	48.31	30.26	2.23	126.76	184.79
Swarm3	3.07	42.28	32.92	8.95	499.72	195.38
3-satellite double differences						
Swarm1	1.34	16.98	23.13	1.26	63.94	115.50
Swarm2	0.77	18.41	14.29	1.43	68.31	68.46
Swarm3	1.93	28.62	19.29	5.93	309.71	98.38

Table 12.10 Formal errors for estimated biases (pm/s^2) and scale factors (part per million) for 24-hr arc (30 July 1999 0:00:00 - 31 July 1999 0:00:00) using multi-satellite precise orbit determinations from double differences. The values are scaled by assuming a double-difference noise of 4 mm.

The formal errors for the estimated accelerometer calibration parameters, as derived from the inverse of the normal matrix, are displayed in Table 12.10. The formal errors are significantly lower than for the single-satellite method (Table 12.7). It has to be noted that the weight of 4 mm for double differences used for scaling the normal matrix is consistent with a weight of 0.6 mm/s ($4 \times \sqrt{2}$ / Δt, where Δt is the observation time interval) for triple differences used to weight the normal matrices for the single-satellite cases. Thus conceptually the double difference method seems to be able to produce more precise accelerometer calibration parameters. It has to be realized that this would be true in case of Gaussian observation errors with zero mean only, but is not sure in case of systematic errors.

The actually estimated biases and scale factors are included in Tables 12.11-12.12 for GPS observation noise and all error sources combined, respectively. It

Satellite	bias			Scale factor		
	X	Y	Z	X	Y	Z
Single-satellite triple differences						
Swarm1	-0.0216	-0.0390	-0.3241	1.0000	1.0001	1.0026
Swarm2	-0.0100	0.2377	0.1845	1.0000	1.0000	1.0030
Swarm3	-0.0160	-0.5883	0.0535	1.0000	1.0006	0.9998
2-satellite double differences						
Swarm1	-0.0210	0.0161	0.0500	1.0000	0.9999	0.9997
Swarm2	-0.0228	0.0419	-0.0103	1.0000	1.0000	0.9999
2-satellite double differences						
Swarm1	0.0035	0.0746	0.0555	1.0000	0.9999	1.0001
Swarm3	-0.0030	-0.0425	-0.0286	1.0000	1.0007	1.0000
2-sat double differences						
Swarm2	0.0017	0.1474	0.0570	1.0000	0.9998	0.9995
Swarm3	-0.0086	0.0134	-0.1087	1.0000	0.9997	0.9999
3-satellite double differences						
Swarm1	-0.0004	0.0191	0.0070	1.0000	0.9999	0.9999
Swarm2	-0.0009	0.0111	-0.0064	1.0000	0.9999	1.0001
Swarm3	-0.0033	-0.0225	-0.0348	1.0000	1.0004	1.0002

Table 12.11 Estimated biases (nm/s^2) and scale factors for 24-hr arc (30 July 1999 0:00:00 - 31 July 1999 0:00:00). Effect of GPS observation noise (Table 12.5). The single-satellite results are included for reference.

can be observed that in general the errors of estimated biases and scale factors are indeed lower when using the method based on double differences. When all error sources are included and all double difference combinations are taken (i.e. all three satellites included), results indicate that some improvement can be obtained (Table 12.12). However, more and longer-period simulations are required to draw final conclusions.

12.2.4 Non-gravitational accelerations

Time series of non-gravitational accelerations have been estimated as well, using the single-satellite approach as outlined in [*Van den IJssel and Visser*, 2003, 2004; *IJssel and Visser*, 2007] and the multi-satellite approach as outlined in Section 12.2.1. Piece-wise linear accelerations along the accelerometer X, Y and Z axes were estimated with a time interval of 15 min. These accelerations were then compared with the true non-gravitational accelerations, where the latter were averaged over the 15 min intervals to have a consistent comparison. Nominally, 6-hr arcs were used on order to limit the computational burden (a few 24-hr arc computations were done as well leading to similar statistics, Table 12.13).

Statistics of the comparisons between true and estimated non-gravitational accelerations are included in Table 12.13 for the absolute single-satellite accelerations, and in Table 12.14 for the pair-wise differential accelerations (compare

Satellite	bias			Scale factor		
	X	Y	Z	X	Y	Z
True values						
Swarm1	500.00	-2000.00	-300.00	0.920	0.900	0.950
Swarm2	-1500.00	-2400.00	800.00	0.910	0.980	0.920
Swarm3	350.00	-2300.00	-600.00	0.830	0.870	0.850
Single-satellite triple differences						
Swarm1	497.48	-2023.59	-336.47	0.919	0.945	0.912
Swarm2	-1500.53	-2421.87	778.67	0.911	1.013	0.970
Swarm3	350.52	-2309.70	-588.64	0.830	1.064	0.840
2-satellite double differences						
Swarm1	500.35	-1998.84	-309.81	0.921	0.897	0.973
Swarm2	-1499.01	-2373.47	795.49	0.912	0.987	0.910
2-satellite double differences						
Swarm1	499.44	-2047.18	-278.59	0.917	0.898	0.892
Swarm3	346.68	-2327.82	-616.05	0.818	0.780	0.752
2-satellite double differences						
Swarm2	-1502.04	-2406.59	741.14	0.911	1.020	1.122
Swarm3	350.13	-2312.48	-579.63	0.825	1.005	1.010
3-satellite double differences						
Swarm1	498.35	-1995.95	-313.60	0.919	0.9065	0.921
Swarm2	-1500.90	-2385.33	787.20	0.910	0.9766	0.932
Swarm3	348.42	-2314.25	-602.54	0.822	0.8262	0.838

Table 12.12 Estimated biases (nm/s^2) and scale factors for 24-hr arc (30 July 1999 0:00:00 - 31 July 1999 0:00:00). All error sources included (Table 12.5).

also with Table 12.4). The estimated and true values are also displayed in Figure 12.13 for the error-free case. It has to be noted that the first and last 15-min time intervals were always ignored in the comparisons, since the estimated non-gravitational accelerations are relatively unreliable for the ends of the arc. It can be observed that even for the error-free case, recovery errors in terms of RMS about mean (indicated by STD) are made of about $30/7/45$ nm/s^2 for the $X/Y/Z$ axes for the lower flying satellite pair (Swarm1 and Swarm2) and $6/5/8$ nm/s^2 for the $X/Y/Z$ axes for the higher flying satellite (Swarm3). It can thus be concluded that even when no observation or other errors are present in the GPS, star tracker and accelerometer observations, and force models, recovery errors are made. This is due to the fact that the accelerations are estimated at a time interval of 15 min, whereas the real non-gravitational acceleration that the satellites experience change all the time (at 10 sec interval in the simulations). This leads to a so-called model error of the size indicated in Table 12.13. For Swarm3, this model error is much smaller which is in agreement with the much smaller signal variation for this higher flying satellite. A striking result are the biases that appear for the Y axis (predominantly cross-track direction). This result is however consis-

Satellite	case	method	axis	mean	STD	mean estimate	STD estimate
Swarm1*	error-free	TD	X	-0.33	30.48	-615.95	165.13
Swarm1*	error-free	TD	Y	17.21	9.07	38.30	45.05
Swarm1*	error-free	TD	Z	-4.84	38.86	2.85	35.40
Swarm1*	all errors	TD	X	-1.51	30.59	-614.78	165.28
Swarm1*	all errors	TD	Y	15.93	15.19	39.58	44.46
Swarm1*	all errors	TD	Z	-24.71	39.82	22.72	36.60
Swarm1	error-free	TD	X	0.84	29.39	-515.47	129.87
Swarm1	error-free	DD 123	X	1.05	28.79	-515.68	130.09
Swarm2	error-free	TD	X	0.25	28.80	-517.02	132.31
Swarm2	error-free	DD 123	X	0.51	28.82	-517.28	131.86
Swarm3	error-free	TD	X	0.42	5.69	-109.40	38.65
Swarm3	error-free	DD 123	X	0.49	5.62	-109.48	39.11
Swarm1	error-free	TD	Y	22.47	7.71	25.37	26.81
Swarm1	error-free	DD 123	Y	19.95	7.23	27.89	26.31
Swarm2	error-free	TD	Y	23.32	9.05	34.89	30.77
Swarm2	error-free	DD 123	Y	19.61	7.99	38.60	30.89
Swarm3	error-free	TD	Y	9.23	2.17	20.19	12.41
Swarm3	error-free	DD 123	Y	8.27	4.51	21.15	11.75
Swarm1	error-free	TD	Z	-2.22	47.33	-3.57	40.76
Swarm1	error-free	DD 123	Z	-2.15	45.26	-3.64	38.92
Swarm2	error-free	TD	Z	-2.02	44.89	-3.63	50.70
Swarm2	error-free	DD 123	Z	-2.13	44.49	-3.53	50.22
Swarm3	error-free	TD	Z	0.20	8.11	-3.25	15.28
Swarm3	error-free	DD 123	Z	-0.11	7.88	-2.94	15.39
Swarm1	all errors	TD	X	-1.25	30.46	-513.38	128.52
Swarm2	all errors	TD	X	-1.28	29.54	-515.49	131.32
Swarm3	all errors	TD	X	2.19	10.56	-111.17	41.22
Swarm1	all errors	TD	Y	25.92	23.47	21.92	33.93
Swarm2	all errors	TD	Y	29.49	21.63	28.73	36.49
Swarm3	all errors	TD	Y	3.48	17.99	25.95	21.72
Swarm1	all errors	TD	Z	-27.62	48.38	21.82	43.09
Swarm2	all errors	TD	Z	-20.68	45.59	15.02	50.53
Swarm3	all errors	TD	Z	15.22	25.80	-18.27	25.82

*: 24-hr arc 30 July 1999, 0:15 - 23:45
STD: RMS about mean
TD: single-satellite POD using triple-differenced GPS observations
DD 123: 3-satellite POD using double-differenced GPS observations

Table 12.13 Differences between GPS-based empirical accelerations for 15-min intervals and 15-min averaged true non-gravitational accelerations (values in nm/s^2). The results hold for a 6-hr arc: 30 July 1999, 0:15 - 5:45 (first and last 15 min ignored).

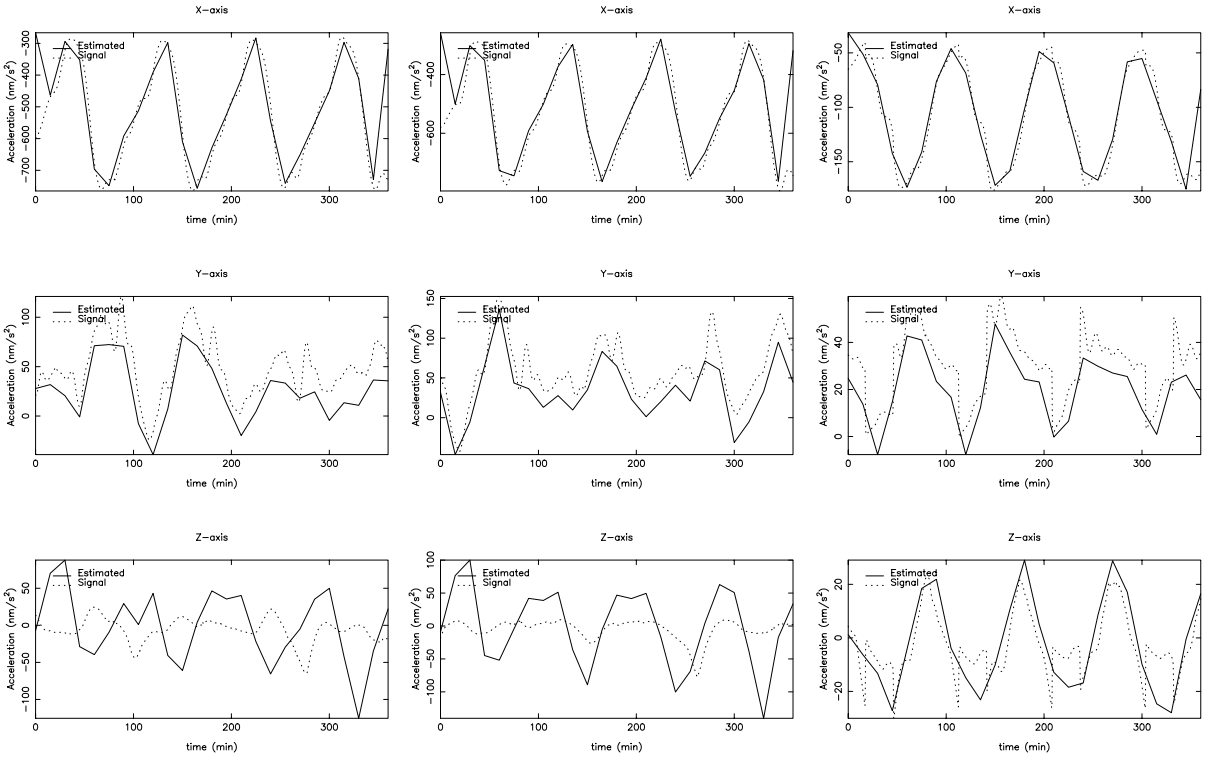

Figure 12.13 Non-gravitational accelerations (15 min interval) for Swarm1, Swarm2 and Swarm3 (left to right columns, respectively) obtained by single-satellite POD using triple differences. No error sources. Time since 30 July 1999, 0:00.

tent with the relatively high formal errors that are predicted for the estimation of the Y axis accelerometer bias (Table 12.10). Estimated radial accelerations are not significant for the lower Swarm pair: the error is much bigger than the signal (Table 12.4). For the higher flying Swarm3 satellite, it seems that significant values can be obtained to some extent (see also Figure 12.13).

In all cases, the double difference method does not seem to lead to significant improvements. Also, the model error seems to be dominant over all other modelled error sources: the recovery errors do not change much for the "all errors" cases included in Table 12.13.

Finally, statistics of the comparisons between true and estimated non-gravitational differential accelerations for Swarm pairs are included in Table 12.14. Again, it can be observed that results do not alter significantly when using the double difference method. For the lower pair (Swarm1-2), the RMS about mean of the recovery error is below 10 nm/s^2 for the X and Y axes, and around 12 nm/s^2 for the Z axis (also in the presence of all error sources). It thus appears that the largest recovery error of the non-gravitational accelerations is common-mode for the lower pair Swarm1 and Swarm2, suggesting that differential accelerometry can be done to a significant extent for this lower pair. For the other pairs (Swarm1-3 and Swarm2-3), results indicate that there are hardly common-mode errors that would cancel, which can be anticipated given the different orbits and altitudes (see also Figure 12.14).

Satellite	case	method	axis	mean	STD	mean estimate	STD estimate
Swarm1-2	error-free	TD	X	-0.59	4.00	-1.55	9.81
Swarm1-2	error-free	DD 123	X	-0.54	3.25	-1.60	10.06
Swarm1-3	error-free	TD	X	-0.43	28.24	406.07	116.44
Swarm1-3	error-free	DD 123	X	-0.55	27.48	406.20	116.77
Swarm2-3	error-free	TD	X	0.17	28.01	407.62	118.36
Swarm2-3	error-free	DD 123	X	-0.01	27.74	407.80	117.94
Swarm1-2	error-free	TD	Y	0.85	4.99	9.52	27.29
Swarm1-2	error-free	DD 123	Y	-0.33	4.65	10.71	27.70
Swarm1-3	error-free	TD	Y	-13.24	8.30	-5.17	17.17
Swarm1-3	error-free	DD 123	Y	-11.68	9.53	-6.74	17.00
Swarm2-3	error-free	TD	Y	-14.09	9.05	-14.70	23.15
Swarm2-3	error-free	DD 123	Y	-11.34	9.43	-17.45	23.55
Swarm1-2	error-free	TD	Z	0.20	7.16	-0.06	14.52
Swarm1-2	error-free	DD 123	Z	0.03	5.78	0.11	16.49
Swarm1-3	error-free	TD	Z	2.42	45.01	0.33	37.95
Swarm1-3	error-free	DD 123	Z	2.05	43.86	0.70	37.21
Swarm2-3	error-free	TD	Z	2.22	42.21	0.39	47.60
Swarm2-3	error-free	DD 123	Z	2.02	42.73	0.59	48.14
Swarm1-2	all errors	TD	X	-0.03	5.57	-2.11	11.17
Swarm1-3	all errors	TD	X	3.44	30.27	402.20	118.58
Swarm2-3	all errors	TD	X	3.47	29.53	404.32	120.78
Swarm1-2	all errors	TD	Y	3.57	8.45	6.81	28.59
Swarm1-3	all errors	TD	Y	-22.44	32.56	4.03	39.70
Swarm2-3	all errors	TD	Y	-26.01	32.32	-2.78	39.66
Swarm1-2	all errors	TD	Z	6.94	12.31	-6.80	14.11
Swarm1-3	all errors	TD	Z	42.84	53.37	-40.09	45.39
Swarm2-3	all errors	TD	Z	35.90	48.72	-33.29	50.95

STD: RMS about mean
TD: single-satellite POD using triple-differenced GPS observations
DD 123: 3-satellite POD using double-differenced GPS observations

Table 12.14 Differences between GPS-based empirical accelerations for 15-min intervals and 15-min averaged true non-gravitational accelerations (values in nm/s^2). The results hold for a 6-hr arc: 30 July 1999, 0:15 - 5:45 (first and last 15 min ignored) and for differential accelerations. The two right most columns provide statistics for the estimated accelerations themselves.

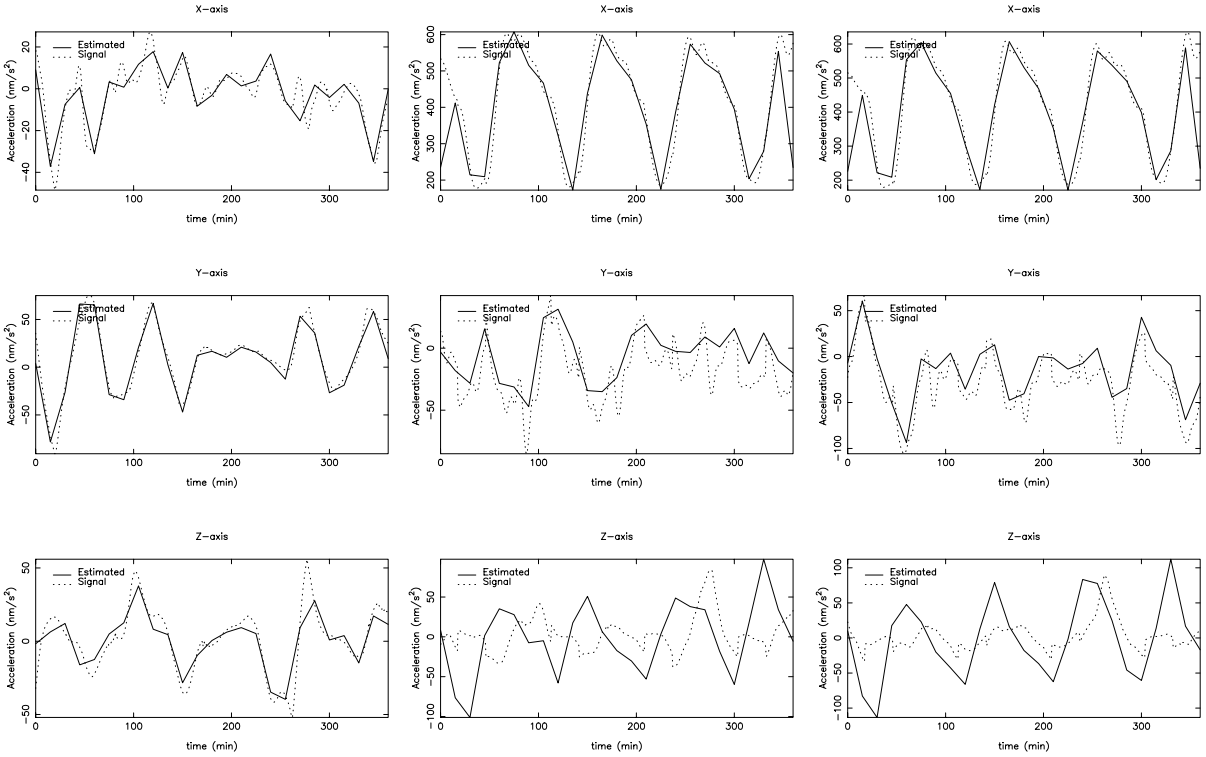

Figure 12.14 Differences between empirical accelerations (15 min interval) for Swarm 1 and 2 (left), Swarm 1 and 3 (centre) and Swarm 2 and 3 (right) obtained by single-satellite POD using triple differences. No error sources. Time since 30 July 1999, 0:00.

12.2.5 Conclusions

A detailed simulation study has been carried out to assess the possibility of estimating accelerometer calibration parameters and non-gravitational accelerations for all three Swarm satellites. In addition to standard single-satellite methods, also a multi-satellite method based on space-borne differential GPS was tested.

Concerning the determination of accelerometer calibration parameters, results indicate that some improvement can be made by the double difference method, but more simulations are required to draw final conclusions.

The method of estimating non-gravitational accelerations was tested as well. Results indicate that especially for the X and Y axes, a large part of the signal variation can be picked up, which is in agreement with results based on analysis of real CHAMP and GRACE data [*IJssel and Visser*, 2007]. For the Z axis, results indicate that hardly a recovery is possible. For the lower Swarm pair, it was found that recovery errors are predominantly common-mode and it is indicated that differential accelerations can be obtained with a much better precision, also for the Z axis.

12.3 Density and wind determination - simulated constellation

The simulated Swarm orbits, quaternions and accelerometer data are used to simulate the density and wind retrieval. Of course, the simulated input data, such as the NRLMSISE-00 densities and HWM-93 crosswind speed, are recovered from

	Wind speed		Density	
	Swarm A	Swarm C	Swarm A	Swarm C
Correlation coefficient r	0.99894	0.99909	0.99997	0.99987
Mean of data/model ratio μ^*			0.99971	1.00059
Std. of data/model ratio σ^*			1.00375	1.00375

Table 12.15 Statistics of the error-free benchmark test over the time period from July 1, 1998 to July 1, 1999. Every sixth measurement (spaced at 60 seconds) was sampled, both from the input models (NRLMSISE-00 and HWM-93), and the result of the iterative density and wind determination algorithm. For the wind, only the Y-component of the spacecraft body-fixed frame was compared.

this processing, when no error sources are introduced. In this way the processing algorithms can be validated, which is done in Section 12.3.1.

It is much more interesting however, to investigate the effect of external error sources in the input data on the density and wind results. Although the magnitude of the input error sources have to be estimated, such an error analysis will give some insight in the achievable density and wind accuracy, how it depends on different circumstances, and which areas offer the most room for improvement. Such an error analysis will be the main topic of the subsequent Sections of this Chapter.

12.3.1 Error-free benchmark

To start off, the results of the iterative density and wind determination algorithm are compared with the models used as inputs in the simulation. If the algorithm works as intended, the output data of the algorithm will be nearly identical to the input data from the models. However, there are a couple of reasons why this might not be exactly so:

- An iterative approach, with a finite convergence limit, is used for the wind derivation (see Section 8.4.3).
- The wind can only be estimated in a single direction (see also Section 8.4.3, about the assumptions made in the wind derivation).
- The computational precision is limited.

It is therefore interesting to make an error-free comparison. The results of this comparison are summarized in Table 12.15. Note that the wind comparison was only made in the spacecraft Y-direction, for convenience. The algorithm estimates a 3D wind vector, which represents the wind component perpendicular to the local satellite velocity with respect to the co-rotating atmosphere, projected on the spacecraft XY-plane (again, see Section 8.4.3 for details).

Nevertheless, the Table shows that the correlation coefficients are very close to one, for the density result even more so than for the wind result, as can be expected. No significant differences can be seen in these results between Swarm A and Swarm C. These results indicate that the algorithm works as expected, and that the influence of the above-listed possible algorithm-related and computational errors is very small.

12.3.2 Error analysis approach

The error analysis approach as outlined in *Bevington and Robinson* [2003] is adopted. This approach considers a computer function named CALCULATE, which returns the final result x when called with arguments corresponding to the input parameters $u, v, w, \ldots$:

$$x = \text{CALCULATE}(u, v, w, \ldots) \tag{12.3}$$

The variations of x with the input variables $u, v, w, \ldots$ are then computed by making successive calls to the function:

$$\begin{aligned} dx_u &= \text{CALCULATE}(u + du, v, w, \ldots) - x \\ dx_v &= \text{CALCULATE}(u, v + dv, w, \ldots) - x \\ dx_w &= \text{CALCULATE}(u, v, w + dw, \ldots) - x \\ &\text{etc}\ldots \end{aligned} \tag{12.4}$$

Under the assumption that correlations between the input errors are small, the total contribution of the uncertainties is then equal to the root sum squared of the individual variations:

$$dx = \sqrt{dx_u^2 + dx_v^2 + dx_w^2 + \ldots} \tag{12.5}$$

The DENSWIND_ITERATIVE2 algorithm, as outlined in Chapter 8, is adopted for this purpose, resulting in the DENSWIND_ITER3 function, which takes the place of CALCULATE above. The input parameters $u, v, w, \ldots$ include the accelerometer measurements, relative velocity components and various outputs of the non-gravitational force modelling. The output x in this case consists of the density and crosswind speed.

12.3.3 Error sources

The error sources in the accelerometer density and wind processing can be subdivided in three major groups: Instrument error, relative velocity error and force model error. Each of these categories can be split into a number of possible error sources:

- Accelerometer instrument error
  - Measurement noise
  - Calibration bias
  - Calibration scale factor
- Relative velocity error
  - Orbit velocity
  - Atmospheric corotation velocity
  - Wind velocity
- Satellite force model error
  - General
    - Satellite panel area
    - Satellite mass
  - Radiation pressure

Cat	Error source	CHAMP	GRACE	Swarm-A	Swarm-C	Units
Acc. instr.	Accelerometer noise, X	3	0.1	3	3	nm/s^2
	Accelerometer noise, Y	3	1.0	3	3	nm/s^2
	Accelerometer bias, X	1	1	1	1	nm/s^2
	Accelerometer bias, Y	5	5	5	5	nm/s^2
	Accelerometer scale, X	0.05	0.05	0.05	0.05	–
	Accelerometer scale, Y	0.10	0.10	0.10	0.10	–
Relative velocity	Relative velocity bias, X	100.0	100.0	100.0	100.0	m/s
	Relative velocity bias, Y	100.0	100.0	100.0	100.0	m/s
	Relative velocity bias, Z	50.0	50.0	50.0	50.0	m/s
	Wind model	50	50	50	50	% of model
Force models	Satellite model area/mass	8	4	8	8	% of model
	Atmospheric temperature	20	20	20	20	% of model
	Helium concentration	5	5	5	5	% of model
	Accommodation coefficient	0.10	0.10	0.10	0.10	–
	Radiation pressure	8	5	8	8	% of model
	Eclipse transition timing	100	100	100	100	% of model

Table 12.16 List of error magnitudes in the input values for the density and wind derivation algorithm.

    - Optical properties of satellite panels
    - Eclipse transitions
    - Albedo and infrared radiation distribution over the Earth
- Aerodynamic interaction
    - Energy accommodation coefficient
    - Atmospheric temperature
    - Atmospheric composition

Note that the accelerometer and relative velocity inputs are vector quantities. They contain components in each of the three satellite body-fixed directions. Not all these error sources will contribute significantly to the density and wind error. For example, the algorithm uses only the X- and Y-components of the accelerometer measurements and disregards the Z (radial) direction of this measurement. The noise and calibration in that direction is therefore not of importance. In addition, the modelled radiation pressure accelerations in the Z-direction has no influence either. The relative velocity in the Z-direction is an exception though, since it changes the aerodynamic interaction with the satellite shape, resulting in different forces for the other two directions as well. Therefore, an error in this input parameter, due to an unmodelled vertical wind, for example, can result in an error in the recovery of density and cross-track wind.

Table 12.16 lists the error sources and their magnitudes that were used for this part of the study. Most of the errors are assumed to be the same for all satellites, except for the noise levels, and the satellite model and optical properties. These latter items are assumed to be more accurately known for GRACE, with its relatively simple geometry, compared to CHAMP and Swarm.

There are various considerations that should be kept in mind when interpreting the results in the rest of this chapter. First of all, the accelerometer noise levels quoted here were taken from the instrument specifications (Chapter 3 can be consulted for CHAMP and GRACE, and information from [*Bock*, personal communication, 2008] was used for Swarm). The use of normal-points (time-averaged

measurements), which can result in a reduced noise level in exchange for limiting the temporal resolution, has not been taken into consideration here.

Most of the other values for the error sources are based on rather crude guesswork, based on the experience gained during the course of the project. Most of these items are compound values, which are far-removed from actual measurement errors. They are based instead on complex calculations and models. Unfortunately, the empirical models used, such as those for the temperature, composition and radiation pressure, do not provide statistical uncertainties as outputs.

Another caveat that should be added here is that some of the error sources are tightly linked in reality, but are considered as independent error sources in equation 12.5. One example is the accelerometer calibration, where the biases and scale factors are highly correlated when estimated from the GPS tracking. A similar issue is the link between the aerodynamic model, wind model and Y-axis accelerometer calibration. With the R03 calibration parameters, the Y-axis bias and scale factor are determined by comparing the accelerometer signal with the force models, in which the accommodation coefficient of the aerodynamic model is an important parameter. An error in this parameter will lead to an error in the Y-axis calibration. However, both these errors have a large constant component, which will tend to cancel each other. Considering these as independent error sources could therefore result in an overly pessimistic total error. In a future version of the analysis, perhaps the Y-axis calibration should be considered an additional output of the algorithm, instead of an independent input. This could add considerable complexity and computation time to the algorithm, and has therefore not been implemented yet.

12.3.4 Density error results

The statistics of the density errors, split out over the various error contributions are summarized in Table 12.17. The entire data set, from July 1997 until the end of 2002, was used for generating these statistics. The minimum, maximum and mean columns are especially interesting for this evaluation. In the minimum column, it can be seen that there is no single density measurement with a near zero error, because of the inherent uncertainty in the satellite geometry and gas-surface interaction. The minimum relative density errors for Swarm A and Swarm C are therefore the same, at 11.2% of the signal. The mean and maximum relative density errors are a lot higher for Swarm C than for Swarm A, however, because of the lower drag signal, which causes errors in the acceleration measurement and modelling to have a larger effect.

For the wind-derivation, the minimum errors are a lot smaller, and the maximum errors a lot larger than for the density-derivation. This indicates that there are special circumstances under which the wind determination is very accurate, and other circumstances under which it is not possible to get good results. The favourable conditions include a large drag signal (with respect to noise and calibration errors), and a favourable orbit geometry with respect to solar radiation pressure accelerations, with the Sun vector preferably in the orbital plane, so that they do not affect the Y-axis acceleration very much.

The maximum errors in both density and wind speed, and for both missions, are dominated by the eclipse transition timing error. Fortunately, this error occurs only for a small fraction of the measurements, which can be edited out.

Figure 12.15 shows the RSS of all the density error contributions, compared with the total density signal for Swarm A and Swarm C (Swarm B is omitted,

	Swarm A					Swarm C				
Error source	min	max	mean	RMS	Std.	min	max	mean	RMS	Std.
Accelerometer noise, X	0.0	9.6	0.5	0.7	0.6	0.0	29.7	2.6	3.4	2.2
Accelerometer noise, Y	0.0	7.1	0.2	0.3	0.3	0.0	21.1	0.9	1.5	1.2
Accelerometer bias, X	0.0	3.2	0.2	0.2	0.2	0.0	9.8	0.9	1.1	0.7
Accelerometer bias, Y	0.0	11.7	0.3	0.6	0.5	0.0	30.6	1.6	2.6	2.1
Accelerometer scale, X	0.0	6.4	5.2	5.2	0.2	0.0	6.3	5.2	5.2	0.2
Accelerometer scale, Y	0.0	10.0	0.4	0.5	0.4	0.0	10.0	0.4	0.5	0.4
Relative velocity bias, X	0.0	2.8	2.7	2.7	0.0	0.0	2.9	2.7	2.7	0.0
Relative velocity bias, Y	0.0	1.1	0.1	0.2	0.1	0.0	1.3	0.1	0.2	0.0
Relative velocity bias, Z	0.0	1.2	0.0	0.0	0.0	0.0	1.2	0.0	0.0	0.0
Wind model	0.0	7.1	0.9	1.2	0.8	0.0	8.0	0.6	0.9	0.6
Satellite model area/mass	8.0	8.0	8.0	8.0	0.0	8.0	8.0	8.0	8.0	0.0
Atmospheric temperature	0.1	3.5	2.8	2.9	0.3	0.0	4.0	3.0	3.0	0.3
Helium concentration	4.8	7.3	6.4	6.4	0.2	4.8	7.3	6.3	6.3	0.2
Accommodation coefficient	2.9	11.7	9.4	9.5	1.0	2.7	10.5	9.1	9.1	0.9
Radiation pressure	0.0	6.6	0.2	0.3	0.3	0.0	28.7	1.0	2.0	1.6
Eclipse transition timing	0.0	60.6	0.2	0.1	1.4	0.0	87.9	0.6	3.8	3.8
RSS of all contributions	11.2	63.0	15.5	15.5	0.9	11.2	90.4	16.2	16.5	2.9

Table 12.17 Statistics of the density error magnitudes as a percentage of the density signal, per error source, for Swarm A and Swarm C. Note that the entire simulated mission has been used and no editing has been performed, except for the removal of the data around the Swarm A orbit-raising manoeuvres.

	Swarm A					Swarm C				
Error source	min	max	mean	RMS	Std.	min	max	mean	RMS	Std.
Accelerometer noise, X	0	78	2	3	2	0	323	10	16	13
Accelerometer noise, Y	0	525	24	37	28	0	1628	114	162	115
Accelerometer bias, X	0	25	1	1	1	0	86	3	5	4
Accelerometer bias, Y	0	890	38	60	46	0	2778	193	279	201
Accelerometer scale, X	0	91	17	21	12	0	98	17	22	13
Accelerometer scale, Y	0	230	34	42	25	0	249	35	44	27
Relative velocity bias, X	0	8	1	1	1	0	7	1	1	1
Relative velocity bias, Y	0	1	0	0	0	0	1	0	0	0
Relative velocity bias, Z	0	1	0	0	0	0	1	0	0	0
Wind model	0	10	0	1	1	0	11	0	1	0
Satellite model area/mass	0	0	0	0	0	0	0	0	0	0
Atmospheric temperature	0	9	1	1	1	0	9	1	1	1
Helium concentration	0	5	0	0	0	0	4	0	0	0
Accommodation coefficient	0	201	45	57	34	0	215	46	58	35
Radiation pressure	0	321	13	25	21	0	1991	79	142	118
Eclipse transition timing	0	5966	10	93	92	0	11710	42	323	320
RSS of all contributions	1	6023	95	140	103	7	11863	300	484	380

Table 12.18 Statistics of the wind error magnitudes, per error source, for Swarm A and Swarm C. Values are in m/s. Note that the entire simulated mission was used, and no editing has been performed, except for the removal of the data around the Swarm A orbit-raising manoeuvres.

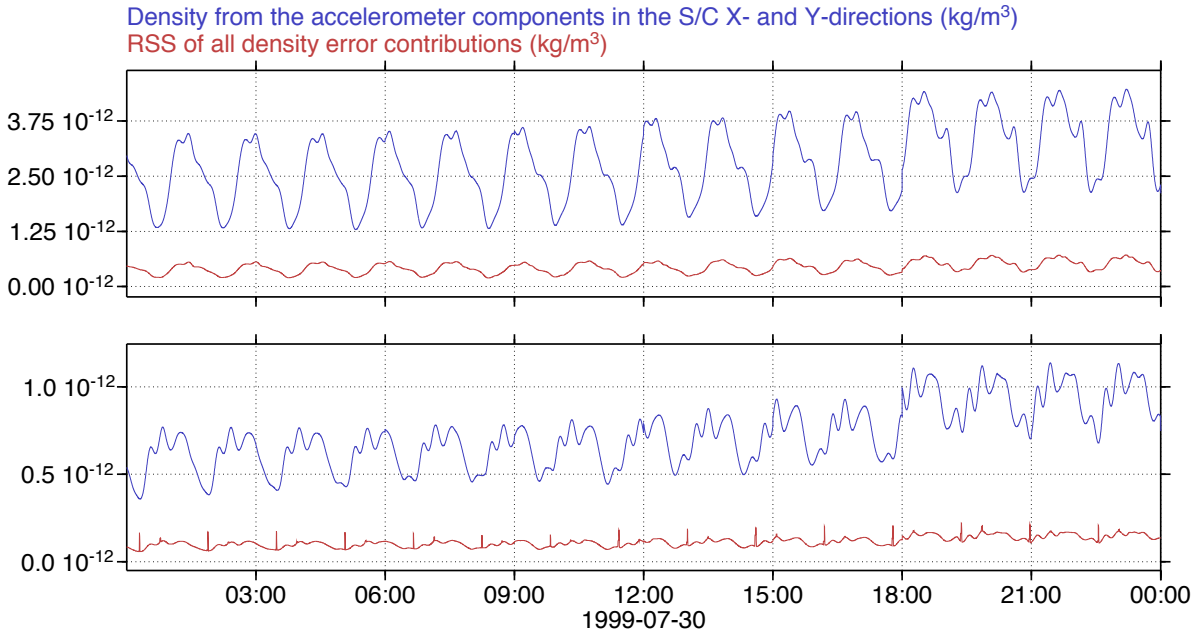

Figure 12.15 RSS of all density error contributions (red line), compared with the density signal (blue line), for Swarm A (top) and Swarm C (bottom).

because it is assumed to show similar performance to Swarm A). It is apparent that the error is at a level of about 10%-20% of the signal in both cases, even though the density at the altitude of Swarm C is about four times lower than for Swarm A.

Figure 12.16 shows the individually computed density error contributions from the accelerometer instrument sources. It is clear that the uncertainty in the scale factor of the accelerometer X-direction forms the largest contributor from that category. The other contributors are minor in comparison for both satellites, but especially for Swarm A. Swarm C has a much higher density error contribution from the accelerometer noise and bias, due to its lower signal strength.

The density error due to relative velocity error is shown in Figure 12.17. As expected, the in-track wind, predominantly in the X-direction, has by far the largest influence. The wind error is also modelled by scaling the HWM-93 output. This results in a pattern with more peaks in the density error, as the HWM-93 in-track wind varies over the orbit. The highest peaks are as large or larger than the 100 m/s in-track wind bias.

The equivalent plots for the force model contributions (Figure 12.18), shows that several factors, all of them related to the drag coefficient, form large contributions. The error due to the uncertainty in the energy accommodation coefficient is largest for Swarm A, nearly twice as large as the scale factor error. Next is the error in the satellite area/mass ratio. A possible error in the atmospheric composition (the presence of Helium, which changes the drag coefficient) is almost as large. At a slightly lower level is the error due to the uncertainty in the thermospheric temperature, which also affects the drag coefficient calculation. Because of their relation to the drag coefficient, these density errors are all scaled to the signal strength, in this case the total density.

The radiation pressure error sources hardly affects the density determination for Swarm A at this point in time. There are no eclipse transitions for the selected day for this satellite. For Swarm C though, these errors are present in the form

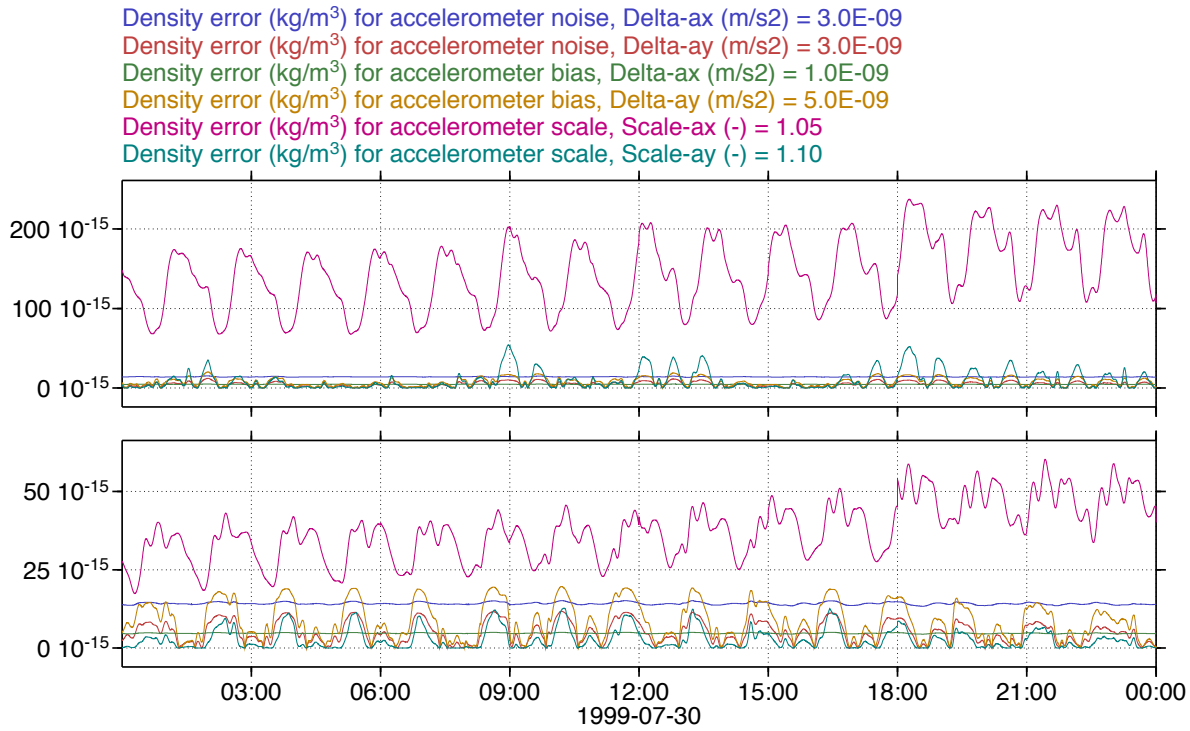

Figure 12.16 Density error due to accelerometer error sources for Swarm A (top) and Swarm C (bottom).

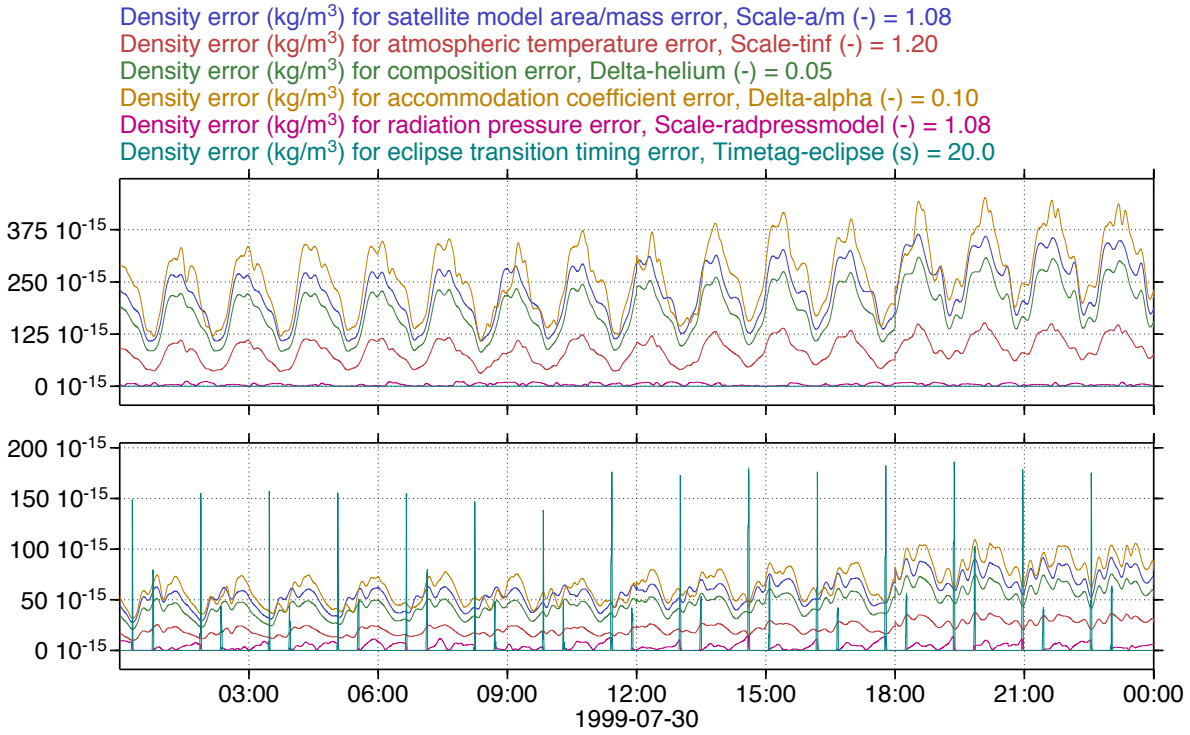

Figure 12.17 Density error due to relative velocity error sources for Swarm A (top) and Swarm C (bottom).

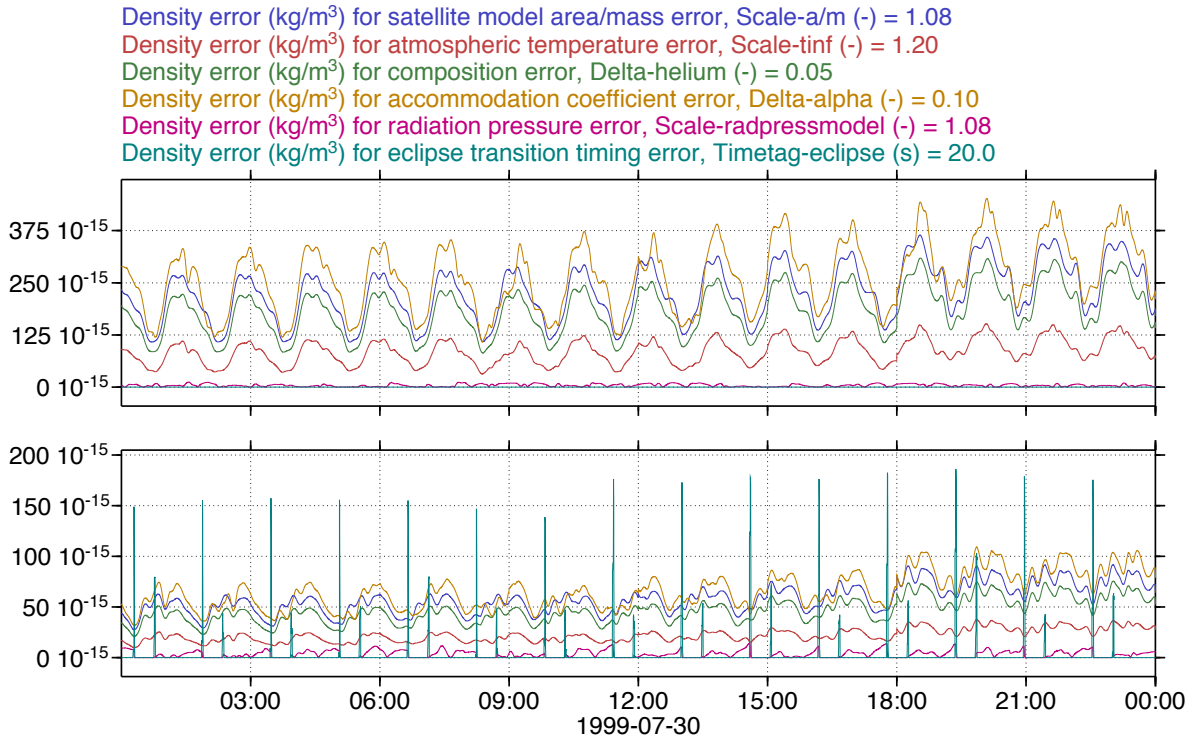

Figure 12.18 Density error due to force model error sources for Swarm A (top) and Swarm C (bottom).

of sharp spikes at the eclipse transitions, due to a possible inaccurate timing of these transitions by the model. There is also a much lower, nearly negligible, contribution for the full period when the satellite is in sunlight. The error is zero during the eclipses themselves.

The above figures showed the results for just a single day. In Figure 12.19, the long-term evolution of the total RSS density error is plotted. Each dot represents the RSS error for a single measurement, which has been sampled every 6 minutes. Since the major error contributors are related to the drag coefficient, the error for the majority of points is around a fixed percentage of the total density. The dots at higher errors are mostly at eclipse transitions, due to the eclipse timing error source.

12.3.5 Wind error results

The RSS of all the wind error contributions for both Swarm A and Swarm C are plotted in Figure 12.20. For Swarm C, the error is much larger than for Swarm A, due to the higher altitude and lower drag. During the eclipse transitions, the wind error reaches physically unpossible wind speed values of 2–3 km/s.

The statistics of the wind errors, split out over the various error contributions, and taken over the entire dataset, are summarized in Table 12.18.

Figure 12.21 shows the individual contributions of the errors due to the instrument and force models. Although many sources have significant contributions, the largest ones are the bias and scale of the accelerometer Y-component, and the radiation pressure and accommodation coefficient. Note that an error in the satellite's area to mass ratio has no influence on the wind determination, and wind errors due to uncertainties in the thermospheric temperature and composi-

Figure 12.19 Long-term evolution of the relative density error (RSS of all contributions) for Swarm A (top) and Swarm C (bottom).

tion are negligible. Errors in the in-track wind also have a very small effect on the crosswind determination.

From the discussion above, it will be clear that the altitude and the level of solar activity will play a major role in the success of wind retrieval from the Swarm satellites. This is illustrated in the long-term RSS wind error plots of Figure 12.22. The best chance at good wind retrieval results will likely be during high solar activity, and during the final months before re-entry of the lower pair, when at their low altitudes, the drag signal will become very large, and radiation pressure related errors will become negligible. Figure 12.22 shows that for Swarm C, sensible crosswind determination at the start of the mission will be very challenging, as most data points will have an uncertainty of at least a few hundred and up to a few thousand meters per second.

12.3.6 Conclusions

The major sources of error for density determination and for wind determination are quite different. For the density, the factors relating to the aerodynamic model

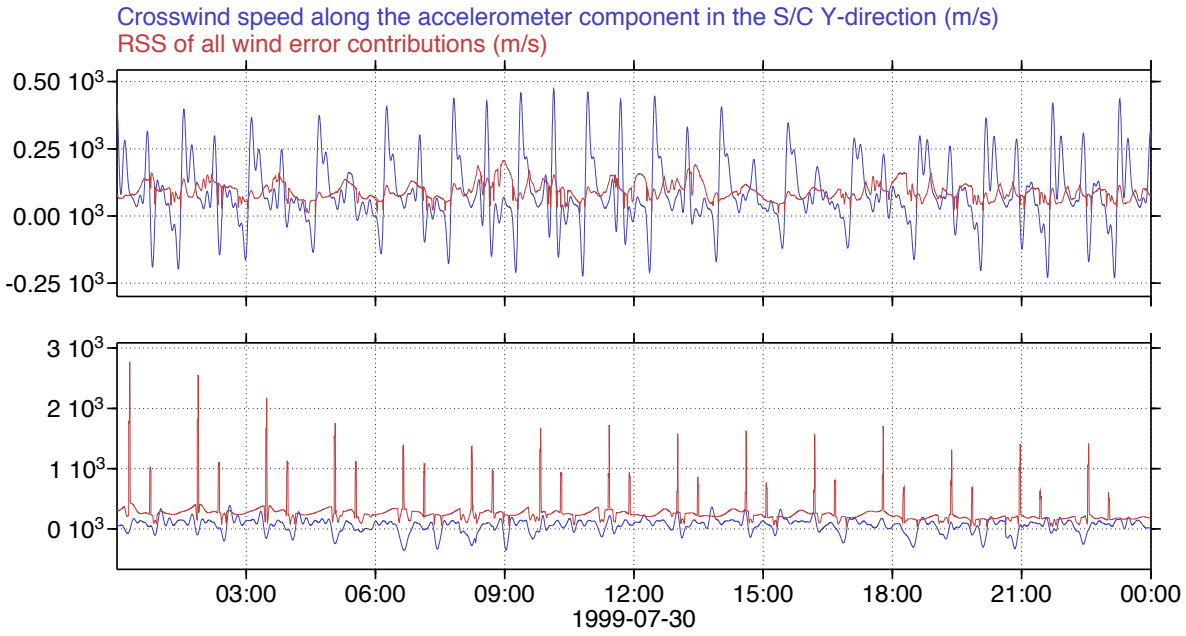

Figure 12.20 RSS of all wind error contributions (red line), compared with the wind signal (blue line), for Swarm A (top) and Swarm C (bottom).

(geometry and drag coefficient) are the most important, while for the wind, the Y-axis accelerometer calibration and solar radiation pressure are dominant. The accommodation coefficient has a large influence on both. Further research into finding the optimal accommodation coefficient values is therefore recommended.

Because of the fact that the density error is dominated by error sources that are multiplicative in nature, the resulting RSS error expressed as a percentage of the density signal is quite constant at around 15–16%. Occasional upward spikes occur for the high altitude Swarm C satellite at low solar activity, around eclipse transitions, when radiation pressure modelling errors can be exceptionally large.

It is more complicated to put a single number on the wind derivation error, because it depends on so many external factors, which continually change during the mission.

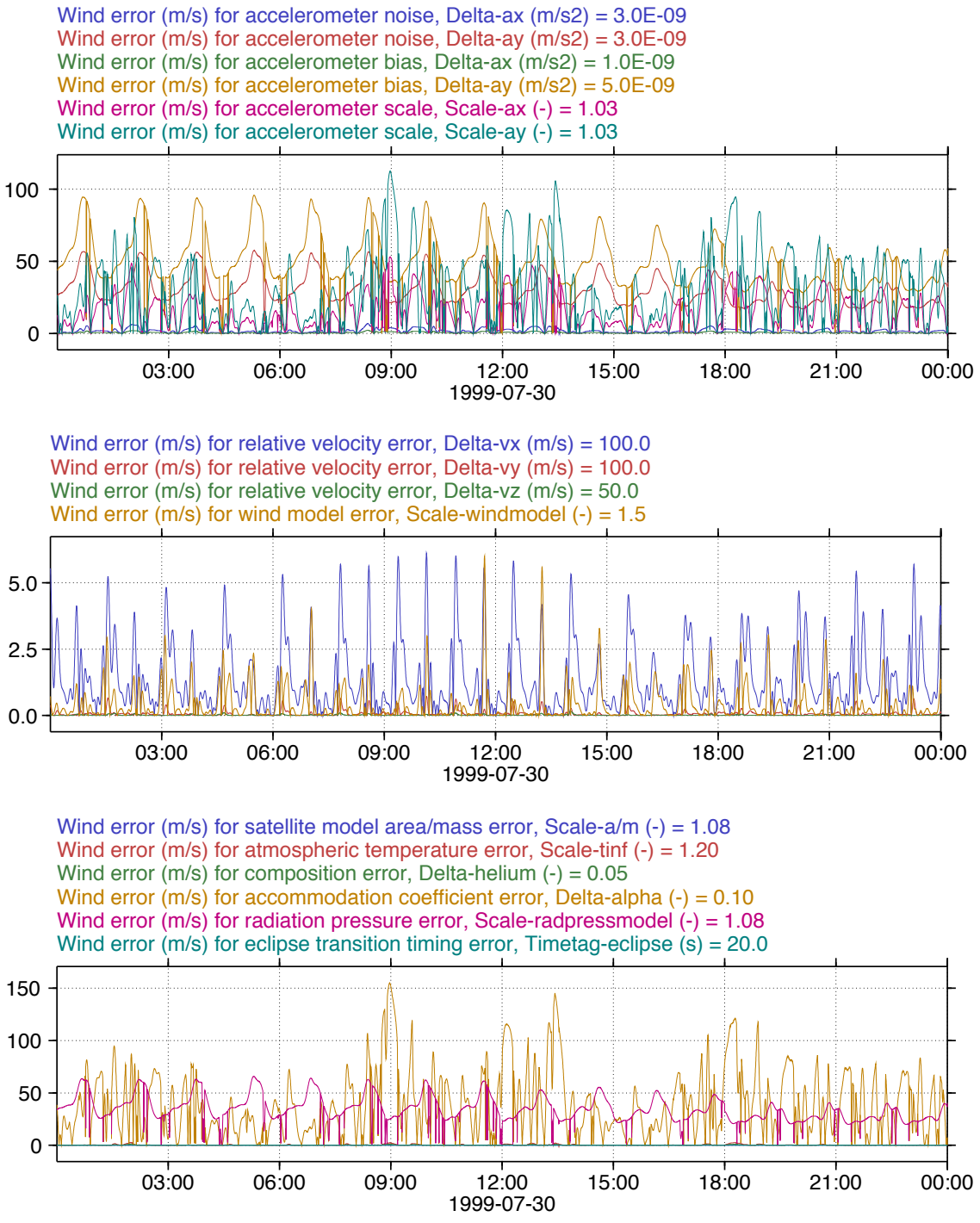

Figure 12.21 Wind errors for Swarm A due to accelerometer error sources (top), relative velocity error sources (middle) and force model error sources (bottom).

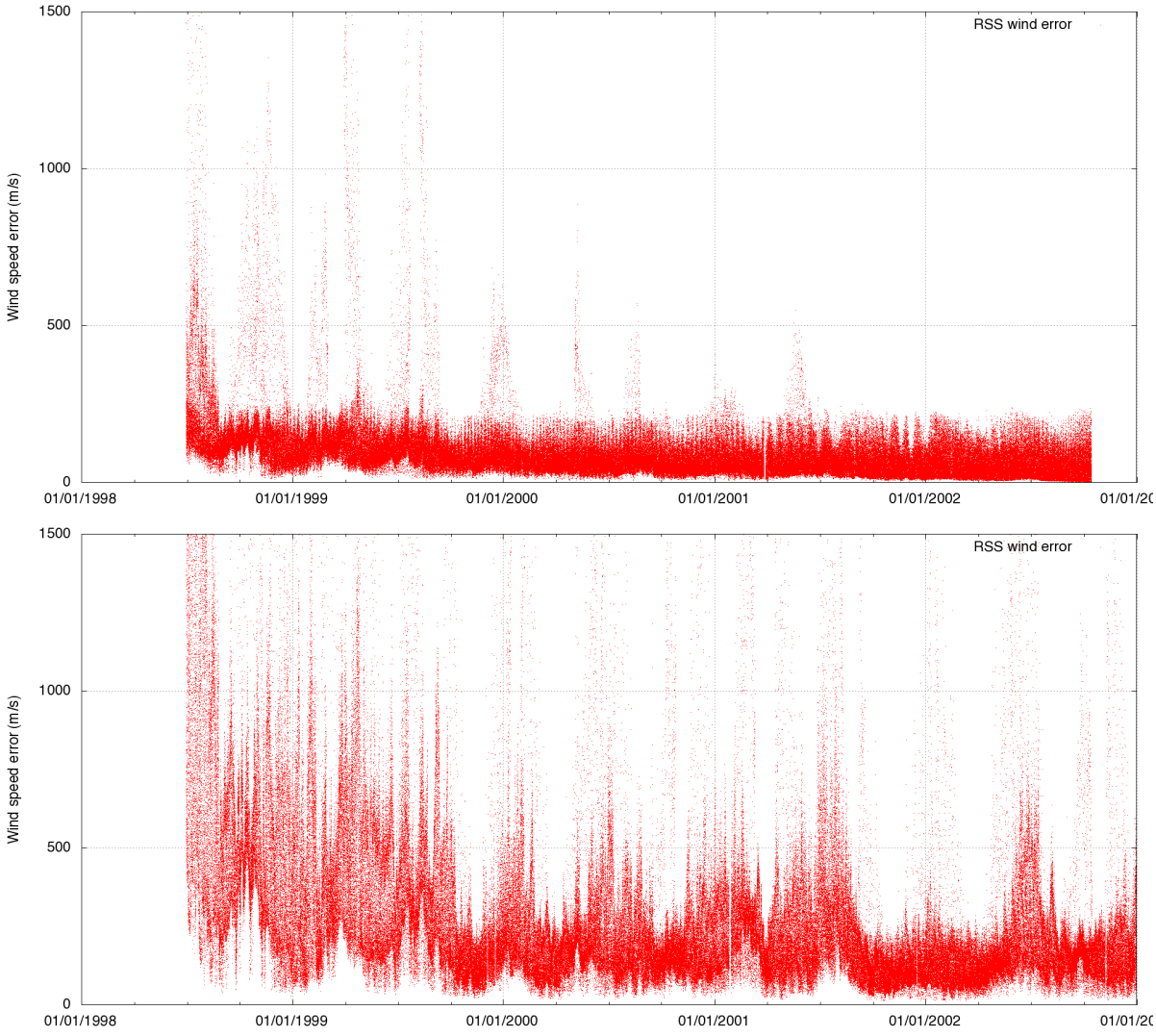

Figure 12.22 Long-term evolution of the wind error (RSS of all contributions) for Swarm A (top) and Swarm C (bottom).

Chapter 13
Other thermosphere missions

This Chapter contains an overview of other dedicated thermosphere missions, in Section 13.1 and missions with an important spin-off possibility for thermosphere research, in Section 13.2. In Section 13.3, several aspects of the Atmospheric Explorer missions, that flew in the 1970s, are reviewed. These missions carried instrumentation that could be of use for a future dedicated accelerometer-carrying thermosphere mission, as discussed in the conclusions of this Chapter, in Section 13.4

13.1 Other recent, current and future dedicated thermosphere missions

13.1.1 Starshine

The three Starshine student satellites were launched in May 1999, December 2001 and September 2001, respectively (Starshine-3 was launched before Starshine-2). These passive satellites flew in approximately circular orbits with low inclinations. The small, spherical satellites, covered with mirrors to aid optical observation from the ground, were designed to educate students about atmospheric drag on satellites. Students were involved both in the building of the satellite and in the recording of visual observations when the satellites were in orbit. The effects of drag on their orbits was later also analyzed using Two-Line Element data by *Lean et al.* [2006], using the method of *Picone et al.* [2005].

13.1.2 TIMED

The NASA TIMED satellite was launched in December 2001 into an orbit at approximately 615 km altitude. TIMED stands for Thermosphere Ionosphere Mesosphere Energetics and Dynamics, and is primarily aimed at the scientific investigation by remote sensing of the region of the atmosphere between 60 and 180 km above the surface. This is just below that of the satellite drag measurements investigated in this study. One of the instruments on TIMED is the Global Ultraviolet Imager (GUVI), which measures the far ultraviolet (FUV) glow of the thermosphere on the dayside limb. From this data, the total mass density can be inferred, which has been compared with satellite drag data by *Emmert et al.* [2006].

13.1.3 ANDE-RR

The Naval Research Lab ANDE (Atmospheric Neutral Density Experiment) and ANDE-RR (ANDE Risk Reduction) missions consists of multiple spherical microsatellites. The two satellites of the ANDE-RR mission [*Nicholas et al.*, 2007], named MAA (Mock ANDE Active) and FCal (Fence Calibration), were launched from the Space Shuttle Discovery payload bay in December 2006, and were designed to test various technologies, including a novel technique for deployment from the Shuttle, for use on the later ANDE mission itself.

The ANDE mission [*Thomas*, 2008], to be launched in 2009, will consist of an active and a passive spherical satellite, each of which will contain laser retroreflector arrays, gyroscopes and accelerometers. In addition, the active sphere will include, among others, a GPS receiver and a wind and temperature spectrometer (WATS), to compute total density and validate drag coefficient models.

13.1.4 DANDE

The DANDE satellite (Drag and Atmospheric Neutral Density Explorer), an innovative student project at the University of Colorado [*Pilinski*, 2008], is designed to measure total density, atmospheric composition and horizontal winds in the region of 100-350 km altitude. The small spherical satellite, covered with solar panels, will carry a wind and temperature spectrometer (WTS) and an array of six low-cost accelerometers, from which the deceleration due to drag will be measured as the satellite spins.

13.1.5 ADMS/TacSat-2

TacSat-2, an experimental satellite build by the Air Force Research Lab, and launched in December 2006 in an orbit at approximately 420 km altitude, carries the Atmospheric Density Mass Spectrometer (ADMS), which measures the composition and total neutral density along its flight path [*Wise*, personal communication, 2007].

13.2 Missions with a spin-off possibility for thermosphere research

13.2.1 GOCE

The GOCE satellite (Gravity field and steady-state Ocean Circulation Explorer) was launched in March 2009 [*Drinkwater et al.*, 2003, 2007]. It is the first satellite that carries a gravity gradiometer, an instrument that consists of six highly accurate accelerometers (with a noise level of 10^{-12} ms^{-2} Hz$^{-1/2}$), arranged in pairs of two along each axis. This instrument allows the accurate recovery of the static gravity field and geoid. To obtain a high sensitivity to the short wavelengths in the Earth's gravity field, the satellite flies in an unusually low circular orbit, at approximately 250–290 km altitude. To maintain this orbit under the influence of the high drag forces, the satellite uses an ion thruster, which acts in the flight direction. The mission is designed so that its orbit can be maintained for an expected duration of about 20–30 months, depending on the level of solar activity, and the chosen altitude profile.

The observable of interest for the GOCE mission objectives is the gravity gradient, which is determined by differencing the measurements of each accelerometer pair. The common mode of all accelerometers contains the signal due to the non-gravitational forces. In this case, this includes the continuous acceleration due to the ion thruster assembly.

If the GOCE data are to be used for thermospheric investigations, the accelerometer processing procedures of this report have to be supplemented with the processing of the ion thruster activation data. This additional complexity is likely to be well worth the required investigation, since GOCE could offer an unprecedented density and wind data set at very low satellite altitudes, which can be well compared with contemporaneous CHAMP and GRACE data. This region of the thermosphere is especially interesting for research involving re-entry analysis of space objects.

13.2.2 Microscope

The objective of the CNES Microscope satellite [*Touboul et al.*, 2001], scheduled to be launched in 2011, is to test the validity of the equivalence principle from Einstein's general theory of relativity. The microsatellite will carry a drag free control system, making use of two differential accelerometers, capable of measuring the non-gravitational forces to an accuracy better than 10^{-12} ms^{-2}. These forces will be compensated by electrical actuators in all three directions. It will be in an orbit at approximately 700 km altitude. Besides the data processing issues concerning the drag free control system that were discussed above for GOCE, the derivation of accurate thermospheric density data from this mission will also require a very high level of accuracy for the radiation pressure modelling, because of the low drag signal at the high altitude. If such a data processing proves successful however, the mission could provide very interesting higher-altitude density data, in a timeframe overlapping the Swarm measurements.

13.3 The Atmospheric Explorers

Chapter 6 showed the dependence of the aerodynamic models on atmospheric temperature and composition. These quantities are not measured by the current, and currently proposed accelerometer missions. Besides their usefulness for a more accurate accelerometer data processing, leading to more accurate density and wind speed results, such measurements are of great interest for the solar-terrestrial physics and thermospheric modelling community by themselves as well.

It is therefore recommended that the accelerometer instrumentation of future satellites for air density and atmospheric wind investigations, such as a possible Swarm successor mission, should be supplemented with additional instrumentation packages. The Atmospheric Explorers (AE) C to E of NASA ([*Burgess and Torr*, 1987]), flown in the 1970s, can serve as a typical reference. These satellites and their instrumentation are therefore described in somewhat more detail below.

Figure 13.1 shows the orbit and orientation of these satellites. Table 13.1 provides additional information.

One important instrument of the AE-C was the accommodation sphere, which on one side had an ideal orifice opening to the external flow and on the other side a connection to a mass spectrometer allowing partial pressure measurement.

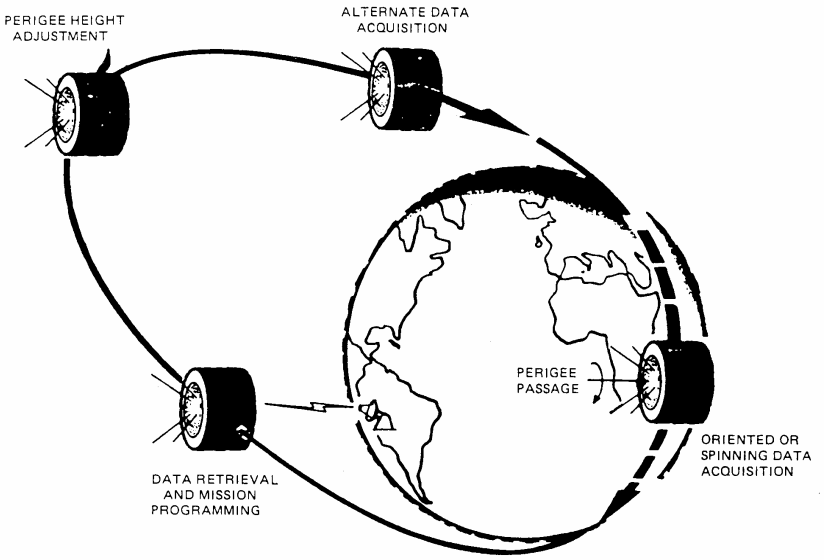

Figure 13.1 Atmosphere Explorer AE-C, with orientation during a typical orbit.

Geometry of AE-C and reference data	Dimension
Height	1.1435 m
Diameter of polyheder enclsing cylinder	1.3350 m
Reference area (projected area in X direction)	1.5242 m^2
Reference length	1.3350 m
Moment reference (X_m, Y_m, Z_m)	0.0 m, 0.0 m, 0.5715 m
Total mass	665 kg + 66.5 kg
Orbit and attitude data	
Apogee height	3000–4500 km, initial
Perigee height	130–160 km
Inclination	68°
Attitude	Flight direction normal to z-axis
Adjustable spin rate	0, or 1–10 rpm
Launch dates	
AE-C	December 13, 1973
AE-D	October 6, 1975
AE-E	November 20, 1975

Table 13.1 Reference information on the Atmospheric Explorer C, D and E missions.

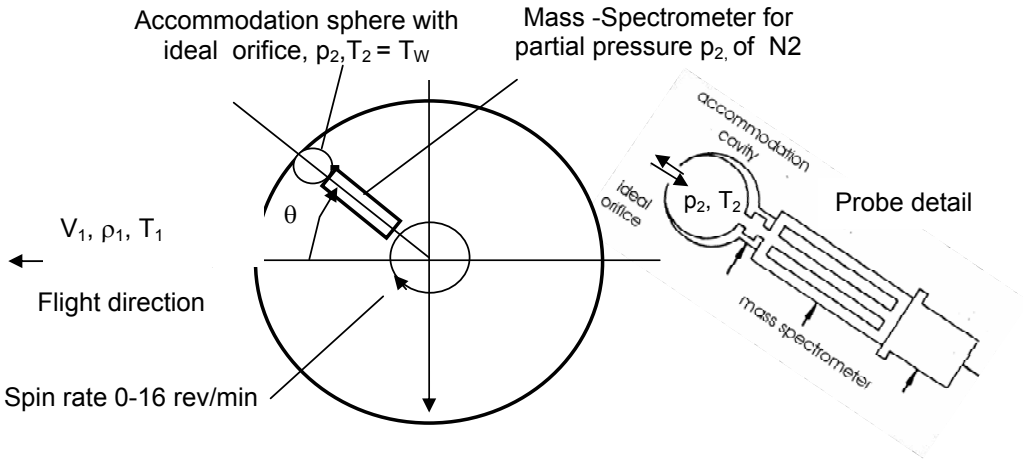

Figure 13.2 Cross section of Atmospheric Explorer C with accommodation sphere and mass spectrometer working as a rotating Patterson probe.

With this instrumentation, the AE-C could be operated like a rotating ideal Patterson probe. The original pioneering development work on free molecular probes was conducted by G.N. Patterson at the University of Toronto (e.g. [*Patterson*, 1956]), and since then this naming is used for the rotating type probe. Additional descriptions are given by *Chue* [1975] and *Koppenwallner* [1984, 1986], who used the probes during testing in ground facilities.

Figure 13.2 shows a principal sketch of AE-C with this instrumentation, including a detail of the ideal orifice with accommodation sphere and mass spectrometer.

In the Atmospheric Explorer, a sharp edged ideal orifice was realized, which guarantees transmission probabilities of $P = 1$ for the probe entering and the probe re-emitted particle fluxes. The mass spectrometer was set to measure the molecular nitrogen partial pressure p_2 at a temperature T_2, which equals the wall temperature T_w of the accommodation sphere.

The free molecular probe function

The free molecular probe function is derived with the balance condition of the incident and reemitted particle fluxes and is given by the following exact relation:

$$\frac{p_2}{p_1}\sqrt{\frac{T_1}{T_2}} = e^{-S_N^2} + \sqrt{\pi} S_N \left(1 + \mathrm{erf}(S_N)\right) \tag{13.1}$$

with

$$S_N = S_1 \cos(\theta), \quad S_1 = \frac{V_1}{\sqrt{2\frac{R}{M}T_1}} \tag{13.2}$$

in which R is the absolute gas constant and M the molecular mass on which the mass spectrometer is set. Depending on the mass spectrometer setting, one can determine the following quantities of the species i in the undisturbed atmosphere, with the rotating probe:

- Molecular speed ratio S
- Atmospheric temperature T

- Density ρ

In the following, the basic evaluation procedure is shortly explained.

Determination of species specific molecular speed ratio S and temperature T

If one selects the measurements at $\theta = 0°$ and $\theta = 90°$ and assumes $S > 5$, equation (13.1) reduces to an extremely simple relation for the molecular speed ratio S_1 of the specific gas component.

$$\frac{p_2(\theta = 0°)}{p_2(\theta = 90°)} = 2\sqrt{\pi}S_1 \tag{13.3}$$

or

$$S_1 = \frac{1}{2\sqrt{\pi}} \frac{p_2(\theta = 0°)}{p_2(\theta = 90°)} \tag{13.4}$$

As the satellite's orbital velocity V_1 is known, one can easily determine the free stream temperature T_1 of the selected gas component.

$$S_1 = \frac{V_1}{2\frac{R}{M}T_1} = (\frac{1}{2\sqrt{\pi}}) \frac{p_2(\theta = 0°)}{p_2(\theta = 90°)} \tag{13.5}$$

$$T_1 = 2\pi \frac{V_i^2}{R/M} (\frac{p_2(\theta = 0°)}{p_2(\theta = 90°)})^2 \tag{13.6}$$

Determination of species specific density

If one selects only the pressure measurement at $\theta = 0°$, the free stream density ρ_1 of a selected species can be derived by the following relation:

$$\rho_1 V_1 = \frac{1}{\sqrt{\pi}} \frac{p_2(\theta = 0°)}{\sqrt{2\frac{R}{M}T_w}} \tag{13.7}$$

13.4 Conclusions

Free molecular probes combined with neutral gas mass spectrometers offer an excellent possibility for diagnostics of the upper atmosphere. They can provide information on composition, temperature and density. Rotating probes need only one mass spectrometer as the sensing instrument and have therefore the following advantages:

- The zero offset can continuously be determined by the orifice position in the wake.
- Temperature measurements require the ratio of two measured pressure values, which requires only a linear characteristic of the sensor. It is therefore insensitive to the sensor signal slope value.

The 'rotating probe' can either be realized by a rotating spacecraft, as was done with the Atmosphere Explorers, or by a specially designed probe mounted on stabilized spacecraft, similar to CHAMP, GRACE and Swarm. In this case, also a direct measurement of the side wind is possible.

Chapter 14
Conclusions and recommendations

The main conclusion from this work is that the accelerometer instruments on CHAMP, GRACE and the future Swarm satellites provide invaluable data on the thermosphere, in the form of mass density and crosswind speeds. In this final chapter, this conclusion will be elaborated on, and recommendations will be given, both for improvements to the current and planned missions, as well as for future missions.

14.1 Conclusions on density and wind processing results

14.1.1 Density processing conclusions

The density-derivation from accelerometer data is quite straightforward, and this procedure has already been extensively used in literature. However, this study shows that the error estimates made previously in literature (e.g *Bruinsma and Biancale* [2003], *Sutton et al.* [2007]) were often still too optimistic. These previous studies often used inappropriate simplifications in the aerodynamic modelling [*Koppenwallner*, 2008], further reducing the accuracy of the results. The uncertainty in the gas-surface interaction, the imprecise knowledge of the exact spacecraft geometry and the instrument calibration uncertainty can introduce significant systematic errors, which have often been overlooked in the past. The error analysis for Swarm made for this study, which is equally applicable to CHAMP and GRACE, shows an estimate of the RSS error of the density measurement of about 15%.

Despite these systematic errors and uncertainties, the density data resulting from this study are very useful for thermospheric modelling, and will continue to be useful for a long time. The current thermospheric density models also suffer from systematic errors, due to similar errors in the calibration and processing of the underlying data, as well as an omission of geophysical phenomena, such as long-term change [*Laštovička et al.*, 2006], which have only recently been accurately measured. A statistical comparison of data and models, presented in Chapter 9, resulted in log-normal (multiplicative) mean offsets of the data/model ratios deviating up to around 30% and log-normal standard deviations between about 15% and 30% for CHAMP and between about 24% and 45% for GRACE.

These model errors are of the same or greater order of magnitude as those in the accelerometer-derived data. It will be a challenge for the next couple of years

to try and reconcile the different density data sets and models, in a physically coherent manner. The availability of more precision data in general, and especially data sets from several instruments flying at the same time, and data sets spanning longer sequences of the solar cycle, will be very helpful for meeting that challenge.

Moreover, the current and future accelerometer missions provide a level of temporal and spatial detail on density variations in the thermsophere, that are currently beyond the capabilities of global models to capture. This brings about another opportunity for research, into the fine structures of thermospheric density changes, such as the response to geomagnetic storms, gravity waves, etc.

These data and models find their usefulness in studies of the physics of the upper atmosphere, and its interaction with the ionosphere, magnetosphere and the Sun, but also in practical applications involving orbit determination and prediction, such as re-entry and debris avoidance operations of spacecraft, and precise orbit determination for altimeter and interferometric SAR missions [*Doornbos et al.*, 2002, 2007].

14.1.2 Crosswind processing conclusions

The wind-derivation from accelerometer data is not as straightforward as the density derivation. A new iterative wind-derivation algorithm was developed for this study, which can be independent of the orientation of the instrument's principal axes with respect to the flight direction. The validity of this algorithm was tested by making use of the CHAMP slew manoeuvres and sideways-flying periods. Previously published algorithms for wind determination from CHAMP data, which assumed the wind to be in the spacecraft body-fixed Y-direction [*Sutton et al.*, 2007] and considered only the drag, but not the lift and sideways forces [*Liu et al.*, 2006], would lead to unrealistic results under such conditions.

Unfortunately, the calibration of the cross-track axis of the accelerometer instrument could not be performed independently of a priori models. Therefore, the resulting wind speeds from CHAMP are also not completely independent of these models. The precise dependence of the wind results on these models remains to be fully investigated. It is also not straightforward to express the estimated accuracy of these measurements in a single number, since it is highly dependent on many external conditions. The Swarm simulations, presented in Chapter 12 led to mean and standard deviations of the wind speed error of the order of 100 m/s for Swarm A, and of the order of 300–400 m/s for Swarm C, over the course of the entire mission. This difference in the simulated performance for the lower-flying Swarm A and higher-flying Swarm C satellites is mirrored in the observed performance of the current wind data from the CHAMP and GRACE missions, respectively.

The current dataset of CHAMP-derived crosswind speeds at high to medium solar activity seems well within the statistical uncertainty of the current empirical models and shows many similarities with results from physical models. This promises very good opportunities for further research.

At low solar activity, and especially at the higher altitude of the GRACE and future Swarm C satellites, accurate crosswind determination will likely remain much more challenging. Because of the low aerodynamic acceleration signal under those conditions, errors in the calibration, the aerodynamic modelling and especially the radiation pressure modelling will have a dominant effect.

14.1.3 Outlook regarding the current and future accelerometer missions

The thermospheric research community is fortunate that the CHAMP and GRACE missions have shown such a good longevity. Nevertheless, the CHAMP satellite is currently at such a low altitude that it will likely decay and burn up in the atmosphere within a year of the start of the expected rise in EUV heating of the atmosphere, towards the next solar maximum.

The data at the lower altitudes which it will soon pass through will be especially interesting for thermospheric studies. The signal strength at those altitudes will be strong enough for a more accurate determination of crosswind. In addition, the last part of its mission will perhaps give the opportunity to study waves and tides propagating up from the lower parts of the atmosphere.

This final mission phase for CHAMP will hopefully coincide with observations by the GOCE mission. The feasibility of processing GOCE observations, under its drag-free control [*Canuto et al.*, 2002], for thermospheric density and wind purposes remains to be investigated. If successful however, there will likely be a synergy between the CHAMP and GOCE observations, that could be very useful for purposes of calibration and scientific interpretation of the observations.

The twin GRACE satellites are currently still at such a high altitude, that they might be able to survive at least a few years of the expected next solar maximum period. If the GRACE mission is kept operational, and their instruments keep functioning, they will keep providing valuable data for thermospheric density studies, in addition to their designed duty of the recovery of gravity field variations. At a certain point, the drag will become high enough so that sensible crosswind measurements can also be derived from GRACE data, as has already been demonstrated now for CHAMP.

If the GRACE mission stays operational long enough, there can also be a very valuable synergy with ESA's Swarm mission. The Swarm constellation approach will ensure the possibility to study density variations with altitude, as well as variations with local solar time. The proximity of the two lower satellites in the Swarm constellation, and the similar design of the three satellites, will also have obvious benefits for the calibration of the resulting data sets. The timing of the Swarm mission with respect to the next solar cycle is also of great interest, since no comparable data are currently available over an ascending phase of the solar cycle.

14.2 Recommendations

During the work on this project, several issues were encountered which more or less stood in the way of an optimal use of the instruments for density and crosswind determination purposes. This is no real surprise, since the main objectives of the missions do not include this goal, so these things were probably never considered as part of the design criteria. Nevertheless, these issues can contain important lessons, either for future work on the current missions, or for the design and implementation of future missions, which is why they are listed in this Section.

14.2.1 Consistency of the CHAMP and GRACE data sets

In Chapter 9 it was seen that, depending on the type of processing, the density data from both CHAMP and GRACE have significant biases with respect to mod-

els used as a reference. These biases are of course due to errors in the models (the models were based on miscalibrated historical density data, did not model long-term change, etc.) and errors in the CHAMP and GRACE data processing (uncertainties in the accelerometer calibration, choice of accommodation coefficient, satellite area, etc.).

In order for these datasets to be used in modelling activities, researchers currently just multiply them with a scale factor, to bring them in line with their a-priori model (see e.g. *Bowman et al.* [2008*a*]). Although this was a valid approach to quickly solve a problem at hand, this is clearly just a stop-gap solution, which prevents development of a full understanding of key issues in current thermosphere models and data. It is therefore recommended that:

> **Further investigations are made into the factors that play a role in creating the observed discrepancy between the CHAMP and GRACE density data sets.**

And, secondly:

> **Look for and identify possible changes in the processing of CHAMP and GRACE data, to make the two data sets more consistent, so that they can be used without the need for a-priori scaling when applied as input to future models.**

Such possible changes could entail, for example, improvements or adjustments in the satellite panel models, the use of composition-varying accommodation coefficients, and others.

Such an investigation is clearly applicable to Swarm as well. It will be interesting to see whether the upper and lower Swarm satellites will also show such inconsistent results. If it turns out that the inconsistency mainly has to do with the modelling of the satellite shape and size, and not so much with environmental aspects due to the difference in altitude, it is expected that it will be much reduced for Swarm.

14.2.2 Data from the GOCE satellite

As mentioned in the introduction to this report (see Chapter 1), the GOCE mission has been outside the scope of this project. The GOCE satellite, launched on March 17, 2009 (just a few weeks before the time of writing), flies its mission at altitudes of about 250–290 km. To maintain this low altitude, and observe the gradients in the gravity field, the satellite is under drag-free control. The effects of drag, as measured by the satellite's gradiometer (consisting of six accelerometers), are counter-acted by an ion-propulsion system. This complicates the application of the processing chain described in this report. In essence, the accelerometers on GOCE will record a near-zero drag acceleration, and the signal on the thermospheric density should be derived mainly from the thruster acceleration that is applied. The movement of the satellite is not controlled in the cross-track and radial directions, so the accelerometer axes in these directions should be able to provide information on the wind speed.

The very low altitude of the GOCE satellite, and the simultaenous availability of its data with that from CHAMP and GRACE, still make it a very interesting mission for use in thermospheric studies. This leads to the following recommendation:

To support the study of thermospheric density and crosswind data using the GOCE mission, by making the necessary data sets (accelerometer(s), ion thruster, star camera, GPS tracking, housekeeping) available to investigators.

14.2.3 GSI modelling and input parameters

This proposal is closely related to the previous one. The atmospheric research groups currently rely on very simple gas surface interaction models like the Schamberg model or the diffuse reflection model with variable energy accommodation coefficient. These models have been introduced more than 60 years ago. In the meantime many different, more physical models have been introduced and partially tested on their consistency. The actual success of this effort was however very limited. The scientific community working in Rarefied Gas Dynamics (RGD) has, since 1956, organized 26 biannual conferences, where GSI is regularly covered in special sessions. The 26 published RGD proceedings contain extremely valuable information on the development of GSI modelling and testing. The following two activities are therefore proposed. First:

Perform a critical review of Gas Surface Interaction modelling.

This should include a review of experimental Gas Surface Interaction:

- Molecular beam experiments with scattering diagnostics
- Ground experiments on direct energy and momentum exchange.
- Observation in orbital environment.

And secondly:

Set up a harmonized proposal for a GSI reference model to be used for air density and crosswind derivation from accelerometers. This model shall incorporate a limited set of experimental input parameters, which can only be varied within a physically realistic span.

14.2.4 Thruster activation periods in the accelerometer data

The current problem of thruster activation periods in the accelerometer data is best illustrated by separately discussing the situations for CHAMP and GRACE.

The situation for CHAMP: Removal of thruster activations

In the CHAMP Level 2 accelerometer data, attitude thruster activation periods have been removed from the data. In general, only the orbit manoeuvre thrusting activations can be found in the data (if data for the day of the manoeuvre is available). The editing of this data likely takes place in an initial processing step. The attitude thruster activations typically take only a fraction of a second. The affected measurement points can therefore easily be removed from the high-rate data. Enough valid points will then remain for the computation of the lower rate (0.1 Hz in the case of CHAMP) Level 2 data.

In principle, this editing is very much desirable for the density and crosswind determination, since accelerations due to thruster activations can otherwise be misinterpreted as density or wind variations. However, for the accelerometer calibration using GPS data, the removal of these accelerations is not desirable. The thruster activations can have a real effect on the orbital dynamics, as measured

by both the GPS receiver and the accelerometer, so removal of the thruster activation times will result in difficulties reconciling the two measurement types in the orbit processing for calibration, resulting in calibration errors. The influence of this effect has not yet been studied.

Note that even attitude thrusters, which are usually fired in equal but opposite pairs, can cause linear accelerations, on top of the desired angular accelerations, because of slight differences between the thrusters of each pair. This can not be thorughly checked with the currently available data for CHAMP, but it is clearly observed in the GRACE data (see Section 4.7.3).

However, as only recently discovered by Park (H Lühr, *personal communication*), there is perhaps some leakage of at least one of the thrusters, which can be observed as regular spikes of approximately 200 m/s in the crosswind speed, for a duration of about 40 seconds. This effect on CHAMP is currently under investigation, but clearly such effects have to be avoided for future missions.

The situation for GRACE: Data filtering/smoothing

For the GRACE Level 1B accelerometer (ACCDAT) data, the situation is different. The attitude thruster activations have not been edited. The activation times are available in a separate Level 1B product (THRDAT). This seems like a good solution, because the unedited data can then be used for the accelerometer calibration, and the user can combine the two products to edit out the thruster activations, before applying the density and crosswind derivation algorithms. In reality however, the ACCDAT data has had a smoothing filter applied, which ensures that the very short-duration thruster activation accelerations have been smeared out over tens of seconds. It is therefore necessary to edit out much more data (up to around 30% of the total) than would otherwise have been the case.

Recommendations

This leads to the following recommendations:

> **To request, for the benefit of scientific research of the thermosphere, that CHAMP and GRACE accelerometer data and/or auxiliary data are (re)processed and made available in a format that is suitable for both accelerometer calibration (with thruster activations included) and density and wind retrieval (by removing or enabling the removal of thruster activations).**

and:

> **To set up from the start a similar approach for the processing of the Swarm accelerometer data.**

A simple, and probably cost-effective way for the responsible agencies/institutes to support these recommendations is to just make available the existing high-rate, unfiltered Level 1 accelerometer data, and leave the details of the further processing to the users of this data.

There is a good chance that such a modification to the data processing of CHAMP and GRACE is beneficial to the primary mission goals of these satellites as well. A better understanding of the accelerometer data and modelling of the instrument behaviour and calibration should in principle result in improved gravity field products. In fact, the current cross-track calibration of CHAMP based on

force models is definitely more consistent with physical reality, than the calibration from the POD, and could perhaps already aid in better gravity field solutions.

14.2.5 Improved modelling of radiation pressure and eclipses

In Chapters 8 and 11, it was shown that residual radiation pressure signals are clearly visible around the eclipse transitions, both in the accelerations and in the derived crosswind data (see e.g. Figures 8.8 and 11.36). The current eclipse model is based on a spherical, not ellipsoidal Earth, and utilizes algorithms for computing atmospheric absorption and refraction that have never been validated or adjusted with real data. As a result, there are timing errors in the eclipse transition, of the order of tens of seconds to minutes, which clearly show up in the 10-second spaced data. This situation leads to the following recommendation:

> **The modelling of eclipse transitions and their effect on the radiation pressure acceleration should be further studied, with the aid of accelerometer (and possibly other) data.**

Such an investigation could start with the current literature (e.g. *Vokrouhlický et al.* [1996] and *Adhya et al.* [2004]), but should lead to clearly defined algorithms and parameters for implementation in accelerometer processing software. Such improved algorithms will also be beneficial for precise orbit determination purposes of other satellites, especially those at higher altitudes, such as navigation satellite systems, for which the eclipse transitions take a longer time and could have a larger effect on the orbit accuracy.

14.2.6 Measurements of the atmospheric state

Chapter 6 showed the dependence of the aerodynamic models on atmospheric temperature and composition. These quantities are not measured by the current, and currently proposed accelerometer missions. This leads to the following recommendation:

> **The accelerometer instrumentation of future satellites for air density and atmospheric wind investigations should be supplemented with additional instrumentation packages.**

The Atmospheric Explorers (AE) of NASA, flown in the 1970s, can serve as a typical reference.

Typical additional instruments could be:

- Free molecular probes for molecular speed ratio S determination.
- Neutral particle mass spectrometer

These probes should work as molecular air data system and thus allow:

- Direct air density determination
- Mean molecular speed ratio determination
- Mean molecular mass determination

With a neutral particle mass spectrometer, molecular composition could be determined as well. A separate instrument that could measure the wind speed could also aid in improving the accuracy of the density measurement by the accelerometer.

14.2.7 Design of the satellite exterior and attitude control

The current and planned low-orbiting accelerometer-carrying satellite missions, including CHAMP, GRACE, GOCE and Swarm, have primary mission goals that are different from the determination of density and winds. For CHAMP, GRACE and GOCE that is the determination of the gravity field, for which the non-gravitational forces are a major error source. For CHAMP and Swarm, the Earth's magnetic field is a major focus of the mission. This requires sensitive instruments that are placed on booms, away from the magnetically and electrically active parts of the satellite, which could disturb such measurements.

These primary mission goals are reflected in the design of these satellites. They are all generally long, slender objects, which are oriented so that their frontal area, exposed to the atmosphere, is minimal. In addition, they each have appendages in the form of antennae, instrument probes, solar array fins, etc.

Unfortunately, these design aspects are very much detrimental for the purpose of density and crosswind determination. The long, slender shapes decrease the drag compared to more compact shapes (providing a given volume of the spacecraft), and therefore the sensitivity to the signal of interest for the determination of density and crosswind. In addition, due to the large areas parallel to the flow, the slender shape adds to the sensitivity of the aerodynamic model to the unknown temperature, composition and accommodation coefficient.

The presence of booms, antennae and other appendages add complexity to the shape, and therefore they add uncertainty in the modelling of the aerodynamics and radiation pressure. Even though sophisticated software packages such as ANGARA can be used to represent the satellite at arbitrary detail, the work on the CHAMP and GRACE models has shown that uncertainties in area of 4-7% can easily occur. Such errors might be due only to the limited accuracy of the available drawings of complexly shaped appendages, or the limited manpower to translate such drawings into computer models. The appendages can cause shadowing of parts of the satellite by other parts, which leads to additional complexity of the computer calculations for aerodynamic and radiation pressure, and more strict requirements on the accuracy of the knowledge of the satellite attitude, in the data processing.

Finally, the limited range of the yaw-, pitch- and roll-angles for attitude control of the current and planned satellites inhibits the accurate determination of the accelerometer bias and scale factor for those accelerometer axes that are not in the flight direction. This is partly because the acceleration signal in the flight-direction is often much larger than in the other two directions, due to the effect of drag. But more importantly, due to the orbital energy-changing nature of accelerations in the flight-direction, such accelerations will be much easier to observe using the GPS tracking data.

The above considerations lead to the following recommendation:

The external satellite design and attitude control design for future accelerometer missions with density and wind investigation objectives should be performed with these objectives in mind.

This will likely result in satellites for which the external design is:

- Is of more compact shape.
- Has a larger area to mass ratio.
- Preferably does not have appendages or booms.

In addition, regarding the attitude control, the satellite:

- Is not, or is more loosely attitude-controlled, or is controlled in such a way to optimize the calibration of all accelerometer axes.

With regard to this last point, such a modified attitude control should result in having each of the accelerometer axes (in turn) be more or less aligned along the satellite flight direction, at intervals that allow the detection of changes in the calibration.

It is recollected that for CHAMP and GRACE, adequately accurate information on the spacecraft exterior geometry and surface properties were not part of the documentation available to the normal users of the satellite's data. Acknowledgements are in order for those colleagues who helped obtain this information for use within the project. With the goal to make this easier in the future, this leads to another recommendation:

> **The spacecraft exterior must be seen as an essential part of the non-gravitational acceleration measurement system. Therefore, information on the detailed geometry of the spacecraft exterior (including appendages, such as antennae, exterior instruments, star camera baffles, etc.), and the surface properties (material, reflectivity properties, etc.) should be made available as part of the standard documentation for users of data products of satellites equipped with accelerometers.**

This recommendation can easily be extended to all other satellites aimed at investigations of the thermosphere and satellite drag, or for which the modelling of radiation pressure and/or drag for precise orbit determination is of importance for the mission goals.

Bibliography

Adhya, Sima, Anthony Sibthorpe, Marek Ziebart, and Paul Cross (2004), Oblate earth eclipse state algorithm for low-earth orbiting satellites, *Journal of Spacecraft and Rockets*, *41*(1), 157–159.

Aksenov, V.P. (1977), *Theory of motion of artificial Earth satellites*, Nauka, Moscow.

Altamimi, Z., P. Sillard, and C. Boucher (2002), ITRF2000: A new release of the International Terrestrial Reference Frame for earth science applications, *J. Geophys. Res.*, *107*(B10).

Altamimi, Z., X. Colillieux, and J. Legrand et al. (2007), ITRF2005, a new release of the international terrestrial reference frame based on time series of station positions and earth orientation parameters, *J. Geophys. Res.*, *112*(B9), B09401.

Antreasian, Peter G., and George W. Rosborough (1992), Predicition of radiant energy forces on the TOPEX/POSEIDON spacecraft, *Journal of spacecraft and rockets*, *29*(1), 81–90.

Arduini, C., G. Laneve, and F.A. Herrero (1997), Local time and altitude variation of equatorial thermosphere midnight density maximum (MDM): San Marco drag balance measurements, *Geophysical Research Letters*, *24*(4), 377–380, doi:10.1029/97GL00189.

Bailey, G.J., N. Balan, and Y.Z. Su (1997), The Sheffield University plasmasphere ionosphere model – a review, *Journal of atmospheric and solar-terrestrial physics*, *59*(13), 1541–1552, doi:10.1016/S1364-6826(96)00155-1.

Baker, R.M. (1966), Radiation on a satellite in the presence of partly diffuse and partly specular reflecting body, in *Trajectories of artificial celestial bodies*, edited by Jean Kovalevsky, p. 85, Springer Verlag.

Barlier, F., C. Berger, J.L. Falin, G. Kockarts, and G. Thuillier (1978), A thermospheric model based on satellite drag data, *Annales de Geophysique*, *34*(1), 9–24.

Bartels, J., N.H. Heck, and H.F. Johnston (1939), Geomagnetic three-hour-range index measuring geomagnetic activity, *Journal of Geophysical Research*, *44*, 411.

Bauer, S. J. (1973), *Physics of Planetary Ionospheres*, Springer-Verlag, Berlin, Heidelberg, New York, ISBN: 3-540-06173-8.

Bauer, S. J., and H. Lammer (2004), *Planetary Aeronomy*, Springer-Verlag, Berlin, Heidelberg, New York, ISBN: 3-540-21472-0.

Berger, C., R. Biancale, M. Ill, and F. Barlier (1998), Improvement of the empirical thermospheric model DTM: DTM-94 – a comparative review of various temporal variations and prospects in space geodesy applications, *Journal of Geodesy*, *72*(3), 161–178.

Bettadpur, S. (2004), Recommendation for a-priori Bias & Scale Parameters for Level-1B ACC Data (Release 00), http://podaac-www.jpl.nasa.gov/, Jan. 21 2004.

Bettadpur, Srinivas (2007), Gravity recovery and climate experiment product specification document (rev 4.5 – february 20, 2007), Center for Space Research, The University of Texas at Austin.

Bevington, Philip R., and D. Keith Robinson (2003), *Data reduction and error analysis for the physical sciences, third edition*, McGraw-Hill, New York.

Bezdèk, A. (2007), Lognormal distribution of the observed and modelled neutral thermospheric densities, *Studia Geophysica et Geodaetica*, *51*(3), 461–468, doi:10.1007/s11200-007-0027-2.

Bird, G.A. (1994), *Molecular Gas Dynamics and the Direct Simulation of Gas Flows*, Oxford Engineering Science, Oxford University Press, Oxford.

Born, Max, and Emil Wolf (1999), *Principles of optics – 7th ed*, Cambridge University Press.

Bowman, B.R., and M.F. Storz (2002), Time series analysis of HASDM thermospheric temperature and density corrections, in *AIAA/AAS Astrodynamics Specialist Conference and Exhibit, 5–8 August 2002, Monterey, California*, AIAA 2002-4890.

Bowman, B.R., and W.K. Tobiska (2006), Improvements in modelling thermospheric

densities using new EUV and FUV solar indices, in *16th AAS/AIAA Space Flight Mechanics Conference, Tampa, Florida, January 22–26, 2006*, AAS 06-237.

Bowman, Bruce R., and Kenneth Moe (2005), Drag coefficient variability at 175-500 km from the orbit decay analyses of spheres, in *AAS/AIAA Astrodynamics Specialist Conference, Lake Tahoe, CA, August 7–11, 2005*, number AAS 05–257.

Bowman, Bruce R., W. Kent Tobiska, Frank A. Marcos, Cheryl Y. Huang, Chin S. Lin, and William J. Burke (2008*a*), A new empirical thermospheric density model JB2008 using new solar and geomagnetic indices, in *AIAA/AAS Astrodynamics Specialist Conference and Exhibit, 18–21 August 2008, Honolulu, Hawaii*, number AIAA 2008–6438.

Bowman, Bruce R., W. Kent Tobiska, Frank A. Marcos, and Cesar Valladares (2008*b*), The JB2006 empirical thermospheric density model, *Journal of atmospheric and solar-terrestrial physics*, *70*(5), 774–793, doi:10.1016/j.jastp.2007.10.002.

Bruinsma, S., G. Thuillier, and F. Barlier (2003), The DTM-2000 empirical thermosphere model with new data assimilation and constraints at lower boundary: accuracy and properties, *Journal of atmospheric and solar-terrestrial physics*, *65*, 1053–1070, doi:10.1016/S1364-6826(03)00137-8.

Bruinsma, S., D. Tamagnan, and R. Biancale (2004), Atmospheric densities derived from CHAMP/STAR accelerometer observations, *Planetary and Space Science*, *52*(4), 297–312, doi:10.1016/j.pss.2003.11.004.

Bruinsma, Sean, and Richard Biancale (2003), Total densities derived from accelerometer data, *Journal of Spacecraft and Rockets*, *40*(2), 230–236.

Burgess, E., and D. Torr (1987), Into the thermosphere, the Atmosphere Explorers, NASA SP 490, Washington D.C.

Cageao, R.P., and R.B. Kerr (1984), Global distribution of helium in the upper atmosphere during solar minimum, *Planetary and Space Science*, *32*(12), 1523–1529, doi:10.1016/0032-0633(84)90019-9.

Caluwaerts, Dries (2006), Atmospheric density retrieval from satellite accelerometer data and surface force modeling, Master's thesis, TU Delft.

Campbell, Wallace H. (1996), Geomagnetic storms, the Dst ring-current myth and lognormal distributions, *Journal of Atmospheric and Terrestrial Physics*, *58*(10), 1171–1187, doi:10.1016/0021-9169(95)00103-4.

Canuto, Enrico, Basilio Bona, Giuseppe Calafiore, and Marina Indri (2002), Drag free control for the european satellite GOCE, part I: modelling, in *Proceedings of the 41st IEEE conference on decision and control, Las Vegas, NV, December 2002*, number WeA03–6.

Carrou, J. P. (ed.) (1995), *Spaceflight Dynamics Part I*, Cépaduès.

Casali, S.J., and W.N. Barker (2002), Dynamic calibration atmosphere (DCA) for the high accuracy satellite drag model (HASDM), in *AIAA/AAS Astrodynamics Specialist Conference and Exhibit, 5–8 August 2002, Monterey, California*, AIAA 2002-4888.

Case, K., G.L.H. Kruizinga, and S.C. Wu (2004), GRACE Level 1B Data Product User Handbook, JPL D-22027.

Cefola, P.J., A.I. Nazarenko, R.J. Proulx, and V.S. Yurasov (2003), Atmospheric density correction using two line element sets as the observation data, in *AAS/AIAA Astrodynamics Specialists Conference, Big Sky, Montana, August 3–7, 2003*, AAS 03-626.

Chandra, S., and P. Stubbe (1970), The diurnal phase anomaly in the upper atmospheric density and temperature, *Planet. Space Sci.*, *18*, 1021–1033.

Chapman, S., and T.G. Cowling (1970), *The mathematical theory of non-uniform gases*, Cambridge Mathematical Library, Cambridge University Press.

Chue, S.H. (1975), Pressure probes for fluid measurements, *Progr. Aerospace Sciences*, *16*(2), 147–223.

Collins, F.G., and E.C. Knox (1994), Parameters of nocilla gas/surface interaction model from measured accommodation coefficients, *AIAA Journal*, *32*(4), 765–773.

Cook, G. E. (1965), Satellite drag coefficients, *Planetary and Space Science*, *13*(10), 929–946, doi:10.1016/0032-0633(65)90150-9.

Cook, S.R., J.B. Cross, and M.A. Hoffbauer (1995), Accommodation coefficients involving hypersonic gas surface interaction, in *Rarefied Gas Dynamics, Volume 2. Proceedings of the 19th International Symposium*, edited by J. Harvey and G. Lord, pp. 967–980, Oxford University Press.

Cook, Steven R., and Mark A. Hoffbauer (1997), Nocilla model parameters obtained from forces exterted on surfaces by molecular beams, *Journal of Spacecraft and Rockets*, *34*(3), 379–383.

Dickinson, R. E., E. C. Ridley, and R. G. Roble (1981), A three–dimensional general circulation model of the thermosphere, *J. Geophys. Res.*, *86*, 1499–1512.

Dickinson, R. E., E. C. Ridley, and R. G. Roble (1984), Thermospheric general circulation

with coupled dynamics and composition, *41*, 205–219.

Domingo, V., B. Fleck, and A.I. Poland (1995), The SOHO mission: An overview, *Solar Physics*, *162*(1–2), 1–37, doi:10.1007/BF00733425.

Doornbos, E., R. Scharroo, H. Klinkrad, R. Zandbergen, and B. Fritsche (2002), Improved modelling of surface forces in the orbit determination of ERS and Envisat, *Canadian Journal of Remote Sensing*, *28*(4), 535–543.

Doornbos, Eelco (2004), Calibrated, high accuracy satellite drag model - esoc contract 16643/02/d/hk(sc) final report, Faculty of Aerospace Engineering, Delft University of Technology, Delft, The Netherlands.

Doornbos, Eelco (2006), NRTDM final report - Near Real-Time Density Model (NRTDM) - ESOC contract 18576/04/D/HK(SC), Delft Institute for Earth-Oriented Space Research.

Doornbos, Eelco (2007), Thermosphere density model calibration, in *Space weather, research towards applications in Europe*, vol. 344 of *Astrophysics and Space Science Library*, edited by Jean Lilensten, Springer.

Doornbos, Eelco, Heiner Klinkrad, Remko Scharroo, and Pieter Visser (2007), Thermosphere density model calibration in the orbit determination and prediction of ERS-2 and Envisat, in *Envisat Symposium, Montreux, Switzerland, 23-27 April, 2007*, edited by H. Lacoste, ESA SP-636.

Doornbos, Eelco, Heiner Klinkrad, and Pieter Visser (2008), Use of two-line element data for thermosphere neutral density model calibration, *Advances in Space Research*, *41*(7), 1115–1122, doi:10.1016/j.asr.2006.12.025.

Doornbos, E.N., H. Klinkrad, and P.N.A.M. Visser (2005), Atmospheric density calibration using satellite drag observations, *Advances in Space Research*, *36*, 515–521, doi:10.1016/j.asr.2005.02.009.

Dow, J.M., R.E. Neilan, and Gendt G (2005), The International GPS Service (IGS): Celebrating the 10th Anniversary and Looking to the Next Decade, *Adv. Space Res.*, *36*(3), 320–326.

Drinkwater, Mark R., R. Haagmans, D. Muzi, A. Popescu, R. Floberghagen, M. Kern, and M. Fehringer (2007), The GOCE gravity mission: ESA's first core Earth Explorer, in *Proceedings of the 3rd international GOCE user workshop, 6-8 November 2006, Frascati, Italy, ESA SP-627*, pp. 1–8.

Drinkwater, M.R., R. Floberghagen, R. Haagmans, D. Muzi, and A. Popescu (2003), GOCE: ESA's first Earth Explorer core mission, in *Earth gravity field from space – from sensors to Earth sciences*, vol. 18 of *Space Sciences Series*, edited by G.B. Beutler *et al.*, pp. 419–432, Kluwer academic publishers.

Drob, D.P., J.T. Emmert, G. Crowley, J.M. Picone, G.G. Shepherd, W. Skinner, P. Hays, R.J. Niciejewski, M. Larsen, C.Y. She, J.W. Meriwether, G. Hernandez, M.J. Jarvis, D.P. Sipler, C.A. Tepley, M.S. O'Brien, J.R. Bowman, Q. Wu, Y. Murayama, S. Kawamura, I.M. Reid, and R.A. Vincent (2008), An empirical model of the earth's horizontal wind fields: HWM07, *Journal of Geophysical Research*, *113*(A12304), doi:10.1029/2008JA013668.

Emmert, J.T., J.M. Picone, J.L. Lean, and S.H. Knowles (2004), Global change in the thermosphere: Compelling evidence of a secular decrease in density, *Journal of Geophysical Research*, *109*(A2), A02301, doi:10.1029/2003JA010176.

Emmert, J.T., R.R. Meier, J.M. Picone, J.L. Lean, and A.B. Christensen (2006), Thermospheric density 2002 – 2004: TIMED/GUVI dayside limb observations and satellite drag, *Journal of Geophysical Research*, *111*(A10S16), doi:10.1029/2005JA011495.

Emmert, J.T., J.M. Picone, and R.R. Meier (2008*a*), Thermospheric global average density trends, 1967–2007, derived from orbits of 5000 near-earth objects, *Geophysical Research Letters*, *35*(L05101), doi:10.1029/2007GL032809.

Emmert, J.T., D.P. Drob, G.G. Shepherd, G. Hernandez, M.J. Jarvis, J.W. Meriwether, R.J. Niciejewski, D.P. Sipler, and C.A. Tepley (2008*b*), DWM07 global empirical model of upper thermospheric storm-induced disturbance winds, *Journal of Geophysical Research*, *113*(A11319), doi:10.1029/2008JA013541.

Escoubet, C.P., R. Schmidt, and M.L. Goldstein (1997), Cluster - science and mission overview, *Space Science Reviews*, *79*(1–2), 11–32, doi:10.1023/A:1004923124586.

Ferraz-Mello, S. (1964), Sur le probleme de la pression de radiations dans la theorie des satellites artificiels, *Comptes Rendus de l'Académie des Sciences*, *258*, 463.

Ferraz-Mello, S. (1972), Analytical study of the earth's shadowing effects on satellite orbits, *Celestial Mechanics*, *5*(1), 80–101, doi:10.1007/BF01227825.

Floyd, Linton, Jeff Newmark, John Cook, Lynn Herring, and Don McMullin (2005), Solar EUV and UV spectral irradiances and solar indices, *Journal of atmospheric and solar-terrestrial physics*, *3*(15), doi:10.1016/j.jastp.2004.07.013.

Flury, Jakob, Srinivas Bettadpur, and Byron D. Tapley (2008), Precise accelerometry onboard the GRACE gravity field satellite mission, *Advances in Space Research*, *42*(8), 1414–1423, doi:doi:10.1016/j.asr.2008.05.004.

Forbes, J.M., R. Gonzalez, F.A. Marcos, D. Revelle, and H. Parish (1996), Magnetic storm response of lower thermosphere density, *Journal of Geophysical Research*, *101*(A2), 2313–2319, doi:10.1029/95JA02721.

Förste, C., F. Flechtner, R. Schmidt, U. Meyer, R. Stubenvoll, F. Barthelmes, R. König, K.H. Neumayer, M. Rothacher, Ch. Reigber, R. Biancale, S. Bruinsma, J.-M. Lemoine, and J.C. Raimondo (2005*a*), A New High Resolution Global Gravity Field Model Derived From Combination of GRACE and CHAMP Mission and Altimetry/Gravimetry Surface Gravity Data, Poster g004_EGU05-A-04561.pdf (316 KB) presented at EGU General Assembly 2005, Vienna, Austria, 24-29, April 2005.

Förste, C., F. Flechtner, R. Schmidt, U. Meyer, R. Stubenvoll, F. Barthelmes, R. König, K.H. Neumayer, M. Rothacher, Ch. Reigber, R. Biancale, S. Bruinsma, J.-M. Lemoine, and J.C. Raimondo (2005*b*), A new high resolution global gravity field model from combination of GRACE and CHAMP mission and altimetry/gravimetry surface gravity data, Poster presented at EGU General Assembly 2005, Vienna, Austria, 24-29 April, 2005.

Förste, Ch. (2002), Format Description: The CHAMP Data Format, CH-GFZ-FD-001.

Förste, Christoph, and Sunchan Choi (2005), CHAMP accelerometer preprocessing at GeoForschungsZentrum Potsdam, in *Earth observation with CHAMP, results from three years in orbit*, pp. 169–174.

Förster, M., S. Rentz, W. Köhler, H. Liu, and S. E. Haaland (2008), IMF dependence of high-latitude thermospheric wind pattern derived from CHAMP cross-track measurements, *Annales Geophysicae*, *26*(6), 1581–1595.

Foster, J.C., J.M. Holt, R.G. Musgrove, and D.S. Evans (1986), Ionospheric convection associated with discrete levels of particle precipitation, *Geophysical Research Letters*, *13*(7), 656–659, doi:10.1029/GL013i007p00656.

Fritsche, B., M. Ivanov, A. Kashkovsky, G. Koppenwallner, A. Kudryavtsev, U. Voskoboinikov, and G. Zhukova (1998), Radiation pressure forces on complex spacecraft, final report, ESOC contract 11908/96/D/IM, HTG, Germany and ITAM, Russia.

Frommknecht, B., H. Oberndorfer, F. Flechtner, and R. Schmidt (2003), Integrated sensor analysis for GRACE – development and validation, *Advances in Geosciences*, *1*, 57–63.

Fuller-Rowell, T. J., and D. Rees (1983), Derivation of a conservation equation for a mean molecular weight for a two–constituent gas within a three–dimensional, time–dependent model of the thermosphere, *Planetary and Space Science*, *31*, 1209–1222.

Fuller-Rowell, T.J., and D.S. Evans (1987), Height-integrated Pedersen and Hall conductivity patterns inferred from the TIROS-NOAA satellite data, *Journal of Geophysical Research*, *92*(A7), 7606–7618, doi:10.1029/JA092iA07p07606.

Fuller-Rowell, T.J., and D. Rees (1980), A three-dimensional time-dependent global model of the thermosphere, *Journal of the Atmospheric Sciences*, pp. 2545–2567, doi:10.1175/1520-0469(1980)037¡2545:ATDTDG¿2.0.CO;2.

Fuller-Rowell, T.J., D. Rees, S. Quegan, R.J. Moffett, and G.J. Bailey (1987), Interactions between neutral thermospheric composition and the polar ionosphere using a coupled ionosphere–thermosphere model, *Jounral of Geophysical Research*, *92*(A7), 7744–7748, doi:10.1029/JA092iA07p07744.

Fuller-Rowell, T.J., D. Rees, S. Quegan, R.J. Moffett, and G.J. Bailey (1988), Simulation of the seasonal and universal time variations of the high-latitude thermosphere and ionosphere using a coupled three-dimensional model, *Pure and applied geophysics*, *127*(2–3), 189–217, doi:10.1007/BF00879811.

Fuller-Rowell, T.J., D. Rees, H.F. Parish, T.S. Virdi, P.J.S. Williams, and R.M. Johnson (1991), Lower thermosphere coupling study: Comparison of observations with predictions of the University College London-Sheffield Thermosphere-Ionosphere Model, *Journal of Geophysical Research*, *96*(A2), 1181–1202, doi:10.1029/90JA02315.

Fuller-Rowell, T.J., M.V. Codrescu, R.J. Moffett, and S. Quegan (1994), Response of the thermosphere and ionosphere to geomagnetic storms, *Journal of Geophysical Research*, *99*(A3), 3893–3914, doi:10.1029/93JA02015.

Fuller-Rowell, T.J., M.V. Codrescu, H. Rishbeth, R.J. Moffett, and S. Quegan (1996), On the seasonal response of the thermosphere and ionosphere to geomagnetic storms, *Journal of Geophysical Research*, doi:10.1029/95JA01614.

Garcia, R.R., D.R. Marsh, D.E. Kinnison, B.A. Boville, and F. Sassi (2007), Simulation of secular trends in the middle atmosphere, 1950–2003, *Journal of Geophysical Research*, *112*(D09301), doi:10.1029/2006JD007485.

Golub, G.H., and C.F. van Loan (1996), *Matrix Computations (3rd ed.)*, Johns Hopkins, ISBN 978-0-8018-5414-9.

Guo, Jinapen, Weixing Wan, Jeffrey M. Forbes, Eric Sutton, R. Steven Nerem, T.N. Woods,

Sean Bruinsma, and Libo Liu (2007), Effects of solar variability on thermosphere density from CHAMP accelerometer data, *Journal of Geophysical Research*, *112*(A10308), doi:10.1029/2007JA012409.

Hargreaves, J.K. (1992), *The solar-terrestrial environment: an introduction to geospace - the science of the terrestrial upper atmosphere, ionosphere and magnetosphere*, vol. 7 of *Cambridge Atmospheric and Space Science Series*, Cambridge University Press.

Harris, Isadore, and Wolfgang Priester (1962), Time-dependent structure of the upper atmosphere, *Journal of the Atmospheric Sciences*, *19*(4), 286–301.

Hays, P. B., T. L. Killeen, N. W. Spencer, L. E. Wharton, R. G. Roble, B. A. Emery, T. J. Fuller-Rowell, D. Rees, L. A. Frank, and J. D. Craven (1984), Observations of the dynamics of the polar thermosphere, *Journal of Geophysical Research*, *89*(A5), 5597–5612.

Heath, D.F., and B.M. Schlesinger (1986), Mg 280-nm doublet as a monitor of changes in solar ultraviolet irradiance, *Journal of Geophysical Research*, *91*(D8), 8672–8682.

Hedin, A.E. (1983), A revised thermospheric model based on mass spectrometer and incoherent scatter data - MSIS-83, *Journal of Geophysical Research*, *88*, 10170–10188.

Hedin, A.E. (1988), The atmospheric model in the region 90 to 2000 km, *Advances in Space Research*, *8*(5–6), (5)19–(5)25, In: COSPAR International Reference Atmosphere: 1986, Part I: Thermosphere models.

Hedin, A.E. (1991), Extension of the MSIS thermospheric model into the middle and lower atmosphere, *Journal of Geophysical Research*, *96*(A2), 1159–1172.

Hedin, A.E., C.A. Reber, G.P. Newton, N.W. Spencer, J.E. Salah, J.V. Evans, D.C. Kayser, D. Alcayde, P. Bauer, and L. Cogger (1977*a*), A global thermospheric model based on mass spectrometer and incoherent scatter data MSIS. i - N2 density and temperature, *Journal of Geophysical Research*, *82*, 2139–2147.

Hedin, A.E., C.A. Reber, G.P. Newton, N.W. Spencer, H.C. Brinton, H.G. Mayr, and W.E. Potter (1977*b*), A global thermospheric model based on mass spectrometer and incoherent scatter data MSIS. II - composition, *Journal of Geophysical Research*, *82*, 2148–2156.

Hedin, A.E., E.L. Fleming, A.H. Manson, F.J. Schmidlin, S.K. Avery, R.R. Clark, S.J. Franke, G.J. Fraser, T. Tsuda, F. Vial, and R.A. Vincent (1996), Empirical wind model for the upper, middle and lower atmosphere, *Journal of atmospheric and terrestrial physics*, *58*(13), 1421–1447, doi:10.1016/0021-9169(95)00122-0.

Hedin, Alan E. (1987), MSIS-86 thermospheric model, *Journal of Geophysical Research*, *92*(A5), 4649–4662.

Hedin, Alan E., *et al.* (1988), Empirical global model of upper thermosphere winds based on atmosphere and dynamics explorer satellite data, *Journal of Geophysical Research*, *93*, 9959–9978.

Hedin, Alan E., *et al.* (1991), Revised global model of thermosphere winds using satellite and ground-based observations, *Journal of Geophysical Research*, *96*(A5), 7657–7688.

Helleputte, T. Van, and P. Visser (2008), GPS based orbit determination using accelerometer data, *Aerospace Science and Technology*.

Hickey, M.P. (1988), The NASA Marshall engineering thermosphere model, NASA Marshall Space Flight Center, Alabama.

Hinteregger, Hans E., Katsura Fukui, and Bruce R. Gilson (1981), Observational, reference and model data on solar EUV, from measurements on AE-E, *Geophysical Research Letters*, *8*(11), 1147–1150, doi:10.1029/GL008i011p01147.

Hurlbut, F.C. (1985), Gas-surface scattering models for satellite applications, in *Thermophysical aspects of re-entry flows*, vol. 103 of *Progress in astronautics and aeronautics*, edited by J.M. Moss and C.D. Scott, pp. 97–119, Washington D.C.

Hurlbut, F.C. (1989), Particle surface interaction in the orbital context: A survey, in *Rarefied Gas Dynamics*, vol. 116 of *Progress in astronautics and aeronautics*, edited by E.P. Muntz, pp. 97–119, Washington D.C.

Hurlbut, F.C. (1994), Two contrasting modes for the description of wall/gas interaction, in *Rarefied Gas Dynamics, experimental techniques and physical systems*, vol. 158 of *Progress in astronautics and aeronautics*, pp. 494–506, AIAA.

IJssel, J. van den, and P. Visser (2007), Performance of GPS-based accelerometry: CHAMP and GRACE, *Adv. Space Res.*, *39*(10), doi:10.1016/j.asr.2006.12.027, 1597–1603.

IJssel, J. van den, and P.N.A.M. Visser (2003), SWARM End-to-end Simulator: CCN 1 - SoW ref. EOP-SM/0847/Is.:1-2, *Final report*, DEOS, September 2003.

IJssel, J. van den, and P.N.A.M. Visser (2004), Determinations of Non-Conservative Accelerations from Orbit Analysis, in *Earth Observation with CHAMP, Results from Three Years in Orbit*, edited by C. Reigber *et al.*, pp. 95–100.

Jacchia, L. G., and J. Slowey (1968), Diurnal and seasonal latitudinal variations in the upper atmosphere, *Planetary and Space Science*, *16*, 509–524, doi:10.1016/0032-0633(68)90165-7.

Jacchia, L.G. (1959), Two atmospheric effects in the orbital acceleration of artificial satellites, *Nature*, *183*(4660), 526–527.

Jacchia, L.G. (1964), Static diffusion models of the upper atmosphere with empirical temperature profiles, *Smithsonian Astrophysical Observatory Special Report*, *170*.

Jacchia, L.G. (1971*a*), New static models of the thermosphere and exosphere with empirical temperature profiles, *Smithsonian Astrophysical Observatory Special Report*, *313*.

Jacchia, L.G. (1971*b*), Revised static models of the thermosphere and exosphere with empirical temperature profiles, *Smithsonian Astrophysical Observatory Special Report*, *332*.

Jacchia, L.G. (1972), Atmospheric models in the region from 110 to 2000 km, in *CIRA 1972: COSPAR International Reference Atmosphere 1972*, pp. 227–338, Akademie-Verlag, Berlin.

Jacchia, L.G. (1977), Thermospheric temperature, density and composition: New models, *Smithsonian Astrophysical Observatory Special Report*, *375*.

Jäggi, A., U. Hugentobler, and G. Beutler (2006), Pseudo-stochastic orbit modeling techniques for low-Earth orbiters, *Journal of Geodesy*, *80*(1), 47–60.

Johannsmeier, D., and G. Koppenwallner (1990), Analytical and numerical formulation of lift and drag for satellites in free molecular flow, *HTG Report 90–3*, HTG.

Johannsmeier, D., G. Koppenwallner, D. Mehrholz, and R.D. Boetcher (1989), Determination of spacecraft parameters using radar data, summary report, esoc contract 8424/89/d/md, contract officer h. klinkrad, HTG.

Kaiser, M.L. (2005), The STEREO mission: an overview, *Advances in Space Research*, *36*(8), 1438–1488, doi:doi:10.1016/j.asr.2004.12.066.

Kang, Z., B. Tapley, S. Bettadpur, J. Ries, and P. Nagel (2006), Precise orbit determination for grace using accelerometer data, *Advances in Space Research*, *38*, 2131–2136, doi:10.1016/j.asr.2006.02.021.

Killeen, T. L., R. W. Smith, N. W. Spencer, J.W. Meriwether, D. Rees, G. Hernandez, P. B. Hays, L. L. Cogger, D. P. Sipler, M. A. Biondi, and C. A. Tepley (1986), Mean neutral circulation in the winter polar *F* region, *Journal of Geophysical Research*, *91*, 1633–1649.

King-Hele, Desmond (1992), *A tapestry of orbits*, Cambridge University Press.

Kisel, V.A. (1973), *Reflection of light*, Nauka, Moscow.

Kittel, Ch. (1971), *Introduction to solid-state physics – 4th ed.*, Wiley, New York.

Knipp, D.J., W.K. Tobiska, and B.A. Emery (2004), Direct and indirect thermospheric heating sources for solar cycles 21–23, *Solar Physics*, *224*(1–2), 495–505, doi:10.1007/s11207-005-6393-4.

Kockarts, G. (2002), Transport phenomena, *Journal de Physique IV*, *12*(10), 235–252.

Kogan, M. (1969), *Rarefied Gas Dynamics*, Plenum Press.

König, Rolf, Grzegorz Michalak, Karl Hans Neumayer, Roland Schmidt, Sheng Yuan Zhu, Heribert Meixner, and Christoph Reigber (2005), Recent developments in CHAMP orbit determination at GFZ, in *Earth observation with CHAMP, results from three years in orbit*, pp. 65–70.

Koppenwallner, G. (1982), Freimolekulare Aerodynamik für Satellitenanwendung, *DLR–FB–82–08*, DLR.

Koppenwallner, G. (1984), The free molecular pressure probe with finite length slot orifice, in *Rarefied Gas Dynamics, Proc. 14th int. symposium*, edited by H. Oguchi, University of Tokyo Press.

Koppenwallner, G. (1985), Low density aerodynamics of satellites, in *Rarefied Gas Dynamics, Vol. 1*, edited by S.S. Kutateladze and A.K. Rebrov, pp. 385–399, Plenum Press, New York.

Koppenwallner, G. (1986), The free molecular orifice pressure probe for mass spectroscopic studies, in *Rarefied Gas Dynamics, Proc. 15th int. symposium*, edited by V. Boffi and C. Cercigniani, B.G. Teubner, Stuttgart.

Koppenwallner, G. (1989), Rarefied gas dynamics, in *Hypersonics Vol. 1, defining hypersonic environment*, edited by J.J. Bertin and others, pp. 519–547, Birkhäuser, Boston, Basel, Berlin.

Koppenwallner, G. (1999), Aerodynamik von satelliten, in *Handbuch der Raumflugtechnik*, edited by W. Hallmann and W. Ley, Carl Hanser Verlag, M unchen.

Koppenwallner, G. (2008), Comment on special section: New perspectives on the satellite drag environments of earth, mars and venus, *Journal of Spacecraft and Rockets*, *45*(6), 1324–1326, doi:10.2514/1.37539.

Koppenwallner, G., and W. Wuest (1979), Concave corner flow problem, *Acta Astronautica*, *6*(9), 1227–1234.

Koppenwallner, G., M. Ivanov, D. Johannsmeier, and A. Kaskhowski (1994), Free molecular and transitional aerodynamics of spacecraft (rarefied aerodynamic modelling system for earth satellites, RAMSES, summary

report, esoc contract 10032/92/d/im, HTG, Germany and ITAM, Russia, ESOC contract 10032/92/D/IM.

Koppenwallner, G., *et al.* (1995), A rarefied aerodynamics and modelling system for earth satellites, (RAMSES), in *Rarefied Gas Dynamics, Volume 2. Proceedings of the 19th International Symposium*, edited by J. Harvey and G. Lord, pp. 1366–1372, Oxford University Press.

Kroes, R., O. Montenbruck, W. Bertiger, and P.N.A.M. Visser (2005), Spacecraft Formation Flying, Relative Positioning Using Dual-Frequency Carrier Phase, *GPS Solutions*, *9*(1), 21–31.

Lala, P. (1971), Semi-analytical theory of solar pressure perturbations of satellite orbits during short time intervals, *Bulletin of the Astronomical Institutes of Czechoslovakia*, *22*, 63.

Lala, P., and L. Sehnal (1969), The earth's shadowing effects in the short-periodic perturbations of satellite orbits, *Bulletin of the astronomical institutes of Czechoslovakia*, *20*, 328.

Landsberg, G.S. (1976), *Optics – 5th ed.*, Nauka, Moscow.

Laštovička, J., R.A. Akmaev, G. Beig, J. Bremer, and J.T. Emmert (2006), Global change in the upper atmosphere, *Science*, *314*(5803), 1253–1254, doi:10.1126/science.1135134.

Lean, J.L., J.M. Picone, J.T. Emmert, and G. Moore (2006), Thermospheric densities derived from spacecraft orbits: Application to the Starshine satellites, *Journal of Geophysical Research*, *111*(A04301), doi:10.1029/2005JA011399.

Lean, Judith (1991), Variations in the sun's radiative output, *Reviews of Geophysics*, *29*(4), 505–535.

Legge, H., K. Nambu, and S. Igarashi (1991), Force and heat transfer on a disc in rarefied flow, in *Rarefied Gas Dynamics, Volume 1. Proceedings of the 17th International Symposium, Aachen*, edited by A.E. Beylich, pp. 679–686, VCH Verlagsgesellschaft, Weinheim.

Lemoine, F., S. Luthcke, C. Cox anc B. Thompson, D. Rowlands, and D. Chinn (2003), New CHAMP gravity solutions: progress towards GEM2003S, Geophysical research Abstracts, Vol. 5, 12626, European Geophysical Society.

Lemoine, F.G., S.C. Kenyon, J.K. Factor, R.G. Trimmer, N.K. Pavlis, D.S. Chinn, C.M. Cox, S.M. Klosko, S.B. Luthcke, M.H. Torrence, Y.M. Wang, R.G. Williamson, E.C. Pavlis, R.H. Rapp, and T.R. Olson (1998), The development of the joint NASA GSFC and the national imagery mapping agency (NIMA) geopotential model EGM96, NASA GSFC, NASA/TP-1998-206861.

Lichten, Stephen M., and James S. Border (1987), Strategies for high-precision global positioning system orbit determination, *Journal of Geophysical Research*, *92*(B12), 12751–12762.

Limpert, Eckhard, Werner A. Stahel, and Markus Abbt (2001), Log-normal distributions across the sciences: Keys and clues, *BioScience*, *51*(5), 341–352.

Liu, H., H. Lühr, V. Henize, and W. Köhler (2005), Global distribution of the thermospheric total mass density derived from CHAMP, *Journal of Geophysical Research*, *110*(A04301), doi:10.1029/2004JA010741.

Liu, Huixin, Hermann Lühr, Shigeto Watanabe, Wolfgang Köhler, Vance Henize, and Pieter Visser (2006), Zonal winds in the equatorial upper thermosphere: Decomposing the solar flux, geomagnetic activity, and seasonal dependencies, *Journal of Geophysical Research*, *111*(A07307), doi:10.1029/2005JA011415.

Lühr, H., and C. Falck (2004), CHAMP attitude calibration manoeuvre, 21-29 June 2004, CH-GFZ-TN-0010.

Lühr, H., L. Grunwaldt, and Ch. Förste (2002), CHAMP Reference Systems, Transformations and Standards, CH-GFZ-RS-002.

Lühr, H., A. Aylward, C. Stolle, T. Spain, M. Förster, P. Ritter, and A. Aruhlia (Dec 2008), Ionospheric current quantification and modelling for improved magnetic and electric field analyses for Swarm, Final Report, SWIO-SST-FR(2); ESTEC Contract No. 20943/07/NL/JA.

Lühr, Hermann, and Stefan Maus (2006), Direct observation of the f region dynamo currents and the spatial structure of the eej by champ, *Geophysical Research Letters*, *33*(L42102), doi:10.1029/2006GL028374.

Marcos, F.A. (1990), Accuracy of atmospheric drag models at low satellite altitudes, *Advances in Space Research*, *10*(3), 417–422.

Marcos, F.A., M.J. Kendra, J.M. Griffin, J.N. Bass, D.R. Larson, and J.J.F. Liu (1997), Precision low earth orbit determination using atmospheric density callibration, in *Astrodynamics. Vol. 97(1)*, edited by F.R. Hoots *et al.*, pp. 501–513, AAS, San Diego, California.

Marcos, F.A., M.J. Kendra, J.M. Griffin, J.N. Bass, D.R. Larson, and J.J Liu (1998), Precision low earth orbit determination using atmospheric density callibration, *Journal of the astronautical sciences*, *46*(4), 395–409.

Marshall, J.A., S.B. Luthcke, P.G. Antreasian, and G.W. Rosborough (1992), Modeling radiation forces acting on TOPEX/Poseidon for precision orbit determination, *TM 104564*, NASA.

Mayaud, P.N. (1980), *Derivation, meaning, and use of geomagnetic indices*, geophysical monograph 22, American Geophysical Union, Washington D.C.

Mayr, H.G., I. Harris, and N.W. Spencer (1978), Some properties of upper atmosphere dynamics, *Reviews of Geophysics and Space Physics*, *16*, 539–565.

McPherron, R.L., and D.N. Baker (1993), Factors influencing the intensity of magnetospheric substorms, *Journal of Atmospheric and Terrestrial Physics*, *55*(8), 1091–1122, doi:10.1016/0021-9169(93)90040-6.

Menvielle, M., and A. Berthelier (1991), The K-derived planetary indices: Description and availability, *Reviews of Geophysics*, *29*(3), 415–432.

Menvielle, M., and A. Marchaudon (2007), Geomagnetic indices in solar-terrestrial physics and space weather, in *Space weather, research towards applications in Europe*, vol. 344 of *Astrophysics and Space Science Library*, edited by Jean Lilensten, Springer.

Menvielle, M., and J. Paris (2001), The aλ longitude sector geomagnetic indices, *Contributions to geophysics and geodesy*, *31*(1).

Millward, G.H., H. Rishbeth, T.J. Fuller-Rowell, A.D. Aylward, S. Quegan, and R.J. Moffett (1996), Ionospheric f_2 layer seasonal and semiannual variations, *Journal of Geophysical Research*, *101*(A3), 5149–5156, doi:10.1029/95JA03343.

Moe, K., and B. Bowman (2005), The effects of surface composition and treatment on drag coefficient of spherical satellites, in *AAS/AIAA Astrodynamics Specialist Conference, Lake Tahoe, CA, August 7–11, 2005*, number AAS 05–258.

Moe, K., M.M. Moe, and S.D. Wallace (1998), Improved satellite drag coefficient calculations from orbital measurements of energy accomodation, *Journal of spacecraft and rockets*, *35*(3), 266–272.

Moe, K., M.M. Moe, and C.J. Rice (2004), Simultaneous analysis of multi-instrument satellite measurements of atmospheric density, *Journal of spacecraft and rockets*, *41*(5), 849–853.

Moe, Kenneth, and Mildred M. Moe (2005), Gas-surface interactions and satellite drag coefficients, *Planetary and Space Science*, *53*, 793–801, doi:10.1016/j.pss.2005.03.005.

Montenbruck, O., and E. Gill (2000), *Satellite Orbits - Models Methods Applications*, Springer, ISBN 3-540-67280-X.

Montenbruck, O., T. Van Helleputte, R. Kroes, and E. Gill (2005), Reduced dynamic orbit determination using GPS code and carrier measurements, *Aerospace Science and Technology*, (9), 261–271.

Montenbruck, Oliver, and Eberhard Gill (2000), *Satellite orbits : models, methods and applications*, Springer-Verlag.

Moré, Jorge J., Burton S. Garbow, and Kenneth E. Hillstrom (1980), User guide for MINPACK-1, Argonne National Laboratory, Argonne, Illinois, ANL-80-74.

Musanov, S.V., A.P. Nikiforov, A.I. Omelik, and A.G. Freedländer (1985), Experimental determination of momentum transfer coefficients in hypersonic free molecular flow and distribution functions of reflected molecules, in *Rarefied Gas Dynamics, Volume 1. Proceedings of the 13th International Symposium*, pp. 669–676, Plenum Press, New York.

Musen, P. (1960), The influence of the solar radiation pressure on the motion of an artificial satellite, *Journal of Geophysical Research*, *65*(5), 1391–1396.

Namgaladze, A. A., Yu. N. Korenkov, V. V. Klimenko, I. V. Karpov, F. S. Bessarab, V. A. Surotkin, T. A. Glushchenko, and N. M. Naumova (1988), Global model of the thermosphere–ionosphere–protonosphere system, *Pure Appl. Geophys.*, *127*(2/3), 219–254.

Namgaladze, A. A., Yu. N. Korenkov, V. V. Klimenko, I. V. Karpov, V. A. Surotkin, and N. M. Naumova (1991), Numerical modelling of the thermosphere–ionosphere–protonosphere system, *53*, 1113–1124.

Namgaladze, A. A., Yu. N. Korenkov, V. V. Klimenko, I. V. Karpov, F. S. Bessarab, V. M. Smertin, and V. A. Surotkin (1994), Numerical modelling of the global coupling processes in the near–earth space environment, in *Proceedings of the 1992 Symposium/5th COSPAR Colloquium*, vol. 5, edited by D. N. Baker *et al.*, pp. 807–811, Pergamon Press, Washington.

Neumayer, Karl Hans, Grzegorz Michalak, and Rolf König (2005), On calibrating the champ on-board accelerometer and attitude quaternion processing, in *Earth observation with CHAMP, results from three years in orbit*, pp. 71–76.

Nicholas, Andrew C., Ted Finne, and Mark A. Davis (2007), Atmospheric neutral density experiment risk reduction (ANDE-RR) flight hardware details, Naval Research Laboratory.

Niell, A.E. (1996), Global Mapping Functions for the Atmosphere Delay at Radio Wavelengths, *J. Geophys. Res.*, *101*(B2), 3227–3246.

Nocilla, S. (1963), The surface re-emission law in free molecular flow, in *Rarefied Gas Dynamics, Volume 1. Proceedings of the third International Symposium*, edited by J.A. Laurmann, pp. 327–346, Academic Press.

Nocilla, S. (1972), Theoretical determination of the aerodynamic forces on satellites, *Astronautica Acta*, *17*, 245–258.

Olsen, Nils, Terence J. Sabaka, and Luis R. Gaya-Pique (2007), Study of an improved comprehensive magnetic field inversion analysis for Swarm, Danish National Space Center.

Owens, J.K. (2002), NASA Marshall engineering thermosphere model - version 2.0, *NASA/TM–2002–211786*, Marshall Space Flight Center, Alabama, June 2002.

Parkinson, R.W., H.M. Jones, and I.I. Shapiro (1960), Effects of solar radiation pressure on earth satellite orbits, *Science*, *131*(3404), 920–921, March 1960, doi:10.1126/science.131.3404.920.

Pater, Imke de, and Jack J. Lissauer (2001), *Planetary sciences*, Cambridge University Press.

Patterson, G.N. (1956), Theory of the free molecule orifice type pressure probes in isentropic and non-isentropic flows, UTIAS Report No. 41.

Paxton, Larry J., Andrew B. Christensen, David C. Humm, Bernard S. Ogorzalek, C. T. Pardoe, Daniel Morrison, Michele B. Weiss, W. Crain, Patricia H. Lew, Dan J. Mabry, John O. Goldsten, Stephen A. Gary, David F. Persons, Mark J. Harold, E. Brian Alvarez, Carl J. Ercol, Douglas J. Strickland, and Ching-I. Meng (1999), Global ultraviolet imager (GUVI): measuring composition and energy inputs for the NASA Thermosphere Ionosphere Mesosphere Energetics and Dynamics (timed) mission, *Optical Spectroscopic Techniques and Instrumentation for Atmospheric and Space Research III*, *3756*(1), 265–276, doi:10.1117/12.366380.

Perosanz, R. (2003), On board evaluation of the STAR accelerometer, in *First CHAMP Mission Results for Gravity, Magnetic and Atmospheric Studies*, edited by Christoph Reigber *et al.*, pp. 11–18, Springer Verlag.

Peymirat, C., A.D. Richmond, B.A. Emery, and R.G. Roble (1998), A magnetosphere-thermosphere-ionosphere electrodynamics general circulation model, *Journal of Geophysical Research*, *103*(A8), 17467–17477.

Picone, J.M., A.E. Hedin, D.P. Drob, and A.C. Aikin (2002), NRLMSISE-00 empirical model of the atmosphere: Statistical comparisons and scientific issues, *Journal of Geophysical Research*, *107*(A12), doi:10.1029/2002JA009430.

Picone, J.M., J.T. Emmert, and J. Lean (2005), Thermospheric densities derived from spacecraft orbits - I. Accurate processing of two-line element sets, *Journal of Geophysical Research*, *110*(A03301), doi:10.1029/2004JA010585.

Pilinski, M.D. (2008), Analysis of a novel approach for determining atmospheric density from satellite drag, Master's thesis, University of Colorado, Department of Aerospace Engineering Sciences.

Press, William H., Saul A. Teukolsky, William T. Vetterling, and Brian P. Flannery (2007), *Numerical recipes - the art of scientific computing, third edition*, Cambridge University Press.

Quegan, S., G.J. Bailey, R.J. Moffett, R.A. Heelis, T.J. Fuller-Rowell, D. Rees, and R.W. Spiro (1982), A theoretical study of the distribution of ionization in the high-latitude ionosphere and the plasmasphere: first results on the mid-latitude trough and the light-ion trough, *Journal of atmospheric and terrestrial physics*, *44*(7), 619–640, doi:10.1016/0021-9169(82)90073-3.

Reber, Carl A., Charles E. Trevathan, Robert J. McNeal, and Michael R. Luther (1993), The upper atmospheric research satellite (UARS) mission, *Journal of Geophysical Research*, *98*(D6), 10,643–10,647.

Rees, M.H. (1989), *Physics and chemistry of the upper atmosphere*, Cambridge Atmospheric and Space Science Series, Cambridge University Press.

Reigber, Ch., P. Schwintzer, and H. Lühr (1999), The CHAMP geopotential mission, in *Bollettino di Geofisica Teoretica ed Applicata, Vol. 40, No. 3-4, Sep.-Dec. 1999, Proceedings of the 2nd Joint Meeting of the International Gravity and the International Geoid Commission, Trieste 7-12 Sept. 1998, ISSN 0006-6729*, edited by I. Marson and H. Sünkel, pp. 285–289.

Reigber, Ch., H. Lühr, and P. Schwintzer (2002), CHAMP mission status, *Advances in Space Research*, *30*(2), 129–134, doi:10.1016/S0273-1177(02)00276-4.

Richards, P. G., J. A. Fenelly, and D. G. Torr (1994), EUVAC: A solar EUV flux model for aeronomic calculations, *Journal of Geophysical Research*, *99*, 8981–8992.

Richmond, A. D., E. C. Ridley, and R. G. Roble (1992), A thermosphere/ionosphere general circulation model with coupled electrodynamcis, *Geophys. Res. Lett.*, *19*(6), 601–604.

Richmond, A. D., C. Lathuillère, and S. Vennerstroem (2003), Winds in the high-latitude lower thermosphere: Dependence on the interplanetary magnetic field, *Journal of Geophysical Research*, *108*(A2), doi:10.1029/2002JA009493.

Richmond, A.D., and R.G. Roble (1987), Electrodynamic effects of thermospheric winds from the NCAR thermospheric general circulation model, *Journal of Geophysical Research*, *92*(A11), 12,365–12,376, doi:10.1029/JA092iA11p12365.

Rishbeth, H. (1971*a*), The F–layer dynamo, *Planetary and Space Science*, *19*, 263–267.

Rishbeth, H. (1971*b*), Polarization fields produced by winds in the equatorial F–region, *Planetary and Space Science*, *19*, 357–369.

Roberts, Charles E. (1971), An analytical model for upper atmosphere densities based upon jacchia's 1970 models, *Celestial Mechanics*, *4*, 368–377.

Roble, R. (2000), On the feasibility of developing a global atmospheric model extending from the ground to the exosphere, *Geophysical Monograph*, *123*, 53–68.

Roble, R. G., E. C. Ridley, A. D. Richmond, and R. E. Dickinson (1988), A coupled thermosphere/ionosphere general circulation model, *Geophys. Res. Lett.*, *15*, 1325–1328.

Roble, R.G., and R.E. Dickinson (1989), How will changes in carbon dioxide and methane modify the mean structure of the mesosphere and thermosphere?, *Geophysical Research Letters*, *16*, 1441–1444.

Rottman, Gary (2005), The SORCE mission, *Solar Physics*, *230*(1–2), 7–25, doi:10.1007/s11207-005-8112-6.

Rowlands, D., J.A. Marshall, J. McCarthy, and et al. (1995), GEODYN II system description, Hughes STX Corp., Greenbelt, Md.

Rubincam, D.P. (1987), Lageos orbit decay due to infrared radiation from earth, *TM 87804*, NASA, January 1987.

Rubincam, D.P., and N. Weiss (1986), Earth albedo and the orbit of LAGEOS, *Celestial Mechanics and Dynamical Astronomy*, *38*(3), 233–296, doi:10.1007/BF01231110.

Sassi, F., R.R. Garcia, B.A. Boville, and H. Liu (2002), On temperature inversions and the mesospheric surf zone, *Journal of Geophysical Research*, *107*(D19), doi:10.1029/2001JD001525.

Sassi, F., B.A. Boville, D. Kinnison, and R.R. Garcia (2005), The effects of interactive ozone chemistry on simulations of the middle atmosphere, *Geophysical Research Letters*, *32*(L07811), doi:10.1029/2004GL022131.

Schaaf, Samuel A., and Paul L. Chambré (1961), *Flow of rarefied gases*, Princeton Aeronautical Paperbacks, Princeton University Press.

Sehnal, L. (1966), The perturbations of the orbital elements caused by the pressure of the radiation reflected from the earth, in *Trajectories of artificial celestial bodies*, edited by Jean Kovalevsky, p. 80, Springer Verlag.

Sehnal, L. (1970), Radiation pressure effects on the motion of artificial satellites, in *Dynamics of Satellites*, p. 262, Springer Verlag.

Sehnal, L. (1988), Thermospheric total density model TD, *Bulletin of the Astronomical Institutes of Czechoslovakia*, *39*(2), 120–127.

Sentman, Lee H. (1961), Free molecule flow theory and its application to the determination of aerodynamic forces, *LMSC–448514*, Lockheed Missiles Space Company.

Spencer, N. W., G. R. Carignan, H. G. Mayr, H. B. Niemann, R. F. Theis, and L. E. Wharton (1979), The midnight temperature maximum in the Earth's equatorial thermosphere, *Geophysical Research Letters*, *6*, 444–446.

Storz, M.F., B.R. Bowman, J.I. Branson, S.J. Casali, and W.K. Tobiska (2005), High accuracy satellite drag model (HASDM), *Advances in Space Research*, *36*(12), 2497–2505.

Sutton, E.K., J.M. Forbes, and R.S. Nerem (2005), Global thermospheric neutral density and wind response to the severe 2003 geomagnetic storms from CHAMP accelerometer data, *Journal of Geophysical Research*, *110*(A09S40), doi:10.1029/2004JA010985.

Sutton, Eric K. (2009), Normalized force coefficients for satellites with elongated shapes, *Journal of Spacecraft and Rockets*, *46*(1), 112–116, doi:10.2514/1.40940.

Sutton, Eric K., R. Steven Nerem, and Jeffrey M. Forbes (2007), Density and winds in the thermosphere deduced from accelerometer data, *Journal of Spacecraft and Rockets*, *44*(6), 1210–1219, doi:10.2514/1.28641.

Tapley, B., J. Ries, S. Bettadpur, D. Chambers, M. Cheng, F. Condi, B. Gunter, Z. Kang, P.Nagel, R. Pastor, T. Pekker, S.Poole, and F. Wang (2005), GGM02 - An improved Earth gravity field model from GRACE, *Journal of Geodesy*, *79*(8), 467–478.

Tapley, B.D., S. Bettadpur, M. Watkins, and C. Reigber (2004), The gravity recovery and climate experiment experiment, mission overview and early results, *Geophys. Res. Lett.*, *31*(L09607).

Thomas, L. (2008), Ande concept, in *16th international workshop on laser ranging, Poznan, Poland, October 2008*.

Thuillier, G., and S. Bruinsma (2001), The Mg II index for upper atmosphere modelling, *Annales Geophysicae*, *19*(2), 219–228.

Tobiska, W. Kent, S. Dave Bouwer, and Bruce R. Bowman (2006), The development of new solar indices for use in thermospheric density modeling, in *AIAA*, AIAA 2006-6165.

Touboul, P., B. Foulon, M. Rodrigues, and J.P. Marque (2004), In orbit nano-g measurements, lessons for future space missions, *Aerospace Science and Technology*, (8), 431–441.

Touboul, Pierre, Manuel Rodrigues, Gilles Métris, and Bernard Tatry (2001), MICROSCOPE, testing the equivalence principle in space, *Comptes Rendus de l'Académie des Sciences - Series IV - Physics*, pp. 1271–1286, doi:10.1016/S1296-2147(01)01264-1.

Troshichev, Oleg, Alexander Janzhura, and Peter Stauning (2006), Unified PCN and PCS indices: Method of calculation, physical sense, and dependence on the IMF azimuthal and northward components, *Journal of Geophysical Research*, *111*(A05208), doi:10.1029/2005JA011402.

Vallado, David A. (2001), *Fundamentals of Astrodynamics and Applications, Second Edition*, Microcosm Press, El Segundo, California.

Vashkovyak, S.N. (1973), Radiation pressure effect on the motion of artificial earth satellites, in *Monitoring of artificial Earth satellites*, p. 124.

Vashkovyak, S.N. (1976), Changes in balloon-satellite orbits induced by light radiation, *Astronomicheskii zhurnal*, *53*(5).

Vellante, M., M. Förster, U. Villante, T. Zhang, and W. Magnes (2007), Solar activity dependence of geomagnetic field line resonance frequencies at low latitudes, *Journal of Geophysical Research*, *112*(A02205), doi:10.1029/2006JA011909.

Vigue, Y., S.M. Lichten, R.J. Muellerschoen, G. Blewitt, and M.B. Heflin (1994), Improved gps solar radiation pressure modeling for precise orbit determination, *Journal of Spacecraft and Rockets*, *31*(5), 830–833.

Visser, P.N.A.M., and J. van den IJssel (2000), GPS-based precise orbit determination of the very low Earth orbiting gravity mission GOCE, *Journal of Geodesy*, *74*(7/8), 590–602.

Visser, P.N.A.M., and J. van den IJssel (2003), Verification of CHAMP accelerometer observations, *Adv. Space Res.*, *31*(8), 1905–1910.

Vokrouhlický, D., P. Farinella, and F. Mignard (1993), Solar radiation pressure perturbations for earth satellites, i. a complete theory including penumbra transitions, *Astronomy and Astrophysics*, *280*, 295–312.

Vokrouhlický, D., P. Farinella, and F. Mignard (1994), Solar radiation pressure perturbations for earth satellites, II. an approximate method to model penumbra transitions and their long-term orbital effects on LAGEOS, *Astronomy and Astrophysics*, *285*, 333–343.

Vokrouhlický, D., P. Farinella, and F. Mignard (1996), Solar radiation pressure perturbations for earth satellites, IV. effects of the earth's polar flattening on the shadow structure and the penumbra transitions, *Astronomy and Astrophysics*, *307*, 635–644.

Weimer, D.R. (2005), Predicting surface geomagnetic variations using ionospheric electrodynamic models, *Journal of Geophysical Research*, *110*(A12307), doi:10.1029/2005JA011270.

Wilkins, Matthew P., Chris A. Sabol, Paul J. Cefola, and Kyle T. Alfriend (2006), Practical challenges in implementing atmospheric density corrections to the NRLMSISE-00 model, AAS 06-170.

Wit, T. Dudok de, J. Lilensten, J. Aboudarham, P.-O. Amblard, and M. Kretzchmar (2005), Retrieving the solar EUV spectrum from a reduced set of spectral lines, *Annales Geophysicae*, *23*(9), 3055–3069.

Wyatt, S. (1963), The effect of terrestrial radiation pressure on satellite orbits, in *Dynamics of satellites*, p. 180, Springer Verlag.

Yurasov, V.S., A.I. Nazarenko, P.J. Cefola, and K.T. Alfriend (2005*a*), Application of the ARIMA model to analyze and forecast the time series of density corrections for NRLMSIS-00, in *AAS/AIAA Astrodynamics Specialist Conference, Lake Tahoe, CA, August 7–11, 2005*, AAS 05-256.

Yurasov, V.S., A.I. Nazarenko, P.J. Cefola, and K.T. Alfriend (2005*b*), Density corrections for the NRLMSIS-00 atmosphere model, in *AAS/AIAA Space Flight Mechanics Conference, Copper Mountain, Colorado, January 23–27, 2005*, AAS 05-168.

Zhang, J., I.G. Richardson, D.F. Webb, N. Gopalswamy, E. Huttunen, J.C. Kasper, N.V. Nitta, W. Poomvises, B.J. Thompson, C.-C. Wu, S. Yashiro, and A.N. Zhukov (2007), Solar and interplanetary sources of major geomagnetic storms (Dst $\leq$-100nT) during 1996–2005, *Journal of Geophysical Research*, *112*(A10102), doi:10.1029/2007JA012321.